22nd Aerospace Mechanisms Symposium

19951024 098

DEPARTMENT OF DEFENSE
PLASTICS TECHNICAL EVALUATION CENTER
ARRADCOM, DOVER, N. J.

Proceedings of a symposium held at
NASA Langley Research Center
Hampton, Virginia
May 4-6, 1988

PLASTEC

Lockheed   CALIFORNIA INSTITUTE OF TECHNOLOGY   NASA

--   ***DTIC DOES NOT HAVE THIS ITEM***
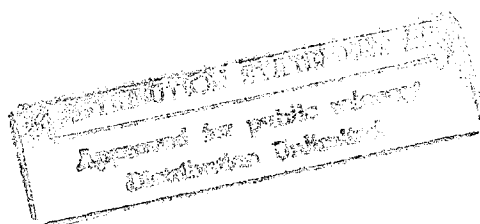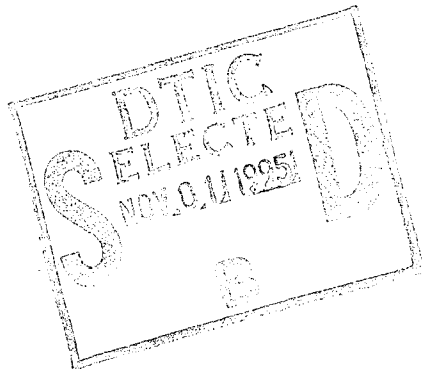
-- 1 -   AD NUMBER: D441857
-- 5 -   CORPORATE AUTHOR: NATIONAL AERONAUTICS AND SPACE ADMINISTRATION
--   HAMPTON VA LANGLEY RESEARCH CENTER
-- 6 -   UNCLASSIFIED TITLE: 22ND AEROSPACE MECHANISMS SYMPOSIUM,
--11 -   REPORT DATE: MAY   , 1988
--12 -   PAGINATION: 426P
--20 -   REPORT CLASSIFICATION: UNCLASSIFIED
--21 -   SUPPLEMENTARY NOTE: PROCEEDINGS: NASA/CALIFORNIA INSTITUTE OF
--   TECHNOLOGY, PASADENA, CA. LOCKHEED MISSILES AND SPACE CO. INC.
--   SUNNYVALE, CA. HELD AT NASA LANGLEY RESEARCH CENTER, HAMPTON, VA.,
--   4-6 MAY 1988. (SEE PL-051808 - PL 051809).
--22 -   LIMITATIONS (ALPHA):   APPROVED FOR PUBLIC RELEASE; DISTRIBUTION
--   UNLIMITED. AVAILABILITY: NATIONAL AERONAUTICS AND SPACE
--   ADMINISTRATION (NASA), WASHINGTON, D.C. 20546.
--33 -   LIMITATION CODES: 1   24

-- END   Y   FOR NEXT ACCESSION   END

Alt-Z FOR HELP3 ANSI   3 HDX 3   3 LOG CLOSED 3 PRINT OFF 3 PARITY

22nd Aerospace Mechanisms Symposium

NASA

National Aeronautics
and Space Administration

Scientific and Technical
Information Division

1988

PREFACE

The proceedings of the 22nd Aerospace Mechanisms Symposium, which was held at the NASA Langley Research Center on May 4 to 6, 1988, are reported in this NASA Conference Publication. The symposium was sponsored by the National Aeronautics and Space Administration, the California Institute of Technology, and Lockheed Missiles and Space Company, Inc.

The purpose of the symposium was to provide a forum for the interchange of information among those active in the field of mechanisms technology. To that end 28 papers were presented on aeronautics and space flight, with special emphasis on actuators, aerospace mechanism applications for ground support equipment, lubricants, latches, connectors, and other mechanisms for large space structures. The papers were prepared by authors from a broad aerospace background, including the U.S. aerospace industry, NASA, and European and Asian participants.

The efforts of the review committee, session chairmen, and speakers contributing to the technical excellence and professional character of the conference are especially appreciated.

The use of trade names or names of manufacturers in this publication does not constitute an official endorsement of such products or manufacturers, either expressed or implied, by the National Aeronautics and Space Administration.

iii

CONTENTS

SESSION V

SESSION VI

SESSION VII

15-METER DIAMETER HOOP/COLUMN ANTENNA SURFACE CONTROL ACTUATOR SYSTEM

Elvin L. Ahl, Jr., and James B. Miller*

ABSTRACT

The design, development, and implementation status of the Surface Control Actuator System (SCAS) for the Hoop/Column Antenna are described with the primary focus on the design of the mechanical elements. The SCAS is an electro-mechanical system that will automatically adjust the antenna shape by changing the length of control cords. Achieving and maintaining the proper surface shape and smoothness are critical to optimizing the electromagnetic characteristics of the antenna.

INTRODUCTION

Future space structures such as large space antennas and the Space Station will have to be assembled in orbit or deployed once they are clear of the launch system. As part of NASA's research program in Large Space Structures, Langley Research Center (LaRC) is proceeding with the development of concepts for deployment and control of these large structures.

The Hoop/Column Antenna is the focus at LaRC for research in the interaction of structures, controls, and electromagnetics for large space antennas. An antenna employing the hoop/column concept is a potential candidate for a future flight experiment. An antenna, possibly as large as 122 meters in diameter with an 85-meter column, could be stored in the STS cargo bay. It could then be deployed while in orbit with the option to be left on station or returned for further evaluation.

A 15-meter diameter Hoop/Column Antenna has been fabricated and has undergone structural and electromagnetic characterization. The antenna, shown in figures 1 and 2, consists of a telescoping column and an upper and lower cord system which suspends a 24-segment deployable hoop. A

---

*NASA Langley Research Center, Hampton, VA

reflector mesh is connected between the hoop and column and shaped by 96 surface control cords to form four parabolic mesh apertures. A non-deployable feed mast with four feeds, which are directed toward the four apertures, is attached to the top of the telescoping column.

The hoop and column are held in relative position by 48 upper cords and 24 lower cords. The upper cords radiate in a bicycle spoke fashion from 24 equally spaced stations located on the bottom side of the upper cap structure to the ends of the 24 hoop sections. The lower cords (96 surface control cords and 24 hoop cords) are divided into 24 groups with four surface control cords and one hoop/cord per group. The cords radiate upward and outward from 24 equally spaced stations, located on the top side of the lower cap structure, to the antenna surface and the ends of the 24 hoop sections. The outer edge of the mesh surface is attached to the ends of the hoop segments and the inner edge is attached to the column.

During deployment the upper cords are stored on spools located on the top side of the upper cap structure and the lower cords (hoop cords and surface cords) are stored on spools on the bottom side of the lower cap structure. As the antenna deploys, see figure 3, the cords unwind from the two sets of spools through the stations. When the antenna is fully deployed a bead located at the end of each cord is captured in a housing. The location of the beads on the cords determines the effective length of the cords, thus defining the shape of the antenna surface.

Electromagnetic characterization tests have been completed. These characterization tests have confirmed the sensitivity of antenna performance to antenna surface contour. Fine tuning the antenna performance was limited by the surface refinement capability of the present manual adjustment system, which has a practical accuracy limit of .010 inch of cord length. Additionally, the manual process requires from 4-8 hours for each surface adjustment and cannot compensate for dynamic changes in the shape of the structure. Also, the need for in-flight adjustment and the limited accessibility of the current adjustment points preclude the use of the manual adjustment system. Therefore, an automated surface control actuator system is being added to the antenna.

DESIGN CRITERIA

The Surface Control Actuator System was designed to control the antenna surface by changing the length of surface cords. The research nature of this program has influenced the specific design requirements. Therefore, the resulting design criteria for this concept may exceed flight system requirements. The following is a general list of the requirements.

2

o System must be a flight qualifiable concept.
o System must not interfere with the stowed antenna's geometry.
o System must control one parabolic mesh aperture (one quadrant) of the surface.
o System must use the existing surface control cord stowage system.
o Each surface control cord must have 1.5 inches of adjustment in length.
o Cord length control accuracy must be .002 inch.
o System must operate for cord loads ranging from 0-25 lbs.
o Antenna must be protected from over tensioning of the cables.
o Dynamic surface control capability must be 4 Hz at 1 inch peak to peak amplitude.

MECHANICAL DESIGN

The SCAS controls one parabolic mesh aperture of the antenna surface. Control of one quadrant, see figure 4, is accomplished through seven stations whose functions are to provide a mechanism to automatically adjust the length of the surface control cords. A mechanical station, see figure 5, consists of four basic subassemblies: Cylinder Block Assembly, Pulley Block Assembly, Take-up Spool Housing Assembly, and Motor Assembly Group.

The Cylinder Block Assembly, see figure 6, contains a cylinder block, piston assemblies, cylinder block springs and bushings, side plates, pulley shafts, and pulley sheaves. The purpose of the Cylinder Block Assembly is to position the piston and to direct the piston control cable below the lower cap structure to the Pulley Block Assembly. In order to achieve 1.5 inches of motion and satisfy the envelope requirements, each piston must be offset from the center line of the cylinder block. A piston assembly consists of the piston, piston control cable, piston retaining screw, and piston bushing. A bead at the end of each surface control cord is captured by the piston. The piston rides in the cylinder block on Teflon bushings which are bonded to the piston and cylinder respectively. The piston and cylinder bushings also form a cavity in the cylinder block for the cylinder block spring. The piston's axial and rotational travel is limited by the piston retainer screw which rides in a slot in the cylinder block. The piston control cable, bonded to the lower end of the piston, is a .036 inch diameter steel cable used to move the piston inside the cylinder block. The cylinder block spring preloads the piston control cable. The side plates provide attachment points for the pulley sheave axles. Slots in the side plates which match slots in the cylinder block provide view ports to observe the location of the piston.

The Pulley Block Assembly, see figure 7, consists of a pulley block, sheaves, axles, and a mounting plate. This assembly directs the piston cables to the proper take-up spools. The Pulley Block Assembly is mounted directly to the Take-up Spool Housing Assembly.

The Take-up Spool Housing Assembly, see figure 7, consists of the take-up spools, ball bearings, a motor mounting plate, and optical sensor assemblies for the surface control cords. The primary function of this assembly is to position the five take-up spools which control the piston control cables. The take-up spools operate in conjunction with the optical sensor assemblies to provide three absolute position reference points. The motor mounting plate, attached to the housing, is used to support and align the Motor Assembly Group with the take-up spools.

The Motor Assembly Group consists of four identical motor assemblies which drive the take-up spools that adjust the position of the piston. Each Motor Assembly consists of a motor plate, planetary gearhead motor, adaptor plate, incremental encoder, brake coupling, brake mount, brake, and two clamps (see figure 8). The motor plate attaches the motor to the Take-up Spool Assembly. The incremental encoder housing is attached to the motor by an adaptor plate. The encoder wheel is bonded to the adaptor shaft which is bonded to the rear motor shaft. The brake mount is attached to the adaptor plate, and the brake is secured to the mount with the clamps. A flexible coupling connects the brake output shaft to the adaptor shaft. Although a mechanical station assembly will accommodate control of the hoop cord, a motor drive assembly has not been implemented. A manual adjustment mechanism, see figure 7, has been incorporated at the station to change the hoop cord length.

The four subassemblies of a mechanical station function together to produce changes in the length of the surface control cords. A surface control cord captured by a piston is adjusted by a piston control cable which is routed through a series of pulleys to the take-up spool. As the piston control cable winds around the take-up spool the position of the piston in the cylinder block changes. The motor drives a surface control cord take-up spool in response to controller commands. An incremental encoder attached to the motor resolves the motion of the take-up spool to .001 degree. Actual control of the piston position should be .002 inch or better allowing for Controller deadband, gear bask lash, and uncertainty in the cable strain. A brake attached to the motor is used to prevent back drive when the power is removed from the motor and brake.

SYSTEM OPERATION

The SCAS control system consists of a host computer, System Interface Unit (SIU), Load Interface Unit (LIU), seven Station Controllers, and seven Mechanical Stations (see figure 9).

The host computer communicates with the system via a MIL-STD-1553B serial communication bus. The host computer provides commands to the control system and receives cord position, cord load, and status information from the system. The SIU handles communications between the

4

system and the host computer, controls access to the system, handles power distribution to the stations, performs position and load limit checks, distributes commands to the stations, and collects and formats data from the stations. The LIU conditions the signals from the load cells located at the surface end of the cords and digitizes, formats, and transmits load data to the SIU and Station Controllers.

Each Station Controller contains four cord controllers. The cord controllers use the signals from the incremental encoders and the three position absolute encoders to determine the positions of the take-up spools. The controllers correct the position command for strain in the piston control cables, operate the brakes, and provide drive signals to the motors as required to obtain the desired piston displacements.

Several safety features have been incorporated into the system to protect personnel and equipment. The cord controllers and the SIU monitor both the position and tension of each cord and compare these values to safe limit values determined by analysis. In the event that either the position or load limits are exceeded the controller and SIU are independently capable of disabling the offending cord actuator. Programmable warning limit checks are also performed by the SIU if requested by the investigator. In the event the electronic control system fails to disable the actuator, two mechanical stops have been incorporated.

STATUS

A prototype SCAS station has been built to evaluate the system sensitivity to fabrication tolerances. The system design has been updated to reflect changes made to the prototype station. The SCAS mechanical parts have been fabricated and are currently being assembled. The mechanical system is scheduled to be integrated into the antenna by early 1988. A prototype of the System Interface Unit, Load Interface Unit, and Station Controller is expected to be completed by early 1988. Total SCAS integration and checkout are expected by the middle of 1988.

CONCLUSIONS

A surface control actuator system has been designed which meets all system requirements. A prototype of the mechanical subsystem has been fabricated and used to verify the feasibility of this concept. It is anticipated that proper control on the antenna surface will lead to a better understanding of the interaction between antenna structures, control, and electromagnetics. Due to the uniqueness of this design, a patent application has been submitted.
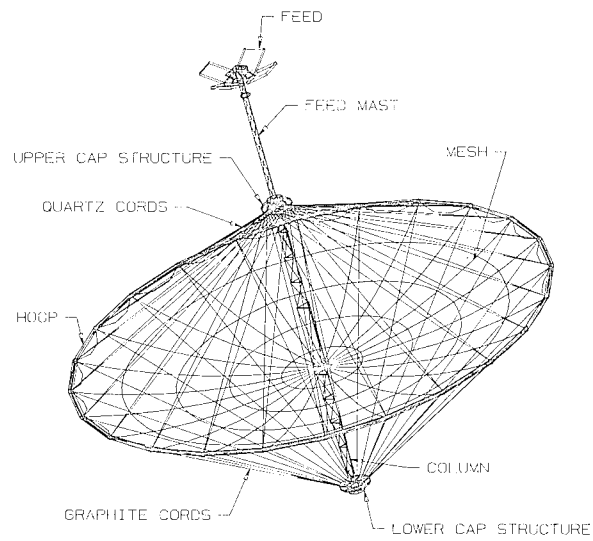
HOOP/COLUMN ANTENNA

FIGURE 1
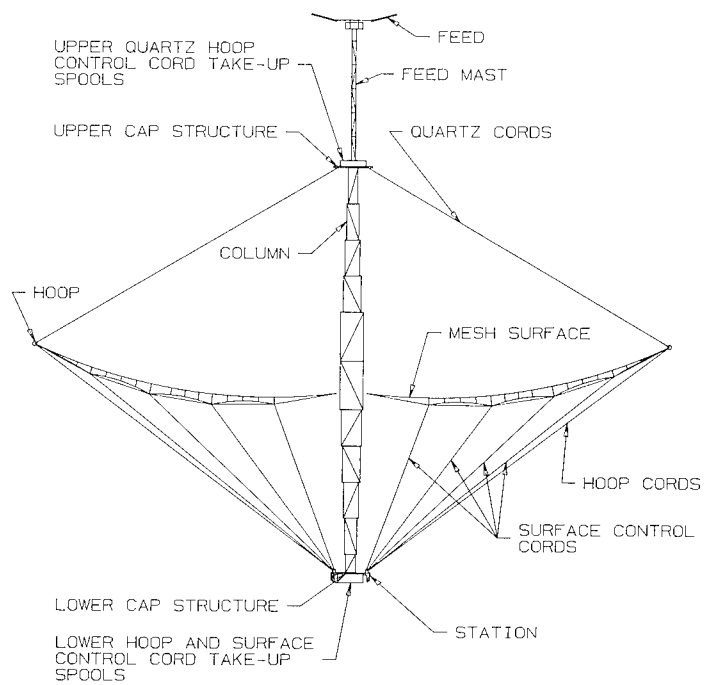
HOOP/COLUMN ANTENNA PROFILE

FIGURE 2

MESH AND MOST CORDS REMOVED FOR CLARITY

FEED MAST AND FEEDS ADDED AFTER ANTENNA DEPLOYMENT

COLUMN DEPLOYMENT
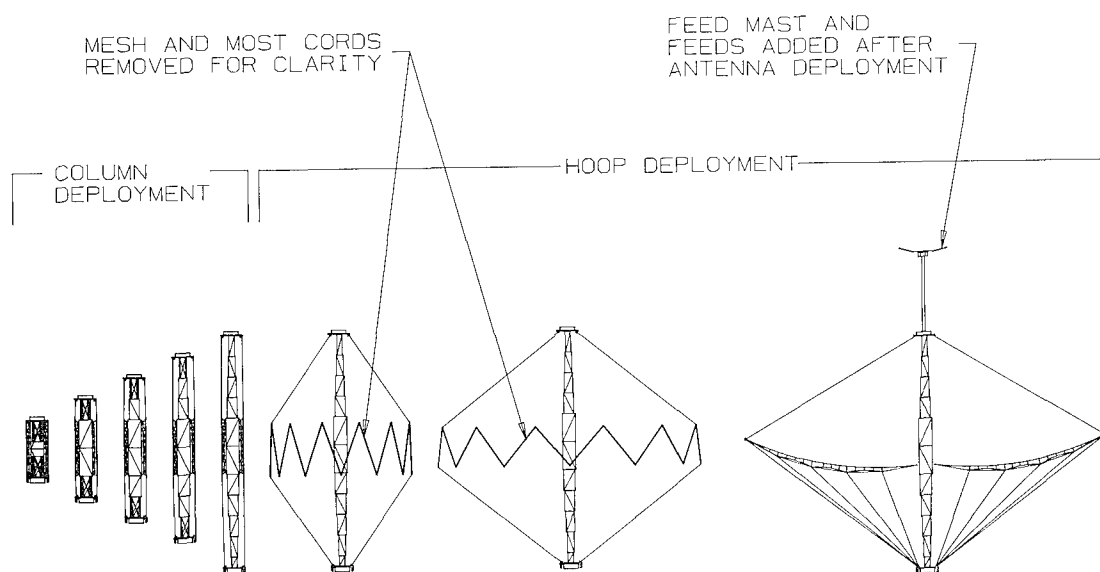
HOOP DEPLOYMENT

DEPLOYMENT SEQUENCE

FIGURE 3

SURFACE QUADRANT TO BE CONTROLLED (OTHER 3 QUADRANTS REMOVED FOR CLARITY)

28 SURFACE CONTROL CORDS
7 HOOP CORDS

SCAS STATION LOCATIONS
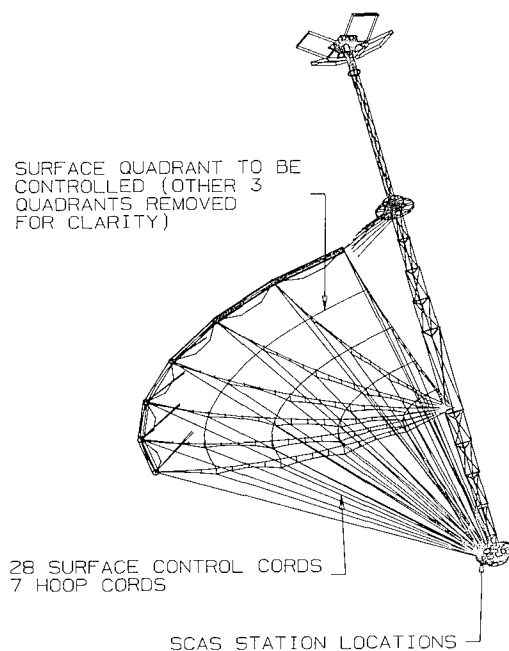
SINGLE QUADRANT WITH CORDS

FIGURE 4

7

SURFACE CONTROL CABLE

G01
G02
G03
G04
HOOP

CYLINDER BLOCK ASSEMBLY

LOWER CAP STRUCTURE

SURFACE CONTROL CORD TAKE-UP SPOOL

TAKE-UP SPOOL HOUSING ASSEMBLY

MOTOR ASSEMBLY

PULLEY BLOCK ASSEMBLY
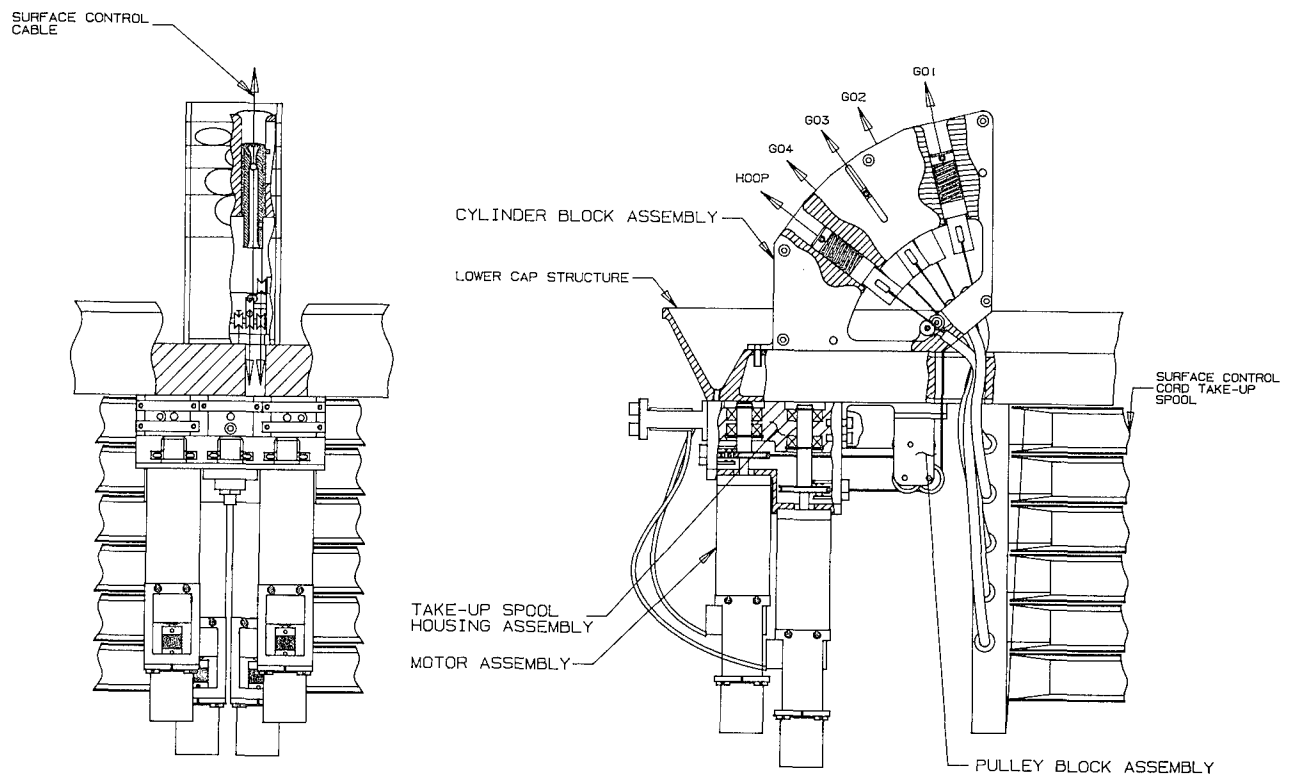
MECHANICAL STATION

FIGURE 5

8

PISTON RETAINING
SCREW

SURFACE CONTROL
CORD BEAD

CYLINDER BLOCK
SPRING

SURFACE CONTROL
CABLE

SIDE PLATES

CYLINDER BLOCK
BUSHING

PISTON CONTROL
CABLE

PULLEY SHEAVES

AXLE

GO1
GO2
GO3
GO4
HOOP

CYLINDER BLOCK

PISTON BUSHING

CYLINDER BLOCK
SPRING

PISTON

CYLINDER BLOCK ASSEMBLY

LOWER CAP STRUCTURE

TEFLON GUIDE TUBE

PISTON CONTROL
CABLE

CYLINDER BLOCK ASSEMBLY

FIGURE 6

9

OPTICAL EMITTER BOARD

OPTICAL SENSOR BOARD

LOWER CAP STRUCTURE

BEARING

MOUNTING PLATE

PULLEY BLOCK ASSEMBLY

TAKE-UP SPOOL

CONTROLLER INTERFACE

SURFACE CONTROL CORD TAKE-UP SPOOL

ABSOLUTE ENCODER BRACKET

HOOP CORD MANUAL ADJUSTMENT MECHANISM

TAKE-UP SPOOL HOUSING ASSEMBLY

AXLE

SHEAVES

MOTOR ASSEMBLY

TAKE-UP SPOOL HOUSING ASSEMBLY
AND PULLEY BLOCK ASSEMBLY

FIGURE 7

INCREMENTAL ENCODER ─┐   ┌─ ADAPTER PLATE   ┌─ MOTOR PLATE

BRAKE ─┐

CLAMPS ─┘

┌─ FLEXIBLE COUPING

└─ ADAPTER SHAFT

─ PLANETARY GEARHEAD MOTOR

MOTOR ASSEMBLY

FIGURE 8

MIL-STD-1553B
SERIAL BUS

CONTROLLER STATION 1	MECHANICAL STATION 1
CONTROLLER STATION 2	MECHANICAL STATION 2

HOST COMPUTER

SYSTEM INTERFACE UNIT (SIU)

LOAD CELL INTERFACE UNIT (LIU)

CONTROLLER STATION 7

MECHANICAL STATION 7
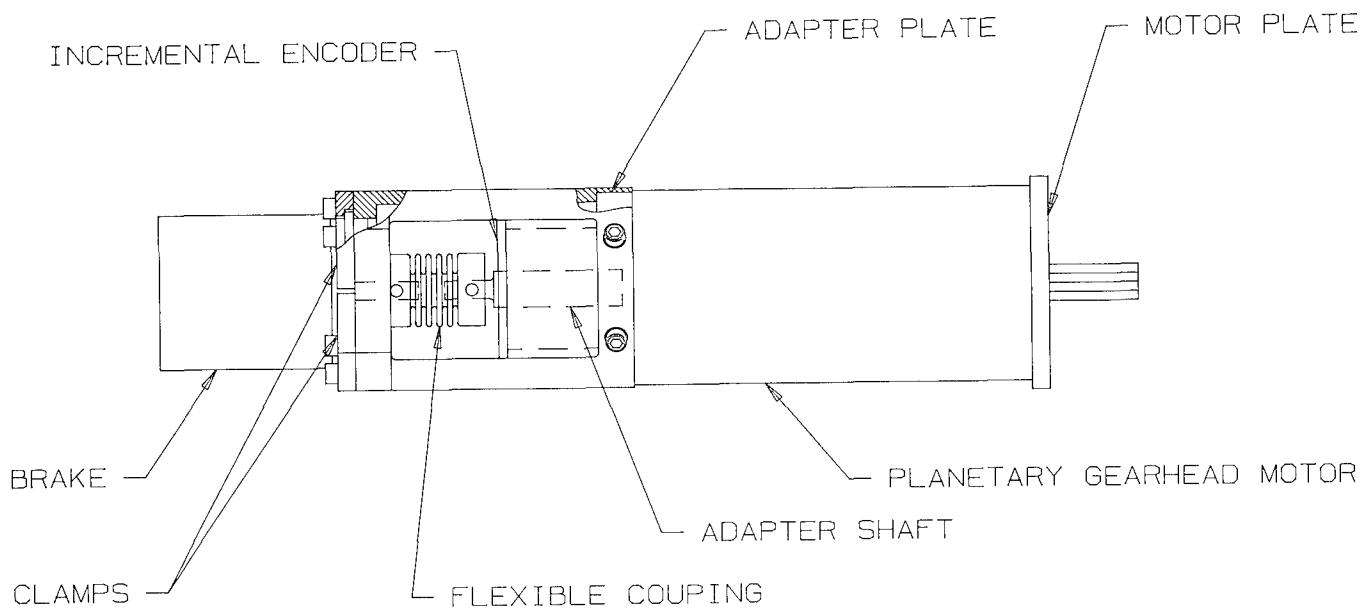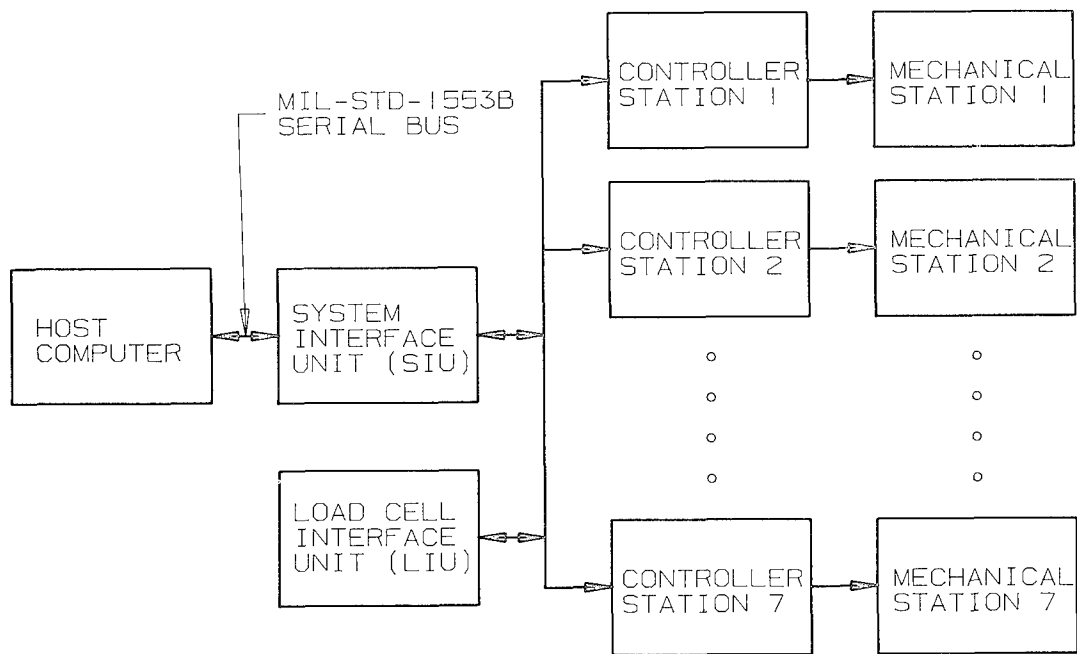
SURFACE CONTROL SYSTEM

FIGURE 9

11

HIGH OUTPUT PARAFFIN ACTUATORS:

UTILIZATION IN AEROSPACE MECHANISMS

Scott Tibbitts [*]

Introduction

The requirement for actuators and pin pullers on spacecraft is typically met by pyrotechnic actuators, electric motors, spring/silicone damper devices and non-explosive initiators. These approaches are sometimes less than optimum:

1) Pyrotechnic initiators generate shock, are limited in their stroke, raise safety concerns, cannot be fully verified before flight, and are not resetable.

2) Electric motors are heavy, complex, and costly.

3) Spring/silicone damper devices require an initiator (typically pyrotechnic), are heavy, and may require heating of the silicone damper fluid.

4) Non-explosive initiators are heavy, limited in their stroke, cannot be fully verified before flight, and are not resetable.

High Output Paraffin (HOP) thermal actuators have been developed to provide an alternative to conventional aerospace actuators: HOP actuators directly convert temperature changes to useful mechanical work. When fabricated with internal resistance heating elements they provide an electric linear motor. For applications in which slower response times (15 seconds - 20 minutes) are acceptable or preferred, HOP actuators have distinct advantages over conventional approaches.

Table 1: Capabilities of HOP Actuators

-Resetable: Can be cycled > 10,000 times.
-Flight hardware can be fully verified before flight.
-Output force to 4000 N (900 lbs).
-Stroke to 10 cm.
-High reliability: One moving part (the actuator rod).
-Can be fabricated magnetically clean.
-Gentle smooth stroke.
-Low power requirement (5-40 watts at 28 volts).
-Non-explosive: minimal safety concerns.
-Weighs less than 30 gms
-Small size

The capability of HOP thermal actuators to convert temperature changes to useful mechanical work also creates a wide variety of potential future aerospace applications in thermal control systems, and systems that can utilize mechanical work from temperature changes or heat (solar) input.

---

[*] Maus Technologies, Boulder, Colorado

In 1985 Maus Technologies was responsible for a development program to design a non-electronic thermal control system. A key component in the system was a device that could translate small changes in temperature into mechanical work (a thermal actuator) to drive a temperature control assembly. The application required the development of a thermal actuator to provide significant mechanical work (2.5 cm stroke, 80 N output force) from a small temperature change (10° C). Paraffin was selected to provide the motive force for the actuator. This type of actuator utilizes the 15 percent volumetric expansion of paraffin that occurs during the solid-to-liquid phase change. The resulting High Output Paraffin (HOP) actuator is similar in function to the commercial low output (1 cm stroke, 120 N output force) wax pellet actuator (Figure 1) which is well established in the thermal control industry:
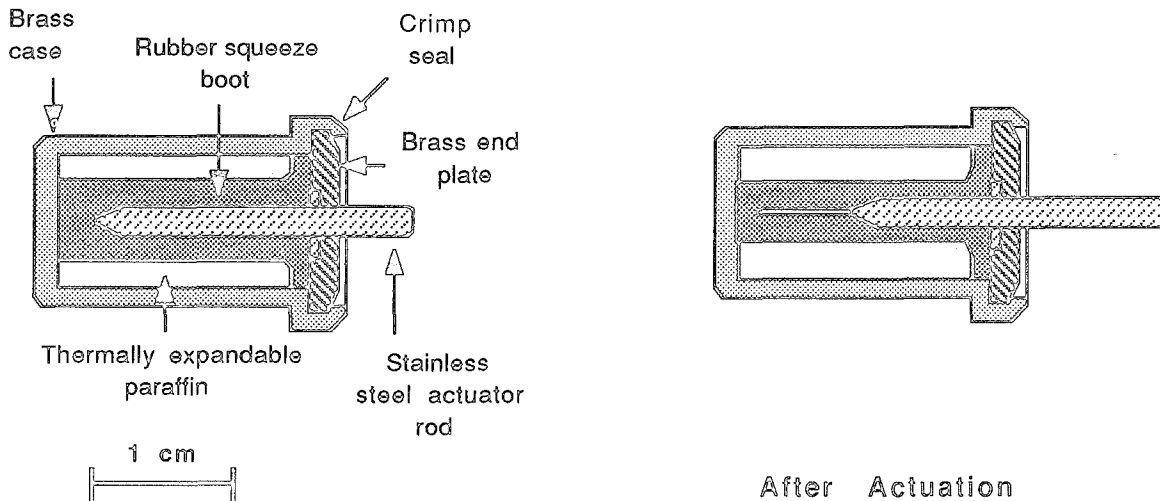
Figure 1: Commercial Wax Pellet Actuator

As the actuator is heated to the actuation temperature, the paraffin begins to melt and expand, creating hydrostatic pressure inside the actuator case. This pressure is translated through the rubber squeeze boot to the actuator rod, causing the rod to extend from the actuator. As the wax cools and solidifies, it contracts, allowing the rod to be pushed back into the actuator.

These commercial actuators are extremely reliable, being capable of cycling 50,000 times in harsh, corrosive environments. The most familiar application is the valve control mechanism utilized in automobile cooling system thermostats.

HOP actuators incorporate a modified squeeze boot design, increasing the mechanical work output, providing strokes to 10 cm and output forces to 4000 N (900 lbs) from the expanding paraffin. A typical HOP actuator is shown in Figures 2a and 2b. This actuator will extend 7.5 cm against a resisting force of 120 N (27 lbs) when heated from 35 ° C to 40 ° C.
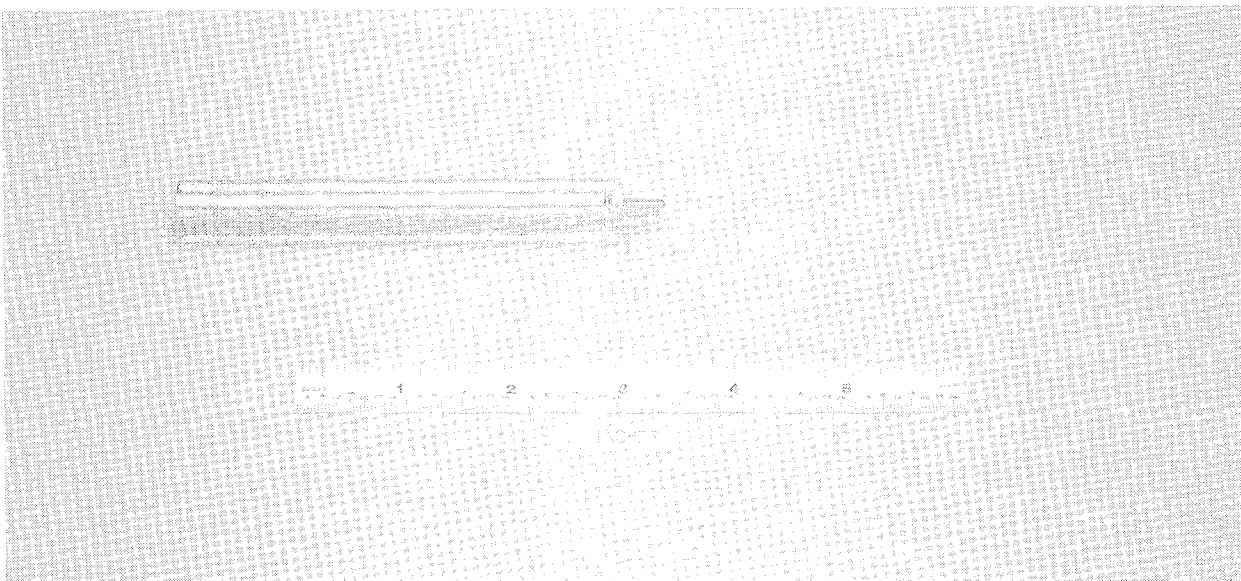
Figure 2a: HOP Actuator Prior to Actuation
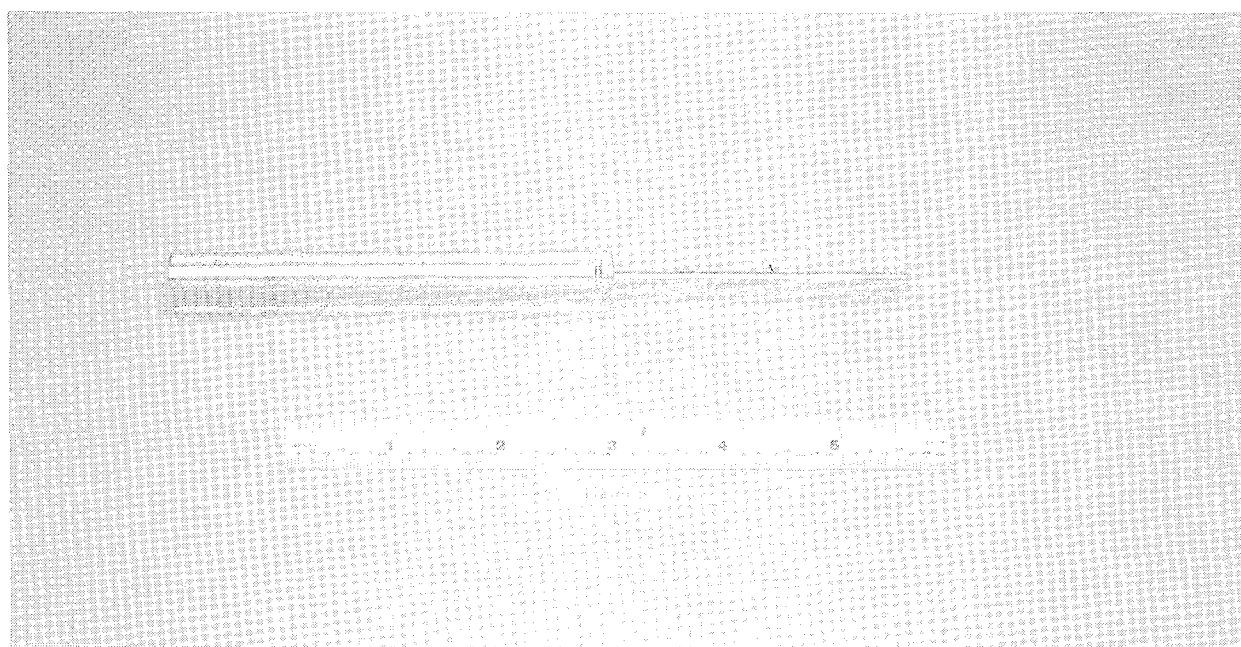
Figure 2b: HOP Actuator After Actuation

The capability of these types of actuators to generate significant mechanical work from small changes in temperature is well suited to aerospace mechanisms, where light weight, simplicity and reliability are prime concerns. As a result, the HOP actuator technology was adapted to the specific requirements of the aerospace industry.

Development of the Aerospace HOP Actuator.

Paraffin actuators are not new to the aerospace community. Mechanisms utilizing commercial wax pellet actuators have been designed and flown on spacecraft. The devices have used external resistance elements to heat the actuator. The most notable example is the magnetometer flipper on the Voyager spacecraft[1]. These mechanisms will be included on future flights (Galileo and the Mars Observer Mission), and the NASA Jet Propulsion Laboratory has an ongoing program to develop a generic launch latch utilizing wax pellet actuators.

Paraffin driven actuators have been utilized in aerospace mechanisms because of inherent characteristics that make them well suited for space applications:

Table 2: Characteristics of Commercial Wax Pellet Actuators

-Low weight
-Gentle stroke
-Non-explosive
-Non-magnetic
-Reliable
-Resetable for up to 50 K cycles
-High force: To 200 N (45 lbs)

During the past year we have met with the Mechanical Devices group at the Jet Propulsion Laboratory and discussed the development of a paraffin powered actuator designed specifically for the aerospace industry. As a result of these discussions the HOP actuator was adapted for aerospace mechanisms to the following requirements:

Table 3: HOP Aerospace Actuator Design Requirements

-All external components qualifiable to outgassing requirements
-Qualifiable to vibration and acoustic requirements
-Internally heated to provide faster response times, efficient heating, and allowing flexibility in
  case material selection (thermal conductivity) not a requirement
-Operating range: - 70 °C to 65 °C
-Redundant, space qualifiable heating element
-Flexible design allowing custom fabrication for specific requirements :
      Fabrication from a wide variety of materials including titanium or stainless steel
      Fabrication from non-gamma emitting or non-magnetic materials
      Fabricated with a wide range of custom paraffin formulations

The result of the development program is the Internally Heated (IH) HOP actuator. Characteristics of the actuator are listed in Table 4.

Table 4: Characteristics of IH-HOP actuators

-Useful stroke: Maximum nominal stroke is 10 cm .
-Output force: Maximum nominal output force is 4000 N (900 lbs).
-Actuation temperature (temperature at which motion begins): Can be varied from -20 °C to 120 °C by selection of paraffin type.
-Actuation temperature range (temperature rise necessary for full extension after start of motion): Can be varied from 5 °C to 60 °C by selection of paraffin.
-Response time (power on to full stroke): 15 seconds to 20 minutes. Dependent on power input, amount of thermal isolation, and initial actuator temperature.
-Stroke time (extension begins to full stroke): 5 seconds to 4 minutes. Dependent on power input.
-Efficiency (mechanical power out/electrical power in): Approximately 5% once the actuation temperature has been reached.
-Actuator size: Proportional to stroke times force (Figure 3).
-Actuator weight: Proportional to stroke times force (Figure 3).
-Cycle Life: >10,000 cycles at rated stroke distance and force.

Actuator Size vs. Stroke and Output Force:
Titanium IH-HOP Actuator

Approximate Actuator Weight (gms) / **Approximate Actuator Volume (cm 3)**

Actuator Stroke X Output Force
Cm - N
(Inch - Lbs)
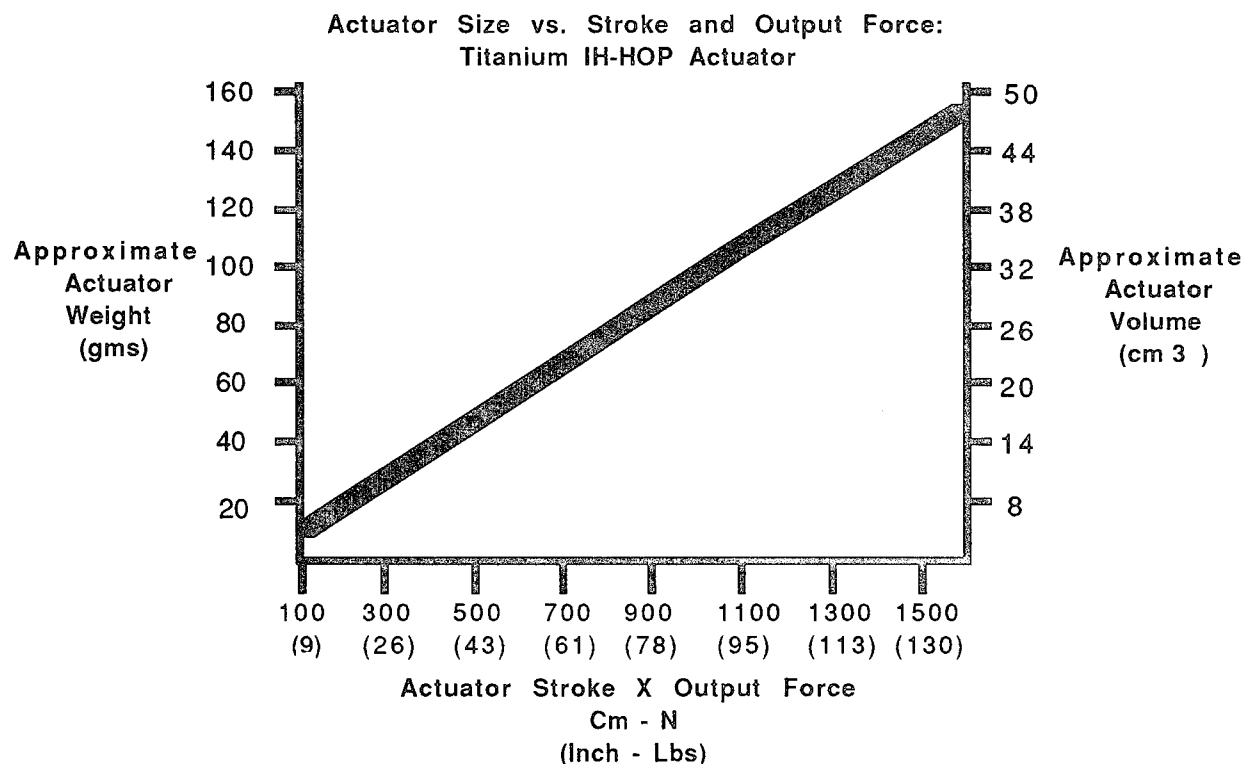
Figure 3: Size and Weight of HOP Actuators

Representative IH-HOP actuators are shown in Figure 4. These specific actuators were designed for mechanisms such as those on the Gamma Ray Spectrometer (GRS) requiring components containing no appreciable nickel, aluminum, chromium or iron. Actuator components are fabricated from commercially pure titanium, resulting in an actuator with total Ni, Al, Cr and Fe at milligram levels. Force-stroke curves, materials of construction, and actuator specifications are listed in Figure 5 and Table 5.
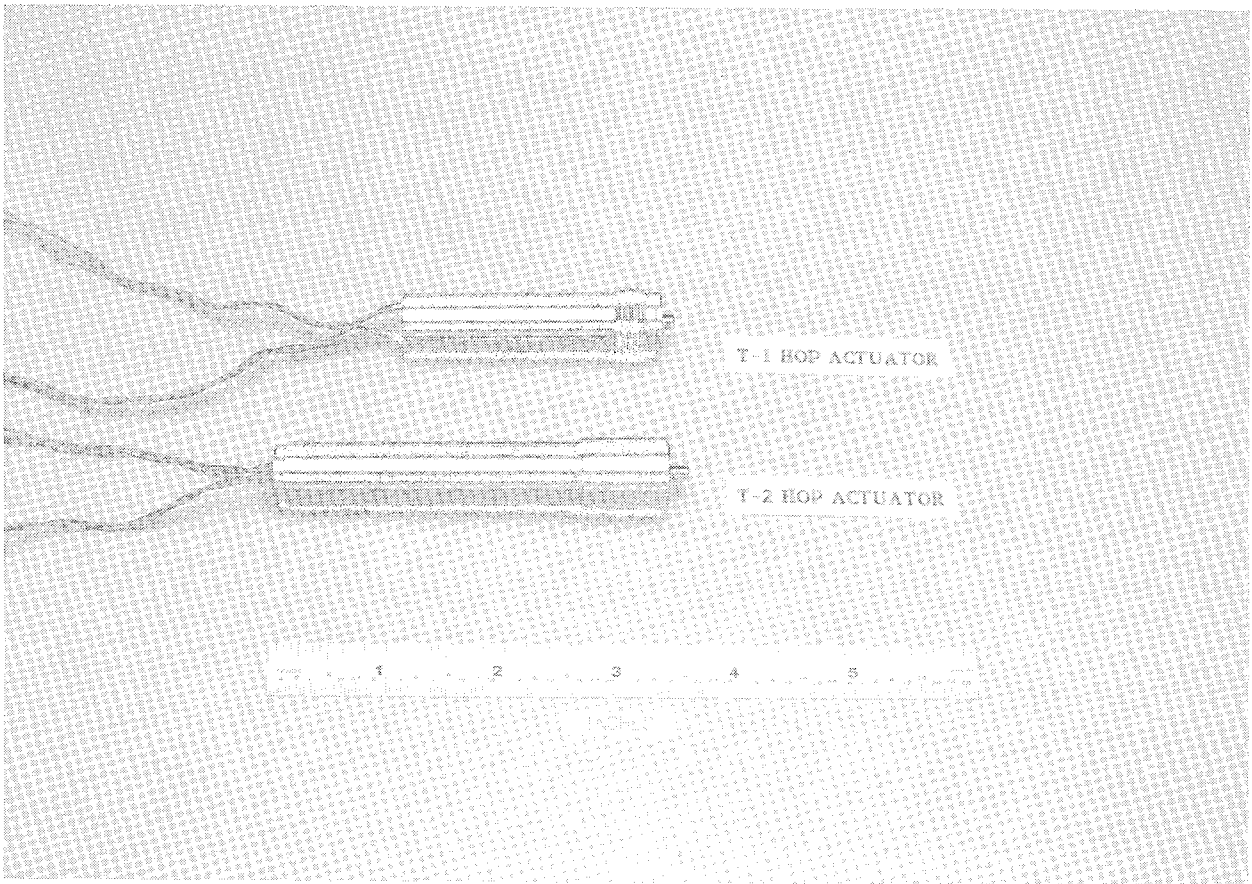
Figure 4: Internally Heated HOP Actuators

T-1 IH-HOP Actuator
Output force vs. stroke

T-2 IH-HOP Actuator
Output force vs. stroke
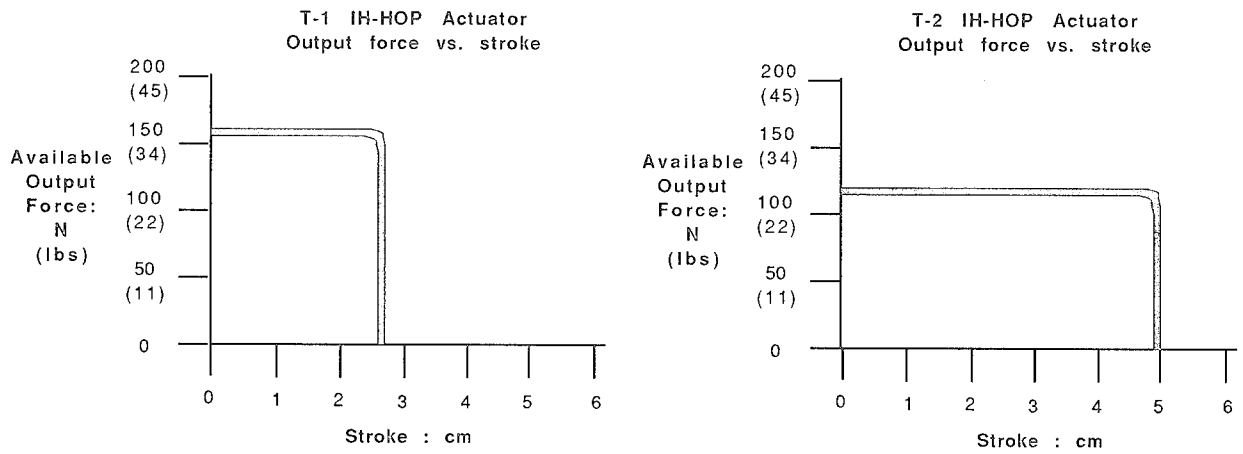
Figure 5: Force-Stroke Curves for IH-HOP Actuators

Table 5: Specifications for IH-HOP Actuators in Figure 4

	T-1 HOP Actuator	T-2 HOP Actuator
Stroke:	2.5 cm	5 cm
Actuation temperature:	90° C	90° C
Output force	160 N	120 N
Weight	25 gms	42 gms
Unactuated length	5.8 cm	9.0 cm
Power requirement	10 watts @ 28 volts	20 watts @ 28 volts
Response time	2 minutes from 70 F	2 minutes from 70 F

	Materials of construction:
Structural components:	Commercially pure titanium
Heaters:	Fully redundant polyimide film heating elements
Lead wires:	PTFE insulated copper conductor
Lead wire pass-through:	Glass-filled high pressure hermetic seal
O-ring seals:	DuPont Viton B
Squeeze boot:	Castable polyurethane or DuPont Viton B
Paraffin:	Distilled thermally expansive paraffin with suspended copper particles.

Design Detail

A cross-sectional detail of a typical actuator is shown in Figure 6. The design requirements are best discussed by reference to this cross-sectional view:

Operating pressure: The actuator is designed to produce the maximum output force from an internal hydrostatic pressure of 20,700 kPa (3000 psi) generated from the expanding paraffin. The case and seals are designed to withstand a minimum of 48,000 kPa (7000 psi), providing a safety factor of 2.5.

Squeeze boot:The key component in the actuator is the elastomer squeeze boot/seal. Castable two-part polyurethane was chosen as the elastomer for the following reasons:

-Thermoset polyurethanes provide superior outgassing performance (correct stoichiometry produces a "single molecule" component).
-Superior toughness/flexibility.
-Tooling is easily modified for different actuator configurations.

Alternatively, compression molded DuPont Viton B is used for higher service temperature applications.

Secondary O-ring seal

Primary O-ring seal

Actuator rod   Actuator body

Electrical leads
(four total)

Elastomer
squeeze boot

Heating
elements

Thermally
expandable
paraffin

High pressure
hermetic
pass-through

After   Actuation
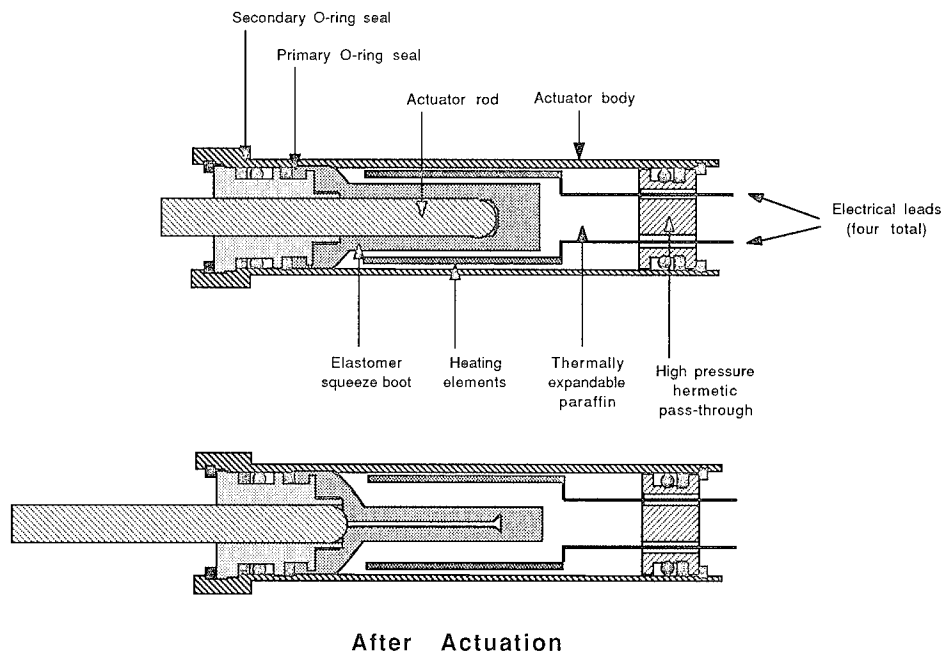
Figure 6:   IH-HOP Actuator Cross-Sectional View

Seals: The actuator is sealed by a redundant O-ring type seal: The squeeze boot is fabricated with an integral O-ring which seals between the actuator body and the actuator plug. This is backed up with a standard DuPont Viton O-ring/backup-ring seal. This arrangement provides sealing for internal pressures in excess of 48,000 kPa (7000 psi). Both the O-ring and the urethane boot meet or exceed outgassing requirements according to ASTM E-595-77 (<1 % total weight loss, <.1 % recondensable weight loss at 125 °C, 10^{-6} Torr vacuum).

Actuator body: The actuator body is typically fabricated from either 303 stainless steel or titanium; however, it can be fabricated from any material that will provide the necessary strength to withstand the internal hydrostatic pressure. It is preferable to fabricate the case from relatively low conductivity metals such as stainless steel or titanium to reduce heat loss through the case. These low electrical conductivity materials also minimize Thompson effect currents in the case of material for magnetically sensitive applications.

Expandable paraffin: The actuator is filled with a mixture of copper particles and purified paraffin. The copper is an optional component that increases heat transfer rates in the wax, providing even melting in the actuator. The paraffin is a distilled single or multi component formulation depending on the application. Typical wax expansion curves are shown in Figures 7a and 7b.

20

Figure 7a is an expansion curve for a paraffin that is used for binary, on-off type actuators that require a quick actuation once the melting temperature is reached. The 15% expansion occurs shortly after the melting temperature is reached. These paraffins are typically a single component formulation.

Figure 7b is an expansion curve for a paraffin that is used for actuators in which actuation over a wide temperature range is desired. In these type of actuators, the temperature of the actuator translates to a specific degree of extension over a wide range of temperatures. These are the types of actuators that can be used for positioning devices or thermal control systems. These paraffins are typically a multi-component formulation.

In both types of actuators the melting temperature of the wax can be varied from -20 °C to 120 °C, depending on the type of paraffin utilized.

Figure 7a: Narrow Melting Range Paraffin

Figure 7b: Wide Melting Range Paraffin
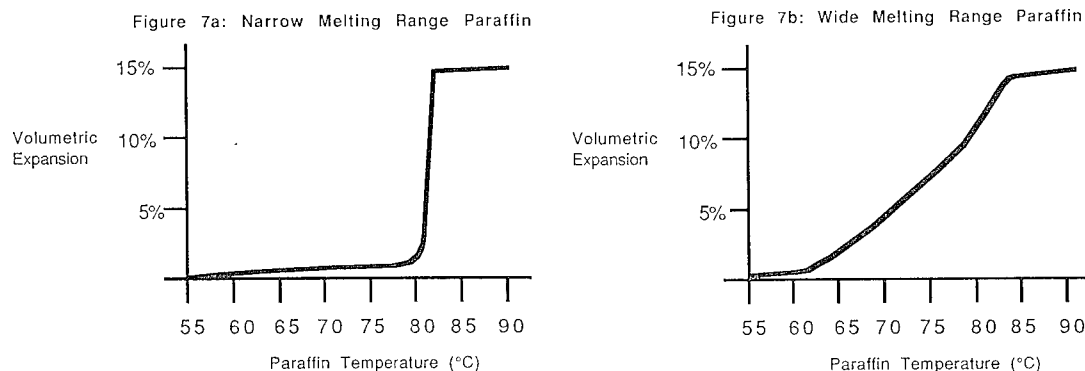
Figure 7: Paraffin Expansion Curves

Heating elements: Two, polyimide film resistance heating elements are used in parallel to provide a redundant heating capability: If one element fails, the actuator will fire with the remaining element. The two elements are mounted midway between the squeeze boot and the actuator case to provide even wax heating. Heating elements are selected on the basis of the application, response time, power requirements, and material requirements. Watt densities in the heaters are currently limited to 12 watts/square cm of element area, which translates to a maximum power input of 30 watts for a 2.5 cm stroke actuator. Satisfactory performance is possible with power inputs as low as 2 watts providing the actuator is thermally isolated.

Pass-through: Power to the internal heating elements is supplied through a four pin high pressure (10,000 psi) glass seal hermetic pass through. The pass-through is sealed to the actuator body with a Dupont Viton O-ring/Backup O-ring seal.

21

Qualification Issues

Outgassing: All external HOP actuator components are fabricated from materials meeting or exceeding the requirement for 1% total weight loss, 0.1% recondensable weight loss according to ASTM E-595-77. The only actuator component that does not meet that requirement is the paraffin, which is hermetically sealed inside the actuator. For applications that require a higher degree of containment the actuator can be fabricated inside a helium leak tight metal bellows assembly.

Vibration/Acoustic: At the time of paper submittal, vibration and acoustic testing of the actuators is scheduled, but has not been performed.

All internal actuator components are potted in place by the paraffin. Feedback from JPL based on qualification experience with similar devices indicates that the actuators should be qualifiable to extreme vibration requirements.

Vacuum operation: At the time of paper submittal, vacuum testing of HOP actuators is scheduled, but has not been performed.

HOP actuators create work from the pressure differential between the melting wax and the ambient pressure. When operated at atmospheric pressure this differential is approximately 21,000 kPa (3000 psi). Operation in vacuum will have an insignificant effect on this differential, and is expected to have no affect on actuator function.

Thermal cycling: The actuators are internally heated during firing; therefore, the actuator components are warmed prior to actuator function. HOP actuators have been repeatedly operated from -30 °C with no affect on operation. Tests to -70° C are planned.

Actuator Applications

The characteristics of HOP actuators allow the design of more complex, multi-function mechanisms utilizing a single actuator. Specific characteristics that can be utilized in these multi-function mechanism include:

-Repeatability: The mechanism can be designed to repeat a function (such as opening or latching) as many times as necessary. Alternatively, a mechanism can be designed to perform distinct functions on subsequent actuations.

-Positionability: The actuation can be stopped, and the position easily maintained at any point during the stroke, allowing a mechanism to be designed that performs distinct functions depending on length of actuation.

-Long stroke times: A device can be designed that performs a sequence of operations, with distinct delays between operations, as the actuator is fired.

Prototypes of two such mechanisms are discussed below:

22

Resetable Launch Latch

This mechanism (Figures 8a and 8b) was proposed for the sunshade on the Mars Observer Mission Gamma Ray Spectrometer (GRS), and is operated by the T-1 HOP actuator. The mechanism is designed to allow the sunshade to be unlatched, and then relatched as many as 100 times during the mission.   It is a "pin pusher" mechanism, that provides a pin puller type function from HOP actuator extension.
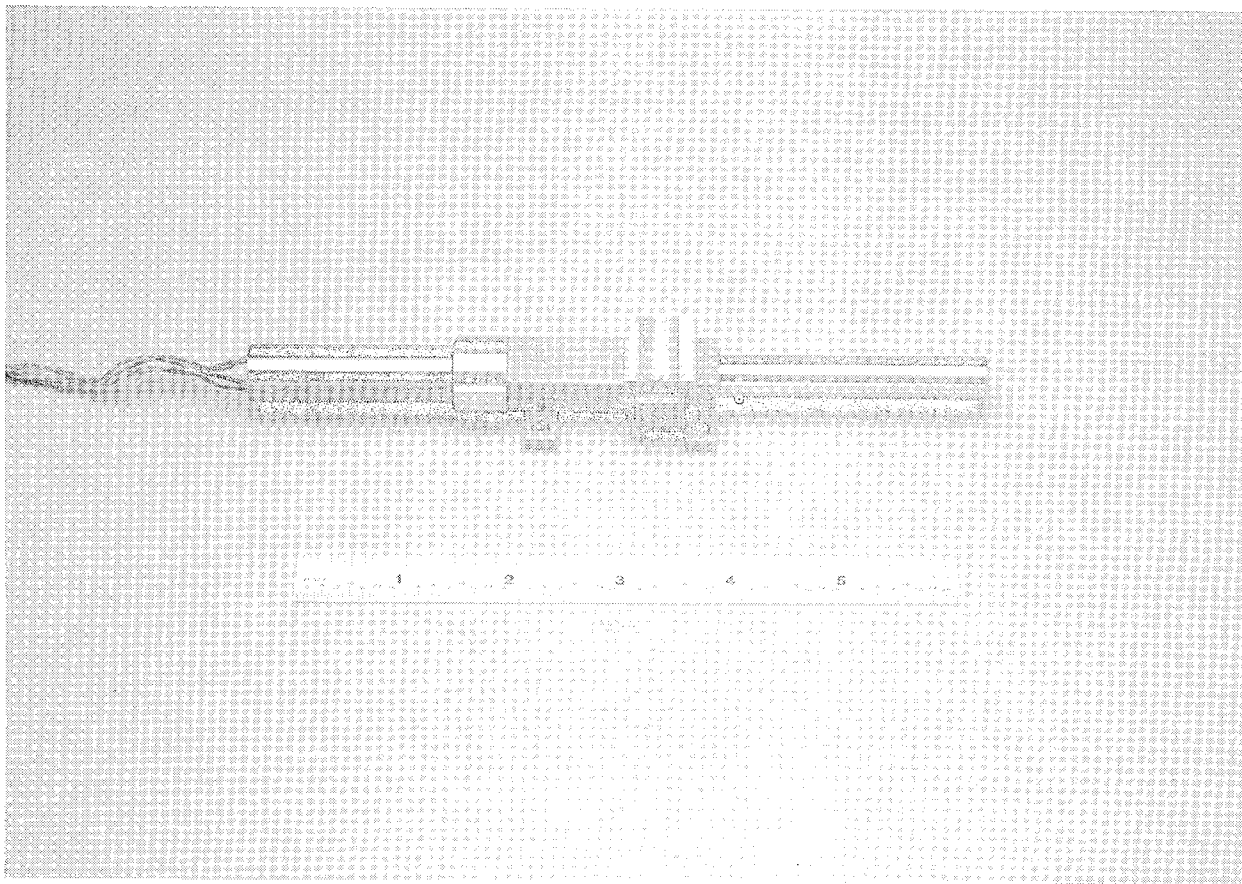
Figure 8a: HOP Actuator Launch Latch
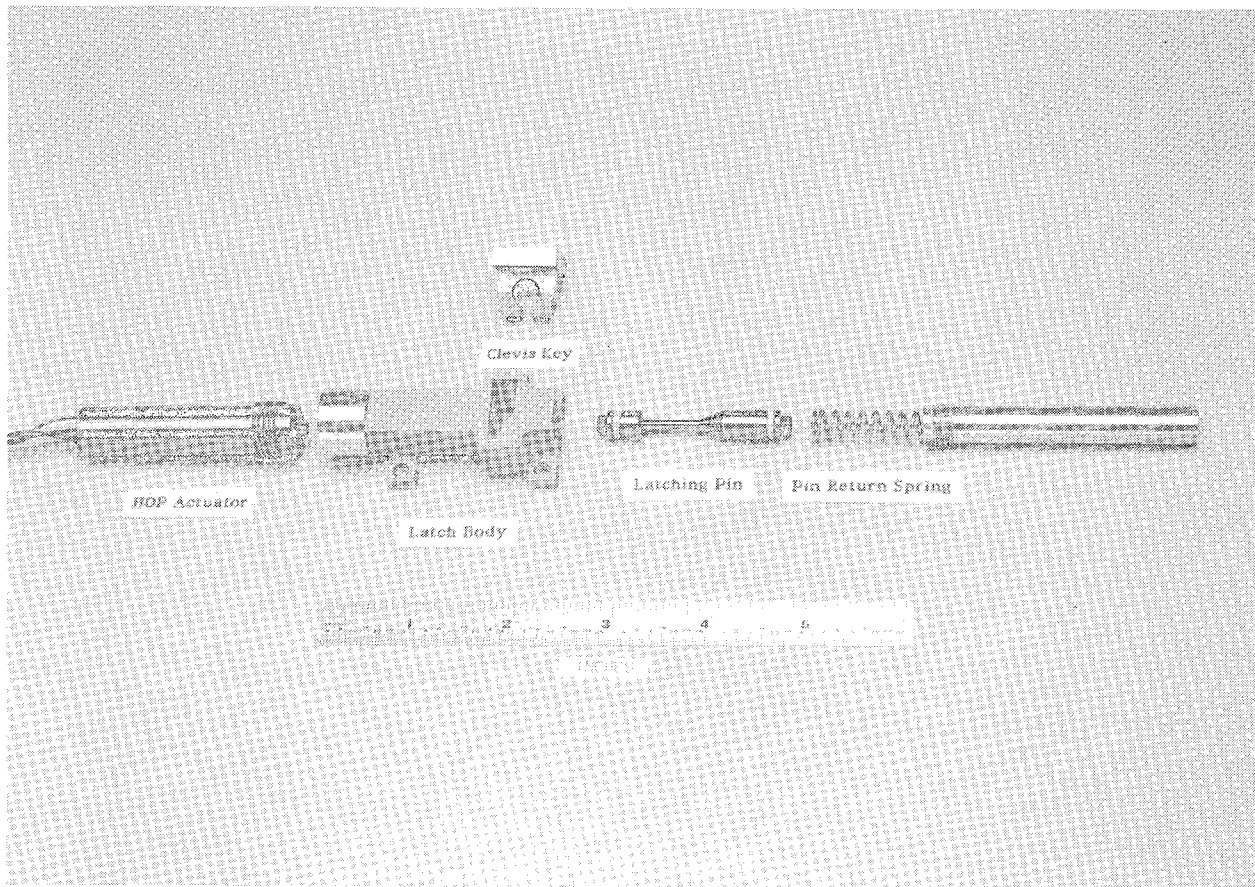
Figure 8b HOP Actuator Launch Latch Components

The sunshade is fabricated with a "clevis key", that mates and latches into an opening on the top of the latch mechanism. The clevis key is a metal tang with a .66 cm ID hole to receive a .64 cm OD pin. , and a .28 cm wide slot below the hole. The latch body contains a latching pin with an OD of .64 cm on one end tapering down to an OD of .25 cm on the opposite end.

In the unactuated position (during launch), the clevis key is held in place by the large diameter portion of the pin, which is in turn held in place by a return spring. The mechanism is unlatched by energizing the actuator, which extends against the latching pin. The pin moves (compressing the return spring) until the small diameter portion of the pin is pushed into the clevis key, releasing the latch (the .28 cm slot allows the clevis key to be pulled from the latch around the .25 cm pin).

The mechanism is relatched by first energizing the actuator, mating the clevis key with the latch body, and then allowing the actuator to cool. As the actuator cools, the return spring pushes the pin back to the original position, locking the clevis key in place.

Sunshade Operator (single actuator/multi-function mechanism)

As an alternative to a discreet latching mechanism and sunshade opening mechanism on the GRS, a single actuator mechanism was proposed to operate both the sunshade and latch. The function of this mechanism illustrates the multi-function capability of HOP actuators. The mechanism will operate the GRS sunshade in the following sequence:

1) Unlatch sunshade.
2) Open sunshade to one of two positions.
3) Latch and hold sunshade in position with no power input.
4) Close door and relatch.
5) Repeat as many as 100 times.

This is accomplished with a single T-2 HOP actuator providing 120 N (27 lbs) of force over a 5 cm stroke . The mechanism is shown in Figures 9 and 10.
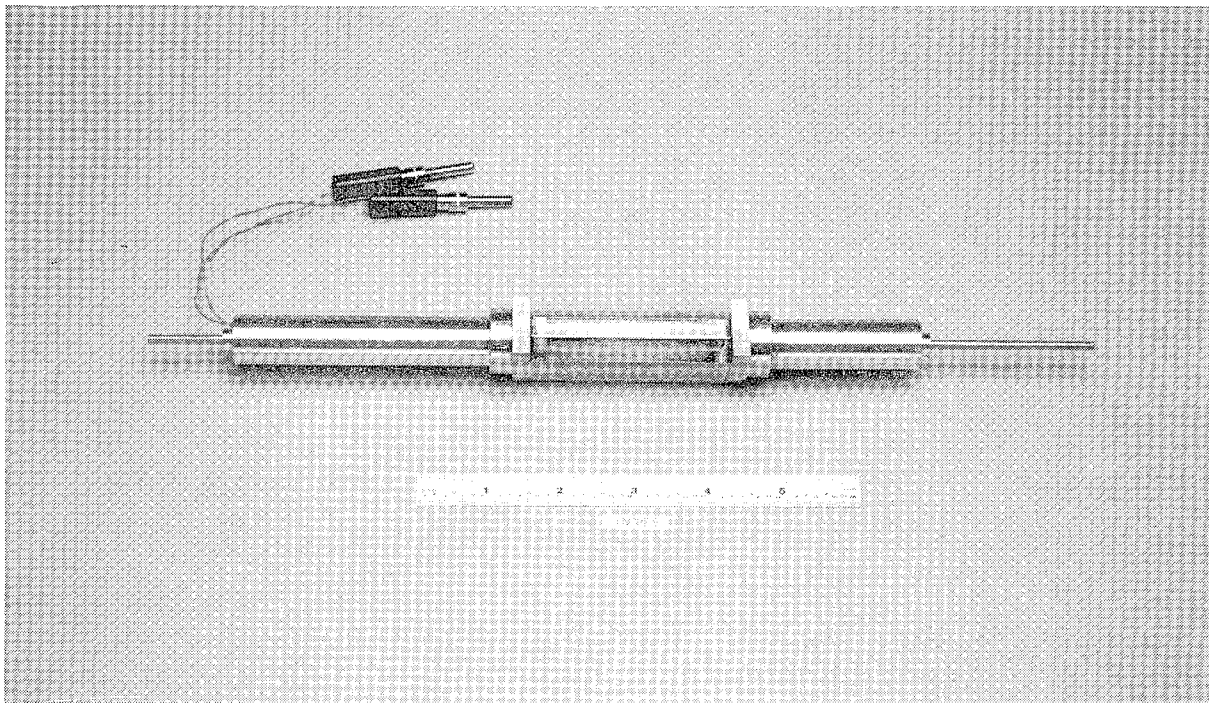
Figure 9: Proposed HOP Actuator GRS Sunshade Actuator

Before Actuation: Latch Engaged and Sunshade Closed

After Actuation: Latch Released and Sunshade Open
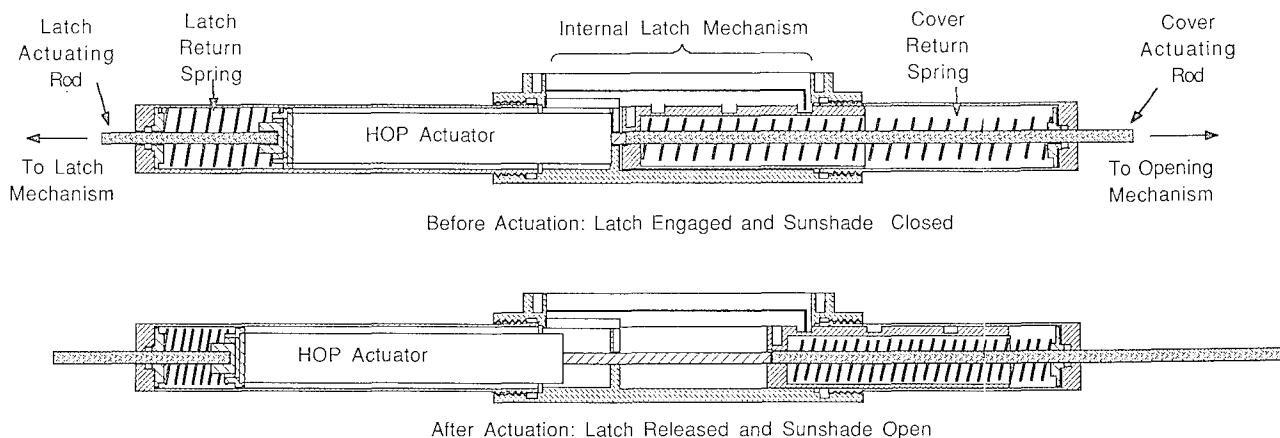
Figure 10: Proposed HOP Actuator GRS Sunshade Operator (cutaway view)

The HOP actuator in the mechanism is located between two bias springs: the latch return spring, and the cover return spring.   The springs are balanced so that on actuation, the following sequence occurs:

1) The linear actuator extends, compressing the latch return spring, extending the latch actuating rod 2.5 cm with 45 N (10 lbs) of force, which unlatches the cover (sunshade).

2) The actuator continues to extend against the cover return spring, extending the cover actuating rod as much as 2.5 cm with 45 N (10 lbs) of force, opening the sunshade.

3) When the sunshade is in the proper position, power to the actuator is turned off. The internal latch mechanism is a mechanical binary device that latches the door actuating rod (and thereby the sunshade) in the proper open position as the actuator contracts (in a similar manner to the latching mechanism in a ball point pen).

When the actuator is energized the subsequent time:

4) The latch actuating rod extends, readying the latch.

5) The actuator then continues to extend against the internal latching mechanism, releasing the mechanism.

6)Actuator power is turned off. As the actuator cools it contracts, allowing the cover actuating rod to contract, slowly closing the sunshade.

7) After the sunshade closes, the actuator continues to contract allowing the latch actuating rod to contract, latching the sunshade.

First Scheduled Flight

The first aerospace mechanism to utilize HOP actuators will be a gimble caging device being designed by Aeroflex Labs for a satellite to be launched in the fall of 1988. The mechanism utilizes two IH-HOP actuators providing 220 N (50 lbs) of force over a 1.25 cm stroke to cage and uncage a gimble. The mechanism will be used for both pre-launch testing, and gimble uncaging after launch.

Future Applications for HOP Actuators

Initial interest has focused on applications in which HOP actuators are used as an alternative to pyrotechnic actuators. However, the capabilities of the actuators extend beyond short stroke, single actuation applications. Potential future applications fall into two distinct categories :

- Electrically powered linear motors: The actuator works in conjunction with a resistance heater providing the necessary heat for actuation:

   Some potential applications:

   As an alternative power source (to pyrotechnic actuators, spring/silicone dampers, and small motors) for pin pullers, cable cutters, deployment and latching/unlatching devices, and equipment covers.

   An HOP actuator working in series with a piezoelectric positioning device would provide a "solid state" long stroke positioning platform with micro-positionability.

-Thermal control systems: The actuator provides mechanical work to drive a control system, as a result of temperature changes in the surrounding environment.

   Some potential applications:

   High force (2000-4000 N) actuators have excellent stiffness, and can provide temperature dependent compensating forces for thermally produced strains in large space structures. These compensating strains could be generated by an electrically heated actuator working with a control system, or they could be directly generated by temperature changes in the structure itself.

   High force HOP actuators working in conjunction with a cooling and heating source would provide hydraulic type power that could be utilized for space tools such as riveters, clamps and jacks. The heating source could be solar radiation, and the cooling means could be radiation to space, providing solar powered space tools.

For spacecraft solar collection devices, the actuators provide a method for aiming both flat-plate and concentrating systems. By combining HOP actuators with a shading device that selectively insolates the actuator (depending on collector position), accurate solar tracking can be provided without electronics.

HOP actuators can provide non-electronic proportional temperature control for fluids or radiators: Perturbations in system temperatures are translated to mechanical work that can directly operate control devices such as valves or louvers.

Conclusion

The High Output Paraffin thermal actuator provides an alternative device to the mechanism designer requiring significant mechanical work from a small, compact, reliable component. The work can be generated from heat provided by internal electrical resistance elements, or from environmental temperature changes.

In the internally heated configuration, the advantages over conventional electrically powered actuators can be significant: low weight, resetability, full verification before flight, high force, long stroke, gentle stroke and flexibility in materials of construction. For thermal control applications, the actuators provide a flexibility of design unavailable in alternative thermal actuator technologies.

With the strong industry emphasis on reliability, safety and simplicity, we expect HOP thermal actuators to be developed for a wide variety of future aerospace applications.

Acknowledgement

The author wishes to acknowledge and express his appreciation to Robert int'Hout of the NASA-Jet Propulsion Laboratory Mechanisms Support Group, who provided support and guidance during the development of the HOP aerospace actuator. Adaption of the technology to the requirements of the aerospace industry would have been a much more difficult process without his frequent and invaluable assistance.

References

1. Stange, William C.: The MJS-77 Magnetometer Actuator. 11th Aerospace Mechanisms Symposium NASA-GSFC, April, 1977.

STRUCTURAL LATCHES FOR MODULAR ASSEMBLY

OF SPACECRAFT AND SPACE MECHANISMS

WILLIAM MC COWN*

NEAL BENNETT*

ABSTRACT

Latching techniques are changing from early approaches due to the advent of berthing technology. Latch selection for a given interface may be conducted by evaluating candidate capabilities which meet functional interface requirements. A judgment criteria system is presented along with an example of its use in choosing the Rollerscrew Structural Latch (RSL) for the NASA Flat Plate Interface Prototype (FPIP).

Details are given on Rollerscrew operation, design, and development difficulties. A test plan is also outlined for the RSL and FPIP.

INTRODUCTION

Assembling spacecraft systems from modular sections has changed the role of structural latching systems. Previous approaches based on docking methods have given way to controlled berthing techniques using end effector and robotic arm systems. Latches are now required to operate reliably over many connect/disconnect cycles and multi-year lifespans. Interfaces can be brought into near-intimate contact and alignment before structural attachment is initiated. These refinements have allowed the use of both latch and fastener techniques for the structural connection of spacecraft and payload interfaces.

TUTORIAL

The primary functions of a latching system are to acquire, hold, and release one object from another. This is usually done by moving some part of a fixed structure into the path of a moveable structure so as to prohibit relative motion between the two. Key features of this concept are

---

* Rexnord Aerospace Mechanisms, Torrance, California

(1) a fixed structure to which a latch is mounted; (2) a moveable structure that is to be latched to the fixed structure; (3) the path of the moveable structure must be controlled relative to the fixed structure; (4) a method must be available by which the latch may grasp or capture the moveable structure; and (5) the capture action must be defined by the latch mechanism.

Most interfaces share connection integrity between three basic elements: (1) the structures to be assembled; (2) an alignment system; and (3) a mechanical latching system. These elements correspond to the key features of the latching function. Spacecraft docking interfaces share torsion, shear and compression loads between the structure and alignment subsystems, while tension and bending are reacted by structure and latching subsystems. Structure and alignment subsystems are usually passive in operation with latches being active.

Every connectable interface has unique characteristics that govern the configuration and operation of its latching system. The goal of the latch engineer is to match the characteristics of a latch system to the functional requirements of the mating interface. Latch selection can consist of seven phases:

(1)   Definition of Functional Latch Requirements
(2)   Proposal of Candidate Techniques
(3)   Establishment of a Weighted Judgment Criteria
(4)   Selection of Final Candidates per Weighted Criteria
(5)   Formalization of Functional Latch Requirements
(6)   Optimization of Final Candidates to Functional Requirements
(7)   Selection of a Final Latch System per Weighted Criteria

Functional latch requirements are often difficult to define early in a program. Table 1 outlines functional characteristics of latch systems that must be understood prior to functional requirement definition. Several varied latching techniques should be proposed for initial evaluation to provide a good cross section of available latching technology. Establishment of a weighted judgment criteria for candidate selection offers an objective decision process for concept evaluation. Selection of final candidates from early proposals allows competitive development toward a latching system best optimized for each interface application. A final latch system can then be selected that represents the optimum choice for interface operation.

TABLE I

FUNCTIONAL CHARACTERISTICS OF LATCH SYSTEMS

I. BASIC CHARACTERISTICS

(A) LOAD CHARACTERISTICS
(B) OPERATIONAL CHARACTERISTICS
(C) ENVELOPE
(D) POWER AND SIGNAL
(E) MASS
(F) ENVIRONMENT
(G) LIFE, RELIABILITY
(H) MARGINS, SAFETY FACTORS
(I) COST
(J) SCHEDULE
(K) MISCELLANEOUS REQUIREMENTS
(L) QUALIFICATION

II. LOAD CHARACTERISTICS

(A) LOAD SPECTRUM
   (1) STATIC
   (2) DYNAMIC

(B) DIRECTION
(C) PRELOAD
(D) PUSH-OFF
(E) TAKE-UP
(F) ADJUSTABILITY
(G) ENVIRONMENT
(H) STIFFNESS
(I) MISCELLANEOUS

III. OPERATIONAL CHARACTERISTICS

(A) PHASE CHARACTERISTICS
   (1) CAPTURE
   (2) ENGAGEMENT
   (3) TAKE-UP
   (4) PRELOAD
   (5) STRUCTURAL LOAD
   (6) UNLATCH
   (7) RELEASE CHARACTERISTICS
   (8) EMERGENCY OPERATIONS
   (9) INSTALLATION AND MAINTENANCE

(B) ACTUATION DYNAMICS
(C) ACTUATION TIME
(D) DIRECTION
(E) POWER
(F) RATE
(G) ALIGNMENT
(H) RELIABILITY
(I) ENVIRONMENT
(J) LIFE
(K) TESTING
(L) OTHER MISSION SPECIFIC REQUIREMENTS

Setting up a weighted judgment criteria is purely a subjective process. Both required and desired characteristics that affect design, operation, fabrication, and management of the interface should be weighted relative to importance. Following this, latch candidates must be evaluated for capabilities in each area and have the weighing factors applied to obtain an objective capability value. Similar selection methods are widely used for the evaluation of spacecraft systems.

Most common spacecraft latch systems in use today are based on actuated hooks or threaded fasteners. While these devices seem very different, they are quite similar in function. Both systems rely on the interlocking of piece parts to retain an object, but differ in their axis and type of movement. Each system has advantages and disadvantages relative to interface requirements.

The primary advantages of hook systems are rapid actuation and high misalignment tolerance. The major disadvantage is that length and preload are relatively fixed. Threaded fastener systems are variable in preload and length but require finer alignment and are slower in actuation than hooks. Fasteners and hooks are complimentary technologies with specific applications in aerospace latching.

Docking systems in the past have incorporated hook systems because of their rapid actuation and relatively high misalignment tolerance, which is useful during interface capture. Berthing technology has reduced the necessity for rapid actuation because closing velocities are low and alignment is more controllable. Fastener systems with reach and alignment flexibility are being developed for connector and standard interface systems where close prelatch orientation is available.

Spacecraft coupling is controlled by both the latch actuation mechanism and its drive system. Often the mechanism to control latch translation is more complex than the interfacing latch element itself. Linkage systems on hook latches and advance/retract mechanisms on powered fasteners correspond and guide the configuration of each system. From a drive standpoint, both linkages and threads act as gear stages with loads being fed back into the motor system.

A problem with both hook and fastener systems is load control. Hook system preload is traditionally preset by rigging. Load changes due to thermal and dynamic fluctuations cannot be compensated under normal circumstances.

Fastener systems usually control load through their drive systems by either power control, active feedback through a sensor system, positional sensing, or mechanical control, such as a clutch system.

LATCH SELECTION FOR THE NASA FLAT PLATE INTERFACE PROTOTYPE

The Flat Plate Interface Prototype (FPIP) is an integrated modular connector designed to transfer thermal energy, electrical power, and signal data between two structures. This interface system is being developed by TRW´s Electronic Systems Group for NASA GSFC, under contract number NAS 5-30080. Figures 1 and 2 illustrate both sides of the prototype design and full-scale mock-up respectively. The FPIP consists of two thermal transfer structures with very flat mating surfaces, a split core power transformer system, an optical data transfer system, a load distribution system, and a central latching system. Thermal heat sinking is accomplished by compressing the structures together under a uniform load generated by the latch through the load distribution system. Requirements on the latching system include high load capability, limited contaminant generation, high reliability and life, and controlled load capability. Functional requirements for this latch system are listed in Table 2.

TABLE 2

FUNCTIONAL REQUIREMENTS FOR THE FPIP LATCH

|		
o	Structural Preload	$\geq$ 3,600 Kg (8,000 Lbf)
o	Ultimate Load	$\geq$ 6,800 Kg (15,000 Lbf)
o	Take-Up Load	$\geq$ 225 Kg (500 Lbf)
o	Preload Adjustable up to	4,550 Kg (10,000 Lbf)
o	Actuation Time	$<$ 100 sec.
o	Lateral, Longitudinal Misalignment	$\leq$ 3 mm (.125 in)
o	Angular Misalignment	$\leq$ 2 Degrees
o	Mass	$\leq$ 20 Kg (40 Lbm)
o	Life	$>$ 1,000 Cycles Over 10 Yrs
o	Power	TBD @ 28 Vdc
o	Negligible Particulate and Gaseous Contamination	
o	Simple Operation, EVA Compatible	
o	Full Retractability into Interface, Damage Resistant Design	
o	Full Accommodation to the TRW Load Distribution and Flat Plate System	
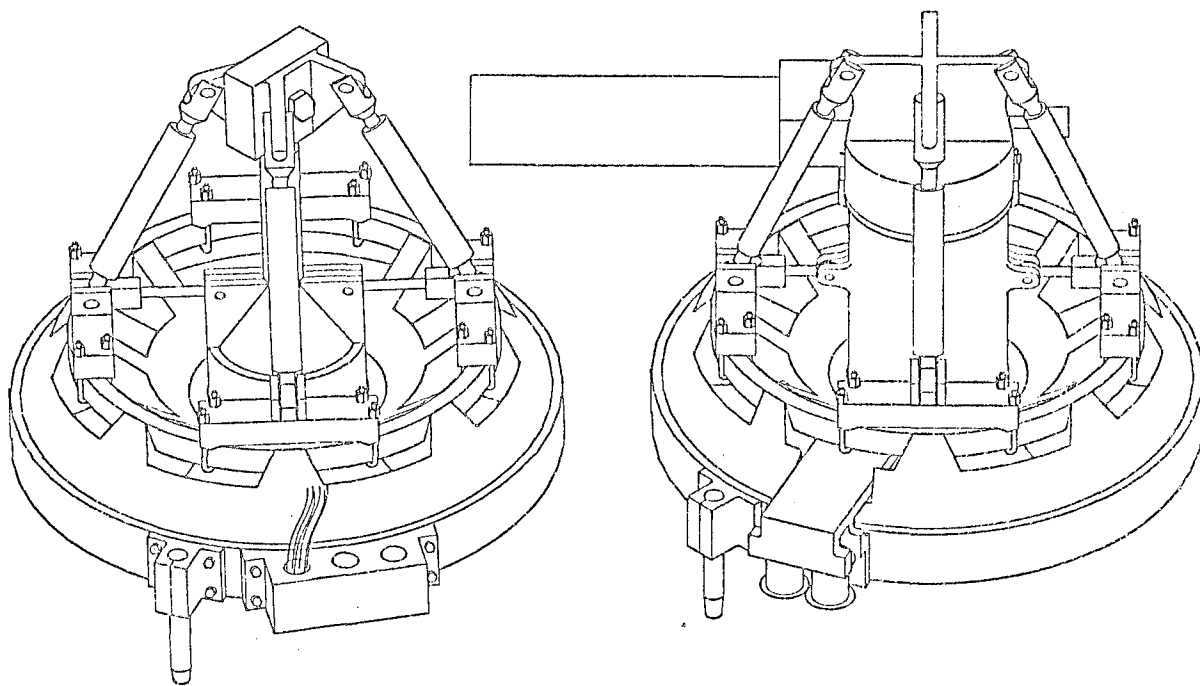
FIGURE 1

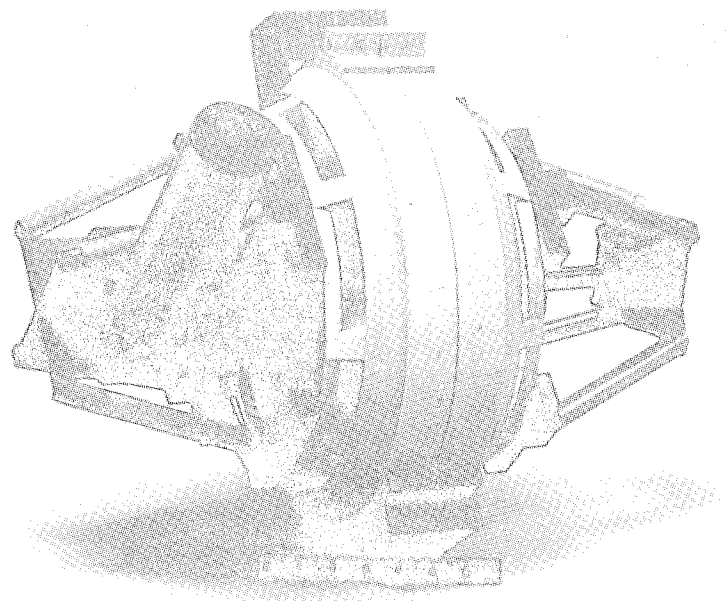FLAT PLATE INTERFACE PROTOTYPES (TYPE I AND TYPE II)

FIGURE 2

FULL SCALE FLAT PLATE INTERFACE MOCK-UP

34

The FPIP does not require gross alignment capacity or rapid engagement. High preload generation, reliability, life, and low contamination are mandatory to the operation of the FPIP system. Candidate latching concepts included a powered pawl latch, a Rollerscrew Structural Latch, a powered claw latch, and a powered nut/bolt latch system. Latches were evaluated against a weighted judgment criteria, as shown in Table 3. The powered pawl latch and Rollerscrew latch were chosen as preliminary candidates due to their limited sliding contact in the area of the interface.

TABLE 3

WEIGHTED JUDGMENT CRITERIA

(PRELIMINARY EVALUATION)

ITEM	CRITERIA	WEIGHT FACTOR (1-10)	FIXED ACME		POWERED NUT/BOLT		ROLLERSCREW		POWERED PAWL	
			VALUE	SCORE	VALUE	SCORE	VALUE	SCORE	VALUE	SCORE
1	COST	8	4	32	5	40	3	24	5	40
2	SIMPLICITY	5	4	20	4	20	3	15	4	20
3	FUNCTION	9	7	63	6	54	9	81	8	72
4	MASS	4	5	20	6	24	3	12	5	20
5	POWER	4	5	20	5	20	7	28	6	24
6	LOAD	9	7	63	8	72	9	81	8	72
7	ENVELOPE	7	4	28	7	49	5	35	5	35
8	RELIABILITY/LIFE	9	5	45	4	36	9	81	8	72
9	SERVICE/MAINTENANCE	5	5	25	4	20	7	35	8	40
10	ENVIRONMENT COMPATIBLE	9	5	45	4	36	8	72	7	63
11	SAFETY	5	4	20	5	25	6	30	5	25
12	DESIGN FLEXABILITY	4	4	16	6	24	8	32	7	28
13	DESIGN MATURITY	2	5	10	6	12	4	8	8	16
14	OPERATION SIMPLICITY	7	7	49	8	56	9	63	7	49
15	ELECTRONICS COMPLEXITY	5	5	25	6	30	6	30	5	25
16	SCHEDULE	6	5	30	5	30	5	30	6	36
17	MISCELLANEOUS FACTORS	7	7	49	7	49	7	49	4	28
18	CONTROL	7	5	35	5	35	7	49	6	42
	TOTALS			595		632		755		707

At this point, latch optimization began as each system was refined. Changes to the Rollerscrew system included structural revision to fit into the load distribution system, contamination control by a wear-in process with multiple clean-up stages, drive system revision to comply to customer request and test requirements, and variable load control through mechanical and electronic techniques. Pawl latch changes included structural revision and variable load control.

A final evaluation was made using the previous judgment system, resulting in the Rollerscrew Structural Latch being chosen as Rexnord's primary candidate for the FPIP docking mechanism. The major criteria that affected this decision were function, environmental compatibility, operational simplicity, cost, and miscellaneous factors. The Rollerscrew latch and pawl latch are very similar with many common components. Both latches would work well for this application. The pawl latch, however, had minor drawbacks in its design and operation, such as additional components, including the hook and its control system, a motion reversal during actuation, and sliding surfaces in the hook/receptacle area.

THE ROLLERSCREW STRUCTURAL LATCH

Construction and Operation

The Rollerscrew Structural Latch (RSL) Assembly is shown in Figures 3 through 9. Figure 3 is an isometric view of the entire assembly while Figures 4 and 5 are photographs of the Rollerscrew Assembly and the Rollernut Receptacle. Figures 6, 7, and 9 show cutaway views of the Rollerscrew Assembly and the Receptacle Assembly. The latch is powered by a brushless DC motor that has been modified for vacuum use through a worm gear drive system that is torque limited by a slip clutch, as shown in Figure 9. A flange at the base of the Screw is driven by an internally splined spool which is connected to the worm gear assembly.

To engage, the drive system advances the Screw through a guide system until its drive flange bottoms. The Screw threads into a floating receptacle and tightens, preloading the interface. When engagement and take-up phases are complete, power is increased to obtain a predetermined load. On full load the motor stalls and is shut down, completing latch-up.

LATCH RECEPTACLE

ROLLERSCREW

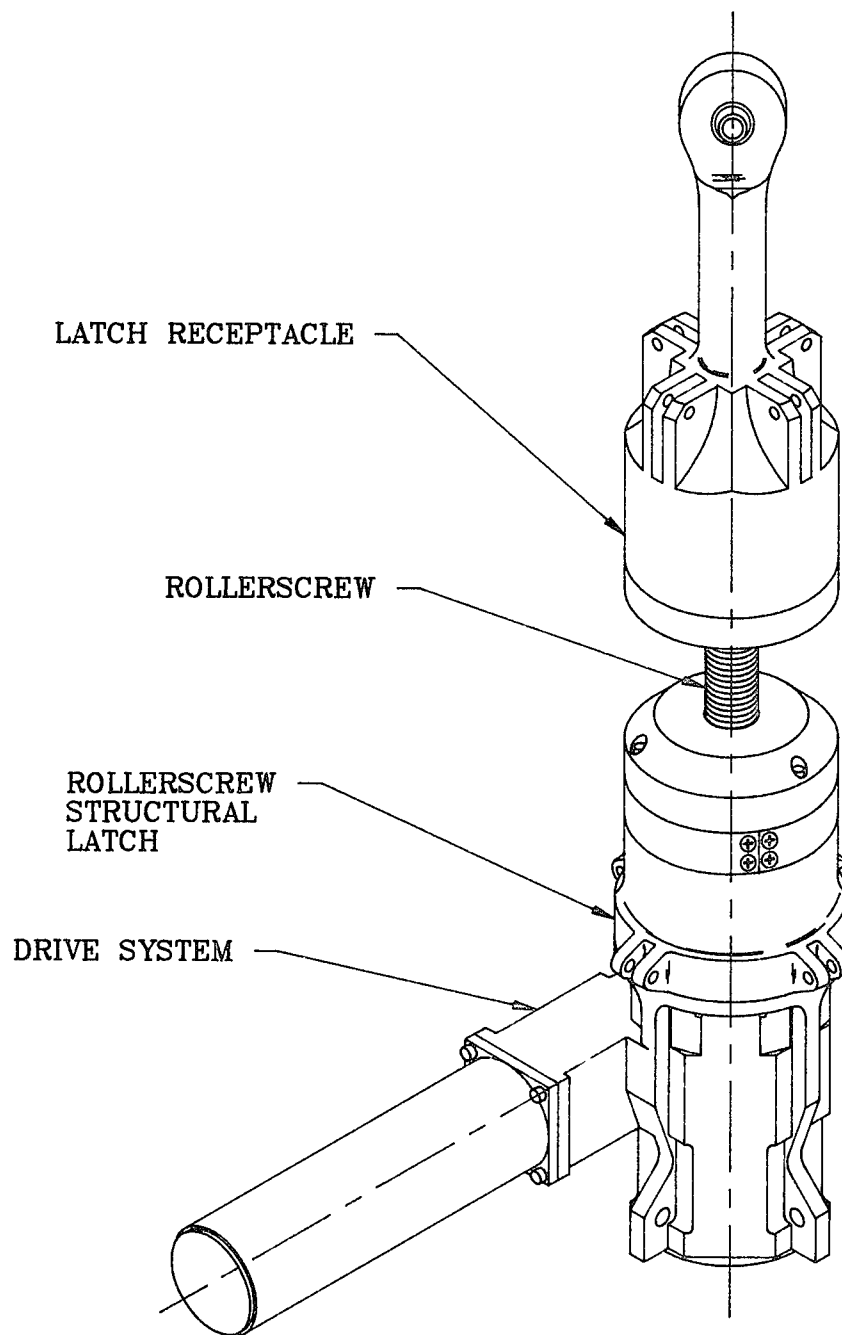ROLLERSCREW
STRUCTURAL
LATCH

DRIVE SYSTEM

FIGURE 3

ROLLERSCREW STRUCTURAL LATCH SYSTEM

37
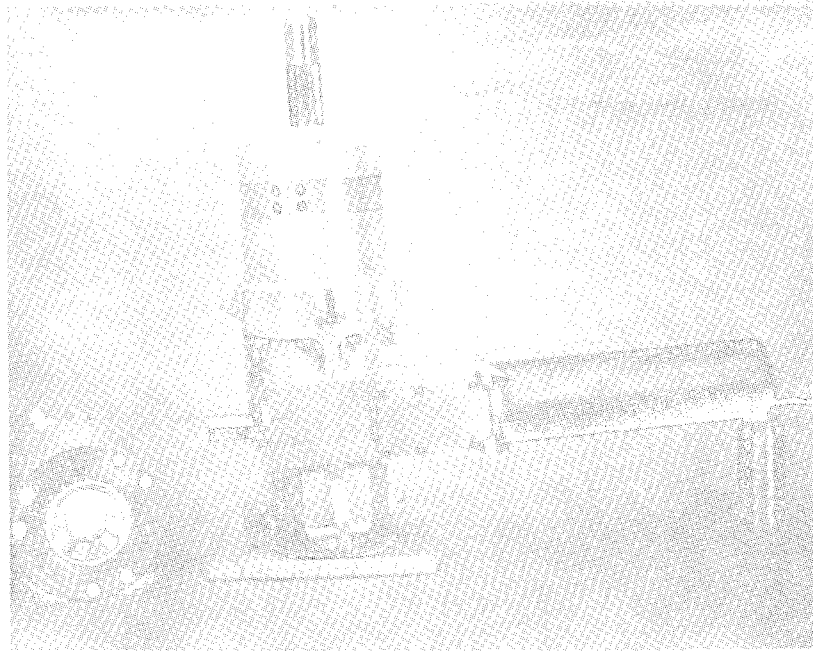
FIGURE 4

RSL ASSEMBLY

FIGURE 5

LATCH ASSEMBLY

SPLINED FLANGE — EVA DRIVE — DRIVE HOUSING

ROLLERSCREW

DRIVE SPOOL

MOTOR

GUIDE HOUSING
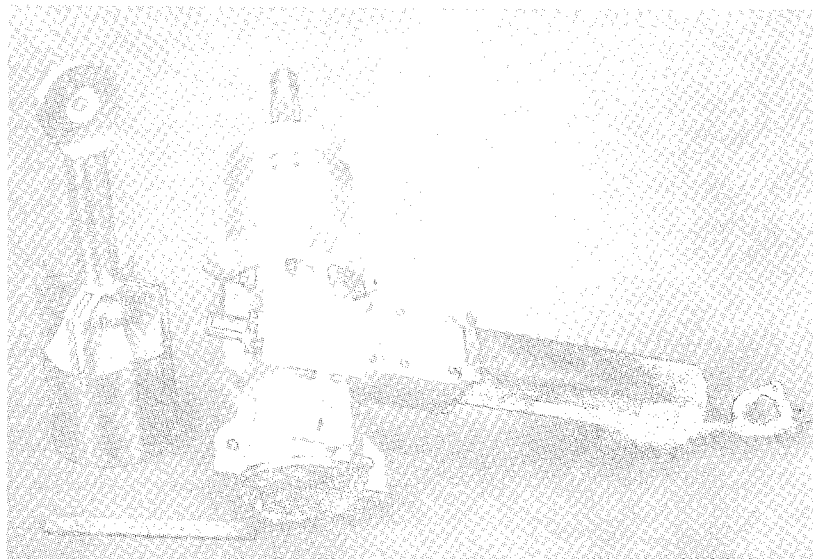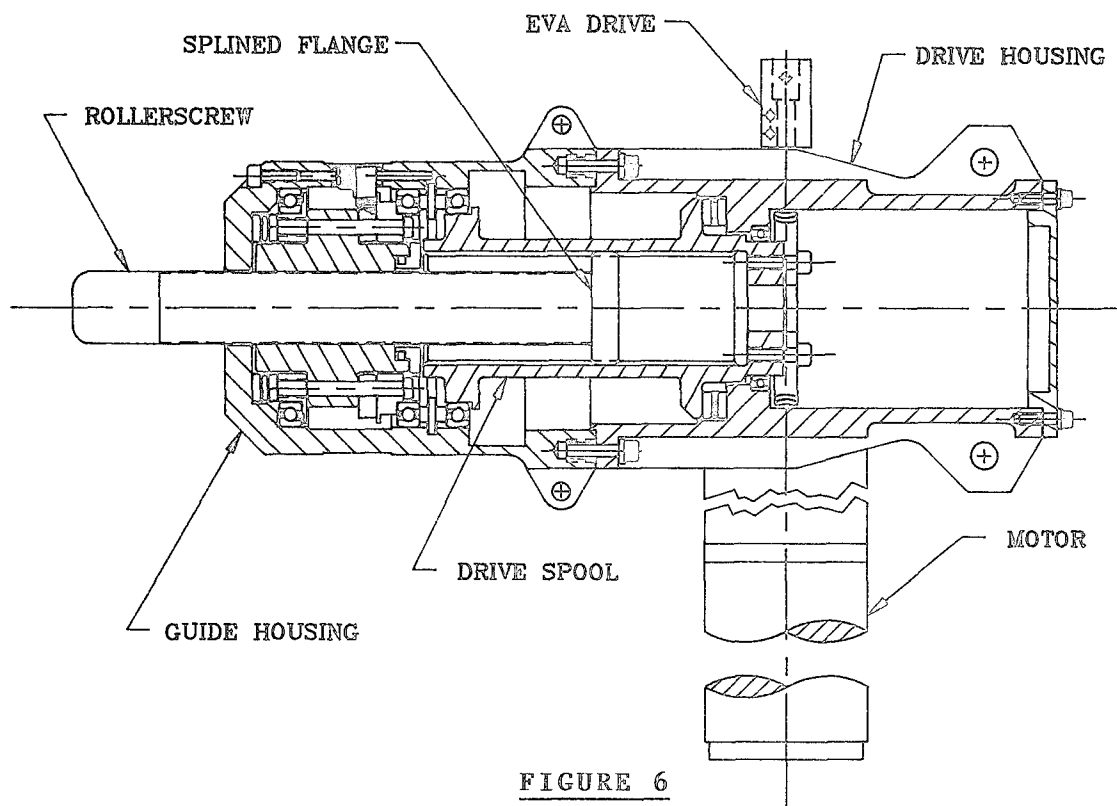
FIGURE 6

ROLLERSCREW LATCH ASSEMBLY

GUIDE CONE

ROLLERNUT

RECEPTACLE HOUSING

SPRING PLUNGER
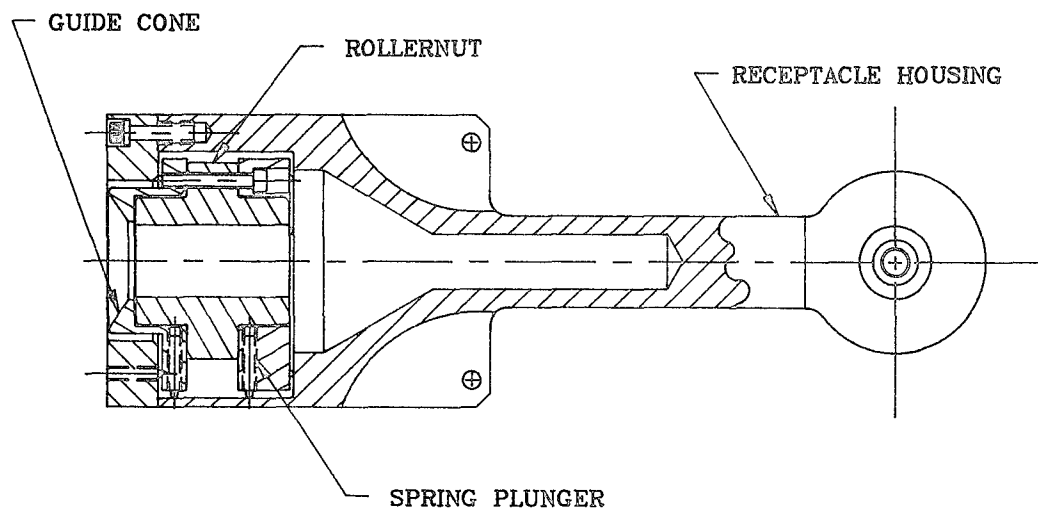
FIGURE 7

RECEPTACLE ASSEMBLY

39

For interface demate, the motor direction is reversed, un-screwing the Rollerscrew from its receptacle and retracting it back into the RSL housing. The motor drive is then shut down.

The Rollerscrew Structural Latch will not loosen preload over extended periods due to worm gear ratio, back drive efficiency, and motor detent torque. No periodic maintenance is planned for this device.

The Rollerscrew/Nut System

The primary element of the RSL is the Rollerscrew and Nut, as shown in Figure 8. A recirculating Rollerscrew was chosen for this application primarily because of its reliability. The Rollerscrew/Nut uses rolling elements as a thread interface, which reduces sliding friction to a minimum. The Nut resembles a rollerbearing with threads. Reduced friction allows high loads to be generated with low input torque, reducing power requirements. The hardened components and materials used in the Nut decrease the opportunity for cold welding over extended load lifetimes. If any degradation or contamination occurs, the Rollerscrew and Nut are very damage tolerant. Rolling element mechanisms with high torque margins insure good reliability.

FIGURE 8

RECIRCULATING ROLLERSCREW NUT

40

The primary failure mode for Rollerscrews is structural overload. Beyond rated loadings the threads or rollers may brinell, causing rough action and decreased efficiency. As loading is increased to failure, roller breakage occurs. A recirculating Rollernut was chosen for this application, partially because it features a cage which reduces the tendency to jam on massive overload failure.

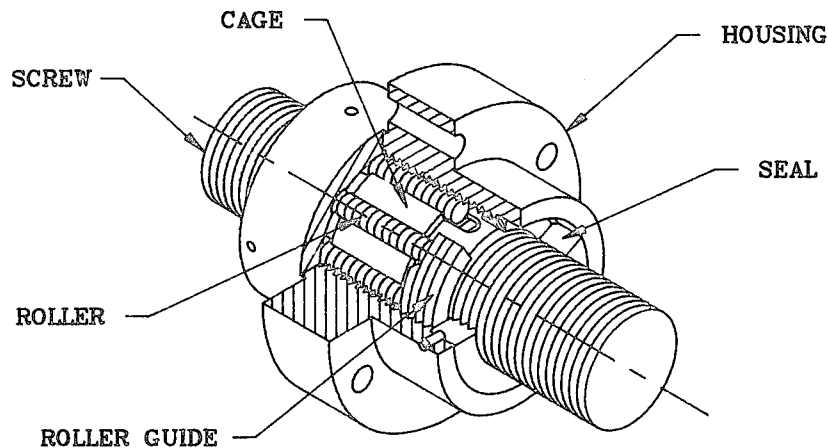Other Rollerscrew failure modes include over-speed, which is not a problem with this device, and re-entry of the rollers inside the housing. No history of re-entry failure has been reported for Rollerscrews; however, this can be a problem with ball-screw systems. A Rollernut uses caged rollers articulated by a cam system for positive control.

The Rollerscrew/Nut are commercially available items modified to engage and disengage smoothly. Materials used for this system are 4140 steel screw, 52100 nut and rollers, 440C stainless case, and a Teflon seal. Screw and Nuts are dry-lubricated with tungsten disulfide, then run-in and cleaned to reduce particle generation.

DESIGN CONCERNS AND SOLUTIONS

Major concerns which arose during the design of the RSL are as follows:

- o   Thread Engagement
- o   Gear System Operation
- o   RSL Load Control
- o   Clutch Operation
- o   Contamination Control

Threading engagement is potentially difficult for Rollerscrews under misaligned conditions. The Rollernut has a 25 mm (.984 inch) diameter thread with a pitch of 1.0 mm (.040 inch). Eleven rollers within the Nut define a pick-up window of .09 mm (.004 inch). Under misaligned conditions the lead window can be missed, cross-threading the Screw and jamming the Nut. A large bullet nose on the Screw coupled with modifications to the internal mechanism of the Nut and lead thread of the Screw eliminated cross-threading concerns.

The worm gear drive system presented difficulties that affected primarily the powertrain efficiency and consistency. Efficiency became a problem when design equations predicted anywhere from 17% to 60% power transmission. Consistency was required because motor power is to govern latch preload.

Losses or gains through the gear train have a direct effect on RSL preload. Gear train stiffness, alignment, and backlash that can affect latch operations have been addressed in the design process.

Worm gear efficiency equations are based on commercial gear reducers with oil bath lubrication running at constant RPM. Worm efficiency can vary due to any number of variables, such as materials, lubrication, rubbing speed, alignment, stiffness, profile, and wear. A statistical average was taken to approximate a theoretical design value for initial motor and clutch sizing. Verification tests are to be run to establish an empirical value for this gearset. However, every gearset is individual and these measurements may have limited design value.

Gear stiffness was found to be marginal on initial designs, and was increased by increasing shaft size, changing assembly techniques, revising housing design, and mounting with preloaded bearing sets, as shown in Figure 9.
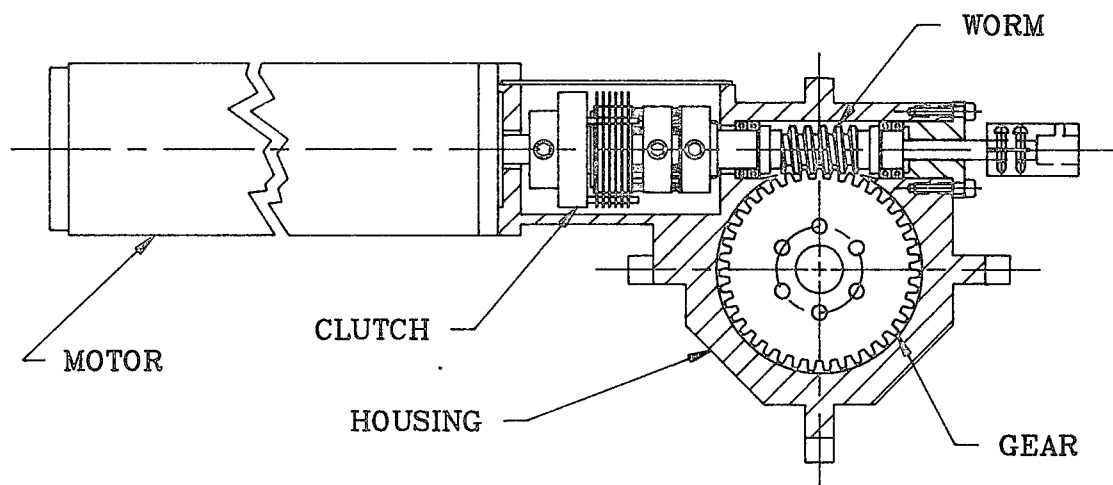

FIGURE 9

ROLLERSCREW DRIVE SYSTEM

To obtain constant load readings, worm sets must be run-in under conditions similar to actual service. The worm is hardened and ground 1045 steel and the gear is Amco Alloy #45 Phosphor Bronze. The worm and gear are lubricated with both tungsten disulfide and Braycote 601 grease.

Load control for the RSL is accomplished by a two stage actuation with motor power determined by current limiting devices. This method allows accurate preload to be consistently applied. A single stage actuation was considered where the drive system is powered to stall, but variables in drive system inertia could vary preload levels beyond acceptable limits.

A polymetric slip clutch was originally used to control RSL preload. Difficulty in predicting a change in friction coefficient between ambient air and vacuum conditions precluded this approach. Commercially available materials could vary in friction coefficient by as much as 2 to 1 between air and vacuum operation. The clutch has been relegated to an overload protection role.

The RSL addresses contamination in a number of ways. Rolling element latch interfaces were selected, in part, to reduce particle generation. In addition, Teflon wiper seals have been added to control any loose particles in the RSL and Receptacle Nut. Both RSL and Receptacle housings are covered, with the exception of the Screw and Nut interfaces. A run-in and clean-up procedure reduces particle generation from initial actuations. Gaseous contamination is reduced by the use of liquid lubrication only in the worm gear area, deep within the housing.

TESTS PLANNED FOR THE RSL AND FPIP

At the time of submittal of this paper, acceptance testing of the RSL was just commencing. Planned testing of the RSL includes calibration of preload versus motor power, life cycling, and misalignment capability tests. Planned testing at the systems level will include cycling tests as well as functional tests of the FPIP system in a vacuum. Results of both the RSL and FPIP tests will be reported as a supplement to the presentation at the Symposium.

CONCLUSIONS

This paper has presented a brief tutorial and evaluation procedure for interface latch selection. An application of this technique is discussed with detail about its operation, construction, and design development.

The Rollerscrew Structural Latch is a viable candidate for interface latching. Careful design and application are required to utilize the Rollerscrew as an autonomous latching/fastening device. The result of this effort promises a significant increase in reliability over standard nut/bolt fastener systems.

THERMALLY STABLE DEPLOYABLE STRUCTURE

Colleen M. Kegg*

ABSTRACT

A deployable structure which meets stringent thermal and strength requirements in a space environment has been developed. A mast with a very low coefficient of thermal expansion was required to limit the movement from thermal distortion over the temperature range of -200 °C to 80 °C to .064 cm (.025 in.). In addition, a high bending strength over the temperature range and weight less than 18.1 kg (40 pounds) was needed. To meet all of the requirements, a composite, near-zero CTE structure was developed. The measured average CTE over the temperature range for the mast was .70 x 10^{-6}/°C (.38 x 10^{-6}/°F). The design also has the advantage of being adjustable to attain other specific CTE if desired.

INTRODUCTION

ABLE's FASTMast (Patent 4,599,832) was used as a basis for the design (Figure 1). The FASTMast is built up from many pieces and its component nature allowed the design to be tailored to meet the strength and CTE requirement while minimizing the weight. The buckled bow rods shown in Figure 1 serve to preload the structure and remove play at the joints due to manufacturing tolerances which would also contribute to the deflection at the top of the mast. A lanyard deployment system was chosen over a canister deployment system to minimize both the weight and stowed volume. The mast and deployment system for a 230 cm (90 inches) high mast was kept below a weight of 18.1 kg (40 pounds) and a stowed height of 20.3 cm (8.0 inches).

CTE tests and strength tests were done to determine the optimum longeron design. A prototype model of the mast was built using aluminum and S-glass/epoxy to check the mast design and deployment mechanism.

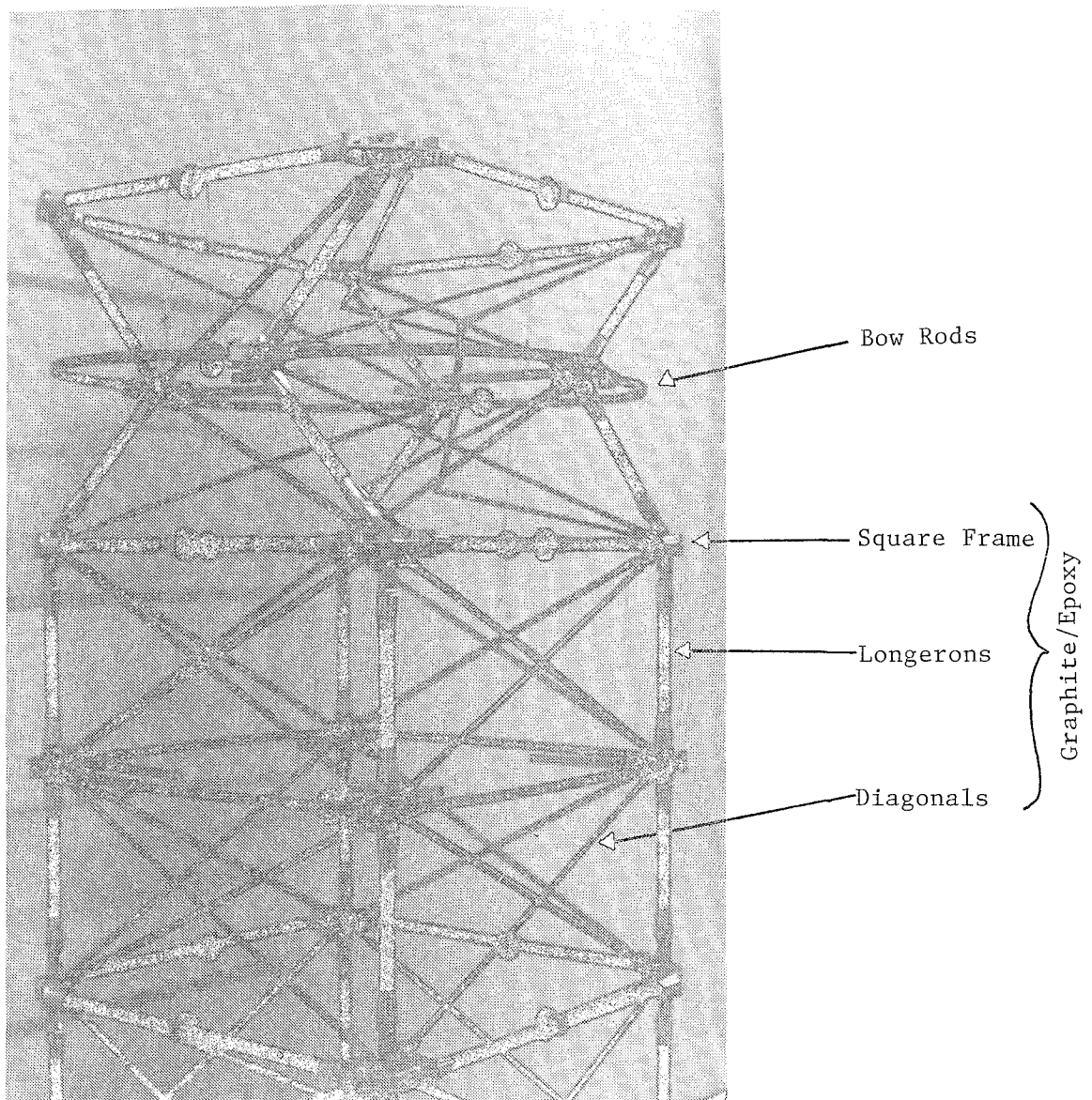* AEC-Able Engineering Co., Inc. (ABLE), Goleta, California

Figure 1. ABLE FASTMast

DESIGN CONSIDERATIONS

Thermal Distortion

The low CTE was required to limit the thermal distortion caused by the large temperature differences which can occur in structural elements in space. The two orientations of the mast to the sun shown in Figure 2 will cause the largest thermal differences and thus distortions. In one case the sun is shining directly onto one longeron while the longeron behind it is shaded. In the second case, the sun is shining directly onto one set of diagonals while the adjacent sets are shaded. The worst-case sun orientation is when both longeron shading and diagonal shading occur simultaneously. To meet the distortion requirement for this condition over the -200 °C to 80 °C temperature range, the mast could have a maximum CTE of $1.0 \times 10^{-6}/°C$ ($.56 \times 10^{-6}/°F$).

Strength and Stiffness

Each longeron had to have a strength of 10,700 N (2,400 lb) for the mast to have 6,770 N-m (60,000 in.-lb) bending strength. Full strength was required over the temperature range so the differences in CTE's between mating parts were critical. The stiffness was designed to be tunable; by using tubes for longerons, the inside diameter could be adjusted to change the stiffness without redesigning the mast.

Materials

P75 graphite epoxy was chosen for the primary members in the mast because of its low CTE of $-1 \times 10^{-6}/°C$ ($-.55 \times 10^{-6}/°F$) and low density of 1.6 g/cm³ (.058 pounds/inch³). In addition, it has a high strength of 8.6×10^8 N/m² (125,000 psi) and a high stiffness of 17×10^{10} N/m² (25×10^6 psi). It was used for the longerons, square frame and diagonals, as shown in Figure 1. Titanium was used for the large corner pieces because of its density and high strength. Titanium has a relatively large CTE of $8.3 \times 10^{-6}/°C$ ($4.6 \times 10^{-6}/°F$), but the corner pieces have a small effect on the overall CTE of the mast. S-glass/epoxy was used for the flexible bow rods which preload the structure but make no contribution to thermally-induced displacements.

Metal end fittings bonded to the graphite/epoxy were used because manufacturing the graphite with end fittings was expensive and limited the design flexibility. The longeron strength was limited by the strength of the metal to graphite bond so thermal compatibility between the two materials was important. Titanium was considered but analysis showed that its CTE would increase the overall CTE of the mast above the required value, and the strength of a titanium-to-graphite bond would be too low at -200 °C due to the differential CTE between the two materials. For a bond strength of 10,700 N (2,400 pounds), a minimum bond length of 2.3 cm

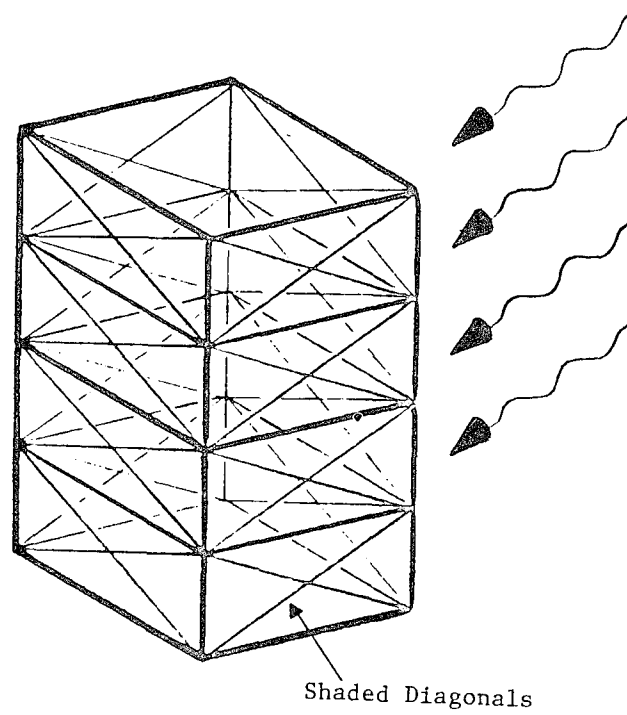Shaded Longerons

Shaded Diagonals
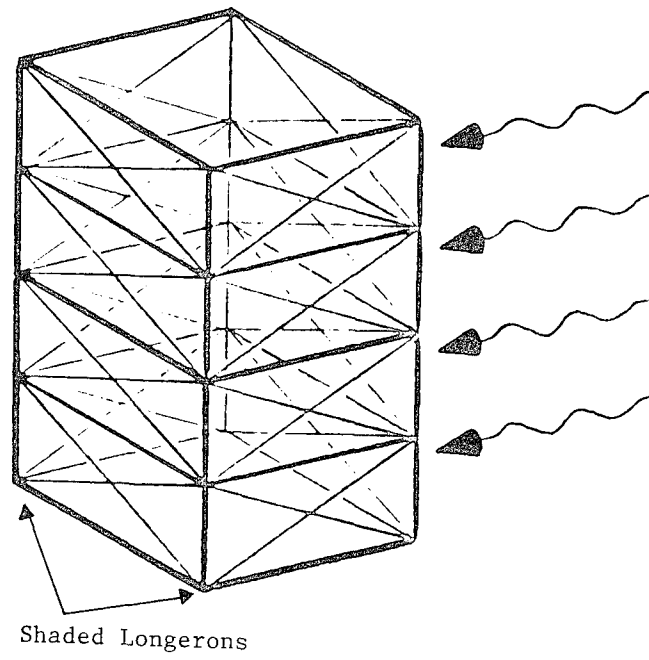
Figure 2. Mast to Sun Orientations

(.9 inches) was required. However, analysis indicated that at low temperatures, the differential CTE between the two materials along that length would cause shear failure in the bond. Invar was also considered because of its low CTE, $1.6 \times 10^{-6}/°C$ ($.9 \times 10^{-6}/°F$), although its density is almost twice that of titanium. The effective CTE and strength of the mast with each metal bonded to graphite had to be determined.

MATERIAL TESTS

CTE Tests

Samples of the two material options, titanium-invar-graphite and titanium-graphite, were made up as shown in Figure 3. Due to symmetry, it was only necessary to simulate a longeron for one half of a bay. The samples were sent to a CTE-measuring lab and the CTE's over the temperature range were determined.

The results of the CTE testing for the titanium-invar-graphite sample are shown in Figure 4. The CTE of invar varies with temperature[1] as shown in Figure 5, and the CTE data for the test sample tracks the characteristic curve for the thermal expansion of invar. The near-zero CTE between -60 °C and -10 °C lowers the average CTE over the temperature range to $.68 \times 10^{-6}/°C$ ($.38 \times 10^{-6}/°F$) and a smaller temperature range could result in an even lower CTE. The predicted CTE of $.25 \times 10^{-6}/°C$ ($.14 \times 10^{-6}/°F$) for the longeron agreed fairly well with the tested CTE. A CTE of $.68 \times 10^{-6}/°C$ ($.38 \times 10^{-6}/°F$) would result in .044 cm (.017 inch) movement at the top of the mast over the temperature range, which is less than the .064 cm (.025 inch) movement allowed.

Figure 6 shows the CTE test results for the titanium-graphite sample. A CTE of $2.56 \times 10^{-6}/°C$ ($1.42 \times 10^{-6}/°F$) was predicted and the tested CTE was $3.28 \times 10^{-6}/°C$ ($1.82 \times 10^{-6}/°F$) which would result in .21 cm (.082 inch) movement at the top of the mast over the temperature range. Further design work would be necessary if titanium were to be used since .21 cm (.082 inch) exceeded the maximum allowed movement. The CTE test results are summarized in Table 1.

---

1.   American Society for Metals, Metals Handbook, Vol. 2, 8th ed., 1961

Longeron (One Bay)

Titanium-Invar
Graphite Sample

Titanium-Graphite
Sample
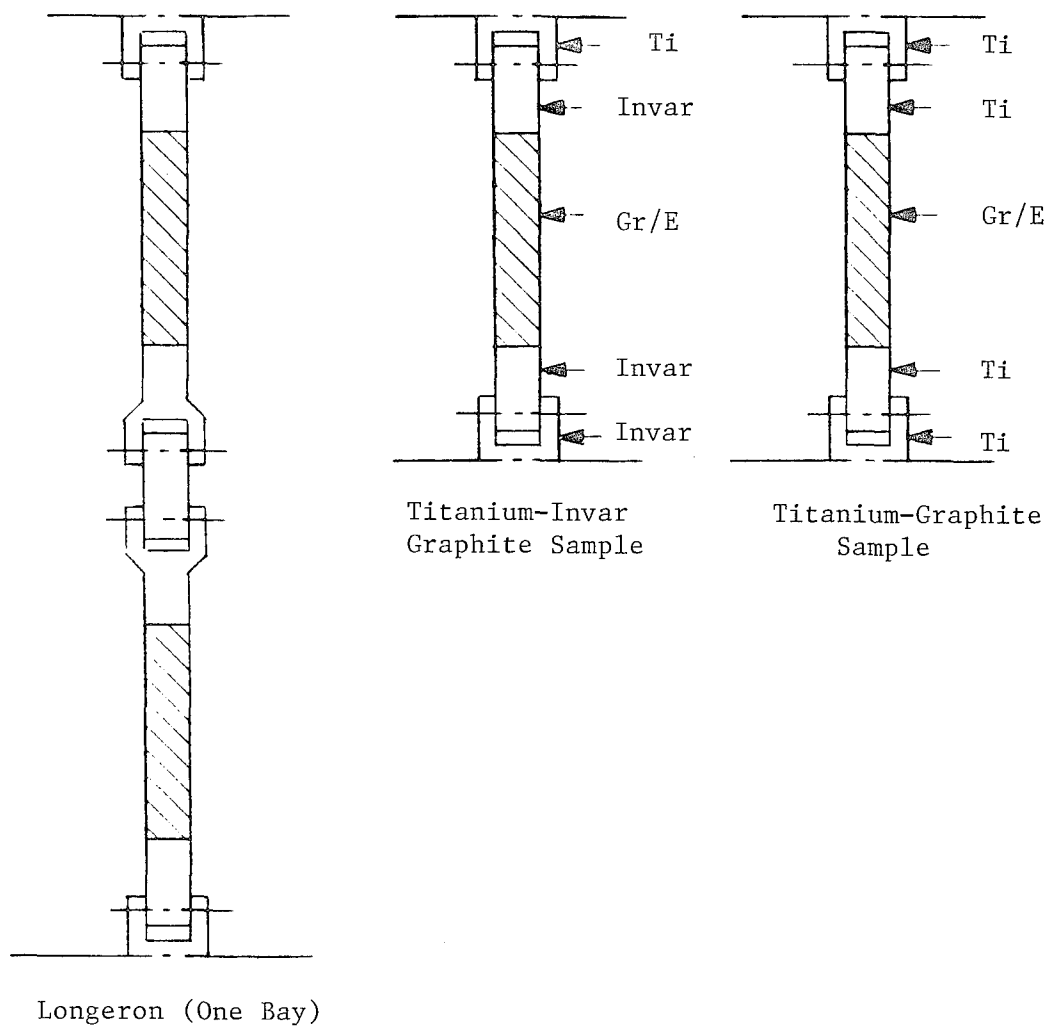
Figure 3. CTE Test Samples
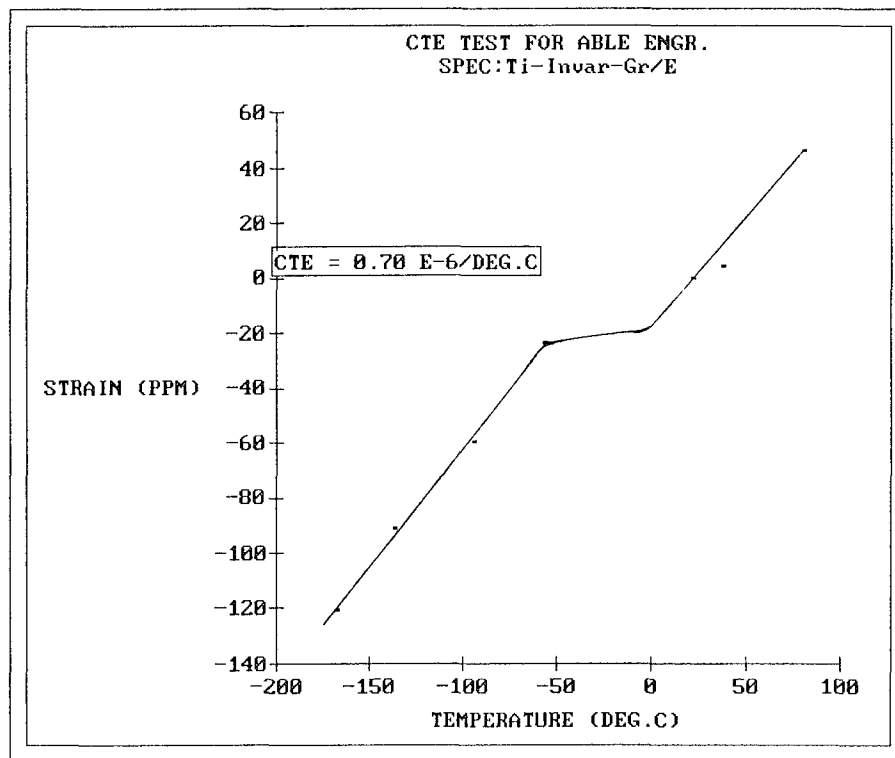
Figure 4.   Titanium-Invar-Graphite Test Results
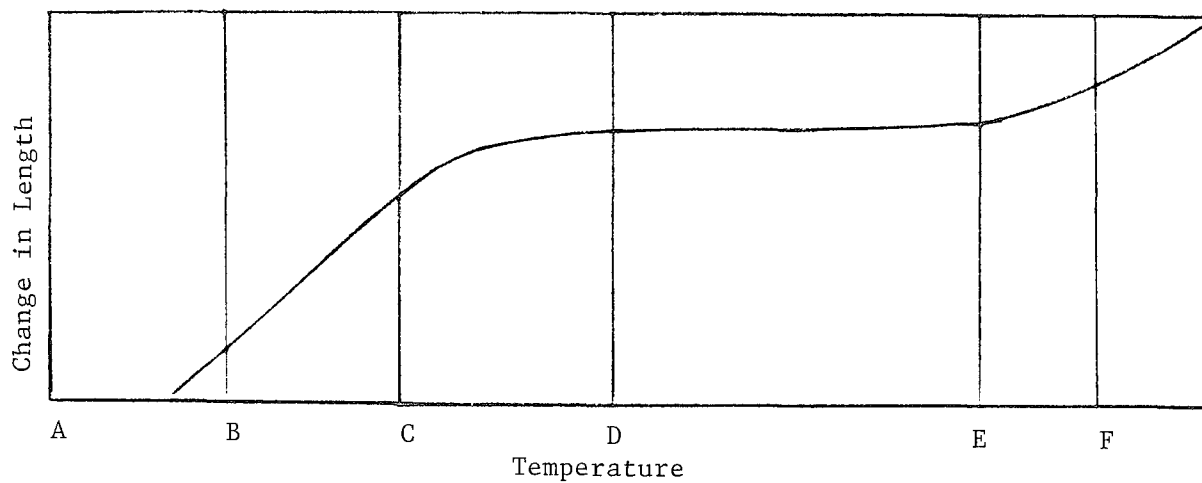
Figure 5.   Change in Length with Temperature of a Typical Invar

51
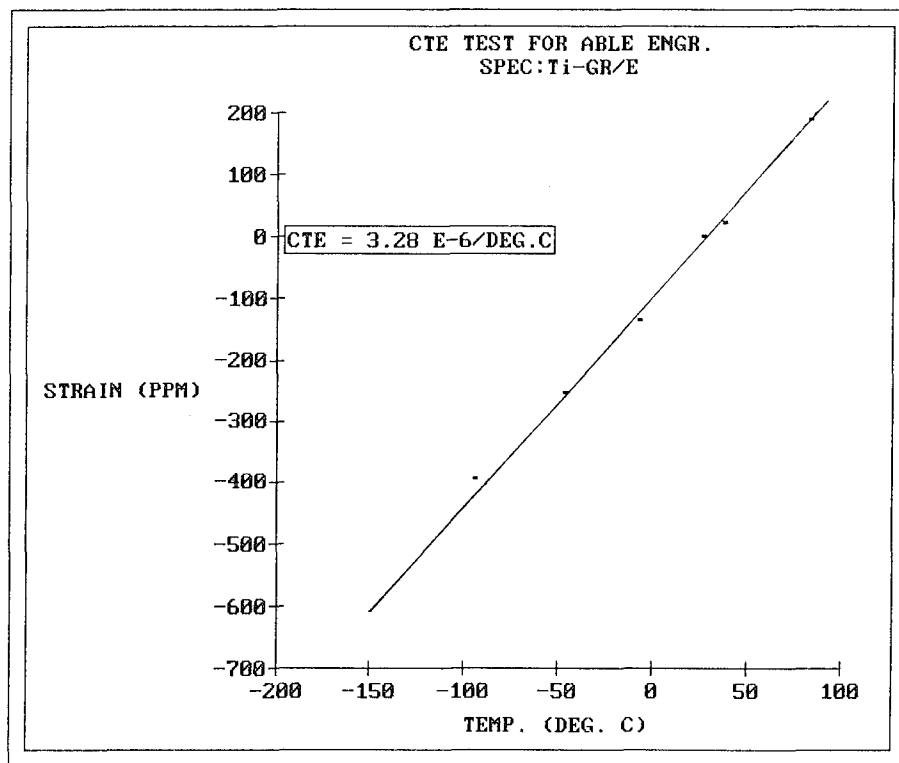
Figure 6.   Titanium—Graphite Test Results

Titanium-Invar-Graphite		
CTE Actual	$.68 \times 10^{-6}/°C$	$(.38 \times 10^{-6}/°F)$
Predicted	$.25 \times 10^{-6}/°C$	$(.14 \times 10^{-6}/°F)$
Calculated Movement	$.044$ cm	$(.017$ in.$)$
Titanium-Graphite		
CTE Actual	$3.28 \times 10^{-6}/°C$	$(1.82 \times 10^{-6}/°F)$
Predicted	$2.56 \times 10^{-6}/°C$	$(1.42 \times 10^{-6}/°F)$
Calculated Movement	$.21$ cm	$(.082$ in.$)$

Table 1.   CTE Test Results Summary

Bond Strength Tests

The strength of the epoxy bond between the graphite and metal end fittings was tested using the fixture shown in Figure 7. The fixture was placed inside a thermal chamber. Liquid nitrogen was sprayed into the chamber to achieve a low temperature of -190 °C and a hot air gun was used to raise the temperature to 80 °C. Thermocouples were used to monitor the temperature of the metal end fittings and the graphite. The LN_2 was regulated by a controller and the duty cycle was adjusted so that the temperatures for the graphite and metal end fittings were kept to within 2 °C of each other. A tensile load of up to 15,100 N (3,400 pounds) on the test samples could be applied with the gaged tensioning system. A bond strength of 10,700 N (2,400 pounds) was needed to meet the strength requirement for the mast.

Two bond configurations were tested and they are shown in Figure 8. With the tapered bond, the OD of the graphite bonding surface and the ID of the metal end fitting had a slight taper. The taper increases flexibility in the least loaded sections which encourages a more even transfer of load along the length of the bond. Bonding along the taper also meant that bonding occurred to some of the internal longitudinal fibers as well as those along the outside of the tube. The parallel bond, with the bond line parallel to the axis of the tube, was the second configuration. With this bond, the OD of the graphite and the ID of the metal fitting remain parallel with the axis of the parts but the inside of the graphite and the outside of the metal fitting are tapered to provide the same load transfer advantage as with the tapered bond. This type of bond has the advantage of the epoxy being entirely in shear where it has its greatest strength, and the overall length of the made-up tube is easier to control.

Test samples simulating the tapered bond proposed for the mast were fabricated from graphite tubing and both titanium and invar end fittings and tensile tests were conducted. At the same time the effect of thermal cycling was also tested by storing the test samples in the thermal chamber while the tests were being run. As a result, the untested samples were thermally cycled between room temperature and -190 °C. Test results are shown in Figure 9. The failure mode for all of the samples was a shear failure at the bond. The invar-to-graphite bond had strength well over the required 10,700 N (2,400 pounds), even at -190 °C. The strength of the titanium-to-graphite bond degraded rapidly as the temperature dropped and at -190 °C had a strength of only 1,780 N (400 pounds).
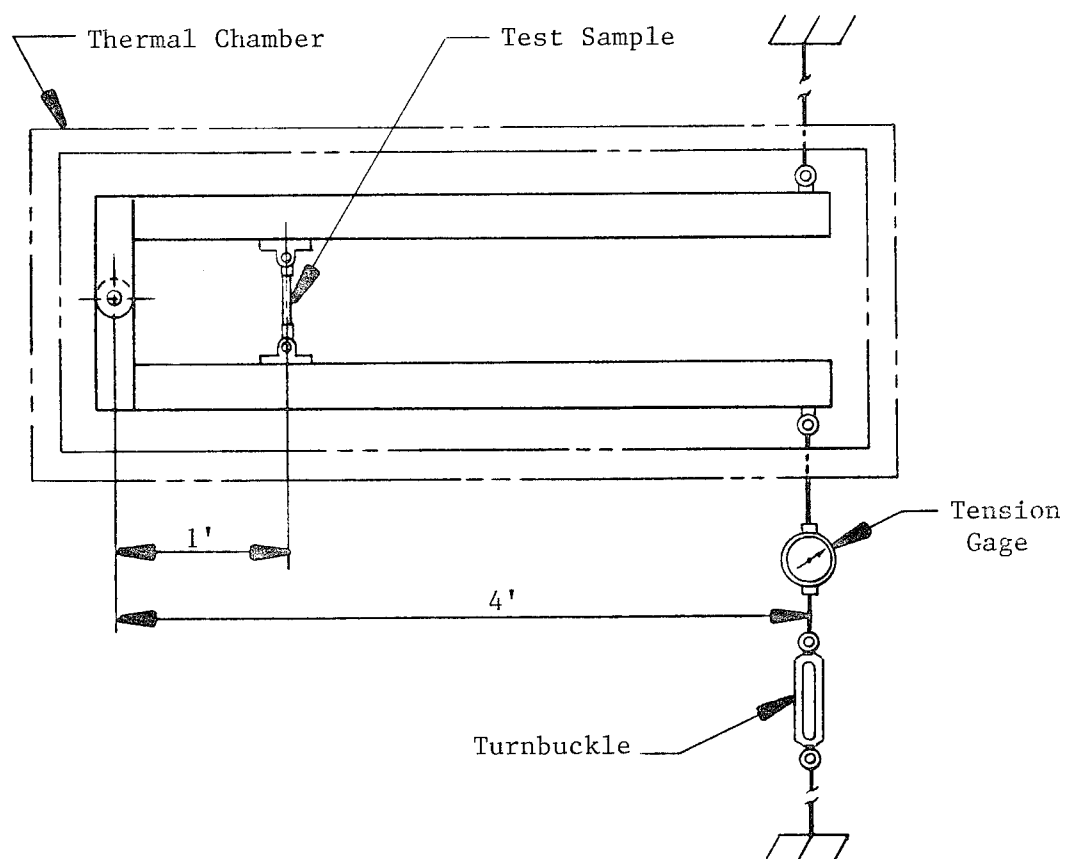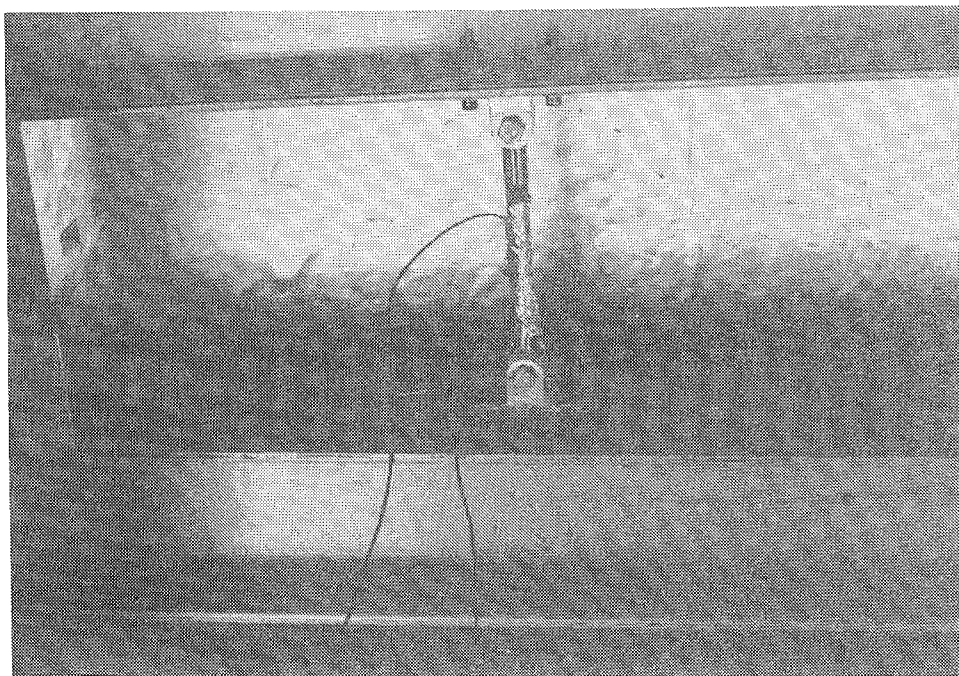
Figure 7.   Graphite to Metal End Fitting Bond Test

Parallel to
Axis Bond

Bond Line
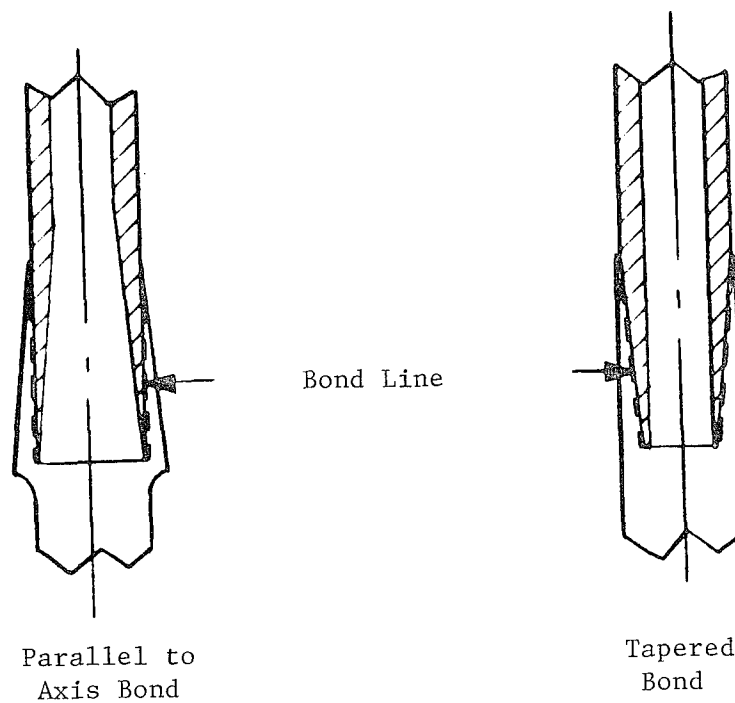
Tapered
Bond

Figure 8.   Bond Configurations
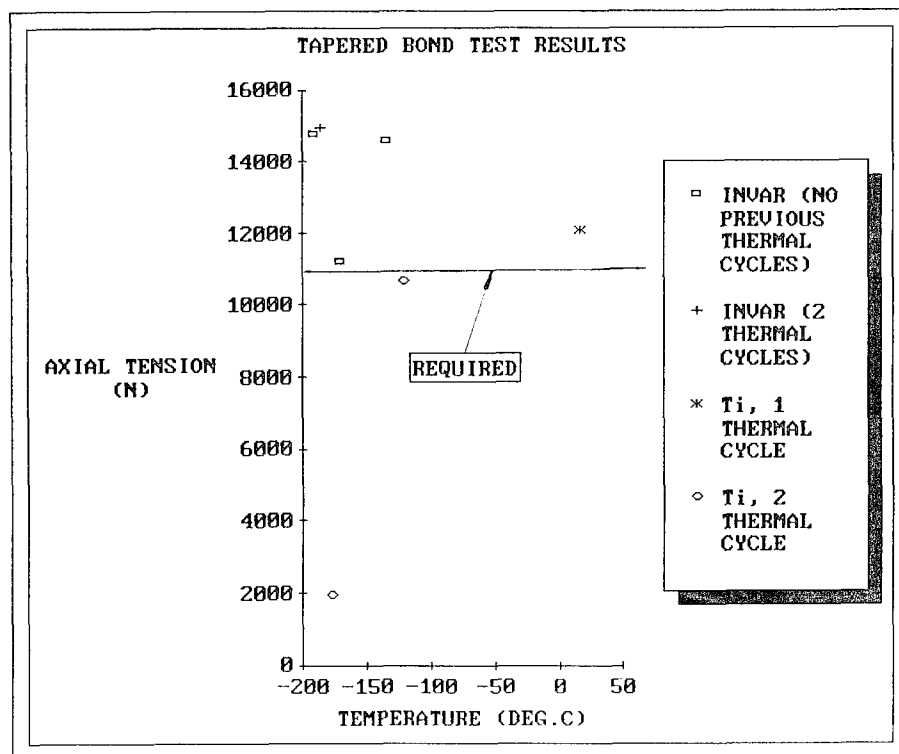
Figure 9.   Tapered Bond Test Results

Titanium-graphite test samples with a parallel bond line were fabricated in an effort to improve the strength of the titanium-to-graphite bond. Axial slots were cut in the end fitting to allow the metal to more easily conform to the radial contraction of the graphite since the radial CTE of graphite is fairly high, $32 \times 10^{-6}/°C$ ($18 \times 10^{-6}/°F$). The results are included with the results from the tapered bond test in Figure 10. The strength of the parallel bond was only slightly improved over that of the tapered bond at -190 °C and was lower than the tapered bond strength at the higher temperatures, potentially due to the decrease in bond area resulting from the axial cuts.

Conclusion from Testing

The trade study between invar and titanium end fittings showed that invar was the better material choice. The overall mast CTE was too large and the bond strength too low with titanium end fittings. Using invar instead of titanium increased the weight by 1.91 kg (4.2 pounds).

SUMMARY

CTE tests and bond tests verified that the FASTMast design could be tailored to fill the need for a deployable mast with a very low CTE and high strength over the temperature range of -200 °C to 80 °C. By combining materials with inherently low CTE, invar and graphite, for the primary mast members and judicious use of high CTE material with high strength, titanium, the CTE of the mast can be kept to a minimum while retaining high strength and low weight. Table 2 contains a summary of the requirements and the thermal and strength characteristics for the thermally stable mast which was developed.

The mast development is being continued. Improvements are being made to the lanyard deployment mechanism and the device which sequences the bay deployment.
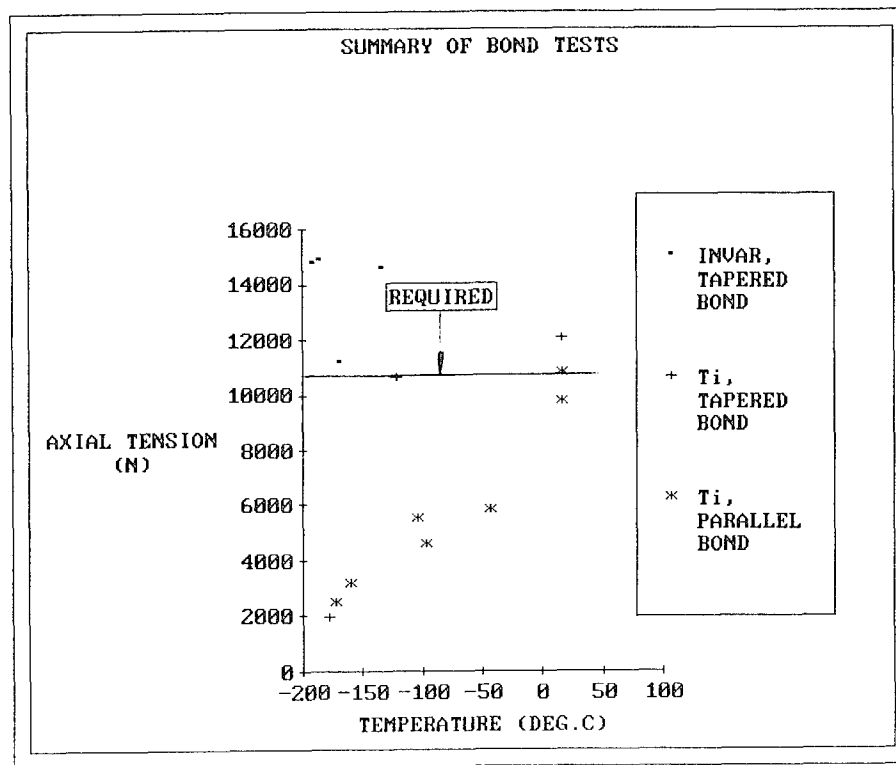
Figure 10. Bond Test Results Summary

	Required	Actual
CTE	$1.0 \times 10^{-6}/°C$ $(.56 \times 10^{-6}/°F)$	$.70 \times 10^{-6}/°C$ $(.38 \times 10^{-6}/°F)$
Maximum Distortion	.064 cm (.025 in.)	.044 cm (.017 in.)
Bending Strength	6770 N-m (60,000 in.-lb)	7950 N-m (70,500 in.lb)

Table 2. Summary of Requirements and Mast Characteristics

THE X-BEAM AS A DEPLOYABLE BOOM
FOR THE SPACE STATION

Louis R. Adams*

ABSTRACT

Extension of antennas and thrust modules from the primary structure of the Space Station will require deployable beams of high stiffness and strength, as well as low mass and package volume. A square boom cross-section is desirable for interface reasons. These requirements and others are satisfied by the X-Beam.

The X-Beam folds by simple geometry, using single-degree-of-freedom hinges at simple angles, with no strain during deployment. Strut members are of large diameter with unidirectional graphite fibers for maximum beam performance. Fittings are aluminum with phosphor-bronze bushings so that compliance is low and joint lifetime is high.

The several beam types required for different applications on the Space Station will use the same basic design, with changes in strut cross-section where necessary. Deployment is by a BI-STEM which pushes the beam out; retraction is by cables which cause initial folding and pull the beam in.

INTRODUCTION

The problems of launching and assembling the Space Station demand minimum package size and weight with maximum stiffness and strength. The design is shown in Figure 1 and embodies the following features:

- The mast articulation is the X-Beam version (patent pending) of the Astromast, shown in Figures 2 and 3, which has the following advantages:

  - Zero strain in the members during deployment allows use of large strut cross sections and high modulus graphite fibers.

  - Simple hinge angles minimize tooling costs.

  - High torsional and bending beam stiffness is maintained during deployment.

  - Maximum mast performance for minimum weight is achieved by using primarily unidirectional graphite fibers for all loaded members.

  - Diagonal members perform as compression and tension members so that only one diagonal is required per face, minimizing mass and maximizing stiffness.

---

*Astro Aerospace Corporation, Carpinteria, California

- The mast hinges are single-degree-of-freedom journal bearings, with precise steel pins turning in lubricated phosphor bronze bushings to produce minimum freeplay hinges, ensuring linear performance of the deployed structure.

- Mast fittings will be made from aluminum alloy in order to minimize weight and price.

- Minimum deployer weight and package size are achieved by eliminating the conventional canister deployer or external framework mechanism. Instead, a BI-STEM, a proven space mechanism, is used to push the mast out while retraction is achieved by pulling in on four lanyards.

X-BEAM CONCEPT

The X-Beam, shown conceptually in Figure 2, packages in a unique way in that frames consisting of longerons and diagonals rotate together to the packaged configuration. These load-carrying members have hinges only at their ends. The only folding members are the battens at alternating bays, which in this structure are unloaded, serving only to stabilize the nodal points where struts meet. Because the diagonals cross each other when packaged, fittings are required near each diagonal midpoint, and the beam name is derived because of this configuration.

The hinges which allow this packaging are all parallel to the batten members associated with the frames, and are therefore at very simple angles. Because the frames do not change shape during deployment, no strain occurs. The folding battens have hinges which are parallel to the beam axis and may fold inwardly or outwardly.

DESIGN ISSUES

Significant issues, and features of the design which address them, are as follows:

High Boom Frequency

Ultra high modulus graphite/epoxy composite materials are used in the longerons, thereby maximizing stiffness and minimizing mass. Non-straining deployment allows this feature.

Low Boom Mass

All strut members are graphite/epoxy, thus minimizing mass. Fitting designs are conservative but determined largely by axial strut loading rather than bending, so that mass requirements are relatively low.

Thermal Distortion

Use of graphite/epoxy struts and aluminum fittings produces a structure which is highly stable thermally. The low temperature excursions expected permit this material combination.

Deployment Reliability

Deployment is sequential as the boom is extended by a sprocket-driven BI-STEM, which is a space-proven device, and each double-bay module is restrained by an escapement mechanism. The number of hinge joints in the structure is minimal, and the hinged batten has a moment-generating hinge which drives toward deployment.

Retraction Reliability

Retraction of the boom is accomplished by a simple system of tethers passed through pulleys in the beam. The load lines generated ensure that a single bay retracts when tension is applied to the tethers. The critical tension required to retract a bay is set by design of the folding batten.

<div align="center">DESIGN</div>

Struts

Longerons are tubes and are hinged only at their ends. Diagonal struts are hinged at their ends and have central cross-over fittings for packaging. Batten A (rigid) struts are rigidly attached at structural nodes and are unhinged. Batten B (folding) struts are hinged at their ends and at their centers, so that they fold inward during packaging. Constant-moment torsion springs are incorporated in the Batten B center hinges to aid deployment.

Fittings

The various fittings, as machined for the prototype X-Beam, are shown in Figure 4. With the exception of the diagonal end fitting, all hinge axes are directed along major machining axes, so that no compound-angle machining is required. The hinge on the diagonal end fitting is oriented at a simple angle relative to the strut centerline. Hinges on all other end fittings are oriented orthogonally to the strut centerline. This simplicity of hinge angles is significant in minimizing complexity and cost of machining, and is also advantageous in terms of fitting stiffness. The proposed cluster fitting design at the rigid batten is shown in Figure 5.

The batten midhinge, shown in Figure 1, generates constant moment in the direction of full deployment. The torsion spring is rated at 3.6 Nm (32 in-lbf) and is of the negator type such that a short length of laminated spring is transferred from one spool to another. There are three major components: the spring and two joint bodies. The three hinges in the batten member (two

ends and mid) are configured so that a compressive load on the batten strut
generates a moment on the midhinge which is in the direction for folding. In
this way, internal loading only is required for retraction; no mechanism is
needed to fold the batten.

DEPLOYMENT

The method of deployment is shown in Figure 1. The stacked portion of
the boom feeds out with the payload two bays at a time, pushed by the
BI-STEM. The boom-to-Space Station interface stiffness is therefore not
degraded during deployment. The outboard end of the boom, however, is
degraded due to the two bays in transition. The stiffnesses of the BI-STEM
and of four longerons in bending are sufficient to provide a minimum outboard
natural frequency of about 4 hertz for the stacked starboard antenna boom
with its 454-kilogram tip mass.

Axial deployment force (about 450 N) is provided by a sprocket-driven,
tabbed, 35-millimeter-diameter BI-STEM which extends up the center of the
boom. The positive nature of the sprocket drive ensures that the stated
force level is achieved; periodic tabs along the internal element of the
BI-STEM prevent rotation relative to the outer element, so that structural
integrity is preserved. The BI-STEM is stabilized every two bays against
lateral deflection by close-fitting rings suspended in the centers of the
rigid batten frames. Sequential bay deployment is assured due to an
escapement mechanism through which each batten frame must be pulled.

RETRACTION

In Figure 6, the method of retraction is shown. Beryllium copper ribbon
cables, which are fed out with the beam during deployment, provide retraction
forces in a sequential fashion due to the path they follow through the boom.
The BI-STEM which deployed the beam is retracted in concert with the retract-
ing boom. The mid-battens fold inward so that utility lines are not
disturbed. The sequence of events, repeated until full retraction, are

1. Mid-battens of double-bay module nearest stack are folded by inter-
   nal loading (225 N tension required per ribbon cable).

2. Double-bay module and associated utilities retract.

3. Boom is pulled through escapement (23 N tension required per ribbon
   cable).

4. Packaged double-bay module seats on stack.
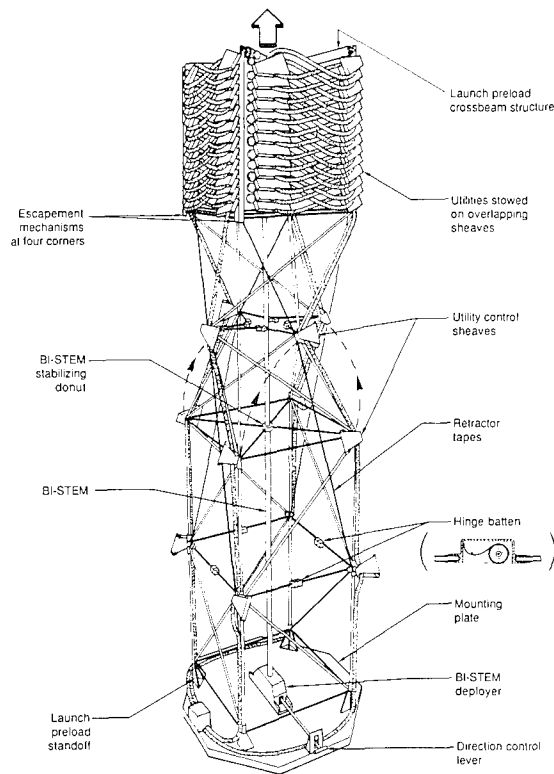
Figure 1. Space Station deployable boom.
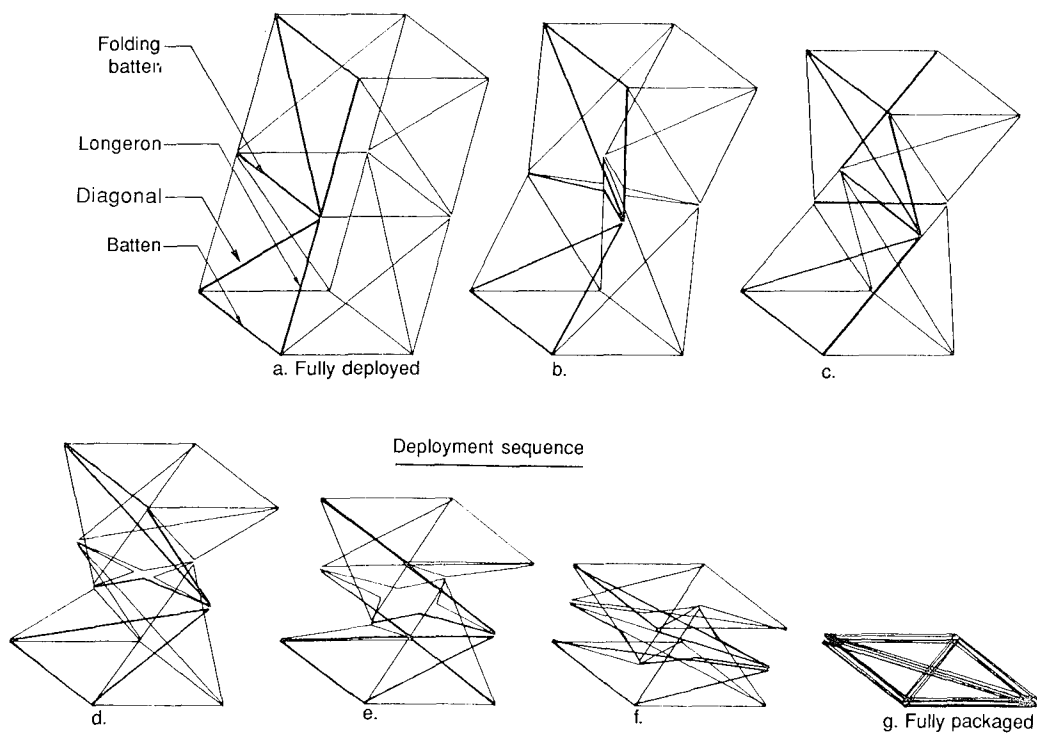
Figure 2. X-Beam concept.

63
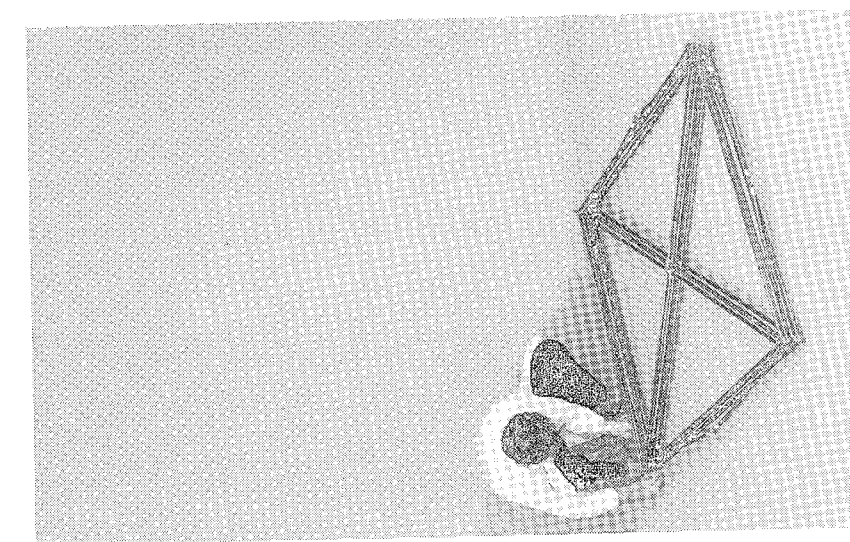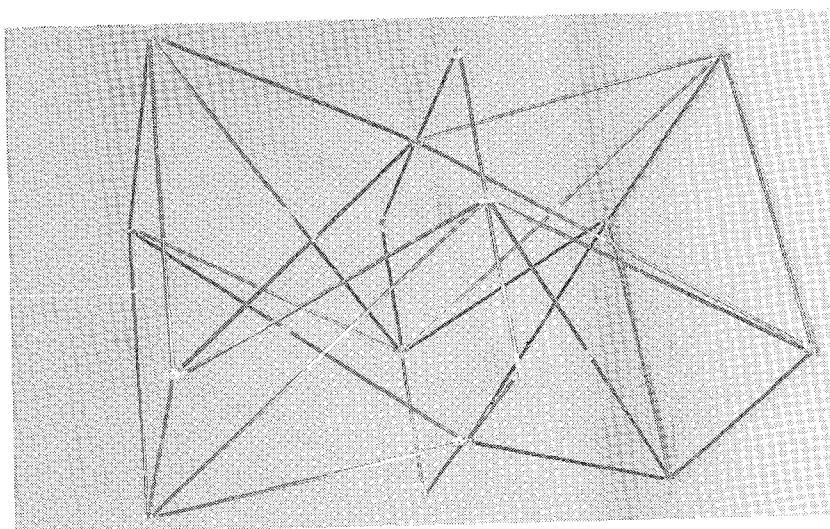
a. Packaged

b. Mid-deployment
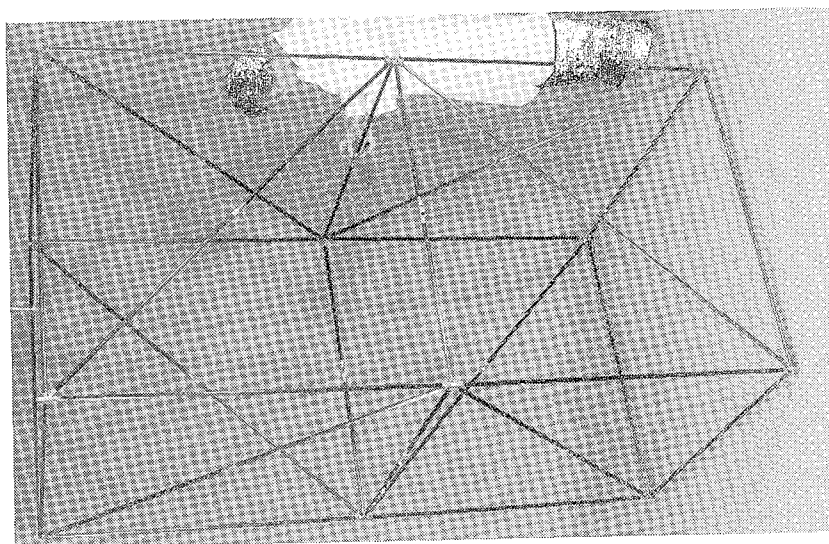
c. Fully deployed

Figure 3. X-Beam prototype model, with outwardly-folding mid battens.
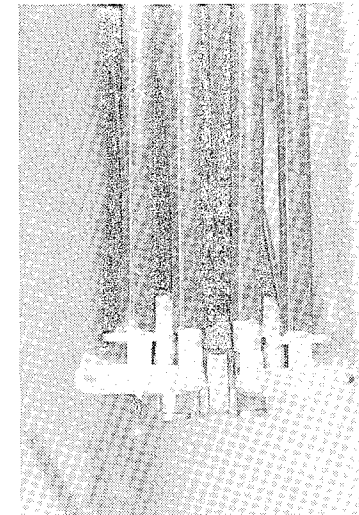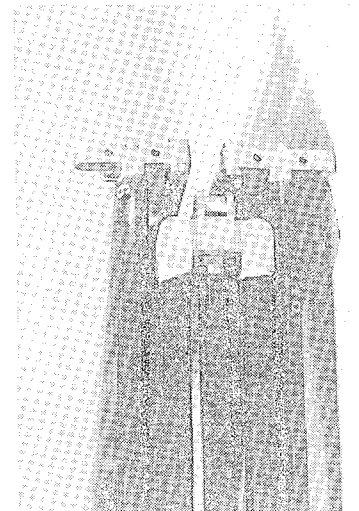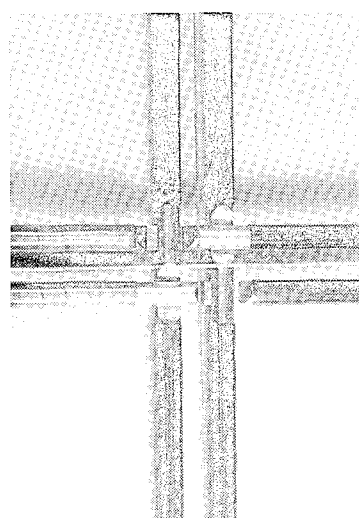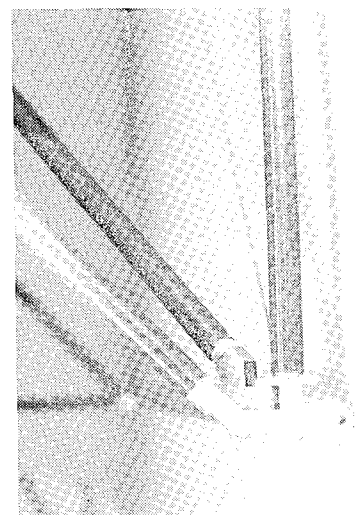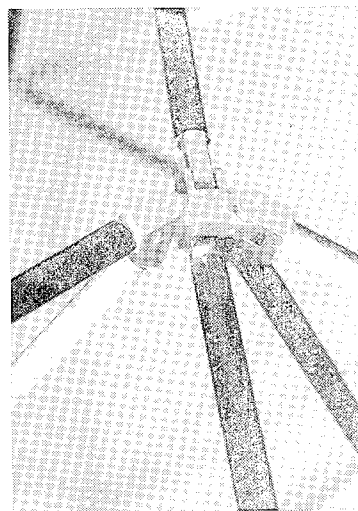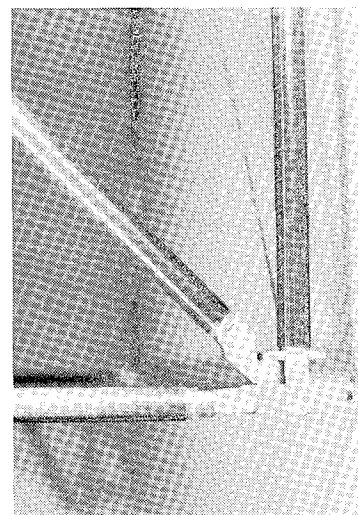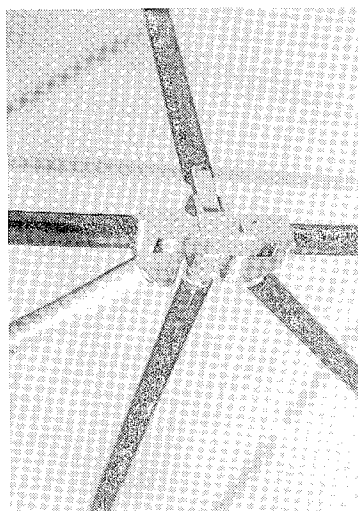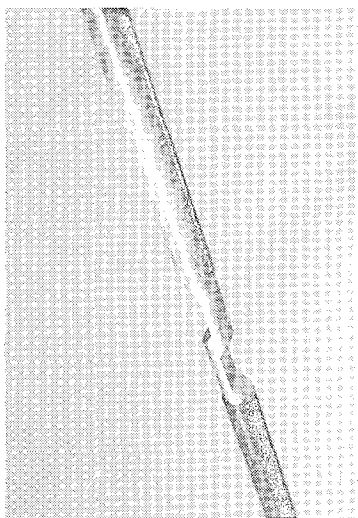
Diagonal cross-overs

Mid cluster

Base hinge cluster

a. Deployed

b. Deploying

c. Packaged

Figure 4.   X-Beam prototype hinge fittings.

65
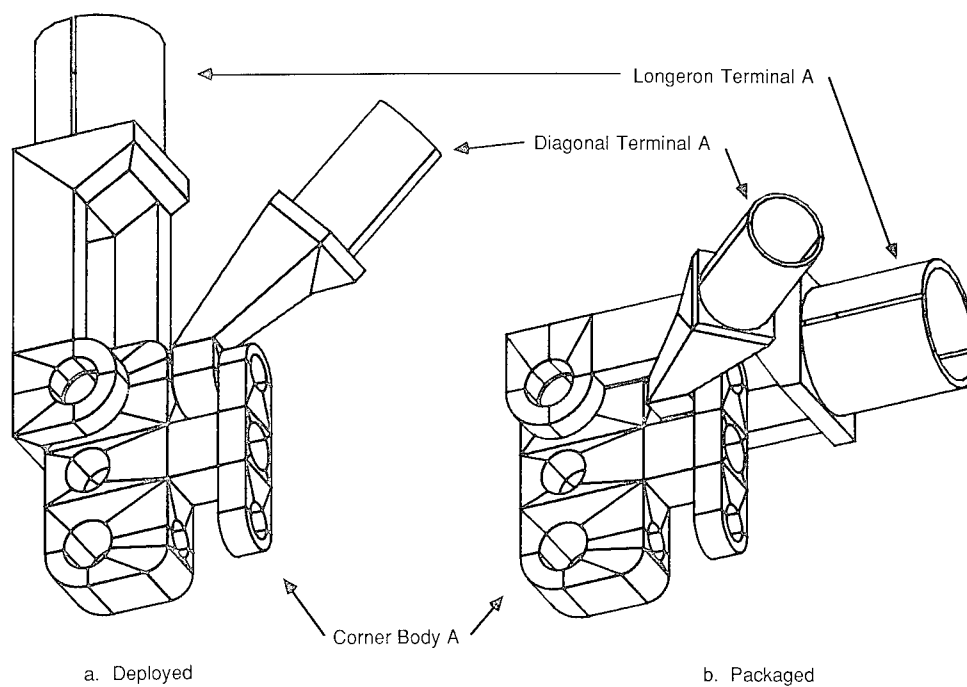
Figure 5. X-Beam Cluster A (at rigid batten).
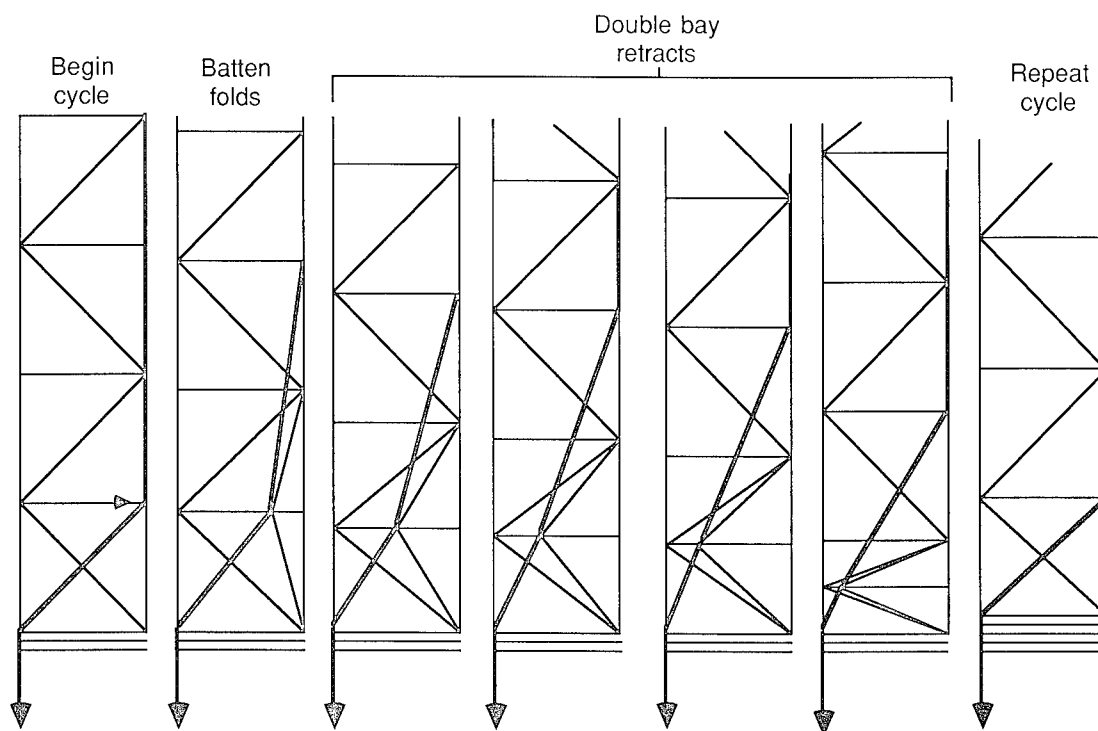
Figure 6. Retraction by ribbon cables.

MOTION SYNCHRONIZATION OF A MECHANISM

TO DEPLOY AND RESTOW A TRUSS BEAM

M. Lucy[*]

ABSTRACT

The functions of the Control of Flexible Structures I (COFS I) deployer and retractor assembly (DRA) are primarily to deploy and retract the Mast 1 beam, and secondarily to latch, unlatch, and restow the DRA mechanism. The objective of this paper is to present the problems associated with the diagonal folding mechanism that retracts the beam, discuss the synchronization requirements critical to the process of restowing the beam, and to present a proposed solution to the problem of synchronization between the mechanical systems. In addition, this paper presents a detailed description of the design and functioning of the DRA.

INTRODUCTION

Future space missions are anticipated to require large truss platforms and beams for a number of structural applications. Under a Control/Structures Interaction (CSI) effort, there is being developed a validated technology data base which includes the areas of controls and structures interaction, deployment dynamics, and system performance for large flexible spacecraft.

The NASA initiated COFS Program, a major element of the CSI effort (figure 1), provides focus for the research and technology base activities in structural dynamics and controls. These activities address technology needs through the development and validation of analytical tools, extensive ground testing of representative structures, and performance of in-space experiments for verification of analysis and ground test methods.

Under COFS, the COFS I Project, involving the space structures and controls research community, consists of a series of planned ground and flight activities that progressively build from large space systems modeling and dynamic characterization to evaluating the more complex issues of flexible-body control.

As a subset of COFS I, the Mast Flight System (MFS), figure 2, incorporating a reusable, generic deployable-restowable truss beam as a test bed, was conceived to bridge the gap between ground and on-orbit verification, and validation of structure and control methodologies. This single test article was planned for use

---

*NASA Langley Research Center
    Hampton, Virginia

in the ground test and two flight tests. The objectives of the two flight tests were to evaluate system identification open-loop dynamics and distributed flexible-body closed-loop controls, respectively.

The sections that follow describe the Mast subsystems involved with the various motion synchronization issues and their possible improvement.

DESCRIPTION

Several subsystems comprised the MFS which was being developed by the prime contractor, the Harris Corporation (figure 3). These were designated as the Integrated Mast Subsystem (IMS), Mast Support Subsystem (MSS), Modular Distributed Instrumentation Subsystem (MDIS), Excitation and Damping Subsystem (EDS), and Power Distribution Subsystem. The IMS was composed of four functional components: the beam, parameter modification device (PMD), motor controller (MC), and deployer and retractor assembly (DRA). The beam, PMD and DRA were to be provided under subcontract by Astro Aerospace Corporation. The MFS's DRA, containing a large deployable and restowable "next-generation" truss beam, was to be attached in a cantilever fashion to the carrier. The carrier was the Spacelab Enhanced Multiplexer Demultiplexer/Space Technology Experiments Program pallet (EMDM/STEP). The carrier would, in turn, be attached within the Space Transportation System (STS) Orbiter payload bay. A detailed discussion of the IMS beam and DRA follows.

Beam

The Astro Aerospace Corporation's Articulating Astromast beam, also referred to as the Z-beam, is shown in figure 4. The beam was a statically determinate, 60.7m long, non-redundant, truss structure that incorporated single degree-of-freedom (d.o.f.) hinges for deployment and retraction. Longitudinal members (longerons) provided bending stiffness and were hinged only at their ends. Alternating diagonal members (diagonals) provided torsional and shear stiffness and were hinged at their ends and near their centers. Transverse members (battens) were positioned at regular intervals along the beam to assure longeron stability. The "B" frame battens were hinged at their ends and near their centers while the "A" frame battens were rigidly attached to the beam nodal (corner) bodies. All beam elements were composed of graphite/epoxy tubes bonded to titanium end fittings. The beam design consisted of a triangular cross section with the longerons located at the vertices of an equilateral triangle. The truss structure repeated itself in two-bay segments. There were 27 repeatable two-bay (bay-pair) segments for a total of 54 bays. Pertinent beam specifications are listed in Table I. This design was specifically chosen for low member loads induced during the deploy and restow process.

The single d.o.f. hinges were designed for low compliance and minimum free play. These hinges also provided control over the kinematics of the structure during deployment and retraction. For this truss configuration, single d.o.f. joints produced strains, derived from moments (figure 5), during deployment and restow, and this effect was quantified and accounted for in terms of induced loads and sizing of members. When compared to other possible configurations, the unique design and folding geometry of the Z-beam minimized the

68

induced strains and eliminated the need for swivel joints. The spatial motions of a typical pair of diagonal hinges, a "B" batten hinge and a "B" corner body are shown on figure 6. Astro's kinematic modeling efforts involved in-house developed code while Langley's verification efforts have utilized ADAMS* code.

The beam was deployed two bays at a time by rotating the longerons of a bay-pair approximately 90° to their upright position. Simultaneously, the diagonals unfolded and were locked in place by mid-span spring-loaded hinges. No net beam rotation was experienced during deployment and restow due to the alternating directions of the diagonals in a bay-pair.

During the process of deployment and restow, the design of the Z-beam necessitated that the "B" batten frame experience large deformations. Mid-span hinges were incorporated in the "B" batten members to permit these large defor-mations with relatively low strain being induced in the truss members (the diago-nals being strained more than the other beam members). The geometry of the truss beam allowed its members to be strain free in the deployed and stowed con-figurations.

The beam stowed efficiently with symmetric (alternating clockwise and counter-clockwise) folding of the longerons about the longitudinal axis. The diagonals and "B" batten frame members were folded at mid-span to allow packaging. The basic packaging of the beam reduced the length to 3.51 percent of the deployed length.

Actuators, instrumentation, and avionics necessary for excitation, measure-ment, and control of the low-frequency modes of this structure were an integral part of the flight system. The truss beam also contained a PMD at the tip which provided the capability of changing the tip inertia during on-orbit testing. This allowed alteration of the frequency spacing and cross axis coupling between modes.

The effective stiffness, coefficient of thermal expansion (CTE) and buckling loads for the truss member assemblies are listed in Table II.

Deployer and Retractor Assembly (DRA)

The DRA was a mechanical device to deploy and retract the beam during orbital operations. The design consisted of a structural container for the beam, an upper drive assembly containing the mechanisms necessary for deployment and restow, a diagonal fold-arm retractor mechanism, telescoping support tubes attached to a base plate, and latch cluster assemblies (not shown) (figure 7). The deploy and restow mechanism (lead-screw drive system) and diagonal fold-arm mechanism (bell-crank linkage system) were housed in the DRA upper drive assembly (figure 8). The stiff, reinforced tubular structural framework (figure 9) was to be covered by a honeycomb shell.

---

*Automatic Dynamic Analysis of Mechanical Systems, Mechanical Dynamics, Inc., Ann Arbor, Michigan

The DRA had to execute four different operations (DRA extension, beam deployment, beam retraction, and DRA restow). There were basically five different mechanisms incorporated in the DRA to perform these operations and the mechanisms incorporated a total of eleven pairs of D.C. motors. Both motor windings of any pair of motors were powered by independent driving sources so that a single failure in the MC (or MDIS computer) would not prevent retraction and restow of the beam.

The DRA deployment and retraction mechanism consisted of a deployer drive motor and gear box, a continuous loop gear and shaft power transmission system, three lead-screw drive assemblies and lead-screws, and a stowed beam stack lifting assembly (not shown). The lead-screws were driven by an assemblage of gearing and six shafts (figure 8)--the latter identified as a recirculating gear arrangement. At each alternate bevel gear cluster, a power take-off drove the lead-screw. This recirculating arrangement of gears and shafts was selected to minimize backlash and permit redundancy in the power transmission path from the deployer drive motor to the lead-screws.

The three synchronized lead-screws engaged partial nut fittings at the beam "A" batten cluster hinge assemblies (corner bodies). Constant rotation of the lead-screws caused bay-pairs to be sequentially deployed and deployment and retraction were continuous. Each deployed bay-pair achieved full structural integrity before exiting the DRA. The deployment process could be stopped at any two-bay increment and the beam locked in place to provide a direct load path through the MSS to the carrier. To minimize the overall height of the experimental MFS package, the DRA itself was stowed and extended using the same lead-screw mechanism.

Deployment of the Mast

Illustrated in figure 10 is the general sequence for deployment of the beam. All DRA functions would be checked prior to committing the DRA or beam to deployment. During deployment, all beam electronics would be active thereby enabling ground personnel to monitor beam acceleration. The sequence was as follows:

The first operation in the deployment was the release of the DRA from its preloaded, stowed configuration by functioning the stowage latch. This swivel latch (figure 11), which holds down the upper drive and tip assemblies, would translate while rotating 90° (using a cam action). This released the preload and provided clearance between the upper drive and beam tip canister assemblies during deployment. Functioning the stowage latch only released the upper drive assembly as the tip canister assembly was still being held down by the tube latch.

The deployer drive motor was operated to start turning the lead-screws in a direction that would elevate the upper drive assembly while simultaneously extracting the lead-screws from the stacks of stowed beam partial nut fittings. This operation extended the DRA's telescoping tubes (figure 10). At maximum extension, the deployer drive motor would stop and the tube latches (figure 12) would lock-up the telescoping tubes. Functioning of the

tube latch would also unlock the beam tip canister assembly retention latch, thereby freeing the stowed beam tip canister assembly.

To raise the tip canister assembly and initiate beam deployment, the deployer motor was reversed and began lifting the beam's first set of "A" corner bodies. When the tip canister assembly reached a position near the top of the DRA's upper drive assembly, the longerons of the first deployed bay-pair were vertical. Contined deployer motor operation caused the extended longerons to pull the next set of "A" corner bodies past detents (figure 13) and onto the bottom of the lead-screws. As will be described later, the spring loaded diagonal hinges acted as energy stowage devices which assisted beam deployment, therefore some space was provided between the detent and stowed beam to allow for this final bay-pair deployment action. Each detent was designed to release the "A" corner body at about 100N of force. The DRA then, in a continuous manner, extended the first deployed bay-pair out of the DRA while the next bay-pair was being deployed within the DRA. Bay-pairs were deployed until the required number of extended bays was reached.

During deployment and retraction, a device called an off-loader (stack lifter) (figure 14) would move the stack of stowed bays toward or away from the deployment and restow mechanism, respectively. The stack lifter, being mechanically slaved to the lead-screw, would prevent partial bay deployment within the stowage canister.

When the required even number of bays had been deployed, the beam latch (figure 15) would be engaged. This latch would transfer any loads from the beam directly into the DRA base structural tube and hence to the Orbiter through the MSS structure and the carrier.

Retraction of the Mast

For retraction, the process was essentially reversed from that for deployment except the diagonal folding mechanism was activated to unlatch and initiate the opening of the diagonal hinges.

Retraction of the Mast began with unlocking the beam latch and operating the lead-screws in the opposite direction from that of deployment. While this operation was under way, the separate diagonal folding mechanism (figure 8) activated the upper and lower diagonal fold-arms to initiate unlatching and opening of the diagonal mid-span hinges and also began simultaneously folding the six diagonals. A compressive load was introduced into the "B" batten member which, in turn, caused the batten to fold at its mid-span hinge.

The fold-arms initiated the diagonal hinge folding action by releasing a secondary mechanical hinge latch and then they began pressing inwards on the hinges. This hinge is a separate mechanism and will not be described in this paper. The fold-arms were most effective only during the initial stages of

restow of a given bay-pair, then they were recycled to their retracted position. In figure 8, the diagonal folding mechanism drive motor activated the diagonal fold drive gear which in turn functioned a continuous loop of bell-cranks and coupler links. At every other bell-crank, linkages led to the upper and lower diagonal fold-arms (a typical set of fold-arms is shown for clarity). These fold-arms pressed on the diagonal hinges during the initial stages of each bay-pair's retraction process.

At the final stage of restow, the tip canister assembly would be retracted. The tube latches would unlock the tubes and simultaneously lock the stowed tip canister assembly. The direction of lead-screw rotation would then be reversed to return the DRA to the stowage position. This final motion would also pull the upper drive assembly down toward the stowed tip canister. Stowage latch actuation subsequently would lock the upper drive and tip canister assemblies.

Table III presents a listing of the status monitoring instrumentation signals that were to be passed to the MDIS computer and which were needed to synchronize and control functioning of the DRA.

If allowable limits were exceeded at any time during deployment or restow, the process would have been automatically interrupted by the MDIS/MC combination. Retraction could be reinitiated at any time by the flight crew. Starting the retraction process would require that the diagonal folding mechanism be cycled back to its retracted position, had it moved, and that the beam would have to be deployed to the next even bay-pair. Once fully retracted, the packaged beam would have been preloaded within the DRA by the clamping action of the stowage latches.

ON THE PROBLEM OF SYNCHRONIZATION DURING RESTOW OF THE BEAM

Conceptually, beam bay-pair restow could have been accomplished by any of three methods, used singly or in combination. The three methods were: rotation of the "B" batten frame with respect to the "A" batten frames (required large displacement mechanisms and would produce high member loads), forcing the upper three "A" corner bodies downwards (required introduction of excessively high loads in the members sufficient to affect diagonal hinge opening), and pushing inwards or applying a torque across the six diagonal mid-span hinges (required large displacement mechanisms and would produce low member loads). A combination of the latter two methods was selected for simplicity and minimum energy expenditure.

It was analytically determined that the fold-arm mechanism required the least amount of energy to affect bay-pair restow during the first 25° of diagonal hinge rotation. This mechanism was designed to apply the necessary forces at the proper point of contact on the diagonal hinge while tracking the path of required spatial motion. Figure 16 presents the torque required to open the diagonal hinge. It was necessary to synchronize the movement of this mechanism with the restowing beam bay-pair member spatial motion that would be associated with the constant rotation of the lead-screws. At the beginning of bay-pair retraction, the lead-

screws started turning to push the "A" corner bodies downward while the lower set was being restrained by the detent device. Simultaneously, the upper and lower diagonal fold-arms began to press on the diagonal hinges. This combined action continued for the first 25° of diagonal hinge rotation. At the 25° position, the constant drive lead-screw mechanism became the most energy efficient restow method; therefore, the fold-arms were disengaged to be recycled back to their retracted position while the lead-screws continued to press downward on the "A" corner bodies. Once the upper and lower "A" corner bodies came together, continued lead-screw rotation drove the lower set of corner bodies past the detent. At that point, a new set of "A" corner bodies was engaged at the top of the leadscrews and the process repeated itself. The synchronization of these functions is extremely crucial.

Suppose, for example, the diagonal fold-arms were not synchronized kinematically and began pushing on the diagonal hinges before lead-screw motion began reducing the distance between the upper and lower sets of "A" corner bodies—the lower set being either still on the lead-screws or restrained by the detents. Conceivably the joints and/or members within the retracting bays could become subject to high loads and hence, the possibility of failure. On the other hand, if the diagonal fold-arms were late in pushing on the diagonal hinges, the downward force on the "A" corner bodies could cause excessive loadings leading to buckling of the longerons or could force the lower set of corner bodies past the detents.

This problem of synchronization arises from the fact that two independent displacement inputs into a single d.o.f. mechanism are being specified. A simple equivalent illustration (figure 17) follows:

Suppose one wishes to apply two displacement inputs into a four-bar linkage. Since a four-bar linkage has only a single d.o.f., a specification of angle θ will give rise to an angle $\hat{\phi}$. If ϕ were specified as well and is different from $\hat{\phi}$, excessive loadings on the joints, buckling of the coupler link, or even bending of the other links may result. In the MFS, such excessive loading could cause failure in any of the beam members or any element of the deployment and restow or diagonal fold-arm mechanisms.

In the same manner, for the lead-screw and diagonal hinge motion synchronization, there exists a 1:1 kinematic relationship between the rotation of the lead-screw and the displacement of the diagonal hinge. If the motion of the diagonal folding arm does not coincide with the displacement of the diagonal hinge for a given lead-screw rotation, then either:

1. The fold-arms are not pushing on the diagonal hinges (and may cause buckling of the longerons at the initial stages of retraction) or

2. The fold-arms are pushing with an excessive force (and may cause failure of the pin joints or bending of some of the battens or longerons).

73

A SOLUTION TO THE SYNCHRONIZATION PROBLEM

In this writer's opinion, it is highly improbable that such closely synchro-
nized motions between lead-screw rotation (and hence, "A" body translation) and
fold-arm actuation of the diagonal hinges can be achieved. Based on a combined
kineto-elastostatic model of the Mast Z-beam and DRA design, optimization tech-
niques should first be applied to the model to minimize the differences between
the desired fold-arm motion and the actual motion. Subsequently, to account for
these differences, it is recommended that a flexible member (such as a constant-
load spring) be incorporated at the point (area) where the diagonal fold-arm pad
is to contact the diagonal hinge such that the remaining differences between the
motions do not result in excessive joint and member loadings. This approach
would prevent the problems stated above. The theoretical basis follows:

> Using the four-bar linkage analogy illustrated earlier (figure
> 17), one would specify the displacement θ to the input link and a
> displacement $\hat{\phi}$, not equal to the displacement, ϕ, of the output
> link. However, the shaft that is connected to the output link is
> flexible such that $\hat{\phi}$ and ϕ, though different, are taken up by the
> flexibility. This flexibility of a member is equivalent to that to
> be attached to the diagonal fold-arm.

A proposed solution would be to design into the flexible element of the
diagonal fold-arm, preferably a constant-load spring effect, then one would not be
loading up the beam elements excessively, thereby increasing reliability.
Furthermore, it is recommended that an optimized system design be performed to
ensure that diagonal fold-arm movement and diagonal hinge motion are sufficiently
close to each other.

SUMMARY

In a complicated mechanism such as the DRA, it is desirable to simplify the
general essence of the mechanical movements of subassemblies. For the particular
case of the beam retractor linkage, the motion of the "A" corner bodies and the
synchronized motion of the diagonal fold-arms in relation to the spatial motion of
the diagonal hinges may be difficult or impossible to achieve. With an analogy to
a four-bar linkage (also a single d.o.f. system), a simple approach (such as use
of a constant load spring) may minimize the loads due to motion errors during the
retraction synchronization process. This constant load spring may relax the
synchronization dimensional accuracy requirements to allow a practical and
feasible design.

Table I: Pertinent Beam Specifications

Number of Bays: 54

Deployed Bay Length: 44.250 inches (1.124m)
Total Deployed Length: 2389.500 inches (60.693m)
Beam Diameter: 55.118 inches (1.400m)

Angle between Deployed Diagonal/Batten: 42.831 degrees

Stowed Bay-pair Height: 3.000 inches (0.076m)
Stowed Beam Height: 84.000 inches (2.134m)
Packing Ratio: 0.035

Maximum Tube Diameters: Longeron - 0.900 inch (22.86mm)

                        Diagonal - 0.945 inch (24.00mm)
                        Batten A - 0.625 inch (15.88mm)
                        Batten B - 0.500 inch (12.70mm)

Table II: Beam Members, Effective Structural and Thermal Properties

	Effective Axial Stiffness, 10^6 lb (N)			Effective CTE 10^{-6} in/in/°F	Local Buckling Loads
	Max.	Design	Min.		
Longeron 1	10.7(47.6)	9.7(42.9)	9.3(41.3)	+0.082	5935 lb (26,400 N)
Longeron 2	9.0(40.1)	8.2(36.4)	7.9(35.2)	+0.082	5070 lb (22,560 N)
Diagonal 1	1.0(4.4)	0.9(3.9)	0.8(3.7)	+1.13	264 lb (1175 N)
Diagonal 2	1.0(4.4)	0.9(3.9)	0.8(3.7)	+1.09	264 lb (1175 N)
Batten A (axial load)				-0.32	343 lb (1525 N)
(frame, 3 radial loads, ea)					594 lb (2640 N)
Batten B				+0.372	201 lb (894 N)

Table III: DRA Status Monitoring Instrumentation

Stowage and tip latch limit switches -- each stowage and tip latch motor
     actuates a redundant limit switch at each end of travel.
     Activation of a switch element is an event and is monitored by the
     MDIS.

Telescopic tube limit switches -- each telescopic tube latch motor
     actuates a redundant limit switch at each end of travel.
     Activation of a switch element is an event and is monitored by the
     MDIS.

Deployed bay-pair encoder -- provides the deployed bay-pair count.

Diagonal latch verification switches -- an optical switch is employed
     to verify that each of six diagonal mid-span hinges of a bay-pair
     are latched before any portion of the bay-pair exits the DRA.

Beam lock limit switches -- each beam lock motor actuates redundant
     limit switch at each end of travel. Activation of a switch element
     is an event and is monitored by the MDIS.

Diagonal folding encoders -- provide the position of the diagonal
     folding mechanism.

Diagonal folding stow limit switch -- the diagonal folding motor
     actuates a single limit switch at a fully stowed position.
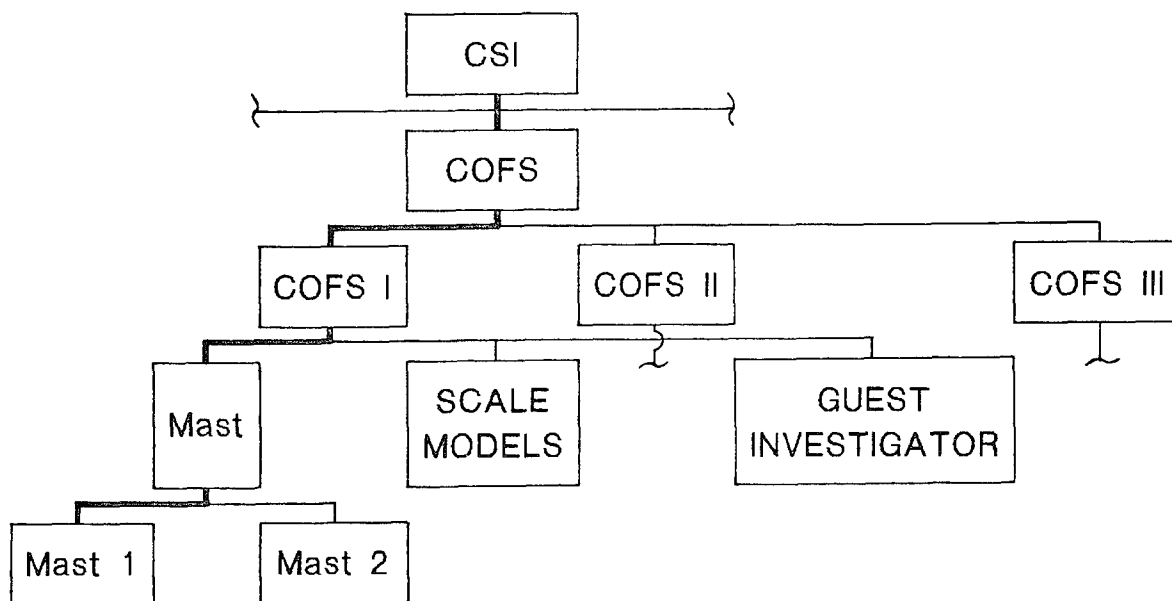
Figure 1.   Control/Structures Interaction (CSI) effort.
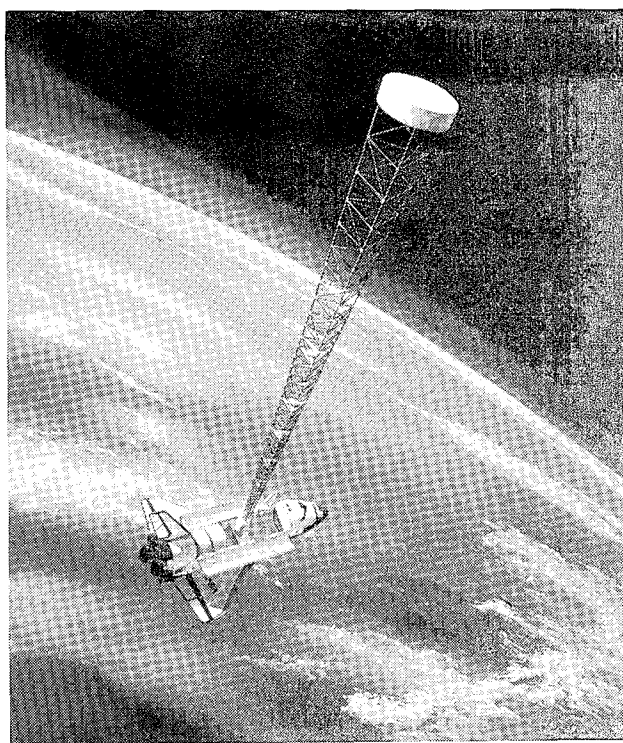
Figure 2.   Deployed 60-meter Mast beam.
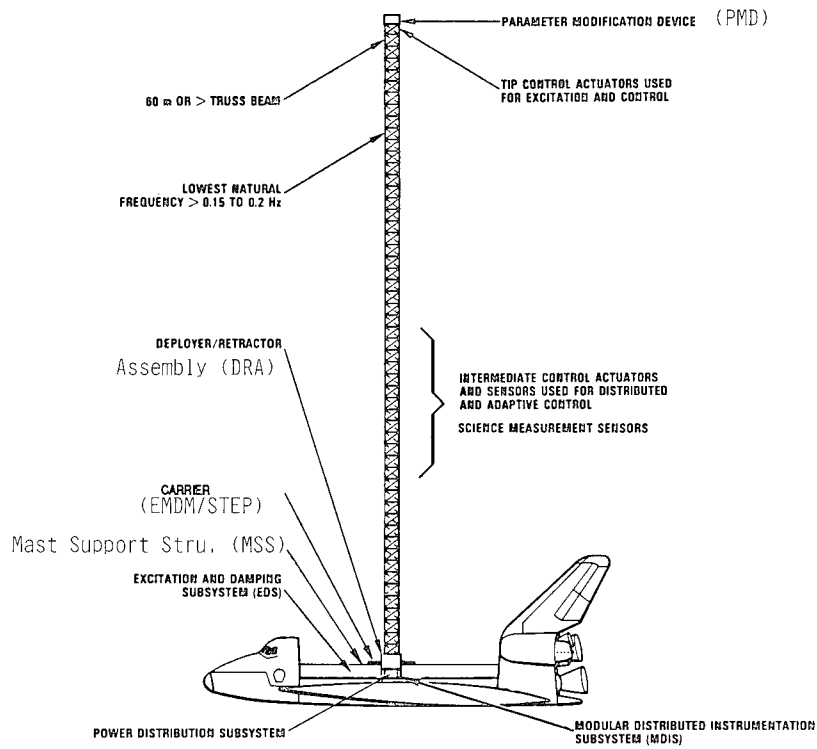
Figure 3. Mast Flight System (MFS).
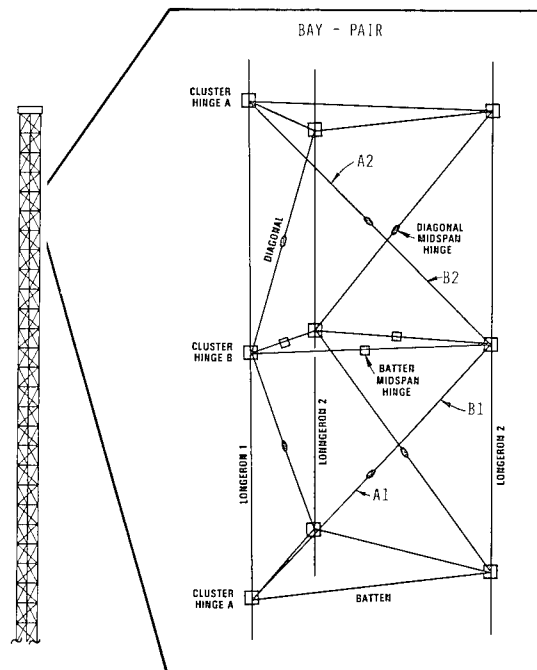
Figure 4. Articulating Astromast beam concept.
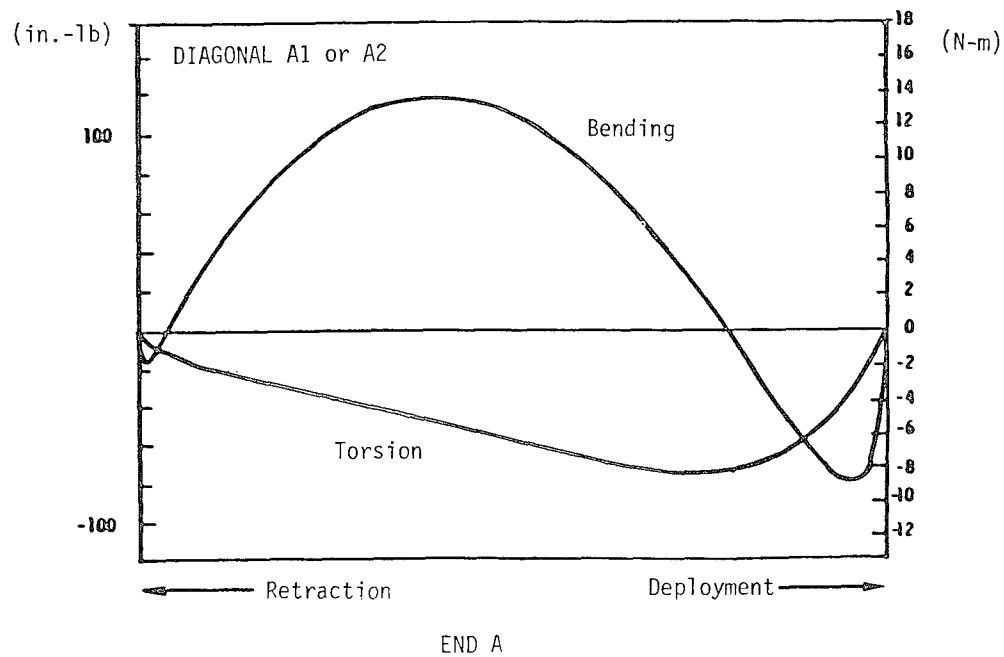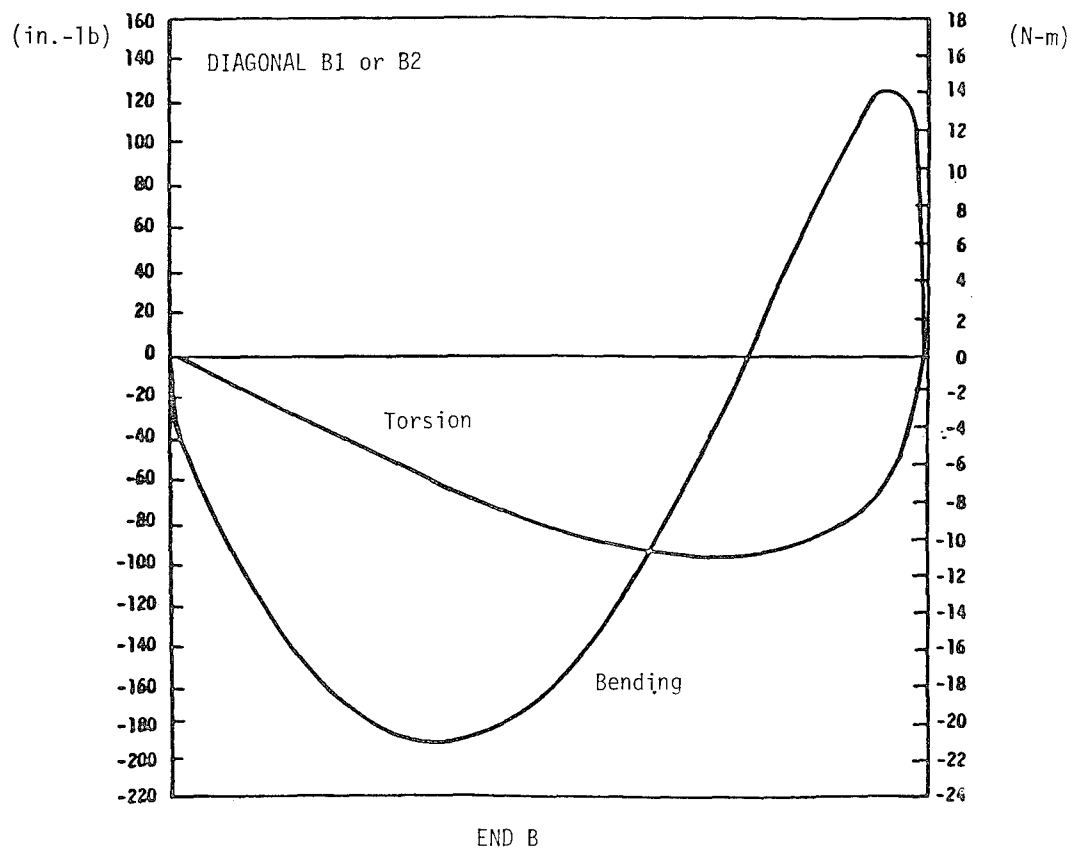
Figure 5. Moments at ends A and B during deployment/retraction cycle.

79
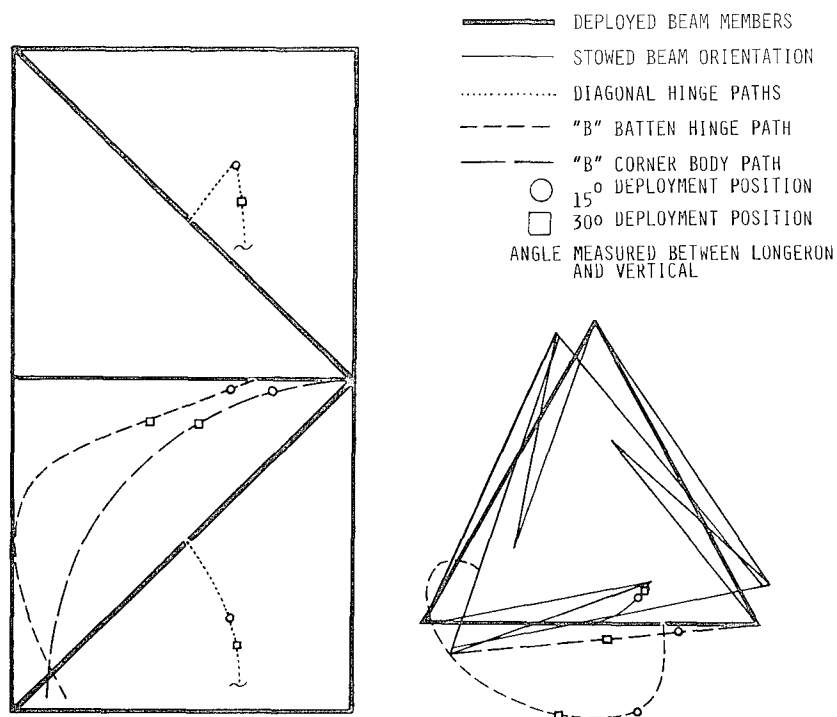
Figure 6. Spatial motion of typical beam members.

LAUNCH CONFIGURATION WITHOUT HONEYCOMB PANELS

Stowage latches at top of each post

Tip Canister

Upper drive assembly

Nut stack with lead-screw threaded thru (3 places)

Base structural tube

Stowed beam

Retractor device (3 places)

"B" corner body retention guide track

Base plate
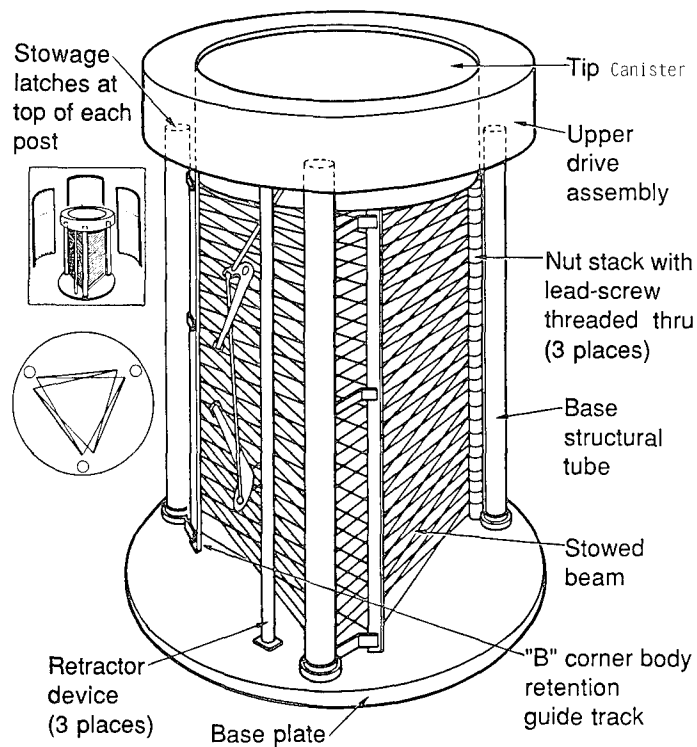
Figure 7. Mast flight system – stowed.

80

LEAD SCREW TRANSMISSION & RETRACTOR LINKAGE
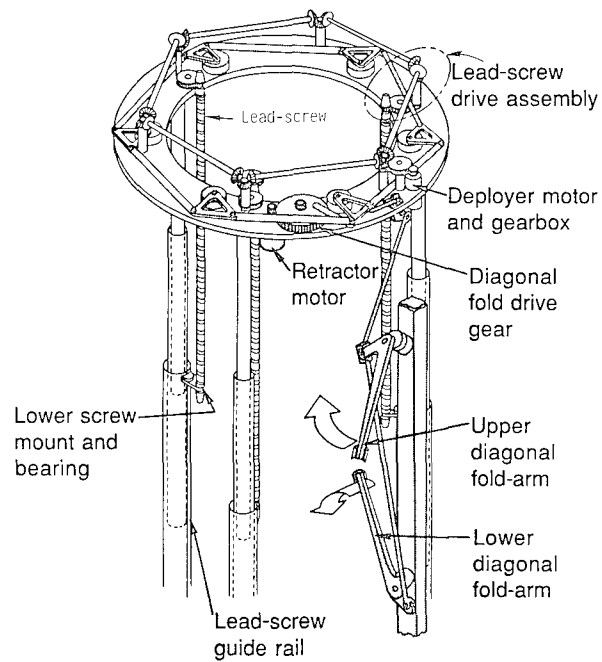
Figure 8. Lead-screw and fold-arm mechanisms.
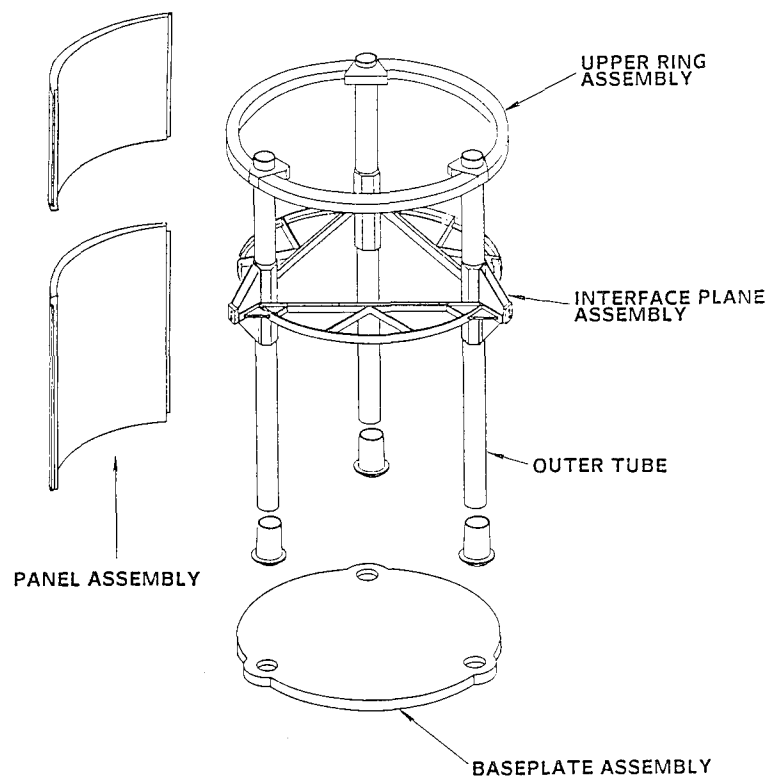
Figure 9. Fixed DRA support structure.

Leadscrew

Telescoping Tube

Detent

Stack Lifter

Delatch from
Stowed Position

Extend and
Latch Deployer
Structure

Beam Stacked,
Leadscrews
Engaging First
Corner Bodies

Deploy Beam

Leadscrews
Elevate Beam,
Stack Lifter
Coordinates
Stack Movement

Fully Deployed,
Beam Latched
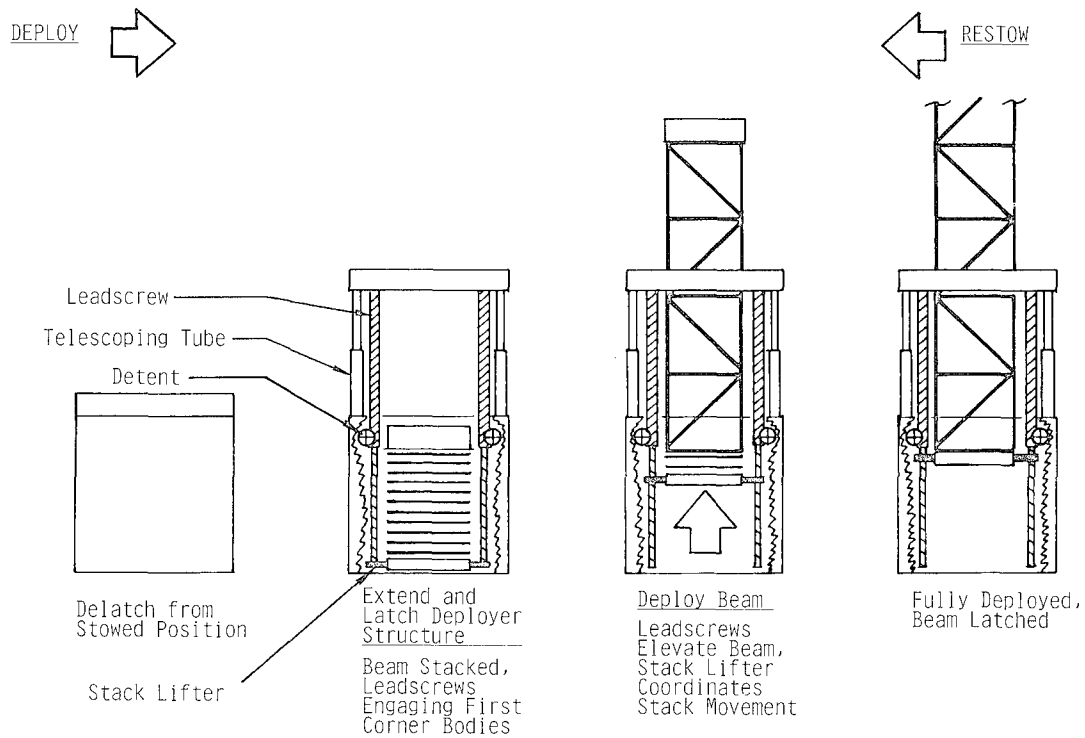
Figure 10.   Deployment/retraction sequence.

Upper drive transmission assembly

Tip canister
assembly

Swivel
catch

Stowage
latch
assembly

Drive
motor
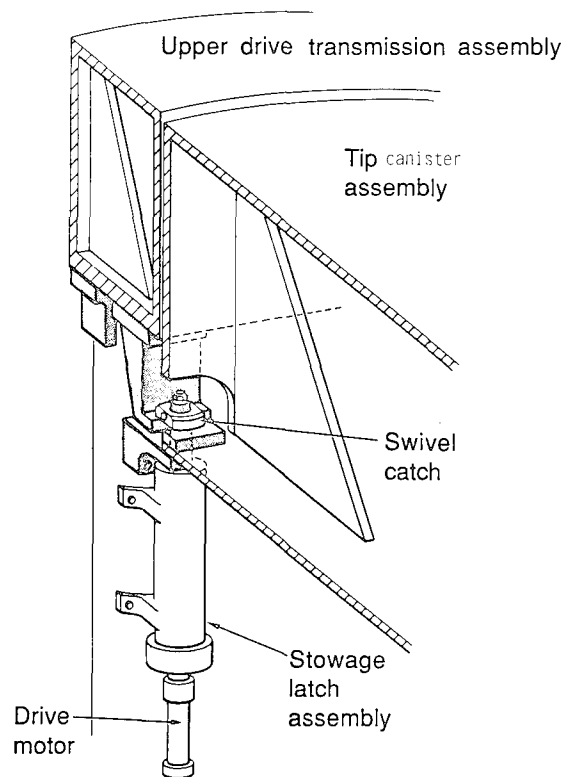
Figure 11.   Stowage latch.

TUBE LATCH, UNLOCKED
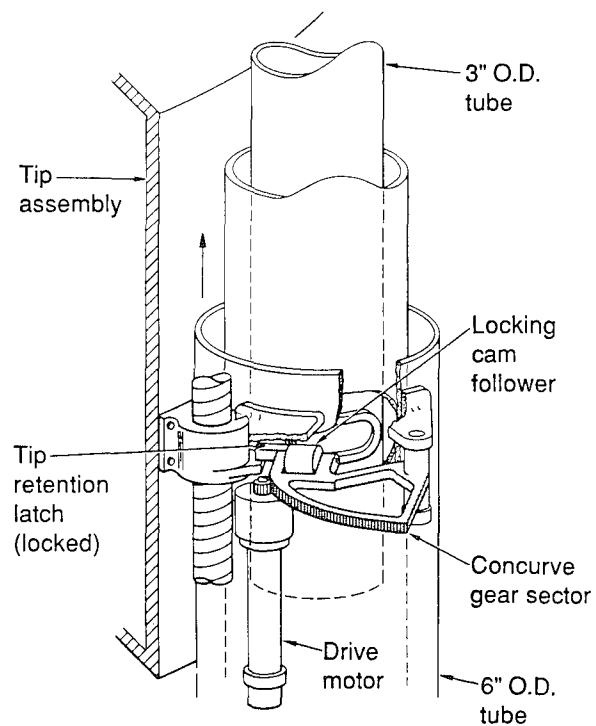
Figure 12.   Telescoping tube latch mechanism.
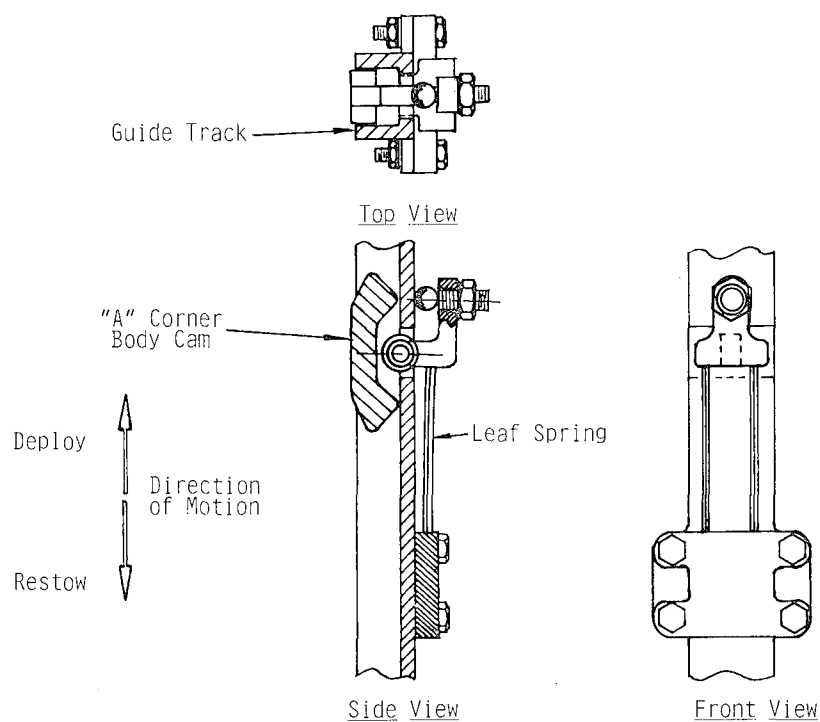
Figure 13.   Detent device.
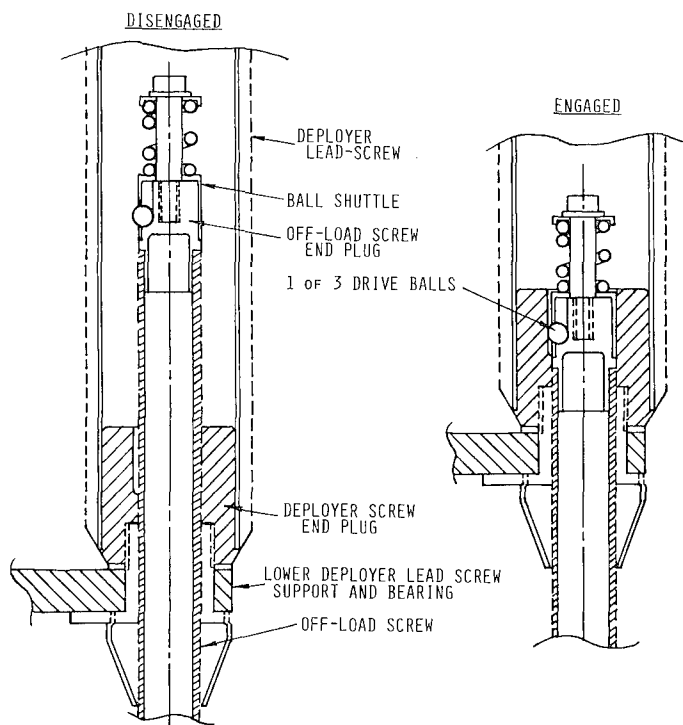
Figure 14. Stack lifter (off-loader).
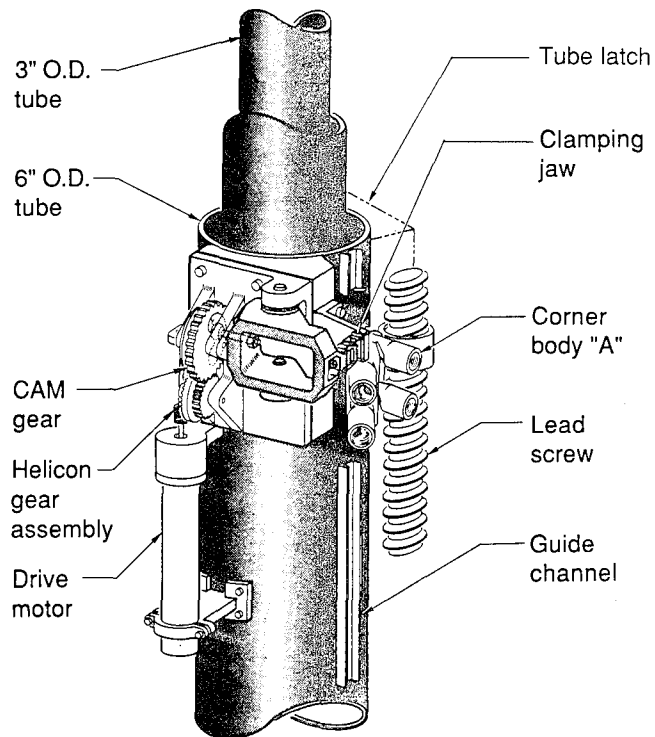
Figure 15. Beam latch mechanism.
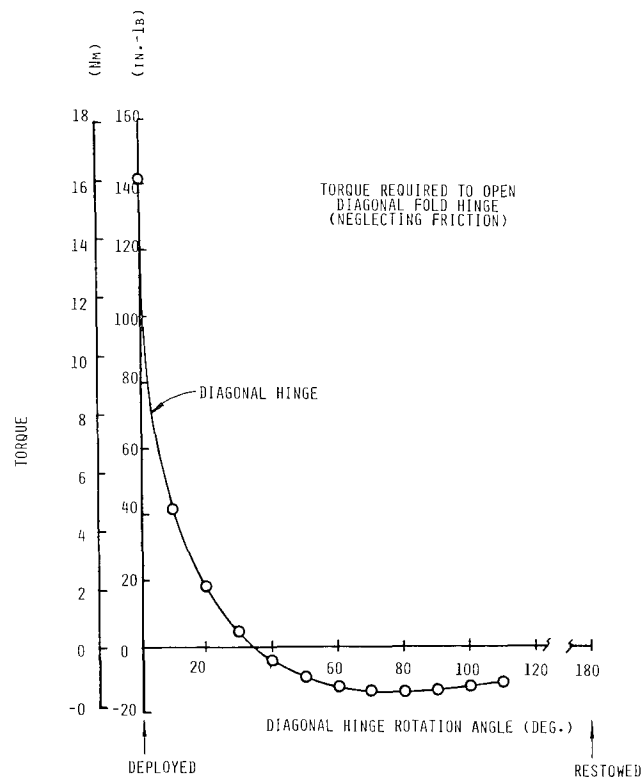
Figure 16. Torque required to open diagonal hinge.
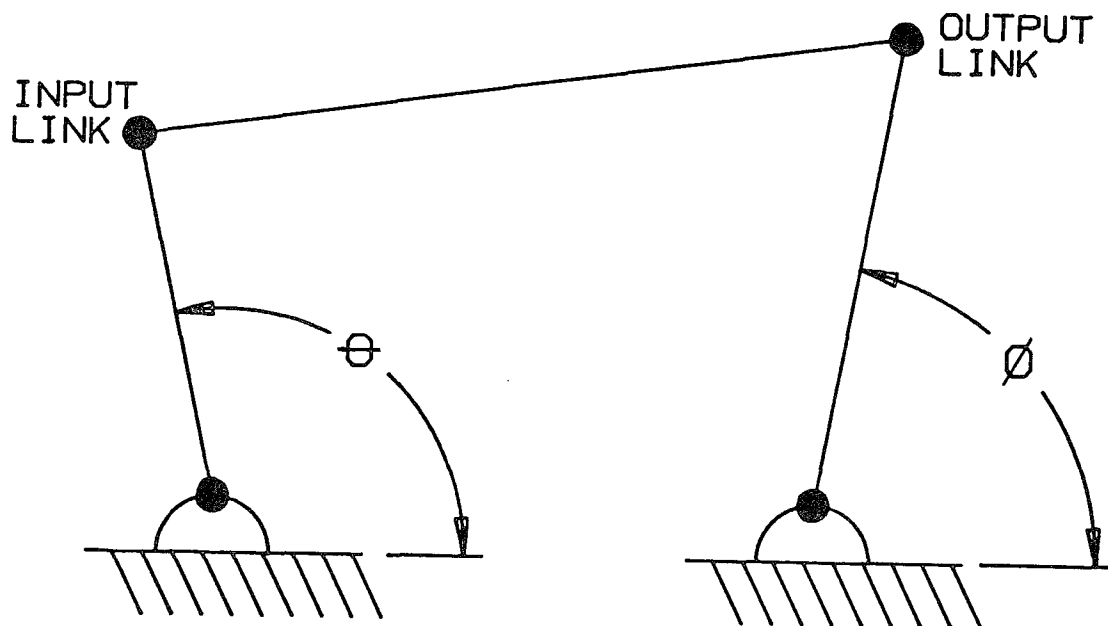
Figure 17. Equivalent four-bar linkage.

85

ON THE DANGER OF REDUNDANCIES IN SOME AEROSPACE MECHANISMS*

M. Chew **

ABSTRACT

This paper attempts to show that redundancies in some aerospace mechanisms do not generally improve the odds for success. Some of these redundancies may even be the very cause for failure of the system. To illustrate this fallacy, two designs based on the Control of Flexible Structures I (COFS I) Mast deployer and retractor assembly (DRA) are presented together with novel designs to circumvent such design inadequacies, while improving system reliability.

INTRODUCTION

One of the general principles held closely and dearly by mechanical designers and engineers is the incorporation of redundancies in the design of their mechanical and electromechanical systems. For good system reliability, redundancies are incorporated to improve the chances for success, and generally do; however, there are some types of redundancies that fail to do so. In fact, this paper, in describing two aerospace mechanism designs, will illustrate that some redundancies may decrease the chances for system success. Although the set of such undesirable types of redundancies described herein is small, it is worth documenting such types that do not perform to expectation. Other approaches can be taken instead to improve the odds. Redundancies can also introduce other penalties (such as space, weight, efficiency and fabrication costs) which should be weighed against the expected benefits of the redundancies introduced into the system.

One type of redundancy that is undesirable relates to conditions within the system. A given failure of a component or subsystem may change the environment such that the redundant component or subsystem does not perform to its expected level. Such a redundancy degradation can, at times, be anticipated so that designs around

the obstacle can be adopted. As an example, failures occurred in some recent development and deployment tests conducted on the Magellan (Venus Mapper) Spacecraft when a particular lot of pyrotechnic pin pullers, ones that incorporate a redundant initiator, failed to function properly. As part of an engineering evaluation, the contractor conducting the tests determined that

1. The shock pulse from the first initiator could prove sufficient to permanently distort the bore of the pin puller, thereby preventing piston motion. A subsequent firing of the second initiator would not improve this situation. Fabrication and quality assurance problems were also present in these units.

2. Further design consideration by others revealed that if the first initiator's output was insufficient, firing this initiator could contaminate the interior surface with sufficient particulate deposits to inhibit free piston movement if such movement had not already taken place. It is possible that enough particulate contamination could be introduced between the piston and bore to prevent any piston motion with a subsequent firing of the second initiator.

This paper considers another type of undesirable redundancy which introduces a condition of over constraint to aerospace mechanisms. To adequately explain and illustrate this type of redundancy, two mechanism designs within the COFS I DRA will be used to show how such a type of redundancy can actually be the cause for system failure. The two mechanisms are the lead-screw drive and the diagonal fold-arm bell-crank linkage. In the sections that follow, a description is given of the design of each of these mechanisms, how they function within the COFS I DRA, how their expected redundancy can cause failure, and how the design can be improved.

BACKGROUND

As a subset of COFS I, the Mast Flight System (MFS), figure 1, incorporating a reusable, deployable-restowable truss beam as a test bed, was conceived to bridge the gap between ground and on-orbit modal verification, and validation of control methodologies. A description of the specific subsystems of the MFS, of which the deployer and retractor assembly (DRA) is one of the major functional components, can be found in reference 1.

OPERATION OF THE COFS DEPLOYER/RETRACTOR ASSEMBLY (DRA)

The main function of the DRA is to deploy and retract the beam out of and into the Shuttle payload bay in a continuous, smooth motion. This sequence of deployment and retraction is shown in figure 2. Figure 3 shows the DRA with

the beam partially deployed. Central to the DRA is an annular box called the upper drive assembly. This box contains two sets of mechanisms. One is a gear train designed for simultaneous power transmission to three lead-screws used to deploy or retract the beam. The other is a spatial linkage designed to unlock and open the beam's diagonal latches and hence initiate folding of the beam during the retraction process. These mechanisms are illustrated in figure 4.

The deploy or restow drive mechanism is powered by a deployer motor via a gearbox so as to enable the lead-screws to change their direction and speed of rotation. The mechanism consists of six drive shafts, laid end-to-end to form a loop, much like the sides of a hexagon. At the ends of each shaft are bevel gears, so that power may be transmitted from one shaft to the next, around this hexagonal loop, back to itself. Power take-offs for the lead-screws occur at every other set of beveled gears. The redundancy arises from the continuous loop--failure of any drive shaft or bevel gear will not disrupt the ability of this mechanism to transmit power to the set of three lead-screws. Such a gearing system is called a recirculating gear train [references 2-4]. Other types of power recirculating arrangements have been used in the testing of belts and chain drives [references 5 and 6].

In the process of deploying the beam, the deployer drive motor rotates in a direction such that the lead-screws move the nodal fittings (corner bodies) located at the corners of the beam. As the corner bodies ride along the lead-screws, the immediate folded stack bay of the beam begins to unfold. Since the lead-screw rotation is continuous, the unfolding, and hence the deployment of the beam, is smooth and continuous. The reverse is also true for the retraction of the beam. At the deployed position for each beam bay-pair, the diagonal links are straightened and the mid-span hinges and latches are spring loaded so that the beam behaves as a structure.

To begin retracting the beam, the same spring loaded latches on the diagonal links must be unlocked to permit the diagonal links to fold. To fold these spring latches, the diagonal fold-arm drive system is used. Simultaneously, as these latches are being folded, the separate deployer motor is driving the lead-screws in the restow direction. This causes the corner bodies to move down into the DRA, thereby completing the folding and stowing of each bay-pair of the beam. This sequence is repeated until the beam is restowed.

In the following sections, an examination of how redundancies in the lead-screw drive gear train and in the bell-crank linkage could be the very factors that can cause failures within the DRA will be presented. This examination begins with the bell-crank mechanism.

BELL-CRANK LINKAGE

In the bell-crank linkage (figure 4) that is located in the upper drive assembly (figure 3) of the DRA, a crank-and-rocker linkage, driven by the retractor motor through a diagonal fold-arm drive gear, is concatenated to the bell-crank. Rotation of the diagonal fold-arm drive motor results in oscillatory motion of the bell-crank linkage. This linkage consists of six triangular oscillatory members, or links, that are located at the corners of a hexagon. These triangular links are connected to each other by six straight members to form a hexagonal continuous

or closed-loop. While minimizing backlash, this loop is anticipated to provide redundancy in the event of failure of any of the bell-crank or straight link members. A power take-off at each alternate bell-crank, transfers the oscillatory motion of the bell-crank linkage drive to a spatial six-bar linkage that transmits power to the upper and lower diagonal fold-arms. These diagonal fold-arms press on the near-over-center hinge latches to effect folding of the diagonal during the initial stages of the retraction process for each bay-pair of the beam.

Next, consider the six couplers that link the bell-cranks together to form the hexagonal loop. Normally, only five such links are needed. In the event any one of these links were to fail, a sixth coupler link was incorporated to complete the loop, thereby ensuring that the bell-crank linkage would still perform its function. In this way, a redundant power path to retract the beam back into the canister is still maintained to all the diagonal fold-arms should any coupler link fail. Such a redundancy has obvious advantages. It absolves the need for a totally separate system that would increase cost, weight, complexity and space requirements; and, according to the subcontract designers, it would also provide some degree of structural integrity to the mechanism in the form of lower system backlash.

General Observations on Mobility

Careful design considerations are needed to introduce this sixth coupler link. In fact, without judicious dimensional choices for the bell-crank mechanism, the resulting hexagonal loop (with the sixth coupler link) will act as a structure, not a mechanism and therefore will not move! A brief proof follows:

> A kinematic equivalent for an arbitrarily dimensioned bell-crank mechanism is shown in figure 5. In this figure, link #1 is the ground (fixed) link. Applying the degree-of-freedom (d.o.f.) equation attributed to Gruebler [reference 7 and 8] for this linkage we have;

Link #1 is the ground link.

Using the d.o.f. equation, $F = \lambda (L-j-1) + \Sigma f_i$

Where for planar mechanism,
  λ = Mobility number   = 3
  L = Total # of links = 13,
  j = Total # of joints = 18, and
  f_i = d.o.f. of the ith joint = 1.

substituting $F = 3(13-18-1) + 18$

so that $F = 0$

Which states that the bell-crank mechanism is a zero d.o.f. system and is therefore a structure and will not move!

Special Dimensions for the Bell-Crank Mechanism

There are special dimensional requirements for this linkage that will permit the bell-crank mechanism to exhibit a single d.o.f. The theory is based on that of a folding linkage [reference 8]. The folding linkage is a four-bar where

90

the dimensions of its opposite links are equal, such that the four-bar constitutes a parallelogram. A principal characteristic of the folding linkage is that any given angular rotation on the input link is exactly duplicated at the output link. Such a linkage therefore (a) ensures a design with one d.o.f., (b) allows the bell-crank and folding arm members to operate as a mechanism, and (c) maintains the synchronization of all the folding arms (upper and lower pairs)--a total of six in the DRA. Based on the characteristics of the folding linkage and on sufficiency conditions, a workable design for the bell-crank mechanism would be

1. All coupler links must be the same length (from figure 5, they are links #3, 5, 7, 9, 11, 13), and that same length must also be equal to the distance between two adjacent ground pivots of the bell-cranks.

2. All rocker links or sides of the bell-cranks (such as links #2a, 2b, 4a, 4b, 6a, 6b, 8a, 8b, 10a, 10b, 12a and 12b) are of the same length.

3. The angles (α) subtended by the bell-cranks at the pivots must all be equal to 60°.

With the above special dimensions, the bell-crank mechanism will exhibit a single d.o.f. and will therefore move. Under this set of circumstances, the d.o.f. equation will no longer apply. While the above design simplifies the choice of dimensions, the number of parts are still a point of concern. The high part count contributes to problems in tolerance buildup, reliability, cost, weight and space. A more optimal approach to the design with improvements in all these factors will be discussed later.

Danger of Over Constraint Redundancies

The loop arrangement for the bell-crank mechanism ensures a dual path for power transmission to the upper and lower diagonal fold-arms in the event that a coupler link within the mechanism fails. However, this redundancy may only be academic. Recall that the bell-crank mechanism under general dimensions forms a structure and is therefore immobile. The introduction of the sixth coupler link as a redundancy has caused the mechanism to become over constrained. Fortunately, with special dimensional requirements, the bell-crank mechanism can be made movable with a single d.o.f. However, these special dimensional requirements must be observed at all times during the planned operation of the DRA. The problem is, in the hostile space environment, temperature gradients across the mechanism could cause these dimensional requirements to be violated. This could result in locking up the bell-crank mechanism (reverting it back to a structure) or could cause high link- and bearing-loadings within the mechanism. Even in the absence of temperature gradients, the costs and complexity of ensuring tight tolerancing may well be undesirable.

This bell-crank mechanism therefore serves to illustrate the danger of introducing a redundancy into a mechanism that will result in an over constrained system. With special dimensional requirements, the mechanism may be made movable. However, the strict requirements of dimensional control in hostile environments may not be readily realized in practice. This could bring about failure of the system, ironically due to that very redundancy.

While this example is based on that for a linkage mechanism, the principle is equally applicable to gear drive mechanisms. The next section discusses the danger of such over constraint redundancies in the lead-screw drive mechanism of the DRA.

LEAD-SCREW DRIVE MECHANISM

The lead-screw drive mechanism is powered by a deployer motor via a gearbox which enables the lead-screws to change their direction and speed of rotation. In an arrangement similar to the bell-crank mechanism, the lead-screw drive mechanism consists of six drive shafts, laid end-to-end to form a loop, much like the sides of a hexagon shown in figure 4. At the ends of each shaft are bevel gears, so that power may be transmitted from one shaft to the next, around this hexagonal loop, back to itself. It can be seen that power take-offs for the lead-screws occur at every other set of beveled gears in the hexagonal loop. The redundancy arises from the continuous loop--failure of any drive shaft or bevel gear will not disrupt the ability of this mechanism to transmit power to the set of three lead-screws. Such a gearing system is called a recirculating gear train which can be found in many machines, although rather infrequently, for a good reason.

A quick investigation into the general mobility of such a gear drive set-up would show a zero d.o.f. A brief proof for this system follows:

> Again applying the d.o.f. equation [reference 7 and 8] for this loop we have;
>
> With link #1 as the ground link.
>
> Using the d.o.f. equation, $F = \lambda(L-j-1) + \Sigma f_i$
>
> Where for planar mechanism,
> λ = Mobility number = 3
> L = Total # of links = 13,
> j = Total # of joints = 24, and
> Σf_i = Total d.o.f. of all joints = 36.
>
> substituting F = 3(13-24-1) + 36 = 0
>
> so that $\quad$ F = 0

Which states that, as in the bell-crank mechanism, this gear train has a zero d.o.f. and is therefore a structure!

This gear train is only operable when special dimensions are instituted into the design. The difficulty of maintaining the special dimensions needed in recirculating gear trains testifies to the generally high tooth loadings and low power transmission efficiencies observed. This is precisely what is observed in gear torque testing machinery which also has similar recirculating gear train arrangements [reference 9]. With inadequate design, the resultant low power transmission efficiency could cause failure of the mechanism to perform its mission

satisfactorily, if at all. In fact, during tests of a DRA feasibility of concept model, a gear box failed and higher than predicted drive motor loads were experienced. This was believed due, in part, to a lack of recognition of the need to achieve and maintain special dimensions.

RECOMMENDATION ON DESIGN IMPROVEMENTS

The introduction of an additional link or drive shaft has caused the respective mechanisms to become over constrained. Such kinematic structures for power transfer, although commonly found within subcomponents such as constant velocity joints and universal joints [references 10 and 11], may not be suitable for aerospace applications. Therefore other approaches should be pursued.

One approach to eliminate the effects of over constraint within the system is not to introduce it in the first place. For example, it is possible to design the coupler links and the gear shafts to ensure that their failure would not occur. Such would be the simplest approach if that is possible within the available space and weight requirements.

Another approach is to use circular ring gear arrangements as illustrated in figure 6. This design consists of two large ring gears that rotate concentric to the axis of the canister. The innermost ring gear is driven by the deployer motor and power is fed off to three gears to drive each of the three lead-screws. The use of a ring gear makes the process of coordinating the rotation of the lead-screws a trivial matter when compared to the present design.

In a similar manner, the outermost ring gear driven by the diagonal folding mechanism motor, pushes and pulls on three push-pull cables as it oscillates back and forth. These cables, after going through a very gradual 90° turn to orient them parallel to the beam axis, drive the upper diagonal fold-arms which in turn are coordinated with the respective lower diagonal fold-arms via a coupler link. To save weight, this ring gear could be made up of gear sectors.

In comparison to the present design, this ring gear arrangement would save space, reduce part count, and improve reliability.

SUMMARY

Two designs of mechanisms that have redundancies built-in have been shown, paradoxically, to be the very elements that can cause failure of the mechanism to perform its function. In each of these designs, the introduction of the redundancy causes the mechanism to become kinematically over constrained. While the over constraint may be eliminated with special dimensional requirements placed on the mechanism, these requirements may not be achievable in the hostile environment of space.

While redundancies do indeed generally improve the odds for mission success, **redundancies also exist that do not follow this general philosophy. The**

dangers of such fallacies, if unexplored and not emphasized, may lead to significant redesign or loss of valuable experiments.

REFERENCES

1. Lucy, M., "Motion Synchronization of a Mechanism to Deploy and Restow a Truss Beam", NASA CP-2506, 1988, pp. 67-86.

2. Lozano-Guzman, A., "Vibration of Power Transmission Timing Belts", Ph.D. Thesis, University of Newcastle upon Tyne, England, 1982.

3. Sanger, P. J., "The Determination of Power Flow in Multiple-path Transmission Systems", Mechanisms and Machine Theory, 7(1), Spring 1972.

4. Laughlin, H. G., Holowenko, A. R. and Hall, A. S., "How to Determine Circulating Power in Controlled Epicyclic Gear Systems", Machine Design, 28(b), March 22, 1956.

5. Turnbull, S. R., Nichol, S. W., and Fawcett, J. N., "An Experimental Investigation of the Dynamic Behavior of a Roller Chain Drive", ASME, Paper 77-DET-168, 1977.

6. Bouillon, G., Tordion, G. V., "On Polygonal Action in Roller Chain Drives", Journal of Engineering Industry, ASME, pp. 243-250, 1965.

7. Gruebler, M., "Getriebelehre:, Springer-Verlag OHG, Berlin, 1917/21.

8. Freudenstein, F., "Kinematics of Mechanisms", Section 4 of Mechanical Design and Systems Handbook; Ed: H. A. Rothbart, McGraw Hill Book Co., N.Y., 1964.

9. Dudley, D. W., "Gear Handbook:, McGraw Hill Book Co., N.Y., 1962.

10. Freudenstein, F., and Maki, E. R., "The Creation of Mechanisms According to Kinematic Structure and Function", International Journal for the Science of Architecture and Design, 1980.

11. Fisher, I., "On the Hooke's Joint", Ph.D. Thesis, Columbia University, N.Y., 1983.
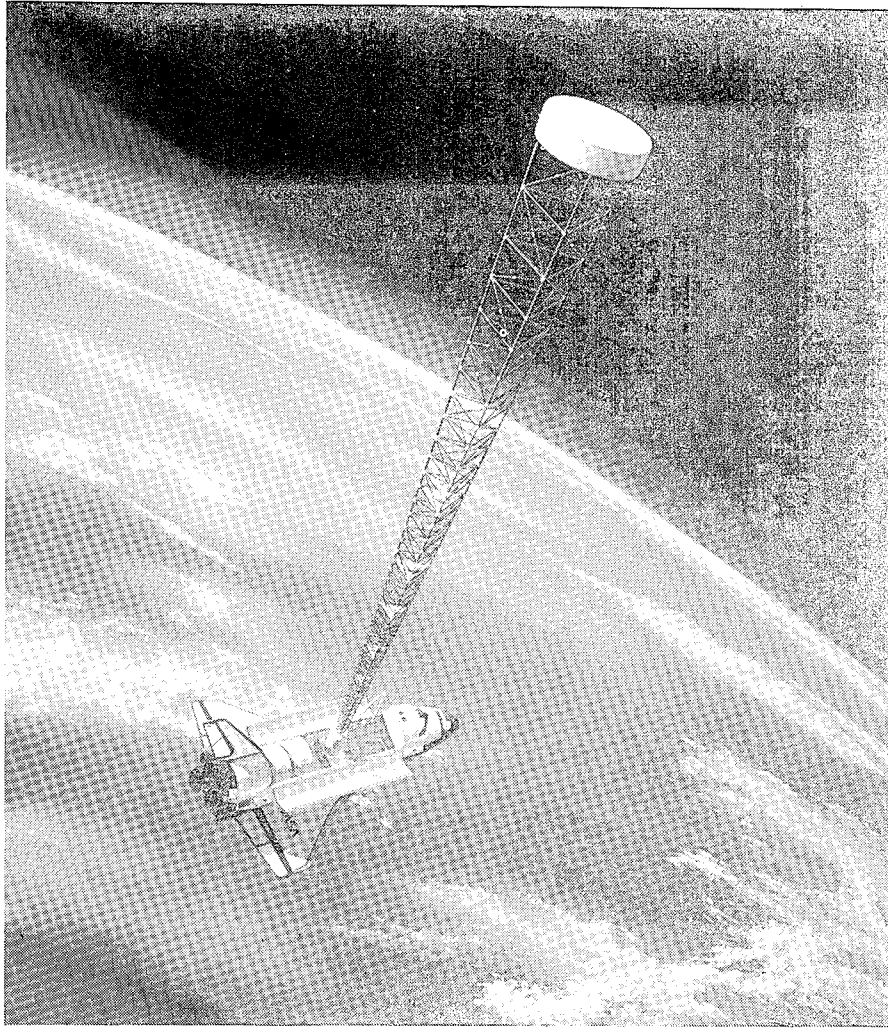
Figure 1.- Deployed 60 Meter Mast Beam

DRA FUNCTION
(DRA Not Shown For Simplicity)

Deployment

Retraction
6 diagonals
delatch and unfold
Continuous
smooth motion

Diagonal latches

"A" Corner bodies

Batten Latches

"B" Corner bodies

Bay-Pair

Beam stowed for launch

Unfolds 2 bays at a time

Erected beam locked in place by diagonals

• Deployer reverses
• Beam retracts 2 bays at a time but with continuous motion
• Retraction mechanism releases 6 diagonal locks and folds diagonals
• Deployer restacks mast

Figure 2.- Mast Beam Deployment/Retraction Sequence

DRA DEPLOYED, BEAM DEPLOYED
(Retractor device shown)

Upper drive assembly

Retractor arms

Drive linkage

Retractor device deployed
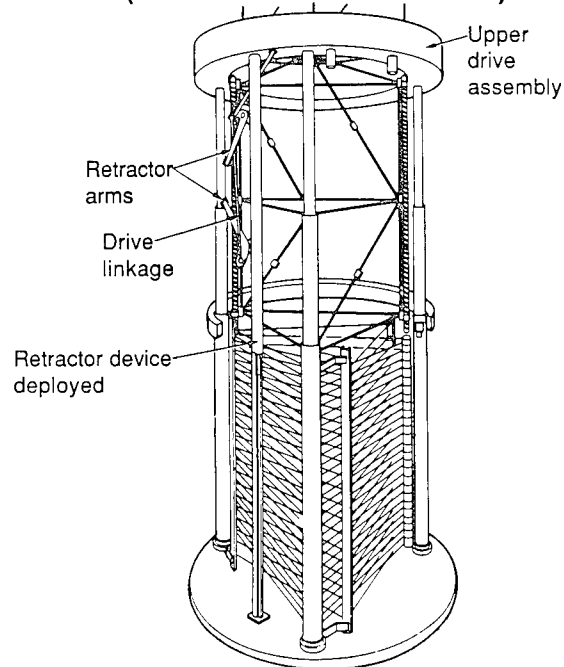
Figure 3.- DRA Deployed, Beam Partially Deployed
(Typical Retractor Device Shown)

LEAD SCREW TRANSMISSION & RETRACTOR LINKAGE

Lead-screw drive assembly

Coupler link

Deployer motor and gearbox

Retractor motor

Diagonal fold drive gear

Lower screw mount and bearing

Upper diagonal fold-arm

Lower diagonal fold-arm

Lead-screw guide rail
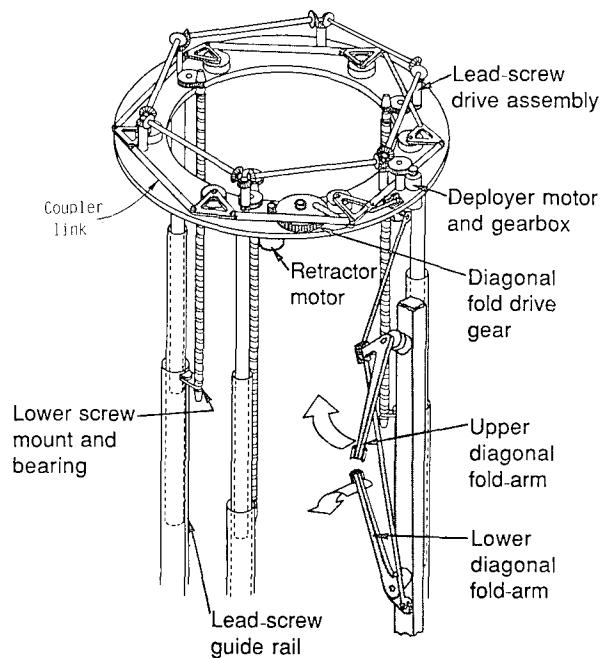
Figure 4.- Lead-Screw and Fold-Arm (Retractor) Mechanism
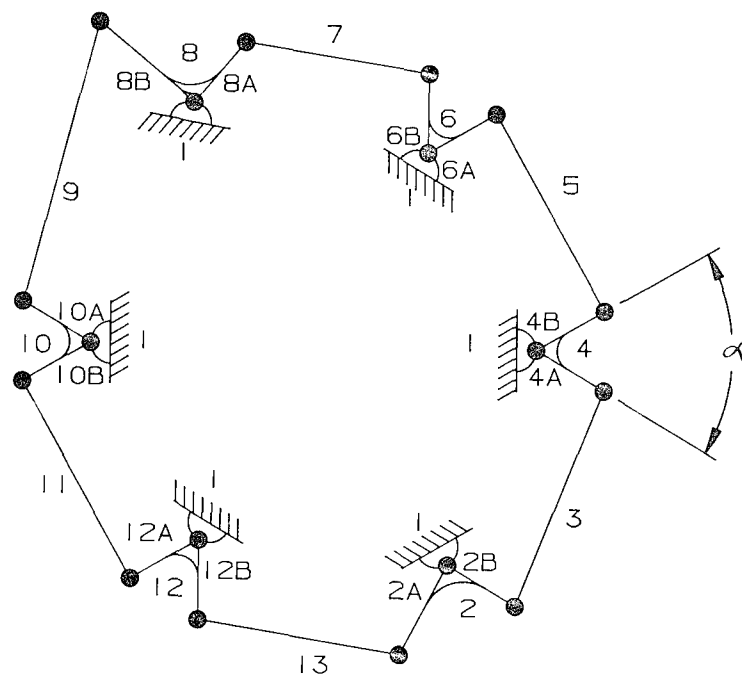
Figure 5.- Bell-Crank Mechanism Kinematic Equivalent

Lead-Screw Motor

Push-Pull Cable

Lead-Screw

Lead-Screw Motor

Telescoping Tube

Push-Pull Cable

Fold-Arm Motor

Lead-Screw

Fold-Arm Ring Gear

Lead-Screw Ring Gear
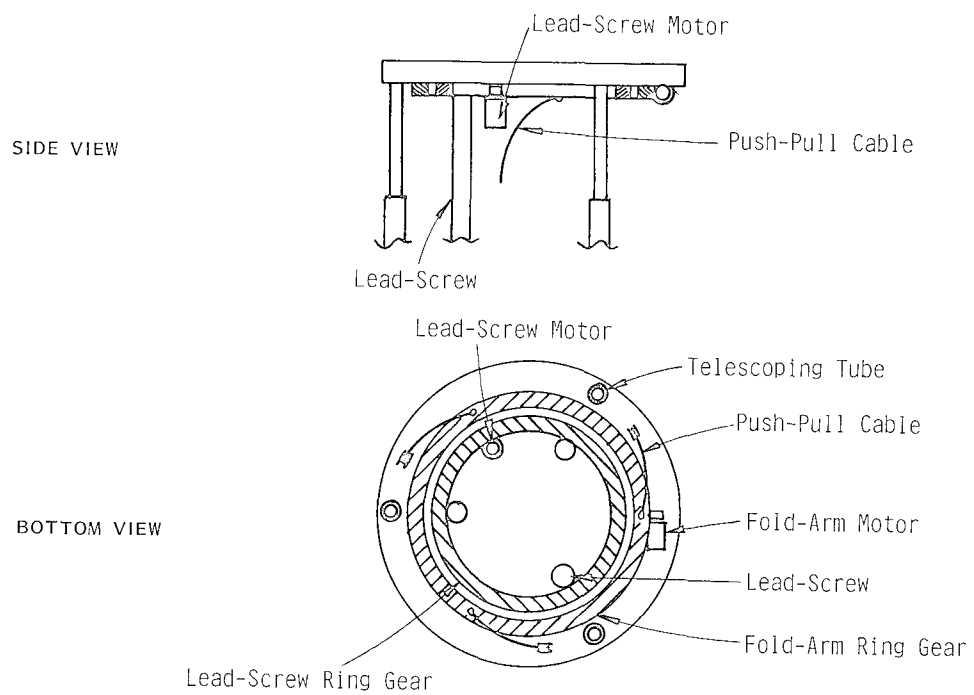
Figure 6.- Circular Gear Arrangement

QUICK ACTUATING CLOSURE AND HANDLING SYSTEM

Johnny W. Allred, Dorsey E. White, III, Benjamin T. Updike, and
Peyton B. Gregory*

Abstract:

A quick activating closure and handling system, which utilitizes conical sections for locking, was developed to allow quick access of the combustor internal components of the 8-FT. High Temperature Tunnel at NASA's Langley Research Center. These critical components include the existing methane spraybar, a transpiration cooled nozzle and the new liquid oxygen (LOX) injection system housed within the combustor. A substantial cost savings will be realized once the mechanism is installed since it will substantially reduce the access time and increase the time available for conducting wind tunnel tests. A need exists for more frequent inspections when the wind tunnel operates at the more severe conditions generated by using LOX in the combustor. A loads anaylsis and a structural (finite element) analysis were conducted to verify that the new closure system is compatible with the existing pressure shell. In addition, strain gages were placed on the pressure vessel to verify how the pressure shell reacts to transient pressure loads. A scale model of the new closure system was built to verify the operation of the conical sections in the locking mechanism. The entire closure system is mounted on a handling cart for ease of operation and eliminates the need for the overhead manually operated crane. The end closure of the pressure vessel is designed to the ASME Boiler and Pressure Vessel Code, Section VIII, Division 2. The mechanism is mounted on a support cart that contains an air motor, gear boxes and screw jacks to drive the conical surfaces into the locked position in the pressure vessel.

Introduction:

The 8-Foot High Temperature Tunnel at NASA-Langley Research Center is a large blowdown wind tunnel which simulates the pressure and temperature environment encountered during Mach 7 flight at altitudes from 80 to 130,000 feet. Figure 1 shows the existing combustor which produces hot gas with maximum stagnation conditions of 27.6 MPa (4000 psig) pressure and $2220^{O}K$ ($4000^{O}R$) temperature. Figure 2 shows the existing end closure assembly with the methane piping attached. Methane is burned in air, with the products of combustion as the test medium, to simulate the temperature environment and provides approximately a 4-foot diameter uniform high temperature test core in the test section.

---

*NASA Langley Research Center
    Hampton, Virginia

This unique research facility is presently being modified to allow research in the area of hypersonic air-breathing propulsion. Liquid oxygen will be introduced into the combustor for testing and evaluating large-size engine modules, full scale air-breathing missiles, flight-weight aerospace vehicle airframes, and engine structures.

Modifications to the existing tunnel will require a more frequent inspection of the combustor internal components. The combustor was designed for an internal pressure of 34.5 MPa (5000 psig) and was fabricated of thick wall material. Figure 3 shows the existing end closure which requires many man-hours for removal to allow inspection or replacement of internal components. Each piece, except for bolts, is presently handled using an overhead crane and special handling fixtures.

Present Method:

The present method is very time-consuming and requires considerable use of equipment and manpower to obtain access to the combustor internals. Figure 3 shows the 16 shear blocks with forty-six 4.45 cm (1-3/4 inch) diameter by 50.20 cm (19-3/4 inches) long bolts, a solid stud ring with twenty-four 4.8 cm(1-7/8 inch) diameter by 60.9 cm(24 inch) long studs, and a compression seal ring. Figure 4 shows the end view of the end closure assembly. The existing shear blocks, which are used in place of heavy flanges, are difficult to handle since they extend into the vessel and must be removed individually with the overhead crane and a special handling fixture. The existing shear blocks are numbered to facilitate proper reinstallation. The 46 bolts must be torqued each time the vessel is closed.

The solid flange ring (bolted to the end closure plug), the compression ring, and the seal ring require special handling fixtures and the overhead crane. The end closure plug is then removed from the vessel by means of an overhead crane and a special handling fixture as shown in Figure 5. These disassembly operations are completed by using special handling fixtures, overhead crane and a rigging crew. Approximately 164 man-hours are required to remove and reinstall the closure plug, plus detail planning, coordinating and integrating this activity between research personnel and the required trades. In the event of an unscheduled shutdown, an average of 2 days is required to remove the closure plug. This time loss translates into increased cost and reduced research productivity.

Therefore, the need exists to replace this end closure system with a design that is reliable and provides quick access to the combustor internals.

New Method:

The new method utilizes a system that includes a self-contained quick actuating closure and handling system which requires 2 hours to remove the end closure. These components are mounted to a handling cart which rolls on guide rails imbedded in the floor of the combustor building. The major components, shown in Figures 6 and 7, of the new method are the four shear blocks, a conical wedge ring to force the shear blocks radially into position for positive locking, a preload ramp that moves the shear blocks axially and

creates an initial preload between these blocks and the pressure vessel, a seal ring, and a modified closure plug. The locking mechanism is driven by an air motor and four screw jacks. The air motor operates four screw jacks to force the conical surfaces against the four shear blocks. Figure 7 shows the locked position of the shear blocks which provides the necessary preload to effectively transmit the internal pressure load directly to the grooves in the pressure vessel. These conical surfaces are designed to give the proper radial movement of the shear blocks, within the constraint imposed by the space available for longitudinal screwjack travel. These conical surfaces transmit the load directly from the plug to the pressure vessel. This new method provides system compactness and does not interfere with the required penetrations of the external piping and other equipment. The engagement of the shear blocks and the sealing of the fluid can be accomplished in a matter of minutes without the use of large bolts. Figure 8 shows the unlocked position.

Figure 9 gives a more detailed cross-section of the new method of sealing the internal gas that is more reliable than the flat metal seal used in the existing method. The seal selected provides a tapered backing ring that prevents extrusion of the o-ring. A finite element analysis shows that the radial deflection of the pressure vessel is extremely small because of the additional reinforcement from the torus which is located on the outside diameter of the pressure vessel near the seal. A backup seal is provided in the seal ring which is deformed by the pressure load acting on the preload ramp. This feature provides a backup to the primary seal. Analysis shows that the vessel is elongated in the axial direction, which unloads the clamping gaskets with the existing method. The shoulder machined in the seal ring restricts the radial movement of the preload ramp. This restriction causes the seal ring to deflect into the shoulder of the vessel. The thickness of the seal ring is sized to give the proper deflection to offset the elongation of the vessel and the compression of the shear blocks. Double seals are provided for safety reasons and provide the ability to monitor leakage from the primary seal. The leakage monitoring is accomplished by a pressure transducer located near the hole drilled through the vessel wall between seals. A lip is machined on the leading edge of the plug to minimize the potential for damaging the primary seal during installation.

This quick actuating system provides a minimum amount of wear on the locking grooves in the vessel since the final engagement is not made between the shear blocks and the vessel until the last few thousands of an inch of radial movement. The present method allows contact between the shear blocks and vessel locking grooves during assembly and disassembly causing severe wear.

This system also allows for proper adjustment of the shear blocks to the pressure vessel grooves by the use of the adjustable rods and the front tee guides shown in Figure 7. The adjustable rods contain a left-hand/right-hand threaded nut assembly to prevent the shear blocks from moving upstream when unlocking. The front tee guides prevent the shear blocks from moving downstream when locking and prevent cocking and binding during both locking

and unlocking operations. Shims are provided to allow proper adjustment. Another adjustment by installing shims exists between the seal ring and the preload ramp shown in Figure 9. This feature permits the proper tolerances for an effective use of the conical surfaces on the preload ramp. Lubrication of the sliding surfaces prevents self-locking of the wedge ring and the shear blocks.

A tee slot and a tee section shown in Figure 10 is used between each of the four shear blocks and the wedge ring to provide proper movement during assembly and disassembly. The tee section is used to lift the two bottom shear blocks from the grooves in the pressure vessel during disassembly. Proper clearance between these two items minimizes the power required to remove the shear blocks from the grooves in the pressure vessel. The initial movement of the wedge ring is accomplished before the initial movement of the shear blocks from the pressure vessel. It should be noted that the static friction of the mating surface are not overcome at the same time. These surfaces are forced together during the locking operation by the use of the air motor. The surface between the wedge ring and the shear blocks (Surface "A") is separated before the clearance between the tee and the shear blocks (Clearance "B") is closed during the disassembling operation. Shim locations are provided for final setup and assembly if needed. After the clearance is taken at the wedge ring, the jack forces are then transmitted through the surface at the bottom of the tee to overcome the static friction forces between the shear blocks and the pressure vessel.

Figure 11 shows a one-eighth scaled model which was constructed to demonstrate the operation of the closure system. The model includes the pressure shell with grooves, the preload ramp, the shear blocks, tee guides, and the wedge ring. This model was used in establishing the tolerances required for the components in the closure system and to demonstrate the design.

The locking mechanism is part of the pressure vessel and is designed in accordance with ASME Boiler and Pressure Vessel Code. The end closure meets the stress limits required by Section VIII, Division 2 of the Code. Figure 12 shows the load path of the forces resulting from the operating pressure in the combustor. A component of this axial force that is transmitted to the grooves in the pressure vessel also acts on the conical portion of the wedge ring. This component acts through the screw jack extensions and is transmitted through the vertical portion of the handling cart. Since the wheels of the cart are free to move as the combustor moves during a tunnel run, the reaction force is taken through the connecting plates and gussets, which are bolted to the closure plug. All stresses are within the ASME Code stress allowables.

Figure 13 shows the handling cart that is designed to maintain a center of gravity for the complete assembly that is well between the front and rear wheels of the cart. All components of the fuel and liquid oxygen mainfold systems are connected to the plug and can be easily inspected when the assembly is pulled from the combustor. The cart is leveled by using the manually operated screw jacks to insure that the spraybar of the methane fuel

system can be inserted into the combustor without interference with the inside diameter of the combustor. The entire system is pulled from the combustor at disassembly and pushed toward the combustor for reassembly by the use of a fork lift. The cart is mounted on tracks for proper alignment during the assembly and disassembly operations. Additional casters are provided to move the assembly laterally after the spraybar has cleared the end of the combustor.

The combustor outer shell and end retaining ring were instrumented with strain gages as shown in Figure 14 to determine if the combustor shell cycled with each pressure run of the tunnel. The instrumentation verified that the vessel did cycle with each pressure run.

Structural Evaluation:
    A finite element computer model of the combustor end closure assembly was constructed for two main reasons. The first was to determine the peak stress in the grooved region of the end closure. This allowed a prediction of the cycle life and the degree to which a preload is required to reduce the number of load cycles. The second reason was to determine the deflection characteristics of the end closure so that the new design could account for such deflections.

Figure 15 shows the finite element model of a 2 degree circumferential portion of the cylindrical shell, two elements thick at 1 degree per element. The load consists of a 27.6 MPa (4,000 psi) internal pressure acting on the inside of the shell and on the face of the shear block. The model is constrained at the downstream face in the (z) direction allowing it to move radially. The load transfer between the shell and the shear block is also only in the (z) direction on the compression faces. The deformed shape is shown in Figure 16.

From the analysis, the peak stress, shown in Figures 17 and 18, is located at the inner corner of the first groove farthest downstream. The peak combined stress is 904.6 MPa (131.2 ksi) at 27.6 MPa (4000 psi) combustor pressure. This assumes full contact across all three faces of the grooved segments. The distribution of load across the first, second, and third grooves is 47%, 39% and 14% respectively. Since there are three combustor conditions, 4.2 MPa (600 psi), 13.8 MPa (2000 psi) and 27.6 MPa (4000 psi) a value of 13.8 MPa (2000 psi) is used to determine the cycle life. The total life is 18,000 cycles. From prior runs, 15.2% of the total life has been used. Therefore, the remaining cycle life is 15,260 cycles. The effect of the grooves not being simultaneously in contact was also considered. A .0254 mm (.001 inch) gap was assumed on the second and third grooves which is ten percent of the average deflection if the other two grooves were never in contact. The peak stress is 957.7 MPa (138.9 ksi) at 27.6 MPa (4000 psi) combustor pressure and the remaining cycle life is 11,500 cycles.

There are three operating conditions of the wedge ring closure mechanism: preload, release, and unload. The preload condition sets the closure plug in place and enables the combustor to take pressure. Under higher values of the coefficient of friction, the jacking force can be relieved and the wedge ring

103

will stay in place. The release condition relieves the wedge ring of the friction forces. After the wedge ring is released, the unload condition moves the shear blocks clear of the combustor grooves and enables the closure plug to be removed from the combustor. The reacting forces are shown in Figure 19. In addition to the normal and friction forces, there is the weight of the shear blocks and the hoop forces in the wedge ring. The reaction equations were solved, and the jacking forces were determined as a function of the coefficient of friction and the hoop force in the wedge ring.

Another variable considered was the angle of the preload ramp. Ramp angles of 5° and 10° were investigated. It was found that a substantial decrease in the preload and releasing jacking forces occurred using a 5° ramp and a slight increase in the unload jacking force using a 5° ramp. Therefore, a 5° ramp is used to minimize the required jacking force. Figure 20 shows a plot of jacking force versus coefficient of friction for the three operating conditions. The jacking force is a per jack force using a total of four jacks. Wedge ring hoop forces of 0 and 44.5 kN (10,000 lbs) were considered, which tends to be the bounds depending on the final tolerances between the wedge ring and closure plug. In Figure 20, four pairs of lines are shown. The upper line is for a zero hoop force and the lower line is for a 44.5 kN hoop force. The plot also shows the variation between a preload ramp of 5° and 10°. Figure 21 is a plot of the normal forces as a function of the coefficient of friction for a 5° preload ramp.

Summary:

A quick actuating closure and handling system has been designed to reduce the projected inspection cost and to increase the research facility productivity. The new closure system, which takes 2 hours to remove, allows easy access to the internal components of the combustor for inspection of the transpiration cooled nozzle, the fuel spraybar, and the liquid oxygen injection system. The structural integrity of the combustor is maintained while reducing the complex handling operations associated with assembly and disassembly of the closure components. The analysis shows that the fatigue life of the combustor is not reduced and that the new design meets the requirements of the ASME Pressure Vessel Code. The new design increases system reliability by providing an improved sealing system and eliminates the possibility of the unsafe handling of the large end closure components.

104

COMBUSTOR ASSEMBLY

Figure 1

Figure 2

105

END CLOSURE
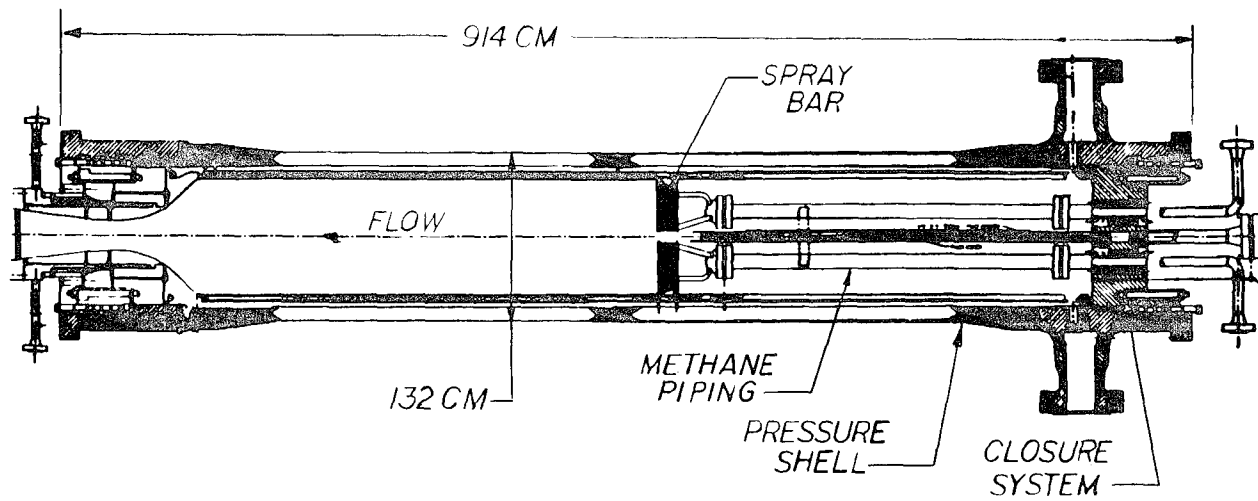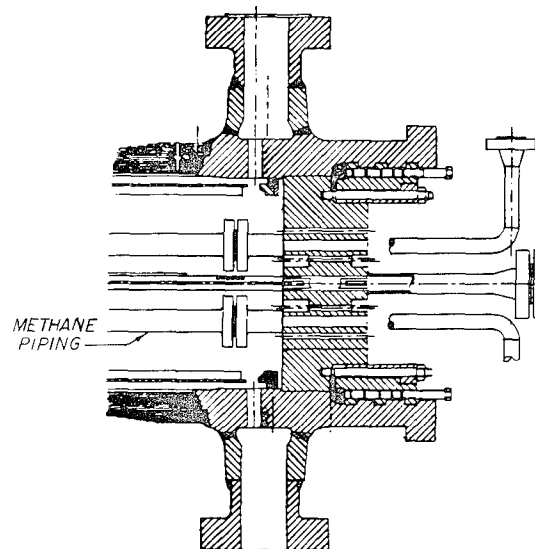
Figure 3

Figure 4

Figure 5

CLOSURE ASSEMBLY

Figure 6

LOCK ASSEMBLY
(LOCKED POSITION)

FRONT TEE — SHIM

PRELOAD RAMP — SHEAR BLOCK

SHEAR BLOCK

COMBUSTOR PRESSURE SHELL

TURNBUCKLE

JACK

WEDGE RING

CLOSURE PLUG

Figure 7

LOCK ASSEMBLY
(UNLOCKED POSITION)

PRELOAD RAMP

COMBUSTOR BARREL

SHEAR BLOCK

SEAL RING

KEY ASSEMBLY

BEARING BLOCK

PUSH ROD

JACK

CLOSURE PLUG

WEDGE RING
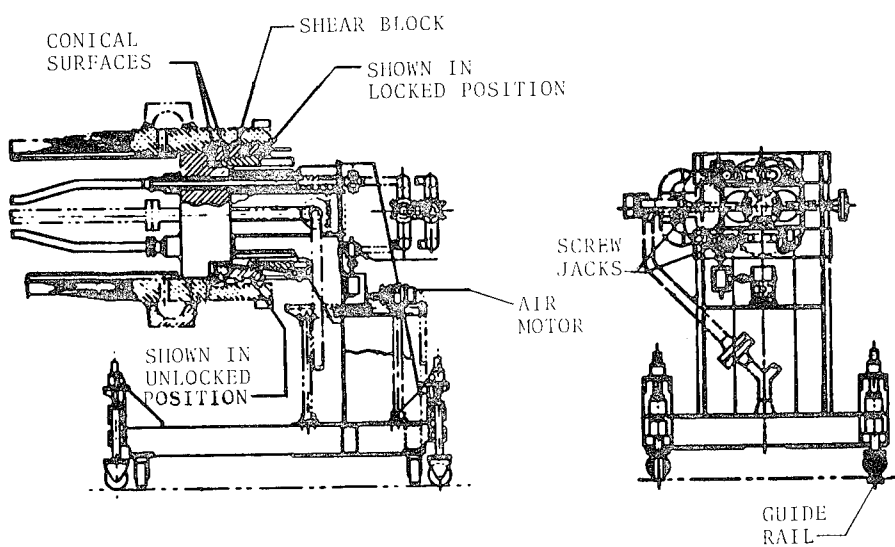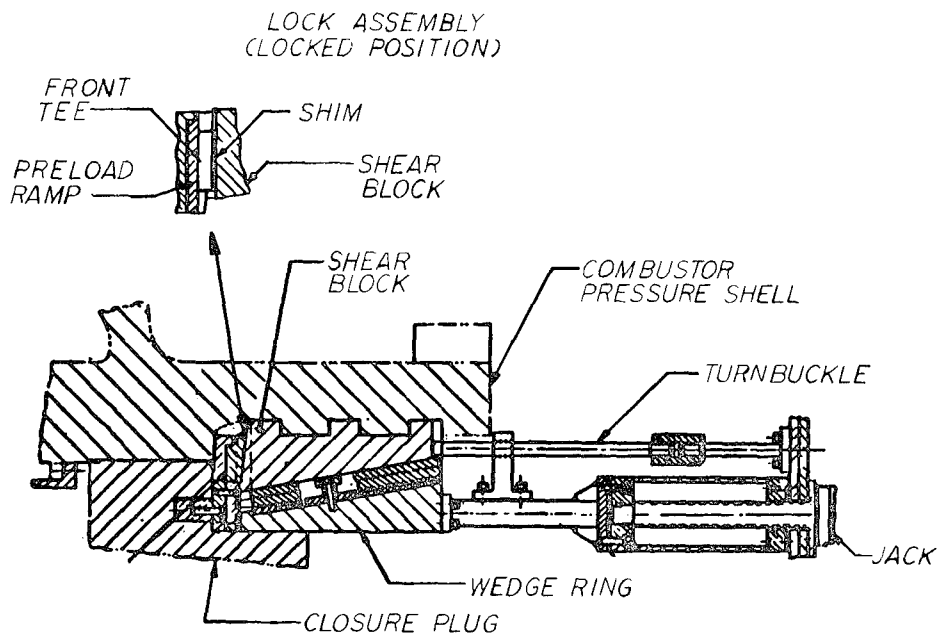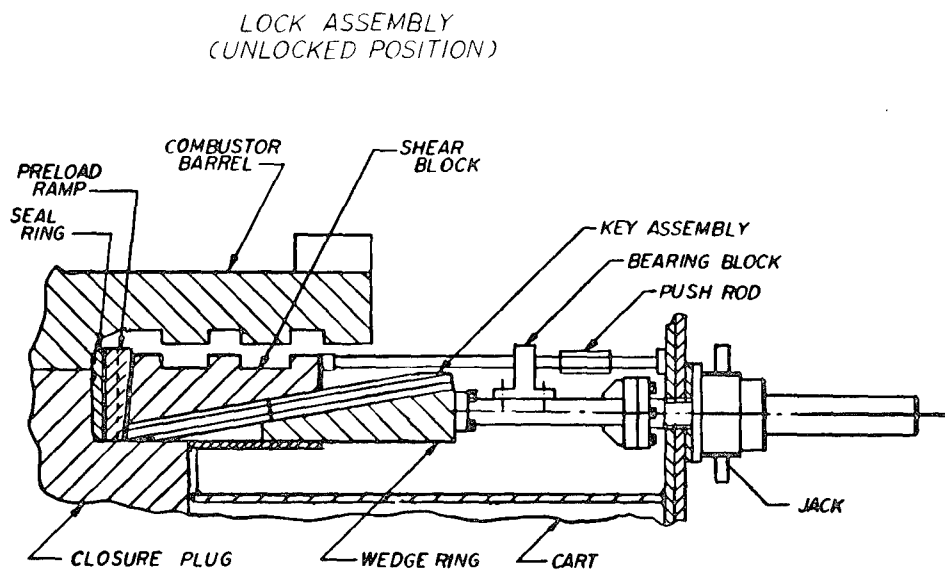
CART

Figure 8

108
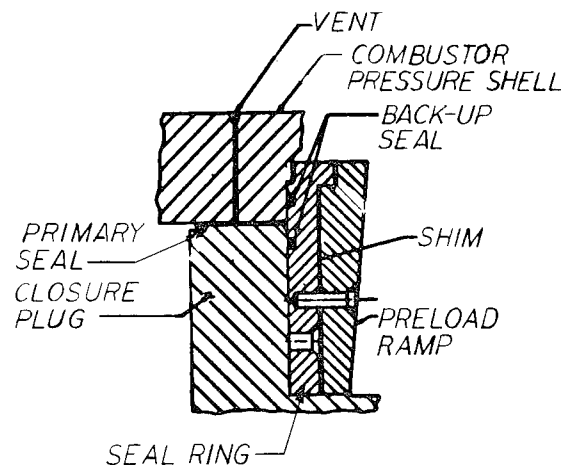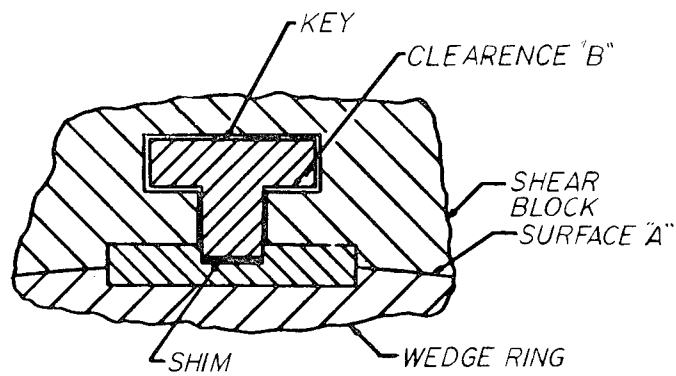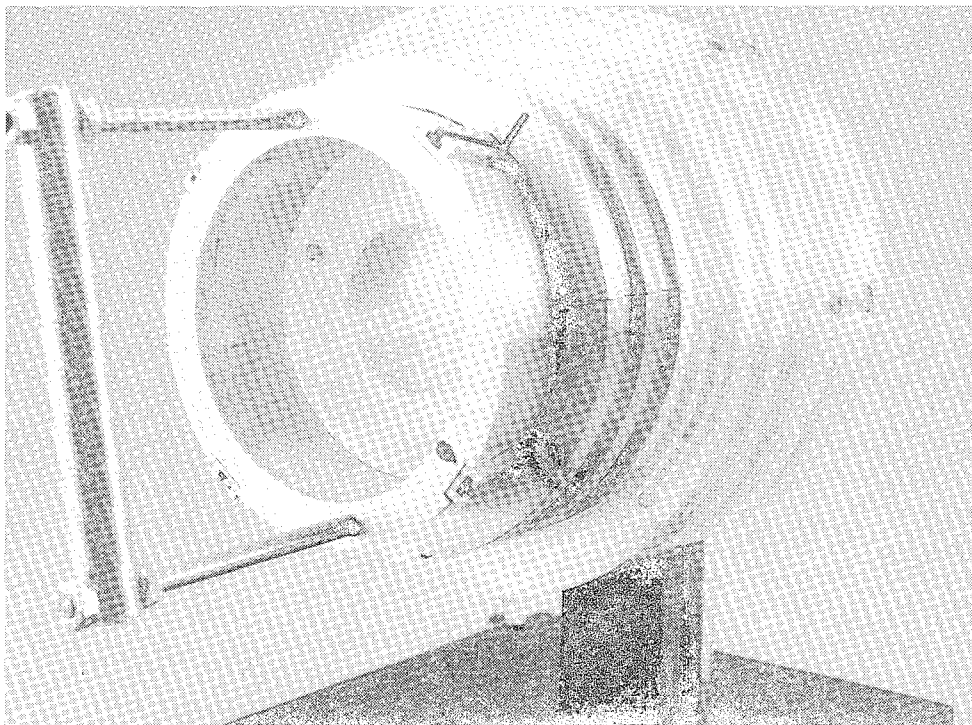
Figure 9

Figure 10

Figure 11

LOAD PATH

Figure 12

110

CART ASSEMBLY

26.67 CM

241.3 CM

143.51 CM

284.48 CM

3107 kg   2104 kg

Figure 13

REINFORCEMENT
RING

STRAIN GAGES

2 LOCATED
180 APART

TORUS

LOCKING GROOVES

AIR INLET

LAMINATED TRANSITION
SECTION

LAMINATED BARREL

TUNNEL
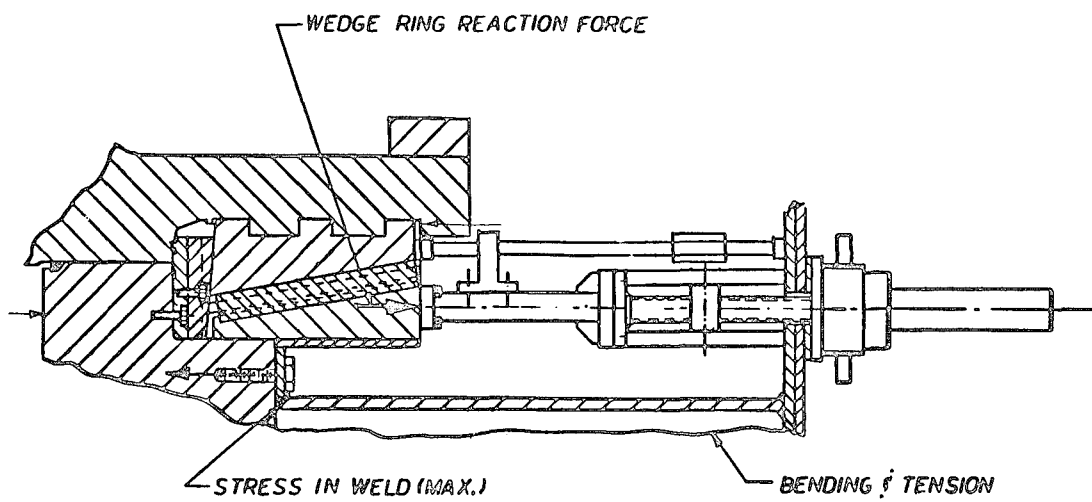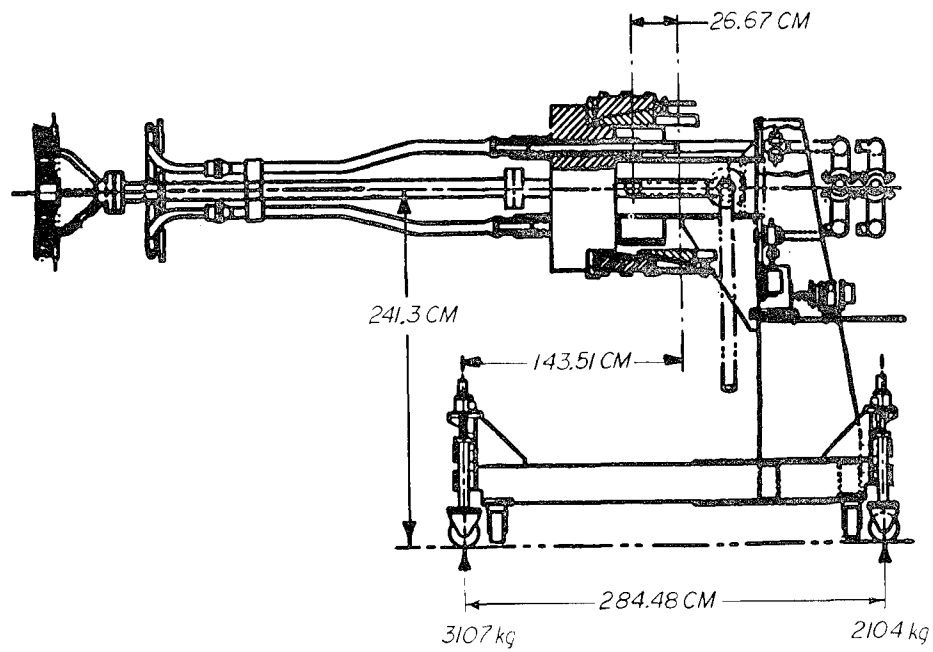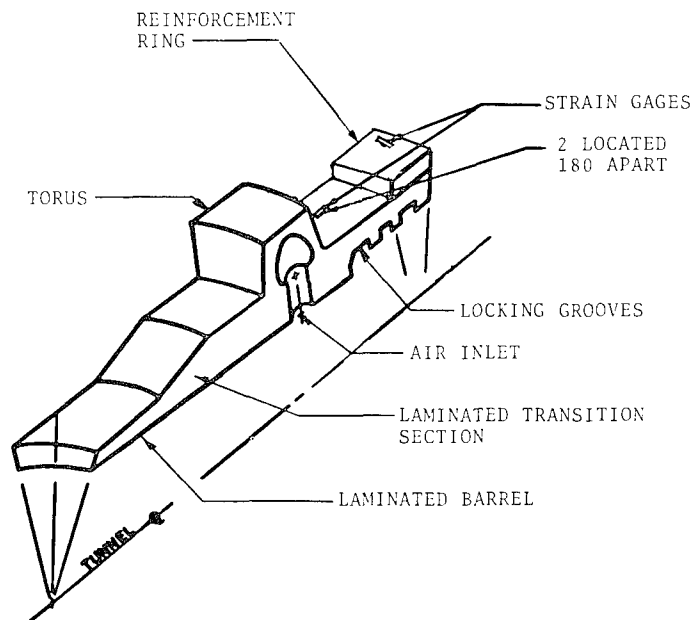
**SKETCH OF
FINITE ELEMENT MODEL**

Figure 14

FINITE-ELEMENT MODEL
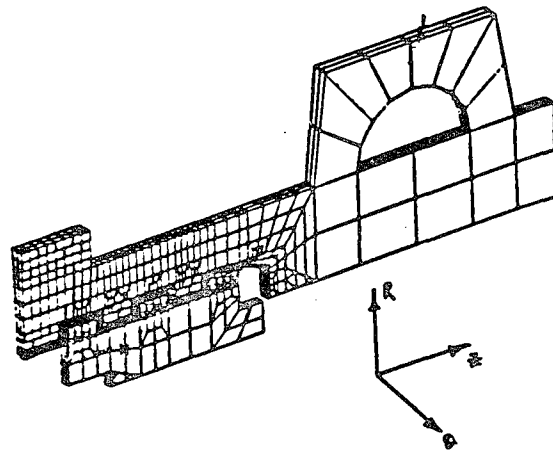
Figure 15

DEFORMED SHAPE

Figure 16

STRESS (MPa)

311.0

248.0

184.5

121.1

57.7

-5.6

-69.1

-132.5

-195.9

Figure 17

Figure 18

COMPONENT FORCES

PRELOAD

RELEASE

UNLOAD
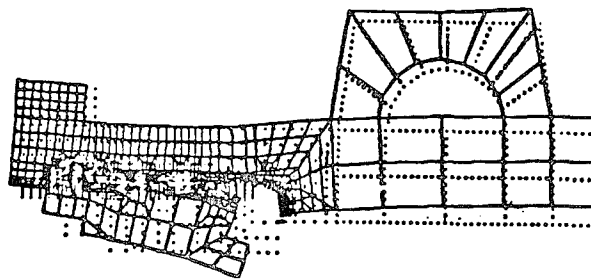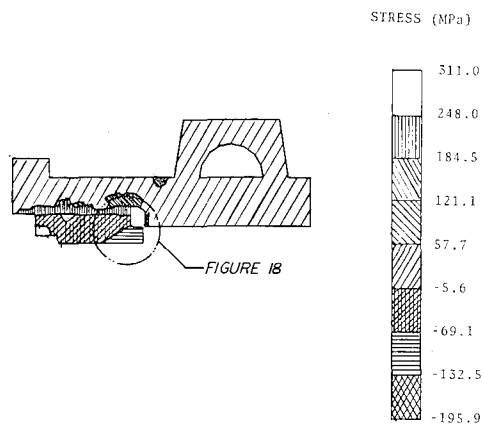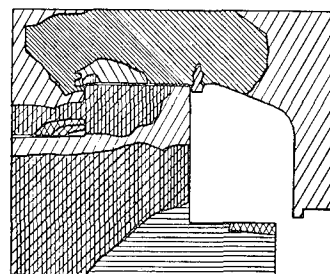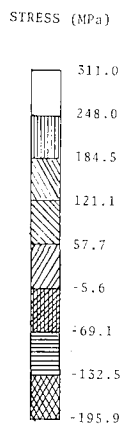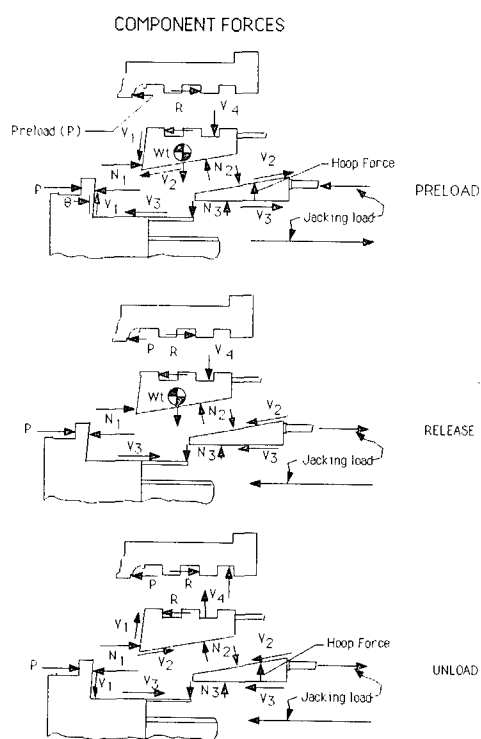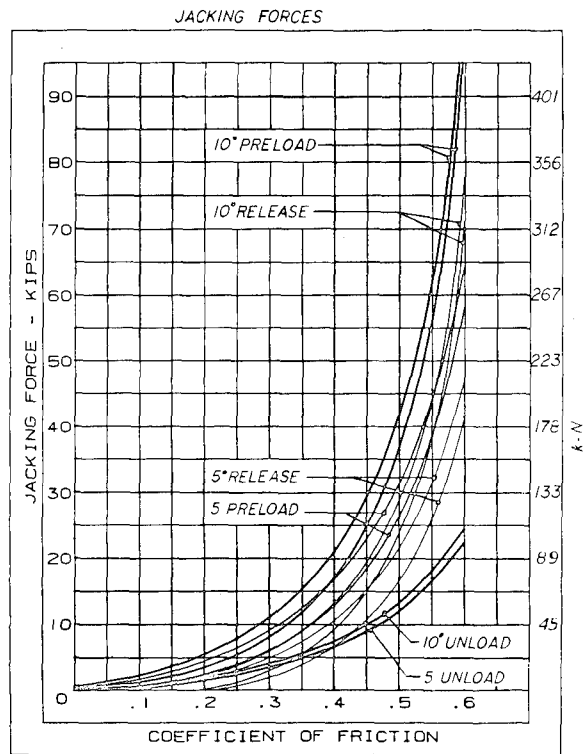
Figure 19

Figure 20

Figure 21

114
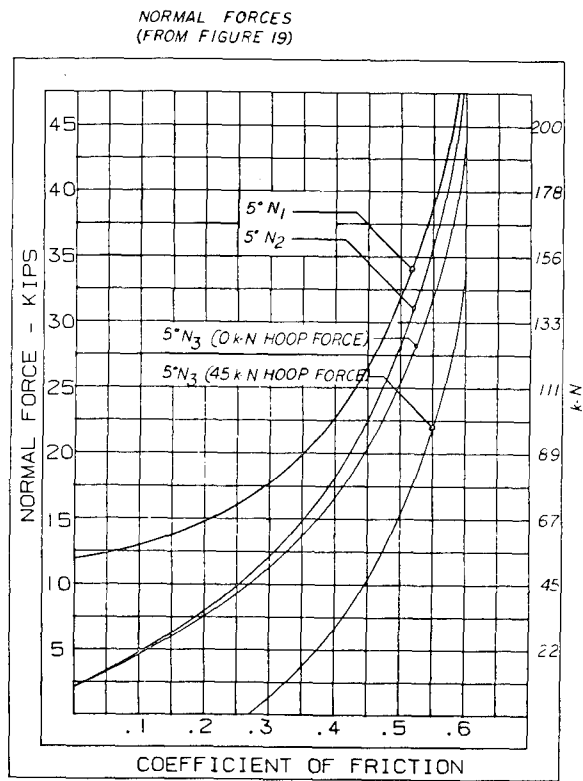
DEVELOPMENT OF A MOTORIZED CRYOVALVE FOR THE CONTROL
OF SUPERFLUID LIQUID HELIUM

K. R. Lorell, J-N. Aubrun, D. F. Zacharie, and D. J. Frank*

ABSTRACT

Recent advances in the technology of infrared detectors have made possible a wide range of scientific measurements and investigations. The Infrared Astronomy Satellite (IRAS), the Cosmic Background Explorer (COBE), the Space Infrared Telescope Facility (SIRTF), and the Infrared Space Observatory (ISO) are all examples of this new generation of instruments. One of the requirements for the use of sensitive IR detectors is that the entire instrument be cooled to temperatures approaching absolute zero. The cryogenic cooling system for these instruments is commonly designed as a large dewar containing liquid helium which completely surrounds the apparatus. Thus, there is a need for a remotely controlled, motorized cryovalve that is simple, reliable, and compact and can operate over extended periods of time in cryo-vac conditions. This paper describes the design, development, and test of a motorized cryovalve with application to a variety of cryogenic systems currently under development at Lockheed.

INTRODUCTION

Recent advances in the technology of infrared detectors have made possible a wide range of scientific measurements and investigations. The Infrared Astronomy Satellite (IRAS), the Cosmic Background Explorer (COBE), the Space Infrared Telescope Facility (SIRTF), and the Infrared Space Observatory (ISO) are all examples of this new generation of instruments. One of the requirements for the use of sensitive IR detectors is that the entire instrument be cooled to temperatures approaching absolute zero. The cryogenic cooling system for these instruments is commonly designed as a large dewar containing superfluid liquid helium (SFHe), which completely surrounds the apparatus. SFHe is capable of providing cooling to temperatures as low as 1.5 K.

Because these experiments are typically flown in space and because many layers of insulation as well as a vacuum shell are required to keep heat leaks to a minimum, the valves that control the filling, venting, and routing of the cryogen are inaccessible. Thus, there is a need for a remotely controlled, motorized cryovalve which is simple, reliable, compact,

---

*Lockheed Palo Alto Research Laboratory, Palo Alto, California

and can operate over extended periods of time in a vacuum at temperatures in the range 1 K to 400 K. In addition, valve operation must produce minimal thermal energy, because any heat input to the cryogen will significantly shorten the useful lifetime of the instrument.

This paper describes the design and test of a 1/4-in.-diameter motorized cryovalve with an orifice of 4.4 mm for the Lockheed Independent Development (ID) SFHe dewar. This dewar, shown in Figure 1, has a 200-L SFHe tank that surrounds the experiment volume and is capable of cooling the enclosed instrument to temperatures as low as 1.6 K. In addition, the dewar uses a special toroidal tank containing normal-boiling-point helium that acts as a thermal guard during extended ground-hold periods. Figure 2 is a plumbing schematic of the system and shows the location of the motorized cryovalves.
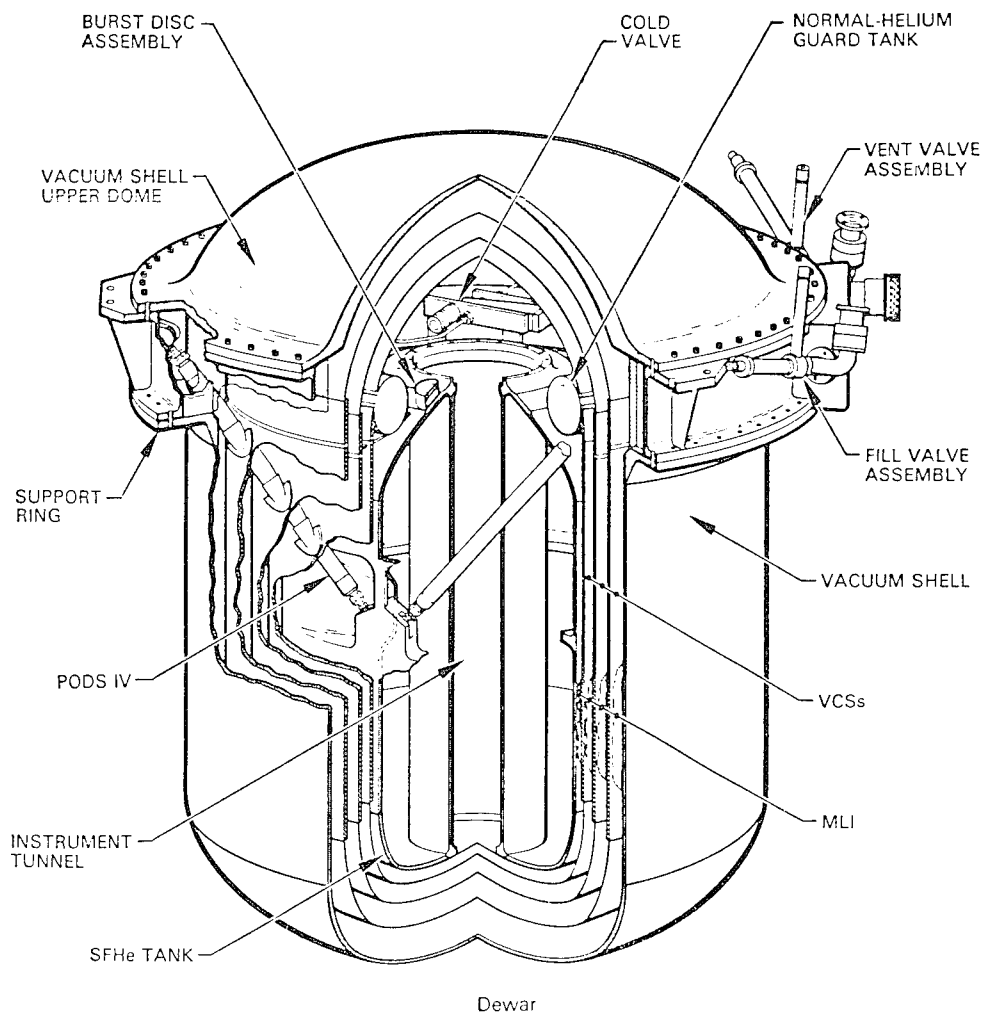
Figure 1   Cross Section of the Lockheed ID SFHe Dewar
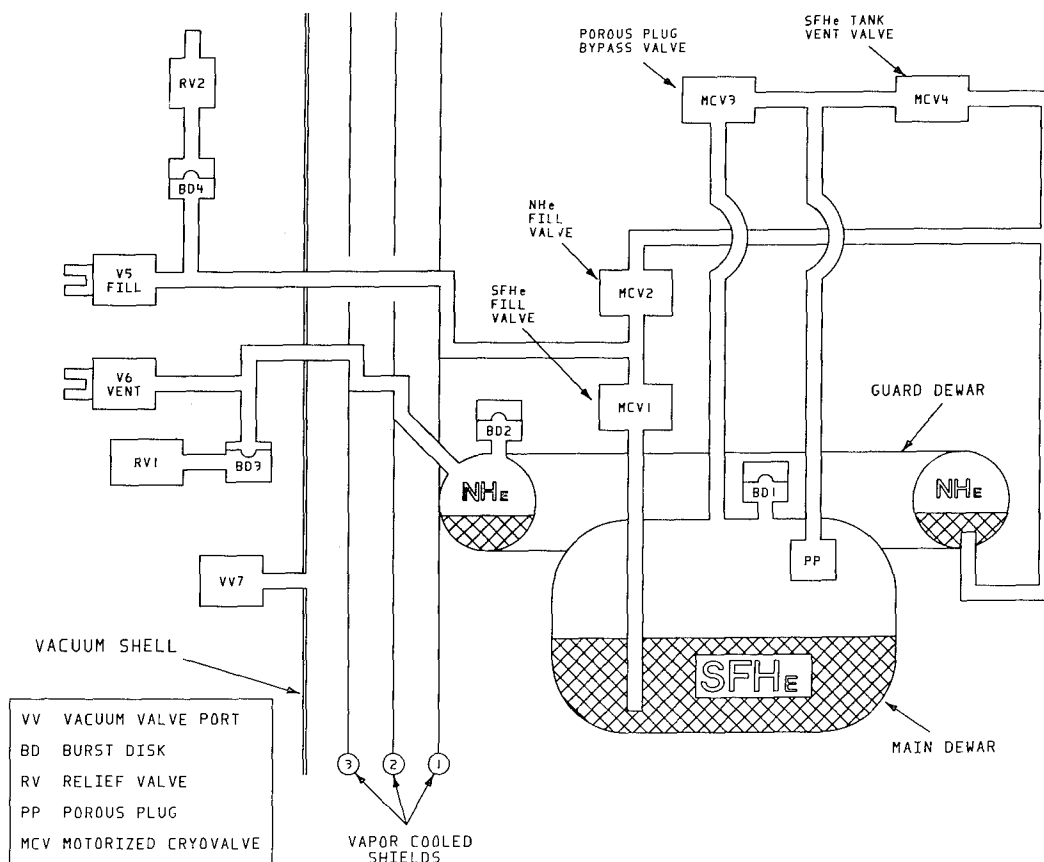
Figure 2   Plumbing Schematic for the Lockheed ID Dewar

CRYOMECHANISMS

This section describes some of the design considerations for
electromechanical devices which must be operated in cryo-vac conditions.

Mechanical

Mechanical design considerations for cryomechanisms center around two
primary concerns: (1) absolute and relative (between mating parts)
dimensional changes as the mechanism is cooled from room temperature to
operating temperature and (2) lubrication (or friction reduction) for
rotating parts. These two problems can interact when a bearing is pressed
into an aluminum housing and the differential in coefficients of thermal
contraction between the steel race and the aluminum housing can cause the
bearing to sieze when cold. The use of gearboxes is especially critical,
because they involve lubrication, rotating parts, and close dimensional
tolerances.

Electrical

Electrical components for use in cryo-vac must be selected to minimize the impact of the severe operating environment. For example, motors must have the appropriate mechanical properties and preferably be of the brushless or stepper design, because brushes have been shown to be unreliable in a vacuum. In addition, motor sizing must be conservative because of substantial increases in friction related to ineffective (or nonexistent) lubrication, and dimensional changes. Sealed switches can be a problem because the hermetic seal usually involves pressurizing the device with nitrogen gas, which freezes at liquid-helium temperatures. The size, current-carrying capacity, and number of wires required to communicate with the mechanism are critical because wires represent a thermal leak from the outside and because incorporating wires in the dewar complicates the thermal design and arrangement of the insulation blankets.

Thermal

The two primary thermal concerns in the design of cryomechanisms are (1) thermal energy generated by the operation of the mechanism and (2) thermal leaks, which are most often related to the electrical connections to the outside. The energy generated by the mechanism can usually be minimized by careful sizing of the actuation device. Because the wires leading to the outside of the dewar represent a continuous source of thermal input, minimizing the number of required wires is essential. In addition, the lower the current the wire is required to carry, the smaller the diameter and resultant heat leak. Thus, the sizing of the actuation device should be heavily weighted in favor of the minimum current configuration capable of meeting the requirements.

Reliability

The reliability of a cryomechanism is a critical issue, even for devices that are not flight hardware. Virtually all such mechanisms become components of a much larger, more complex system and are usually located in the most isolated part of a cryogenic system, inside a vacuum shell and numerous layers of insulation and cooled shields. The dewar is often required to remain cold for long periods of time before launch or use in an experiment. This dormant period can last from several days to many months. In addition, the cryomechanism is often in the critical path for successful operation of the experiment; for example, cryomechanisms are typically used to position optical elements and to operate cryogen fill and vent valves.

Magnetic Fields

Although the usual reason for cooling an apparatus to cryogenic temperatures has to do with increasing the sensitivity of measurements in the infrared, a novel NASA/Stanford University/Lockheed experiment (Gravity Probe-B) utilizes the quantized property of magnetic fields in a film of superconducting lead niobate to provide an extremely sensitive readout of the orientation of the axis of rotation of a gyroscope. Cryomechanisms

located near the section of the dewar that is sensitive to magnetic fields must therefore operate with a minimum of stray flux. This dictates the use of the smallest, simplest actuation device which meets the basic mechanical requirements, so that the flux around the mechanism can be minimized.

REQUIREMENTS FOR THE SFHe CONTROL VALVE

In addition to the concerns discussed in the previous section, additional constraints and requirements were addressed in the design of the SFHe control valve.

Mechanical Requirements

Mechanical design is driven by two main concerns: (1) the valve sealing mechanism itself must be leak-proof to superfluid helium, and (2) the mechanism that opens and closes the valve must be precise in both position and force exerted on the seal and must operate reliably near absolute zero.

The conventional approach to the first problem is to apply a large force (in the case of a 1/4-in. valve, about 1000 N) to push the stem against the valve seat. This may produce plastic deformation of the stem and of the seat, and it is thus essential to carefully control the amount of force exerted by the drive mechanism in order to prevent permanent damage and loss of sealing performance. This mechanism must be able to function at ordinary temperature as well as the specified operating temperature to allow preflight checks. Thus dimensional change due to temperature variation and differences in coefficients of thermal expansion between the various materials can be severe, and the design must be as insensitive to these changes as possible.

Producing such a large seat force requires some kind of gear reduction system to minimize the size of the drive motor and to prevent back driving when no power is applied to the motor. This is a critical design problem because it involves lubrication, rotating parts, and close dimensional tolerances. The required force may be obtained by directly closing the valve with the gear/drive-motor system. However, it is then difficult to produce the exact force level because, as soon as there is contact between stem and seat, the relationship between current in the motor and force on the seat depends strongly on such factors as friction, compliance of the gear train and stem/seat assembly, and the angular position of the motor shaft.

Electrical Requirements

Besides the general problems posed by using electrical components in a cryo-vac environment, the design of the cryovalve had to meet additional requirements specific to the ID dewar application. Reducing the cryogen losses was especially important; most of these losses result from the thermal conductivity of the wires carrying signals and drive current to the

motor across the dewar interface. The low temperature prevents the use of certain electronic components. For instance, brushless motors that use semiconducting Hall-effect detectors for commutation cannot be used because these devices cannot operate at cryogenic temperatures. Similarly, most of the electronic components have to be situated in a warmer part of the spacecraft and lead wires must be used to communicate with the mechanism sensors and actuators.

Sealing Requirements

The valve must be able to effectively seal against SFHe down to temperatures of 1 K. The maximum allowable leak rate across the seat is 10^{-6} scc/s* with no detectable leakage through the valve body.

Design Optimization

The various requirements are obviously coupled, and trade-offs have to be considered between power dissipation, opening/closing time, gear ratio and gear-box complexity and reliability, and motor-drive system complexity. Additional constraints are the size and weight of the device. Since no lubrication is possible, reducing the number of bearings and bushings is important as well as reducing the transverse loads applied to these bearings and bushings to minimize friction and stiction.

CRYOVALVE DESIGN

Compression Spring

The approach taken for Lockheed cryovalve is very similar to that used for the valves on automotive engines. The valve seat force is provided by a compressed spring and valve opening is accomplished using a lever-and-pivot arrangement. Figure 3 shows the principle of operation and the location of the spring and lever mechanism relative to the valve. This concept has the advantage that the seat force is constant, predictable, and repeatable. While designs using motor torque to drive the stem into the seat may be more compact, the drive unit is more highly stressed and the seat force, which is critical to a good seal in the case of superfluid helium, is much less predictable. Belleville washers were used because they provided the required force in a relatively compact package. In addition, the spring constant was such that the increase in force over the range of motion of the stem was minimal.

Spindle/Tape Drive

The difficulty in implementing a motor-driven valve was in developing enough force with a small motor to be able to compress the seat spring in order to open the valve. Even at room-temperature conditions using a conventionally lubricated drive unit, the force/motor-size problem is difficult to solve. Figure 4 illustrates how the drive unit is connected to the lift arms so that the small motor/gearbox combination produces the

---

*scc - standard cubic centimeter per second

120
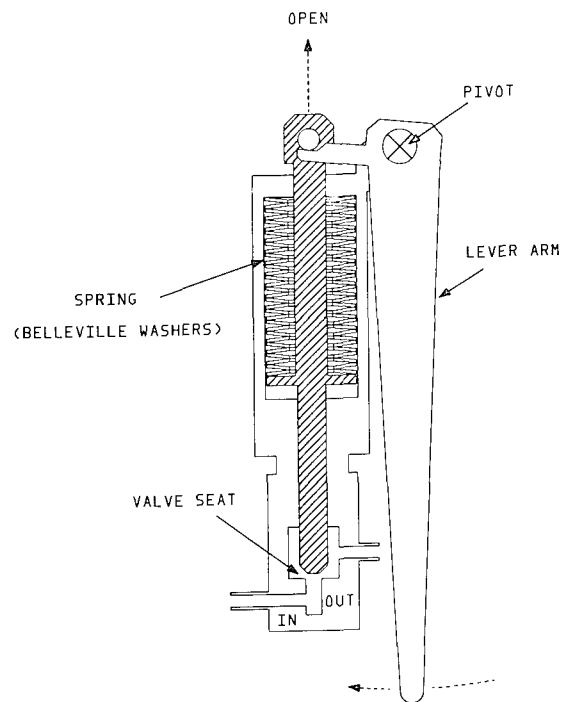
Figure 3   Valve Actuation Showing Spring and Lever Mechanism
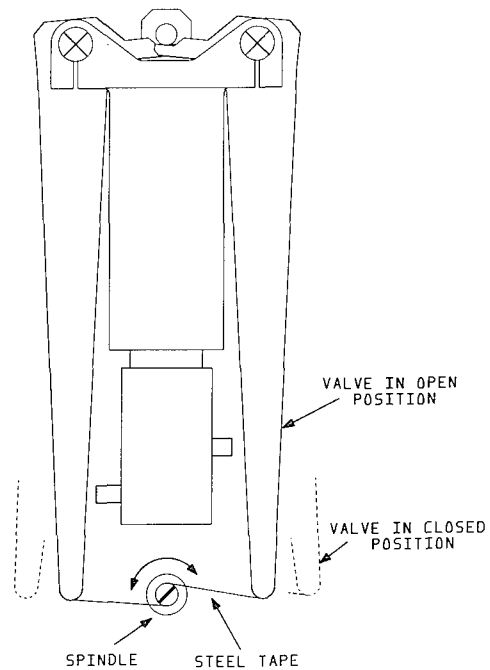
Figure 4   Spindle and Steel-Tape Drive for Lift-Arm Actuation

required actuation torque. The lift arms are designed to have a 6-to-1 lever ratio, thereby reducing the required actuation force from 956 N to 160 N (or 80 N per arm).

The spindle and tape arrangement shown in Figure 4 has several advantages. It is a simple and direct way of translating rotary motion into linear motion. It requires no pivots or gears and attaches directly to the lift arms. Finally, because the tape pulls on the spindle from both sides, there is zero net side force on the gearbox output shaft. This is especially important because the gearbox must run without lubrication and the friction losses through the gearbox are a noticeable part of the motor torque requirement.

The other aspect of the spindle and tape drive is the means of balancing the forces on each of the lift arms. If the tape were attached directly to each of the arms, even a slight decentering of the spindle with respect to the arms will cause the arms to have very different engagement forces at the lift pin. This problem was solved as shown in Figure 5. Instead of being directly attached to the arm, the metal tape is made as a continuous loop, and thus the tension force of each arm is automatically balanced.
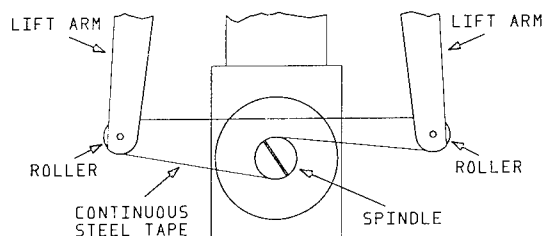
Figure 5   Continuous Steel-Tape Drive

Motor/Gearbox

The torque required to actuate the valve mechanism is provided by a stepper-motor/gearbox combination as seen in Figure 6. The motor is a four-pole stepper with a nominal output torque of 0.007 N-m. The 500:1 planetary gearbox combined with the 1.25-cm-diameter spindle generates a maximum theoretical tension force in the tape of 285 N, which is approximately 3 times the calculated required force. However, because of the high friction losses in the gearbox, which are especially apparent at cryogenic temperatures, a conservative design philosophy was used to size the motor. It was subsequently determined that the motor need not run at maximum current, due primarily to the extra torque capability.

STEPPER MOTOR

500:1
PLANETARY
GEARBOX

ROLLER

LEVER ARM

STEEL TAPE

LIMIT SWITCHES

CAMS

SPINDLE

LEVER ARM

ROLLER
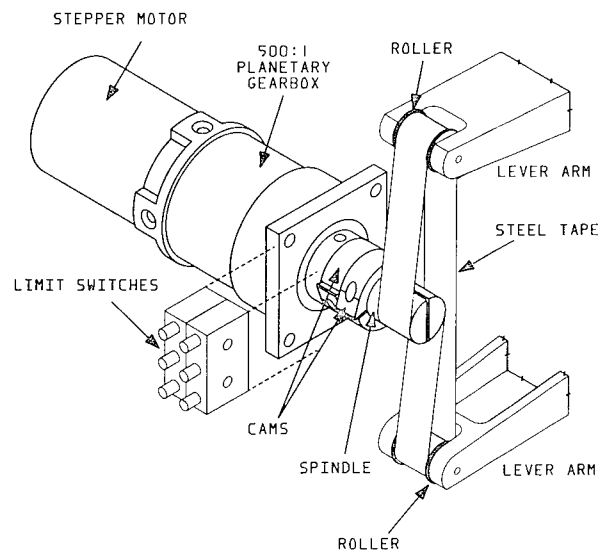
Figure 6   Motor and Gear-Box Drive Mechanism Detail

Because lubrication has been a continuous source of difficulty on
previous cryomechanism designs, the motor and gearbox operate completely
free of lubricant. Before integration, both units are completely
disassembled and thoroughly cleaned. The planetary gearbox utilizes only
two ball bearings, located on the output shaft. The remaining components
turn on bushings. The motor has two Bar-Temp bearings, both of which are
also cleaned. Since the speed of operation is so low, the total number of
duty cycles in the lifetime of a given unit is limited, and the motor has
excess torque capability, no operational problems caused by the lack of
lubricant have developed.

The motor is controlled by an off-the-shelf motor drive integrated
circuit, which is integrated into an electronics package and designed to
control up to five valves. Completion of the open and close cycles is
controlled by two limit switches that are actuated by cams located just
behind the spindle and the gearbox output shaft. The cams and limit
switches are shown in Figure 6. A schematic diagram of the control
electronics is shown in Figure 7.

Valve

The valve itself is a commercially available sealed-stem unit
manufactured by Nupro. Because the valve body is stainless steel and the
bellows surrounding the valve stem are hermetically sealed to the body,
essentially no modification was required for use in a cryogenic system. The
valve body acts as the central structure for the attachment of the actuation
mechanism. The drawing in Figure 8 and the photograph of Figure 9 show the
assembled cryovalve.
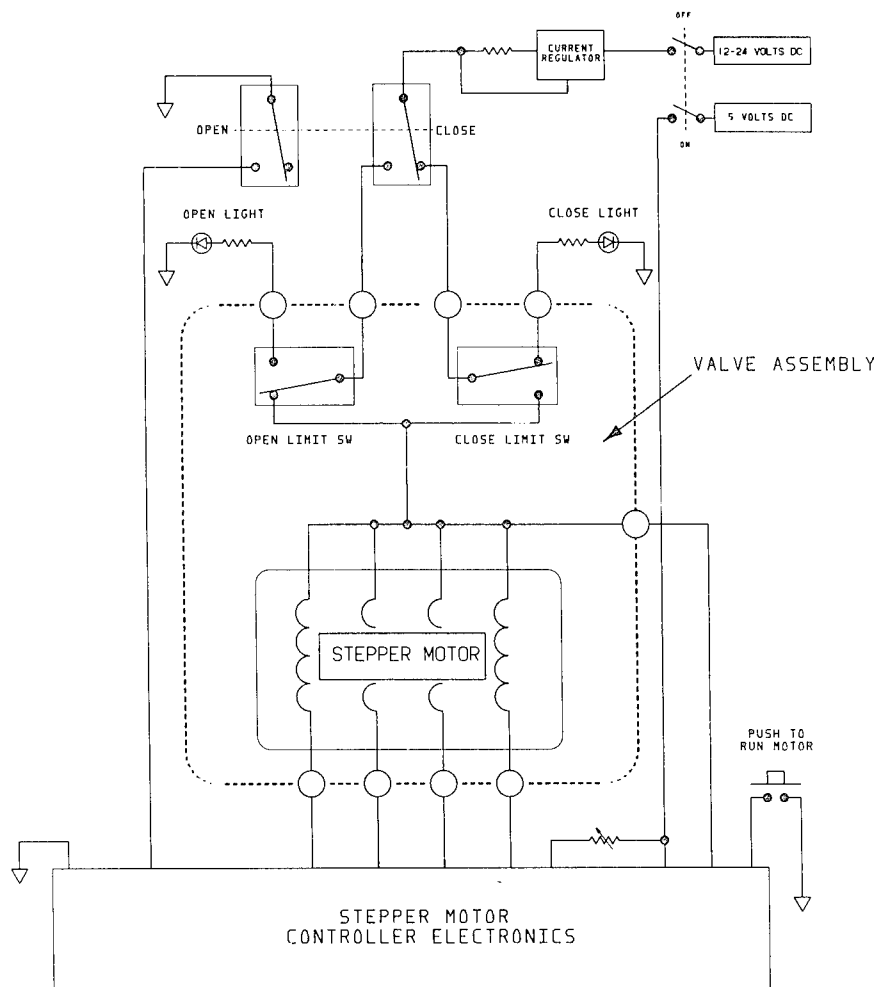
Figure 7 Motor Drive Electronics Schematic
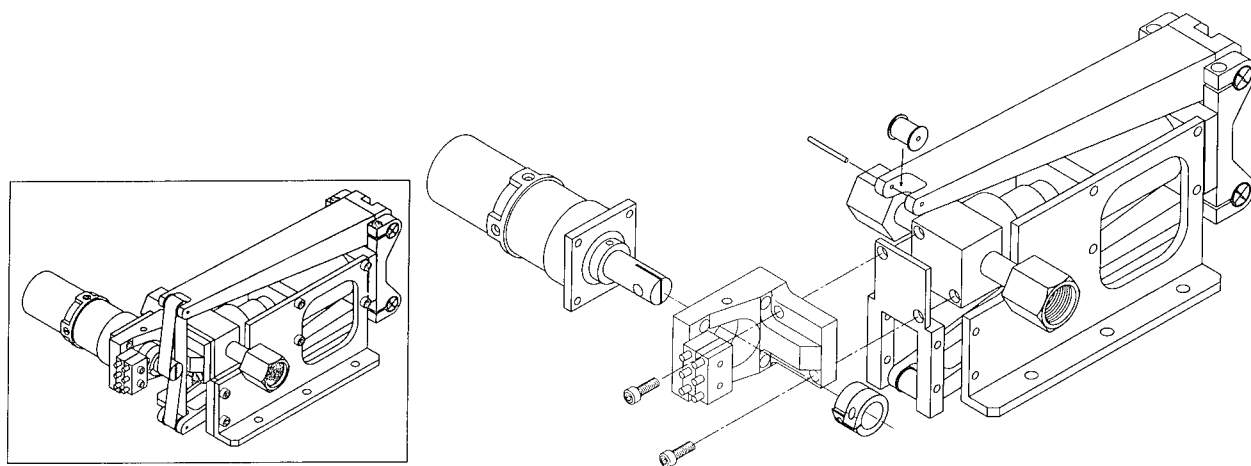
Figure 8 Cryovalve Assembly
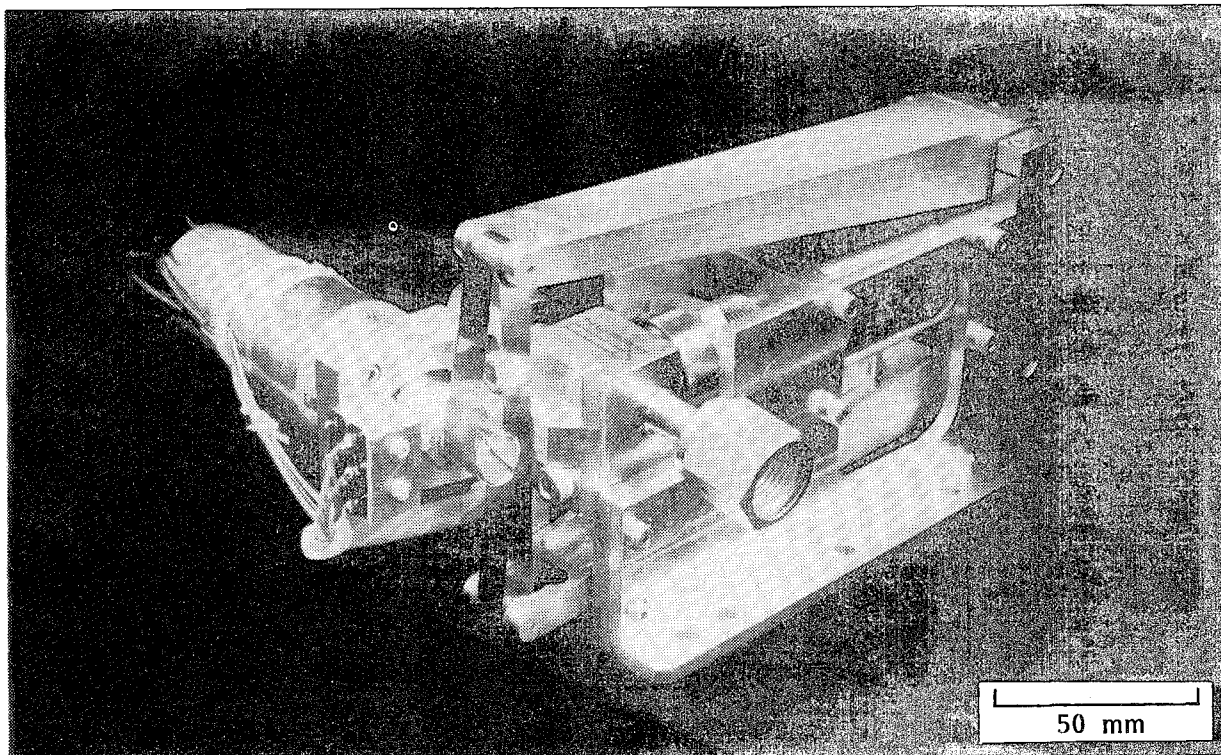
Figure 9   Lockheed Cryovalve

TESTING/PERFORMANCE EVALUATION

Objective

The primary objective of the tests was to determine whether or not the basic goal of an electrically driven mechanism to actuate a valve capable of sealing a cryogenic liquid had been met. However, a number of other objectives associated with the operation of the valve and the mechanism were also explored by the test program. These objectives are:

- Measurement of leak rate and degradation of leak rate as a function of number of operation cycles
- Measurement of leakage from the valve body assembly
- Determination of the minimum current required to operate the motor under increased load (friction) conditions at cryogenic temperatures
- Determination of thermal energy (approximate) dissipated to cryogen
- Observation of behavior of the stainless steel tape drive and potential embrittlement at cryogenic temperatures

Although the operational environment is SFHe at or below a temperature of 2.1 K, tests on the cryovalve were performed using liquid nitrogen (LN_2) at 77 K and LHe at 4.2 K. All cryogenic testing is time consuming and expensive, but using LN_2 and LHe is considerably simpler and less

125

expensive than testing with SFHe. Test results described by Siebert indicate that leak-tight performance at LN_2 temperatures is directly correlated with leak-tight performance under SFHe conditions (Ref. 1).

Test Apparatus

An apparatus was designed and fabricated to perform ambient and cold cycling of the cryovalve assemblies. The test setup included instrumentation to measure temperatures at various locations on the valve assembly and to measure leak rates both at the valve seat and from the valve body. Each of the valves to be used in the ID dewar was subjected to a minimum of 50 cycles at LN_2 with leakage rates measured every 10 cycles. Leak rates were also measured following each cooldown or warmup of the valve assembly. One of the valves was tested at LHe temperature as well.

The test apparatus is shown schematically in Figure 10. The valve assembly can be seen located inside of an evacuated container which is submerged in either LN_2 or LHe. Access to the valve is obtained by separating the upper and lower halves of the container, which remain sealed during a test. Because the valve is in a vacuum, valve cooling takes place primarily though conduction by the support bracket. The container was

Figure 10 Cryovalve Test Apparatus

backfilled with gaseous He to improve the cooldown rate and to help condense
He in the lines at the valve seat during leak checking at LHe temperature.

Temperature sensors were installed at three locations: the support
bracket, the valve body, and the case of the motor. The motor temperature
measurement was of special interest because continued cycling of the valve
at LN_2 resulted in a noticeable temperature rise in the motor. Under
actual operating conditons, this phenomenon is not important because (1) the
valve is cycled very infrequently, and (2) the amount of heating at SFHe
temperatures is about a factor of 10 less than at 77 K because the resistance
of the motor windings has decreased by that amount. Nevertheless, during
the LN_2 tests, the cycle rate was controlled so that the motorcase
temperature did not exceed 100 K. Figure 11 shows a valve installed in the
test container before the vacuum seal is applied and Figure 12 shows the
test setup in the laboratory.
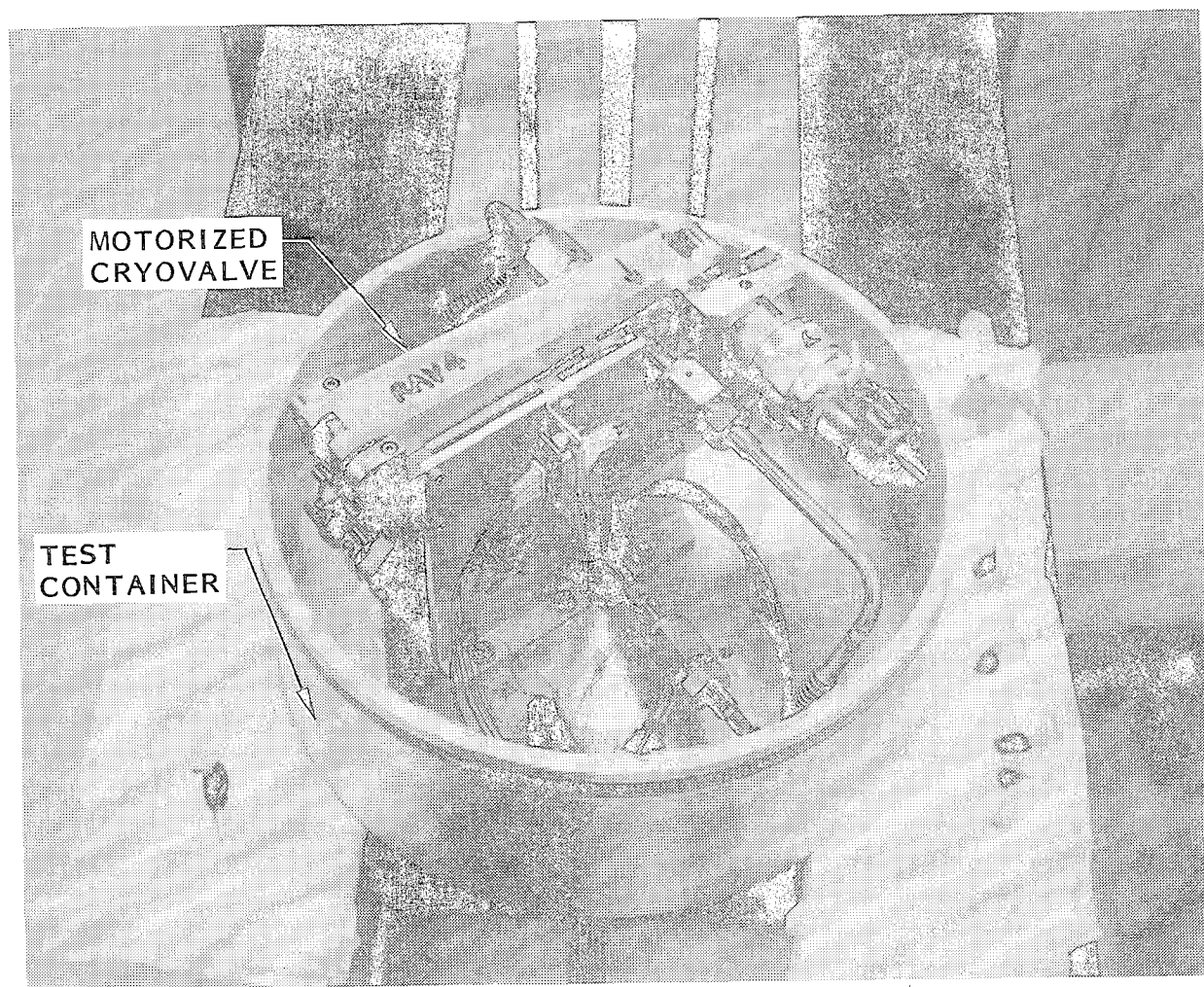
Figure 11   Cryovalve Mounted in Test Container
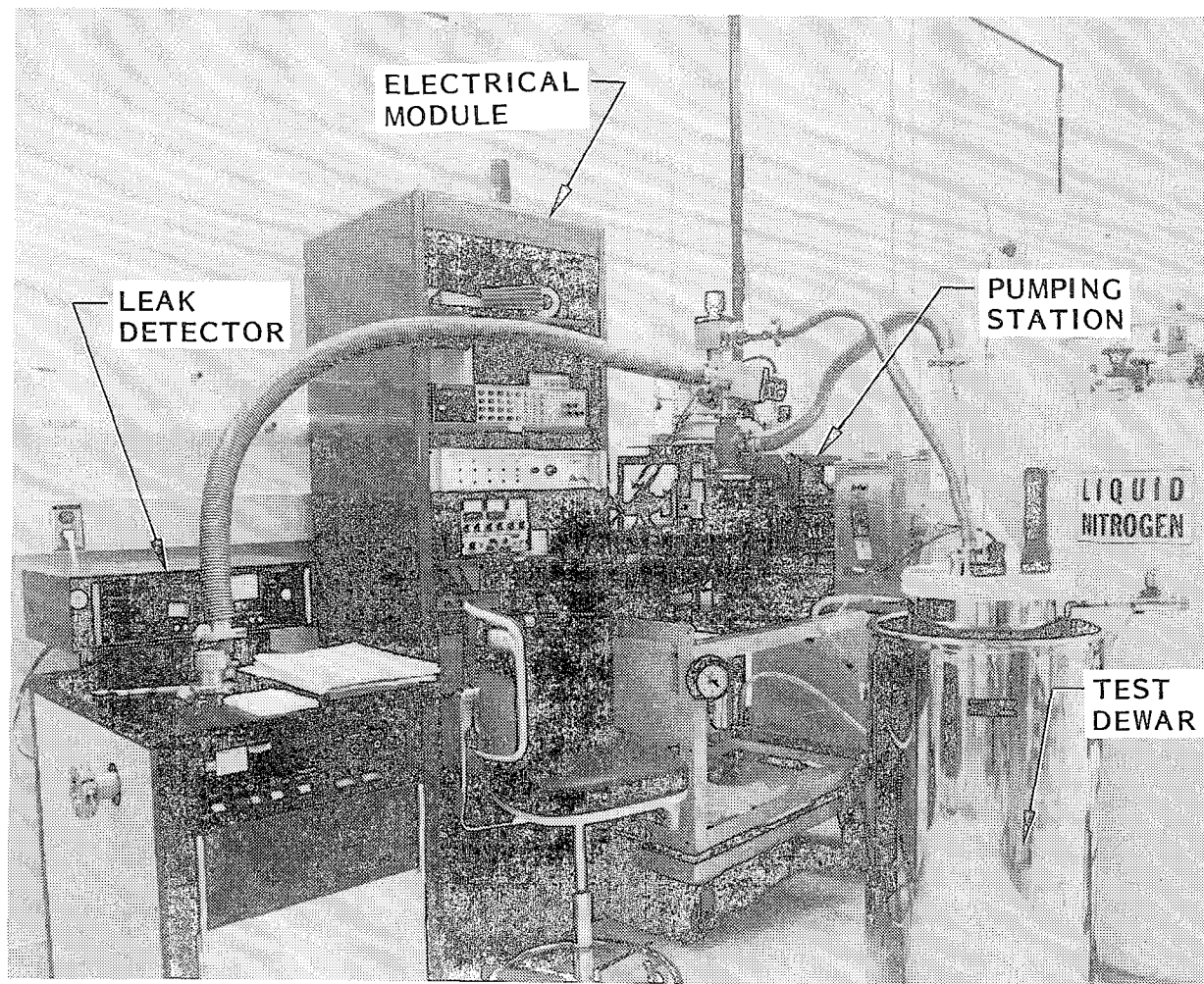
Figure 12   Laboratory Arrangement of Test Apparatus

Leak Checking

A leak detector with a sensitivity of 10^{-10} scc/s was used for all tests. The valve-seat seal was tested by first evacuating both the inlet and outlet lines with the valve open, then closing the valve. The input line was then pressurized with 20-psig gaseous He, and measurements of the leak rate were made at 1 min intervals for 3 min.

Leak checking of the hermetic seal between the bellows and the valve body required opening the valve and pressurizing the valve inlet and outlet lines with gaseous He. Leaks from the valve body into the evacuated test container were then examined with the leak detector. The same three leak rate measurements at 1 min intervals were used.

128

Background levels of gaseous He in the 10^{-8} scc/s range were found. They were due primarily to residual helium from the most recent leak check which was not completely pumped out of the lines. This was intentional in that the time required to pump to the 10^{-10} level would have been prohibitive. Since the acceptable leak rate is in the 10^{-6} scc/s range, a background of 10^{-8} is sufficiently small.

Test Results

Five valves were tested; all were tested at ambient and LN_2 temperatures, but only one was tested at LHe temperature. None of the valves had detectable leaks in the valve body. Lead rates through the valve seats at LN_2 temperature ranged from not measurable (below 10^{-8} scc/s) to a high of 10^{-6} scc/s. One of the unexplained phenomena observed during LN_2 cold cycling was the variability of the leak rate. When a valve exhibited a high leak rate (that is, a 10^{-6} scc/s range), cycling the valve one or more times would cause the leak rate to return to the 10^{-8} scc/s range or lower. One possible explanation is that the 1000-N seat force may have been detrimental to the copper valve stem. Deformation of the stem was observed on posttest disassembly, indicating that the seat force was excessive. If the stem did not locate itself on the seat in exactly the same way during each close cycle, it is possible that a small leak could develop.

A modification was made to the lift rod and the spring housing on the valve that was tested at LHe temperature so that the stem relative to the seat could be better controlled. When this valve was retested at LN_2, only one of the leak rates was larger than 10^{-8} scc/s, the high leak rate excursion being 8×10^{-7} scc/s.

Tests at LHe temperature showed no detectable leakage (i.e., a leak rate at or below the background 10^{-8} scc/s rate) with the exception of one cycle. Measurements during this cycle indicated no detectable leakage for the first minute. By the third minute, the leak rate had increased to 1.5×10^{-5} scc/s (slightly out of specificaton); however, on the subsequent and all later cycles, the leak rate returned to its previous low value. The leakage behavior was very different during this cycle. Typically, when one of the values had a detectable leak, the leakage appeared as soon as the helium was introduced upstream of the valve and remained constant throughout the 3-min period.

Conclusions and Comparisons

On the basis of these test results, the valve design was considered acceptable for laboratory testing of the ID dewar. As previously mentioned, four units were required. Figure 13 shows the units installed during fit-checking of the plumbing.
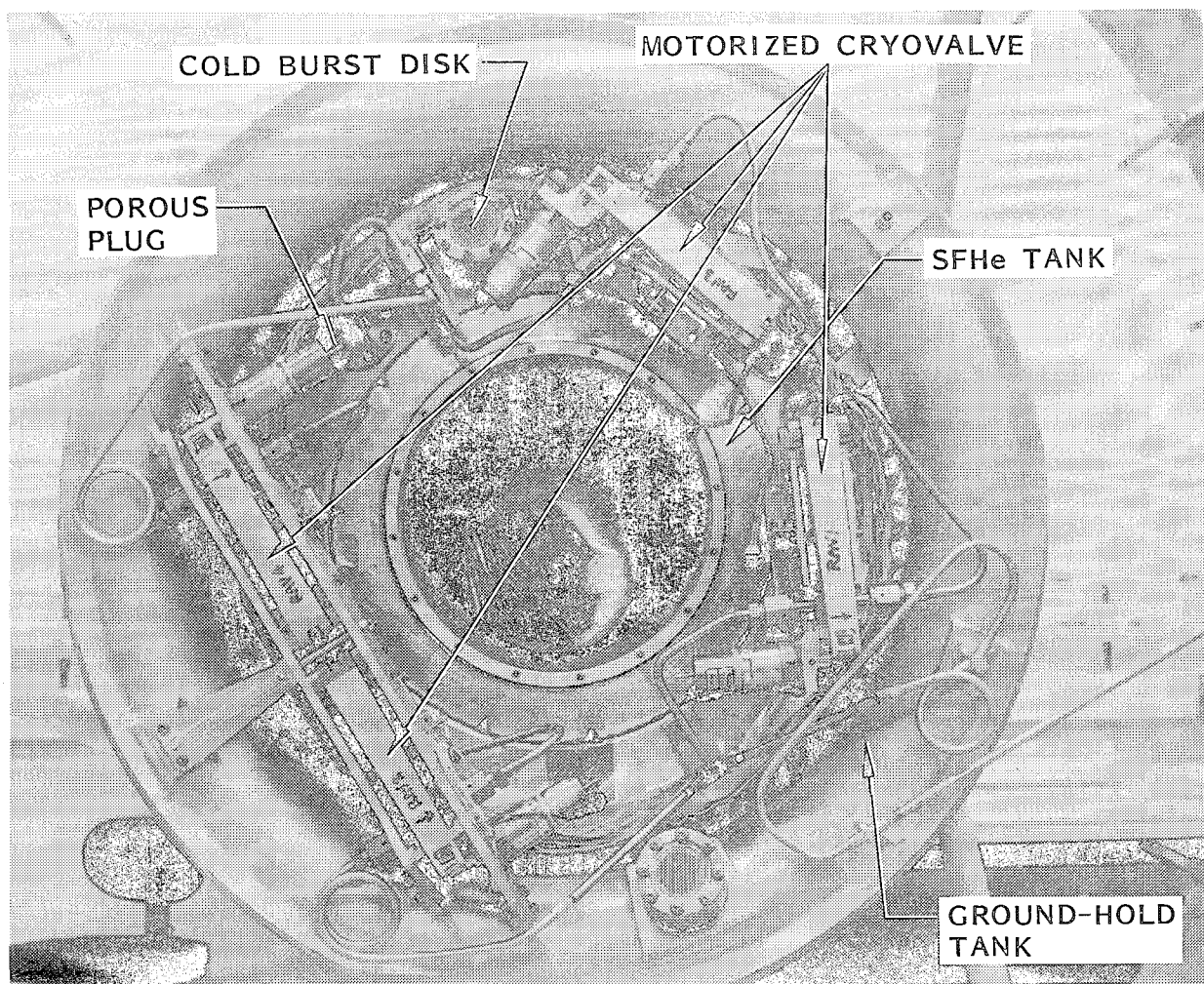
Figure 13   Motorized Cryovalve Installed on ID Dewar

A number of other valve assemblies have been developed or are in the development stage for various NASA or European Space Agency (ESA) programs. Table 1 shows some of the features of these valves and the one described in this paper. The unit developed by Ball Aerospace Division (BASD) (Ref. 2) has been qualified for space and has been used on IRAS and COBE. The units by Utah State University (USU) (Ref. 3) are in the development stage and the characteristics shown in the table will most likely change by the time they are produced for NASA for the Superfluid On-Orbit Transfer Experiment to be flown on the Shuttle. All of these units (BASD and USU) use Nupro bellows valves, as does the Lockheed unit. The unit built for ESA is also shown (Ref. 4).

Table 1   VALVE CHARACTERISTICS

	LMSC	BASD	USU	USU	MBB
Valve Orifice Diameter (mm)	4.4	7.9	7.9	15.9	9.0
Assembly Weight (kg)	1.3	1.6	0.9	2.6	0.9
Envelope					
Length (cm)	8.6	16	7.6*	9.7*	9.1
Width (cm)	1.4	10.9	7.6*	11.4*	7.6
Height (cm)	19.3	10.9	2.5*	5.8*	5.0
Open/Close Time (s)	30.0	8.0	8.0	2.7	.06
Seat Force (N)	957	1669	1335	4005	205
Valve Throw (mm)	2.5	2.5	3.2	5.1	2.4
Current (A)	0.33	?	0.3	0.6	0.42

*Driving mechanism only

Acknowledgement

REFERENCES

1. J. F. Siebert et al. "Experimental Comparison of Helium Leak Rates and Detection Techniques at Temperatures Above and Below the λ-Point," Proceedings of the Space Cryogenics Workshop, p.89 (1984).

2. J. F. Siebert et al., "Development of a Launchworthy Motor-Operated Valve for Containment of Superfluid Helium," Proceedings of ICEC9, p.182 (1982).

3. Superfluid Helium On-Orbit Transfer Preliminary Design Review, Vol. 1, 1987.

4. F. Fuchs and A. Seidel, "Directly Operated Valve for Space Cryostats," Cryogenics Vol. 27, p. 15 (1987).

DEVELOPMENT OF A MAGNETICALLY SUSPENDED, TETRAHEDRON-SHAPED ANTENNA POINTING SYSTEM

Kenichi Takahara*, Tamane Ozawa*, Hiroshi Takahashi*,
Shitta Shingu*, Toshiro Ohashi**, Hitoshi Sugiura**

ABSTRACT

A magnetically suspended, tetrahedron-shaped antenna pointing system is proposed for use in a multibeam broadcasting satellite system in the future. This paper presents the structure of this system, its design concept and the functional test results which were obtained in a laser tracking system in the laboratory. According to these results, it has been confirmed that the system has many advantages over conventional systems and excellent performance.

INTRODUCTION

Satellite broadcasting, which aims at regional services such as high definition television and digital television, is planned in the near future in Japan using 22 GHz-band beams. In one of the plans for this broadcasting system, Japan will be served with 6 precision beams for regional broadcasting as shown in Fig. 1 (ref. 1).

Whereas the distance between a geostationary satellite and the earth is about 36000 km, the attitude control error (0.1 degree in conventional control methods for a satellite stabilized in three axes) corresponds to about 60 km distance on the earth. In order to realize an effective regional broadcasting system, this corresponding distance should be less than 6 km on the earth. Accordingly, the required pointing error for the antenna system is less than 0.01 degree. An offset Cassegrain antenna consisting of a main reflector, a sub reflector, and horns will be mounted in the satellite antenna system shown in Fig. 2. Since the main reflector is fixed to the satellite body, directly driving this large reflector is almost impossible. Rather, the small sized sub reflector must be driven by an Antenna Pointing Mechanism (APM). By driving the sub reflector to compensate for the satellite perturbation movement, the transmitted and received electric waves will be correctly directed to Japan in conformity with the RF beacon from the earth station.

In conventional APMs, lubricated ball bearings or flexible pivots are used (refs. 2 and 3). On the other hand, an APM using magnetic suspension has

Toshiba Corporation, Kawasaki, Japan
 * Research and Development Center, Mechanical Engineering Laboratory
** Komukai Works, Space Programs Division

such advantages as no wear, no friction and no lubrication requirement (ref. 4). For this application, the magnetically suspended, tetrahedron-shaped APM (T-MAPS: Toshiba type Magnetically Suspended Antenna Pointing System) is proposed. The important feature of the T-MAPS is the use of a tetrahedral armature. Because of the simplicity of the tetrahedron, the T-MAPS is able to drive the armature contactlessly in 6 degrees of freedom and is therefore clearly superior to other mechanical APMs. The T-MAPS has demonstrated a 0.002 degree pointing accuracy during laboratory tracking tests utilizing a laser beam.

REQUIREMENT

According to the plan for the satellite broadcasting system, aperture diameters for the main and sub reflectors are about 3 meters and 0.7 meters respectively.

In the total antenna system, the pointing error based on RF sensor signals should be less than 0.01 degree. However the required pointing accuracy for the T-MAPS, which drives the sub reflector with 0.7 $kg \cdot m^2$ moment of inertia and 2.0 kg mass, is 0.002 degree. The pointing ranges required are +1.5 degrees which includes satellite movements and misalignment between the antennas and the satellite body. Specified power consumption is less than 0.2 W in orbit.

Mechanical life is expected to be virtually infinite. Life limiting items are limited to electronic devices.

DESIGN CONCEPT

REDUCTION IN NUMBER OF ELECTROMAGNETS

For the previously manufactured 6 degree-of-freedom APM, it was necessary to use more than 12 electromagnets, because the electromagnets exerted only a pull force. The mechanism was very complicated, requiring a large number of displacement sensors and electromagnets. Furthermore, it became too heavy to be practical in a flight model. In the redesigned APM, the authors carefully considered a reduction in the number of electromagnets and arrived at the tetrahedron configuration. The tetrahedron is a most simple geometric shape and is nonorthogonal. Using these factors, the 12 active electromagnets were reduced to 9 without any functional loss. Consequently, reduced weight and increased reliability were obtained.

REDUNDANCY

Though an electromagnet generates only a pull force in one direction, a displacement sensor is available in both plus and minus directions. Therefore, essentially only 6 sensors are required. Accordingly, even in the case of damage to any of the three sensors, the T-MAPS maintains normal operation by changing the sensor signal processing algorithm.

Similarly, the minimum number of electromagnets required to maintain freedom positioning is 7. Therefore, the T-MAPS with 9 electromagnets has redundant actuation capability.

MECHANISM DESCRIPTION

The T-MAPS is illustrated in Fig. 3. Fig. 4 shows a photograph, illustrating the sub reflector fixed to the mechanism. The T-MAPS consists of a tetrahedral armature fixed to a support shaft, 9 electromagnets, 9 eddy current displacement sensors, several support members and a base. The sub reflector will be fixed to the top of the support shaft. Nine electromagnet and sensor units are placed so that 3 units are attached to the top face of the armature, and 6 units attach to 3 side faces. Each electromagnet consists of a horseshoe-shaped ferromagnetic material with coils wound around the yoke. The armature is enclosed inside 4 support members, to which each electromagnet and sensor unit is fixed. The clearance gap between individual magnet units and the armature corresponds to the pointing range for the T-MAPS. Consequently, the T-MAPS is simpler than any other mechanical APM.

On the other hand, the T-MAPS requires two special considerations with regard to its control method, due to adopting the tetrahedron and the electromagnet units, as described later.

The specifications for the T-MAPS are shown in Table 1.

Since the T-MAPS is a bread board model, a launch lock device, thermal protection (if needed) and other special equipment suited to space environment have not been built. However, these technologies are already established, so the T-MAPS can easily be converted into a flight model with conventional technologies. Similarly, it is expected that the mechanism and its drive electronics will be substantially lightened for the flight units.

MAGNETIC SUSPENSION CONTROL SYSTEM

CONTROLLER DESCRIPTION

The magnetic suspension control system is shown in Fig. 5. In this servo control system, each electromagnet is independently controlled by an individual analog PD controller in a local coordinate system with each electromagnet. The displacements between the armature and the sensors are detected by each sensor. These signals are then fed back to compensators. In this control block diagram, there are two special transformers which need careful treatment. One is a command transformation matrix, R, in which commands in a Cartesian coordinate system are transformed into local commands in local (actuator) coordinates. The other is a position transformation matrix, P, in which displacement signals of each sensor are transformed into displacement signals in the local (actuator) coordinates.

COMMAND TRANSFORMATION

Six independent commands, which determine the armature position, are described in vector form by C (c_1, $\cdots$, c_9) and the displacement vectors perpendicular to the plane, which a magnetic force operates on, are described by A(a_1, $\cdots$, a_9). The relationship between the commands and the displacements is as follows:

$$A = F_1(C) \tag{1}$$

where F1 is a high order vector function which is geometrically obtained from the armature dimensions, electromagnet arrangement and magnetic force vector directions. In practice, the command transformation circuits should be as simple as possible. So applying the linear approximation around the center of the pointing ranges, the eq. (1) becomes:

$$\Delta A = R \cdot C \tag{2}$$

where R is a command transformation matrix, which is obtained from the mathematical model under the above geometrical conditions.

POSITION TRANSFORMATION

Similarly to the previous procedure, displacement vectors perpendicular to the sensor positions are described by S (s_1, $\cdots$, s_9). The relational equation between C and S is shown as:

$$S = F_2(C) \tag{3}$$

where F_2 is another vector function. Applying the linear approximation to the eq. (3), the following relationship is obtained.

$$\Delta S = D \cdot \Delta C \tag{4}$$

Eliminating ΔC using eqs. (2) and (4), the instant transformation matrix, P, with which sensor position displacements can be transformed into operating force point displacements, will be obtained. However, the transformation matrix, D, does not have an inverse, because ΔA and ΔS differ from ΔC in matrix order.

Therefore, using the method of least squares, the position transformation matrix P is finally obtained as follows:

$$A = P \cdot S \tag{5}$$

$$P = R \cdot (D^T \cdot D)^{-1} \cdot D^T \tag{6}$$

where D^t denotes the transposed matrix for D and $(D^T \cdot D)^{-1}$ represents the inverse matrix for $(D^T \cdot D)$.

The two transformation matrices, R and P, have only constant elements. Accordingly, the transformation calculation involves simple multiplication of matrices, and its analog circuits can be easily constructed.

PD COMPENSATOR

The transfer function for the PD compensator in the magnetic suspension system is shown in Fig. 6. This figure indicates the typical phase lead-lag compensation. The tetrahedral armature can be stably levitated by use of this PD compensator in all actuator coordinates. In order to suppress excitation over 1 kHz, the gain would be gradually reduced. It was realized, in experiments, that the frequency range for phase lead should be adjusted to the natural frequency of the magnetic suspension system in consideration of mechanical conditions.

FUNCTIONAL TEST

Functional tests were performed in atmosphere at room temperature, on the following three items:

(a) Magnetic levitational characteristics.
(b) Frequency response.
(c) Resolution.

(a) Using the controller shown in Fig. 5 and adjusting the compensators to magnetically levitate the armature fixed to the sub reflector, it was demonstrated that the system could be stably levitated without a gravity-compensating support. The armature was magnetically levitated in a nominal position by applying a 3 A bias current to each of the 3 electromagnets mounted to the top face of the armature. The magnetic suspension rigidity was 200 N/mm in each of the three lateral directions.

(b) Frequency response for the suspended system was obtained by converting swept sine signals into commands. Test results are shown in Fig. 7. In the z-axis case, the armature precisely tracked the command with no phase lag in the frequency range up to 2 Hz. Similar results were obtained for other axes.

(c) The resolution of the T-MAPS was evaluated by converting micro-rectangular signals into commands. The test results are shown in Fig. 8. In these figures, the upper plot is the input command, and the lower plot shows the signal from the displacement sensor. Jagged signals observed in these figures are natural noises. These figures show that the translational resolution of the armature is less than 0.5 um. Similarly to the measurement in Fig. 8, the rotational motion resolution is less than 5×10^{-4} degree, as shown in Fig. 9.

LASER TRACKING SYSTEM

TEST EQUIPMENT DESCRIPTION

A system using a laser beam instead of an RF beam (see Fig. 10) was constructed to confirm the T-MAPS pointing accuracy. This optical system consisted of a laser generator substituted for a feed horn, a tracking mirror for an antenna, a corner cube reflector for an earth station and a two-dimensional photo detector for an RF sensor.

The corner cube reflector was rotated with some eccentricity. In this test system, the corner cube reflector rotation corresponded to the satellite perturbation movement. In an actual situation, the earth station is fixed and the remaining system components which are mounted on the satellite are moving.

The pointing closed loop, shown in Fig. 11, consisted of PID controllers, the magnetic suspension system described already, and the optical system. This control loop simulated the tracking control for the RF beacon. The deviation between the photo detector outputs and disturbances corresponded to the pointing error. In order to obtain high pointing accuracy, an integral compensator furnished an effective means to obtain the desired characteristics. Ordinarily, integral compensator use not only stabilizes the system, but also decreases the deviation. The disadvantage, however, is that pointing response frequency would be low. However, the 2-ton class satellite considered has a low perturbation motion natural frequency, below 0.1 Hz; therefore integral compensation is sufficiently useful.

As a result, the pointing error, with integral compensation, was virtually zero.

LASER TRACKING TEST

In this laser tracking system, when the tracking servo was not working, a circle was drawn on the screen by a laser beam, in accordance with the corner cube reflector rotation with constant eccentricity. The rotation frequency was about 0.1 Hz, as in the case of the satellite movement. For closed-loop operation, a circle was drawn on a two-dimensional semiconductor photo detector.

When the sensed signals from the detector were converted into $0y$ and $0z$ commands, the tracking mirror tracked the corner cube reflector and the deviation signals in the controller became virtually zero. At the same time, the laser beam on the screen showed no observable motion.

Fig. 12 shows the x and y output signals for the photo detector. In this figure, tracking started at the time corresponding to maximum y direction value. The pointing accuracy for the T-MAPS was confirmed to be as precise as 0.002 degrees.

Test results, including those from the functional test, are shown in Table 2.

CONCLUSIONS

It has been clearly proved that the newly developed T-MAPS is well adapted for multi-beam broadcasting satellite systems. The use of magnetic suspension and a tetrahedral armature offers T-MAPS numerous advantages. These advantages are realized in a concrete manner, as follows.

(a) High pointing accuracy, 0.002 degree with no wear, no friction, and no lubrication required.

(b) Low power consumption, less than 0.2 W in orbit except for power consumption in electronics.

(c) Simple construction and easy manufacturing of electromagnet/displacement sensor units and support members.

(d) Light weight with a reduction in the number of electromagnets.

(e) Sensor redundancy, with 9 displacement sensors. (Only 6 sensors are needed.)

(f) Electromagnetic redundancy, with 9 electromagnets. (7 electromagnets are needed.)

(g) Reliability, with contactless drive and the above mentioned redundancies.

(h) High resolution capability; the minimum sensed displacement was less than 0.5 μm in translation, and 5×10^{-4} degrees in rotation.

(i) Possibility of changing the rotational center, by adjusting misalignments between the satellite body and the antennas, in order to increase the antenna gain.

(j) Flexible adaption to other applications; for example, jitter isolation mounts, laser communication equipment and other drive mechanisms.

The identification of damaged electromagnets and displacement sensors has been considered.

Improvement and development will be continued until the flight model is completed.

REFERENCES

1. S. Yoshimoto, et al., A Trade-Off Study on 22 GHz-Band Multibeam Satellite Broadcasting Systems, AIAA 11th Communication Satellite Systems Conference (1986)

2. H. Heimerdinger, AN ANTENNA POINTING MECHANISM FOR LARGE REFLECTOR ANTENNAS, 15th Aerospace Mechanism Symposium, NASA CP-2181 (1981)

3. B. Hubert and P. Brunet, SOFA: SYSTEME D'ORIENTATION FINE D'ANTENNE, 15th Aerospace Mechanism Symposium, NASA CP-2181 (1981)

4. W. Anderson and S. Joshi, The Annular Suspension and Pointing (ASP) System for Space Experiments and Predicted Pointing Accuracies, NASA TR R-448 (1975)

BIBLIOGRAPHY

1. D. Cunningham, et al., Control System Design of the Annular Suspension and Pointing System, J. GUIDANCE AND CONTROL, Vol. 3, No. 1 (1980)

2. S. Iwaki and R. Matsuda, Testing and Investigation of Magnetically Suspended APM, Proceedings of 15th ISTS, Vol. 1 (1986)

Table 1   SPECIFICATIONS

ITEMS	CHARACTERISTICS
DEGREES OF FREEDOM	6
PAYLOAD MOMENT OF INERTIA PAYLOAD MASS	$0.7 \ kg \cdot m^2$ 2.0 kg

POINTING RANGE
    x, y, z
    $\theta x, \theta y, \theta z$
	
	± 2 mm
	± 1.5 deg.

ARMATURE MASS	2.1 kg
TOTAL MASS (WITH SUPPORT MEMBERS)	8.0 kg
TOTAL SIZE (WITHOUT PAYLOAD)	□ 250×200 mm

Table 2   PERFORMANCE
(confirmed by laboratory tests)

ITEMS	PERFORMANCE
NATURAL FREQUENCY	4 Hz

COIL WATTAGE
    ON EARTH
    IN ORBIT
    (CALCULATION)
	
	10 W
	0.2 W

RESOLUTION
    TRANSLATION
    ROTATION
	
	0.5 μm
	5×10^{-4} deg.

POINTING ACCURACY	0.002 deg.

FREQUENCY	BEAM #
F_1	1,4
F_2	2,5
F_3	3,6
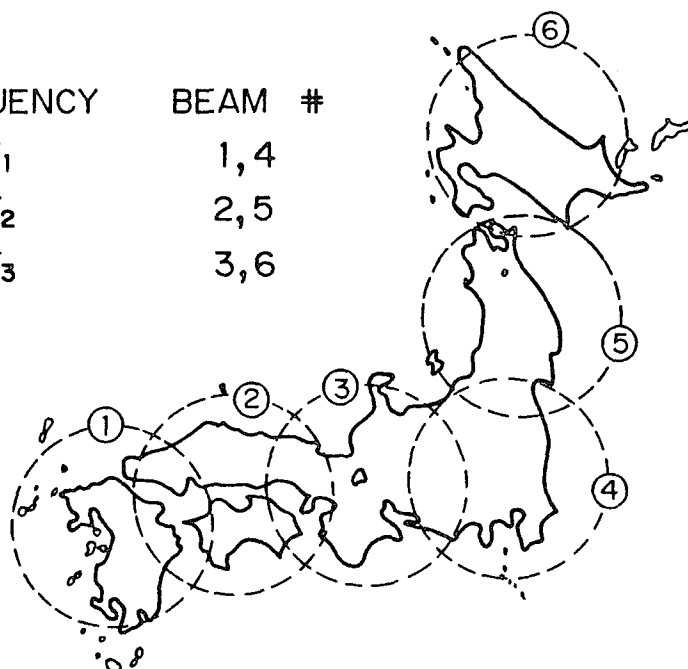
Figure 1   Beam Allotment of Regional Broadcasting
for 6 Beams in the Future

SOLAR PADDLE

THE
EARTH

RF BEACON

MAIN REFLECTOR

SATELLITE BODY
(ATTITUDE CONTROL
ACCURACY : ± 0.1
DEGREES)

ANTENNA
POINTING
MECHANISM

(POINTING ACCURACY :
±0.01 DEGREES)

SUB REFLECTOR
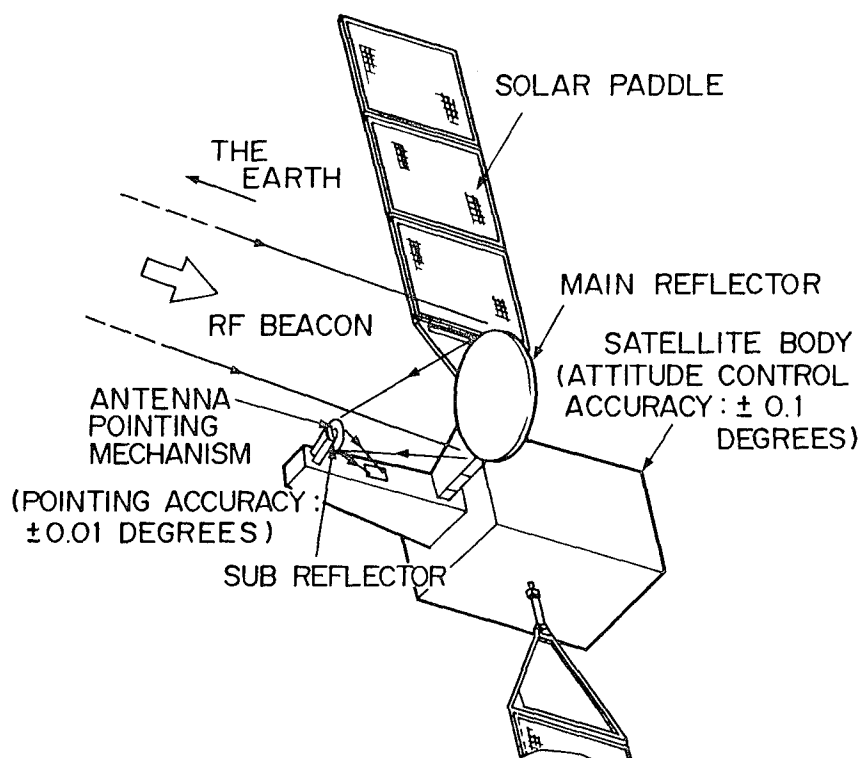
Figure 2   Broadcasting Satellite Antenna System
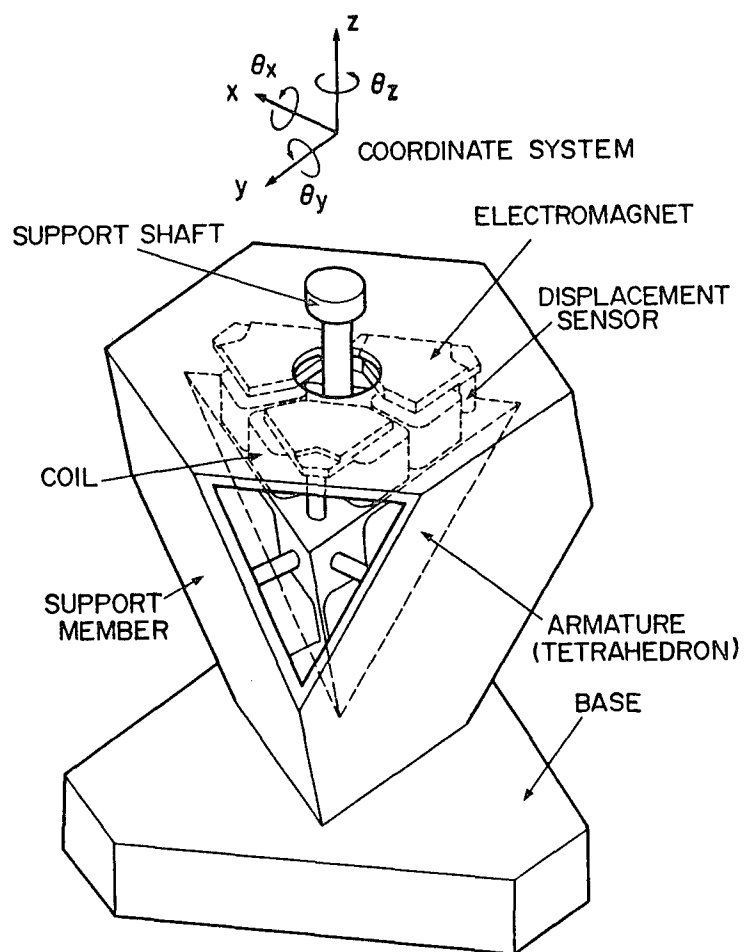
Figure 3   Magnetically Suspended, Tetrahedron-
Shaped Antenna Pointing Mechanism

Figure 4   The Mechanism (T-MAPS)
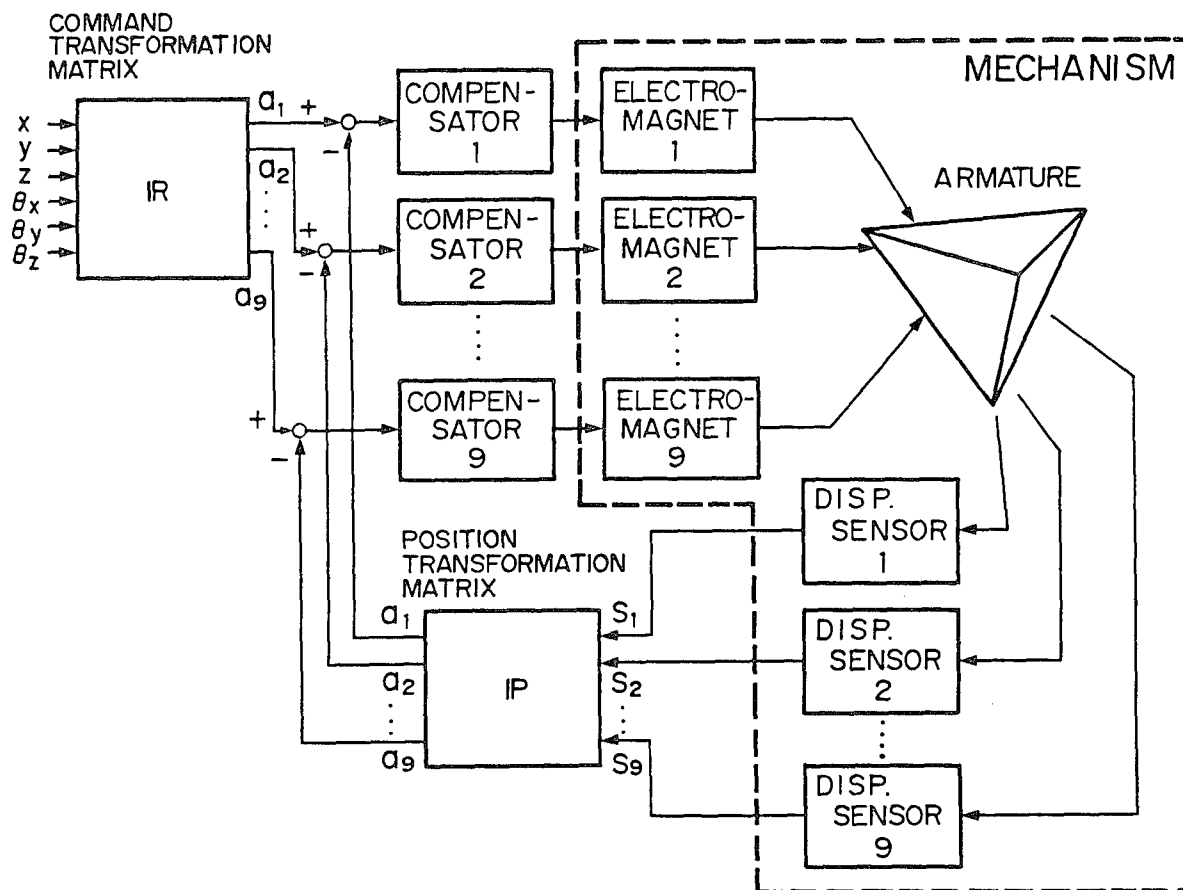
Figure 5   Control Block Diagram for Magnetic Suspension System

143
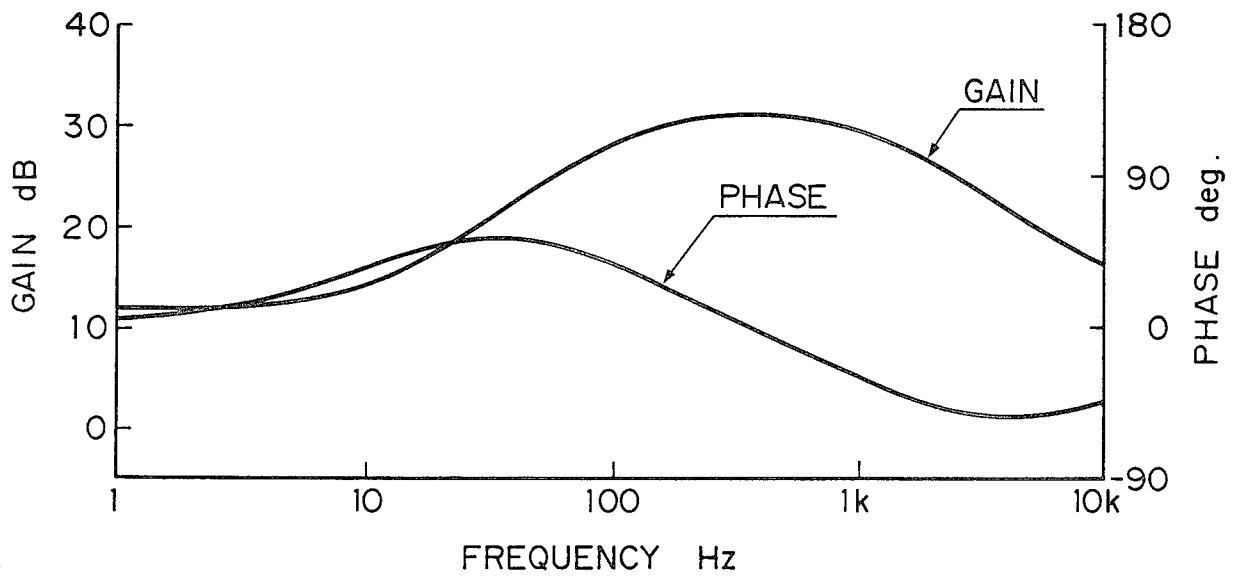
Figure 6   PD Compensator Transfer Function
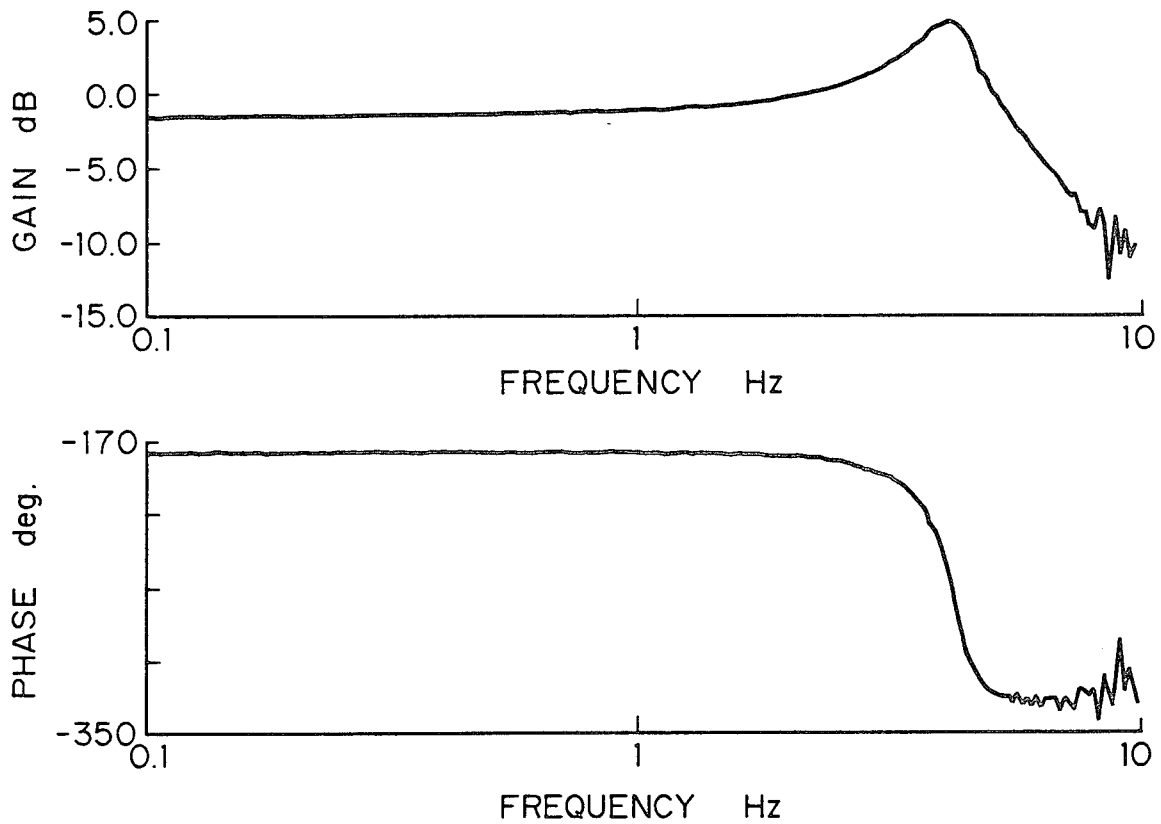
Figure 7   Frequency Response with Antenna Attached
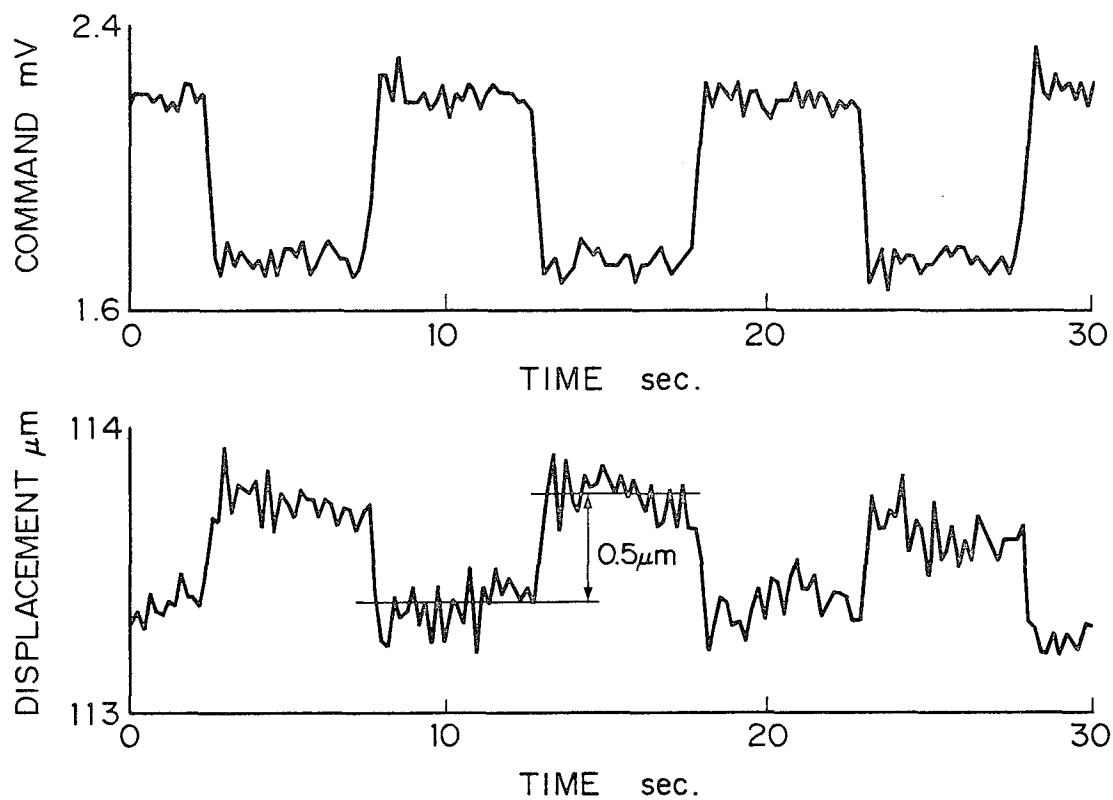
Figure 8   Resolution in z-axis with Antenna Attached
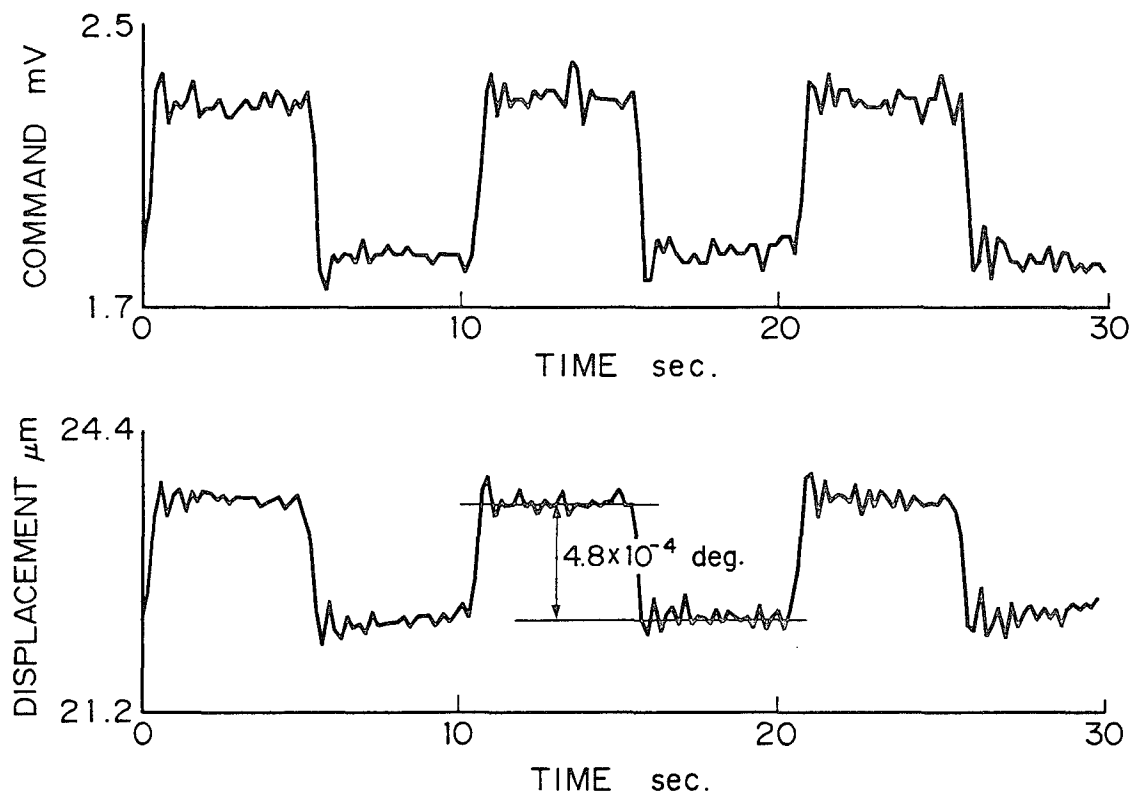
Figure 9   Resolution in Rotation around x-axis with Antenna Attached
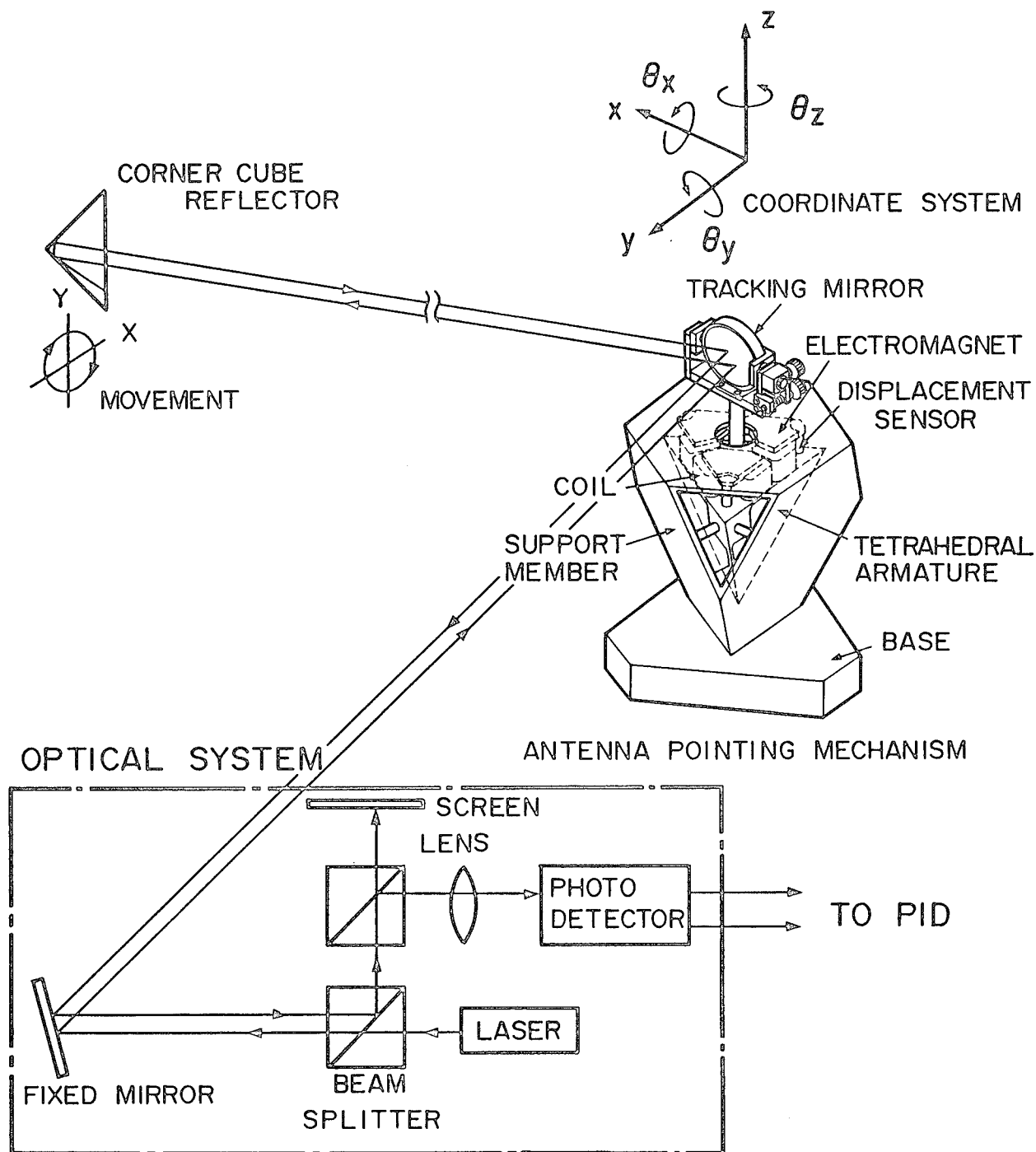
Figure 10   Laser Tracking System
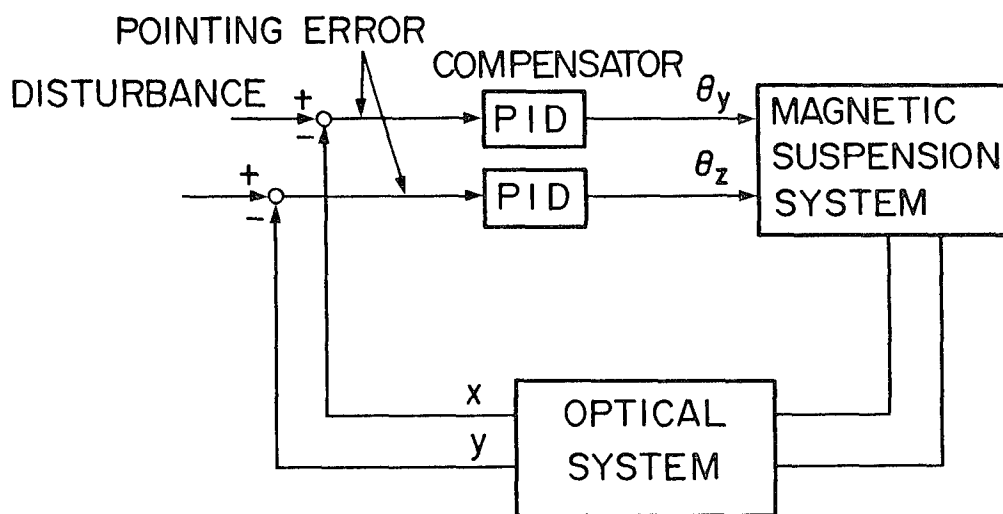
Figure 11   Pointing Closed Loop for Laser Tracking System
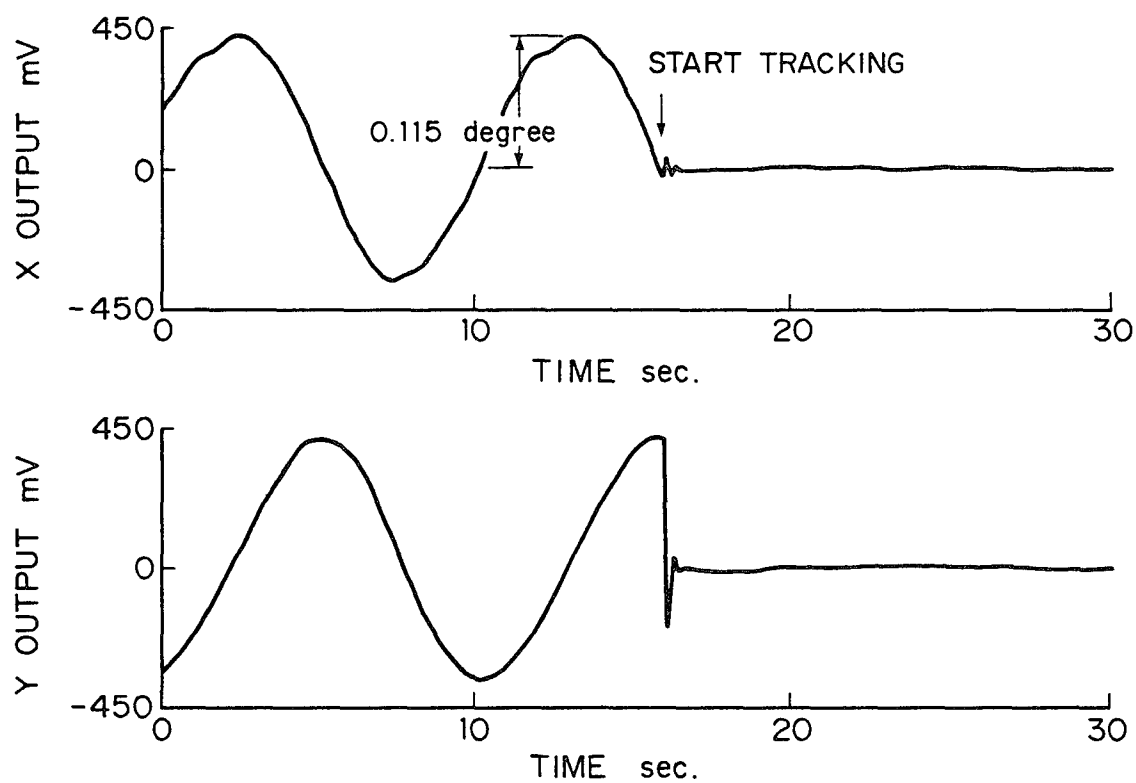
Figure 12   Tracking Characteristics
(Two-dimensional photo detector outputs)

A SPIN AND DEPLOYMENT MECHANISM

David W. Preston * , Todd A. Girkins *

ABSTRACT

The spin ejector was developed as a simple and reliable
mechanism to spin and deploy small payloads from an earth orbiting
platform. It is one component of a complete system for retaining
a payload during vehicle ascent, releasing the payload for
deployment, deploying the payload, and securing the payload
canister after deployment. The complete system was designed,
fabricated and qualified for flight in just over one year, with
the flight article delivered to the launch site in October, 1987.
This paper will briefly describe the complete system, and then
focus on the deployment mechanism (spin ejector) design concept
and test program.

INTRODUCTION

The system described herein was designed to retain, release,
spin and deploy four payloads from the canister cluster assembly
(see Figure 1). Each payload, retained in individual payload
canisters and cradles (see Figures 2 thru 4), weighed less than
400 pounds and was to be deployed at a predetermined spin rate and
a velocity of 3 meters per second (9.84 feet per second, ±10
percent). The spin ejector (see Figures 5 thru 8) was chosen as
the deployment mechanism over design concepts utilizing two
independent systems (one for spin and one for deployment with
motors, controls, batteries, etc.) because of its relative
simplicity and reliability. A compact pneumatic system utilizing
high pressure helium controlled through an orifice was chosen to
power the deployment in order to minimize weight. Because of the
amount of new hardware, an extensive development and qualification
test program was required to prove the system for flight.

---

* McDonnell Douglas Astronautics Company, Huntington Beach, CA

SYSTEM DESCRIPTION

The body of the system is the payload canister assembly (see Figures 2 and 3). Its major components are the cover, latch, cradle, pneumatic system, spin ejector, and closer mechanism. For this specific mission the canister had to be atmospherically sealed, requiring a vent system to be incorporated in the design. Both the vent and pneumatic system are operated by redundant normally closed ordnance valves. The latch release is initiated by redundant ordnance pin pullers. Torsion springs open the cover after latch release. The spin ejector mechanism, functioned by release of the source pressure and controlled by an orifice, deploys the payload. The cover closer mechanism closes the cover using residual pressure from the spin ejector after piston stroke.

Each payload is supported within the canister by four pins located in the cradle retainers and two pins located in the cover. These pins are preloaded against the payload to support it from the time of vehicle launch to deployment.

DEPLOYMENT SEQUENCE

Listed below is the deployment sequence (see Figures 4 and 5) –

- 400 seconds prior to deployment the ordnance vent valve is fired, allowing the trapped atmosphere to leave the canister (vacuum is achieved in approximately 350 seconds)

- 20 seconds prior to deployment the ordnance pin pullers are fired allowing the latch to release. Torsion springs are assisted by the cover pins (preloaded against the payload) in opening the cover, leaving the payload supported by the four cradle retainer pins. The cover rebounds and comes to rest in approximately 7 seconds against the stop.

- Deployment is initiated by functioning the ordnance valve, releasing source pressure into the spin ejector cylinder. The piston drives the lead shaft and cradle, accelerating the payload. When the piston reaches its stop (approximately 0.070 seconds) the payload is moving at its required deployment conditions.

- The lead shaft withdraws from the piston allowing the cradle
  to follow the payload. Springs help to retract the cradle
  retainers in the expanding cone area of the canister,
  releasing the payload and allowing it to fly free. The
  retainers contact the cradle stop (approximately 0.022
  seconds after piston stop), stopping and retaining the
  cradle.

- The cover closer mechanism receives residual pressure from
  the spin ejector, closing the cover approximately 10 seconds
  after piston stop. Spring plungers lock the cover closed. A
  separate orifice and plenum retard the pressure going to the
  closer mechanism, allowing time for the payload to clear the
  cover prior to its closing.

CANISTER DESCRIPTION

The canister assembly (see Figures 2 and 3) consists of three
machined rings connected by 1.27 mm (0.050 inch) riveted sheet
metal. The bottom ring provides an attach point for the spin
ejector mechanism. The middle ring, which connects the conical
and cylindrical sheet metal sections, contains these integrally
machined features; a cradle support shelf, spin up cylinder,
payload release expanding cone, and cradle stop. The forward ring
is machined with a precision diameter chamfer to mate with an o-
ring in the cover and form an atmospheric seal. Additionally,
this forward ring includes a mounting flange used to attach the
canister to the cluster bulkhead.

The shelf in the lower half of the middle ring supports the
cradle and payload prior to launch and during ascent. Above the
shelf is a cylindrical bore which holds the retainers against the
payload during acceleration. The first 5.0 cm (2.0 inch) of this
cylinder is machined with a precision diameter required to hold
the retainer pins at the desired preload. During deployment, the
retainers move quickly past this precision diameter and roll on a
slightly larger bore. The majority of the linear and rotational
acceleration occurs within the 11.7 cm (4.6 inch) constant
diameter section.

The retainer rollers are at the cylinder/cone intersection and
the payload is fully accelerated when the piston reaches its stop.
The retainers then retract into the expanding cone, allowing the
retainers and preload pins to rotate away from the payload. After
the pins are fully disengaged from the payload, the retainers

contact the stop located at the top of the cone. This action
stops and retains the cradle within the canister while the payload
flies free.

CRADLE/RETAINER DESCRIPTION

Each canister contains a cradle assembly (see Figure 3). The
cradle assembly consists of a lead shaft, a 1.27 mm (0.050 inch)
aluminum sheet metal cone connecting two machined rings, and four
cradle retainers containing rollers and preload pins. The cradle
transfers the linear and rotational acceleration forces from the
spin ejector piston to the payload.

Mounted to the cradle's top ring are four retainer assemblies.
Two self aligning rollers on the outside of each retainer guide it
along the canister cylindrical section during payload
acceleration. These are aligned with the lead shaft helix to
eliminate sliding. The preload pins are threaded into bushings
press fit into the retainers. Threading permits easy pin
adjustment for accurate preloading and centering of the payload
within the cradle. This preloading operation occurs in a
simulated canister middle section prior to payload installation
into the canister.

Each preload pin has a spherically tipped surface which engages
a conical receptor of the payload. The pins are mounted in a
threaded bushing containing a series of belleville washers. The
belleville washers create a compact, high spring-rate suspension
system to support the payload against launch and ascent loads.

SPIN EJECTOR DESCRIPTION

The spin ejector (see Figures 5 thru 8) consists of a pneumatic
piston/cylinder assembly which drives the lead shaft. The shaft
is machined with opposing helical tracks which bear against
rollers fixed to the drive plate mounted at the cylinder top.
Therefore, as the piston translates the shaft, the shaft must
rotate. The helical tracks are cut at the appropriate lead angle
to cause the shaft to rotate at the desired spin rate when it is
translated at the required velocity.

The radius to the center-line of the lead shaft helix is made large (3.18 cm/1.25 inch) to reduce the force on the rollers (normal to the helical track) generated by the accelerating payload's rotational moment of inertia. Because of the magnitude of these loads, it is critical that each of the rollers contact the lead shaft equally (creating a balanced spin-up couple). To provide for this, laminated shim stock (0.05 mm/0.002 inch laminations) positions both rollers radially and tangentially (see Figure 7). This adjustment provides a method to accurately center the shaft within the bushing, and reduce forces between the shaft and bushing.

The bushing is positioned close to the rollers in order to react system unbalances without creating large moments. It is made of 17-7 corrosion resistant steel and lined with a Teflon impregnated fabric liner; the lead shaft mating diameter is hard anodized. These materials and finishes were chosen because of the low friction between them. Cutouts machined in the bushing allowed it to be positioned near the rollers (see Figure 8). Flats on the bushing keep it from rotating and binding a roller.

A thrust bearing in the piston bears on the lead shaft to permit free relative rotation. The bearing is lubricated with a vacuum compatible perflourinated polyether-based lubricant. This proved to be a satisfactory lubricant; however, it did not prevent the bearings non-cadmium coated surfaces from corroding. This required the bearings unprotected surfaces to be painted with a corrosion resistant primer.

Because one atmosphere of pressure is trapped under the piston after the canister is vented in orbit, detent assemblies are required to retain the piston and cradle/payload assembly prior to deployment (see Figure 9). These are fixed to the drive plate and mated to a ring on the top of the lead shaft. The detent plunger and ring are fabricated from steel to withstand the high contact stresses. The plunger is heat treated to a slightly lower level than the ring to permit a custom fit of the two parts.

Because the detents retain the piston and cradle/payload assembly prior to deployment, the helium flow is allowed to develop before the cylinder volume begins to expand. Also, the detent assemblies, in combination with a leaf spring acting on the piston bottom, keep the lead shaft and piston in contact. This prevents any chance of impact damage due to gapping.

To stop the piston, a Shore 90 polyurethane rubber pad is used. Its reusability for the development and qualification test program made it preferable over crush blocks.

PNEUMATIC SYSTEM DESCRIPTION

The pneumatic system used to power the deployment consists of a source pressure bottle, ordnance activated isolation valves, corrosion resistant steel tubing, and a control orifice. The 885 cc (54 cubic inch) source, pressurized to 5.0 MPa (725 psi), is controlled by sharp edged orifices ranging in diameters from 0.193 cm (0.076 inch) to 0.320 cm (0.126 inch). Varying the orifice size permits equal pressurization of each system, thus eliminating the possibility of incorrect pressurization of the canisters. These parameters create choked flow at the orifice throughout the piston stroke, thus greatly simplifying the gas flow analysis and minimizing the upstream line losses. The relatively large orifice diameters eliminated the need for a filter in the system.

Limited space dictated the spin ejector base be designed with the pneumatic input at the side. Because positioning the control orifice at the base inlet (for easy inspection) would create a second choke point in the gas flow, it is located on the mounting surface of the base (cylinder inlet). This simplified the pneumatic analysis but made orifice size verification more difficult.

The residual pressure in the spin ejector cylinder is released to the cover stop and closer mechanism (see Figures 2 and 4) after the power stroke. This mechanism, which stops the cover on its opening, utilizes a small pneumatic cylinder to close the cover. A 1.5 mm (0.060 inch) diameter hole in the spin ejector cylinders wall allows the pressure to exit without causing damage to the piston seal. The pressure is controlled by a 0.25 mm (0.010 inch) diameter orifice and 283 cubic centimeter (17.3 cubic inch) plenum in route to the cover stop and closer cylinder. This delays the cover closer cylinder action until the payload clears the cover. Two spring loaded plunger assemblies lock the cover closer mechanism in the closed position so it can not retract as the pressure is lost.

Weight was not a major concern during the system development. This became a favorable condition for sizing hardware due to uncertainties in predicting the pneumatic response during payload

154

deployment. The complete pneumatic system was designed for a conservatively high operating pressure of 20.7 MPa (3000 psi). The working pressure determined from the development test program was 5.0 MPa (725 psi). The maximum dynamic pressure within the spin ejector was found to be 173 psi. This corresponds to a peak axial force of 16,661 N (3745 lbs) thrust.

ANOMALIES

The initial spin ejector design utilized a self aligning roller bearing to bear against the lead shaft helix. This choice allowed the rollers to align themselves normal to the lead shaft helix during the power stroke. However, during development testing, this roller failed at its loading slots due to excessive normal loading. Marks on the lead shaft helix also indicated high forces present at this interface. Furthermore, the self aligning aspects of this roller created difficulty verifying initial roller alignment with respect to the lead shaft's helical track during payload installation.

The failed bearing was replaced with a crown roller bearing which is designed to roll on a surface. One suitable for the mechanism loading and requiring only a slight shim adjustment was found allowing testing to continue after a two day delay. The new roller proved to be satisfactory; no anomalies were encountered. Additionally, the problem of verifying the initial roller alignment was eliminated.

TESTING

One of the more challenging aspects of this program was testing. Two methods of testing the deployment were devised: one deploying vertically up and one deploying vertically down. The vertical up tests utilized a counter balance and bungee-cord system. The bungee-cord was sized to keep the suspension system tight while the payload was being accelerated at greater than one G. The counter balance was sized to negate the effects of gravity. These tests were used to determine the deployment velocity and corresponding spin rate.

The vertical down technique involved deploying the payload into a capture net. These tests utilized rate gyros to determine the payload cone angle of deployment.

For the upward tests, bar charts attached to the accelerating payload were filmed with high speed cameras to yield deployment velocity. The spin rate was calculated from this linear velocity and lead shaft helix angle (linear and rotational velocities are directly related through the lead shaft helix angle). For the downward tests, rate gyro data yielded the spin rate directly. The velocity at the moment of piston stop could then be calculated from the lead shaft helix.

A pressure transducer was inserted in the spin ejector cylinder to gather dynamic pressure data. This data provided –

- maximum thrust forces within the system used to determine component stress and strength margins.

- data with which the pneumatic model could be matched for verification.

A thermocouple was added to further verify the analytical model. However, the deployment event occurs faster (0.070 seconds) than the thermocouple **can react.**

CONCLUSIONS

The spin ejector mechanism has proven to be a simple and reliable mechanism for spinning and deploying payloads in space. A thorough test program verified its simplicity and reliability which are attributes required due to the limited development time allowed for this program. The design, which benefits from its adaptability to many payload configurations and deployment conditions, is suitable for both non-space and space uses.

PAYLOAD CANISTER

PNEUMATIC SOURCE

ORDNANCE VALVES

SPIN EJECTOR

SHIPPING FIXTURE
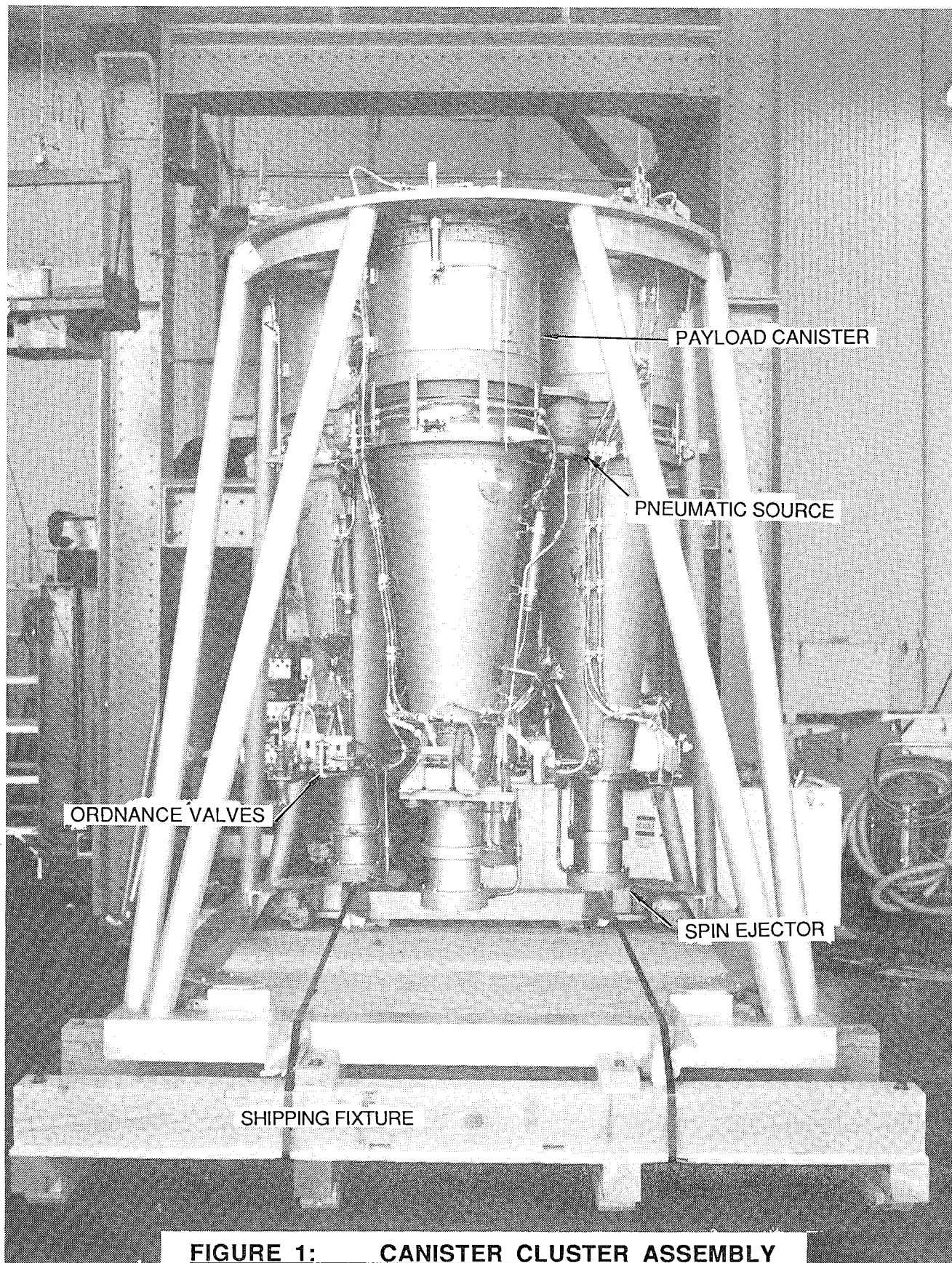
FIGURE 1:   CANISTER CLUSTER ASSEMBLY
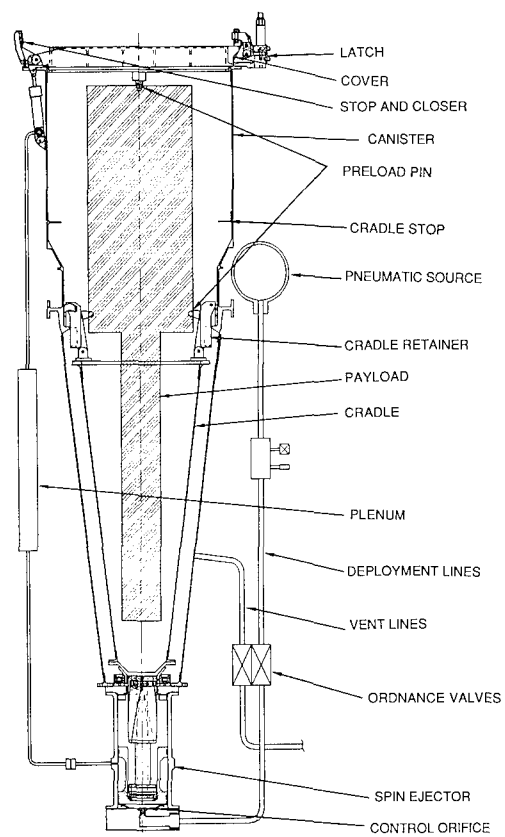
FIGURE 2:   CANISTER ASSEMBLY SYSTEM

Labels (Figure 2):
- LATCH
- COVER
- STOP AND CLOSER
- CANISTER
- PRELOAD PIN
- CRADLE STOP
- PNEUMATIC SOURCE
- CRADLE RETAINER
- PAYLOAD
- CRADLE
- PLENUM
- DEPLOYMENT LINES
- VENT LINES
- ORDNANCE VALVES
- SPIN EJECTOR
- CONTROL ORIFICE
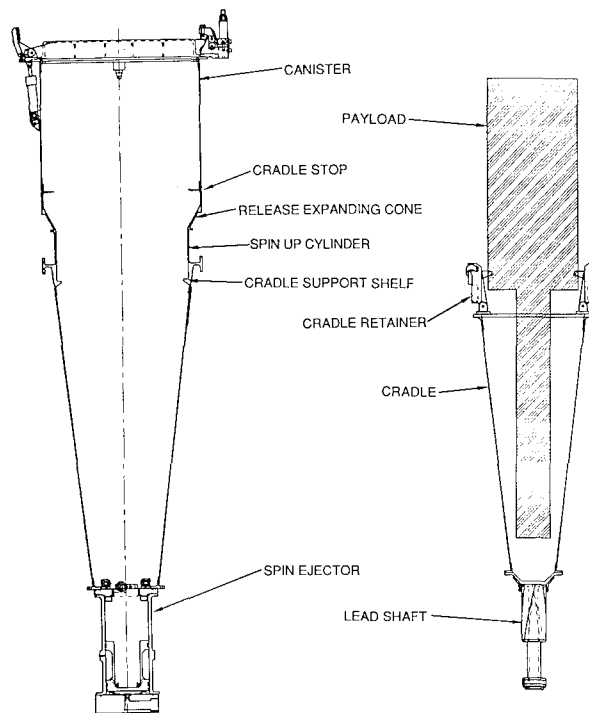
FIGURE 3:   CANISTER AND CRADLE SEPARATED

Labels (Figure 3):
- CANISTER
- PAYLOAD
- CRADLE STOP
- RELEASE EXPANDING CONE
- SPIN UP CYLINDER
- CRADLE SUPPORT SHELF
- CRADLE RETAINER
- CRADLE
- SPIN EJECTOR
- LEAD SHAFT

158

INITIAL POSITION   COVER OPEN   PISTON STOP   CRADLE STOP   COVER CLOSE
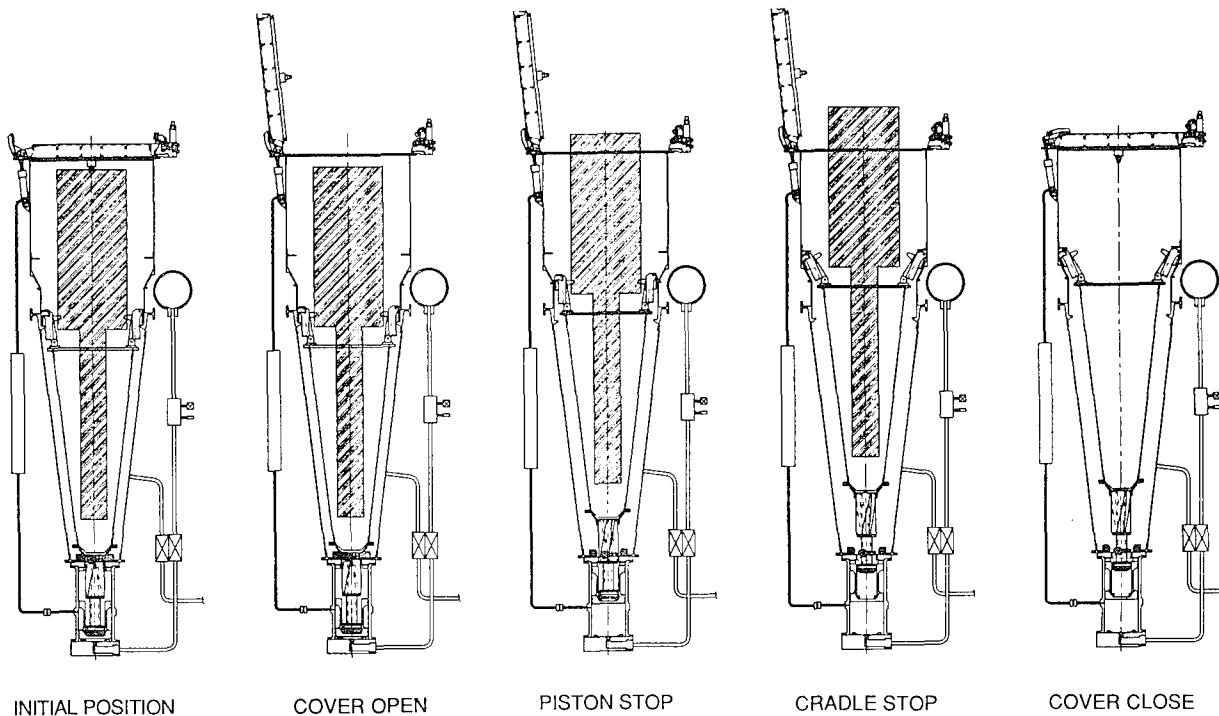
FIGURE 4:   CANISTER DEPLOYMENT SEQUENCE

INITIAL POSITION   PISTON STOP   CRADLE STOP
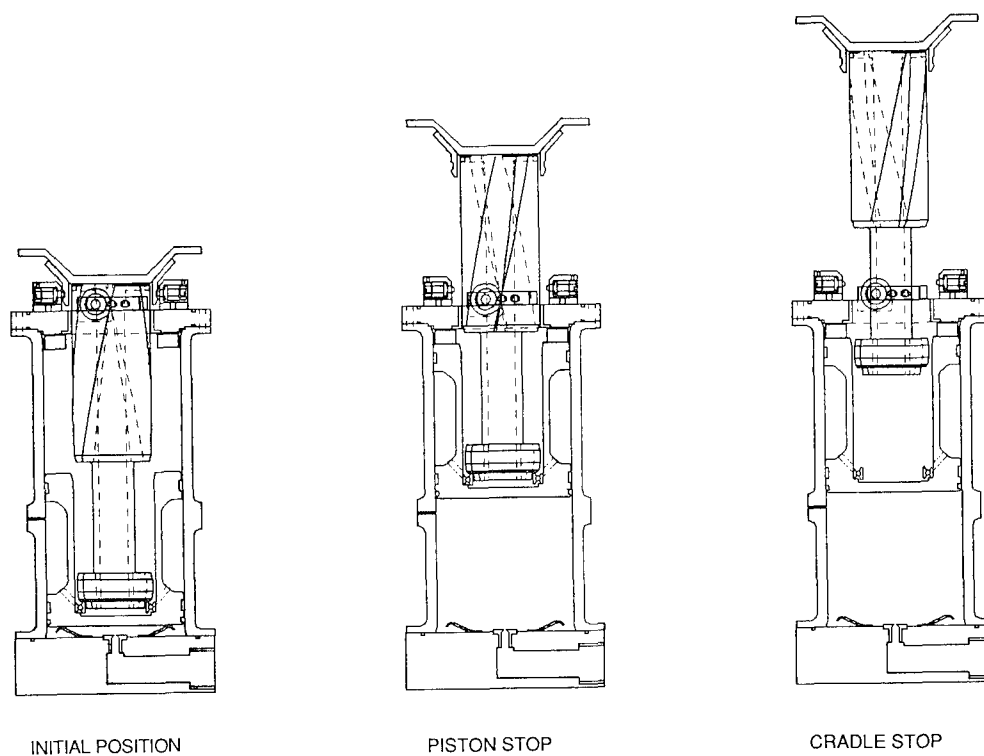
FIGURE 5:   SPIN EJECTOR DEPLOYMENT SEQUENCE

159
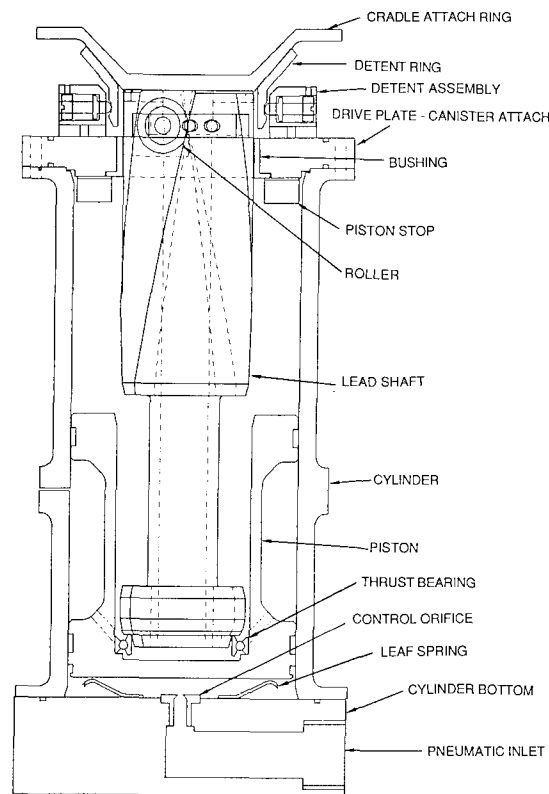
FIGURE 6:   SPIN EJECTOR ASSEMBLY

CRADLE ATTACH RING
DETENT RING
DETENT ASSEMBLY
DRIVE PLATE - CANISTER ATTACH
BUSHING
PISTON STOP
ROLLER
LEAD SHAFT
CYLINDER
PISTON
THRUST BEARING
CONTROL ORIFICE
LEAF SPRING
CYLINDER BOTTOM
PNEUMATIC INLET
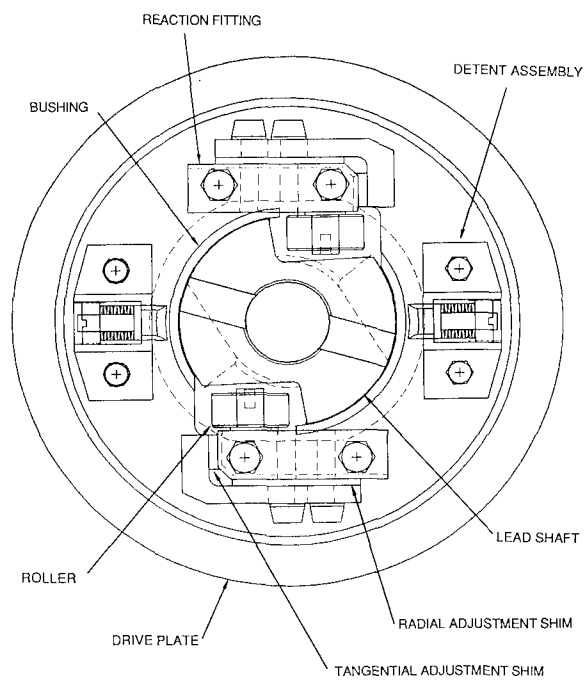
FIGURE 7:   SPIN EJECTOR ASSEMBLY - TOP VIEW

REACTION FITTING
DETENT ASSEMBLY
BUSHING
LEAD SHAFT
ROLLER
RADIAL ADJUSTMENT SHIM
DRIVE PLATE
TANGENTIAL ADJUSTMENT SHIM

160

ROLLER

REACTION FITTING

BUSHING

BUSHING - ROLLER CLEARANCE CUTOUT

HELICAL TRACK
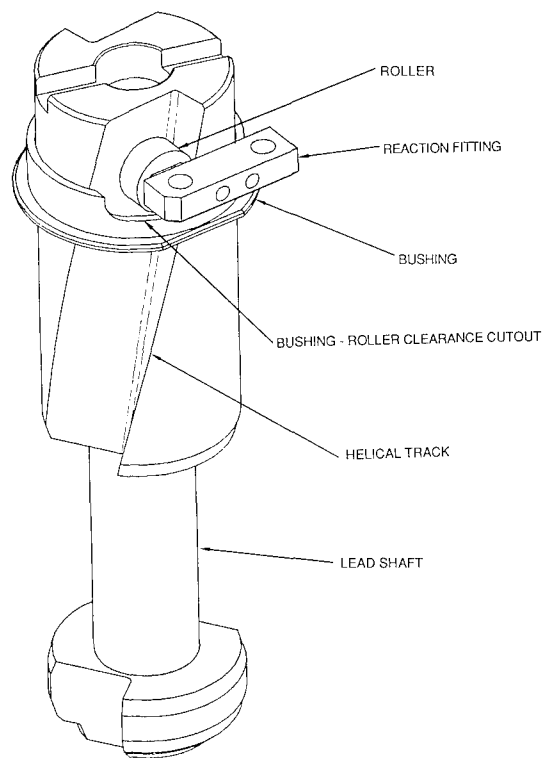
LEAD SHAFT

FIGURE 8:   LEAD SHAFT - BUSHING - ROLLER ARRANGEMENT

ISOMETRIC VIEW

ENGAGEMENT RING ON CRADLE - LEAD SHAFT

BELLIVELLE WASHERS (10)

HOUSING

PLUNGER

ADJUSTMENT NUT
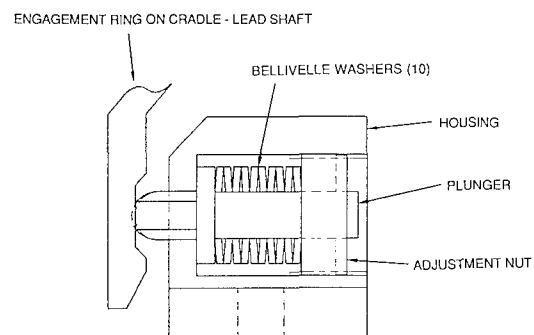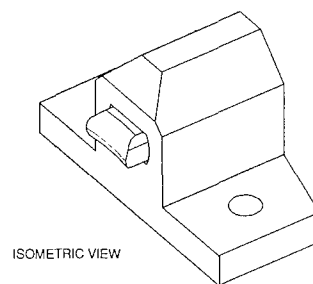
FIGURE 9:   DETENT ASSEMBLY DETAIL

161

CONTROLLING STRESS CORROSION CRACKING IN MECHANISM
COMPONENTS OF GROUND SUPPORT EQUIPMENT

W. A. Majid *

ABSTRACT

This paper deals with the selection of materials for mechanism components used in ground support equipment so that failures resulting from stress corrosion cracking will be prevented. It also provides a general criteria to be used in designing for resistance to stress corrosion cracking. Stress corrosion can be defined as combined action of sustained tensile stress and corrosion to cause premature failure of materials. Various aluminum, steels, nickel, titanium and copper alloys, and tempers and corrosive environment are evaluated for stress corrosion cracking.

INTRODUCTION

A failure of Hold Down Post of solid rocket booster occurred during the application of the pretension load on Mobile Launcher Platform (MLP). A portion of the tensioner containing the fractured surface was studied using scanning electron microscope. The study concluded the tensioner failed catastrophically in a brittle mode initiating a corrosion pit and propagating intergranularly as stress corrosion. The tensioner was fabricated from 18 Ni maraging steel of Rockwell Hardness (HRC) 55.

The National Transportation Safety Board has investigated four recent Boeing 727 mishaps involving structural failures in the landing gear due to corrosion. The first two incidents which occurred in Denver, Colorado on Sept. 29, 1985, and Norfolk, Virginia on January 16, 1986 concern stress corrosion failures discovered in the main landing gear (MLG) actuator support link assembly. Investigation found stress corrosion cracking (SCC) went undetected until the link failed. The third incident, which occurred in Memphis, Tennessee on January 9, 1986 involved failure of MLG shock strut outer cylinder. Examination showed that fracture of the strut stemmed from an area of stress corrosion cracking that initiated on outer diameter of the outer cylinder. Fretting and corrosion pitting were found on the surface of the cylinder in the area contacted by the clamp. The fourth incident which occurred in Miami, FL. on March 3, 1986 involved a nose landing gear (NLG) uplock actuator rod end. The examination disclosed that the rod end separation was the result of severe corrosion of threaded shank of the rod end. Heavy corrosion was found on the mating threads of the uplock actuator.

---

* Lockheed Space Operation Company, Kennedy Space Center, FL.

As shown in Figures 1 and 2 stress corrosion cracking is a mechanical environmental failure process in which a sustained tensile stress and chemical attack combine to initiate and propagate fracture in a metal part. As shown in Figure 3, SCC failure is caused at a tensile stress well below the yield strength of the metal. There have been a number of stress corrosion failures for which design stresses were intermittent, short duration and surfaces of failed parts are not visibly corroded. Many SCC failures are caused by metal equipment to corrosive environment before the equipment is put into service. These environments include those associated with fabrication, testing, shipment, storage and installation. Marshall Space Flight Center (MSFC) had published guidelines for controlling SCC. However, it did not account for chloride and halide SCC in 300 alloy series. 300 series were listed as having high resistance to SCC.

Failed mechanism components analyzed at NASA Malfunction Analysis Lab., K.S.C., indicated that SCC was the major contribution to failures in Ground Support Equipment. Recently SCC has become a major concern in ground support equipment at KSC. Also there is no effective protection against SCC. Not only higher tensile strength play a role in SCC but also susceptibility of metal to SCC. Seventy five percent of all stress corrosion failure could have been prevented if the persons responsible for design, construction and maintenance of equipment had been sufficiently aware of the problem.

SOURCES OF STRESS IN METAL COMPONENTS

The principal sources of tensile stress in components include

    a. Externally applied loads
    b. Pretension loads such as in bolts and screws
    c. Sources of stress in manufacturing
    d. Sources of stress in services.

Externally Applied Loads: Externally applied loads are those loads that are directly applied on the mechanism to perform work. Tensile stresses are thus introduced in the components like links, actuators, fasteners, fittings, etc. of the mechanical equipment. Stresses also arise from reciprocating or rotary motion of mechanical devices either from normal operation or from abnormal effects such as vibration, resonance and fluid flow.

Pretension Loads: Most components are held together with fasteners and fittings. Fasteners such as bolts and screws require pretension loads. A majority of failures in ground support equipment occur in bolts. Tightening of fitting nuts in order to obtain liquid tight seal results in sustained tensile stress in the form of hoop stresses which initiate SCC. Fit-up and assembly operation are sources of tensile stress. Press fitting, shrink fitting and assembly welding are source of tensile stress that would lead to SCC. In a certain case stress produced by an interference fit of bushing in a hole in a fitting contributed to failure of the fitting which was exposed to a marine atmosphere. Forming operation used in assembly to retain component can produce residual tensile stresses that can induce SCC.

164

Sources of Stress in Manufacture: The principal sources of high local stresses in manufacture include thermal processing, stress raisers, surface finishing and fabrication. One of the frequently encountered source of thermal processing stress is welding. Shrinkage of weld metal during solidification impose restraints on the adjacent metal, can produce severe residual tensile stresses. Other thermal processing effects during manufacture include solidification of castings, improper heat treating practices, temperature non-uniformity in furnaces and quenching practices too severe. Residual stresses are introduced at notch in related mechanical component designs, notches created during accidental mechanical damage, electric arc strikes, deficiencies in post weld heat treatments, severe surface irregularities produced in grinding and rough machining, cladding, rolling, electroplating, spraying, brazing or soldering. Residual stresses are produced during electrical discharge machining. High residual tensile stresses result from bending, stamping, deep drawing and other cold forming operations.

Sources of Stress in Service: Stresses in addition to those that a component was designed to withstand are introduced in service by accidental mechanical impact, local electrical arching, local wear, fretting, erosion, cavitation such as pitting, selective leaching, intergranular attack and concentration-cell, cervice or galvanic corrosion. Exposure of metal part to high and low temperature is a major source of stress in service.

GRAIN ORIENTATION AND ENVIRONMENTAL EFFECTS ON SCC

In wrought mill products particularly aluminum such as shown in Figure 4, the grain orientation produced by rolling and extruding have directional effects. For susceptibility to stress corrosion cracking, the directional variation can be appreciable and must be considered in design of fabricated hardware of ground support equipment. Resistance of metals, particularly alloys of aluminum to stress corrosion cracking is always high when stressed in the direction of rolling or in the longitudinal direction, less in the direction perpendicular to the longitudinal or long transverse direction, and least in the direction through the thickness of the plate or short transverse direction. For forgings the direction perpendicular to parting plane or short transverse has the least resistance to stress corrosion.

Stress corrosion cracking often depends upon environmental impurities, alloy composition and structure. Impurities that are present in the environment often cause stress corrosion cracking. Sensitized austenitic stainless steel crack at room temperature in water containing 100 ppm of chloride or 2 ppm of fluoride. SCC in copper alloys are caused by environment that contains ammonia or ammonia like complexing agents. Marine and industrial environment contains halide ions are particularly aggressive in causing crack in high strength steels, corrosion resistant steels and aluminum alloys. Service environment, atmosphere containing SO_2, chlorides, ammonia, oxides of nitrogen, hydrogen sulfide, arsenic and antimony compounds cause by damaging substances

165

such as chlorides or sulfur compounds can be leached from concrete, gasket materials, insulating materials and polyvinyl chlorides and similar plastic materials. Many SCC failures are caused by exposure of metal equipment to corrosive environments before the equipment put into service. Pre-service environments include those associated with fabrication, testing, shipment, storage and installation. Refer to Table 1 for various environments and their impurities have effect on commercial alloys.

STRESS CORROSION CRACKING IN COMMERCIAL STEEL ALLOYS

In several references it is stated that commercial steels containing 0.05% carbon concentration is very susceptible to stress corrosion cracking. However, pure iron is less susceptible to stress corrosion failure. Small amount amounts of carbon promotes stress corrosion cracking and it becomes less severe as carbon contents increased over 0.10%.

A large amount of information has been available on stress corrosion cracking with high yield strength. The term "high strength steel" as used in this paper to steel having yield strength of 900 MPa (130 ksi) or greater, whether the strength is developed by heat treatment of any sort or by cold working. A survey of the information has shown that the strength level of the steel is the most important single factor determining sensitivity to environment induced cracking. Most stress corrosion cracking service failures in high strength steel structure are due to a combination of design plus assembly loads, susceptible alloys and a number of environments including natural environments, salt solutions, organic solvents, various gases containing relatively small amounts of water vapor and hydrogen gas. For many small components such as bolts and springs made of high strength heat treated steels for stress causing service failures are the design stresses. For large forgings, the heat treating stresses are the most important cause of failures.

The initial step in the stress corrosion process is the formation of pits which are likely to form at inclusions. A threshold stress is observed below which cracking does not occur. However, there is no absolute threshold stress for stress corrosion cracking and it vary with specific service application and corrosive environment. The path of cracking in the higher strength steels may be intergranular or transgranular.

A primary measure to avoid SCC should be the selection of a steel with good stress corrosion properties in particular and selecting one with no higher strength than needed. This practice of specifying minimum strength on drawings will not only be of benefit with respect to stress corrosion cracking but also with respect to brittle fracture.

Table 2 at the end of the paper lists alloys that are least susceptible to SCC. Table 3 lists alloys that should be avoided in SCC environment.

166

STRESS CORROSION CRACKING IN ALUMINUM ALLOYS

The most prevalent form of stress corrosion cracking service failures in aluminum alloys is caused by a combination of water, aqueous solutions or atmospheric moisture, alloy of susceptible composition and structure, and sustained tensile stresses, most often caused by heat treatment or assembly. Both initiation and propagation of cracking are accelerated by moisture, temperature, chlorides and other industrial contaminants. Stress corrosion cracking in aluminum structure for atmospheric service is increased through accumulation of water in pockets and crevices. Not only is liquid water more aggressive than undrained pockets may collect salts which concentrate during evaporation and further accelerate stress corrosion.

The relative susceptibilities of various aluminum alloys vary widely. Members of 2000 series and 7000 series are particularly vulnerable in some tempers, and some of the more highly alloyed 5000 series in some strained hardened tempers. When these alloys are extruded, rolled, forged or drawn, the grains are elongated in the direction of maximum flow to produce a structure or texture which is of major importance to SCC behavior of these alloys. The longest grain axis is designated as the longitudinal direction, the shortest is designated as short transverse and the direction of intermediate grain dimension is designated as the long transverse direction. Shown in Figure 5, practically all service SCC failures of aluminum alloy components involve the short transverse properties.

The tensile stress which cause SCC in aluminum alloys may be provided by working stress, but large majority of service failures are caused by assembly stresses, or heat treating stresses, or both. To control SCC in aluminum alloys 1) select alloy with minimum susceptibility, 2) avoid tensile stresses in short transverse direction, 3) keep water and water vapor away from metal surface and 4) minimize chlorides to concentrate.

STRESS CORROSION CRACKING IN IRON-NICKEL-CHROMIUM ALLOYS

The four classes of stainless steels are

1. Martensite: Fe-Cr alloys which are hardenable by heat treatment and contains 11-18% chromium.

2. Ferritic: Fe - Cr alloys which are not hardenable by heat treatment and contains Cr in from 15 to 30%.

3. Austenitic: Fe-Cr-Ni alloys which are hardenable by cold working and contains 6-22% Ni and 16-26% Cr.

4. Precipitation Hardening Alloys: Fe-Ni-Cr which are hardenable additionally by precipitation.

The most serious stress corrosion cracking within stainless steel is caused by chlorides, extreme care is be taken to minimize chloride introduction. To avoid thermal insulation and gasketing materials high in chlorides, avoid sensitizing, minimize fabrication stress. Fluoride ion can cause SCC much the same way as chloride but with lesser concentration. SCC of Fe-Ni-Cr alloys occurs at high concentration of pH in the absence of chlorides.

STRESS CORROSION CRACKING IN COPPER ALLOYS

Copper and copper alloys have excellent SCC resistance in many industrial environment, in sea water and in marine atmosphere. Most service failures by stress corrosion cracking in copper alloys are caused by conjoint action of water, oxygen, tensile stress, alloy composition and structure, and ammonia or compounds of ammonia. SCC is also caused by moist SO_2 and mercury.

STRESS CORROSION CRACKING IN TITANIUM AND TITANIUM ALLOYS.

Titanium and its alloys have excellent SCC resistant properties. A number of environments that cause SCC are HCl, methyl and ethyl alcohol and fuming nitric acids. Alloys containing more than 6% aluminum are especially susceptible to stress corrosion cracking.

CONCLUSIONS

Stress corrosion cracking (SCC) is the major cause of failures in ground support equipment. There is no effective protection against SCC. In designing components of ground support mechanism a designer should take into account and evaluate:

1. Tensile properties of metals
2. Material Susceptibility to SCC
3. Fracture toughness
4. Type of corrosive environment

REFERENCES

1. B. F. Brown, "Stress Corrosion Cracking Control Measures," National Bureau of Standards Monograph 156, June 1977.

2. D. B. Franklin, "Design Criteria for Controlling Stress Corrosion Cracking," Marshall Space Flight Center, Document No. MSFC-SPEC-522A November 18, 1977.

3. R. W. Staehle, "Stress Corrosion Cracking," American Society of Metals Handbook, pp 205-227.

4. "Proceedings of Conference, Fundamental Aspects of Stress Corrosion Cracking," The Ohio State University, Sept. 11-15, 1967, Published by National Association of Corrosion Engineers, Houston, TX, 1969, pp. 214-307, 411-419.

5. "NTSB Safety Recommendations," Aviation Equipment Maintenance, Dec. 87. pp. 6-8,74.

TABLE 1. COMMON ENVIRONMENT EFFECTS FOR SCC

	ENVIRONMENT	DAMAGING SUBSTANCES	TYPE ALLOYS SUSCEPTIBLE
1.	Marine	Chlorides in aqueous or water solution	High Strength Aluminum alloys High Strength Steels Austenitic Stainless Steels Titanium Alloys
2.	Industrial	Sulfur dioxide *	Copper Alloys
		Ammonia	Copper Alloys
		Hydrogen Sulfide	High Strength Low Alloy Steel
3.	Atmospheric	Oxygen	Copper Alloys **
		Hydrogen Sulfide	Many Commercial Alloys
		CO - CO_2 & Moisture	Carbon Steels
		Ammonia	see above in industrial Envr.
		As & Sb Compounds +	High Strength Steels
		Sulfur dioxide	see above in industrial Envr.
		Chloride + Moisture	see marine environment

Notes: * The oxide produces H_2SO_3 & H_2SO_4
      ** Depends upon O_2 concentration
       + Contains in insecticides & other sprays

TABLE 2. ALLOYS LEAST SUSCEPTIBLE TO SCC

ALLOYS	CONDITION
STEEL	
Carbon Steel (1000 series for C>=0.10%)	UTS < 1240 MPa
Low Alloy Steel (4130, 4340, D6AC, etc.)	UTS < 1240 MPa
Music Wire (ASTM 228)	Cold drawn
HY-80, HY-130, HY-140, 1095 Spring Steel	Q and T *
21-6-9, Carpenter 20 Cb, Carpenter 20Cb-3 Stn. Stl.	All
AM350, AM355 Stn. Stl.	SCT 1000 & Above
Almar 362, Custom 455, 15-5 PH	H1000 & Above
PH 14-8 Mo Stainless steel	CH900, SRH950 & Above
PH 15-7 Mo, 17-7 PH	CH900
Nitronic 33, A 286 S.S.	All
NICKEL ALLOYS	
Hastelloy C, Hastelloy X, Incoloy 800, Incoloy 901,	All
Incoloy 903, Inconel 718, Inconel X-750	All
Monel K-500, Ni-Span-C 902, Unitemp, Waspaloy	All
Inconel 600, Inconel 625	Annealed
ALUMINUM ALLOYS	
Wrought **	
1000, 3000, 5000 (+) (++), 6000 series	All
2011, 2024 Rod & Bar, 2219	T8
2219	T6
7049, 7149, 7050, 7075, 7475	T73
Cast	
355.0, C355.0	T6
356.0, A356.0, 357.0, B358.0(Tens-50), 359.0	All
380.0, A380.0	As Cast
514.0 (214), 518.0 (218), 535.0 (Almag 35)	As Cast ++
A712.0, C712.0	As Cast

Notes: * Quenched and Tempered.
      ** Mechanically stress relieved (TX5X or TX5XX) were possible.
       + High Mg alloys should be used in controlled tempers (H111, H112, H116, H117, H323, H343) should be used.
      ++ Mg>3% not recommended for application temperature >66°C (150°F).

TABLE 2. ALLOYS LEAST SUSCEPTIBLE TO SCC (Continued)

ALLOYS	CONDITION
COPPER ALLOYS	
CDA NO. *	(Max % Cold Rlld.
110, 194, 422, 510, 521	37
170, 172	AT and HT **
195	90
230, 619 (9% B phase), 619 (95% B phase), 688	40
443	10
706	50
725	50, Annealed
MISCELLANEOUS ALLOYS (Wrought)	
Beryllium S-200C	Annealed
HS 25 (L605), HS 188, MP35N	All
Titanium: 3Al-2.5V, 6Al-4V, 13V-11Cr-3Al	All
Magnesium: M1A, LAZ933	All
Magnesium: LA141	Stablized

Notes: *   Copper Development Association Alloy number
       ** AT - Annealed and precipitation hardened.
           HT - Work hardened and precipitation hardened.
Source: Marshall Space Flight Center document No. MSFC-SPEC-250A

TABLE 3. ALLOYS LOW RESISTANCE TO SCC

ALLOYS	CONDITION
STEEL	
Carbon Steel (1000 series)	UTS > 1380 MPa
Low Alloy Steel (4130, 4340, D6AC, etc.), H-11	UTS > 1380 MPa
440C	All
18 Ni Maraging Steel - 200, 250, 300 & 350 grades	Aged at 482°C
AM350, AM355 Stn. Stl.	Below SCT 1000
Custom 455	Below H1000
PH 15-7 Mo, 17-7 PH Stainless steel	All Except CH900
ALUMINUM ALLOYS	
Wrought	
2011, 2024	T3, T4
2024	Forgings
2014, 2017, 7039	All
7075, 7175, 7079, 7178, 7475	T6
Cast	
295.0(195), B295.0(B195), 707.0(607, Ternalloy 7)	T6
520.0(220)	T4
D712.0(D612, 40E)	As Cast
COPPER ALLOYS	
CDA NO. *	(Max % Cold Rlld.
260, 353, 782	50
443	40
672	50, Annealed
687	10, 40
762	A, 25, 50
766	38
770	38, 50 Annealed
MAGNESIUM ALLOYS	
AZ61A, AZ80A	All

Notes: *   Copper Development Association Alloy number
Source: Marshall Space Flight Center document No. MSFC-SPEC-250A
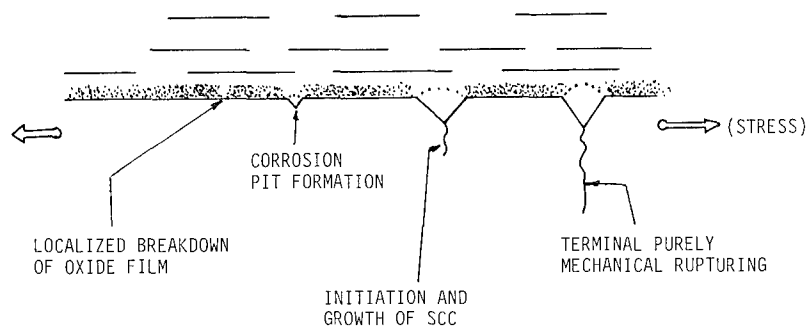
FIGURE 1.   COMMON EVENTS IN SCC, LEFT TO RIGHT
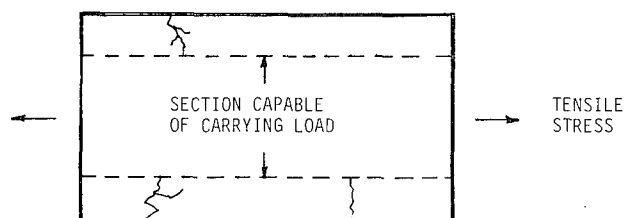
FIGURE 2.   ENVIRONMENTALLY INDUCED CRACKS IN METAL SECTION

STRESS

Normal fracture stress
when tested in an inert
laboratory atmosphere

Normal Engineering Tensile Curve

Premature fracture at lower stress
due to active environment

STRAIN
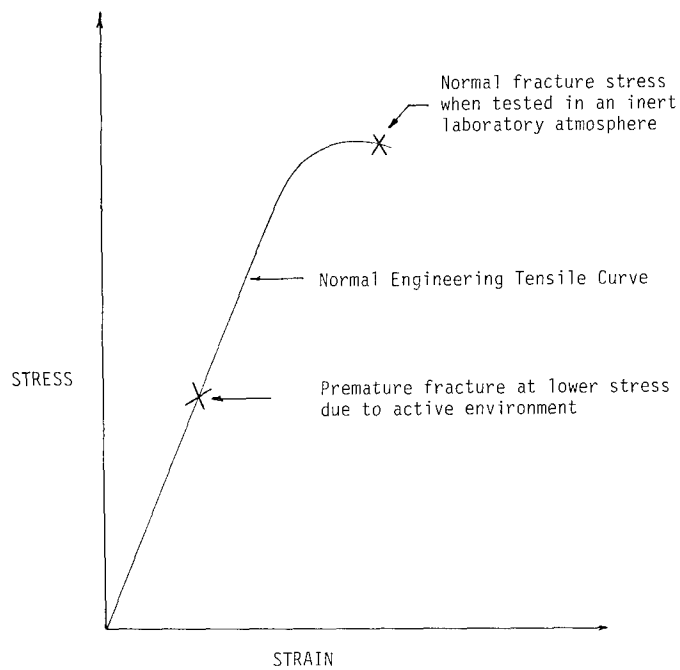
FIGURE 3.   EFFECTS OF STRESS CORROSION CRACKING ON TENSILE CURVE

LONGITUDINAL

LONGITUDINAL

DIRECTION OF
FLOW

LONG
TRANSVERSE

SHORT TRANSVERSE

(A)

LONG TRANSVERSE

SHORT TRANSVERSE

(B)

LONGITUDINAL

LONG
TRANSVERSE

LONG
TRANSVERSE

SHORT TRANSVERSE

(C)
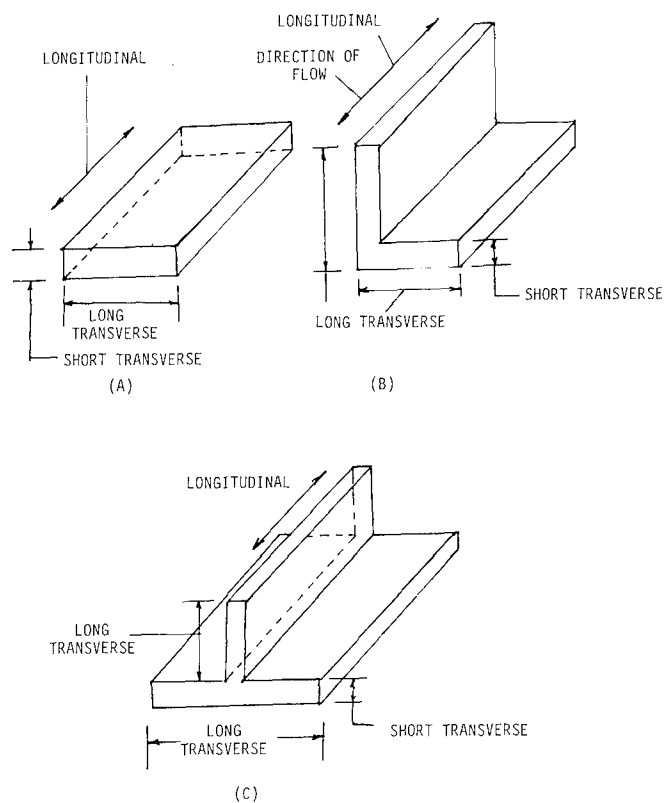
FIGURE 4.   GRAIN FLOW PATTERN IN MILL PRODUCT

173
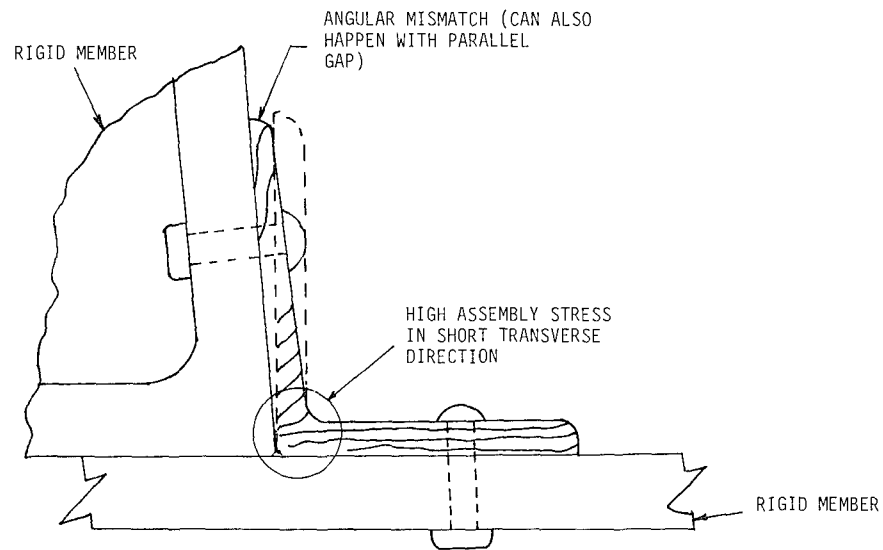
FIGURE 5.   HIGH SUSTAINED STRESS GENERATED DUE TO ASSEMBLY MISMATCH

KINEMATIC SUPPORT USING ELASTIC ELEMENTS

Árni Geirsson * and Daniel B. DeBra **

ABSTRACT

In this paper we review the design of kinematic supports using elastic elements. The two standard methods (cone, Vee and flat and three Vees) are presented and a design example involving a machine tool metrology bench is given. Design goals included thousandfold strain attenuation in the bench relative to the base when the base strains due to temperature variations and shifting loads. Space applications are also considered.

INTRODUCTION

The application of kinematic principles to the support of devices is quite old. Evans [1987] traces its evolution to the eighteenth century. Maxwell (Niven [1890]) gives the clearest early statement of principles and is often quoted. The idea is to constrain only as many degrees of freedom as are required by the application but no more. For example, a slideway that must move in one direction only should be constrained by exactly five points, no more or no less. If less, there are extra degrees of freedom and the motion will not be rectilinear. If there are more constraints, there can be stresses built up between the support points, which results in strain in the supported body. In this discussion, we are considering the mounting of strain-sensitive bodies such as optical benches, inertial systems with several components that must have accurate relative orientation, precision measuring systems such as a metrology bench, etc. These bodies must be supported. Six degrees of freedom must be fixed, but if the base upon which they are mounted is strained, it must not be propagated into the device.

There are two classical configurations for accomplishing this (See Fig. 1a and b):
- cone Vee and flat
- three Vee's

---

* Graduate student, Dept. of Mechanical Engineering, Stanford University
** Professor, Dept. of Aeronautics and Astronautics, Stanford University

In Fig. 1a, the left corner is fixed by the contacts of its mount in three degrees of freedom of translation. However, with only this support, the device can be rotated about any of the three axes. The right hand forward mount rests in a Vee which provides two more constraints, but allows rotation about the line joining the two first mounts. The final constraint is supplied by a flat upon which the third corner rests. Similarly, for the three Vees, there are two constraints at each of the corners. In both cases, six degrees of freedom are constrained.

On the earth, this is frequently done by letting gravity press three balls against the constraints. The assumptions are that
- the weight places the balls in contact with their constraints and holds them there.
- if strain occurs, the balls are free to slide along the surfaces on which they rest.

Thus, the strain of the base is not propagated into the supported device. While these mounts provide a high degree of repeatability if the device is removed and returned, the assumptions are not always satisfied. In space, there is no weight to ensure that the constraints are active. It is necessary to provide a force pushing the balls against the hard points. Since this process can cause strain in the body, care is required to keep the constraining force constant. Furthermore, if the base strains, the surfaces are not frictionless and a small and unfortunately unpredictable amount of strain gets propagated to the body. Both of these disadvantages can be overcome by employing elastic elements in supporting the device. Proper scaling permits adequate stiffness for support while providing acceptable compliance for the attenuation of strain induced in the base.

ELASTIC ELEMENTS

The most common form of elastic element is the flexure which is a flat sheet of material (see f. ex. Jones[1961], Jones[1962], Andreeva[1962], Geary[1954]). For example, the Bendix crossed-flex hinges use these plates in bending. Each plate has three degrees of freedom that are stiff. In Fig. 2a, one can see by inspection that the flexible degrees of freedom are in translation along Z and rotation about the X and Y axes. Combinations of these plate flexures can be used to increase or decrease the number of degrees of freedom. For example, the figure shown in 2b is flexible only in translation along Z, whereas in Fig. 2c, the combination shown provides stiffness only in the X direction.

A more direct way of providing stiffness in one degree of freedom with compliance in the other five is to use a rod. Rods can be combined easily to constrain additional degrees of freedom by mounting them perpendicular to each other at a single location. When the rods are piston actuators, six degrees of freedom can be

controlled as is done in some moving base simulators for pilot training and research (Stewart[1965], Dagalakis[1987]).

In a satellite project at Stanford, supported by sub-contract to Lockheed Missiles and Space Company, we intend to mount a solar array with six rods of this type to avoid over-constraints that could produce unnecessary stresses on the solar arrays or the vehicle (see Fig. 3). We are also involved in some precision manufacturing work in which a machine tool is being developed that requires a separate metrology bench which will be free from the strains in the machine due to temperature variations, changing locations of weight and machining forces. In the latter example, we have made individual supporting elements which are the kinematic equivalent of three elastic V's.

Thus by starting with a requirement for adequate strength and some minimum level of stiffness, one can establish the necessary size and slenderness ratio which will provide an adequate mounting employing elastic elements. Depending upon the application, one may choose to use three V's or a cone V and flat configuration, as shown in Figure 4. If there is one point in the body whose position has special significance with respect to the base, then a cone, V and flat may be the most appropriate. The three rods of the cone should be placed and oriented so that they pass through the critical point, thus minimizing any translation of this point due to rotation of the body relative to the base.

The problem of damping the motions of the supports has not been solved satisfactorily. Jim Bryan has suggested using wire cable for the rods to allow internal friction in applications where slight stick slip within the cable would be an acceptable disturbance. This would also allow much shorter cables than rods of equal strength due to the cable's softness in bending.

DESIGN FOR PERFORMANCE

Kinematic mounting of a body on a base poses two kinds of questions regarding performance:
- How well does each support constrain its assigned degrees of freedom.
- How rigidly do all supports collectively mount the body on the base.

The first class of questions arises from our need to simulate the motion of a ball resting in a conical hole with three sides, in a V-shaped groove with two sides or on a flat surface in all cases without any friction. When using flexible elements in order to eliminate sliding contact in hinges or bearings, some stiffness in unconstrained degrees of freedom is unavoidable. However, this is often better than the erratic stick-slip motion of two surfaces. In the following we shall concentrate on pairs of flexible perpendicular rods used as depicted in Fig. 5 for kinematic mounting.

Each pair simulates a ball in a V-shaped groove. Defining a coordinate system and symbols as in Fig. 5 we obtain the following stiffness matrix:

$$K = \begin{pmatrix} \frac{EA}{L} & 0 & 0 & 0 & 0 & 0 \\ 0 & \frac{24EI}{L^3} & 0 & 0 & 0 & -\frac{12EI}{\sqrt{2}L^2} \\ 0 & 0 & \frac{EA}{L} & 0 & -\frac{REA}{L} & 0 \\ 0 & 0 & 0 & \frac{EI}{L}\left(\frac{24R^2}{L^2}+6.79\right) & 0 & 0 \\ 0 & 0 & -\frac{REA}{L} & 0 & \frac{E}{L}(8I+AR^2) & 0 \\ 0 & -\frac{12EI}{\sqrt{2}L^2} & 0 & 0 & 0 & \frac{4.8EI}{L} \end{pmatrix}$$

which relates forces and torques to displacements through the equation $f = Kd$ where

$$f = [f_x, f_y, f_z, M_x, M_y, M_z]^T$$
$$d = [d_x, d_y, d_z, \theta_x, \theta_y, \theta_z]^T$$

The above stiffness matrix reflects our choice to mount each rod at 45 degrees from the vertical to provide equal stiffness in x and z directions. In the stiffness matrix, we want elements corresponding to F_x/d_x and F_z/d_z to be as large as possible while keeping all other entries close to zero to attenuate the propagation of strain in the base to the body. Examination of the entries leads to the intuitive conclusion that we should keep the rods long (large L) and thin (small D) and they should be attached as close as possible to their point of intersection (small R). We can look at the ratio between F_x/d_x and F_y/d_y as a measure of quality and notice that this ratio is only proportional to the slenderness ratio (L/D) squared with no dependence on material properties. If we make the rods very long and thin, we either compromise their ability to constrain the degrees of freedom that the support is designed to eliminate or they get excessively long. In the stiffness matrix, this appears as a decrease in the F_x/d_x and F_z/d_z stiffnesses although the ratio between F_x/d_x and F_y/d_y increases (unless we keep D^2/L constant as we increase L). This ratio, L/D, is therefore not a sufficient measure of the quality of the design, which leads to the second class of questions, namely those of collective performance of all three supports.

For each application there are normally several criteria that the design must meet. We may have to consider
- adequate strength of the mount
- overall stiffness of the body's mounting on the base
- natural frequencies and modeshapes of the kinematically mounted body
- strain propagation from base to body

The issue of strain propagation is addressed both by the design of each support, their location and orientation and the stiffness of the body. Since there is some stiffness

in unconstrained degrees of freedom, there will always be some strain introduced in the body when the base strains. By carefully laying out the location and orientation of the supports it is possible to influence the nature of the strains generated in the body. We can for example arrange the supports so that for a given strain in the base, minimum strain energy is accumulated in the body or arrange them so that angular distortion of the body (when, say, the base expands uniformly due to increase in temperature) is minimum.

Although analysis of the problem must reflect each application, a simple example is in order. Let us assume that the body to be suspended is an isosceles triangular frame with supports, characterized by the above stiffness matrix, mounted at its corners. Referring to Fig. 6, a relationship is sought between the displacement of the supports at the base (z_3 and z_4) and the resulting displacement of the corners of the triangle (z_1 and z_2).

Let angles ϕ and θ, frame stiffnesses s_1 and s_2, support stiffness (i.e. F_y/d_y) k, and lengths L_1 and L_2 be as defined in Fig. 6. The following relationships then hold for the geometry of the frame as it strains:

$$\delta L_1 = cos(\phi)z_1 + cos(\theta - \phi)z_2$$

$$\delta L_2 = 2z_2 sin(\theta)$$

The total potential energy resulting from strains may then be written in terms of displacements:

$$E = s_1(\delta L_1(z_1, z_2))^2 + \frac{1}{2}s_2(\delta L_2(z_1, z_2))^2 + \frac{1}{2}k(z_3 - z_1)^2 + k(z_4 - z_2)^2$$

Now differentiating this with respect to z_1 and z_2 and setting the result to zero provides a relationship between frame displacements and base displacements:

$$\begin{pmatrix} 2(\frac{s_1}{k})cos^2(\phi) + 1 & 2(\frac{s_1}{k})cos(\theta - \phi)cos(\phi) \\ 2(\frac{s_1}{k})cos(\theta - \phi)cos(\phi) & 2(\frac{s_1}{k})cos^2(\theta - \phi) + 4(\frac{s_2}{k})sin^2(\theta) + 2 \end{pmatrix} \begin{pmatrix} z_1 \\ z_2 \end{pmatrix} = \begin{pmatrix} z_3 \\ 2z_4 \end{pmatrix}$$

One might now, for example, set the z_3 and z_4 values as proportional to the distance of the corresponding corners to the point where lines of unconstrained translation for each support intersect. Again referring to Fig. 6 this corresponds to uniform strain (ϵ) in the base resulting in $z_3 = \epsilon R_1$ and $z_4 = \epsilon R_2$. Now if no angular distortion is required, the angle θ would have to be adjusted until the solution z_1 and z_2 is also proportional to R_1 and R_2. If minimal strain in the frame is the object, the expression for the total potential energy can be minimized by adjusting θ. Our calculations have led us to the following conclusions:

- If all three members of the frame are equally stiff, both minimum strain energy and no angular distortion of the frame are achieved by letting the lines of free translation intersect in the centroid of the triangle.
- If the compliance of the members of the triangle is proportional to their length (as in the case of straight, homogeneous beams of uniform cross section), minimal strain and no angular distortion require different angles θ. However, strain energy in the no distortion case is insignificantly higher than in the minimal strain case (order of 1%).

As pointed out earlier, these considerations must only go as far as allowed by requirements for overall stiffness and natural frequencies.

For the more complex case of nonsymmetric geometry, the analysis proceeds in a similar fashion, only with more symbols to manipulate. It is interesting to note that if the lines of unconstrained translation do not all intersect in one point, the frame may rotate as well as undergoing distortion.

A MACHINE TOOL METROLOGY BENCH

The motivation for our study comes from the field of precision machine tools. In our laboratory at Stanford, we are building an ultra precision turning machine to be capable of turning parts with surfaces of optical quality and repeatability on the order of microinches. This machine is composed of a hydraulic laminar flow spindle, a hydraulically controlled cross-slide on hydrostatic bearings and a high bandwidth tool actuator. All these parts along with the granite slab on which they are mounted are showered with tightly temperature controlled oil to prevent dimensional changes due to temperature fluctuations.

To achieve such high precision in machining it is necessary to employ sophisticated metrology which in our case is based on laser interferometry. All metrology equipment is mounted on a separate metrology bench of granite which surrounds the machinery (Bryan[1979]). Since the geometry of this metrology bench is the standard to which all measurements of the machinery is referred, we require that any strains that may arise in the foundation of the machine should not propagate into the metrology bench while at the same time it is rigidly fixed to the foundation. These requirements are met by kinematic mounting. Since no particular point on the metrology bench is more significant than others, we chose to use the three V configuration, this giving the advantage of identical design of all three supports.

The metrology bench weighs 680 kg (1500 lb), it is shaped like the letter C and made of 0.254 m (10 in.) thick granite. Primary considerations in design of its supports were:
- Sufficient strength to carry its weight.

- The weight carried in tension to avoid buckling.
- High stiffness in constrained directions for natural frequencies greater than 40 Hz.
- Low stiffness in free directions to attenuate strain by 10^3.
- Supports located symmetrically about the mass center for equal loading.
- No rubbing contact.
- Stops to prevent yielding of flexible parts.
- Easy manufacture.

Each support must be functionally equivalent to two rods in a V arrangement (see Fig. 3b). Due to the heavy weight of the bench, it is best to load the rods in tension rather than compression to prevent buckling. In our design this is done by suspending the rods from a column rising from the base with the bench attached to the lower end of the rods. They are set at an angle of 45 degrees from the vertical to make the supports equally stiff in all directions in the plane of the rods. It is important that the first natural frequency of the bench, when moving as a rigid body on all three supports, be sufficiently high that the mass attenuates greatly the associated motion. The orientation that was chosen for the supports (see Fig. 7) reflects this and a desire to make the collective stiffness of the supports equal, i.e. an external horizontal force acting on the bench would cause equal deflection independent of direction. As admitted earlier, no good way has been found to passively damp motions of the supports without compromising other necessary qualities.

Design for fabrication involved several considerations:
- Monolithic or assembled
- Methods of assembly: brazing or bolting
- Material suitable for strength, machining and brazing
- Cost of material and fabrication
- Corrosion resistance

Making each support truly monolithic is difficult in fabrication and since no disassembly is needed after fabrication, it was decided to make each support of five pieces and braze them together: footplate, column, carrier beam and two rods (see Fig. 8). Being easy to machine and corrosion resistant, stainless steel alloy 303 was chosen for all pieces other than rods. Drillrod was chosen as the material for the rods for its strength, cost and availability. Minimum diameter to support the load was found to be 6.35 mm (1/4 in.) while the length could be no greater than 0.119 m (4.7 in.) due to space constraints. This results in a stiffness ratio for constrained and free directions of 234 and an overall strain attenuation from base to bench of 1000.

The first modeshape is shown in Fig. 9. We see that two of the supports are moving in their flexible direction. The associated natural frequency is 46 Hz. The next five natural modes, the highest frequency of which is 80 Hz, also principally

involve the supports, with the bench nearly rigid. The seventh mode is the first one to include significant strain of the bench and occurs at 200 Hz.

CONCLUSIONS

Kinematic support using elastic elements offers some advantages. In a weightless environment it can constrain in tension or compression so external loading is not needed. The strain propagation is systematic and smooth which may be preferred over the stick-slip adjustments of contacting surfaces that must slide. Rods offer a simple design choice with one degree of freedom constrained by each of six rods. Greater lateral and rotational compliance for a given strength can be achieved with stacked flexures however. By selection of location and orientation as well as support design, the strain propagated can be managed in a variety of different ways permitting some selection in design to minimize distortions which may be particularly undesirable.

ACKNOWLEDGEMENT

REFERENCES

Andreeva, L. E., *Elastic Elements of Instruments*, Edit. Feodosev, V. I., Moskva 1962, Israel Program for Scientific Translation.

Bryan, J. B., "Design and Construction of an Ultraprecision 84 inch Diamond Turning Machine", *Precision Engineering*, vol. 1, n. 1, 1979.

Dagalakis, N. G., "Stiffness Study of a Parallel Link Robot Crane for Shipbuilding Applications", NBS internal CME paper, 1987.

Evans, C. "Precision Engineering: an Evolutionary Perspective", MSc thesis, Cranfield Institute of Technology, College of Manufacturing, March 1987.

Geary, P. J., *Flexure Devices*, B.S.I.R.A Bibliographical survey of instrument parts, no. 1, research report M18, 1954.

Jones, R. V. "Anti-distortion mountings for instruments and apparatus", *Journal of Scientific Instruments* v. 38, Oct 1961.

Jones, R. V. "Some uses of elasticity in instrument design", *Journal of Scientific Instruments* v. 39, 1962, p. 193.

Maxwell, J. C., "General considerations concerning scientific apparatus" from *The Scientific Papers of James Clark Maxwell* ed. W. D. Niven, Dover Press 1890

Stewart, D., "A Platform With Six Degrees of Freedom", *Proc. of the Inst. of Mech. Eng.*, vol. 180, part I, n. 15, 1965-1966.
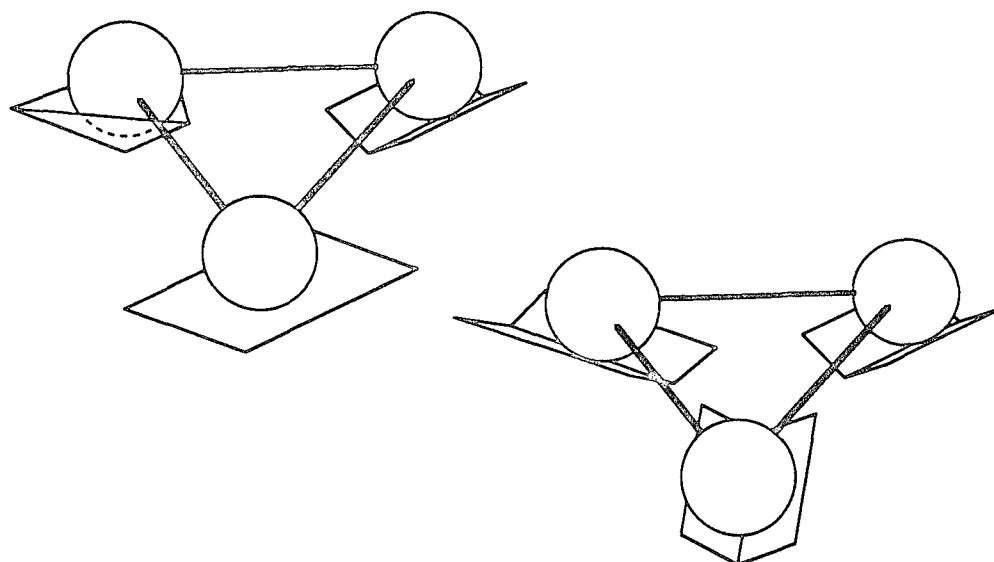
Figure 1: a) Balls resting in conical hole, in V-shaped groove and on a flat surface. b) All three balls in V-grooves.
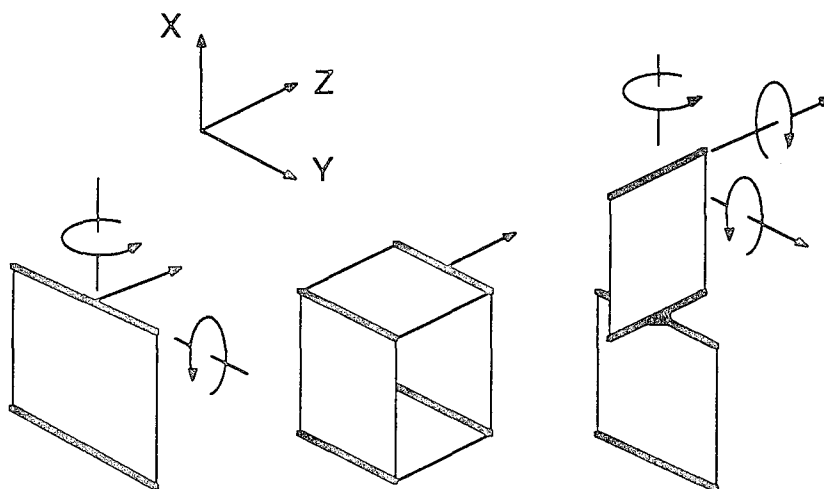
Figure 2: Flexures with a) three, b) one and c) five compliant degrees of freedom.
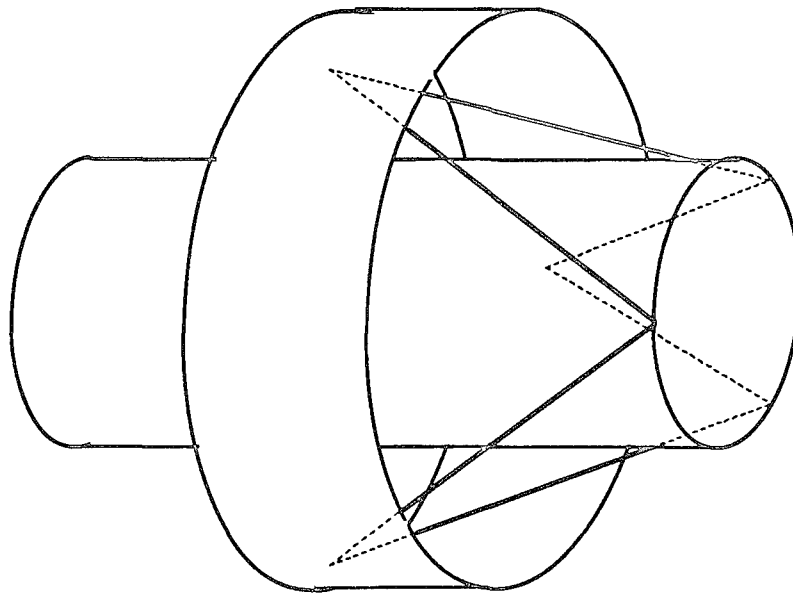
Figure 3: Kinematic suspension of solar array on satellite.

CONE, V
AND FLAT
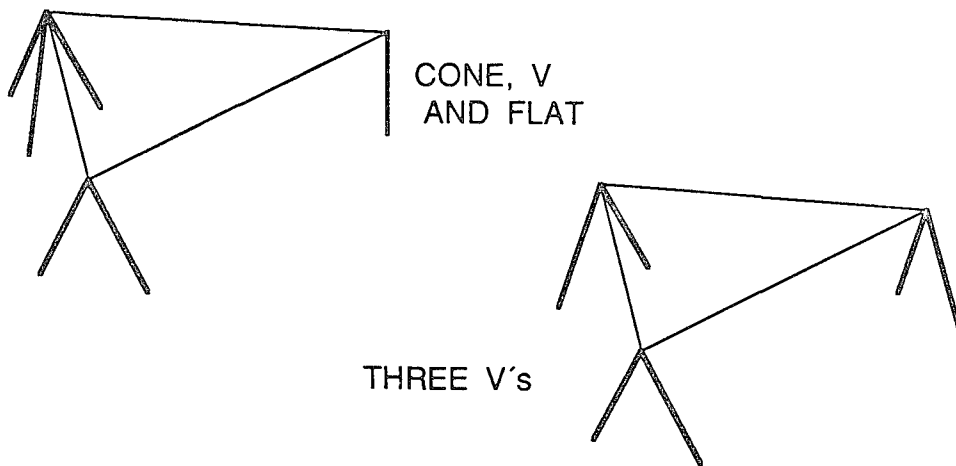
THREE V's

Figure 4: Cone, Vee and flat or three Vees implemented with flexible rods.

185

Figure 5: Two rods in tension simulate ball in V-groove.

Figure 6: Definition of symbols for analysis.

Figure 7: Orientation of supports for metrology bench.

Figure 8: Design of supports for metrology bench. The bench rests on the carrier beam which is suspended by rods from a fixed column.

Figure 9: First modeshape of metrology bench resting on supports.
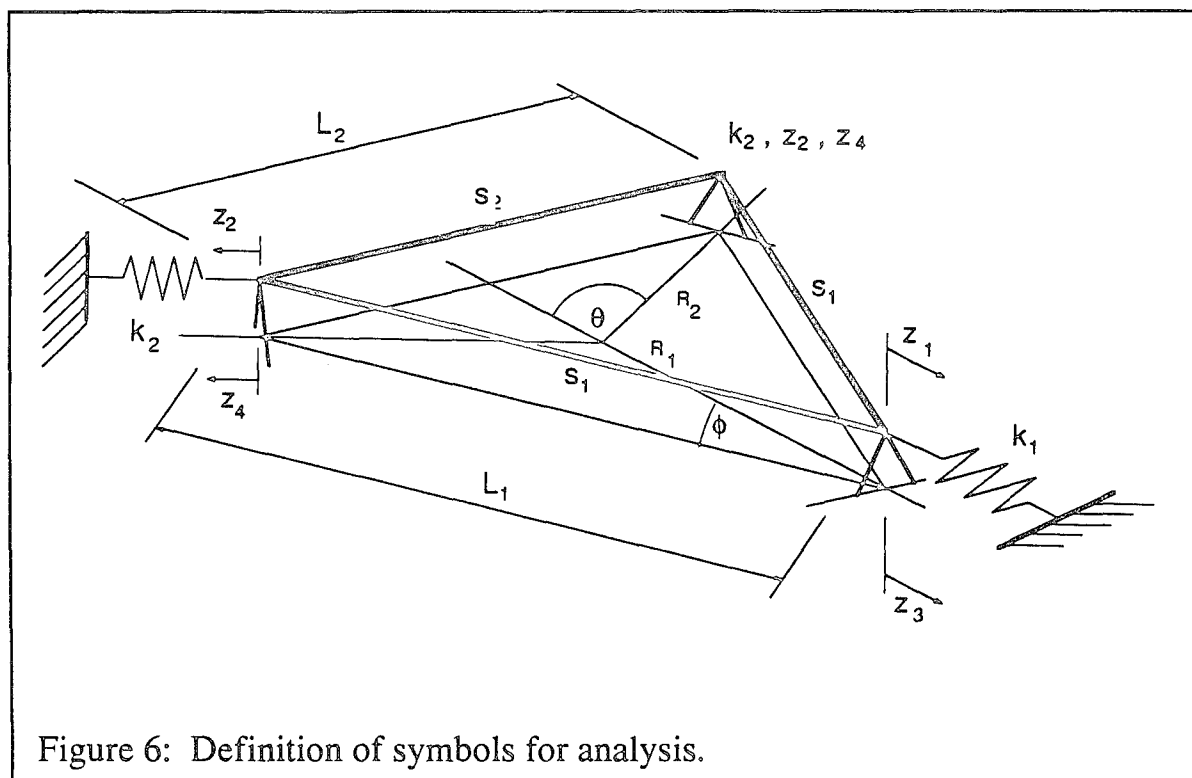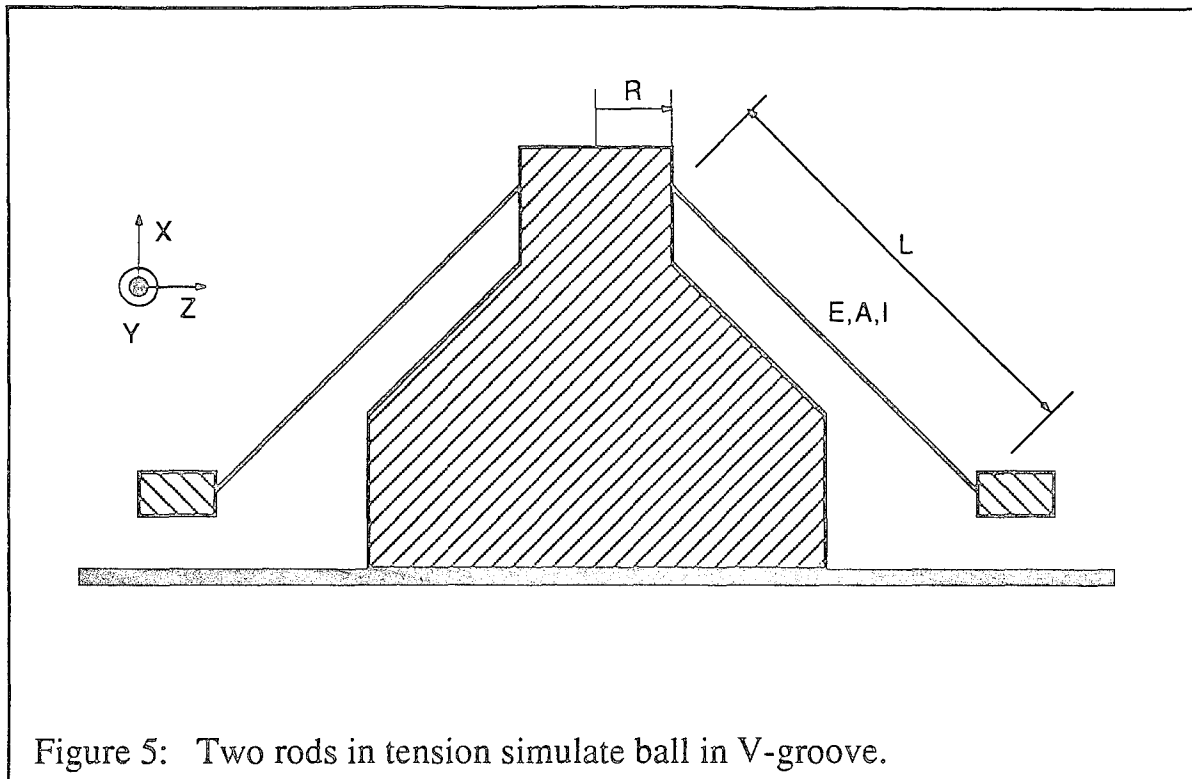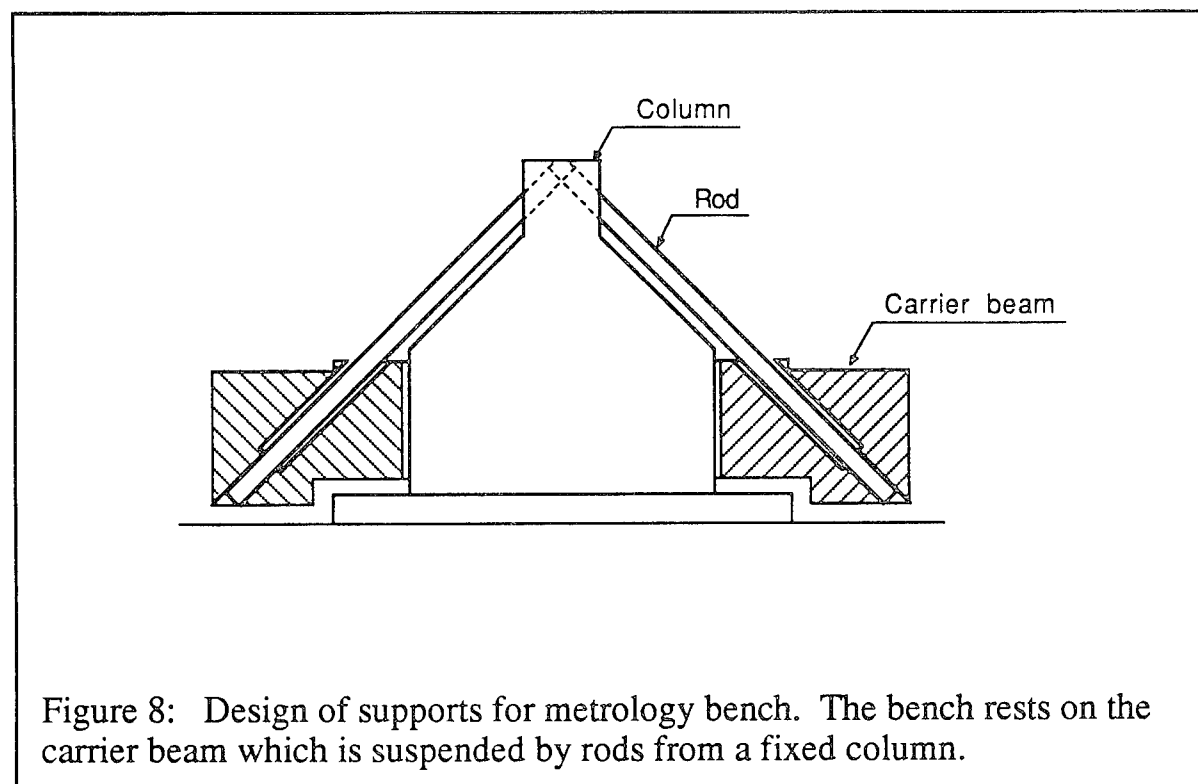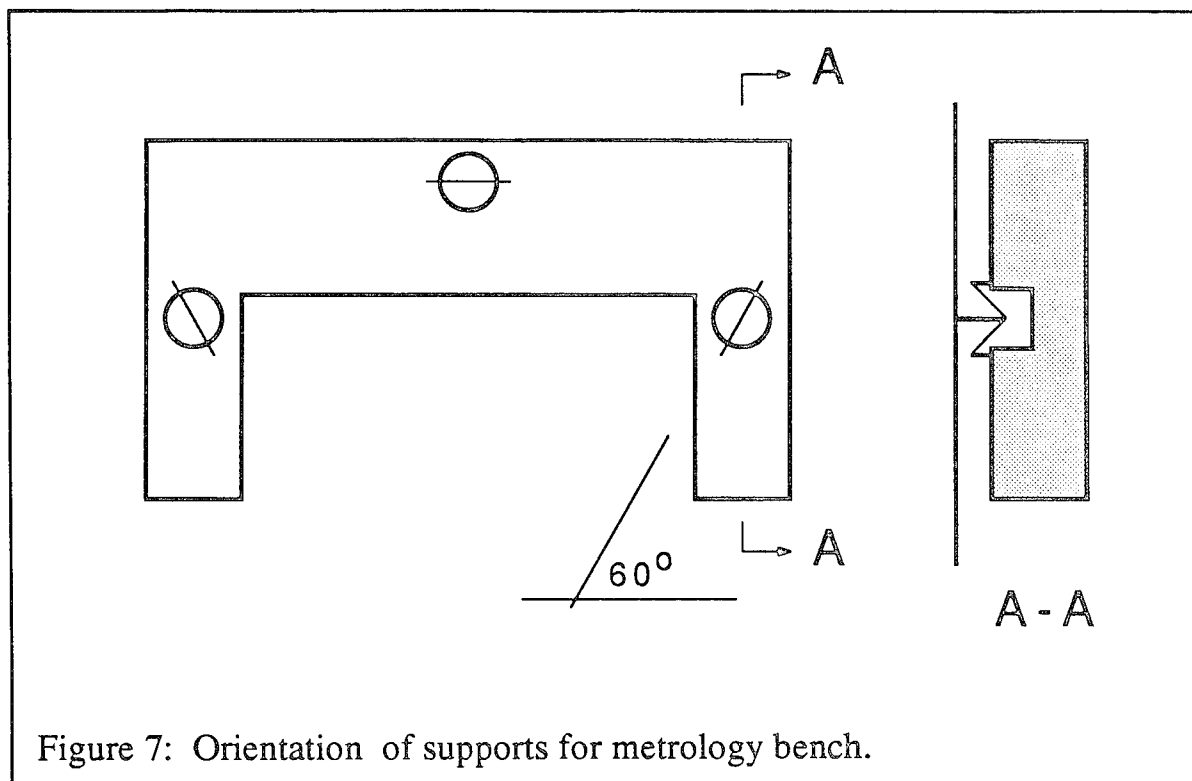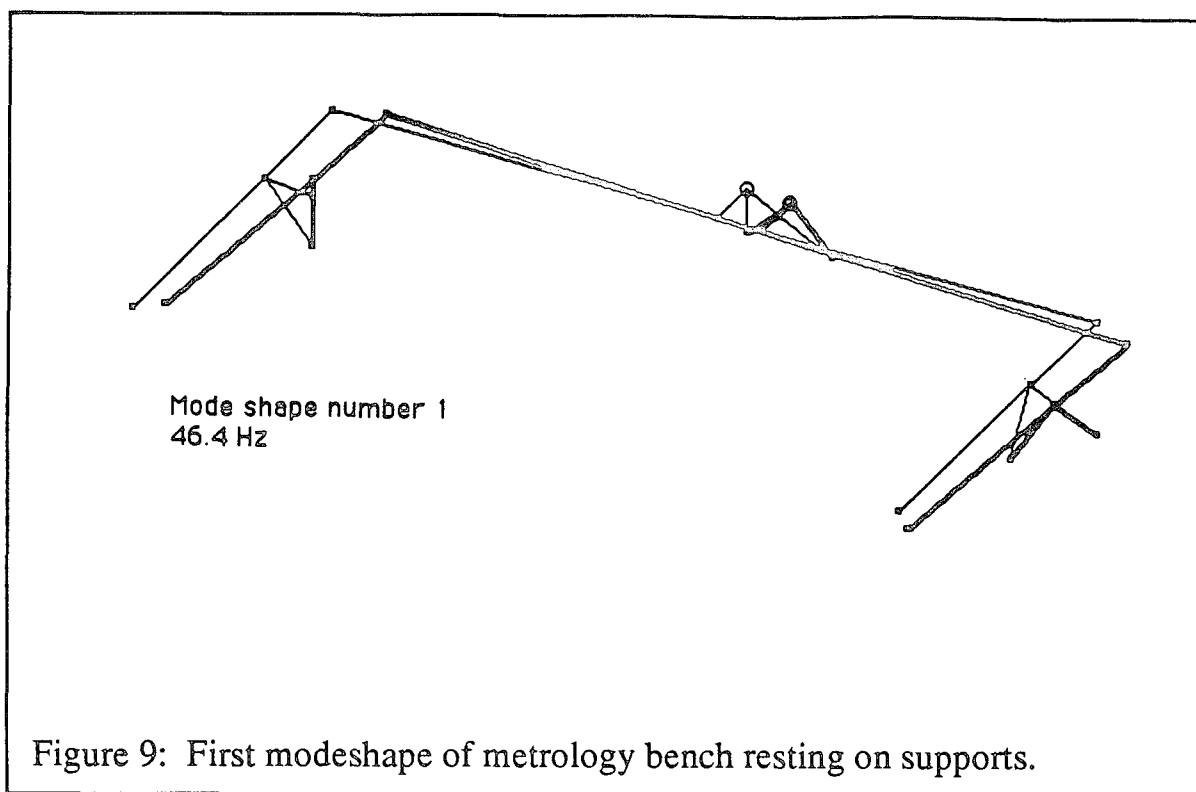
DEVELOPMENT OF DRIVE MECHANISM
FOR AN OSCILLATING AIRFOIL

Clifford D. Sticht*

ABSTRACT

This paper describes the design and development of an in-draft wind tunnel test section which will be used to study the dynamic stall of airfoils oscillating in pitch. The hardware developed comprises a spanned airfoil between schleiren windows, a four bar linkage, flywheels, a drive system and a test section structure.

INTRODUCTION

The purpose of the experiment is to investigate dynamic stall which is a phenomenon associated with an airfoil moving beyond its static stall angle. Examples of where dynamic stall is present are in jet engine compressors, helicopter rotor blades and aeroelastic effects on aircraft wings where small amplitude and high frequency oscillations are present. When an airfoil is moved rapidly through an angle-of-attack range that includes the static stall angle, maximum lift can be greatly increased and becomes strongly dependent on the rate and amplitude of oscillation. There is a hysteresis loop developed in both lift and pitching moments with much larger magnitudes developed than in steady flow as shown in Figure 1. At the end of the cycle, where the vortex leaves the airfoil, there is an abrupt drop in lift and moment.

The test section, described in this paper, will be installed at the new Fluid Mechanics Laboratory at Ames Research Center, which has been developed to pursue basic research in aerodynamic science and technology. The Lab consists of four in-draft tunnel bays and a central experiment bay. These bays house a variety of small research wind tunnels, many of which will be driven by the Laboratory's 113 m^3/s (240,000 cfm) compressor. The wind tunnel, containing the test section being discussed in this paper consists of an intake with screens joined to a contraction section as shown in Figure 2. Downstream of this is the test section, followed by a variable throat to control the flow velocity. The flow then passes through a manifold and finally to the Lab's 6.0 MW (8000 hp) compressor.

---

*   Research Engineer, NASA-Ames Research Center

DESIGN REQUIREMENTS

The oscillating spanned airfoil and test section were designed to meet the following specifications:

1. Variable angular displacement of oscillation with maximum adjustment of oscillation of 10 degrees, with specific indexing at 0, 2, 5, and 10 degrees, but with intermediate positioning capability

2. Mean angle-of-attack position of the airfoil to be adjustable from 0 to 15 degrees in 5 degree increments, with intermediate positioning capability

3. Angle-of-attack accuracy within 0.1 degrees

4. Motion of the airfoil to be simple harmonic within 10% and to have variable driving frequency up to 100 hertz

5. Viewing of the airflow around the airfoil to be unobstructed through windows near the wing

6. Maximum flow velocity of Mach 0.5

7. Airfoil NACA 0012, 7.62 cm (3in.)

8. Test section having a cross section of 25 by 35 cm

DESIGN

After studying several concepts, it was decided that a four-bar type mechanism was the optimum drive for the airfoil (Figure 3). This type of mechanism offered good load transfer, accurate positioning and produced simple harmonic motion within 3% of the ideal. It was necessary to have duplicate drives on both ends of the airfoil, since the wing has poor torsional stiffness and large relative masses at the ends.

The primary difficulty in design was to meet adequate structural integrity at 100 hertz and properly transfer loads to glass windows. Other difficulties were the geometric constraints imposed by the airfoil limiting the size of wing support.

The final wing design is of solid aluminum construction. It is simply supported at the ends to reduce the contact stress in the glass by transferring only concentrated loads to the center of glass plates. It is spanned between the tunnel walls as shown in Figure 4. The airfoil used is a NACA 0012 with the wing having a 7.62 cm (3 in.) cord and a span of 25 cm. When the window is driven at the maximum frequency of 100 hertz, peak angular velocity is 110 rad/s (1047 rpm) corresponding to a maximum angular

acceleration of 68,800 rad/sec^2. The maximum aerodynamic loads on the NACA 0012 airfoil occur at an angle-of-attack of 25 degrees, driving frequency of 100 hertz and flow velocity of Mach 0.5. The load magnitude compared to a statically fixed wing is 2.5 times greater in lift and 5 times greater in pitching moment. For the load case where the tunnel is off, the amplitude of oscillating torque acting on wing is 10.9 Nm (96.7 in-lbs). Aerodynamic loading of the airfoil reaches a distributed lift of 681 N (13 lbs.), a drag of 307 N (69 lbs.), and a pitching moment of 10.2 Nm (91 in-lbs.) which tends to rotate the leading edge downward. This aerodynamic load combined with the inertia load of the airfoil is transferred through pinned supports at the ends of the wing. The ends of the wing are supported through tapered pins with spherical ends fabricated from 18% nickel maraging steel. The design of the pins is based upon the requirement to transfer concentrated loads to the center of the glass plate without bending. The pins are located at 30% and 70% of the cord and have maximum diameters of 5.89 mm and 4.24 mm, respectively. The loads are transfered to cylindrical inserts which slip fit into holes in the glass windows. The inserts are split along the diameter and held together by a band and a soft plastic tip (Fig. 5). At 100 Hertz and Mach 0.5, the peak dynamic loads are 356 N (80 lbs.) on the large pin and 160 N (36 lbs.) on the small pin.

The wing is supported at both ends by 15.2 cm (6 in.) diameter, 2.54 cm (1 in.) thick, optical scheliern windows that oscillate with the wing. This configuration was necessary to meet the requirement of unobstructed viewing of the airflow around the airfoil. Support of the windows is achieved through a circular magnesium frame mounted in the tunnel wall on radial contact and four-point contact bearings. The material used is borosilicate glass (BK-7), which has a breaking stress of about 34 MPa in tension and ultimate compressive strength of 593 MPa in contact with hardened steel. This design is based upon the relationships developed by Hertz, for cylindrical elastic bodies in contact, which predict that all principal stresses are compressive. In the cord direction, positioning of holes was chosen to minimize contact stresses. The hole size was restricted by the design requirement of using an airfoil NACA 0012 with a 7.62 cm. (3in.) cord. It was necessary to go to a D-shaped window to provide adequate edge distance at the driving pin locations. Transferring loads to the glass plate presented an interesting design problem because brittle materials do not behave as well under stress as do ductile materials. The strength of glass in compression is much greater than in tension. Consequently, the design was developed to take advantage of this property. Verification of the structural integrity and optical quality of the windows has been tested by applying the maximum dynamic loads statically.

A flywheel was incorporated in the design to store kinetic energy through each cycle and keep speed fluctuations to less than 1%. Mounted flush with the face of the flywheel is an eccentric disk for adjusting the amplitude of oscillation. The disk is clamped to the flywheel by a ring clamp to allow for infinite positioning of the wing amplitude from 0 to 10 degrees. Both eccentric disks are coupled by a smaller tubular shaft within the flywheel shaft as shown in Figure 6. This will produce equal amplitude adjustments on

both sides of the tunnel. An axial hole in the shaft is symmetrically placed to balance the shaft for the eccentric disk coupling. From the inertia loads of the oscillating window and frame, peak dynamic loads of 6672 N (1500 lbs) act on the disk drive pin. The drive disk can be positioned for wing amplitudes with infinite adjustment between 0 to 10 degrees with indexed positions of 2, 5 and 10 degrees.

Adjustment of the airfoil mean angle-of-attack position prior to a test run is accomplished by rotation of the entire drive mechanism about the window bearing retainer (Figure 7). Side plates supporting the flywheel assembly on both sides of tunnel are capable of positioning the wing mean angle of attack continuously from 0 to 15 degrees, with specific angular indexing at 5 degree increments within this range. The side plate is centered through contact with the outer cylindrical surface of the window bearing retainer, which is fixed to the test section side wall. This will produce rotations about an axis which is coaxial with the window axis. The advantage of this method of changing the wing's mean position is that the movement is uncoupled with changes in amplitude of oscillation. Other design studies were conducted on a concept where mean angle-of-attack was achieved by translating the flywheel shaft vertically. This presented problems with changes occuring in amplitude of oscillation with a change in the mean over the range of 0 to 15 degrees.

The wing oscillation drive motion is provided by a DC servo motor with tach feedback which ensures minimum frequency drift. The support of the DC motor is centered at one end with the flywheel axis in order to maintain the same belt drive pulley centerline distance with a mean airfoil angle-of-attack adjustment. The opposite side of the support translates in elongated slotted brackets at the top of the test section.

INSTRUMENTATION

The tunnel is instrumented to provide airfoil amplitude of oscillation, mean angle-of-attack and driving frequency. Actual position of the airfoil is obtained through optical incremental encoders which are coupled through gears at the window frame and mean angle-of-attack indexing plate.

The mean angle-of-attack encoder is coupled through gears to the tunnel side plates. This encoder provides digital output of mean airfoil position and measures this statically during test setup. Measurement of amplitude of oscillation is achieved through another optical position encoder, gear-coupled to the window with a gear segment and pinion gear. With a coupling ratio of 10.8 to 1 and a resolution of 1024 counts per turn, a resolution of 31 counts per window degree is achieved. The encoder experiences a maximum angular acceleration of 743,000 rad/sec^2 when the driving frequency is 100 Hertz. Driving the encoder from one window frame produces unsymmetric loading of the mechanism. To minimize the loads transfered to the pinion, the gear diameter and tooth face width was kept small, using a steel with a high specific strength. This results in a peak tooth loading of 356 N (80 lbs.) at 100 Hertz.

Flow measurements will be made by a number of sophisticated optical techniques including laser velocimetry, strobic color schlieren and holographic interferometry.

PROJECT STATUS

The osillating wing drive mechanism and test section have been fabricated and will be integrated into the Fluid Mechanics Laboratory at Ames in early 1988. Testing is currently being conducted to verify the structural integrity and proper functioning of the drive. The development of this test section will benefit aerodynamic prediction for helicopters and aeroelastic response on wings by making important contributions to the study of dynamic stall.

$\alpha = 15^\circ + 10^\circ \sin \omega t \qquad k = \dfrac{\omega c}{2U_\infty} = 0.15 \qquad Re = 2.5 \times 10^6$

$c_{N_{MAX}}$

BEGIN
MOMENT
STALL

NORMAL FORCE, c_N

STATIC

DECREASING
INCIDENCE

BEGIN
MOMENT
STALL

PITCHING MOMENT, c_M

STATIC

| 0 | 5 | 10 | 15 | 20 | 25 |
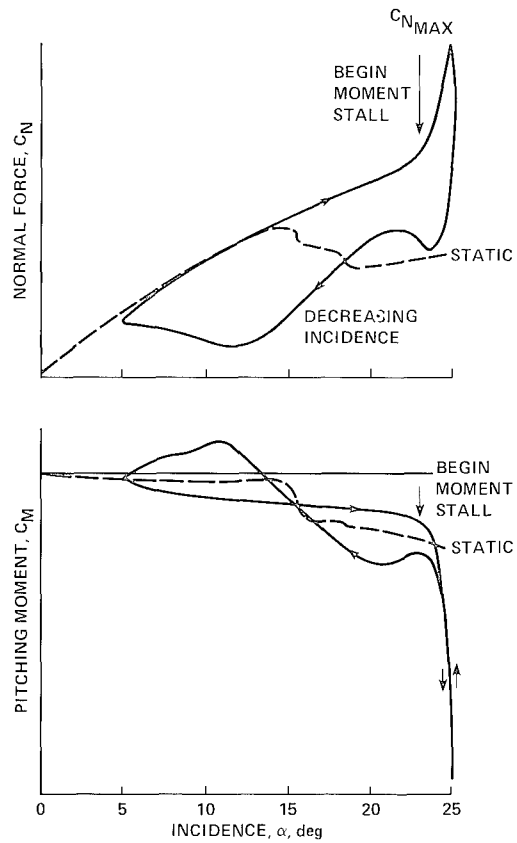
INCIDENCE, α, deg

Fig. 1. Typical static and dynamic variation of normal force and pitching moment as function of angle-of-incidence.

⊚ M_{MAX} = 0.5

INTAKE

TEST
SECTION

VARIABLE THROAT

FLOW ⟹
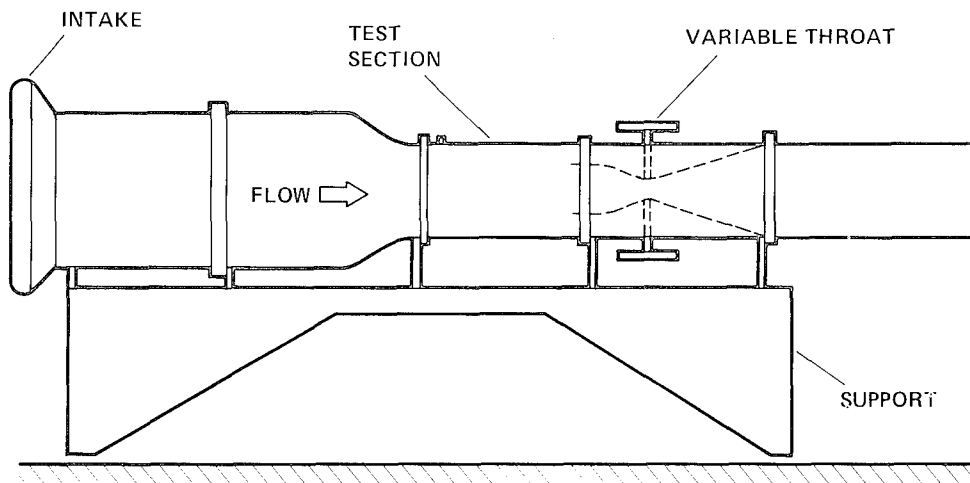
SUPPORT

Fig. 2. Test section installation at fluid mechanics laboratory.
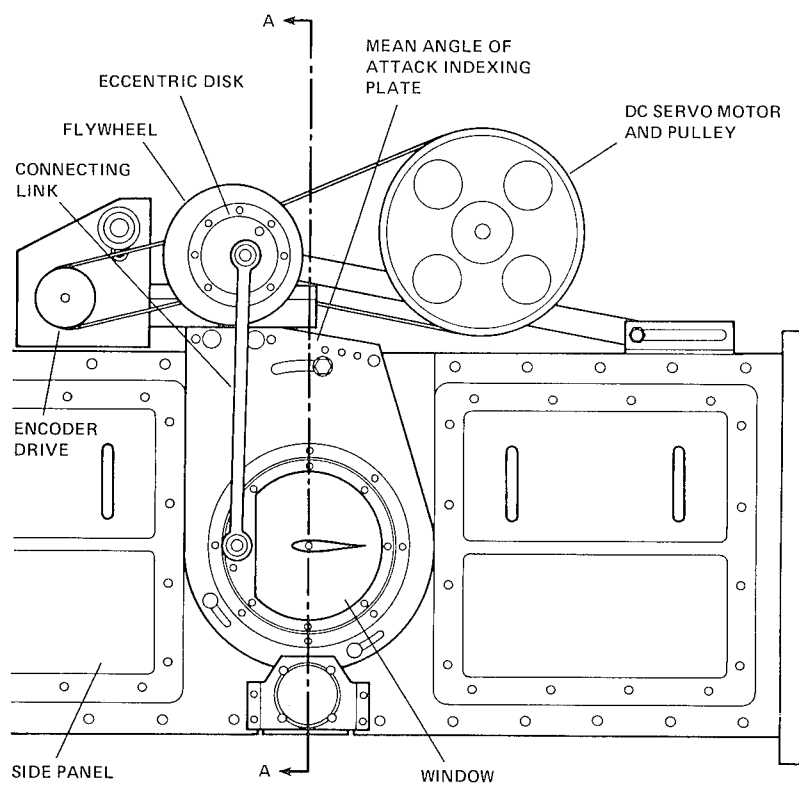
Fig. 3. Test section side view.

SECTION A—A
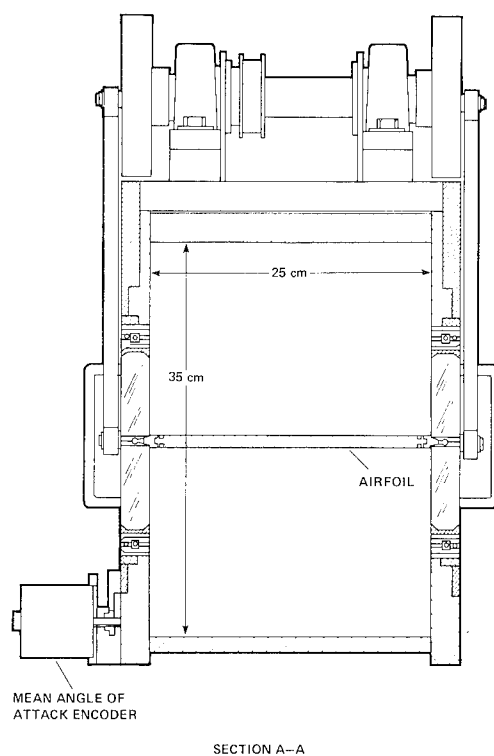
Fig. 4. Upstream view.
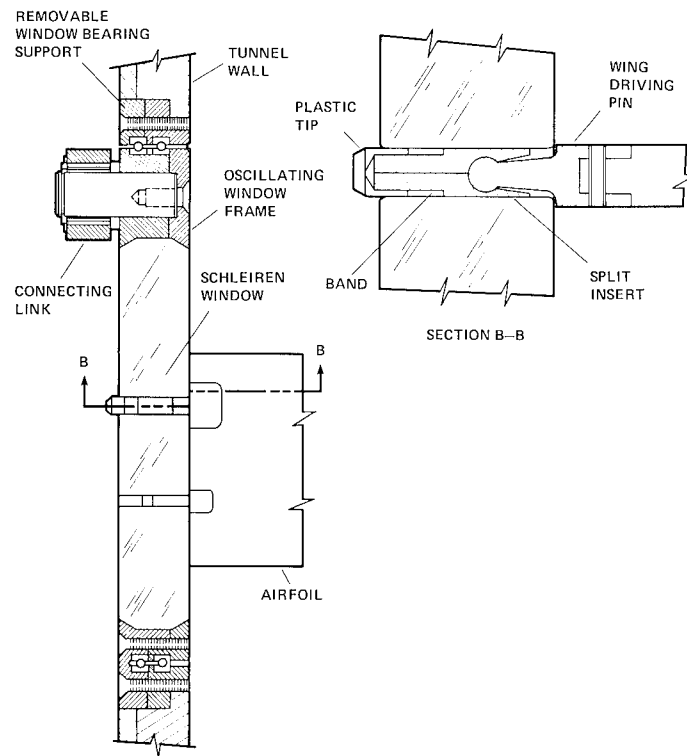
Fig. 5. Airfoil support at window.
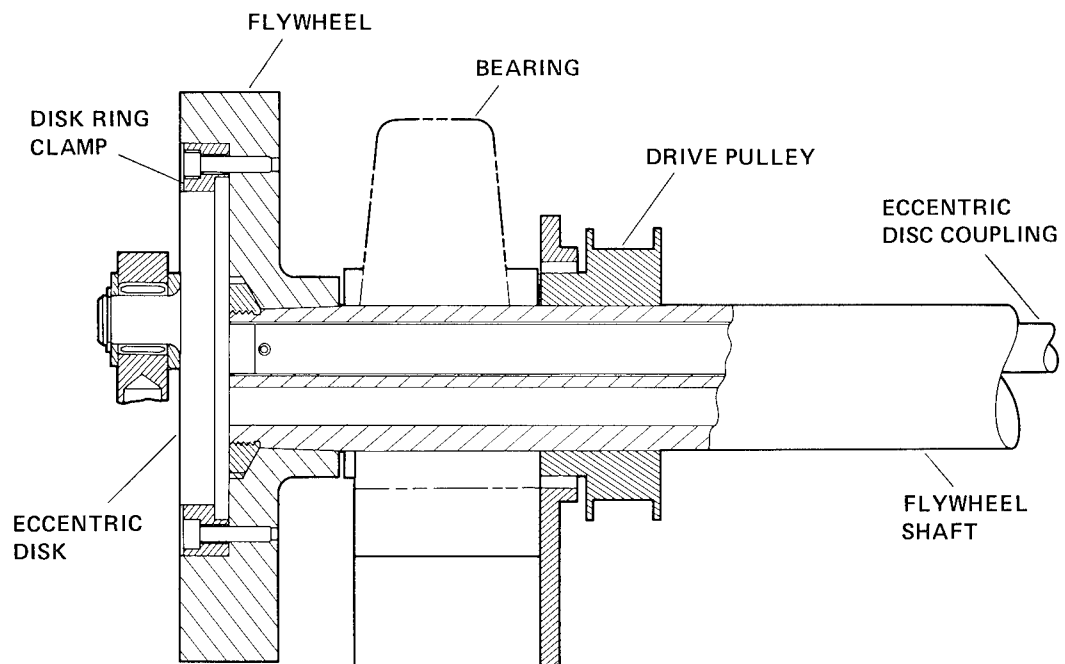
Fig. 6. Flywheel shaft assembly.

WINDOW BEARING RETAINER
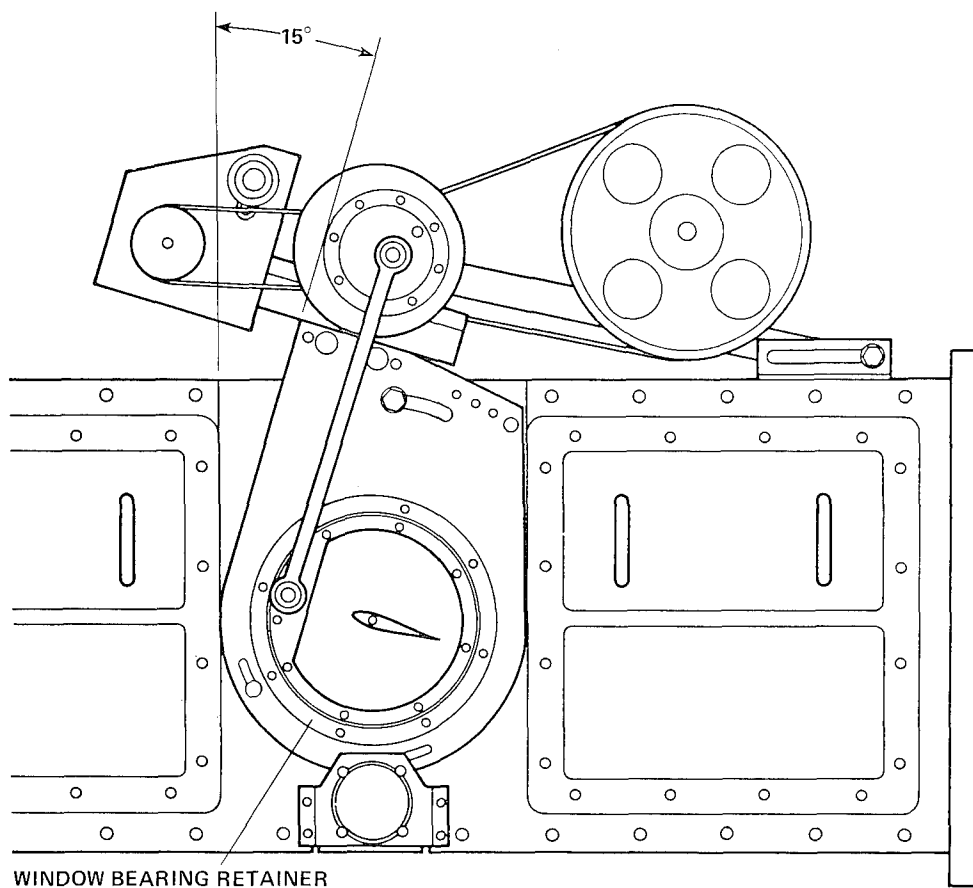
Fig. 7. 15 degree mean angle-of-attack position.

Vibration Isolation System for the Stratospheric Observatory for Infrared Astronomy (SOFIA)

T. Kaiser and N. Kunz*

ABSTRACT

The subject of this paper is the Vibration Isolation System for the Stratospheric Observatory for Infrared Astronomy, SOFIA. Included are discussions of the various concepts, design goals, concerns, and the proposed configuration for the Vibration Isolation System.

INTRODUCTION

NASA - Ames Research Center has recently completed a phase A feasibility study for the Stratospheric Observatory for Infrared Astronomy (SOFIA), an advanced airborne astrometric facility. (See Figure 1.) SOFIA will consist of a three meter F1 telescope mounted in a Boeing 747SP aircraft. The technology for the system will be an extension of that used for the Kuiper Airborne Observatory (KAO), a 0.9 meter (36 inch) diameter F1.8 telescope mounted in a C141 aircraft that has been highly successful in infrared astronomy for the past ten years.

Infrared astronomy involves the study of the spectrum of electro-magnetic radiation between the wavelengths of 0.3 to 1200 micrometers from celestial bodies in the universe. Unfortunately, a large portion of the infrared spectrum is not visible at ground level due to absorption by water vapor, carbon dioxide and molecular oxygen which lie between the ground and 12 kilometers (40,000 ft). Therefore, it is highly desirable for infrared astronomers to make observations at altitudes above the tropopause which is an inversion layer located generally between 12 and 13 kilometers (39,000 to 41,000 feet). Approximately 99% of the moisture in the atmosphere is contained below this layer. SOFIA will be designed to fly for extended periods of time above these altitudes.

SYSTEM CONFIGURATION

The telescope structure will be located in an open cavity between two full depth bulkheads at body stations 520 and 700 on the Boeing 747SP. (See Figure 2) The optical axis will be located at body station 600. The cavity has an opening on the port side of the aircraft that allows the telescope to point from a 20 degree elevation angle to a 60 degree elevation angle. There is also a ± 4 degrees freedom of rotation in cross elevation and line of sight. The estimated weight of the complete floating telescope structure is approximately 13,600 kg (30,000 lb).

Once the telescope is oriented to the desired tracking position, infrared

---

*NASA, Ames Research Center

images are reflected through the Cassegrain telescope, then redirected by a tertiary mirror to pass along the optical tube, through the aft bulkhead to the experimenter instrument package. (See Figure 2.)

Since the objects of interest are essentially at infinity, pure rigid body displacements of the telescope do not affect the image quality. However, rotations do have an effect and any angular displacements must be minimized to obtain good image quality. During tracking the telescope structure is floated on a spherical air-bearing/stator-ring assembly. The spherical air bearing is located at the center of mass of the telescope system and is part of the structural interface between the telescope structure and the instrument-package and counter-weight structure. The thin layer of air that flows over the spherical surface of the air bearing allows for isolation of the three rotational degrees of freedom of the telescope from the aircraft by providing nearly frictionless rotation. In order to achieve this isolation it is required that the center of gravity of the "floated" assembly be located at the center of rotation of the air bearing. This centering is accomplished by controlling the amount and position of counter weights applied on the cabin side of the telescope. Ideally, due to the frictionless behavior of the air bearing, no torque would be required to maintain tracking. However, there are several factors which require the use of reaction torques to prevent telescope rotation: aerodynamic loading, a slightly offset center of mass, cable loads, motion or mass changes within the instrument, or the small amount of friction that does exist. The torquers used for these corrections are also used to position the telescope and to provide the nod (telescope sweeping) required for infrared astronomy.

The torquer system consists of three orthogonal sets of electromagnetic arc shaped segments which are attached to the telescope structure with a corresponding segment attached to the stator of the air bearing. Because the only physical connection between the floating telescope system and the stator is a magnetic force across an air gap, the torquers are allowed to be completely frictionless when they are not in use. Each torquer has a range of plus or minus four degrees. In addition, the elevation angle torquer is in series with a spur gear to provide the total elevation range of the telescope system of 20 to 60 degrees. The design goal of the torquers in conjunction with the pointing and control system is to maintain a tracking position with a maximum error of one arcsecond.

Finally, the stator of the air bearing is supported by the Vibration Isolation System which ties directly to the aft bulkhead. Although pure translation of the telescope does not contribute to image degradation, the effects of translational accelerations, which can include angular displacements or telescope structural distortions, are undesirable and therefore must be minimized to obtain optimum image quality. The Vibration Isolation System will act to attenuate aircraft vibrations from the telescope in the three translational directions in order to maintain the desired image quality. This system will be described in the next section of this paper.

VIBRATION ISOLATION SYSTEM

The primary design goal of the SOFIA Vibration Isolation System is to

minimize image distortion during tracking. This can be accomplished by first analyzing the telescope structure natural frequencies and aircraft/airframe structure vibrations, and then choosing the natural frequency and damping characteristics of a vibration isolation system that minimizes image distortion.

Another important design requirement is that the vibration isolation system must prevent damage to the telescope during gusts and turbulence, as well as during takeoff or landing. To avoid excessive displacement and still allow for these types of loadings requires the use of a dual mode isolation system. These modes include the "tracking" mode which maintains a low natural frequency to maximize vibration attenuation, and the "caged" mode which still provides attenuation, but with stiffer springs to limit the maximum displacement of the floating structure. Additional system design goals include, high reliability, low weight, minimum power consumption and low or no maintenance. Since this is an infrared telescope that is cooled to the outside ambient temperature, heat sources and heat paths must also be minimized or eliminated.

Among the concepts initially considered were metal springs, elastomeric/composite pads and pneumatic isolators. Reviewing the requirements and the advantages and disadvantages of each concept leads to the choice of pneumatic isolators. Metal springs were not feasible due to their large static deflection for the weight and frequency requirements. Composite or rubber pads in general have natural frequencies between 5 and 10 Hz for the size required to carry the load, and would therefore act as amplifiers rather than isolators in the critical frequency range making them infeasible.

Pneumatic isolators were chosen because of their ability to attenuate low frequency vibration. This type of isolator can be designed to have both low stiffness and low static deflection, due to the ability of the air to be compressed to the pressure necessary to support the system load. The pneumatic isolator can be designed as a simple spring, having only one chamber for compressed air. Alternately, by having two chambers connected by a variable orifice, the pneumatic isolator can become a tuneable spring damper. The tunability will be discussed later in this report.

In designing the vibration isolation system it was assumed 1) that the center of mass of the telescope structure will be located at the center of the air bearing and 2) that the isolators will be mounted in a vertical plane also passing through the center of the air bearing. This configuration decouples the modes of vibration and allows the system to be analyzed as a single degree of freedom system in each of the three translational directions.

AIRCRAFT RESPONSE

In order to begin design of the Vibration Isolation System, it was necessary to estimate the vibration that would be transmitted to the isolation system from the aircraft. The first estimates were based on the actual aircraft power spectral density (PSD) plots provided by Boeing. These plots were provided for several locations throughout the aircraft for various

flight conditions.   Vibration analysis for SOFIA was based on the Boeing PSD plot for body station 310 at an altitude of 40,000 ft. and a speed of M=0.8, this data being the closest to the proposed isolation system location and flight conditions for SOFIA during tracking.

Because the PSD's were random plots, a cubic spline curve fitting was performed to generate continuous functions representative of the PSD's in the lateral and vertical directions.   The area under the PSD curve represents the variance (square of the standard deviation) of the probability distribution curve for the random vibration.   For a single degree-of-freedom system, the mean square response of the structure to a random excitation is the integral of the product of the PSD and the complex frequency response for the structure. The value resulting from the square root of the integration is multiplied by a peak response factor of 3 to account for 99.7% of the random vibrations based on a Gaussian probability distribution.   The resulting RMS accelerations were plotted versus natural frequencies for damping factors of 1%, 2%, 5% and 10%. (See Figure 3.)   Using these plots, optimal design frequencies were determined for the lateral and vertical directions.   These plots show that the isolation system should have resonant frequencies of 1 Hz and 1.5 Hz in the vertical and lateral directions, respectively, in order to provide optimum attenuation of vibration for the Boeing 747SP.

As explained above, preliminary optimum natural frequencies for the Vibration Isolation System were determined on the basis of standard flight condition data supplied by Boeing.   However, SOFIA will be subjected to additional non-standard flight conditions (for which no vibration data exists) namely, the effects of opening the cavity and raising the boundary–layer control fence.   Moreover, since a modified 747 does not exist, the tracking mode vibration levels could not be measured.   To determine these effects, vibrational data was collected on the Kuiper Airborne Observatory.   The data was recorded to establish a correlation between the vibration on the aircraft near the telescope in "standard flight mode", with the cavity door closed and the boundary–layer control fence down, to that in the "tracking mode" with the cavity door open and the boundary–layer control fence up.   PSD's were recorded in three locations, below the two rear isolators on the airframe and directly on the left rear isolator.   It was found that below 30 Hz the effect of opening the telescope door was very minor.   In this frequency range there was an increase in the magnitude of the vibrations by a factor less than 10. Between 30-55 Hz and 80-100 Hz, vibrations during tracking increased approximately 10 times over that of standard flight vibrations.   The largest increase occurred between 60-80 Hz where there was a factor increase as large as 60.   Opening the cavity resulted in a PSD nearly equivalent to that for white noise.   Based on this data and for simplification of analysis, a conservative level of white noise was assumed.   The increase in vibration caused by opening the cavity door and raising the boundary–layer control fence could then be determined.

To obtain an estimate for the vibration of the 747SP   with a cavity door open, the square root of the areas under the Boeing 747SP PSD's was calculated to first determine the RMS g accelerations for that aircraft during normal flight at 12.2 kilometers (40,000 ft) and a speed of 0.8 Mach.   These accelerations were then multiplied by the square root of the ratio of

[door open] to [door closed] vibrations measured on the KAO to determine the estimated RMS accelerations that will be transmitted to the vibration isolation system on the 747SP during tracking. It should be noted that no information was provided for the fore/aft levels of vibration for the 747SP. Therefore, the fore/aft vibrations were assumed to be the same as the lateral vibrations based on the data collected on the C141.

The resulting estimated magnitudes of vibration experienced during tracking on the 747SP were found to be approximately 0.21 g's vertically and 0.14 g's in the lateral and in the fore/aft directions. (See Figure 4.) Because these values were lower than the specified flight conditions outlined in the SOFIA project requirements, the isolation system was designed to meet the original SOFIA specifications. These specifications require designing to a maximum acceleration during tracking of 0.25 g's in all directions. The maximum gust/maneuvering loads, when the system is in the "caged" mode, are 3.04 g's upward and 1.04 g's downward, $\pm$ 0.63 g's in the lateral and $\pm$ 0.20 g's in the fore/aft direction. One final criterion for the vibration isolation system is to survive the crash loads. The crash loads are 4.5 g's upward, 2.0 g's downward, $\pm$ 1.5 g's laterally, 9 g's forward and 1.5 g's aft. The criteria for crash loads require that the system not come free in the aircraft. Damage to the system, however, is acceptable for crash loads.

PROPOSED SYSTEM

The proposed vibration isolation system consists of eight pneumatic isolators all located in a plane parallel to the aft cavity bulkhead and acting through the mass center of the telescope system. (See Figure 5.) Four of the pneumatic isolators will be aligned in the vertical plane passing through the mass center. In the tracking mode these four isolators will need to carry the dead weight of the floating telescope structure. These will be semi-active in their axial directions, and a height control valve will be used to react any input displacements by permitting air to transfer to/from the surge tank when a displacement occurs. Also, internal snubbers are to be connected in series with these isolators. When the system is active, these snubbers minimally affect the system stiffness, however when the system is lowered or caged, they provide the primary vibration isolation. The additional four pneumatic springs will be connected at the same locations as the first isolators, but will be aligned in the fore/aft direction. The total system stiffness in each of the three translational directions is, therefore, a combination of the stiffness of the lateral and vertical pneumatic isolators and the internal snubbers.

As mentioned previously, the proposed isolation system will have two modes of operation, the "tracking" mode and the "caged" mode. In the first mode, the isolators will have natural frequencies of about 2.5 Hz up to a maximum acceleration of 0.25 g's. If the 0.25 g limit is reached, the isolators will enter the locked mode where the internal snubbers will provide vibration isolation at a stiffer natural frequency of about 7 Hz. These internal snubbers will restrict deflections up to the maneuvering/gust limit load. If the acceleration reaches the level of the crash limit loads, the external snubbers will prevent metal-to-metal contact.

The maximum deflection of the system for each mode of operation is

based on the total stiffness of the isolators and the maximum acceleration in that mode. When the system is "caged", the pneumatic isolators act as rigid supports and deflection is governed by the stiffnesses of the internal snubbers. In this mode the system is designed to the gust/maneuvering limit load, this is also the mode to react the crash loads. The maximum deflection in any mode is limited by external snubbers to a maximum displacement of one inch. (See Figure 5.)

The design of the isolators will incorporate relaxation damping principles in the "tracking" mode. The system consists of compressed air flowing from a surge tank into a load-carrying chamber through an orifice which acts as a capillary flow restrictor. The size of the orifice will determine the amount of system damping as well as the stiffness and natural frequency of the system. This in turn controls the magnitude of vibration transmitted to the telescope.

By varying the orifice size, the system's damping factor, as well as its natural frequency, can be controlled. The system can then be adjusted or tuned to an optimum response. Small variations in the orifice can result in pronounced variations in resonant frequency. When the orifice is small, flow is highly restricted and the system characteristics (i.e. natural frequency and stiffness) will be determined by the pressure and volume in the load carrying chamber. For a large orifice the restrictions are lowered and the system characteristics are determined by the pressure and volume of both the surge tank and the load carrying chamber. By using a variable orifice in the design, an optimum orifice size can be determined upon installation based on actual aircraft response. (See Figure 6.)

Once the system damping requirements are determined, the accelerations transmitted through the isolators to the telescope can be found based on the input level of vibration and the system natural frequency. For example, a 2.5 Hz critically damped isolation system will transmit 0.065 g's in the lateral fore/aft directions and 0.098 g's vertically (based on the Boeing PSD's.) The resulting deflections during tracking will be 0.38 cm (0.15 in.) vertically and 0.26 cm (0.10 in.) in their lateral and fore/aft directions, based on the system stiffness and input accelerations.

CONCERNS AND RISKS

While basic feasibility of a candidate concept has been demonstrated, several areas which require further analysis and trade-off activity still exist for the SOFIA vibration isolation system. In the area of aircraft response, new 747SP PSD's should be measured at approximately body station 700, with additional fore/aft data included. The data provided by Boeing is somewhat suspect; one would expect lower vibration levels for a 747SP than for the C141 (KAO). From our measured data this is not the case. It is suggested that additional vibration data be collected for an unmodified 747SP which would address the added requirements.

The effect of a slightly offset center-of-mass, which would affect the response of the isolators, needs to be evaluated. Also of concern is the fact that the current design has the torquers reacting through the vibration isolation

system. This not only affects the torquer response, but could also couple together translations and rotations.

A final trade-off study that should be performed in greater depth is the "soft system versus stiff system" problem. There is a trade-off between minimizing response to aircraft vibration, (where a soft system is more advantageous), to minimizing response to aero loads (where a stiff system would be better). The resolution of the problem depends on the relative levels of structure-borne versus aero-generated loading. The aero loading on the telescope is largely unknown at present and depends on several factors. It is, therefore, a good candidate for near-term analysis or testing.

PROJECT STATUS

The Phase A study has been completed and has demonstrated feasibility. Currently, the project is awaiting additional funding for further studies.
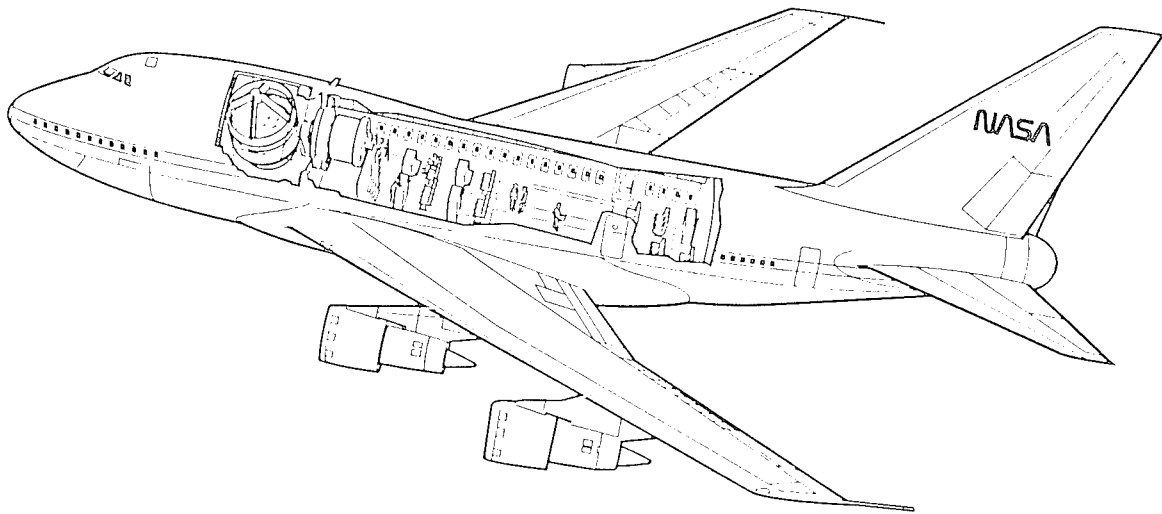
Figure 1. Stratospheric observatory for infrared astronomy.
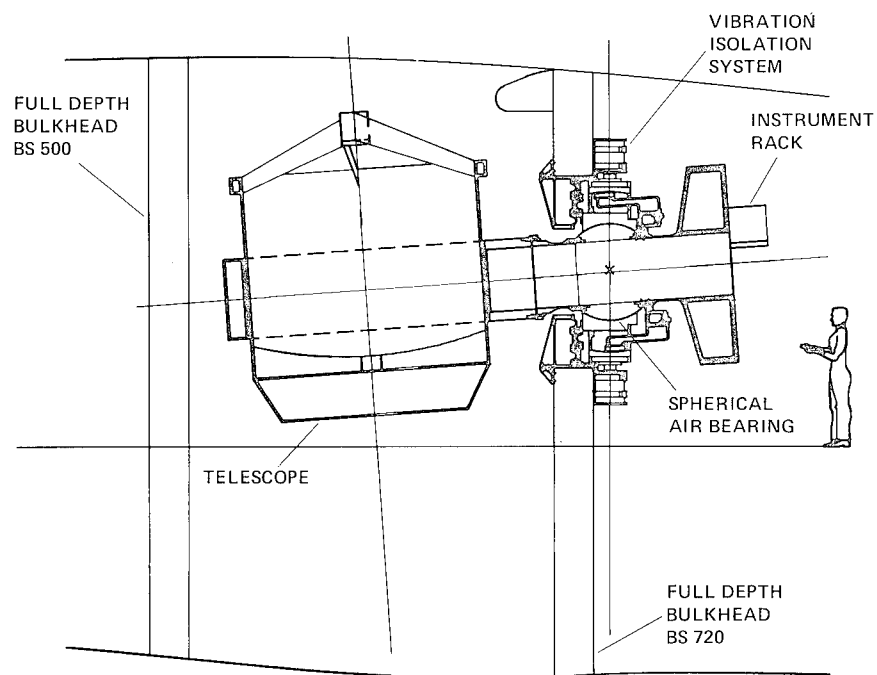
Figure 2. Stratospheric observatory for infrared astronomy.

$$F^2(t) = [H(f) H^*(f)] S(f) \, df$$
$$F(t) = \sigma [F^2(t)]$$

WHERE:

$F^2(t)$ = MEAN SQUARE RESPONSE OF THE STRUCTURE TO A RANDOM EXCITATION (g^2)

$F(t)$ = RMS MEAN ACCELERATION

σ = PEAK RESPONSE FACTOR (PROBABILITY OF $F(t)$)

$S(f)$ = POWER SPECTRAL DENSITY FUNCTION (g^2/Hz)

$[H(f) H^*(f)]$ = COMPLEX FREQUENCY RESPONSE FUNCTION FOR THE STRUCTURE (SINGLE DEGREE OF FREEDOM)

WHERE:

$$H(f) = \frac{1}{[1 + (f/f_n)^2] - i[2\xi(f/f_n)]}$$

$$H^*(f) = \frac{1}{[1 - (f/f_n)^2] - i[2\xi(f/f_n)]}$$

f_n = NATURAL FREQUENCY OF STRUCTURE (Hz)

ξ = DAMPING COEFFICIENT

VARIABLE DAMPING

VERTICAL MOTION AT 40,000 ft, M = 0.8

LATERAL MOTION AT 40,000 ft, M = 0.8

Figure 3. Structural response to random vibration.

	RATIO TRACKING DOOR CLOSED, g^2/g^2	AREA UNDER PSD CURVE NORMAL FLIGHT, g^2	RMS ACCELERATION NORMAL FLIGHT, g	RMS ACCELERATIONS DURING TRACKING, g
C141[1] (0–100 Hz)				
VERTICAL	17	0.00012	0.011	0.045
LATERAL	14	0.00032	0.018	0.067
FORE/AFT	45	0.00008	0.0089	0.067
BOEING 747SP (0–20 Hz)				
VERTICAL	$20^{[4]}$	0.0022	0.047	$0.21^{[2]}$
LATERAL	$15^{[4]}$	0.0013	0.036	$0.14^{[2]}$
FORE/AFT[3]	—	—	—	$0.14^{[3]}$

[1]VALUES BASED ON ACTUAL TEST DATA TAKEN ON THE KAO

[2]ESTIMATED ACCELERATION FOR 747SP = (NORMAL FLIGHT ACCELERATIONS) X (TRACKING/DOOR CLOSED RATIO)$^{1/2}$

[3]NO FORE/AFT DATA WAS PROVIDED BY BOEING FOR THE 747SP IN THE FORE/AFT DIRECTION; LATERAL AND FORE/AFT ACCELERATIONS ASSUMED EQUAL BASED ON C141 DATA

[4]RATIO OF TRACKING/DOOR CLOSED VIBRATIONS FOR 747SP IS ASSUMED EQUIVALENT TO THAT FOR THE C141

Figure 4. Boeing 747SP estimated vibrational accelerations.

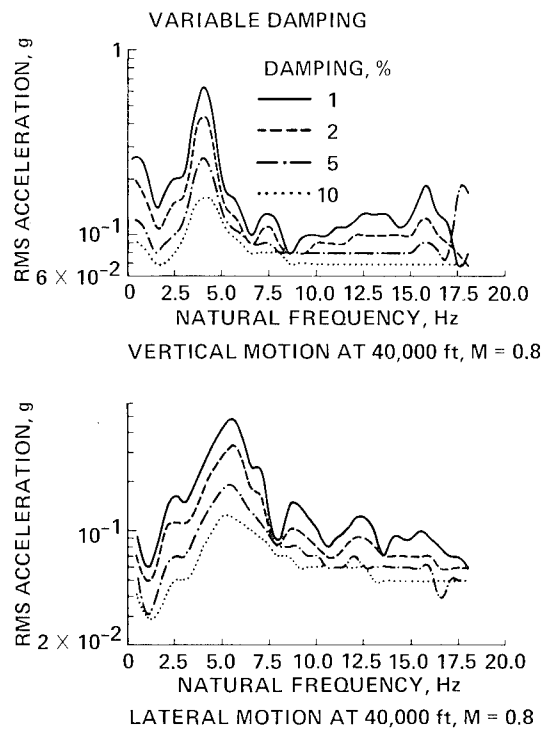|	NATURAL FREQUENCY, Hz	STIFFNESS, MN/m, lb/in.	MAXIMUM ACCELERATION, g's	DEFLECTION, m, in.
TRACKING[1]				
VERTICAL	2.48	3.33 (19,000)	0.25	0.95 (0.375)
LATERAL	2.48	3.33 (19,000)	0.25	0.95 (0.375)
FORE/AFT	2.54	3.45 (19,700)	0.25	0.95 (0.375)
LOCKED SYSTEM[2]				
VERTICAL	6.9	25.57 (146,000)	+3.04	1.59 (0.625)
			−1.04	0.51 (0.20)
LATERAL	6.9	25.57 (146,000)	0.63	0.76 (0.30)
FORE/AFT	5.9	18.74 (107,000)	0.20	0.25 (0.10)
CRASH LIMIT LOADS[2]				
VERTICAL	6.9	25.57 (146,000)	+4.5	2.36 (0.93)
			−2.0	1.04 (0.41)
LATERAL	6.9	25.57 (146,000)	1.5	0.79 (0.31)
FORE/AFT	5.9	18.74 (107.000)	$+3.5^{[3]}$	2.54 (1.00)
			−1.5	1.07 (0.42)

[1]STIFFNESS AND NATURAL FREQUENCY DETERMINED BY PNEUMATIC ISOLATORS, AIR SPRINGS AND INTERNAL SNUBBERS

[2]STIFFNESS AND NATURAL FREQUENCY DETERMINED BY AIR SPRINGS AND INTERNAL SNUBBERS

[3]MAXIMUM FORWARD CRASH LOAD IS 9 g's; EXTERNAL SNUBBERS MINIMIZE MOTION BEYOND 1" DEFLECTION AND 3.5 g's (FORWARD DIRECTION)

Figure 5. Proposed vibration isolation system.
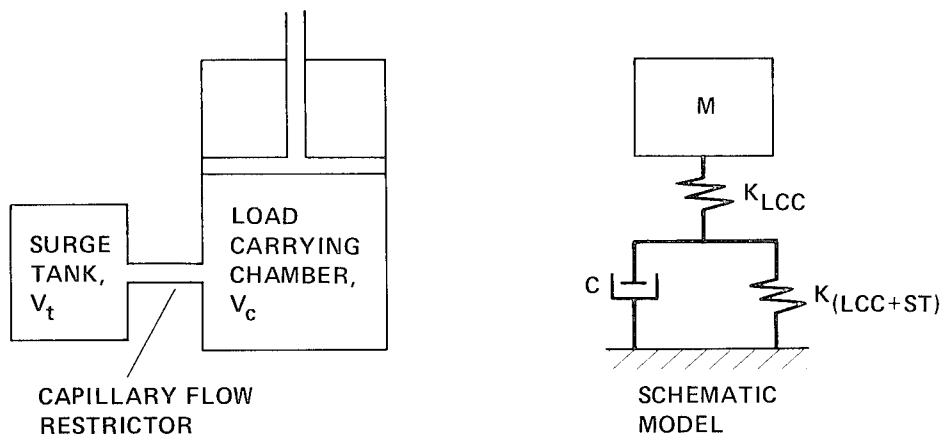
ORIFICE SIZE DETERMINES DAMPING

SMALL ORIFICE — HIGH RESTRICTION

$C = \infty$ $K = 2nPA^2/V_c = K_{LCC}$

LARGE ORIFICE — LOW RESTRICTION

$C = 0$ $K_0 = 2nPA^2/(V_c + V_t) = [(K_{LCC})(K_{ST})]/[K_{LCC} + K_{(LCC+ST)}]$

WHERE:

C = DAMPING CONSTANT

K = ISOLATOR STIFFNESS

n = 1.4 FOR COMPRESSED AIR

P = PRESSURE IN CYLINDER

V_c = LOAD CARRYING CHAMBER VOLUME

V_t = SURGE TANK VOLUME

A = PISTON AREA

Figure 6.   Damped pneumatic isolators.

EXPERIENCE WITH DUPLEX BEARINGS
IN NARROW ANGLE OSCILLATING APPLICATIONS

D.D. Phinney,* C.L. Pollard,* and J.T. Hinricks*

INTRODUCTION

Duplex ball bearings are matched pairs on which the abutting faces of the rings have been accurately ground so that when the rings are clamped together, a controlled amount of interference (preload) exists across the balls.

Because duplex ball bearings have no internal clearance and no freedom for the rings to shift relative to each other, they are vulnerable to

- Radial temperature gradients (inner rings hotter or colder than outer rings) that change the preload and can cause it to disappear or become excessive.

- Blocking in oscillating applications

- Increased sensitivity to contamination

Experience with the last two problem areas on a gimbal that used duplex bearings at both ends of its inner axis is discussed. Motion on this axis would consist of rotation to a pointing direction, followed by narrow angle oscillation (less than ±0.3 deg) at a six cycle per minute rate that could last as long as several years in one position. This is considered a difficult lubrication problem because the low speed and narrow angular range prevent formation of significantly thick lubricant films. The bearings operate continuously with boundary lubrication. Although bearings with one BASD space lubricant demonstrated their ability to operate successfully for many years in a narrow-angle dithering mode, a different lubricant with improved properties was to be used for the gimbal application. Consequently, it was decided that an accelerated thermal vacuum life test should be conducted.

This paper describes the test apparatus and results and presents the rationale for reducing a multi-year life test on oil-lubricated bearings to less than a year. Of the five bearing sets tested, two performed very well, one was marginal, and two were unacceptable. The diagnostic effort on one of these latter sets and the results of additional tests demonstrating the validity of the findings are described herein. Finally, details of the actual gimbal bearing installation and some of our experiences with it are covered.

DESCRIPTION OF TEST APPARATUS

Five life test duplex bearing sets were made by SBB[+]. They were taken from a standard production lot and matched by SBB into face-to-face (DF) duplex sets with a very light preload. The only special provision was that they were lubricated for SBB tests with oil provided by BASD, to avoid potential lubricant incompatibility problems. The characteristics of these inch-series bearings were:
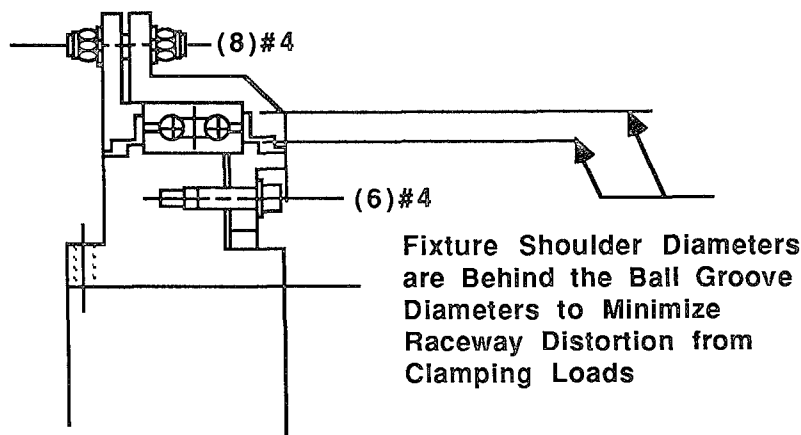
- SBB part number: 3TAR37-46 SUDF 3/5
- Ball and race material: 440C

211

- Separator material: Cotton cloth phenolic laminate
- Inside diameter: 58.74 mm (2.3125 in.)
- Outside diameter: 73.025 mm (2.875 in.)
- Number of balls 48
- Ball diameter: 3.18 mm (0.125 in.)
- Raceway conformities: 0.52-0.528 (inner and outer)
- Contact angle: 18-25 deg
- Raceway surface finish: ≤0.05 µm (2 µin.) AA
- Ball grade: 5
- ABEC tolerance class: 7T (SBB Super Ultra)
- Preload: 13.3-22.2N (3-5 lb)

Bearing sets were installed in the test cartridges shown in Figure 1. As the hub and housing were dimensioned, inner ring fits varied from line-to-line to 0.0125 mm (0.5 mil) loose; outer rings varied from 0.0025 to 0.015 mm (0.1 to 0.6 mil) loose. Deliberate gaps at the flanges of the inner and outer race clamp plates were provided to assure positive clamping. As shown in Figure 1, contact surfaces between the plates and bearing rings were located behind the raceway grooves to minimize race distortion from clamping force. The bearing mounts were made of cold rolled steel and were electroless nickel plated, except for the bearing mounting diameters. These diameters were specified for 0.4 µm (16 µin.) surface finishes.

Fixture Shoulder Diameters are Behind the Ball Groove Diameters to Minimize Raceway Distortion from Clamping Loads

A/N 8505/MD76.8

Figure 1. Life test bearing sets were mounted in steel cartridges with plates clamping the races.

Figure 2 shows the test assembly before installation in the vacuum chamber. The five test cartridges were mounted on a single 25.4 mm steel shaft suspended top and bottom on Bendix flexures. The shaft was oscillated by a lever which was driven by a small bearing. This bearing was on an eccentric so that ±0.3 deg (0.6 deg total) of test cartridge oscillation occurred with each rotation of the eccentric shaft. The eccentric shaft was mounted on dry-lubed ball bearings inside the vacuum chamber and driven from outside with a magnetic feedthrough.
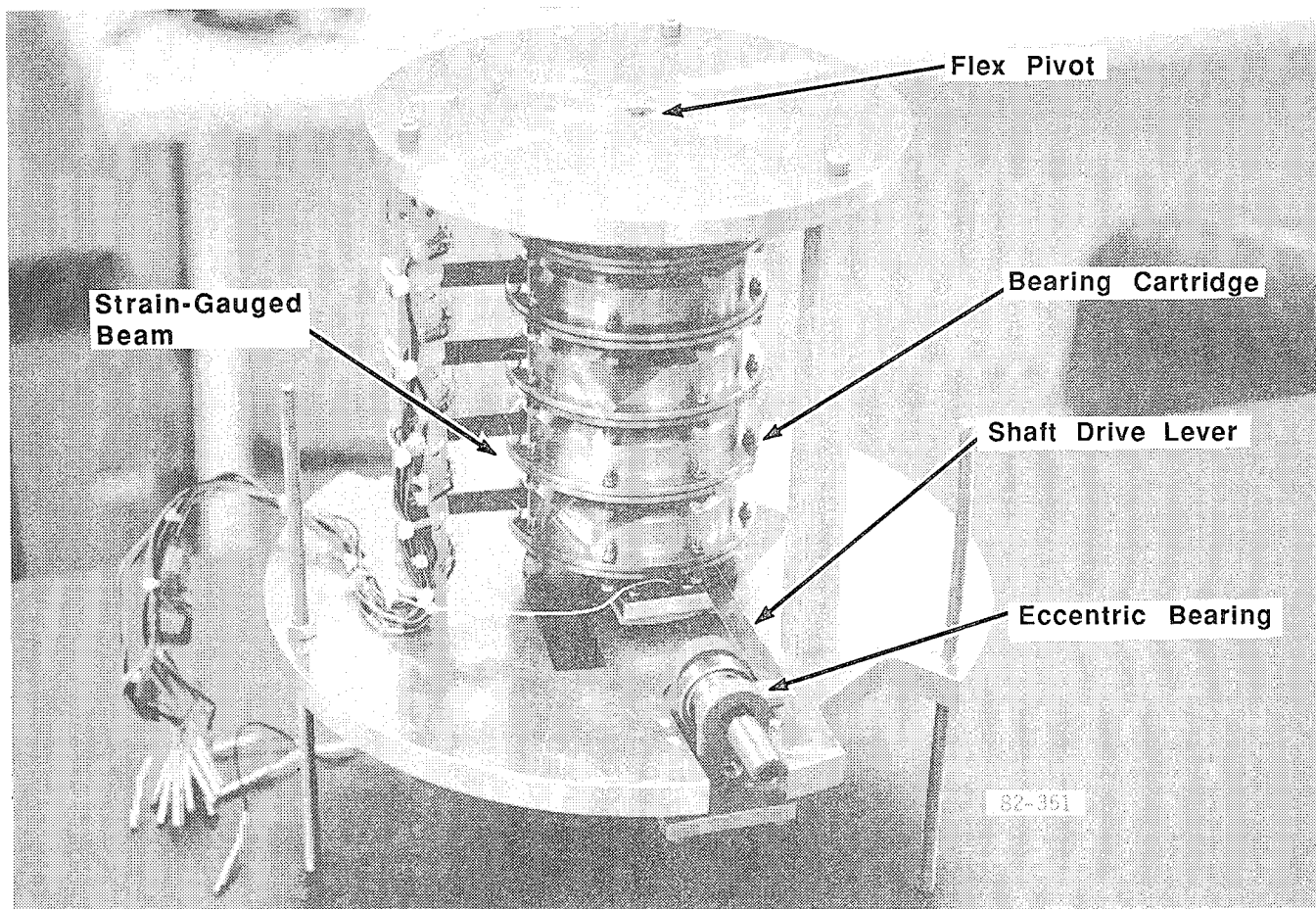
212

Figure 2. Five life test cartridges were mounted on a common shaft, oscillated by a lever and bearing on an eccentric. Strain-gauged beams measured bearing torque.

Test bearing torque was determined by strain gauged steel cantilever beams, which gave a torque sensitivity of 0.007N (0.025 oz-in.) or better. Angular displacement was measured with a Spectrol conductive film potentiometer.

During the test, torques were read out daily on a strip chart recorder. From time to time during the first 14 weeks, hysteresis (torque vs. displacement) plots were made with an X-Y plotter.

TEST ACCELERATION RATIONALE

Our goal was to simulate six years of operation at six cycles/min in a year or less, without introducing effects that would invalidate results. With dry lubricants, bearing life tests are sometimes accelerated because lubricant effectiveness is not considered speed-dependent over a moderate speed range. With liquid lubricants, however, formation of elastohydrodynamic (EHD) oil films at the contact spots may have a major effect on performance and the thickness of this film (h) varies with speed. Since h also varies with viscosity, and viscosity can be controlled by temperature, a mechanism exists for maintaining h while raising the test speed; however, then all other lubricant properties (such as evaporation rate) must be adequately accounted for if the test is to remain valid.

213

To determine the effectiveness of an EHD film, h is divided by the composite surface roughness (σ) of the balls and raceways to produce film parameter λ. If λ≥2, negligible asperity contact occurs, and bearing lifetimes predicted from standard bearing life test data can be expected. As h gets thinner, asperity contact increases, the bearing enters the boundary lubrication regime, and life reduction occurs. In our case, λ was only 0.002 using an h based on the average speed. This was so deep into the boundary lube regime (our nearest tests had been at λ=0.03) that we felt it would be satisfactory to double the speed after producing an otherwise dynamically similar accelerated test.

The life test was designed to simulate the following assumed, real-time temperature profile:

Temp (°C)	Operating Time (yr)
5	0.5
15	1.5
25	3.0
35	1.5
40	0.5

Lubricant loss, which is evaporation-rate dependent, was then calculated, and the single constant temperature that would produce the same loss was determined to be 30°C. Random temperature distribution with time was assumed in the absence of a defined mission temperature profile. Because fractionation of the lubricant causes a large reduction in the evaporation rate as lighter fractions evaporate, the amount of lubricant escaping depends on the temperature profile.

Next, a test temperature was calculated to give a lubricant viscosity that would theoretically result in the same bearing wear. Assuming that wear is inversely proportional to h (Note 1), it was calculated that 26°C would produce this viscosity. Under this assumption, a number of wear cycles at 26°C would cause as much wear as the same cycles distributed over the temperatures and times given above. This temperature was adopted as the baseline for the test.

Considering only EHD film theory of bearing lubrication, we could now accelerate the cycling rate as much as desired by reducing viscosity (raising temperature) so that the product of speed and viscosity remained constant. By going too far with this, however, lubricant evaporation would exceed our normal design limit (10 percent). This would cause abnormally high viscosity (viscosity increases as evaporation proceeds) that might skew test results. The following table shows the results of the calculations of allowable speed increase with temperature and the associated lubricant loss in the accelerated test period.

NOTE 1. This was a pure assumption. Data presented by Winer and Sanborn[1] show that under boundary conditions (film-thickness-to-surface-roughness ratio (λ) of 0.33), more than one-half of the contact load is still carried by the lubricant film. However, in this application with an average speed of 0.02 rpm at 26°C, our calculations using 36234011 indicated a λ of only 0.002. While we had run tests in the range of λ=0.03, no data existed in the range of this test.

214

Lubricant Evaporative Loss During Test
Baseline: 26°C, Viscosity = 101 c.s.

Temp (°C)	Viscosity (c.s.)	Permitted Speed Increase to Keep Same Film	Lubricant Loss, Percent of Initial 0.1g
26	101	1.0X	4.9
40	52	1.9X	7.8
50	36	2.8X	10.4
60	25	4.0X	13.9
70	18	5.6X	18.2
30	(equivalent orbit temp for comparison)		6.1

With a 10-percent limit on lube loss, 50°C became the nominal test temperature. The
corresponding acceleration factor of 2.8x, however, resulted in a 2.1-year test,
which was too long. It was therefore decided to accelerate the cycling rate further
by a factor of 2.5. This would increase λ from 0.002 to slightly less than 0.004, a
vanishingly small value from the standpoint of normal EHD film theory, which we felt
would not affect the results. We then had test conditions of 50°C and 42 cycles/
min, and six years of orbit operation would be simulated in 8.6 months. Because of
the shorter test time, evaporative loss would be reduced to nearly the baseline
estimate of 4.9 percent. Finally, the rule of thumb for chemical processes (rate
doubling for a 10°C increase in temperature) would indicate rough equivalency be-
tween the eight months at 50°C and six years at 26°C.

In addition to the testing at 50°C, occasional short tests at 25°C and 5°C were
scheduled to assure that lower temperature torques were acceptable.

TEST RESULTS

When the life test was started, torques quickly became erratic and increased sev-
eralfold over starting values, which were in the 0.0035 Nm (0.5 oz-in.) range. Two
bearing pairs, Sets 1 and 2, developed especially high torques. After 151 hours,
the test was interrupted and all bearings were disassembled, recleaned, and relubri-
cated. At this time, the phenolic separators in Sets 1 and 2 were replaced with
Teflon toroids. To make room for the toroids, 18 of the 48 balls were removed from
each bearing. When the test cartridges were assembled, 5.3N (1.2 lb) springs were
installed under the clamp screws because it had been found during initial assembly
that bearing torques were extremely sensitive to clamp screw torque.

The bearings were then subjected to a test that lasted 39.5 weeks. Figure 3 shows
the torque behavior of the five bearing pairs during this 39.5-week test. Torque is
the peak-to-peak amplitude during a representative oscillating cycle of ±0.3 deg.
Bearing sets 3 and 4 behaved properly throughout the test and ran at approximately
.0035 Nm (0.5 oz-in.) or less. Set 5 torque gradually climbed away from its low
limit each time the setup was opened and restarted, finally finishing with a 4x
increase. Sets 1 and 2 quickly developed very high torques. Torque increases in
Sets 1, 2, and 5 were eventually attributed to blocking. Blocking occurs if some of
the bearing balls jam into the ends of the separator pockets as a result of creeping
away from their centered positions. Reference 2 contains a more complete discussion
of this phenomenon, as well as recommendations for preventing it. Coincidentally,
Reference 2 was issued the same month (May 1981) the 39.5-week test started, and was
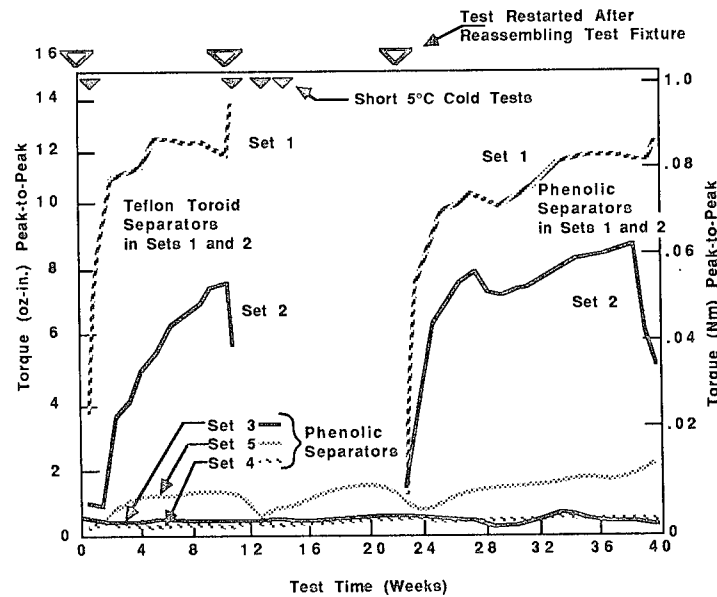a great help to us in understanding the results.

215

Figure 3. Two bearing sets were perfect through the entire 39.5-week test. The other three developed blocking.

The 39.5-week test was interrupted twice for Sets 1 and 2. These bearings were taken out in the tenth week and examined with great care. Neither lubricant degradation nor contaminant buildups could be detected. They were cleaned, rebuilt with phenolic separators, relubed, and returned to testing in the 23rd week. Their performance repeated almost exactly that obtained with Teflon separators. Later in this paper, we discuss our analysis of one of these bearing sets and the corrective action taken.

Bearing Set 3 showed excellent performance during the 39.5-week test. Let us look at it further.

When the fixture was first operated in the vacuum chamber, all bearing sets showed increasing torque with time. At 151 hours, the test was interrupted with set 3 showing the highly irregular hysteresis loop of Figure 4. This loop was drawn using an X-Y plotter with shaft position (potentiometer output) on the X-axis and torque on the Y. When the outer race was rotated just enough to relocate the ball contacts away from their initial position, the regular and low-torque upper loop of Figure 4 was produced.

No raceway degradation was visible when the bearings were inspected, but visual and SEM*observations showed thin surface films of unknown material. When the bearings were cleaned, significant particulate contamination was present in the rinses. A more thorough cleaning process was then implemented, and the bearings were relubricated.

Figure 5 shows a hysteresis loop from Set 3 when the test was restarted, and one of the last loops taken 12 weeks later. Torques are low and quite smooth. Although no other hysteresis loops were taken during the last 22 weeks of the test, it is safe to infer from the low constant torque for Set 3 (shown in Figure 3) that loops at the end of the test would have been similar.

*Scanning Electron Microscope

216

.31 oz-in.

After 150 Hours and Rotating
the Outer Rings 0.4 Deg

1.98 oz-in.
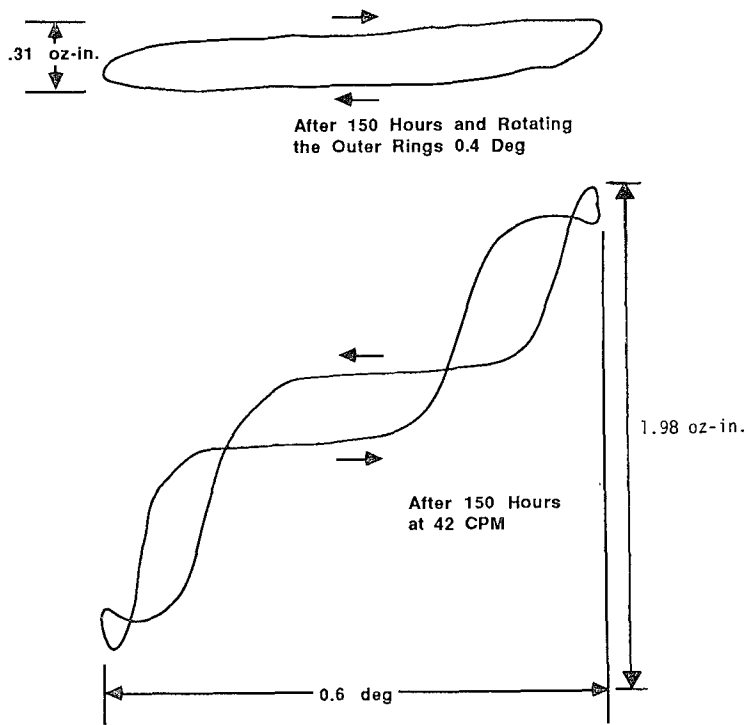
After 150 Hours
at 42 CPM

0.6 deg

Figure 4. After 150 hours, Set 3 had developed a high, irregular torque that was corrected by moving ball contacts to new locations on the raceways.
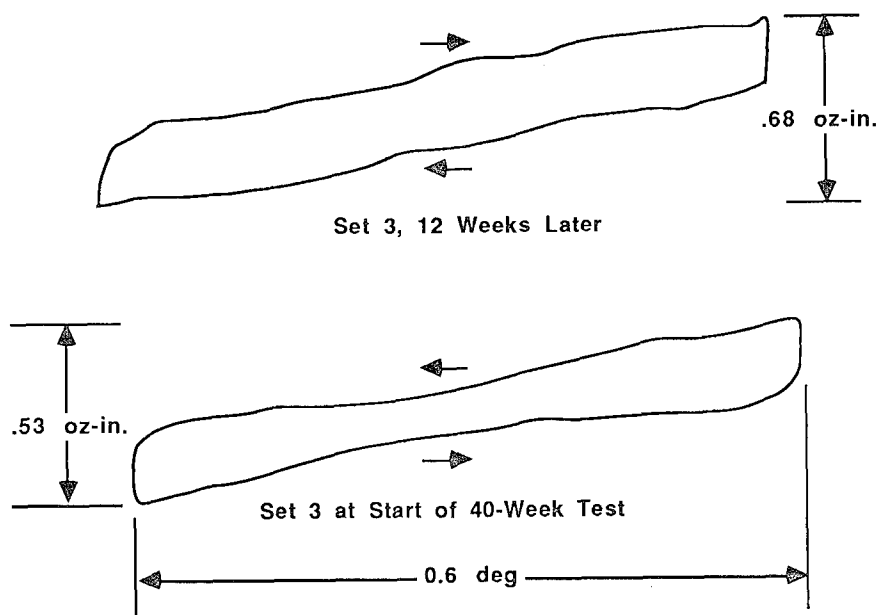

.68 oz-in.

Set 3, 12 Weeks Later

.53 oz-in.

Set 3 at Start of 40-Week Test

0.6 deg

Figure 5. After cleaning, Set 3 shows smooth hysteresis loops when the 39.5-week test started, and 12 weeks later.

217

Hysteresis loops from the other excellent bearings of Set 4 were very similar to those for Set 3. These results show the importance of thoroughly cleaning critical bearings, as well as the ability of properly lubricated and installed duplex bearing sets to operate in low-speed, narrow-angle oscillations in the same place for 16 million cycles. The value of hysteresis in revealing problems is also shown.

Set 5, which also ran the full test but at up to 4x the torque of the good sets, displayed irregular hysteresis loops (Figure 6). A Set 4 loop taken the same day is shown for comparison. The reason for the difference was never determined. No hysteresis loops were made for Sets 1 and 2 during the 39.5-week test.
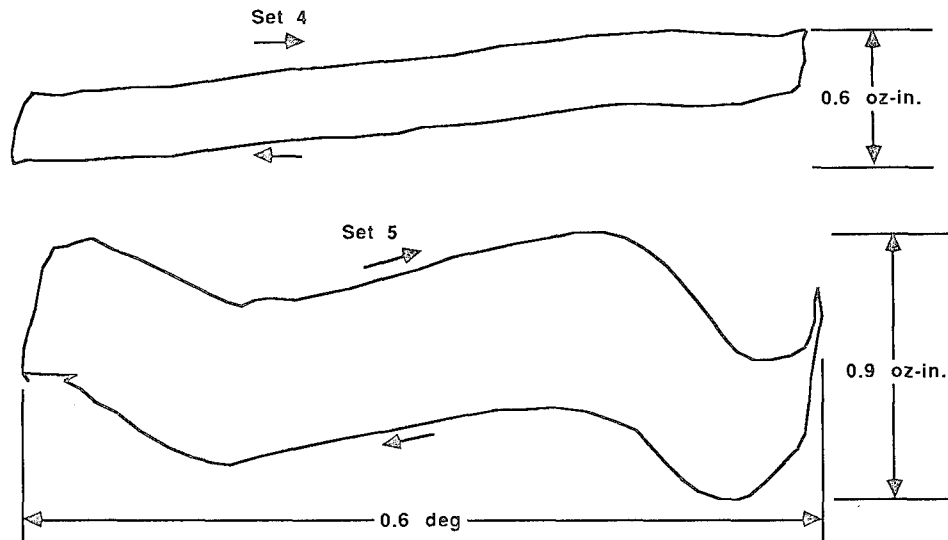
Figure 6. After 12 weeks, Set 5, which had higher torque during most of the test, shows an irregular hysteresis loop, while Set 4 is very smooth.

At the end of the test, a new drive shaft with an eccentric for ±1-deg oscillation was installed without moving the test cartridges from their 16 million cycle positions. The idea was to determine whether any ridges had formed at the limits of travel. Sets 3 and 5 were smooth crossing the ends of the ±0.3-deg tracks and had peak torques (at ±1 deg) of 0.0049 and 0.0064 Nm (0.7 and 0.9 oz-in.). Set 1 showed anomalies inside and outside the ±0.3-deg track but indicated no ridges. It was concluded that no detectable wear scars had been formed and no debris had accumulated at the track ends.

INVESTIGATION OF BEARING SET 1

Bearing Set 1 did not run properly during any part of the 29 weeks it was tested, either with Teflon toroid separators or with the original phenolic ones. Behavior with the two separator types was essentially the same. Sets 1 and 3 were subjected to a thorough post-test inspection to discover any differences, and Set 1 was subjected to further tests to confirm the findings.

Visually, the bearings were in excellent condition, with a large oil meniscus at each ball/race contact. Infrared spectra of oil from both bearings showed no changes from the original oil. Small amounts of contaminants were visibly present and

218

showed up on the rinse filters, but the quantity was judged to be in the irreducible minimum range.

One bearing from each set was inspected under a microscope. The Set 1 bearing had barely visible rectangular spots on the races at some ball contact points; the Set 3 bearing did not show these spots. Both bearings from these two sets were then returned to SBB for inspection, which led to the following:

• All characteristics described in the Description of Test Apparatus section were confirmed except preload on Set 1, for which it was 162N instead of 13.3 to 22.2N, when the outer races were just brought in contact. .

• The Set 1 bearings had 18 balls interchanged between the two bearings, one of which had balls that were 0.0762 mm (0.0003 in.) larger than those of the other.

This ball interchange occurred inadvertently at BASD when the Teflon toroids were replaced with the phenolic ones. It had been necessary to remove 18 balls from each bearing when the toroids were installed. If the outer races of the Set 1 bearings had been firmly clamped, the high preload would have resulted in a several-fold torque increase. However, the springs under the clamp screws limited preload to about 40N. At SBB, when the balls were restored to their proper bearings, preload dropped to 22N. Profilometer measurements on the raceways, with a sensitivity of .25 μm across the ball contact zones and away from them, showed no detectable differences for the visible contact spots. (These spots may have been caused by the oversized balls, which would have carried the full preload, or by a few balls which were found to be slightly outside sphericity limits for Grade 5.) In short, except for the assembly error at BASD, all four bearings were essentially perfect according to original requirements.

The mounting fixtures for Sets 1 and 3 were also inspected by SBB. Roundnesses of the bearing mounting surfaces were within 0.0025 mm, but surface finishes appeared to exceed the drawing limit of 0.4 μm.

The important finding was that the bearings in Set 1 were tight fits in their fixture instead of slip fits. This suggested that improper seating could have occurred, followed by the blocking phenomenon described by M.J. Todd (Reference 2). We do not know how the misassembled balls were spaced; however, if the 18 bigger balls in one bearing were adjacent to each other and not spaced around somewhat uniformly, then the condition for race misalignment and blocking would have been built into the bearings themselves.

The Set 1 bearing fixtures were reworked by lathe polishing until inner and outer bearing rings could be assembled with less than 9N of force (approximately 0.0025 mm loose fits). The bearings were cleaned and relubed, and then installed in the fixtures without springs under the clamp screws. The effect of clamp screw tightening torque on bearing torque was then evaluated at up to 0.45 Nm. Bearing torque remained constant, increasing at 0.7 Nm with lockup at 0.9. In spite of having the clamp surfaces behind the raceway grooves, excessive clamping loads (approximately 45N per bolt at 0.7 Nm bolt torque) produced detrimental race distortion.

The Set 1 bearings were then tested in air for 57 days (3.5 million cycles) with clamp screws torqued to 0.45 Nm, followed by a 30-day test with the 5.3N springs under the screw heads. The springs had been inserted one bolt at a time without

disturbing or rotating the bearings. Figure 7 shows the torques during these two
tests as well as the torque for 51 days of the original test with phenolic sepa-
rators (from Figure 3). Opening up the race fits caused the maximum torque to drop
from 0.06 to 0.014 Nm with the solid preload, but a two-fold increase with operation
still occurred. Soft preloading restored the initial 0.007 Nm torque level that
existed at the start of the solid preload test, and this torque was essentially con-
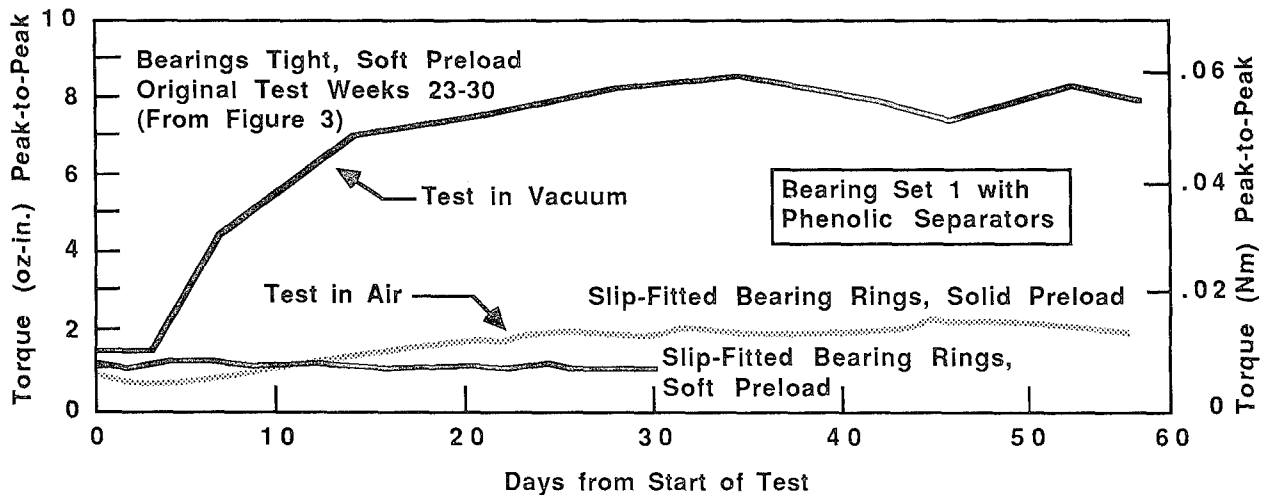stant for 1.8 million cycles.

Figure 7. When Set 1 bearings were made slightly loose in their test fixture,
           torque dropped to 0.007 Nm (1 oz-in.) and was constant for 30 days. With
           solid preload and slipfits, torque increased from 0.007 to 0.014 Nm in 25
           days and then stabilized.

The post-test effort showed the value of mounting the bearing rings in duplex sets
with slightly loose fits, as well as the benefits of "soft" preloading. We did not
discover why Set 1 torque was about twice the level achieved on Sets 3 and 4.

TEST CONCLUSIONS

The following conclusions were drawn from this test program:

- When properly made and installed, lightly preloaded duplex bearings having
  phenolic laminate separators and lubricated with thin films of BASD 36234
  liquid lubricant can withstand more than 16 million low-angle oscillating
  cycles without any signs of degradation whatsoever and without significant
  torque variation.

- Blocking can occur in oscillating duplex bearings at even extremely narrow
  angles of motion.

- Races should be slip fits, if possible, to assure proper performance and
  prevent blocking.

- Soft (spring) preloading is better than hard preloading if bearing torque
  is critical. This confirms a Reference 1 recommendation.

- Bearings must be scrupulously clean.

220

As a result of these findings, we decided to follow the recommendation of Reference 1 to use more open raceway conformities in the actual gimbal bearings, and to use soft preloading. (As will be seen, soft preloading had to be abandoned.)

GIMBAL BEARING INSTALLATION

The original concept for mounting the inner axis duplex pair bearings is shown in Figure 8. Belleville washers were used to provide a soft preload. This design was abandoned when it was determined that the bearing outer ring fits could not be loose (in order to meet axis perpendicularity specifications). Slip fits are necessary for the Belleville to be able to restore the bearings to the preloaded condition after vibration.
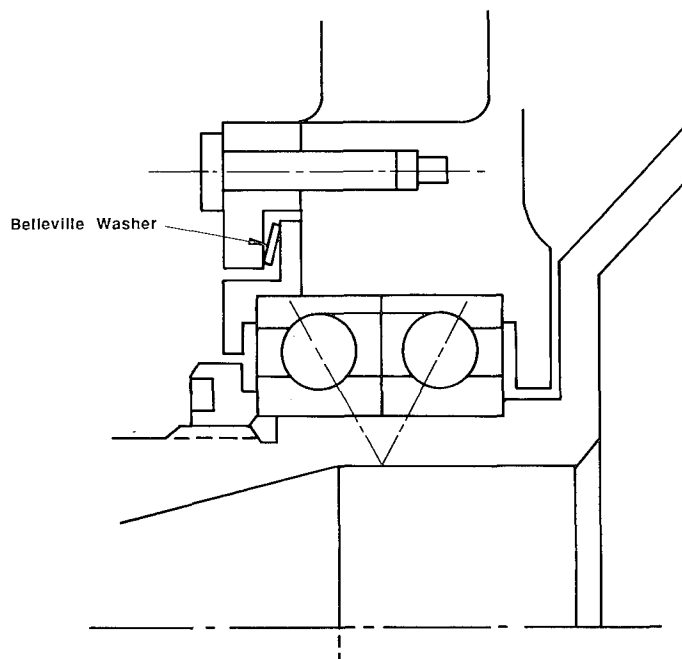

Figure 8. The initial gimbal design used Belleville washers to provide soft preload on its duplex bearings.

The final configuration for inner axis driveline components is shown in Figure 9. A payload mass-simulator connects the two shaft hubs during BASD tests. The bearing seats are match-machined to each bearing pair to provide a 0.0025 mm slip to 0.0025 mm press fit on the diameter. This close fit is not ideal from the blocking stand-point, but was felt to be the best possible compromise. The gap between the outer race retaining ring and housing is shimmed to 0.025 mm maximum when the bearing outer races are just brought into contact with each other, making clamping force on the races independent of torque on the clamping screws. We experienced no problems with bearing race distortion by the large nuts used as inner race retainers. The bearings are ABEC 7 with nominal raceway conformities of 0.549 outer and 0.528 inner. Outer race conformity is more open than usual, in keeping with a life test conclusion. The shafts, diaphragm, and yoke are titanium 6AL-4V. Bearings are lubricated with BASD 36234 oil, which has such a low outgassing rate that reservoirs are not required when closures, as shown with barrier film, are provided.
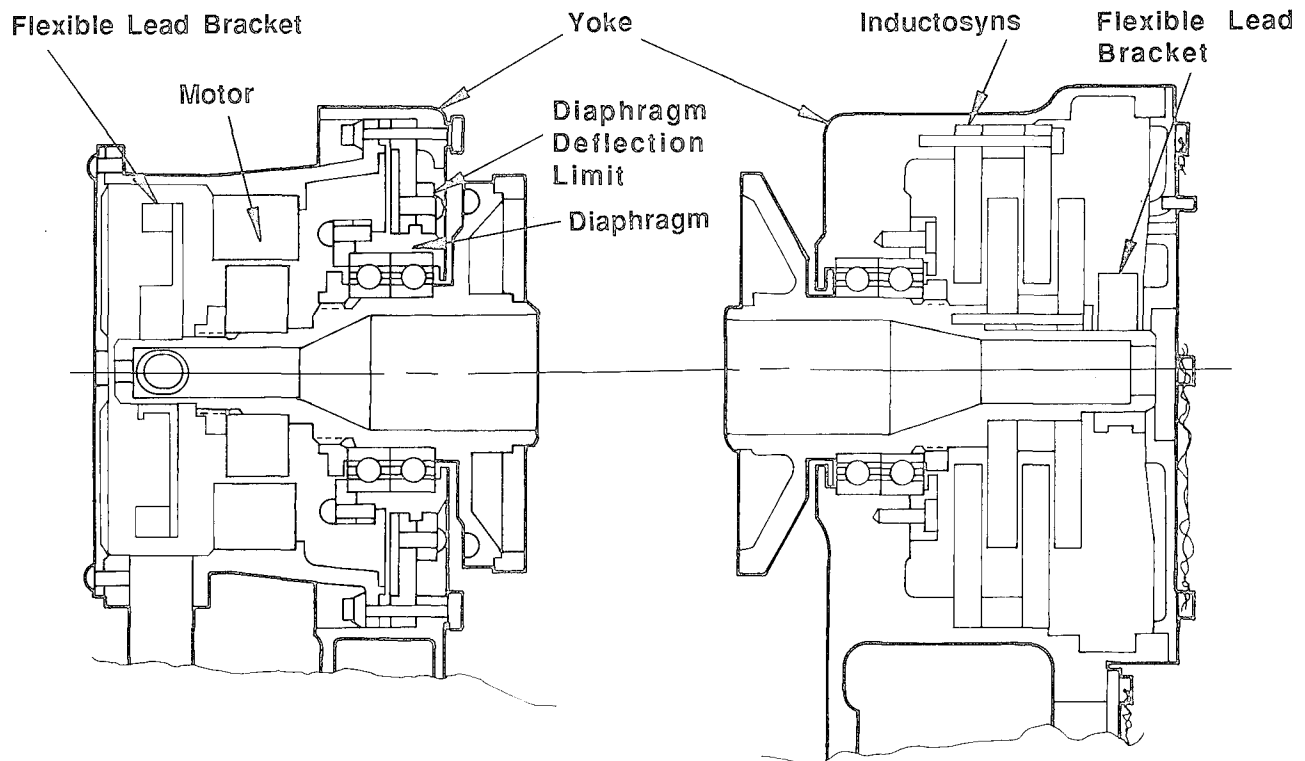
Figure 9. Final configuration of inner axis driveline components. Soft preloading of the duplex bearings could not be used.

The inner axis has a rotation range of 31 deg, but its normal mode is narrow-angle oscillation in one location. Spring-loaded stops are installed at each end of the travel range.

EXPERIENCE WITH GIMBAL BEARINGS

Inner axis drag torque is measured as a part of gimbal acceptance testing. The axis is rotated at a constant speed (approximately 30 deg/min) by an external motor. Torque is measured with a torque transducer, producing the typical trace shown in Figure 10. The top trace indicates rotation from the +30.5 deg stop to the -0.5 deg stop. At end-of-travel, the axis is driven into the stop slightly, compressing the stop spring, to assure complete travel. The lower trace shows rotation in the opposite direction, again reading left to right. The slope in the traces is caused by spring torque of the flexible electrical leads at both ends of the axis. These leads are wound in opposition to each other, and their torques cancel in the middle of the travel range.

Four of the six gimbal assemblies tested had torque traces similar to those shown in Figure 10. Two assemblies exhibited traces as shown in Figure 11. Note the large spikes just inside the stop locations. Following is a summary of the investigation and analysis of this anomaly.

Extensive investigation of the test setup removed it from the list of possible causes. Blocking in the bearings was proposed next. To see if the spikes would grow, the axis was cycled stop-to-stop by hand, with torque traces taken after every 100 cycles. The spikes increased from 0.028 Nm to almost 0.35 Nm after 300 cycles, then stayed at the same level for 700 more cycles. Random movements within the stop
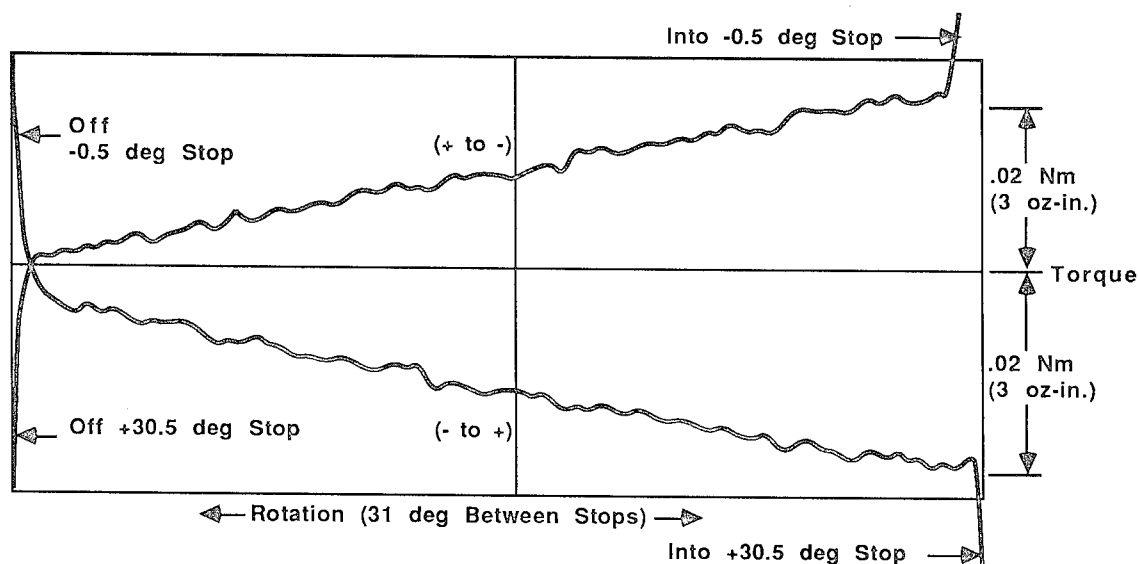
Figure 10. An acceptable inner axis torque trace. Only minor torque ripple is seen between stops.
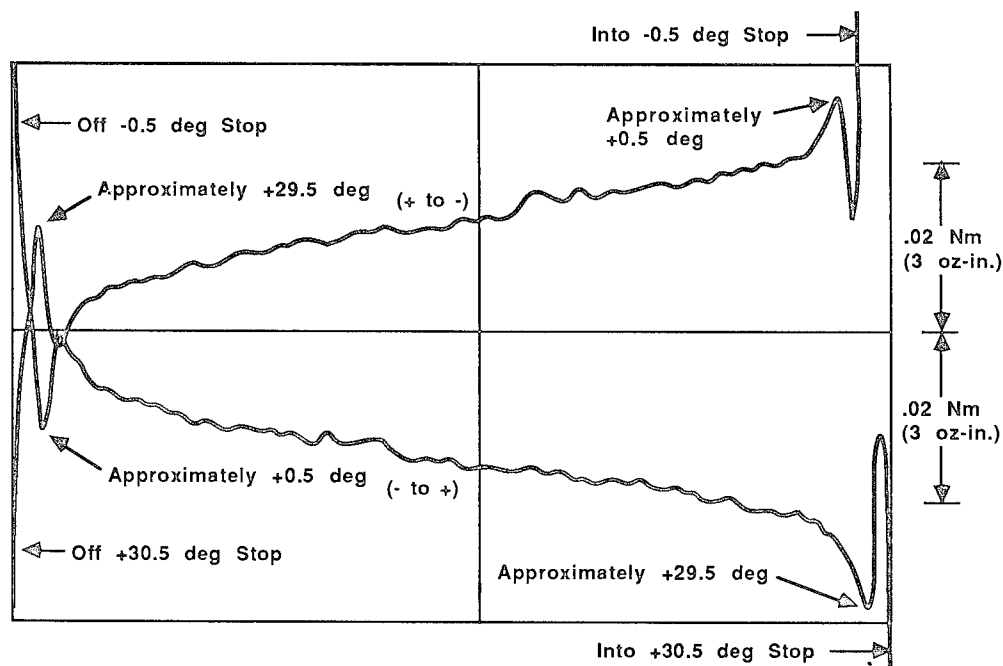
Figure 11. An unacceptable inner axis torque trace showing gross torque anomalies just inside the stops. These anomalies developed during several hundred step-to-step cycles.

range had no effect on the spikes. Neither of these pieces of data suggest blocking, nor does the large torque drop after the spike. Finally, the springs were removed from the stops to allow approximately 40 deg of travel, and the trace in

223

Figure 12 was taken. If this anomaly were blocking, the spikes should have disappeared after the first pass. Since the spikes were still present on the return part of the cycle, blocking was not the problem.
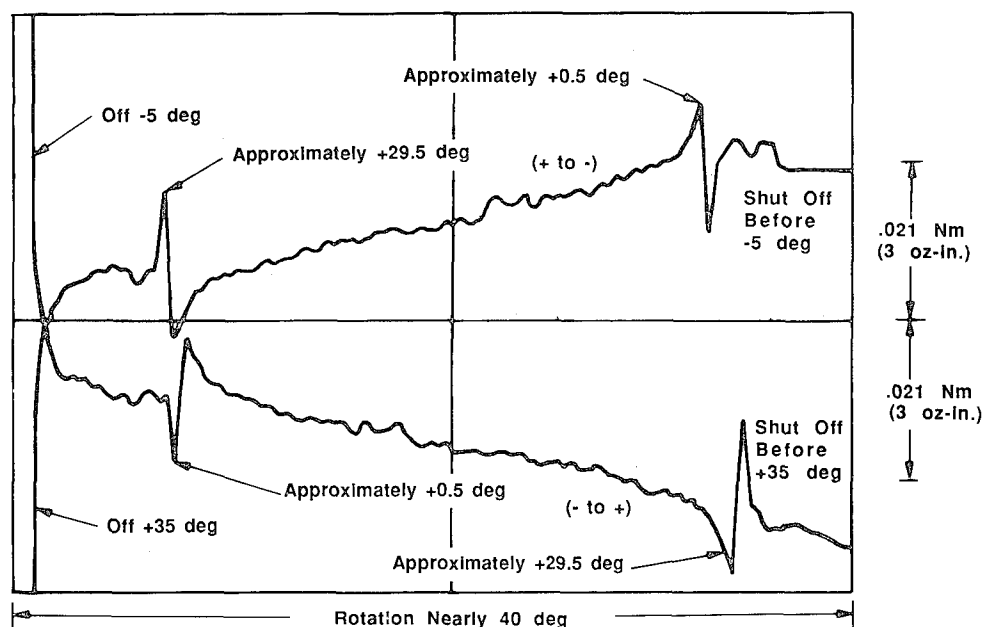

Figure 12. When the drive was rotated beyond the original travel limits, torque spikes remained in their previous locations.

At this point, the torque anomaly felt, by hand, rather like a magnetic detent. The mass simulator, the motor side flex cable and all wires, and the motor housing (including the motor stator) were removed to eliminate all possible hardware problems outside the bearings. A torque trace run on just the motor-side bearings still showed spikes. Two possible explanations were considered.

● There could be a defect or a problem with assembly that caused the race to pinch the balls.

● There could be debris piling up in small hills behind the balls, thereby causing the spike.

To explore the first possibility, the inner race retaining nut on the motor side bearings was removed and replaced finger tight. No change was evident in the torque trace. The outer race retaining ring was also loosened, again with no effect. Thus, debris became the prime suspect.

Assuming that debris caused the anomaly, it should be possible to produce spikes in other locations; therefore, blocks were attached to the second discrepant gimbal to limit travel to 24 deg. Initially, no spikes were present at the new stop locations; cycling block-to-block generated new ones. Traces taken after the 24-deg stops were removed show the new spikes and the original ones (Figure 13). The spikes remained after several stop-to-stop and random cycles. A trace taken after the gimbal sat overnight, to see if the debris hills would flow away, still showed all the spikes. Just to be positive, the travel was reduced to 21.7 deg and again

spikes were created. The blocks were removed as were the stop springs, to permit 40 deg of travel, and all six spikes were visible. Cycling at 40 deg did not generate any new spikes, however, and after 500 cycles the existing spikes were noticeably smaller. After 1000 cycles they were gone. Subsequent attempts to create spikes by shortening travel were unsuccessful.
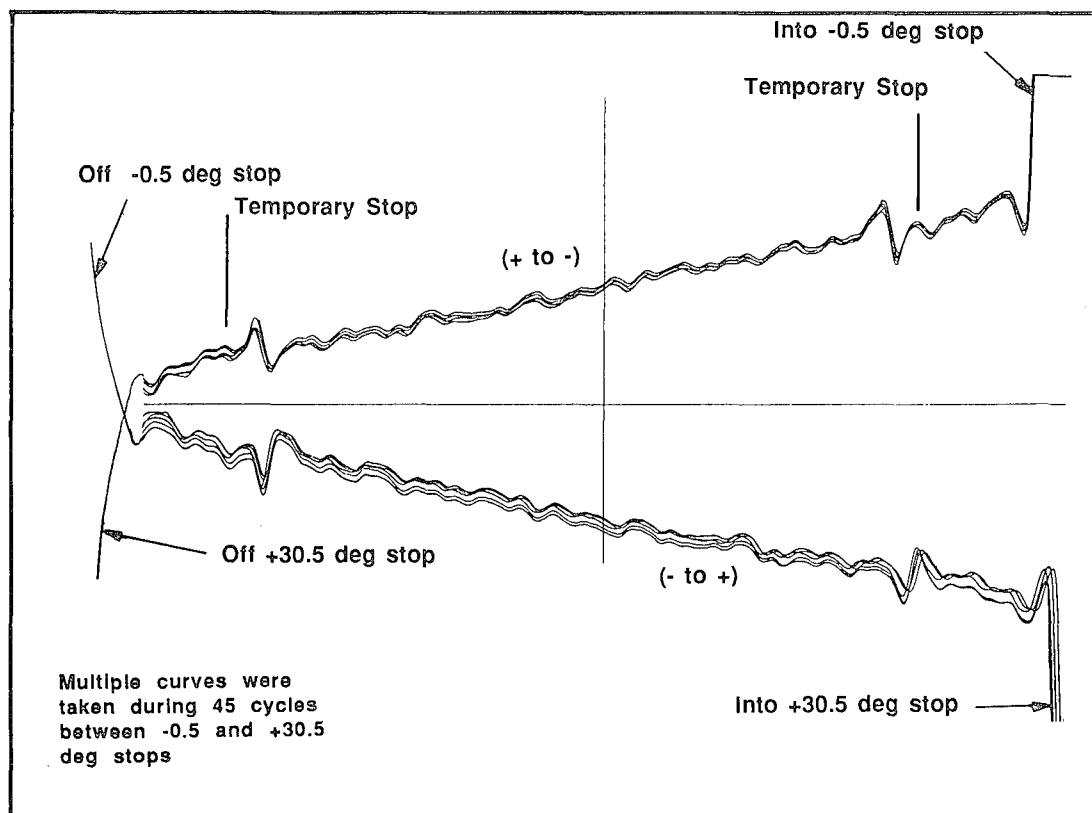

Figure 13. Cycling between temporary stops set inside the original travel limits produced new figure spikes which persisted for more than 45 cycles when the travel was increased again.

Analysis of the bearing geometry shows that with 31 deg of travel, the ball paths do not overlap; however, with 40 deg, ball paths do overlap. It was then evident that the torque spikes were caused by debris piling up just before the ends of the ball paths, under repeated cycling, at fixed angles too short to overlap the ball tracks.

While the mechanism for debris piling is not understood completely, the torque traces indicate that hills build up behind the balls at the end of their travel. Apparently, the hills are formed by compaction of debris just as ball motion begins and before a bow wave builds up that can carry any particles off to the side and back into the track again behind the ball.

Having established debris as the cause of the torque anomaly, it remained to find the source of the debris. At BASD, bearings are run-in, thoroughly cleaned and relubed, and then put in clean bags until assembly time. Assembly takes place in a clean room.

The bearings were removed from the unit, visually inspected, and cleaned. A particulate check on the cleaning rinses showed primarily many small aluminum particles. A much smaller amount of titanium was also present. A few dry-lube particles were

found, but not enough to cause a pile or thicken the wet lube. (The inner race retaining nut threads are dry lubed.) The separators did not show wear, nor were any separator particles found. Bearing raceways were neither pitted nor gouged, and there was no significant amount of iron in the rinse.

The aluminum particles present in the solvent rinses were thought to be the primary problem. The source of these particles, on the motor side, was most likely the aluminum tools used for assembly. These same tools were used on the Inductosyn side as well. In addition, the Inductosyns are basically aluminum plates which are pressed in at assembly. Other hardware pieces are aluminum, but they are not considered primary debris generators.

In summary, it was concluded that the torque anomalies experienced during testing were caused by small debris hills building up in the bearings. These hills could only build when the ball tracks did not overlap. Once the ball tracks overlapped, the debris was redistributed such that it could no longer build up when travel was shortened. The debris was generated during assembly by press fits of the hardware and the tools used for the installation.

As a result, several changes were instituted:

- Assembly procedures were modified to minimize debris producing operations inside the bearing cavities and to increase the number of vacuuming cycles.

- Aluminum assembly tools were changed to titanium because aluminum chips and flakes much more easily than titanium.

- The bearings are now run-in (360-deg rotation) overnight in the gimbal to distribute any assembly debris. This is in addition to the run-in they receive before assembly.

- Experience shows that the torque anomalies form within a few hundred cycles after assembly, if they are going to occur at all. Therefore, a test consisting of 1000 stop-to-stop cycles has been added to the acceptance testing. Although the oscillating life test showed that as many as a million narrow angle cycles might be necessary to produce blocking, we believe that the 1000 wide-angle cycles will probably also reveal any blocking tendency that may be present.

ACKNOWLEDGMENTS

REFERENCES

1. W.O. Winer and D.M. Sanborn: Surface Temperatures and Glossy State Investigations in Tribology. NASA Contractor Rpt. 3031 on NSG Grant 3160, June 1987.

2. M.J. Todd: Investigation of Torque Anomaly in Oscillating PDM Bearings. ESA (ESTL) 49 European Space Tribology Laboratory, May 1981.

ON THE TORQUE AND WEAR BEHAVIOR OF SELECTED THIN FILM MOS_2 LUBRICATED GIMBAL BEARINGS*

John J. Bohner and Peter L. Conley**

ABSTRACT

During the thermal vacuum test phase of the GOES 7 spacecraft, the primary scan mirror system exhibited unacceptably high drive friction. The observed friction was found to correlate with small misalignments in the mirror structure and unavoidable loads induced by the vehicle spin. This paper describes an intensive effort to understand and document the performance of the scan mirror bearing system under these loads. This effort involved calculation of the bearing loads and expected friction torque, comparison of the computed values to test data, and verification of the lubrication system performance and limitations under external loads. The study culminated in a successful system launch in February of 1987. The system has operated as predicted since that time.

SYSTEM DESCRIPTION

The GOES 7 spacecraft is a spin-stabilized geosynchronous vehicle which provides near hemispherical images of earth's weather patterns. Storm warnings from this and earlier spacecraft have saved many lives and millions of dollars in property damage. As such, the complete and continuous production of such weather images is a vital national asset. Indeed, almost no evening news telecast is complete without the weatherman's review of the satellite image.

GOES 7 now provides such images using a Visible Infared Spin Scan Radiometer (VISSR). The VISSR can scan the earth once every 20 minutes by using a scan mirror to reflect an image of the earth over a series of photodetectors. The image is built up like a TV image from a series of horizontal lines. Spacecraft spin provides a west to east image motion for the scan mirror. Then while the VISSR is pointed away from earth, the scan mirror is stepped one line from north to south. Thus a series of lines is collected building a complete image of the earth. It is the scan mirror's support bearings which are the subject of this report.

Figure 1 illustrates the scan mirror system. The mirror is attached at four points to a beryllium support structure. This structure is mounted between a pair of motor, ball bearing and optical encoder assemblies referred to here more compactly as encoders. The beryllium support is hard mounted directly to the beryllium shaft of each encoder. The primary encoder is hard mounted to the instrument frame while the redundant encoder is mounted to the frame through a flexible diaphragm as shown. This diaphragm permits axial motion while maintaining high radial stiffness.

Each encoder contains a preloaded pair of angular contact bearings which support the shaft. In operation, the shaft position is sensed by the encoder and compared to a command value. Any error signal is inverted, amplified and supplied to the drive motor. Any mechanical resistance to achieve the desired position is thus sensed as a voltage which is relayed to earth in the telemetry train. Such resistances include inertial and dynamic imbalance effects as well as the various components of ball bearing friction (References 1-4).

The angular contact bearings' solid lubrication system had evolved towards thinner coatings over 10 years. For GOES 7, the coating of molybdenum disulfide was applied by radio frequency sputtering and was only 3×10^{-8} meters thick. This thickness was selected[5] to provide the maximum operational life before the lubricant would form "torque bumps", common in solid lubricated oscillatory bearings. These bumps were believed to form due to the minute, but repeated accumulation of solid lubricant at the ends of the ball path. As will be shown later in this paper, we found that these torque bumps are not simply due to debris accumulation, but may also represent significant race damage.

DESCRIPTION OF VEHICLE TEST ANOMALY

During spacecraft spin testing, the main scan mirror friction torque had to remain below a prescribed maximum throughout the entire mirror scan. During anechoic testing, the mirror drive torque for the spinning vehicle reached a peak of 0.1 N-m. The launch requirement was 0.076 N-m.

A brief test program was conducted on the vehicle to determine the cause of the high friction torque. During the test, it was noted that the mirror drive torque climbed significantly as the vehicle spin speed increased. Test results at 0 and 100 RPM are shown in Figure 2.

INTRODUCTION TO ANALYSIS

The relationship between average scan mirror drive friction and spin speed was examined with the results shown in Figure 3. It was noted that the friction increase with spin rate followed a curve typical of ball bearing friction trend with increasing load.

The encoder bearings are thin section angular contact ball bearings duplexed back to back with beryllium spacers. The bearing geometry and loading are summarized in Table 1. Using the techniques described in Appendix A, we plotted the expected friction torque increase vs. cross-axis moment per bearing pair for these bearings, obtaining the curve shown in Figure 4. The figure also gives mean contact stress levels for the bearings at the indicated loads. Comparing this curve to Figure 3, it can be seen that the loads required to produce the observed mid-frame torque on a single bearing pair are not unreasonably high, and that the operating stress level for the bearings at this load is well below ball or race damage limits for lubricated bearings.

Checks of the motor drive and data acquisition systems indicated that these systems were functioning properly. Other aspects of the testing supported the theory that unexpected bearing loads were the problem.

It did not matter which of several test encoders was installed on the redundant side of the vehicle. The mounting diaphragm on this side (see Figure 1) does not transmit axial or moment loads to the redundant encoder bearings. Also, those cases in which a development model encoder was mounted on the primary side produced consistently low torques. The bearings in this encoder were not preloaded, hence were insensitive to small misalignments. Finally, it was discovered that the bearings on earlier vehicles, which had exhibited a smaller torque increase upon spinup, had been designed with slightly different race curvatures which would reduce the alignment sensitivity. This is discussed in Appendix B.

TEST DESCRIPTION

Having found the probable cause for the observed friction torque, it was determined that it was not possible to quickly change the VISSR/ vehicle in such a way to eliminate these loads. The amount of misalignment which would cause the observed friction was well within the likely manufacturing tolerances (see Appendix B). Contact stresses which exist at this load are compared to those which correspond to the design preload in Table 2. The projected mean contact stress levels were not so high that lube failure was by any means certain. However, there was no relevant life data available at these stress levels.

It was agreed with NASA that a two-phase life test should be carried out in parallel with launch preparations. Spare flight quality bearing pairs would be tested at loads which encompassed the worst case loads, calculated from encoder motor drive voltage measurements under load (Appendix C). We needed to develop an understanding of the method and rate at which the lubricant coating would be consumed, and the margin which could be confidently maintained with an available motor

torque of 0.56 N-m. Earlier vehicles in this series had exhibited a small but steady increase in drive friction at each end of the scan. We needed to be certain that this effect would not suddenly become much worse at these higher loads.

The initial test phase was an accelerated life test of twice the mission duration, to verify that there would not be a sudden breakdown of the lubrication system and reduction in life. These bearings were analyzed to determine the performance of the lubrication system at relatively high loads.

The second test phase more closely approximated orbital scan rates, and used a spare encoder for a drive. This phase allowed us to observed the gradual buildup of torque bumps in the system, as well as test possible sequences of scan alteration to preserve the lubricant should this be required on orbit.

The assembly used for life testing the encoder bearing pairs is shown in Figure 5. Several bearing pairs were tested simultaneously. Table 3 gives the test parameters for each phase of testing.

TEST RESULTS

TORQUE HISTORY, PHASE I

The accelerated life test was halted periodically and the mid-frame and end-of-frame torques measured by hand. The results are shown in Figures 6 and 7.

It is apparent that the friction torque response of this lubrication system is highly load dependent. The end-of-frame torque in particular increases dramatically for the loaded bearings between 1 and 1.5 lifetimes. Of even more interest is the difference in mid-frame torque between the two identically loaded bearings. This would indicate that at the stress level shown in Table 2, we are very close to a damage threshold for the lube system. Subsequent analysis of the bearings showed this to be true.

At the end of two lifetimes, the frame limits for the worst of the loaded bearing pairs were extended and the test continued by hand. Figure 8 shows the rate at which the end-of-frame torque decreased during this process. It can be seen that the end-of-frame torque was brought within manageable (0.28 N-m) limits rather quickly, although it did not reach the beginning of life level.

TORQUE HISTORY, PHASE II

The second phase of the life testing used new bearings in the same fixture (Figure 5), except we used a spare encoder to drive the test bearings. Using the VISSR drive electronics, the maximum scan rate was considerably slower than that used in the first test phase. This method resulted in precise repeatability of the frame limits, and in the same step and settle wear dynamics which would occur in flight (see Table 3). This phase offered an opportunity to study the changes in torque over the scan. Changes such as the growth of torque bumps at the end of scan were thought to form due to the repeated deposition or extrusion of solid lubricant at the end of the ball path. Such deposits would decrease the bearings' radial clearance and lead to complex torque/position profiles.

It was initially agreed that torque bump rolldown procedures would be implemented when the total end-of-frame torque (three bearing pairs) reached 0.175 N-m. This rolldown limit was subsequently raised to 0.21 N-m. With this provision, the torque bumps at each frame limit were maintained by shifting the frame limits approximately 0.5° in each direction when required. Figures 9 and 10 show sample torque traces before and after a rolldown. The torque shown is the sum for all three test bearing pairs. It can be seen (Figure 9) that through most of the scan, the average torque remains fairly constant with some lumps and noise. Approaching the CW end of the scan, the required torque drops to zero and then climbs to a peak of approximately .25 N-m. With rolldown, this peak is considerably reduced (Figure 10).

The end-of-frame (CW) torque history of the experiment is shown in Figure 11. The figure indicates that the end-of-frame torque was easily maintained within reasonable limits through simple rolldown procedures. At the end of the test (1100 orbital days), the contribution of each individual bearing pair was measured. The results for the loaded bearings are shown in Figure 12.

POST-TESTING BEARING EXAMINATION

Following the completion of each test, the bearings were disassembled for study. Bearing components were examined by visual and Scanning Electron Microscopy (SEM) as well as limited chemical analysis using Energy Dispensive Analysis of X-Rays (EDAX). Following microscopy, the bearings were mechanically inspected using profilometry.

Examination of the normally loaded bearings from both test phases found the ball path lubricant severely reduced. SEM images showed no signs of distress beyond the partial loss of lubricant. No piles of debris or lubricant were found. A typical view is seen in Figure 13

left. Profilometry did find evidence of race wear, particularly at the ends of travel where the races had worn by as much as 4.1 x 10^{-7} meters.

The moment loaded bearings did not fare so well. Phase I bearings visually showed wear paths with severity corresponding to ball load. The most heavily loaded balls had very patchy lubricant coatings on the race and some evidence of metallic damage. Serial Number 101 was the worst with large areas of metallic damage as seen in Figure 13 right. Figure 14 shows details of Phase I ball paths. Some ball paths ended in accumulations of lubricant as seen in Figure 14 right, but many more were devoid of lubricant and were just torn up steel as shown in Figure 14 left.

Phase II moment loaded bearings were visually indistinguishable from the normal load bearings; this is consistent with their lower accumulated life and good torque performance to that point.

Circumferential profilometry of the Phase II bearings did not reveal the presence of debris bumps at the ends of scan. Instead, we found wear pits at each end of travel, but only on the outer race as shown in Figure 15. Data from any Phase I loaded bearing showed a badly roughened surface consistent with the surface seen in Figure 13 right.

ENERGY APPROXIMATION

It is informative to calculate the work which should be required to elastically deform a ball rolling through the wear scar of Figure 15 as the bearing is rotated. The normal ball load will tend to decrease as the ball rolls into a wear depression. Conversely, the ball will need to be compressed to fit between unworn sections of the races. This compression/relaxation of the ball will require work which is supplied by torque acting through some angle. The same effect should also occur as the ball rolls over debris in the ball path (see Figures 9 and 10).

A detailed analysis of this action would need to include the race out-of-roundness and the ball size variations, and is beyond the scope of this paper. However, we can compare the magnitude of the torque "bumps" shown in Figures 9 and 10 with the expected torque based on the profilometry data shown above. Under preload alone, the normal approach of the ball to the outer race is approximately one micron. The work stored and recovered in the contact as it is cycled by the 0.6 microns indicated in Figure 15 may be calculated to be approximately seven micro-Joules. Using our torque traces through a scan, we can estimate the work in any of the bumps using the formula as follows:

Work (J) = [Torque (N-m)/pitch radius (m)] x arc-length (m)

This gives in Figure 9 for the CW "bump" growth of 0.15 N-m over 0.002 radians, a work of approximately 300 micro-Joules. This corresponds to some 43 balls climbing out of a depression such as that in Figure 15.

In the Phase II testing, one bearing pair was under moment loading. Under this condition, approximately half of the balls (or 36 of 72) share the load.

CONCLUSIONS

The GOES 7 spacecraft in now on orbit and functioning as designed. Early ground tests indicated that unexpected, higher VISSR bearing loads were present. These loads increased the torque required to drive the scan mirror. Concerns that the high torque might continue to increase led to a search for the cause and testing to demonstrate acceptable performance despite the high loads. Analysis showed that increased torques were due to spacecraft spin and instrument alignment difficulties.

Life of the MoS_2 sputter lubricated film was greater than two mechanism lifetimes under normal loads. Addition of the moment load reduced that life to between one and two lifetimes. Increases in end-of-frame torque due to debris and race wear were found to be manageable by periodic changes to the VISSR frame limits.

It is apparent that there are two major contributors to the observed friction torque behavior of the scan mirror drive. Looking at any of the torque traces (see Figures 9, 10, and 12), we see that there is an average drive torque hysteresis loop on which is superimposed a large amount of low-frequency noise.

The average torque hysteresis represents a frictional loss due to sliding at the ball-race contacts. We have shown that both the magnitude and the load dependence of this term can be readily determined using the methods (and in the case of the software) of Jones (reference 3). The magnitude of this torque is proportional to the coefficient of sliding friction at the interface. This is very apparent from the large increase of average mid-frame drive torque as we wear through the MoS_2 (see Figure 6). For new bearings with this lubrication system, a coefficient of sliding friction of 0.16 is appropriate. This implies that some metal-to-metal contact is occurring even at the beginning of life.

The second contributor to the system drive torque is the work which much be done to roll over the debris and through the wear scars which develop as the lubricant film wears. This friction is not a loss term; the elastic nature of the ball compression is evident in the manner in which the CW and CCW torque traces of Figures 9 and 10 parallel one another.

ACKNOWLEDGEMENTS

REFERENCES

1)   Mullin, J.V., and Speece, A.L., "Prediction of Bearing Torque Variation Based on Profilometry Data", ASME 69-WA/Lub-4, November 1969.

2)   Dahl, P.R., "A Solid Friction Model", SAMSO Report TR-77-131, DTIC Number AØ4192Ø, May 1968.

3)   Jones, A.B., "The Mathematical Theory of Rolling-Element Bearings" in "Mechanical Design and Systems Handbook", H.A. Rothbart, ed., McGraw-Hill, 1964.

4)   Stevens, K.T., and Todd, M.J., "Experiments on the Torque of Ball Bearings Over Small Angles of Moment", ESA/ESTL/34, Risley, England, 1979.

5)   Christy, R.I., and Barrett, G.C., "Sputtered MoS_2 Lubrication System for Spacecraft Gimbal Bearings", Lubrication Engineering, Volume 38, 8 437-443, 1978.

APPENDIX A - BALL BEARING FRICTION

THEORETICAL SUMMARY

The computation of ball/race sliding friction under load involves a numerical integration of the frictional forces generated across each contact zone. In preparation for this, the individual ball loads, pressure ellipse dimensions, orientations, and motions must be determined. This is a formidable computational effort and we have used the A.B. Jones ball bearing analysis program for the task. Reference 3 gives details of the analysis which is summarized here.

In any ball bearing, the pressure ellipse has a marked curvature in the plane of the major axis. This curvature is the major cause of sliding friction in ball bearings. Integrating the frictional forces across the contact zone, we may determine a net moment about an axis which skewers the curved pressure ellipse for each ball/race contact.

The sum of these torques for all of the contacts in the bearing provides the major source of bearing rolling friction.

In a radial bearing under radial load, the contact zones at each race may be described as above. In the case of an angular contact bearing, at least one race will have a spinning motion superimposed upon the rolling motion, giving rise to additional frictional forces. These forces can also be integrated over each contact area to determine a net contribution to bearing friction torque. Typically, the spinning motion described will occur at only one race. The race which rolls without spin is termed the 'controlling' race. We found rather dramatic differences in the wear which occurred in the presence of ball spin compared to that on the controlling race (see Figure 15).

APPENDIX B - BEARING RACE CURVATURE EFFECTS

The encoder bearings are mounted back-to-back to provide maximum stiffness for an individual encoder. Unfortunately, with two encoders defining the mirror axis, each must accommodate some slight angular misalignment of its preferred axis.

The bearing manufacturer which had been used for early GOES vehicles stopped producing these bearings and with this change the program received bearings with slightly tighter race curvatures (greater ball/race conformity). Using the methods of Jones, the effect of a few percent change in race curvature can have a significant effect on the sensitivity of the bearing friction to misalignment. This is shown in Figure B-1.

The GOES 7 encoders are mounted on a flange of approximately 0.06m in diameter. A misalignment of 100 microradians corresponds to a flange runout of only six microns. The VISSR is a very complex and stiff structure. It is quite likely that the primary encoder bearings had to accommodate the loads discussed above.

APPENDIX C - EXPERIMENTAL VERIFICATION

In support of the GOES 7 vehicle, the flight encoders were retro-fitted with new bearings having maximum race curvatures. During final encoder buildup, the units were calibrated to determine the individual motor characteristics and bearing pair sensitivity to external loads. Based on this information, we were able to more accurately calculate the loads existing in the final spacecraft assembly and verify that they were less than those of the life test.

These results correlate well with the ball bearing friction torque calculated for new bearings using the methods described above. The results are summarized in Figure C-1 for moment loads.

TABLE 1 BEARING GEOMETRY AND LOADING

BEARING TYPE	THIN SECTION ANGULAR CONTACT
MATERIAL (BALLS)	AISI 440C STAINLESS
MATERIAL (RACES)	AISI 440C STAINLESS
SPACING	.0518m
PRELOAD	222N (DB)
NUMBER OF BALLS	36
BALL DIAMETER	.00476m
PITCH DIAMETER	.0735m
O.R. CURVATURE	53%
I.R. CURVATURE	52%
CONTACT ANGLE	0.3 radians

TABLE 2 BALL-RACE MEAN CONTACT STRESS (MPa) (HEAVIEST LOADED BALL)

	OUTER RACE CONTACT	INNER RACE CONTACT	ELLIPSE CONTAINMENT
PRELOAD	587	570	100%
TEST LOAD (63 N-m)	997	969	100%

TABLE 3 LIFE TEST PARAMETERS

	PHASE I	PHASE II
EXCURSION	.175 radians (10°)	.175 radians (10°)
DURATION	245,000 Cycles	58,000 Cycles
VELOCITY	Sinusoidal, 0.2 Hz	Mid-frame ($\pm$ 860 lines): Retrace Frame end (last 50 lines): Normal
TEMPERATURE	21°C	21°C
PRESSURE	1×10^{-6} Torr	1×10^{-6} Torr

NOTE:

Retrace velocity is .00017 rad/sec average.
Normal scanner velocity is 0.000016 rad/sec average.

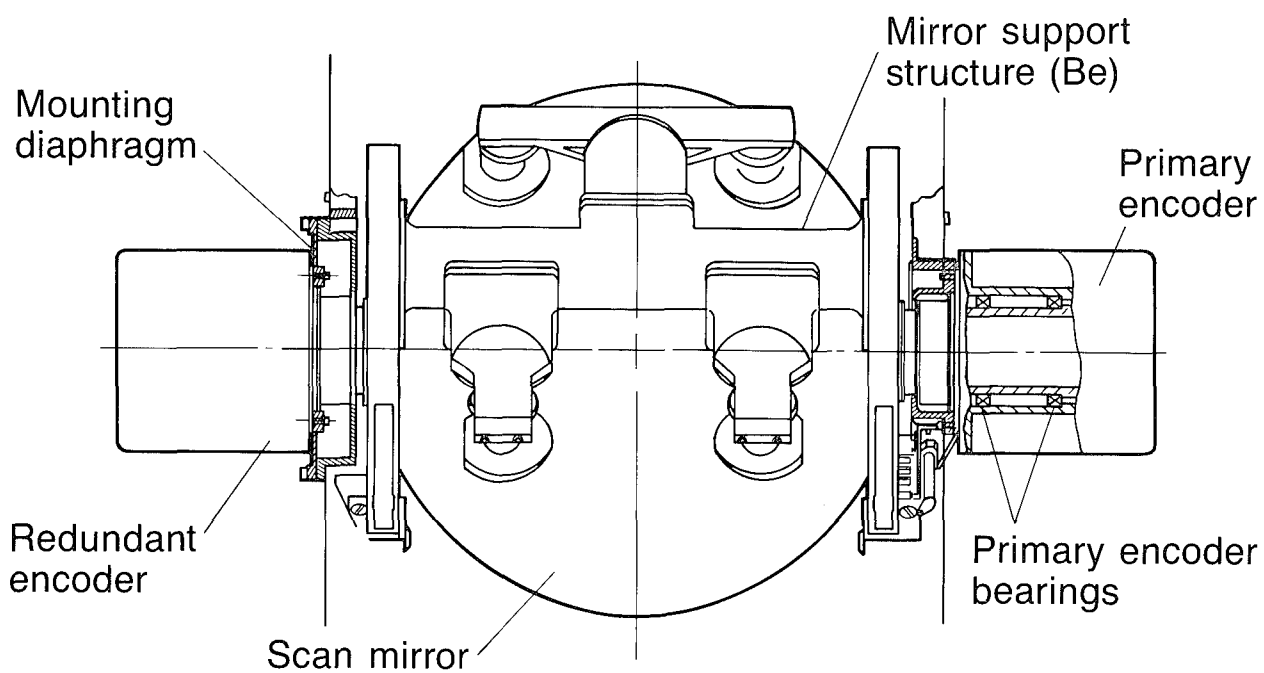Both normal and retrace are stepping motions. Step duration is approximately 0.05 seconds.
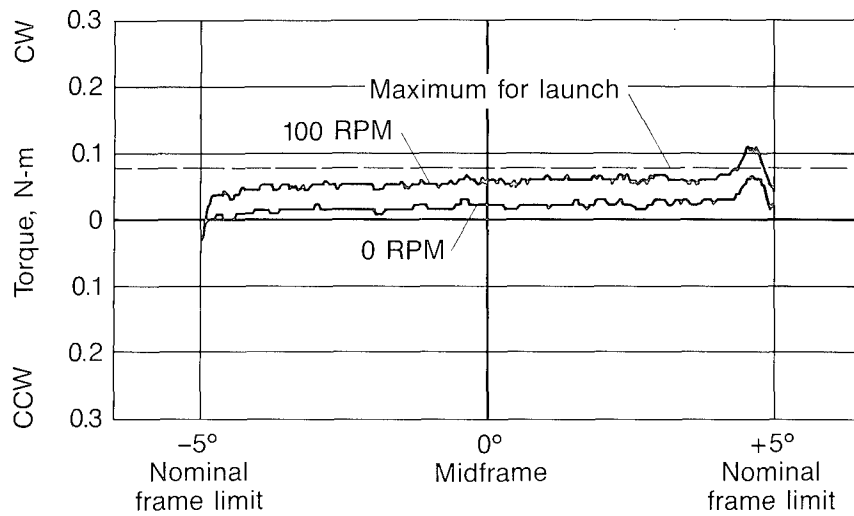
FIGURE 1. GOES-7 SCAN MIRROR DRIVE

FIGURE 2. TORQUE THROUGH SCAN — ANECHOIC TESTING
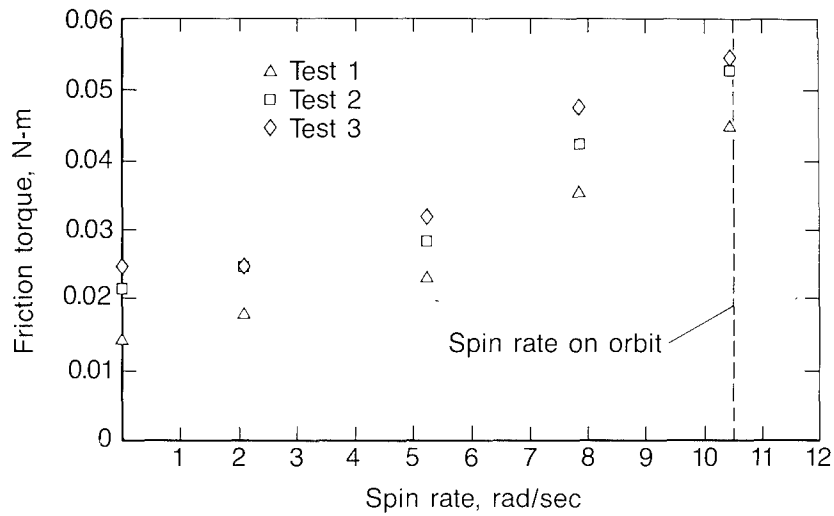
FIGURE 3. FRICTION TORQUE vs VEHICLE SPIN RATE
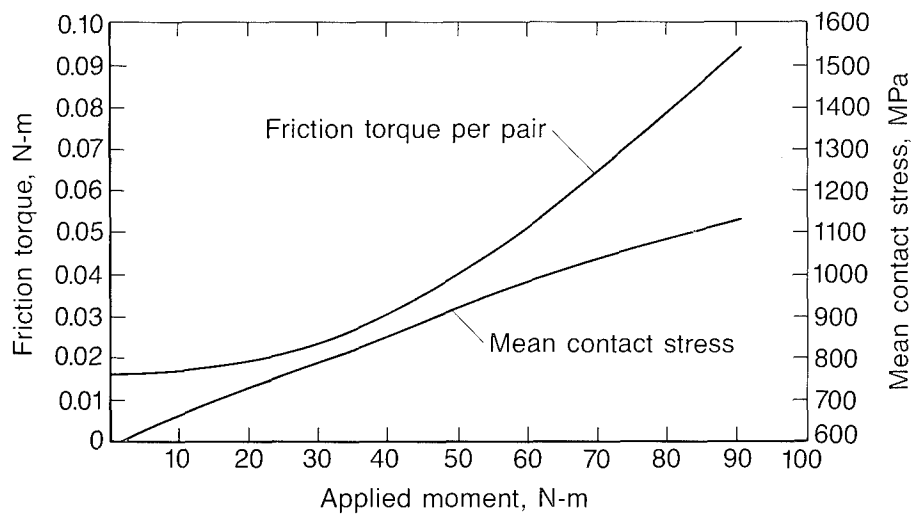
FIGURE 4. BEARINGS UNDER A MOMENT LOAD

Tension spring

Bellcrank
mechanism

Drive linkage

Site   A   B   C   D
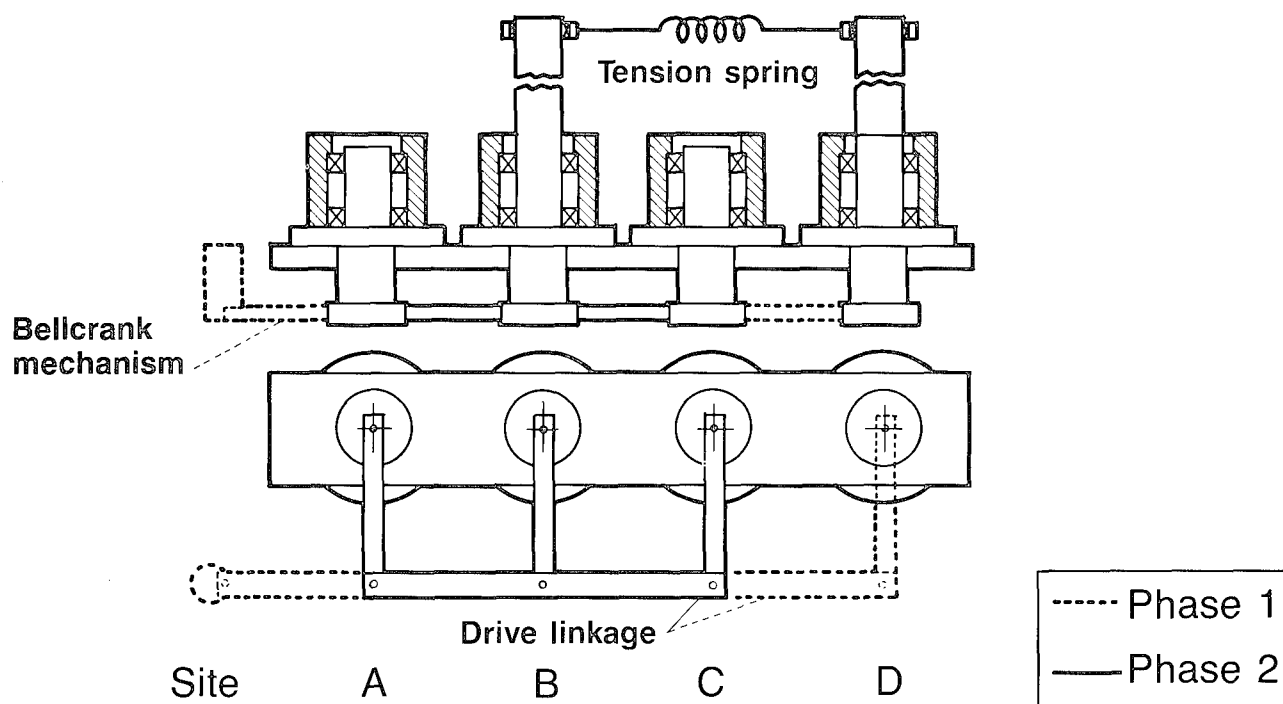
----- Phase 1
——— Phase 2

FIGURE 5. EXPERIMENT SCHEMATIC
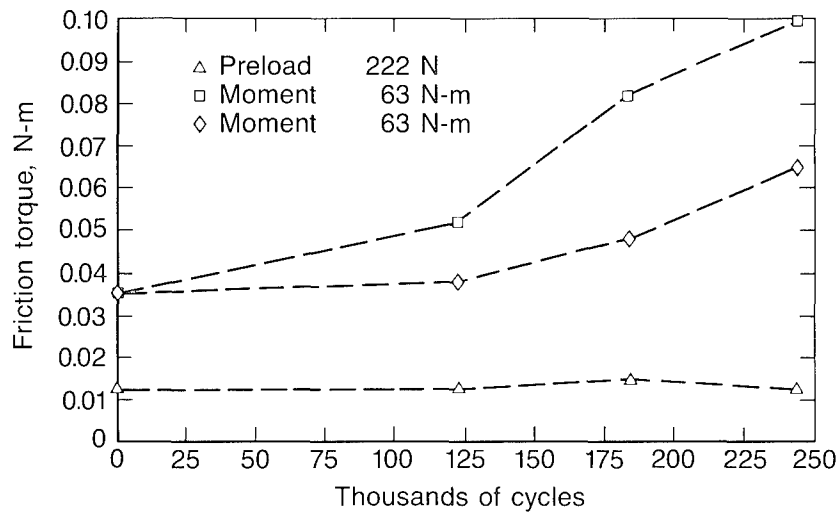
FIGURE 6. ACCELERATED LIFE TEST RESULTS — MIDFRAME
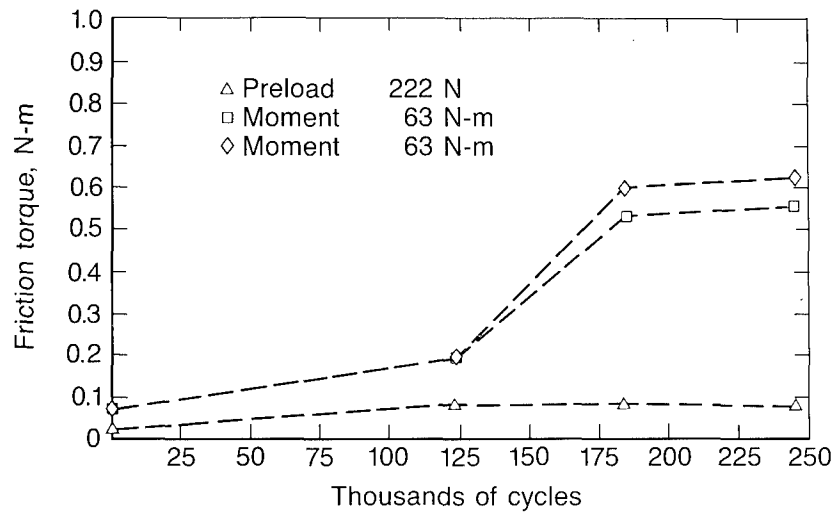
FIGURE 7. ACCELERATED LIFE TEST RESULTS — END-OF-FRAME
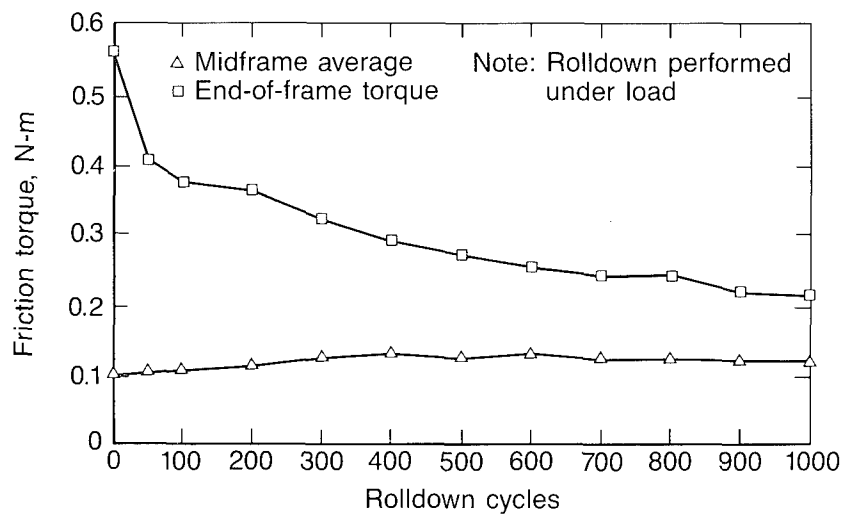
FIGURE 8. POST-ACCELERATED LIFE TEST MANUAL ROLLDOWN
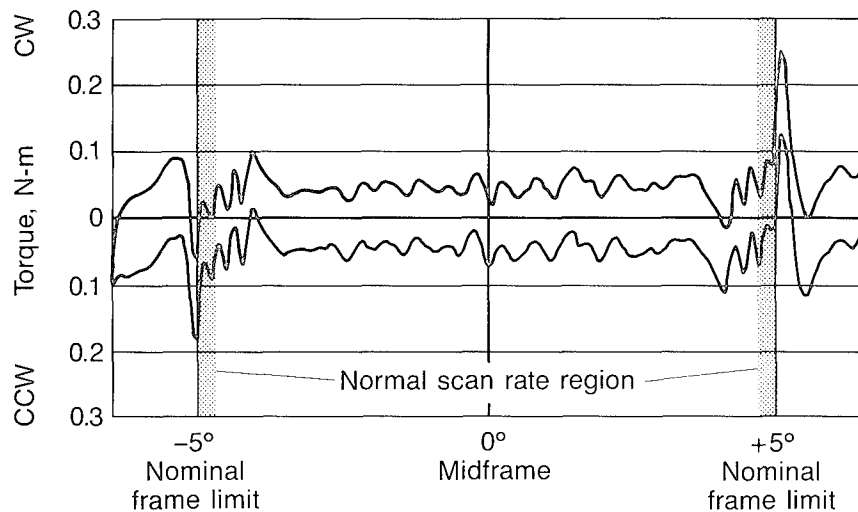
FIGURE 9. LIFE TEST PHASE II (943 DAYS) — TORQUE TRACE
BEFORE ROLLDOWN
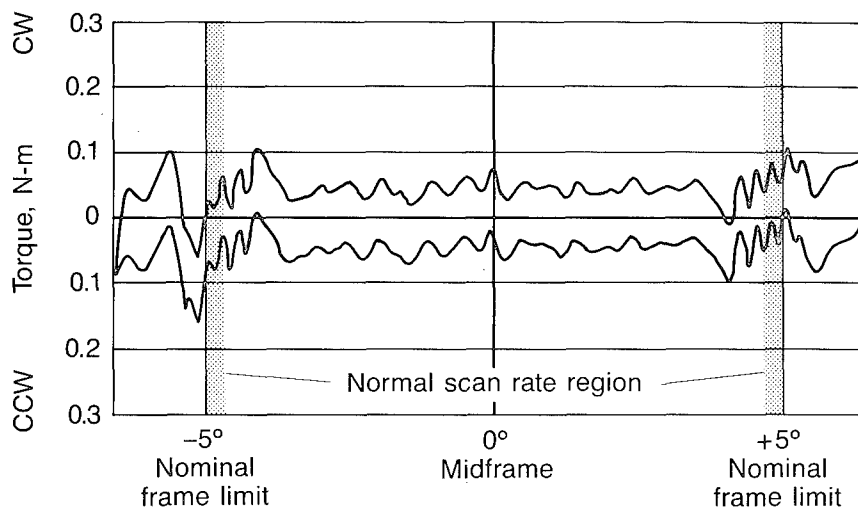
FIGURE 10. LIFE TEST PHASE II (943 DAYS) — TORQUE TRACE
FOLLOWING ROLLDOWN
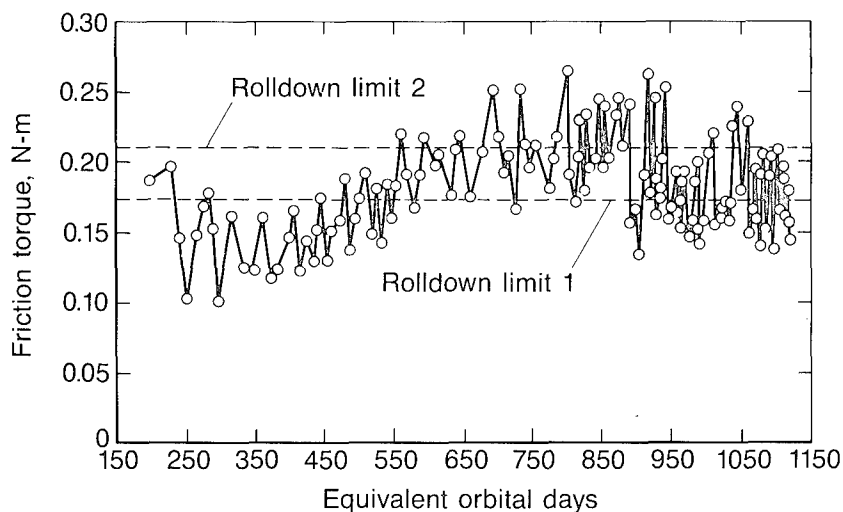
FIGURE 11. LIFE TEST: PHASE II TORQUE HISTORY —
CLOCKWISE END-OF-FRAME PEAK TORQUE

241
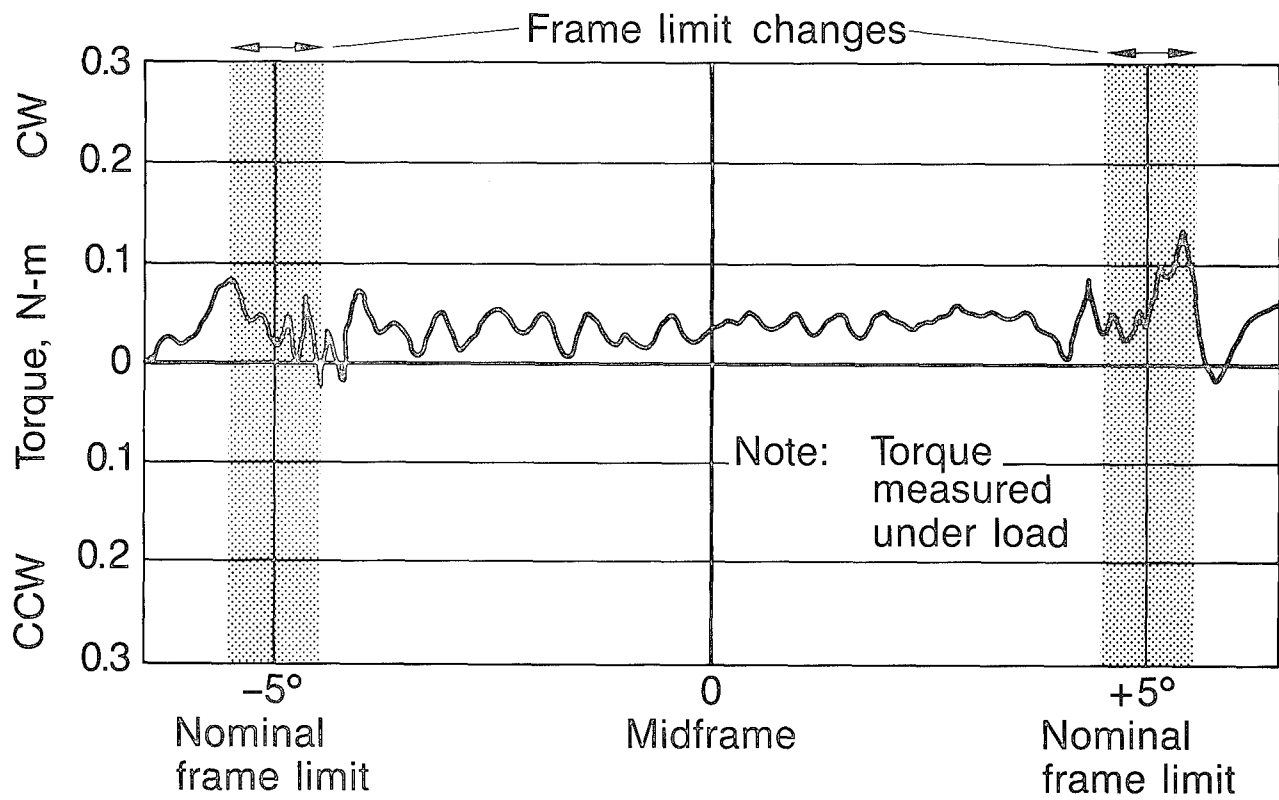
FIGURE 12. TORQUE FOLLOWING PHASE II TESTING — MOMENT LOADED PAIR
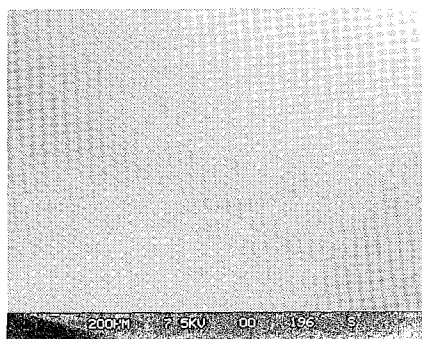
Phase II bearing showing "hole" and typical surface condition
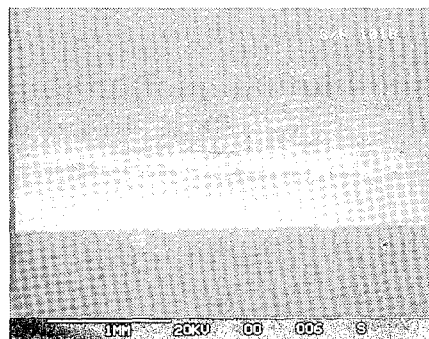
Phase I bearing showing damage in ball path

FIGURE 13. OUTER RACE BALL PATHS (SEM)

Showing metal damage but no lubricant buildup
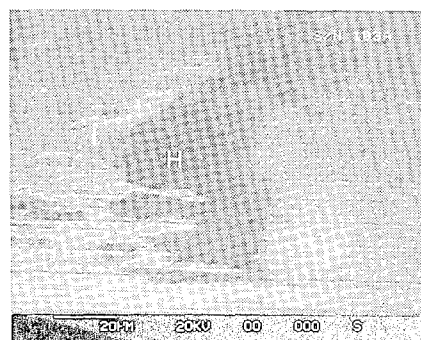
Showing lubricant buildup Region I is earlier accumulation with less steel wear debris than H

FIGURE 14. END-OF-FRAME BALL PATH DETAILS
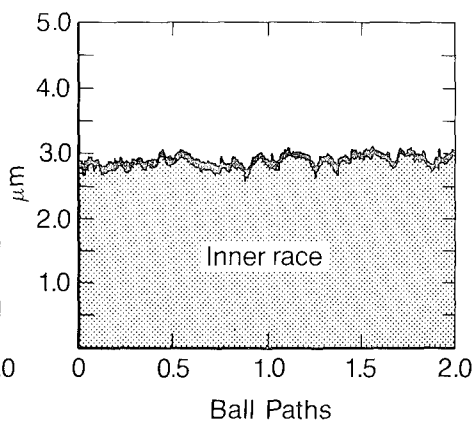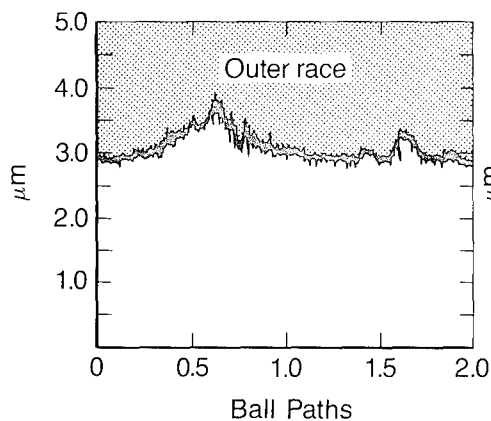
FIGURE 15. TYPICAL WEAR SCARS FROM MOMENT-LOADED BEARING

243
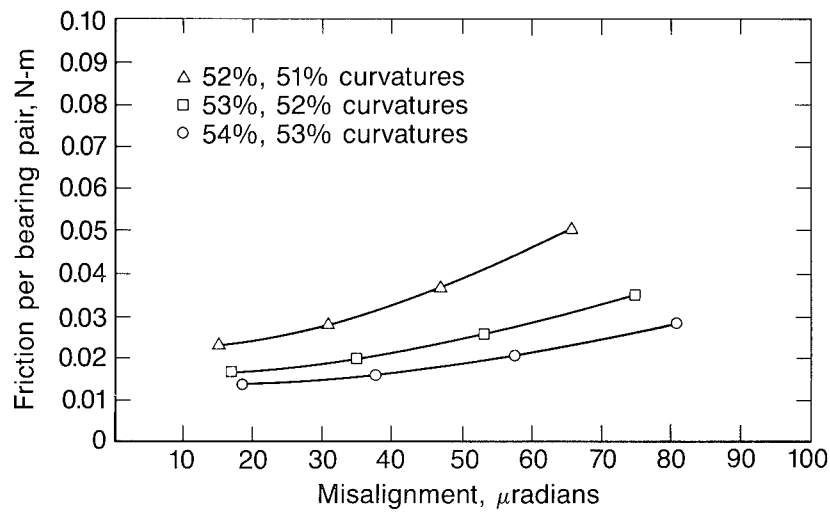
FIGURE B1. RACE CURVATURE EFFECTS
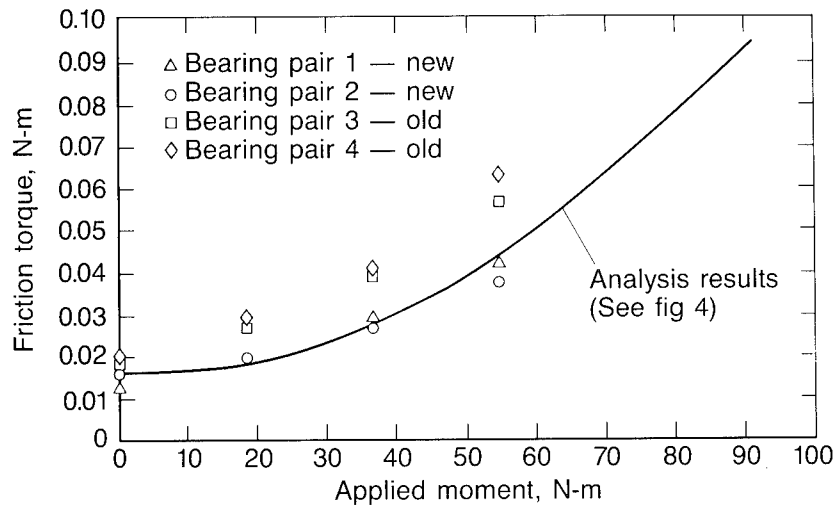
FIGURE C1. BEARINGS UNDER A MOMENT LOAD — TEST

TITANIUM CARBIDE COATINGS FOR AEROSPACE BALL BEARINGS

Hans J. Boving, Werner Haenni, Hans-E. Hintermann*

ABSTRACT

In conventional ball bearings, steel to steel contacts between the balls and the raceways are at the origin of microwelds which lead to material transfer, surface roughening, lubricant breakdown, and finally to a loss in the bearing performances.

To minimize the microwelding tendencies of the contacting partners it is necessary to modify their surface-materials; the solid to solid collisions themselves are difficult to avoid.

The use of titanium carbide-coated steel balls can bring spectacular improvements in the performances and lifetime of both oil-grease lubricated and oil-grease free bearings in a series of severe applications.

INTRODUCTION

In the age of space exploration many different kinds of bearings have been developped such as gas bearings, foil bearings, and magnetic bearings; each of these bearings excels in a specialized field of application. Ball bearings are not quite so limited and are encountered in a wide variety of applications. Recently, improved manufacturing techniques provide rolling bearings with increased accuracy and smoother surfaces; improved bearing-steel making processes provide higher quality steel, and improved fluid and dry lubrication techniques have served to considerably increase the bearing performances in most modern applications. Nevertheless, the useful lifetime of ball bearings remains strongly influenced by the roughness and tribological properties of the balls and races which are in rolling and sliding contact. Indeed, colliding surface peaks lead to cold weldings, material transfer, lubricant breakdown, and therefore to increased torque, noise and vibration levels.

Any surface modification of the contacting components which will result in smoother surfaces and/or in improved tribological properties will mean, for the ball bearing, not only a longer lifetime, but in some cases also increased performances.

This paper is concerned with the surface modification obtained by means of titanium carbide (TiC) coatings on AISI 440C steel balls. To avoid the direct steel to steel contact, it is in principle enough that the surface of

---

* Swiss Center for Electronics and Microtechnology, Inc., Neuchâtel, Switzerland

one of the two contacting components is modified: the balls or the races.

In order to provide the reader an overall view of bearing technology, which will provide him a better understanding of this paper, a series of mechanical, tribological and materials aspects are briefly described (ref. 1). Next, the deterioration of ball bearings for material-related reasons, and what can be done to avoid this type of deterioration, will be considered; e.g. surface modification by means of a TiC-deposit on the steel balls. Finally, the geometrical properties of TiC-coated steel balls will be examined and compared with uncoated steel balls.

The different components used in ball bearings are shown schematically in figure 1. Only the components taking an active part in the bearing operation are considered in this paper; these are the rings, the balls and the cage or ball retainer. In a ball bearing the following sliding and/or rolling contacts can take place: balls to races, balls to cage and cage to rings.
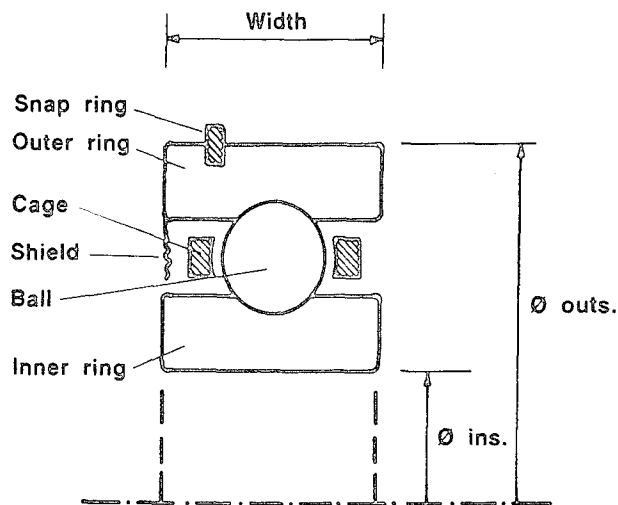
Figure 1. Schematic view of a section through a conventional ball bearing.

BALL BEARING

To assure a successful bearing application it is necessary to consider in detail aspects of different nature.

Mechanical Aspects

The mechanical design engineers are concerned with the bearing dimensions (∅ outs., ∅ ins., width: figure 1) because of optimum interface conditions with the corresponding mechanism. From tables provided by the bearing producers, they can read the static and dynamic load bearing capacities, which have to be compatible with the actual preloads and the loads seen in duty. Operating temperatures have to be examined carefully to evaluate their influence on the bearing loads through differential thermal expansions and gradients. In addition they will have to check if the bearing stiffness and elasticity correspond to what is required by the precision level of the mechanism.

Tribological Aspects

It is a well known fact that there is a rolling and sliding contact between the balls and the races. Although the rolling to sliding proportions are variable and influenced by the bearing geometry and load, it must be stated that the tribological properties of these components are important. Therefore for each specific bearing application, the design engineer has to make a decision as to what lubricant type is to be used (solid or fluid); this decision is influenced by the expected lubricant lifetime, by the static and dynamic torque values, and by the wear rates of the bearing components.

Materials Aspects

Conventional bearings are most often made of steel (balls and rings). Over 90% of the bearings produced are of 52100 steel; the remaining are made of special purpose steels such as T15 high speed steel or AISI 440C stainless steel. For most aerospace applications the stainless steel is used. The cage material can be metallic or organic depending on the bearing application and the lubricant type. The radial and axial loads seen by the bearings are transmitted by the actual ball to race contacts. Figure 2 shows a schematic view of a ball to race contact in the case of a conventional, lubricated bearing.
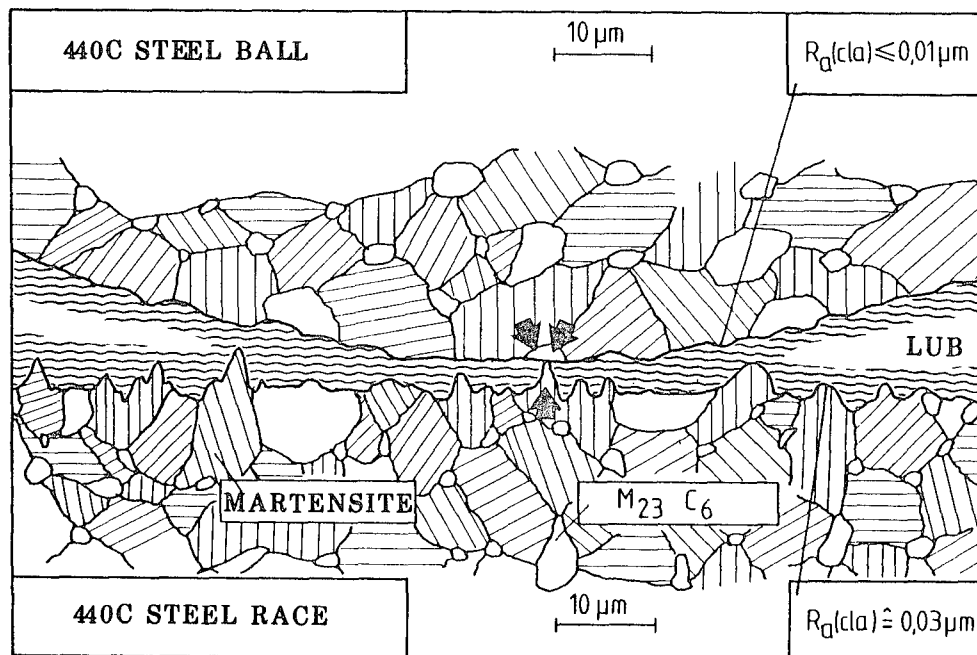
Figure 2. Typical presentation of a lubricated ball to race contact. The steel microstructure is on scale; the surface roughness and curvature scales are arbitrary. The race is approx. 3 times rougher than the ball. Despite the lubricant film, metal-to-metal contacts (microwelds) occur.

The purpose of the lubricant (solid or fluid) is to separate the contacting components and to ease their respective movement. Unfortunately peak to peak collisions do occur due to surface irregularities, to insufficient lubricant film thickness, to lubricant breakdown or to exaggerated momentary or continuous bearing loads. Whatever the reason of such peak to peak collisions, as shown in figure 2, their results are usually similar: microwelding between the steel ball and steel race surfaces. Due to the uninterrupted movement of the bearing the microweld has a very short lifetime and upon rupture there will be material transfer accompanied by a surface roughening. At the rupture site a hot spot is created which in its turn can cause damage to the lubricant by molecule cracking (ref. 2). The deterioration rate of the ball bearing is therefore strongly influenced by the frequency and intensities of the microwelds.

A good understanding of the exact reasons of bearing deterioration is of course very helpful when the useful lifetime has to be extended. It is difficult to completely avoid peak to peak collisions between the contacting surfaces. To minimize the microweld tendencies. one has therefore to work with the material choice. In other words the surface-materials have to be modified.

Modified Contacting Surfaces

The surface modification can basically be achieved in 2 different ways:

a) by using bulk materials of different nature. If the balls and/or races are made of ceramic materials like Si_3N_4 or SiC, their contacts will not lead to cold weldings as with steel to steel. The elastic properties of the ceramic materials are very different from those of steel; therefore the geometry of ceramic bearing components has to be adapted accordingly. Several authors have published papers on ceramic bearings and their performances (ref. 3,4).

b) by applying appropriate coatings on the surface of the contacting steel components. This solution has the advantage that the basic elastic properties of the steel bearing are not modified since the steel is still determining the load bearing capacity of the bearing; the geometry of the different components does not have to be modified.
   Dictated by the application, the engineer has a choice of organic and inorganic coatings, which are available on an industrial or development basis. Examples of coatings are: PTFE, Pb, Ag, TiC, BN, MoS_2, WSe_2, etc...

Figure 3 shows schematically a ball to race contact, when a TiC-coated ball is used. The race roughness is unchanged; TiC-coated balls, on the contrary, can be polished to an exceptionally smooth surface which is estimated at about 5 times better than the race surface. When peak to peak collisions do occur, there is no microwelding since TiC and steel have an insignificant welding tendency.

248
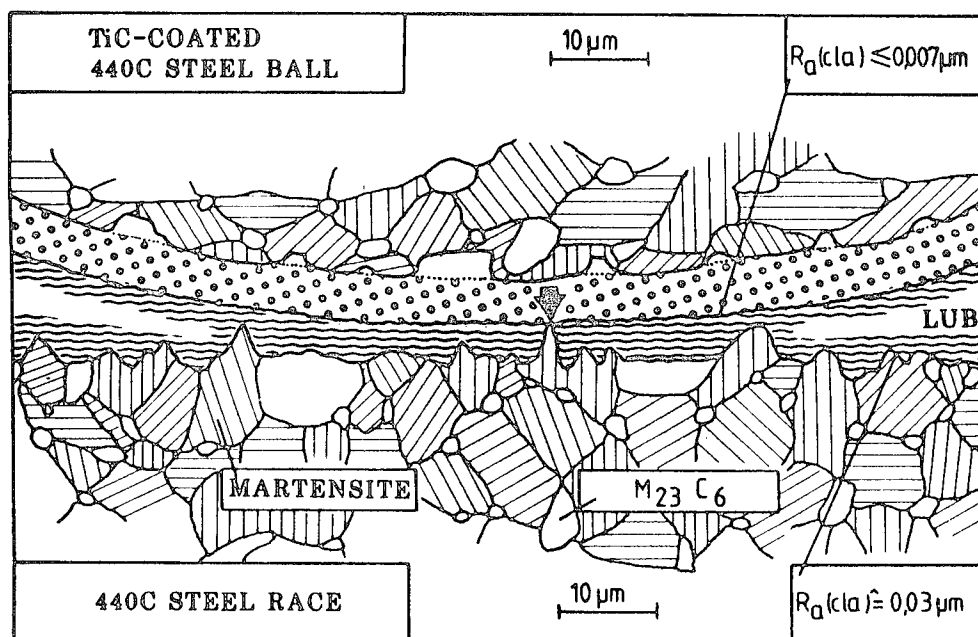
Figure 3: Typical presentation of a lubricated TiC-coated ball to race contact. The steel microstructure and the coating thickness are on scale; the surface roughness and curvature scales are arbitrary. The race is approx. 5 times rougher than the ball. Despite the lubricant film, solid-solid contacts (no microwelds!) occur.

TiC-COATED BALLS

The TiC-coated 440C steel balls are of precision GRADE 3 (according to AFBMA*), which is the highest precision grade used to specify metallic balls for ball bearings. GRADE 3 precision specifications concern the characteristics of both individual balls and ball lots. At this point the main interest lies with the degree of precision which is reached with the individual balls. It has indeed been observed that balls coming from one polishing lot are perfectly identical; no physico-mechanical instrument would be able to find noteworthy differences between two balls of one polishing lot.

Ten TiC-coated balls (3/32" diam.) are hereafter compared with 2 lots of ten uncoated GRADE 3 440C steel balls coming from 2 different producers; it will be seen that even within GRADE 3, important differences in quality exist between TiC-coated and uncoated balls.

---

* Anti-Friction Bearing Manufactures Association, Inc., Arlington, Va

Ball diameter and sphericity

The instrumentation which is currently used for the measurement of the ball diameter and sphericity allows verification that the balls of the 3 examined series indeed satisfy the GRADE 3 specifications. It is, however, difficult to observe notable differences between the coated and uncoated ball series. Therefore, these two aspects are not pursued any further.

Ball surface roughness

The surface roughness of the races and the balls has a strong influence on the useful lifetime of the ball bearing. Therefore, this geometrical characteristic will be given more attention.

The AFBMA standards specify the roughness of the balls; the roughness of the races, however, is not specified. In high precision bearings the race roughness is seldom below R_a = 0.025 μm (or cla = 1 millionth of one inch), which corresponds to the roughness allowed for GRADE 10 balls. Figure 4 shows the results of the R_a (cla) surface roughness measurements performed on 10 balls from each of the 3 series; the extreme and the average values are shown on the graph. It can be seen that although all 3 sets of data correspond to GRADE 3 precision, the TiC-coated balls have a much smoother surface and, in addition, their roughness values present a definitely smaller dispersion.
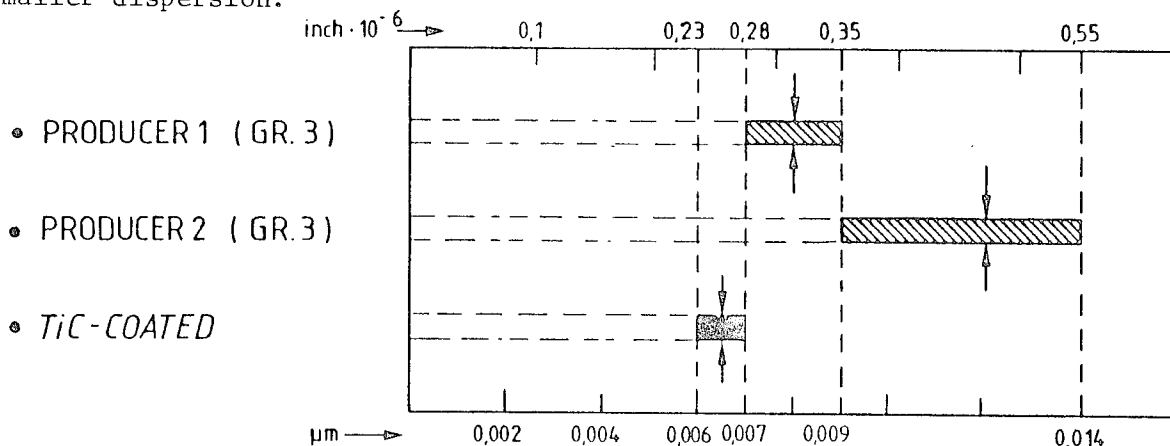
Figure 4: Comparison of the surface roughnesses (arithmetical average: R_a in μm or cla in millionth of an inch) of 3 series of ten 440C steel balls each – diameter 2.381 mm (3/32") – precision GRADE 3 (AFBMA); producer 1 and 2 correspond to uncoated balls. The arrows indicate for each series the average of the measurements on 10 different balls (the maximum allowable surface roughness corresponding to GRADE 3 is Ra = 0.014 μm).

APPLICATIONS

Due to the space environment and to contamination problems, it is often impossible to use conventional oil/grease-lubrication in ball bearings onboard spacecraft. In these and other bearing applications under hostile environments, the use of TiC-coated balls can assure the requested bearing

lifetime and performance. Space-related examples where TiC-coatings are used have been described in the literature: METEOSAT (ref. 5) and the SPACE TELESCOPE (ref. 6). Briscoe mentions in a review on lubricants for space, that TiC-coatings are frequently used to prevent fretting damage on highly loaded contacts in hold down and release mechanisms and latches on deployables (ref. 7).

It has been shown that especially in permanently oil/grease – lubricated bearings, the use of TiC-coatings increases notably the bearing performances. This is very much the case with bearings for spin axis gyro applications (ref. 8).

CONCLUSIONS

- CVD TiC-coated 440C steel balls can be lapped/polished to extremely high precision (better than GRADE 3 according to AFBMA).

- In oil/grease-lubricated bearings the use of TiC-coated steel balls presents two basic advantages:

  . the very low surface roughness of the coated balls; this leads to very low bearing vibration and noise levels

  . the TiC-modified surface avoids microwelds at the metal-to-metal contacts between balls and races; a consequence of this is that the lubricant remains in good condition.

- In oil/grease-free bearings the use of TiC-coated steel balls enables operation in extreme environments such as vacuum, elevated and cryogenic temperatures, etc. As a function of the requested duty cycle, the TiC-coated balls can be used as such or combined with a solid lubricant (e.g. MoS_2).

REFERENCES

1. Harris, T.A.: Rolling Bearing Analysis. John Wiley and Sons, Inc., 1984.

2. Baxter, B.H.: Chemical Processes Occuring in the Regions of Rubbing Contact in S 166 Bearings for Satellite Type Recorder Use, Proc. Int. Ball Bearings Conf., Charles Stark Draper Laboratory, 1973.

3. Hanson, R.A.: The Effect of Advanced Materials Technologies on Wear in Instrument Bearings. Proc. 1987 Ball Bearing Symposium, DoD/Instrument Bearing Working Group, Charles Stark Draper Laboratory, 1987.

4. Hamburg, G., Cowley, P., Valori, R.: Operation of an All-Ceramic Mainshaft Roller Bearing in a J-402 Gas Turbine Engine. Lub. Eng., 37 (7) 1981, 407-15.

5. Jouan, J.: ESA METEOSAT Radiometer Focalising Mechanism. Proc. 11th Aerospace Mechanisms Symp., NASA Conf. Publ. 2038, NASA GSFC, 1977, 13-22.

6. Veit, A., Chandler, D.P.: SPACE TELESCOPE Solar Array Primary Deployment Mechanism. Proc. First European Space Mechanisms and Tribology Symp., ESA SP-196, 1983, 27-34.

7. Briscoe, M.M.: Some Considerations on Lubricants for Use in Spacecraft, Proc. of Int. Symp. on Spacecraft Materials in Space Environments, ESA SP-178, 1982, 27-34.

8. Brown McKee, F.: Gyro Spin Axis Bearing Performance using Titanium Carbide Coated Balls. Proc. 1987 Ball Bearing Symposium, DoD/Instrument Bearing Working Group, Charles Stark Draper Laboratory, 1987

TWO GIMBAL BEARING CASE STUDIES:
SOME LESSONS LEARNED

Stuart H. Loewenthal*

ABSTRACT

In this investigation, two troublesome, torque related problems associated with gimbal actuators are discussed. Large, thin-section angular contact bearings can have a surprisingly high torque sensitivity to radial thermal gradients. A predictive thermal-mechanical bearing analysis, as described, was helpful in establishing a safe temperature operating envelope. In the second example, end-of-travel torque limits of an oscillatory gimbal bearing approached motor stall during limit cycling life tests. Bearing modifications required to restore acceptable torque performance are described. The lessons learned from these case studies should benefit designers of precision gimbals where similar bearing torque related problems are not uncommon.

INTRODUCTION

It is clear to the experienced space actuator designer that meager torque margins necessitate an accurate prediction of bearing drag torque. Furthermore, it is important that these torque levels remain stable with time.

Torque anomalies are among the most common problems for space mechanism bearings and among the most debilitating. This is because of the

- need to keep motor torque margins, hence motor weight, low.

- use of lightweight structural materials with coefficients of thermal expansion (CTEs) different than bearing steels and thus, sensitive to both thermal effects and thermally induced mechanical deflections.

- wide temperature ranges, often 100°C or more, both during qualification tests and in flight.

- likelihood of significant temperature gradients due to the difficulty of heat transfer and cooling within the mechanisms.

- extremely low operation speeds, typically 1 rev/hr or less, which pushes the bearing lubrication mode into the boundary regime, thus, amplifying both the magnitude of the friction coefficient and the uncertainty in its prediction.

This paper attempts to illuminate some of these special problems unique to space mechanism bearings by reviewing two not uncommon, torque related problems encountered on gimbals of different designs.

---

* Lockheed Missiles & Space Company, Inc., Sunnyvale, California

LARGE GIMBAL ACTUATOR

In the first example, the need to maintain the precise location of a high precision encoder under ascent loads necessitated a very stiff bearing mount for a Large Gimbal Actuator (LGA). Hard-preloaded, thin-section, duplex bearings (see Figures 1 and 2) were mounted
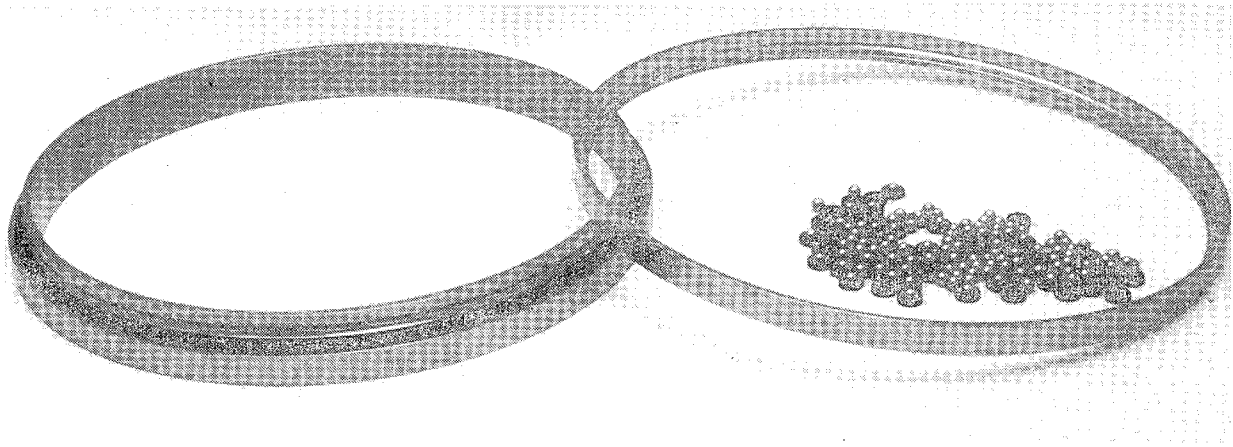

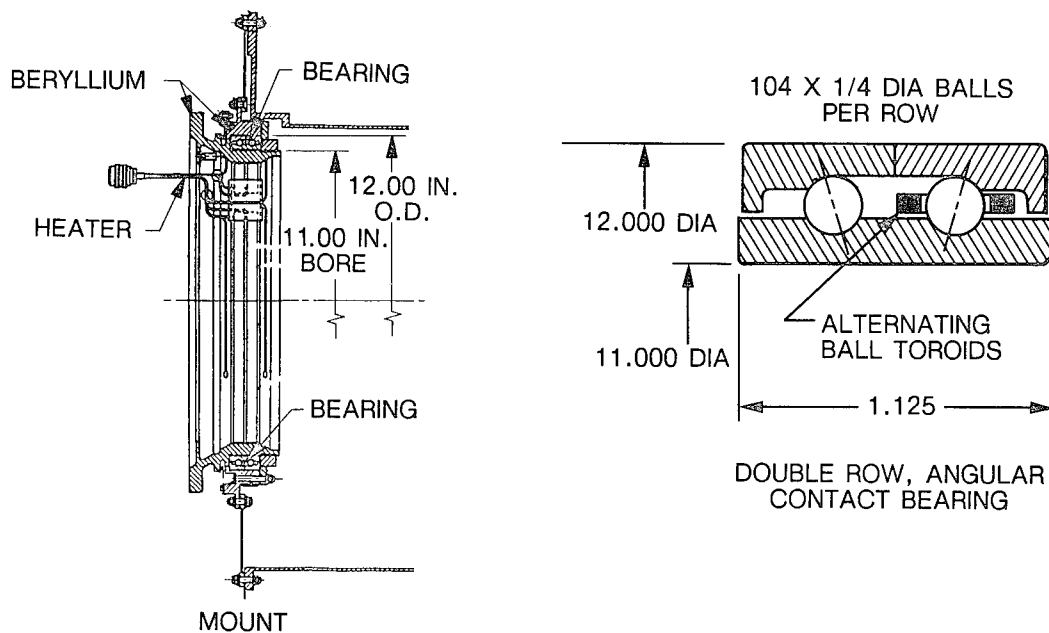**Fig. 1 Large Gimbal Actuator Bearing**

Fig. 2 Geometry of LGA Bearing and Mounting to Beryllium Structure

between a beryllium shaft and housing for maximum stiffness on both the yaw and pitch axes. Internal preload sensitivity, hence torque sensitivity of these bearings to temperature gradients was particularly great due to their hard mount. The coefficient (CTE) of thermal expansion disparity between the steel bearing races and the beryllium mounting structure in combination with the bearing's large size, also contributed to this sensitivity. The immediate concern was the effects that bulk temperature and radial thermal gradients may have on the magnitude of bearing preload and drag torque. Loss of significant bearing preload might permit a shift in encoder position, causing some count error while increased torque might exceed the bearing's allocated torque budget.

Thermal-Mechanical Bearing Analysis

The author found it more expedient to construct a special purpose thermal-mechanical bearing code to solve this class of problem than modify existing general purpose, commercial bearing codes. This also overcame the maximum 30/40 rolling-element limitation of these commercial codes and the need to scale the results to the 104 ball bearing at hand.

The developed program, BRGFIT, calculates the ball contact stresses, bearing displacements and stiffnesses of a thrust loaded, single or duplex angular or deep groove ball bearing. It accounts for the operating bulk temperature, temperature gradients across the bearing and either hollow or solid shafts and housings made of materials dissimilar to the bearing. Furthermore, it predicts bearing drag torque based on bearing internal geometry and user supplied friction coefficients.

The method of solution is based on Jone's bearing theory (reference [1]). The program first calculates the mounted contact angle and axial race displacements (bearing "stickout") for the given desired preload at room temperature and zero temperature gradient. The mounted contact angle is always less than the free contact angle for an interference fit between the inner race and the shaft or between the outer race and housing, due to a reduction in diametral internal clearance. The relationship between the mounted contact angle β_o and the free contact angle β is given by:

$$\cos(\beta_o) = \cos(\beta) + P_D*/2Ad \qquad (1)$$

where

P_D* = reduction in diametral clearance due to press fit or due to a thermal gradient where $T_{i/r} > T_{o/r}$

A = (inner race conformity + outer race conformity -1)

d = ball diameter

The reduction in diametral clearance term P_D* is not directly equal to the race interference fit. It must account for the relative-contraction of the hollow shaft under interference pressure and/or the relative expansion of the hollow housing. Both tend to mitigate the magnitude of the interference fit passed on to the bearing.

Next, the bearing is taken to operating temperatures with the specified temperature difference between the inner and outer race. If the inner race temperature is increased relative to the outer race then the internal preload within the bearing is increased since the races are rigidly clamped in the axial direction. The program iteratively solves for the internal preload and race axial deflection

based on the radial deflection of the shaft/inner race and housing/outer race under changing internal ball load. Axial stiffness (or spring rate) is taken as the derivative of the force-deflection curve at the preload point.

Thermal Effects

The effect of radial thermal gradients on LGA bearing internal preload and contact stress can be significant, as shown in Figure 3. This is because the bearing is large (280 mm [11 inch] bore diameter), the Hertzian deformations are small due to the small balls, and the races are rigidly clamped in the axial direction. A relative modest 5.6°C (10°F) increase in inner race temperature will raise the internal preload from 1100 N (250 lbs) with a nominal race fit to well over 4400 N (1000 lbs). This, of course, will also increase bearing drag torque, as will be discussed later.
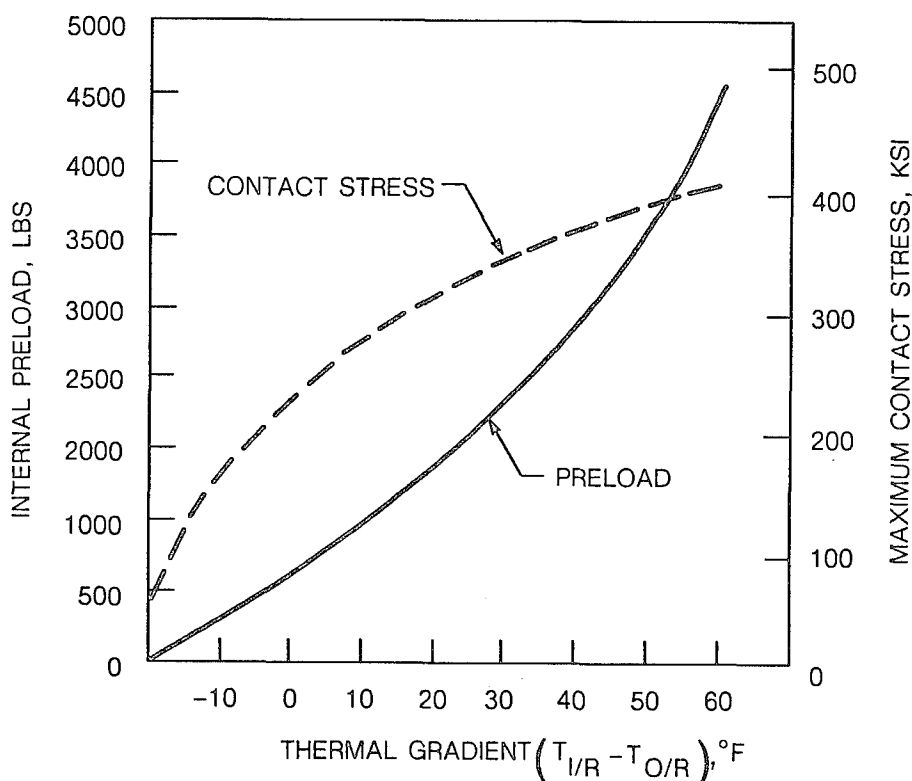
Fig. 3 Effect of Thermal Gradient on Bearing Internal Preload and Contact Stress (Race fits = 0.0002 inch Interference)

The bulk temperature effect is not as dramatic. This is illustrated in Figure 4, which shows the "safe" temperature operating region for the LGA bearings. The beryllium shaft and housing have a slightly larger CTE (by 7×10^{-7} in/in °F) than the stainless steel bearing. As the bulk temperature increases, the housing expands faster than the outer race, creating a potential gap as illustrated by the upper right boundary in Figure 4. This gapping will take place at a higher temperature than one might initially expect, since the outer race will mechanically expand as the support containment of the housing is removed. Thus, the outer race will try to "catch" the expanding housing until the bearing internal preload has dropped completely to zero. At this point, the bearing has become unloaded as defined by the right most boundary in Figure 4.
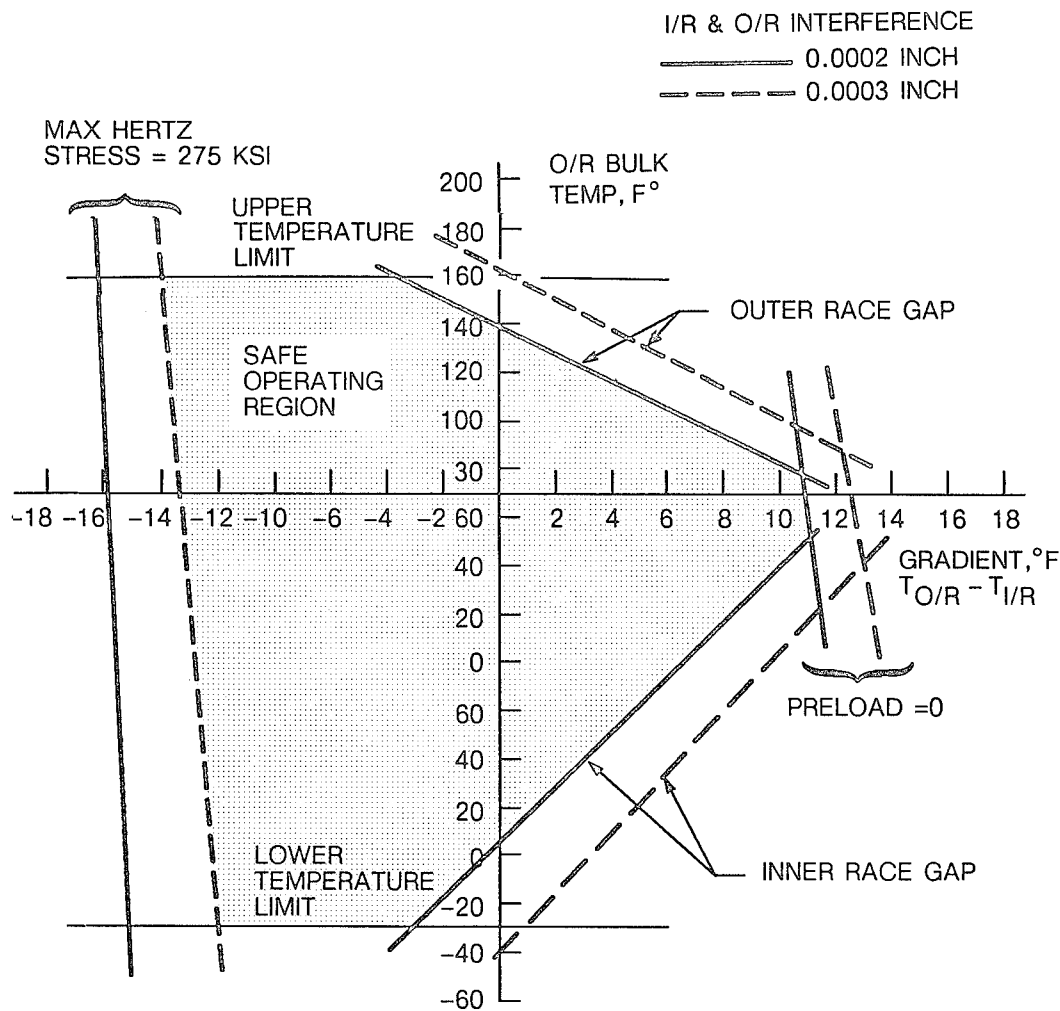
Fig. 4   Bearing Predicted Safe Temperature Operating Region

At cold temperature, the beryllium shaft contracts faster than the steel inner race and a similar gap at the inner race can occur. The upper and lower operation temperature limits for the LGA naturally bound these temperature excursions.

On the other hand, if the inner race is expanding faster than the outer race, the internal preload will increase, as mentioned. There reaches a point where the ball/race contact stresses become unacceptably high as indicated by the left boundary in Figure 4. Thus, all of the above constraints form a thermal operating window that the bearing must operate within.

Drag Torque

Perhaps the most sensitive (and most difficult to predict) parameter to thermal effects is the bearing drag torque. The analysis, due to Jones [2], considers the "scrubbing" friction between the balls and the sides of the tightly conforming raceway ("Heathcoate" slip). It also considers the "spin" friction due to circumferential slip within the contact due to the angular contact between the

ball and the race. *(The origins and implications of spin friction will be covered in greater depth in the second part of this paper.)* This analysis is quite rigorous and has been omitted here but can be found in reference [2].

Applying the thermal analysis to arrive at internal ball loads and using the torque analysis, as described, provides a prediction of the LGA bearing's drag torque as a function of temperature gradient as shown in Figure 5. Test data from our bearings have been included for comparison. A prerequisite for all bearing torque analysis is knowledge about the operating sliding coefficient of friction between the ball and race. For this analysis, the sliding friction coefficient was selected to be 0.15, which turns out to provide acceptable results. If room temperature bearing torque results are available beforehand, which wasn't the case here, the friction coefficient can then be adjusted to give proper torque predictions at different thermal conditions.
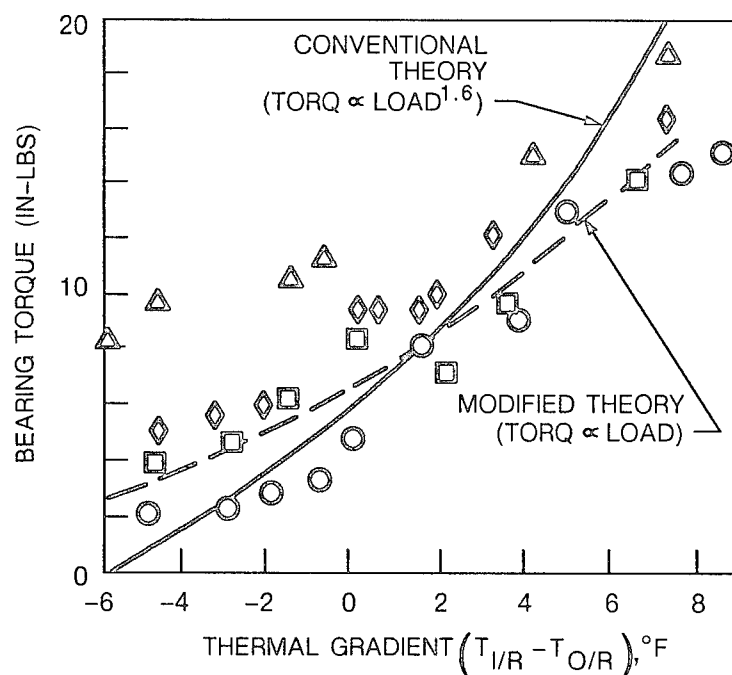
Fig. 5 Comparison Between Predicted and Measured Torque

Two predictive lines appear in Figure 5. The one labelled conventional theory makes use of the Jones method in which torque is proportional to the 1.6 power of load. This exponent considers that not only that the friction forces increase directly with the load, but that the rolling friction and spinning friction are also proportional to the load-expanded contact area as well. One can see from Figure 5 that conventional theory tends to overpredict the torque sensitivity to thermal gradient, although the general magnitude agreement is reasonable. Other low speed, large bore diameter angular contact bearing torque data in the open literature (for example, see references [3] and [4]) also show significantly lower torque sensitivity to thrust load than predicted by conventional theory. In reference [3], Burgmeier measured torque load exponents on the order of 0.7 to 1.0 for a thin-section bearing of similar size to the LGA bearing. Using a relationship that torque is directly proportional to load, indicated by the modified theory line in Figure 5, gives much better trend agreement than before.

Lessons Learned

The torque sensitivity of the LGA bearing to thermal gradients is quite large,as evidencedby the torque doubling in just a 3.3°C (6°F) change, as shown by the data of Figure 5. *In contrast, only a 10% torque change resulted from more than a 63°C (100°F) change in bulk operating temperature [not shown]).* This exceptional torque sensitivity to thermal gradients is a consequence of the bearing's large bore and thin section and the need to rigidly clamp the bearing to ensure encoder position. While wavy spring washers or Belleville springs are often used to decrease thermal sensitivity, axial stiffness is compromised and the position of a position-critical sensor, as in this case, cannot be guaranteed. To insure positive torque margins throughout the flight envelope with a hard mounted bearing, it may be necessary to thermally manage bearing race temperature via active heater control. Such was the case for the LGA bearings (see the heater element in Figure 2).

SPACE TELESCOPE GIMBAL BEARINGS

The Hubble Space Telescope will be the largest and most powerful astronomical instrument ever placed in orbit. It will allow cosmologists to view objects 14 billion light-years away. These targets can be tracked with a pointing stability of 0.007 arc-seconds provided by four reaction wheels which comprise the Pointing Control System (PSC). Ground station communication, via the satellite TDRS, is by way of low gain antennas mounted on the aft shroud and a pair of high gain antennas mounted on the forward shell as shown in Figure 6.

Two High Gain Antenna (HGA) drives, pictured in Figure 7, are cross-mounted to provide pitch and yaw positioning over a hemispherical field of view in excess of 180 degrees. The gimbal contains redundant torque motors and resolvers together with appropriate electrical and data transfer devices.

HIGH GAIN
ANTENNA
GIMBAL
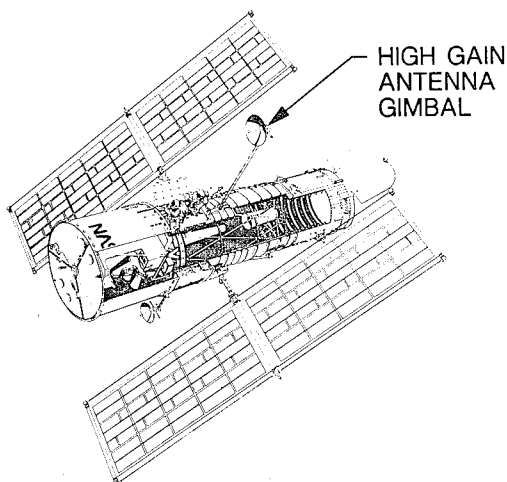
Fig. 6 Hubble Space Telescope Two Axis Gimbal
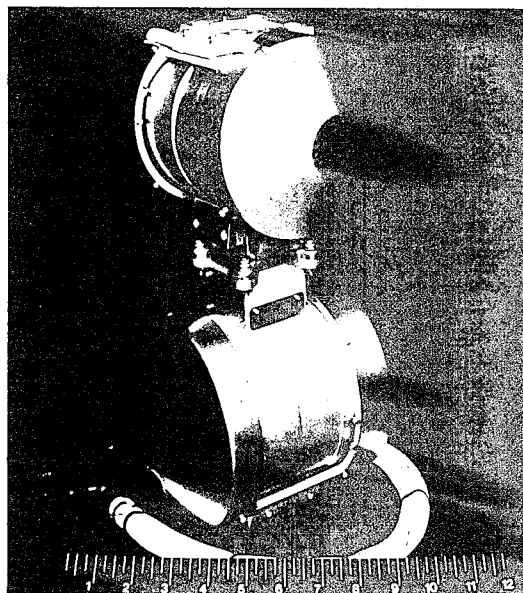
Fig. 7 High Gain Antenna Drive

Bearings - The HGA gimbal is supported by a hard preloaded, pair of A541 size, duplex angular contact ball bearings face-to-face mounted. They contained 24 balls of 3.18mm (0.125 inch) diameter, having an inner and outer race conformity of 51.8%. The one-piece, inner land riding, phenolic, laminated cage and balls were lubricated with a Kendal super refined mineral oil, KG-80.

Torque Anomaly

During life tests under repeated limit-to-limit cycling, the gimbal drag torque increased precipitously from a nominal 14 N-mm (2 in-oz) to as high as 127 N-mm (18 in-oz). This drag approached the stall torque of the motor. There were several curious aspects to this problem. The
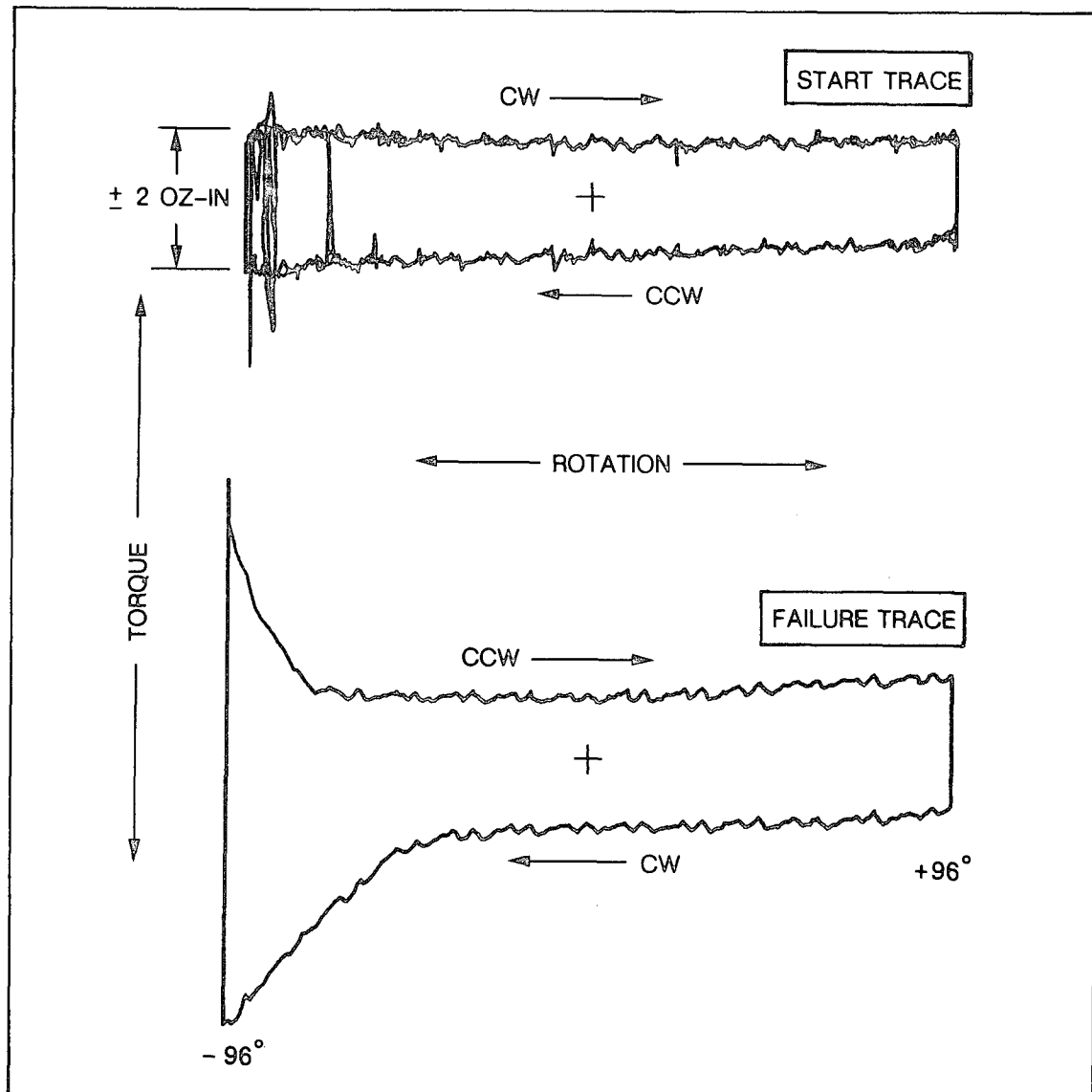
Fig. 8 Bearing Torque Signature at Failure

260

anomalous drag torque always took some operating time to develop, from a few hours to a few weeks at the 0.5 deg/sec cycling rate. The highest torques only occurred at the end-of-travel reversal point. The torque trace always assumed a characteristic saddle-shape that could be symmetric, but was more often nonsymmetric, as shown in Figure 8. Tapping and/or inverting the gimbal caused the torque to temporarily disappear, but it would eventually return. Finally, torque anomalies were observed with all six of the HGA gimbals, even though their design was essentially identical to an earlier gimbal which exhibited no such problem.

The Possibilities

The only possible contacting sources of drag were the flex capsule which contains contacting flex tape wraps and the bearings. Eliminating the flex capsule from the gimbal did not resolve the problem, so the bearings were the prime suspect. The fact that the high torques occurred only at the end of travel and only after many cycles of operation were the two biggest mysteries.

Ball Speed Variation - One hypothesis was that the phenomena often referred to as "cage wind up" was occurring. This refers to the cage pinching forces that can occur when individual balls are orbiting at different speeds due to small variations in contact angle or ball size. This *ball speed variation* (BSV) and its effects on cage loading, have been known for sometime as discussed in detail by Barrish [5]. The most common cause of BSV is due to misalignment as illustrated in Figure 9 from reference [5]. The inner race contact pattern shows that the balls at the top of the bearing must move faster to cover a greater circumferential distance in the same period of time as that of the bottom balls which have a shorter distance to travel. Thus, the balls advance or retard from the average speed and can "squeeze" the cage's ball pockets, increasing drag. Under severe loading conditions, excessive BSV have been observed to cause rapid cage failure.

CONTACT PATTERN DUE
TO MISALIGNMENT
(NOTE CHANGE IN CONTACT ANGLE)

BALL SPEED VARIATION
CAGE "WIND UP"
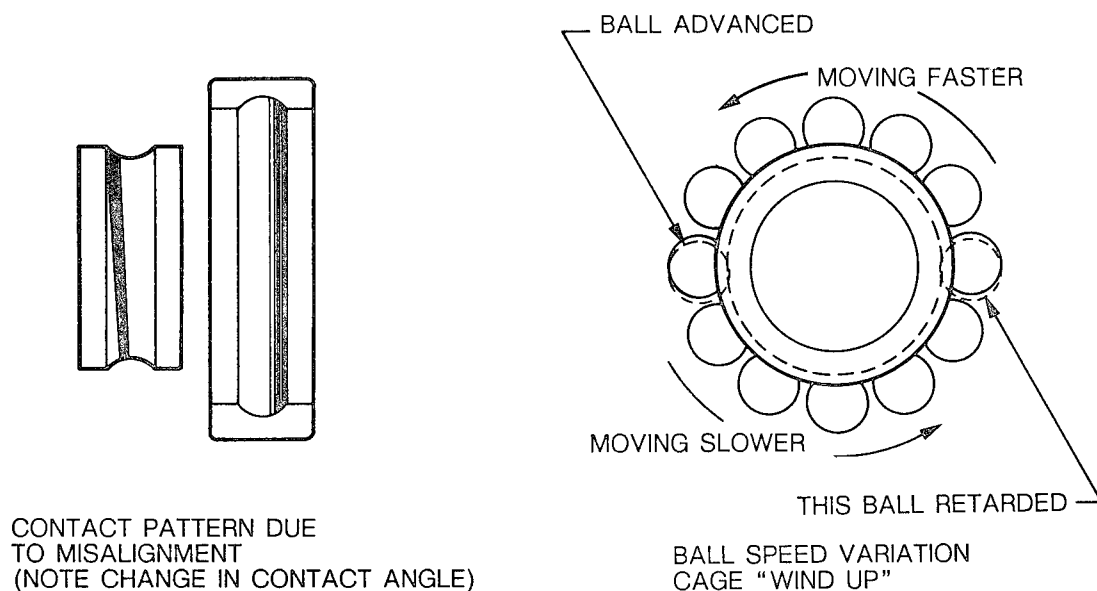
Fig. 9 Effect of Misalignment on Cage-Windup

In an oscillatory bearing, as described here, the distance errors between the balls and hence, the severity of the cage loading ("wind up") would increase with rotation, reach a maximum at

end-of-travel, and then decrease as rotation is reversed. This tends to explain the saddle-shaped torque trace that was observed. Furthermore, this torque buildup due to BSV would be more severe with: (a) a one-piece cage rather than individual toroids or spring separators; (b) low speed, boundary friction rather than the much lower friction which accompanies elastohydrodynamic lubrication; and (c) thrust bearings where all the balls are always loaded rather than a radially loaded bearing where ball spacing can freely adjust in the unloaded zone. The fact that all of these conditions were present with the HGA bearings suggests that BSV is at least a major contributing factor.

A common approach to minimize BSV is to use alternating toroid ball separators to permit the balls to more freely adjust their spacing. A switch was then made from the baseline one-piece phenolic cage to ball toroids as shown in Figure 10. While this change eliminated the "runaway" torque at end-of-travel, drag torque continued to increase over time by about 60%, on the average.
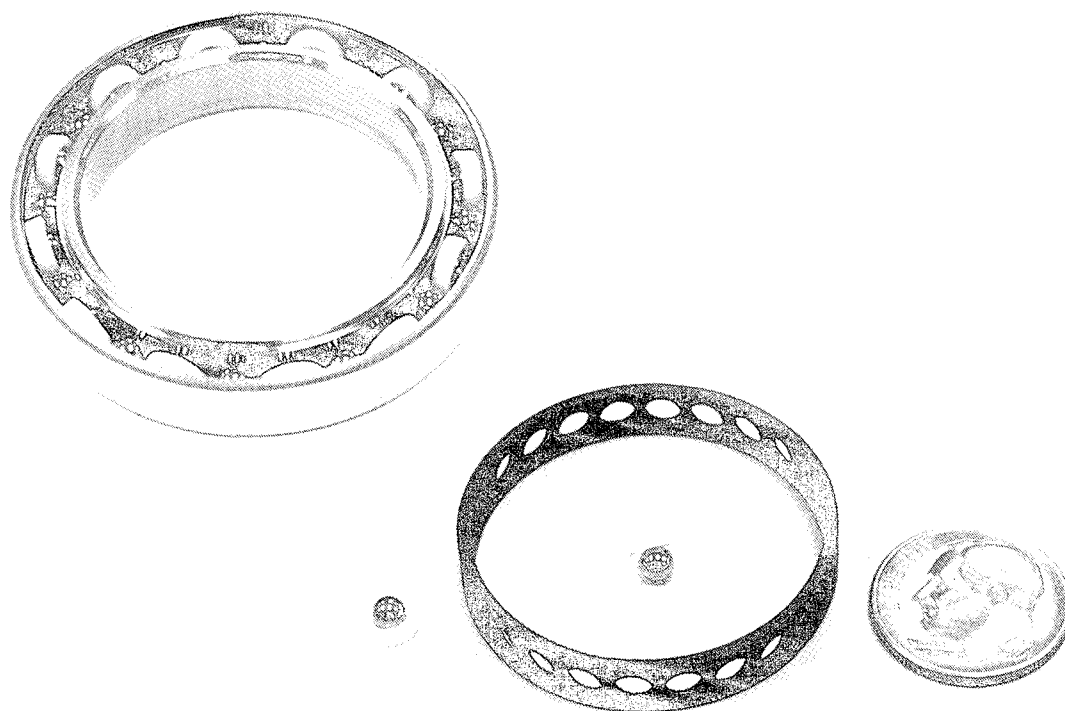
Fig. 10 Comparison of Toroid Ball Separator with Baseline Phenolic Cage

Blocking - Another possible source contributing to the torque anomaly is the effect of contact spin. The European Space Tribology Laboratory (ESTL) reported [6] progressive torque increases with hard-preloaded pairs of ball bearings that were oscillated over an arc of 90 degrees. ESTL referred to this phenomena, which bears a strong resemblance to that observed here, as blocking. One of the mechanisms attributed to cause blocking was Ball Speed Variation, as just discussed. In the ESTL tests, blocking occurred with the "tight" (51.8%) conformity bearing under significant preload (200 N) but was never observed with the "loose" (57%) conformity bearing, otherwise of identical in geometry [6]. It so happens that the HGA gimbal bearings had

the identical "tight" (51.8%) conformity as the ESTL bearings where "tight" and "loose" conformity is illustrated in Figure 11. The second explanation offered by ESTL for *blocking* was due to transverse ball creep, a phenomena first investigated by Prof. Ken Johnson [7].

OPEN   TIGHT

$$\text{CONFORMITY} = \frac{\text{RACE RADIUS}}{\text{BALL DIAMETER}}$$
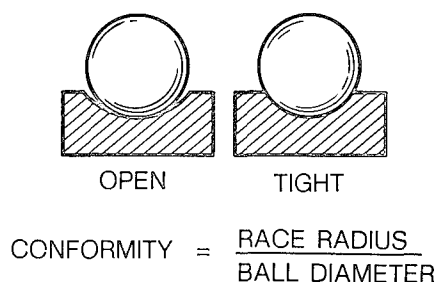
Fig. 11 Bearing Race Conformity

In Prof. Johnson's now-classic experiment with a simple counter rotating thrust bearing, (see Figure 12), the balls were observed to advance radially outward a small amount each revolution. This occurred at extremely slow velocities where centrifugal force effects were negligible. The explanation offered by Prof. Johnson was that circumferential slip *(spin)* velocities normal to the contact produced surface tractions predominantly in the rear of the contact which give rise to transverse ball creep. Thus, the ball radially creeps outward up the groove until, after a few revolutions, the outward *spin* transverse creep force is balanced by the inward axial component of the contact force, as shown in Figure 12. It is this same phenomena which causes a spinning and rolling bowling ball to "hook" into the pins.
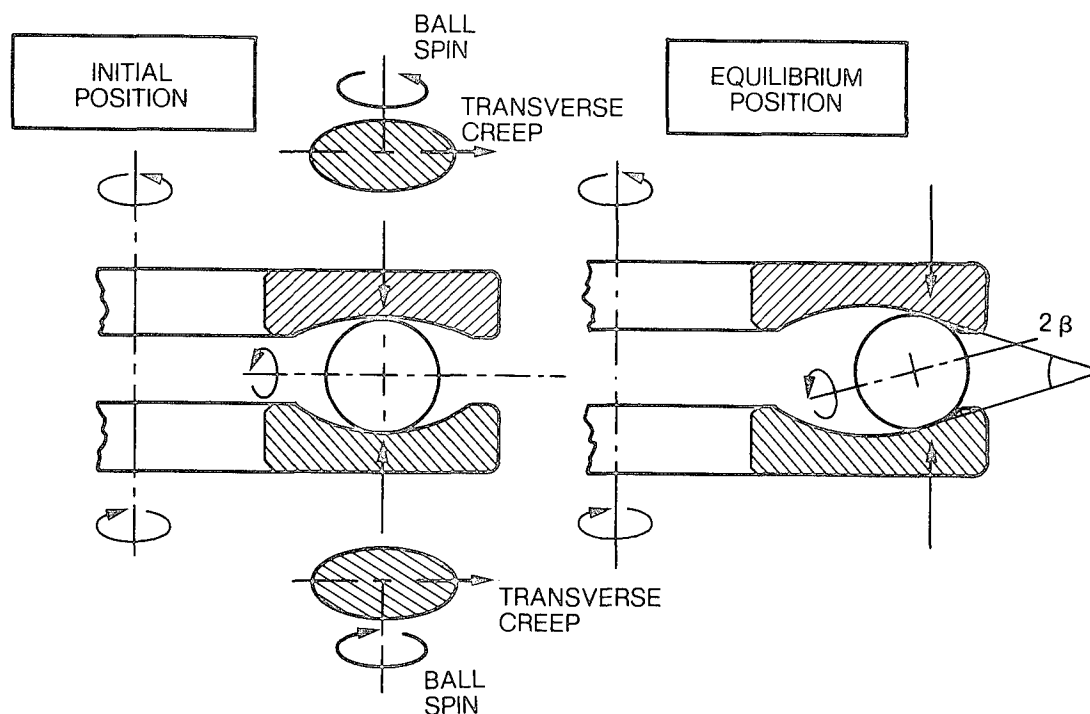
Fig. 12 K.L. Johnson's Spin Experiment with Ball Thrust Bearing

263

Spin and Stress Analysis - At first blush, transverse creep appeared to be a plausible explanation for the time-buildup of torque as the balls attempted to climb the race with time, thereby increasing the contact angle. However, a question still remained as to how large a transverse creep force would be generated and how much more open must bearing conformity be made to eliminate or minimize this *blocking* phenomena. A real concern was that the ball/race contact stresses at liftoff would exceed recommended limits if %-conformity had to be greatly increased (made looser).

A contact stress calculation, using a large general purpose bearing code, indicated that conformity could be safely increased from the baseline 51.8% to 54% under the "worst case" combination of gimbal loads at liftoff. Next a *spin* analysis was conducted.

The spin velocities at each contact, as shown in Figure 13, were calculated according to the methods of reference [7]. These spin velocities are due to the presence of a higher velocity at the upper edge of the contact than the lower one, as illustrated by the vectors in Figure 13. The contact spin engenders transverse creep forces which tend to increase the contact angle with time as shown. The increase in contact angle would aggravate the situation further since the spin velocity is proportional to the sine of the contact angle. It is unclear what resulting ball motion would occur with time, except there would be a tendency for the ball to spiral upward as it rolled along the race. However, it is instructive to note that the direction of the transverse creep force will be the same even if the bearing rotation is reversed. This illustrated in Figure 14 in which the ball rolling rearward is experiencing a hook from a "right-handed" bowler while the ball rolling into the foreground is experiencing a hook from a "left-handed" bowler. This unidirectionality would tend to support the monotomically increasing torque observed with the HGA gimbal bearings as they rotated back and forth between limits.
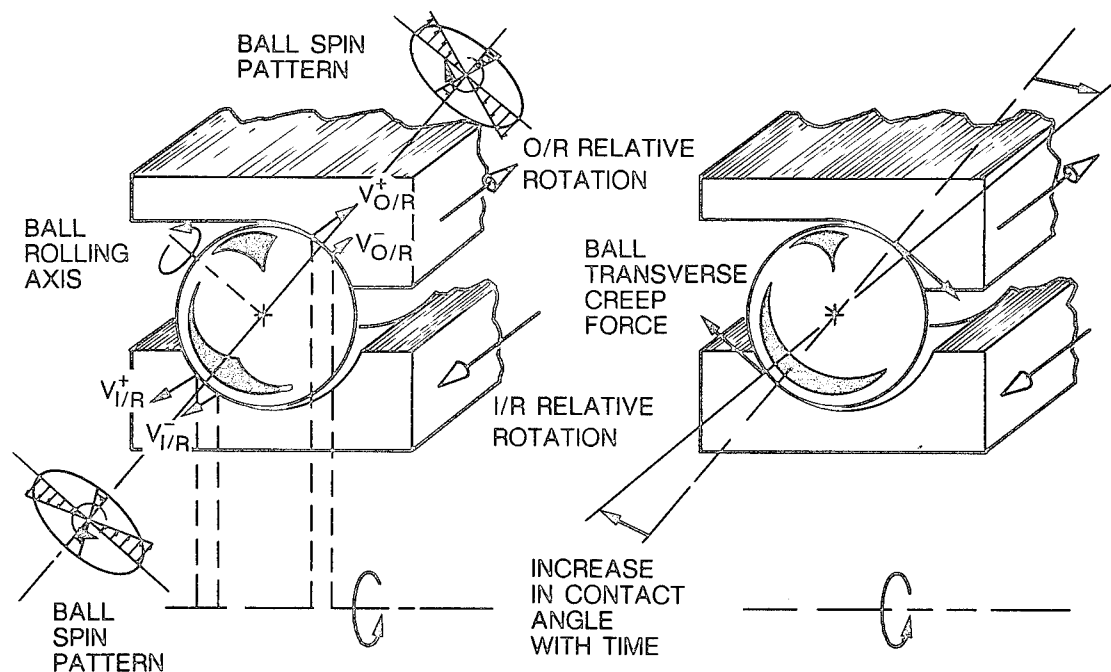
Fig. 13. Spin Generated Transverse Creep Force

264
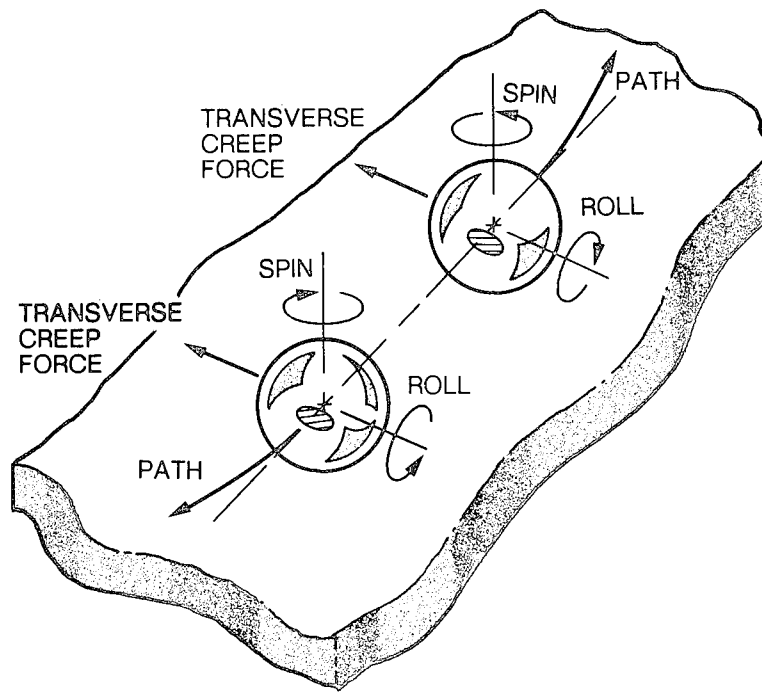
Fig. 14 Transverse Creep Unaffected by Rolling Direction

A proper analysis of these effects would require a time dependent individual ball/race motion analysis under the presence of misalignment. To simplify this sort of full-up analysis, a quasi-steady analysis was performed under uniform axial loading ignoring the effects of misalignment. The analysis is based on the constitutive traction equations of Johnson and Tevaarwerk [8]. Briefly, the *J&T theory* considers the lubricant film in the contact to behave elastically at low strain rates, until the shear stress reaches some limiting value. At this point, the film shears like a plastic material. Their constitutive model relates shear strain and shear strain rate at each point within the contact to the local shear stress (traction force). By integrating these local traction forces across the contact, the net traction force in the direction of rolling, as well as in the transverse direction, can then be computed.

In the case of the HGA bearings, it was necessary to estimate the shear modulus and limiting shear strength of the KG-80 oil film from property data of similar lubricants. Figure 15 summarizes the results of this analysis for different levels of race conformity. The spin torque is a measure of the torque normal to the contact (twisting force). The drag torque considers the combined effects of the spin torque and rolling torque (Heathcoate slip) as discussed in the first *case study*.

As expected, increasing %-conformity, reduced both spin torque and drag torque at the expense of increased contact stress. At 54% conformity, which provides an acceptable contact stress at launch, the predicted spin torque is 45% less and the predicted drag torque is 39% less, than the 51.8% conformity, baseline bearing. The measured torque reduction of a corresponding test bearing was even greater than these predicted values. This data, spotted on Figure 15 for comparison, shows that the drag torque reduction for the 53% inner race/54% outer race test bearing was larger for the ball toroid separators than the one-piece cage. This %-reduction is relative to the baseline bearing's starting torque. However, it is clear that a relatively subtle

increase in the race's transverse groove radii, on the order of 0.05 mm (.002 in), has a profound effect on bearing drag.
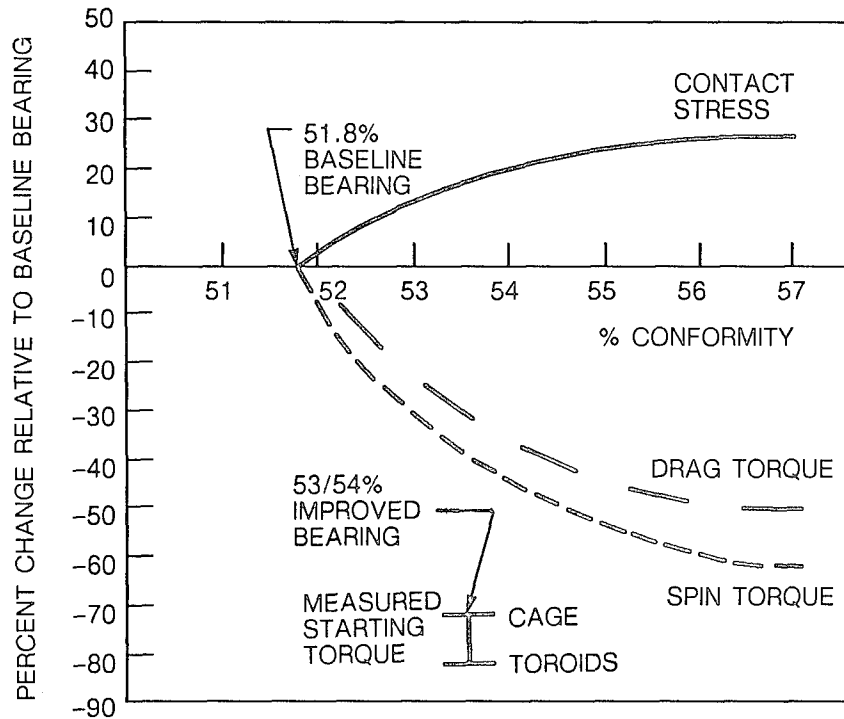
Fig. 15 Predicted Effect of Conformity on Bearing Stress and Friction

Test Results - This dramatic improvement in the torque characteristics of the HGA bearing from the seemingly small increase in %-conformity is readily apparent in Figure 16. In fact, the improvement is even more dramatic when one looks back at the baseline torque failure trace, appearing in Figure 8, rather than the intermediate trace of Figure 16 (a).

The flat trace in Figure 16 (b) shows that the switch to the toroidal separators at the baseline 51.8% conformity definitely got rid of the cage wind-up problem due to BSV. However, as Figure 17 shows, the ball toroids by themselves did not prevent the drag torque from escalating with cycling by about 60% over the starting levels. This cycle effect was hypothesized to be the result of spin generated, transverse ball creep which increases the ball's tendency to climb the shoulder.

It is clear from both Figures 16 and 17, that the dominant factor is the loosening of bearing conformity. The looser bearings not only have flat, small torque traces, but they are also far less sensitive to cycling (25 to 35% torque rise), *no matter what the cage*. This is not totally in concert with the spin analysis, which predicted that although there would be a substantial reduction in the spin torque with a looser conformity, as observed, the transverse creep force would actually increase by about 15%. If this is so, the cycle dependent torque due to transverse creep should be more noticeable. Despite this quirk, predicted gimbal bearing pair torque levels of 1.0 N-mm (0.65 oz-in) compare reasonably well with the measured 0.8 N-mm and 1.3 N-mm (0.5 oz-in and 0.8 oz-in) for the toroid and phenolic cage bearings, respectively.

266
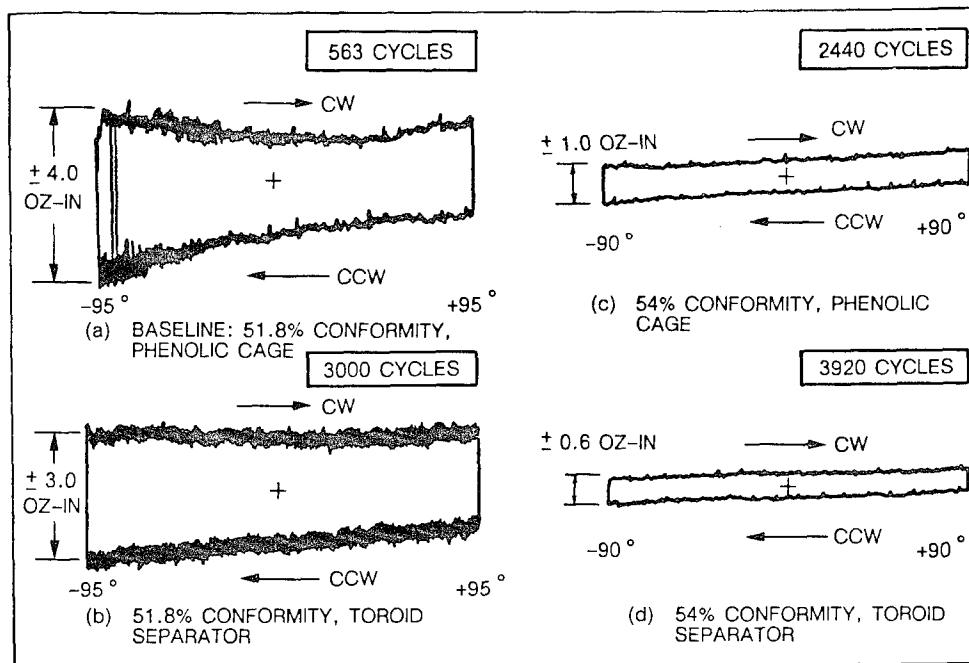
Fig. 16 Gimbal Bearing Torque Trace Summary
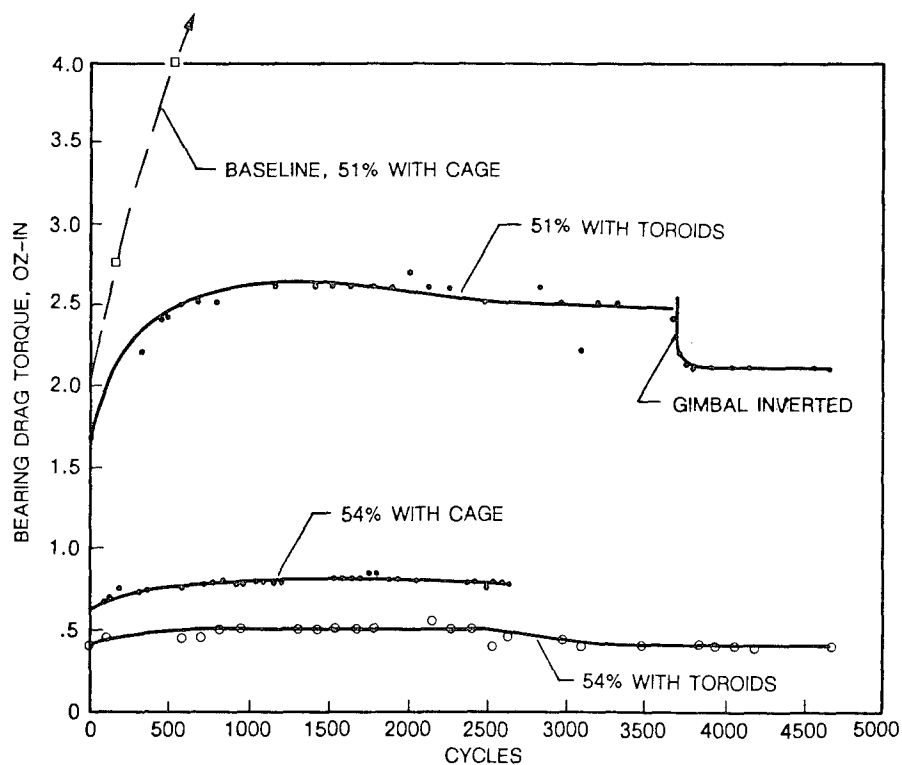
Fig. 17 Effect of Cycles on Bearing Drag Torque

Lessons Learned

The *blocking* torque anomaly was best combatted by increasing %-conformity, although switching to individual ball toroids did tend to lessen cage wind-up. The physical mechanisms responsible for blocking have not been conclusively identified. However, *ball speed variation* does provide a plausible explanation for the high end-of-travel torque. *Transverse ball creep due to spin* appears to be connected with the observed torque/time dependency, although this connection is still a bit illusive at this point.

TABLE I - FACTORS TENDING TO INCREASE BLOCKING

FACTOR INCREASED	EFFECT
• CONFORMITY (TIGHTER)	INCREASES SPIN - HIGHER SPIN TORQUE & DRAG
• CONTACT ANGLE	INCREASES SPIN - HIGHER SPIN TORQUE & DRAG
• ONE-PIECE CAGE	RESTRICTS BALL SPEED SPACING - INCREASES CAGE "WIND-UP"
• MISALIGNMENT	INCREASES BALL SPEED VARIATION - INCREASES "CAGE WIND-UP"
• PRELOAD	INCREASES TRACTION FORCES - INCREASES ANOMOLOUS TORQUE
• FRICTION COEFFICIENT	INCREASES TRACTION FORCES - INCREASES ANOMOLOUS TORQUE
• CONTACT ANGLE VARIATION	INCREASES BALL SPEED VARIATION
• BALL DIAMETER TOLERANCE	INCREASES BALL SPEED VARIATION
• THRUST VS. RADIAL BEARING	THRUST BEARING HAS ALL BALLS LOADED - NO OPPORTUNITY FOR BALL SPACING TO READJUST

Encountering the *blocking* phenomena for a gimbal bearing can be most disconcerting at any time, but particularly late in a flight program. Table I lists many of the likely factors that can contribute to either BSV and/or cage wind-up. They represent sort of a qualitative checklist on how to skirt *blocking*. The last item in the table points to the observation that *blocking* is not often observed in radially loaded bearings or those with a predominant radial load. Apparently, the balls traveling into the unloaded zone have a chance to relax their contact with the ball cage pocket. Perhaps a similar relaxation occurred with the HGA bearings when either tapping or inverting the gimbal temporarily restored lower torque levels.

SUMMARY AND CONCLUSIONS

This investigation focussed on two subtle, but not uncommon, torque problems that can be encountered with spacecraft gimbal bearings. The first example illustrated the surprisingly high torque - thermal sensitivity of a hard preloaded, thin section bearing. A thermal bearing performance code was useful in establishing the acceptable operating temperature envelope. Active heater control was then used to manage bearing torques.

In the second case study, a *blocking* torque anomaly was encountered with oscillatory gimbal bearings during life cycling tests. The remedy was slightly opening the race conformity and switching to alternating ball toroid separators. Bearing analysis, again, was illustrative in assessing the relative options to combat this problem.

REFERENCES

1. A. B. Jones, *Analysis of Stresses and Deflections*, New Departure Engineering Data, Bristol Conn., 1946

2. A. B. Jones, "The Mathematical Theory of Rolling-Element Bearings", Section 13, *Mechanical Design & Systems Handbook*, Rothbart editor, 1st Edition, 1964

3. L. Burgmeier, "Predicting Bearing Torque In Large-Diameter, Thin-Section Bearings", *Machine Design*, Jan. 29, 1964, pp. 118-124

4. W. Ward, "Evaluation of a 90 MM Bore Bearing in a Simulated Space Environment", *ASME J. of Lub. Tech.*, Vol. 40, No. 5, May 1984, pp. 290-298

5 T. Barrish, "Ball Speed Variation in Ball Bearings", *ASLE Lubrication Engineering*, March 1969, pp. 110-116

6. M. J. Todd, "Investigation of Torque Anomaly in Oscillating PDM Bearings", *European Space Agency (ESTL)* Report No. 49, May 1981

7. S. H. Loewenthal, "Spin Analysis of Concentrated Traction Contacts", *ASME J. of Mechanisms, Transmissions, and Automation in Design,* Vol. 108, March 1986, pp. 77-85

8. K. L. Johnson and J. L. Tevaarwerk, "Shear Behavior of Elastohydrodynamic Oil Films", *Proc. Royal Society*, London A, Vol. 356, No. 1685, Aug. 24, 1977, pp. 215-236

SPACE STATION MOBILE TRANSPORTER

James Renshall,* Geoff W. Marks,* Grant L. Young*

ABSTRACT

The first quarter of the next century will see an operational Space Station that will provide a permanently manned base for satellite servicing, multiple strategic scientific and commercial payload deployment, and Orbital Maneuvering Vehicle/Orbital Transfer Vehicle (OMV/OTV) retrieval replenishment and deployment. The Space Station, as conceived at the time of writing, is constructed in orbit and will be maintained in orbit.

The above construction, servicing, maintenance and deployment tasks, when coupled with the size of the Station, dictate that some form of transportation and manipulation device will be required.

The Transporter described in this paper will work in conjunction with the Orbiter and an Assembly Work Platform (AWP) to construct the Work Station. The Transporter will, later in its life, work in conjunction with the Mobile Remote Servicer to service and install payloads, retrieve, service and deploy satellites, and service and maintain the Station itself. Figure 1 shows the Transporter involved in Station construction when mounted on the AWP and later supporting a maintenance or inspection task with the Mobile Remote Servicer and the Flight Telerobotic Servicer.

INTRODUCTION

The Mobile Transporter is the device that will carry the Station manipulators, tools, payloads and orbit replaceable units around the Station. It has to be able to move around on a truss structure fabricated from cubic bays. It has to provide a firm base structure for the Space Station remote manipulators to operate from. It has to move in a variable rate controllable manner to avoid destabilizing the Space Station when carrying large payloads.

The Mobile Transporter must be able to reach any point on the external truss structure by virtue of its own mobility mechanisms; consequently, it must be able to move in a straight line, turn right angle corners and make 90-degree external plane changes.

The Mobile Transporter also has to be stowable within the Orbiter bay for launch and be deployed or erected to the same size as the Space Station truss for use.

---

*Astro Aerospace Corporation, Carpinteria, California

DESCRIPTION

The Mobile Transporter is comprised of three principal structures, a number of drives, an electronics control unit, and thermal protection and harnessing. Mobile Transporter operations are controlled in detail by the drive electronics unit. It receives high-level commands either from the Orbiter (when the Transporter is building truss) or from the Mobile Remote Servicer (MRS). The drive electronics unit consists of a multiplexing unit, a data processor, and a mechanism drive electronics unit. The data processor contains the detail algorithms that control the operation of the heaters and drive mechanisms. The multiplexer is an interface unit to the drive electronics which monitors and powers instrumentation. The mechanism's drive electronics unit generates DC power for the drive motors and heaters, and AC power for the drive module resolvers.

The Mobile Transporter has three degrees of freedom: translation, in-plane rotation, and a normal-to-plane rotation. There are three major structures in the Mobile Transporter: the upper base, the track base, and the lower base.

The general arrangement, in exploded form, is depicted in Figure 2.

The upper base is a self-deploying truss structure fabricated from a combination of two-inch-diameter and four-inch-square graphite tube. The upper base structure carries the MRS in its center position and it transfers the forces and torques generated by the MRS during payload manipulation into the Space Station truss. The upper base also attaches the Transporter to the AWP and transfers any Orbiter-induced perturbation loads into the truss segment that is being built.

The upper base has four node pin latches at its extremities. These are the latches that grip pins on the Space Station truss nodes, thus ensuring that the upper base is firmly attached to the Station truss when it has to be.

The upper base is attached by means of a ring in the center of its lower face to a turntable assembly. The turntable provides the in-plane rotational degree of freedom that the Mobile Transporter needs in order to be able to turn corners.

The turntable assembly itself is attached to the second major structural item, the track base assembly. The track base is an EVA* unfoldable graphite beam structure fabricated from square section tube, and as the name suggests, it is the linear track on which the translational degree of freedom drive runs. Attached to the underside of one of the track base longerons, which is 6.219 meters long, is a gear rack and track assembly. There are flat steel tape tracks attached to the top face of the "rack" longeron and to the top and bottom faces of the other longeron.

---

*Extravehicular activity

The track base assembly can run back and forth by 5.21 meters through the drive hinge assembly. The drive hinge assembly, which contains the normal-to-plane rotational and in-plane translational degrees of freedom, is attached to the lower base assembly. Consequently, the upper base can move 5 meters back and forth with respect to the lower base. Thus, the Mobile Transporter can move 5 meters one step at a time. Since the drive hinge assembly has the normal-to-plane rotational degree of freedom built into it, the upper base can be tilted up by 90 degrees, thus allowing the Mobile Transporter to change plane from one truss face to another.

The lower base assembly is an EVA unfoldable planar structure fabricated from graphite square section tubes. The lower base also has four node pin latches, similar to the ones on the upper base, which serve the same purpose as the upper base. The lower base assembly forms the attachment between the Mobile Transporter and the Space Station, while the upper base, MRS, payload combination is being translated or rotated. Sequential or combined use of the Mobile Transporter degrees of freedom, when properly latched to the Space Station truss by the relevant piece of Transporter structure, thus ensures secure progress around any part of the Space Station truss exterior.

A one-bay translation sequence is shown in Figure 3, "Translation motions and rates."

Photograph 1 shows both the upper and lower bases, one on top of the other and both fully locked to four node pins on the structure. This is the mode the Transporter would be in for any static operations of the Mobile Remote Servicer, which is normally attached to the upper base.

Photograph 2 shows that the upper base node pin locks have released the station truss node pins, fully retracted so as to allow movement, and that the upper base is moving. Translation motion is effected and controlled by the drive hinge and track base. When the upper base moves, the track base moves and the drive hinge is stationary; thus, the drive hinge rolls down a fixed track. The translation drive mechanism is described in greater detail elsewhere in the paper.

Photograph 3 shows that the upper base has arrived at the next bay, which is not quite the fullest extent of its possible travel, with the node pin latches closed onto the node pins. The Transporter is now attached to two bays at eight points.

Photograph 4 shows that the lower base has released itself from the station truss node pins, the latches have fully retracted to allow movement of the base, and the lower base is advancing.

Photograph 5 shows the lower base has fully advanced to the same bay that the upper base is attached to and has locked itself to the structure. The Transporter has now moved one complete bay. The time taken to perform this sequence is dependent upon payload mass. Predicted average rates for various size payloads are shown in Figure 3.

A direction change is shown in Figure 4, "Rotation motions." The Transporter would perform a direction change at a junction between a transverse boom and keel, or immediately prior to making a plane change.

Photograph 1 shows the Transporter as it was in Photograph 5 of Figure 3. Both bases are locked onto the same bay and the track base is aligned with the truss.

Photograph 2 shows that the lower base node pin latches have been opened and fully retracted, and the lower base is being rotated by the turntable. The turntable connects the upper base to the track base. This mechanism is fully described later in the paper.

Photograph 3 shows the lower base drive hinge and track base fully rotated through 90 degrees and relatched onto the node pins. The track base is now realigned with a new direction of travel, and translation could proceed at this point. However, Photographs 4 and 5 show the sequence being completed by a rotation of the upper base performed similarly to the lower base rotation shown in Photographs 1, 2 and 3.

A plane change is shown in sequence in Figure 5, "Plane change motions." Plane changing amounts to stepping out over the side of the truss, rotating about an axis parallel to the truss longerons into a plane parallel to the new plane, and grasping the new plane bay node pins with one of the bases. That motion is followed by the other base to complete the sequence.

Photograph 1 shows the two bases locked onto a side face of the truss. A direction change has just been completed and the track base is aligned at 90 degrees to the truss in the correct direction for a plane change.

Photograph 2 shows the upper base released itself from the node pins and advancing vertically upwards.

Photograph 3 shows the upper base tilting over toward the new plane. It can be seen that the upper base has translated to an approximate midpoint of the travel prior to the tilting motion. This is done so as to minimize tilting inertia and torque on the Space Station. The mechanism that controls the plane change is the rollover drive portion of the drive hinge assembly. It is described in detail later in the paper.

Photograph 4 shows the upper base fully tilted over through 90 degrees and rolling across the upper face on the track base toward the node pins.

Photograph 5 shows the two bases now firmly latched to the truss on two faces at eight node pins.

Photograph 6 shows the lower base has been released from the node pins, and the rollover drive is now pulling it up toward the new plane.

Photograph 7 shows the lower base fully rotated through 90 degrees and ready to be rolled in by the translation drive.

Photograph 8 shows the lower base rolled in underneath the upper base toward the node pins where it is latched 90 degrees away from where it started.

MECHANISMS INSTRUMENTATION AND LUBRICATION

Key requirements that have driven the concept design of the Transporter generally, and the mechanisms particularly, are the need for 30 years lifetime with maintenance and full single failure tolerance without any loss of performance. The first requirement will drive the lubrication system design

and cause the mechanisms to be configured as orbit replaceable units. The second requirement causes the mechanisms to be fully redundant, both mechanically and electronically.

The Tranporter mechanisms are the node pin latches, a turntable and the drive hinge assembly. All the mechanisms use a common motor resolver and brake module even though the mechanisms are somewhat different. The node pin latches are shown in Figure 6. The node pin latches are grippers, they have a pair of jaws attached by pivots to the front of the latch body. The jaws are opened or closed in the following manner. The motor module contained within the latch body causes a threaded shaft, which protrudes from the rear of the latch body, to rotate. There is a gimbal mounted nut running on the threaded shaft and the nut is part of a "U" bracket which "wraps" around the latch body toward the front of the latch. When the threaded shaft is rotated, the "U" bracket moves back or forth. The front of the "U" bracket is connected to the latch jaws by a pair of pivoted push/pull rods.

Consequently, as the motor rotor turns, the threaded shaft rotates, the "U" bracket is moved forward, the push rods are moved forward, and the latch jaws close onto the node pin.

The motor resolver and brake are all dual wound and the Transporter can still function if only three out of the four latches are functional.

Each latch is mounted on a spring compliance system that allows motion in a radial direction only. Thus, the pattern of four latches can "breathe" to allow differential expansion between the Transporter and the truss.

The turntable assembly is shown in Figure 7. It is electrically quadruple redundant and mechanically dual redundant. It has two crossed roller wire race bearings, two drive modules, an upper housing, a lower housing, and a "floating" internal ring gear. The bearings are 40 inches in diameter. Figure 7 shows the turntable sectioned, the wire race crossed roller bearing concept, and the predicted force-speed characteristic.

The bearings and drive are fully redundant and operate in the following manner. When the prime drive is running, the redundant drive is locked by its integral power-off brake. Because the redundant drive cannot rotate, the internal ring gear is rotationally grounded to the lower housing, so in consequence, the upper housing rotates on the upper wire race bearing and the prime drive pinion rolls around the internal ring gear. When the redundant drive is running, the prime drive is locked, consequently, the ring gear is rotationally grounded to the upper housing. Thus, the lower bearing rotates in the lower housing and the redundant drive pinion drives the ring gear and upper housing around.

The turntable is configured to be removable from below through the track base.

The drive hinge assembly contains two separate drives; the rollover drive for plane changing and the translation drive for moving in a straight line.

Figure 8 shows a side view of the rollover drive. It is a double-ended screw jack with a common, high precision, threaded, tubular shaft having two motor-driven planetary roller nuts running on it. One of the motor-driven nuts is gimbal mounted to the Transporter lower base structure, the other motor-driven nut is similarly attached to the drive hinge structure. The threaded shaft is prevented from rotating so that when either of the roller nuts is rotated, the threaded shaft is passed through that roller nut. The linear motion of the jack shaft is converted into rotary motion of the drive hinge by having the rollover hinge pivot offset from the jack shaft line of action.

Dual redundancy is achieved because either motored nut can rotate the drive hinge. The threaded jack shaft exterior is protected, over its ends, by tubular shields attached to the drive module housings and by an expandable metal bellows between the drive module housings. The two characteristics shown in Figure 8 relate jack output force to jack extension rate and output torque at the hinge pivot to the angle of rotation of the hinge. The shape of the second characteristic is so because the distance from the jack line of action to the hinge pivot changes as the hinge rotates.

Figure 9 is a composite view of the various translation drive components and the translation drive characteristic. The translation drive is a rack and pinion drive, the rack is attached to the underside of the track base along its full length. The rack has two rows of teeth, one prime and one redundant, with a full tooth depth separation groove between them. The bearing roller strips can be seen in Figure 9 attached to the track base. The rolling strips on the left hand longeron, as shown, only provide normal to plane location. The rolling strips on the right-hand longeron provide in-plane as well as normal-to-plane location by virtue of the vee roller arrangement and the two inclined strips on the underside. The rollers that bear on the rolling strips are mounted "fore" and "aft" on the drive hinge structure on a 40-inch stance to provide pitch stability for the track base.

The rollers that run on the upper bearing strips, as shown, are compliantly mounted to allow for manufacturing tolerances and differential expansion.

The translation drive has two separate drive modules attached to the drive hinge structure by rocking brackets mounted on a common pivot. Drive torque from the drive module is transmitted through a drive spindle and pinion to the drive rack. The drive pinion is held in mesh with the rack by a changeover actuator which pulls or pushes the relevant rocking drive mount over to its driving position. When the prime drive is engaged, the redundant drive is completely disengaged. If the prime drive experiences a complete mechanical failure, then the changeover actuator rotates the redundant

drive into loose mesh with the rack on the redundant tooth row, then rotates the prime drive completely out of mesh and then finally correctly meshes the redundant drive with the rack. This is accomplished by the changeover actuator interacting with cam profiles in the rocking drive mounts.

During its 30-year lifetime, the Mobile Transporter will experience 160,000 temperature cycles associated with orbital eclipses. Lubrication systems that would be used on geosynchronous satellite mechanisms have to withstand 3,700 temperature cycles for a 10-year lifetime. A low earth orbit spacecraft mechanism may have 11,000 cycles due to orbital eclipses. The Mobile Transporter is clearly in a different regime with regard to lubricant lifetime. Maintainability analysis, using such data that may be available within NASA from orbiter missions, will predict lubrication life and as a consequence, mean time between maintenance actions.

The above predictions will be verified by development testing to be performed during the design, development, test, and evaluation phase of the contract.

The Mobile Transporter lubrication concept is based on the use of Braycote grease. For the most part, the mechanisms are fully housed and sealed, the translation rack, however, is exposed. The volatility of the grease, albeit very low, may be such that some form of reservoir or replenishment method may be required. The reservoir may take the form of a sintered plastic pinion gear inpregnated with grease or oil that is attached to the drive hinge and permanently runs on the rack. To aid deposition of the lubricant on the rack, the pinion could be heated to create thermal siphoning.

The Transporter instrumentation consists of resolvers in each drive module, an absolute encoder on the drive hinge axis for measuring rollover angle and geared encoders on the turntable and translation drive.

The translation geared encoder is a multi-turn encoder with a resolution of eight bits corresponding to 0.05 inches of linear displacement. The absolute position is determined by viewing four linear encoder tracks etched onto the the track base with redundant reading heads.

The Mobile Transporter also has to detect which bay it is on at any time. Various methods of encoding truss locations and reading the codes will be studied. The possible coding methods may be optical, magnetic, capacitive or inductive.
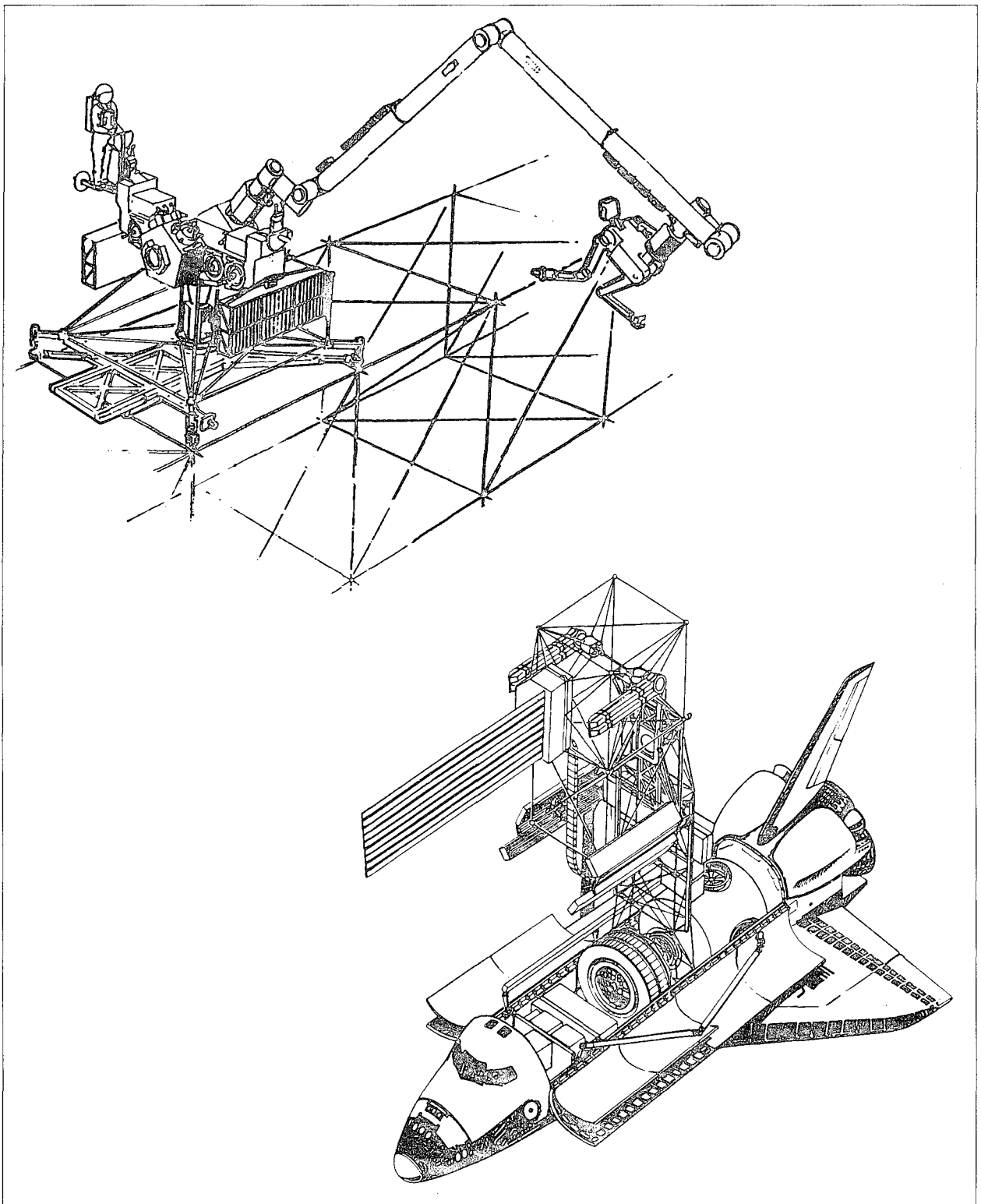
Figure 1. Transporter uses.

Track Base
- Unfoldable graphite track structure for translation

Turntable Assembly
- Fully redundant drive & bearing system
- On-orbit replaceable

Upper Base
- Deployable graphite truss structure
- Supports MRS and payloads

Transporter Degrees of Freedom

ROTN

TRANS

ROTN

Drive Hinge
- Fully redundant roll-over & translation drive & bearing system
- On-orbit replaceable

Lower Base
- Unfoldable graphite structure
- Supports transporter during movement

Node Pin Latch
- Electrically redundant
- Any three latches will support a base

Figure 2. Transporter general arrangement.

279
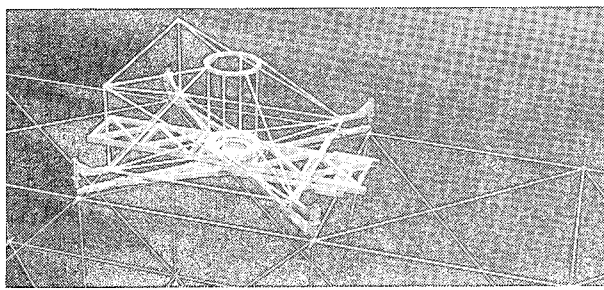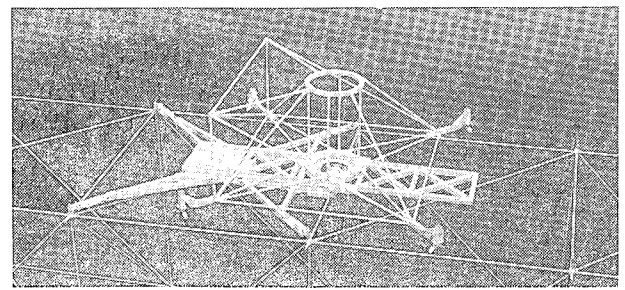
1. Both bases locked.

2. Upper base unlocked and moving.
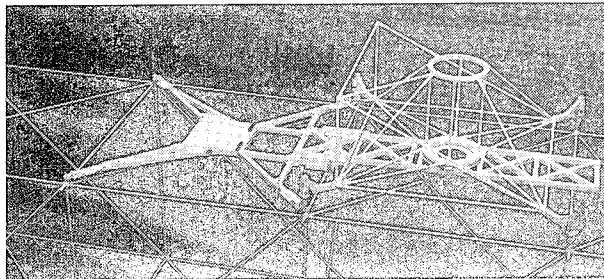
3. Upper base locked down one bay ahead.
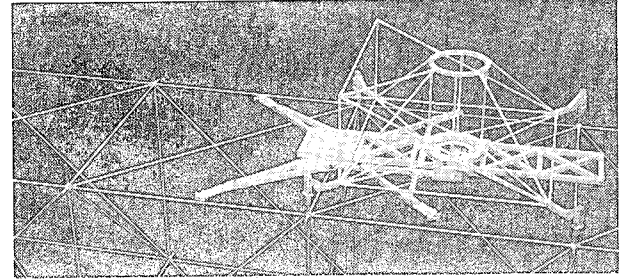
4. Lower base unlocks and moves.
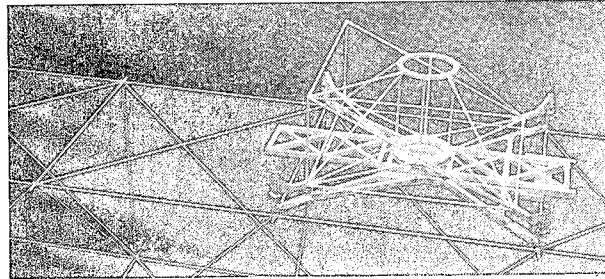
5. Both bases realigned and relocked.
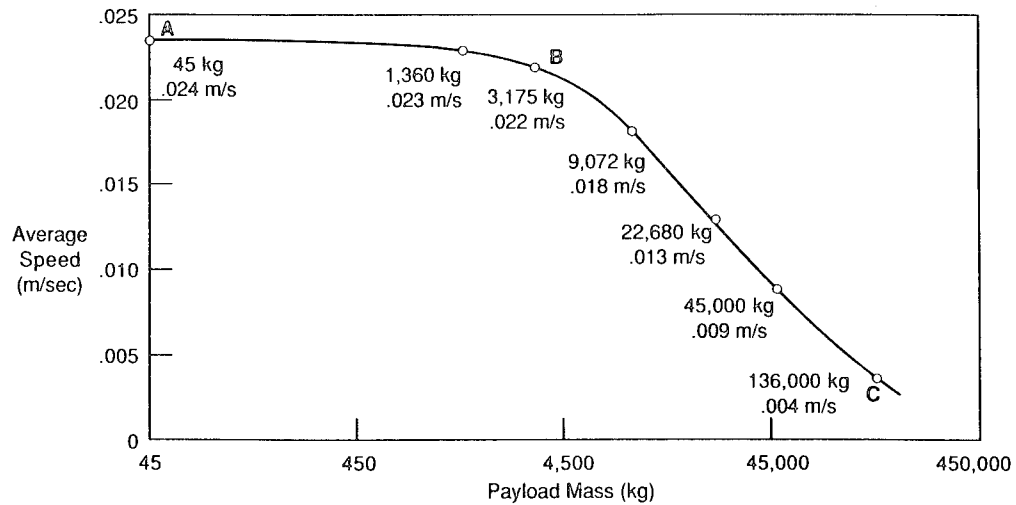
Figure 3. Translation motions and rates.
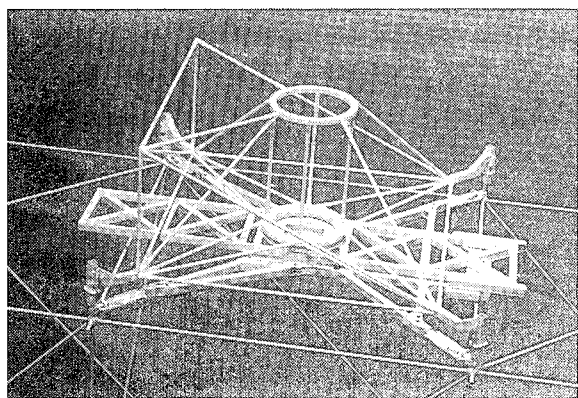
1. Both bases locked onto one bay.
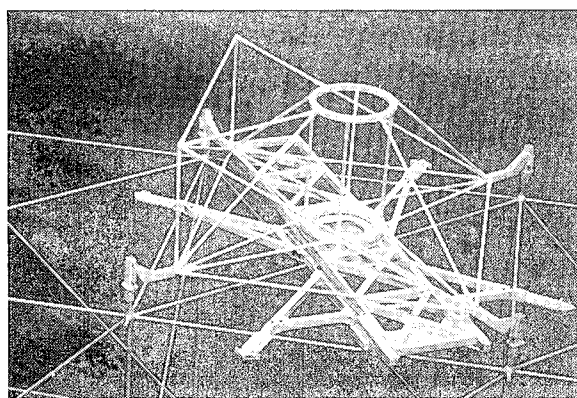
2. Lower base rotates.
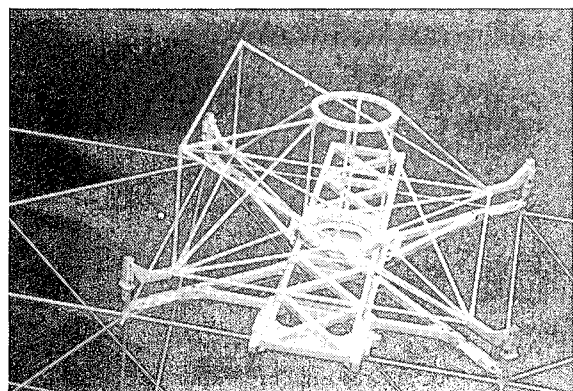
3. Lower base locked down fully rotated.
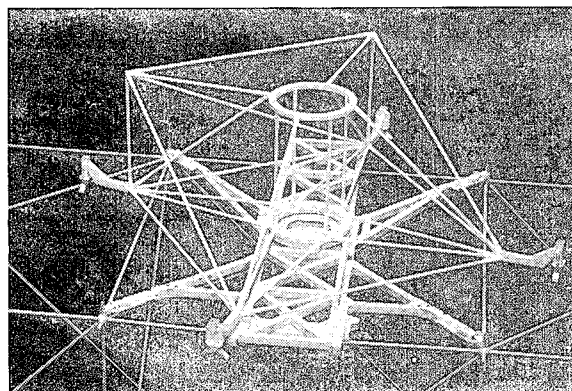
4. Upper base rotates.
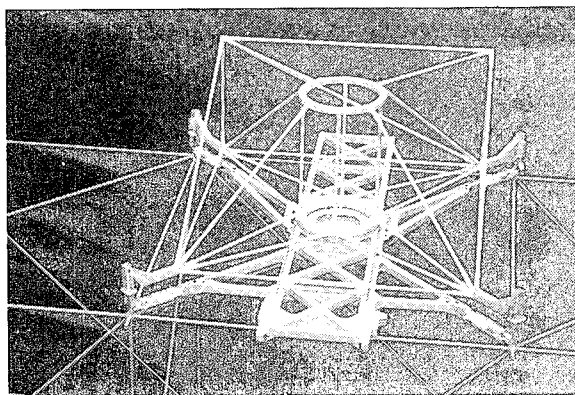
5. Both bases fully rotated.

Figure 4. Rotation motions.
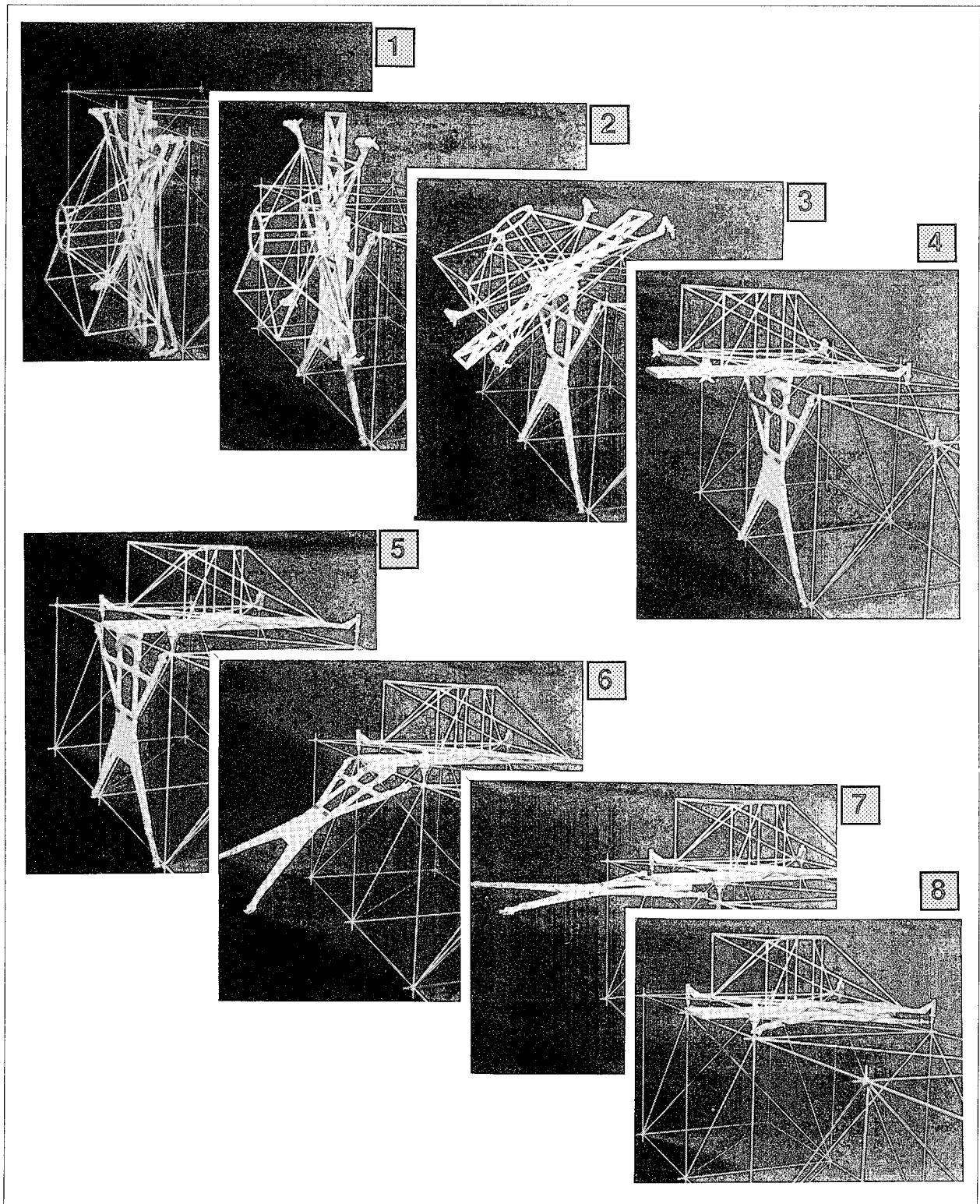
Figure 5. Plane change motions.
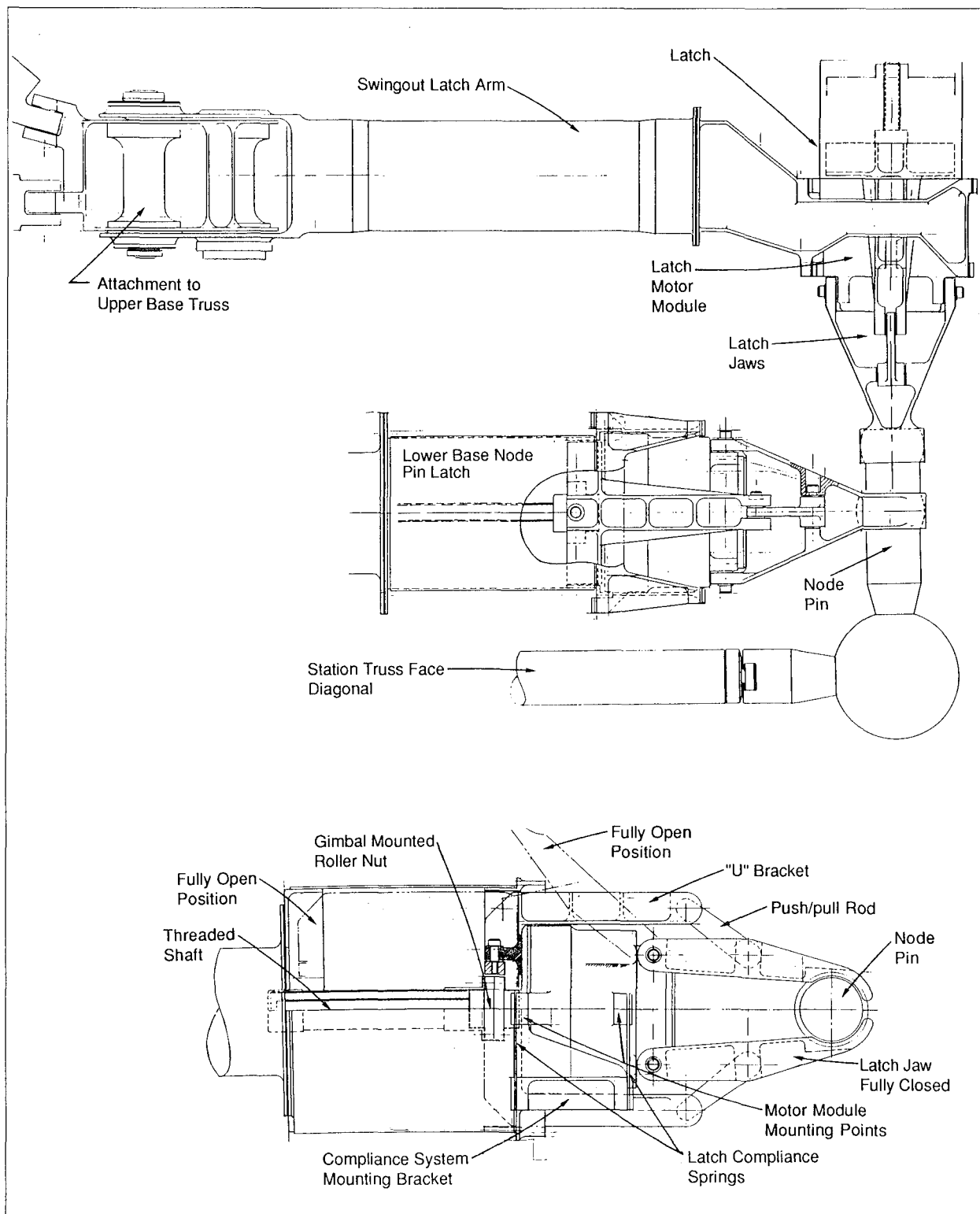
Figure 6. Node pin latches.
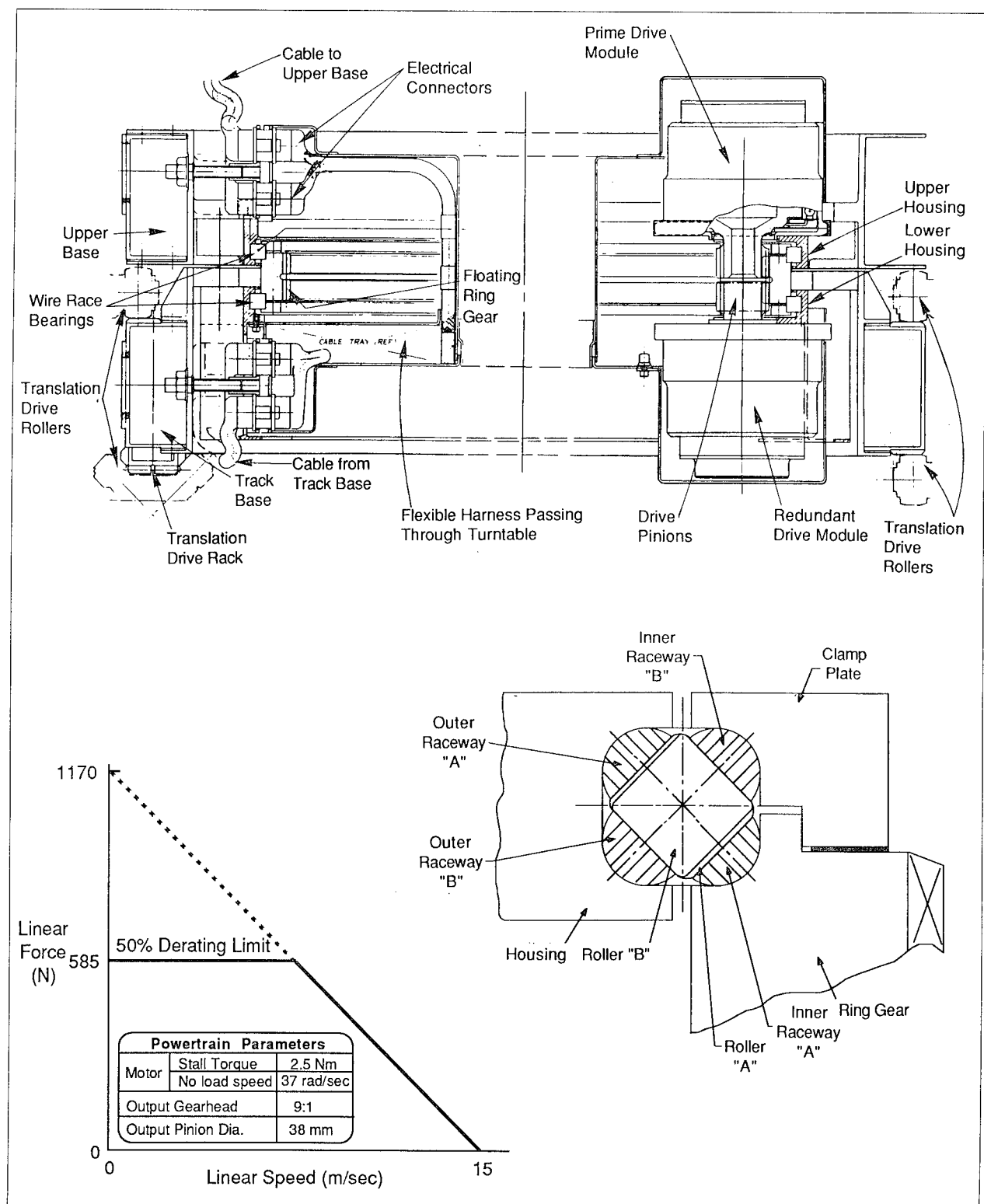
Figure 7. Turntable components and characteristics.
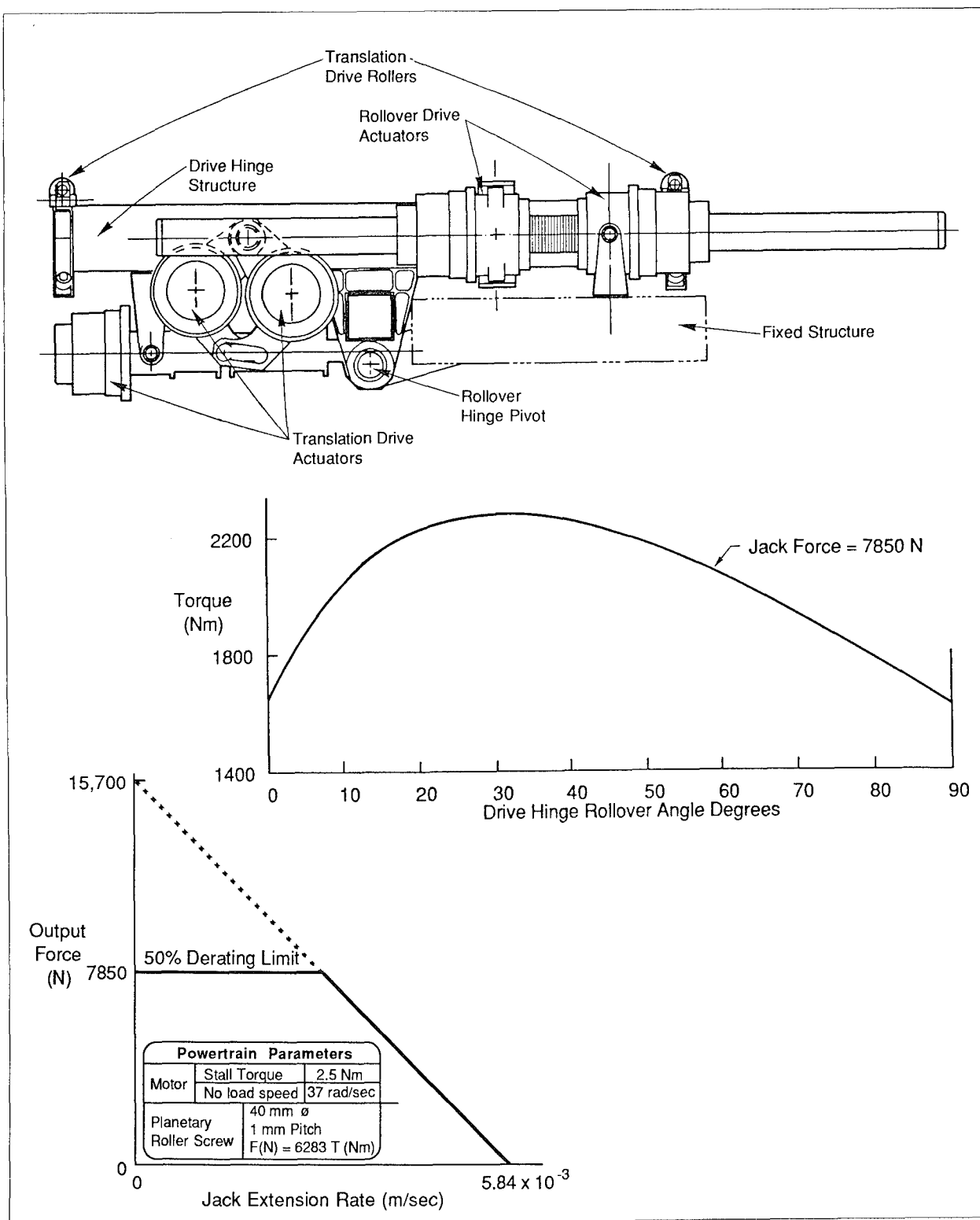
Figure 8. Rollover drive components and characteristics.
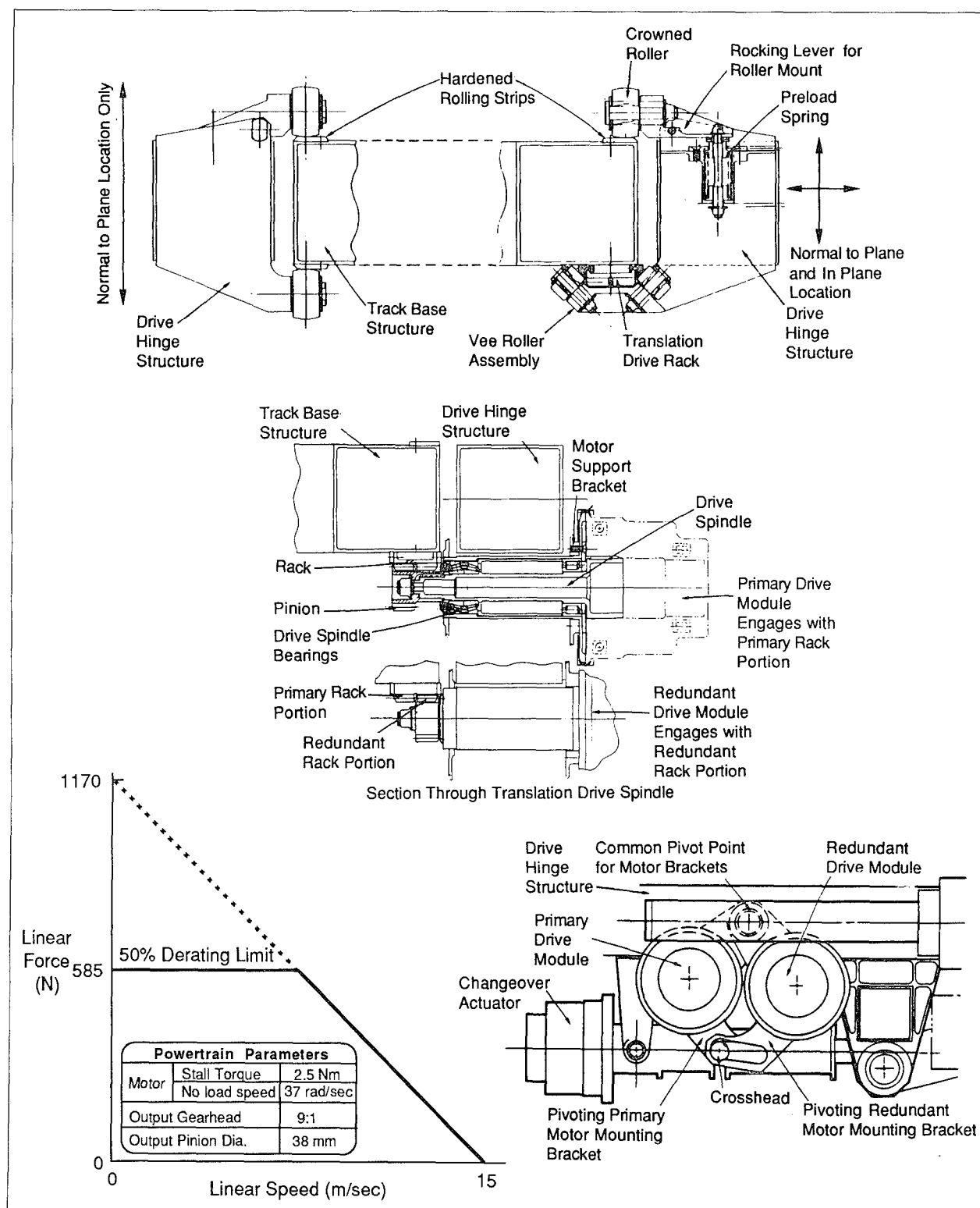
Figure 9. Translation drive components and characteristics.

OPERATIONAL EXPERIENCE AND DESIGN RECOMMENDATIONS
FOR TELEOPERATED FLIGHT HARDWARE*

T. W. Burgess and D. P. Kuban**
W. W. Hankins and R. W. Mixon†

ABSTRACT

Teleoperation (remote manipulation) will someday supplement/minimize astronaut extravehicular activity in space to perform such tasks as satellite servicing and repair, and space station construction and servicing. This technology is being investigated by NASA with teleoperation of two space-related tasks having been demonstrated at the Oak Ridge National Laboratory (ORNL). This paper discusses the teleoperator experiments conducted at ORNL for the Langley Research Center and summarizes the results of these experiments and the related equipment design recommendations. A general discussion of equipment design for teleoperation is also included.

INTRODUCTION

The level of man's activity in space is increasing at a very high rate and is accompanied by an accelerating requirement for more and more astronaut extravehicular activity (EVA) to deploy, repair, service, and resupply orbiting facilities. A possible alternative to EVA is to use automated and teleoperated manipulators, but both types have unresolved issues. Automated devices operate extremely well if the tasks are very precise, well defined, pre-programmed, and repetitive,but they do not perform well in an unstructured environment.

Teleoperation, having direct human control, is not dependent on structured environments, but will require a high level of manipulator dexterity and controlability for realistic space tasks. One of the difficulties in deciding where and how to apply teleoperators has resulted from not having a confident knowledge of their dexterous capabilities to perform complex tasks or of how long they will take to accomplish such tasks. The objective of this paper is to address these issues by employing a teleoperated manipulator controlled by highly skilled, experienced operators to accomplish typical tasks already accomplished by astronauts. This would demonstrate both the successful application of this technology as well as establish a data base of task completion times. The tasks chosen were the Fairchild satellite refueling coupling and the Assembly Concept for the Construction of Erectable Space Structures (ACCESS) I assembly. The Central Research Laboratories' (CRL) model M-2 teleoperator at ORNL was selected to perform these experiments.

TELEOPERATOR FACILITIES

The model M-2 teleoperator is part of ORNL's Remote Operation and Maintenance Demonstration (ROMD) facility. The ROMD facility was developed by the U.S. Department of Energy's Consolidated Fuel Reprocessing Program to demonstrate

remote maintenance techniques for advanced nuclear fuel reprocessing equipment.[1] The model M-2 is a dual-arm, bilateral force reflecting, master-slave system developed jointly by CRL and ORNL and represents the state of the art in commercially available teleoperated manipulators.[2] The model M-2, in operation since FY 1983, incorporates a distributed, microprocessor-based digital control system. Two major assemblies comprise the M-2: (1) the slave package shown in Fig. 1 and (2) the master control station shown in Fig. 2. The slave performs "man-like" handling tasks in the remote environment. This package consists of a pair of arms, three television viewing cameras, lighting, and a 230-kg (500-lb) capacity auxiliary hoist. Each slave arm has a 23-kg (50-lb) continuous capacity, a 46-kg (100-lb) time-limited (peak) capacity, six degrees-of-freedom (D.F.), and a tong-type end effector. The slave is transported by a three-axis positioning system consisting of an overhead gantry bridge and trolley and telescoping tube assembly. A motorized joint at the telescoping tube interface provides 520 degrees of slave rotation in the horizontal plane.

Control of the slave is performed by a single operator from the master control station which consists of a pair of master arms, three 19-inch color television monitors, and an operator console. The master arms are kinematic replicas of the slave arms; each has a peak capacity of 25 lb. The handle on the master is a pistol grip and trigger type that provides slave tong control. The operator interfaces with the control system for other functions primarily through a CRT and touch-screen mounted in the operator console. Operating mode selection, force-reflection ratio selection, camera-lighting control, and system status diagnostics are available through this interface. Master-to-slave arm control is in real time with slave arm tip velocity capabilities up to 152 cm (60 in.) per second. The minimum slave arm loading which can be detected or "felt" at the master control arm is on the order of 1 lb or 1% of peak capacity.

Operator viewing of the remote work site is provided by the cameras mounted on the slave package. These include two boom-mounted cameras with four positioning D.F. (pan, tilt, boom extend-retract, and boom pivot) and motorized lens controls (zoom, focus, and iris) and one fixed camera mounted between the slave arms. The two boom-mounted cameras, one on each side, provide orthogonal views for depth information and viewing flexibility. The lower camera produces a wide angle view of the work site from a fixed position to give additional viewing information and information concerning master-to-slave arm spacial relationships. These camera views are commonly supplemented with facility and transporter mounted cameras. Camera and auxiliary hoist controls are also on the operator console. A joystick is used for overhead camera positioning, while rotary potentiometers provide camera lens zoom, focus, and iris control.

SATELLITE REFUELING COUPLING TELEOPERATION

Satellite refueling operations have been identified by NASA as a potential candidate for development as a remote operation. The refueling coupling, shown in Fig. 3, was developed by Johnson Space Center for manual operation by EVA astronauts. It was successfully demonstrated on the space shuttle by astronaut Sullivan.

This coupling was also operated using the model M-2 teleoperator. The coupling operation required the dexterous manipulation of both arms. This task was more intricate than those normally encountered in fuel reprocessing applications for which the design of the M-2 was optimized. The M-2 has a 100-lb capacity per arm, and the coupling weighed less than 7 lb; therefore, the

operators were urged to use the utmost care during handling. This undoubtedly increased the amount of time required to complete the task. The bayonet-type mount on the coupling halves was engaged and disengaged without incident. The valves used to start and stop flow were operated using a standard-type ratchet wrench that had not been modified for the remote handling operation. Proper seating of the valves was remotely determined using the force reflecting feature of the M-2 teleoperator. Valve torques as low as 30 in./lb could be detected. Operation of the relatively fragile mechanical lockout device that prevents inadvertent opening of the fuel valves was also accomplished without incident.

Complete operation of the coupling was successfully demonstrated in accordance with NASA criteria and without modification for remote handling operation. Task time was about 35 min for the M-2 and about 15 min for the suited astronaut — a time factor of about 2:1. A complete video recording was produced to compare directly with suited astronaut operation.

As a result of the teleoperation of the refueling coupling, several comments and recommendations can be made relative to its design suitability for remote handling. On the positive side, it is somewhat self-aligning, has no loose parts, and has relatively short, simple motions to operate. On the negative, the gross alignment could be readily improved, the round handles were difficult to hold (for the astronaut as well), and there was poor access to the valves. The lockout mechanism which guards the fuel valves should not require two hands to operate, and the valves should be replaced with some that do not require as many revolutions. In general, the device was too delicate and should be considerably more rugged.

ACCESS I TRUSS ASSEMBLY TELEOPERATION

Truss assembly may be quite time consuming in the construction of the Space Station and has been identified as a task potentially well suited for teleoperation. The ACCESS I is an existing truss design which was developed and tested by NASA both in water tank simulation and in Space Transportation System (STS) experiments. Although the ACCESS I had no design considerations for remote handling, experimentation with this truss assembly provided information about the capabilities of teleoperator systems as well as the design considerations applicable to remotely serviced equipment. Since flight testing of the ACCESS I had been completed, astronaut and teleoperator performance could be compared.

ACCESS I Flight Experiment

The ACCESS I was a structural assembly flight experiment intended to study and verify the ability of astronauts to assemble in space a repetitive truss structure representative of the type likely to become a part of the Space Station. It was conducted in November 1985 as a part of the Shuttle Mission STS-61b (Fig. 4).

The truss was assembled from basic hardware which consisted of interchangeable, aluminum nodes and columns which can be snapped together to form connected bays of structure with a triangular cross section as shown in Fig. 5. The horizontal batten and vertical longeron members were 1.4 m (4.5 ft) long and the diagonals 2.0 m (6.4 ft) long (about 1/4 the anticipated size for the Space Station) with a two position locking sleeve on each end of each member. Each

node had six nubs to which the columns could be attached. The columns were mated to a node by sliding back the sleeve on the column's end. Finally, the sleeve was slid back over the joint to make it secure.

Figure 5 shows the equipment and general setup for the flight task with the astronauts in their designated places (Nos. 1 & 2). The nodes and columns were supplied from the canisters (Nos. 3, 4, & 5), which were located so that the astronauts did not have to leave their stations to build the truss. They used the assembly fixture (No. 6) as a frame on which to place and hold parts as the truss sections were being put together. Nodes were slid up the guide rails (No. 7) from the bottom to latching positions on the fixture. The columns were attached to these to form a finished bay which was subsequently released and slid up along the guide rails to a new latched location to make room for the assembly of an additional bay on the lower half of the fixture where the raised bay had been.

ACCESS I Teleoperation Experiments

Two separate experiments were conducted at ORNL; the first demonstrated the assembly and disassembly of the truss by teleoperator alone, while the second experiment included the addition of a person at the test site working in concert with the teleoperator in order to duplicate standard NASA procedures (requiring a two-person team) and provide data for comparison with assembly by astronauts. Results of the second experiment have been previously reported by NASA.[3] Data recorded for both experiments included video recordings of operations, task and subtask completion times, task performance errors (e.g., hardware damage or drops), and test personnel observations and recommendations.

Experiment I Scope and Procedure

The purpose of the first remote handling experiment was to investigate the feasibility of remotely performing selected ACCESS I assembly and disassembly tasks. The selected operations investigated included the construction and disassembly of two truss bays and operations required in set-up of the assembly fixture guide rails. This was performed without making any modification to the ACCESS equipment or the model M-2 teleoperator, or by the use of any special tools.

Remote handling operations were performed by a two-person operator team from the remote control room. One person operated the model M-2 master control arms, and the second person operated the transport system and the model M-2 and facility cameras. The ORNL operators were very experienced at operating the model M-2, and each operator received approximately ten hours of experience assembling the truss remotely prior to any data collection for the purpose of developing procedures. Operators were usually exchanged between each series of task runs to minimize fatigue. Most tasks required dual-arm operations in support of positioning and connecting the truss struts to the nodes.

The ACCESS I assembly and disassembly procedures were modified to better suit operations using a teleoperator system since the standard NASA procedures were intended for a two-person astronaut team. Modifications were made primarily in the order of procedure steps. Only one of the two strut storage canisters was used and positioned upright on the facility floor in front of the ACCESS where the struts could be vertically extracted using the M-2 slave as shown in Fig. 6.

To assemble the first bay, operators installed nodes on each of the three assembly fixture guide rails (Fig. 7), and then installed the diagonal, longeron, and batten struts of the three bay faces around the lower section of the fixture. The upper battens were then installed and the upper end of the diagonal and longeron struts were connected to the nodes. The assembled bay was then moved to the upper position on the assembly fixture by releasing a securing latch at one of the mid-position nodes and raising the bay using the teleoperator and transport system.

Assembly of the second bay was essentially the same procedure used for the first bay except the upper batten struts were already in place from assembly of the first bay. The two bays were disassembled in reverse order of the assembly procedures.

To raise and latch a guide rail, the lower link and vertical links of the rail were raised and locked in position by inserting a captured detent-type pin at the link between the two joints. This procedure was reversed to lower the rail.

Experiment I Results

Each of the assembly-disassembly tasks discussed in the procedure section was successfully completed. Because of time and schedule constraints, the decision was made to concentrate efforts on the truss assembly tasks. Operators completely assembled the two truss bays eight times each and completed the disassembly and guide rail tasks twice per operator.

Combined task completion times for the primary truss assembly tasks stabilized after approximately five trials as shown in Fig. 8. The figure exhibits typical learning curve characteristics experienced in remote handling operations. Complete assembly of two bays by the operators required approximately 60 to 75 min. The average time to complete each task trial per operator is listed below.

	Task	Completion Time (min.)	
		Operator 1	Operator 2
1.	Assemble first truss bay	35.6^a	50.5^a
2.	Raise assembled bay	0.5^a	0.7^a
3.	Assemble second bay	23.0^a	26.9^a
4.	Disassemble lower bay	19.8	33.4
5.	Lower upper bay	0.5	0.8
6.	Disassemble remaining bay	30.6	54.4
7.	Release and lower a mast guide rail	2.6	6.1
8.	Raise and latch a mast guide rail	1.0	3.0

^{a} - Average taken of final three trials for each operator.

Recognizing that a significant amount of time was required for retrieval and transport of task components relative to the time required to make the component connections, subtask completion times were recorded for several of the truss assembly trials. Task completion times were divided into component retrieval-transport time, and component alignment-install time. Strut and node alignment-install time started when the strut or node was in proximity (within approximately

six to eight inches) to the connection point(s) and ended when the required connection(s) was completed and the tong grips were released. The remaining time was recorded as transport-retrieval time.

Subtask completion data were reduced for three of the final Task 1 trials completed by each operator which consisted of nine node installations and 27 strut installations per operator. On the average, 121 sec were required to install a node and 80% of this time was required simply in retrieval and transport. Struts required 146 sec to install and 65% of this time was required for retrieval and transport. As suspected, a significant portion of each component's total installation time was required in simply getting the component to the approximate location of installation.

Of the three types of struts handled, the batten (horizontally oriented) struts were generally the most difficult to install. This was due to the pivoting action of the node around the guide rail for the batten connection points which are orthogonal to the guide rail axis. The other connection points were much less prone to pivot when making the strut-to-node connection. The pivoting of the node made proper alignment of the strut difficult and, many times, required that the node be held secure with the teleoperator which further complicated the task.

Truss struts and nodes were occasionally dropped. The majority of the drops that occurred were an accidental release of a strut or node during withdrawal from the storage canister because of resistance to removal caused by misalignment. The struts were vertically stored in individual tubular cavities and would bind if not removed straight along the longitudinal axis (Fig. 9). The nodes were stored on pins and, like the struts, would bind on removal if pulled at an angle to the pin's axis. Binding occasionally resulted in a release of the component, allowing it to fall back into the storage canister. This type of release was recorded separately from releases that occurred after removal from storage since it is a different type of error in comparison to a free-space drop and may not result in the loss of the component. On the average, 2% of the struts handled were dropped and 6% were released during removal from the storage canister. Of the total nodes handled, 6% were dropped and 4% were released during removal from the storage canister.

Recommendations

Recommendations for design modifications to the ACCESS truss for improved remote handling based on Experiment I are summarized below.

- Strut-to-node connections should be simplified in operation. Ideally, the connections should be self-aligning and connect with a simple push-type motion once the strut is roughly aligned with the node. This type of design should also improve performance by suited astronauts.

- All lockout and latch mechanisms could be improved for operation by manipulator. Most of the ACCESS mechanisms were better suited for hands-on operation than for operation by teleoperator and end effector.

- Strut and node designs should include grip points for teleoperator end effector.

- Nodes should be designed for increased self-alignment to the guide rails. The brackets between the node connection points and node body were occasionally bent out of alignment when making strut connections and should be more rigid in design. The tolerance in the pivoting action of the nodes around the guide rails should be reduced to minimize difficulties in aligning and installing the batten struts.

- Storage of the struts and nodes should be closer to the installation locations on the assembly fixture so that teleoperator arm range is sufficient to retrieve and install the components without transporter motion. This will significantly reduce the time required for assembly.

Experiment II Scope and Procedure

The first experiment successfully demonstrated the ability to remotely assemble and disassemble the ACCESS I truss. It also provided data for evaluating these tasks but did not provide data which could be easily compared to performance by more conventional methods since assembly procedures were modified. The purpose of the second experiment was to investigate remote assembly of the truss by standard procedures so a more direct comparison to other assembly methods could be made.

The second experiment investigated assembly of two bays by a two-person team; one person performing assembly tasks using the M-2 teleoperator while working in cooperation with a person stationed at the ACCESS site. The M-2 operator and ACCESS site operator alternated between the two truss assembly stations to provide data for remote operations at each of these stations. Positioning of the teleoperator and the man at each of these stations is shown in Figs. 10 and 11. Two-way communication was provided for the teleoperator and ACCESS site operators by transmitter-receiver headsets which allowed hands-free operation.

Once positioned for operations at a station, the model M-2 slave and closed-circuit television (CCTV) cameras did not require repositioning. This allowed the M-2 operator to concentrate on the strut handling tasks which required near continuous operation of both arms and eliminated the need for transporter motion. All remote operations were performed by the M-2 operator without assistance from another control room operator.

From Station 1, operators installed the nodes and struts assembled around the lower section of the assembly fixture. This accounted for approximately 70% of the operations required. A single bay face was assembled at one time in cooperation with operations at Station 2. First, a node was installed on the guide rail while a diagonal strut was being placed in position from Station 2. The lower connection point of the diagonal was then made from Station 1. The lower batten and longeron struts of the respective bay face were then installed, the assembly mast rotated, and the process repeated until all three faces had been assembled. All assembly mast rotations were performed from Station 1.

From Station 2, the diagonal struts were positioned and the upper connections made for each bay face. For the first bay, the upper batten struts were installed and for all bays the upper connection of the longeron struts was made while the lower batten struts of the bay face were being installed from Station 1. Raising of the assembled bay was performed from Station 2.

Experiment II Results

The truss assembly tasks were successfully performed from both Stations 1 and 2. Eight repetitions per manipulator operator and station were obtained (a total of 64 bays assembled). The quality of task performance was comparable to Experiment I, and completion times were reduced by a factor of three. The average completion time of the final three task trials per operator and station are listed below. The combined task completion time (tasks 1 and 2) versus task trial for each of the operators is shown in Figs. 12 and 13, respectively.

		Completion Time (min.)			
		Operator 1		Operator 2	
	Task	STA 1	STA 2	STA 1	STA 2
1	Assemble First Bay	9.7	7.9	13.6	11.5
2	Assemble Second Bay	7.9	3.0	12.0	3.1
	Total	17.6	10.9	25.6	14.6

Station 1 consistently resulted in the longest task completion time since the majority of the truss assembly tasks (approximately 70%) are performed from this station. Assembly of the first bay required more time than the second since it included more strut connections and also included raising the assembled bay. Assembly of the second bay from Station 2 did not require the installation of any horizontal struts, only the diagonals, and consistently required the least task completion time since it required the least number of operations.

The effects of learning and practice were not as pronounced in Experiment II in comparison to Experiment I. This becomes evident when comparing the straight line profiles of Figs. 12 and 13 to the exponential profile of Fig. 8. This is attributable to operators having learned truss component handling techniques during Experiment I and the very repetitive, production-like operation of Experiment II.

Task completion times varied more from trial to trial during Experiment II than Experiment I primarily because of two factors. First, operator fatigue was greater during Experiment II because handling operations were essentially continuous at the model M-2 control station; in Experiment I, operations were divided between two operators and tended to produce breaks for an operator while the other was performing his tasks. Frequently, the second task trial completion time increased for an operator because of this effect. Secondly, the M-2 was moved from one station to the other after a few task trials per operator were completed to spread any learning and practice effects to both stations evenly. This, however, prevented operators from smoothly stabilizing at either station.

In addition, the slopes of Figs. 12 and 13 show that task completion times had not quite stabilized for either operator after eight trials each. Undoubtedly, completion times would have decreased with more experience, but significant improvements are unlikely. Practical time and schedule constraints did not permit more testing, and further testing was not deemed cost effective.

There was no detectable damage to the truss components or manipulator during the task trials of Experiment II. As in Experiment I, nodes occasionally

required straightening to ensure optimum alignment with the struts so movement of the assembled bay on the guide rails was as smooth as possible. Dropping of truss components was the only error committed with any frequency during Experiment II. The majority of the struts dropped were accidental releases which occurred because of binding with the storage canister during vertical extraction at Station 2. Fatigue during Experiment II was significant and certainly was a factor in errors committed. On the average, less than 1% of the struts handled at Station 1 were dropped and 12% of the nodes handled were dropped. At Station 2, less than 1% of the struts handled were dropped, but 4% were accidentally released during removal from the storage container.

The M-2 slave positioning at each of the two stations was generally a compromise from ideal task positions for separate tasks in order to perform all of the tasks at each station without having to reposition using the transporter system. The objective was to save time by eliminating transporter operation, but the ease of performing all tasks was sacrificed. This, in turn, increased the error rate and fatigue factor.

Comparison to Other Assembly Methods

The primary purpose of the second experiment was to acquire assembly time data which could be directly compared to assembly by other means. The bar graph of Fig. 14 presents a comparison for assembly by a variety of means including (1) shirt sleeves, (2) ground-based water immersion simulation with pressure suits, (3) Shuttle Mission STS-61b, and (4) teleoperator assembly at ORNL. All data are normalized to the completion of two bays. The teleoperator assembly time shown is an averaged figure computed from the last three runs of both M-2 operators (a total of twelve runs). The value for the water immersion facility is an average of times from Johnson Space Center's Weightless Environment Training Facility and Marshall Space Center's Neutral Buoyancy Simulator and includes some results from development tests with untrained subjects. The tele-operator assembly took about three times as long as did the pressure-suited astronauts in space to achieve the operation. The teleoperator time is very good, however, when one considers that neither the hardware being assembled nor the manipulator itself had been designed to accommodate this task. Historically in the nuclear industry, tasks completed by teleoperators such as the model M-2 or through-the-wall mechanical master-slave systems typically take eight times as long (on the average) to perform a task compared to hands-on operation. The five-to-one time factor achieved for shirt-sleeve comparison indicates that this task is well suited for remote handling. An average time computed from the two very best runs made at each of the two stations was only about two and one half times as long as for the astronauts.

In reality, the total time, including preparation and recovery, required for a human to perform a task directly must be considered. For example, in the case of EVA, the time required to suit up, depressurize, and pressurize must be included since it is necessary in order to perform a task directly and involves a significant amount of time. Of course, one must also consider personnel hazards eliminated through remote handling when analyzing the advantages and disadvantages of remote handling versus direct handling. This is frequently a more important consideration than performance time.

295

GENERAL DESIGN PHILOSOPHY FOR REMOTELY HANDLED EQUIPMENT

When designing flight equipment for remote handling (RH), several general principles are recommended. First and foremost, the equipment designers must be cognizant of the RH system that will be used on their equipment. This must be known before design can begin. Features of the teleoperator system such as reach and motion capabilities, operating envelope, lifting capacities, force threshold, and positioning accuracy will all affect the design of the equipment. Once these characteristics are known, the design can proceed using guidelines which are particularly important for remote handling. The most important of these are:

- Design with modular components - keep assemblies and subassemblies small and in easily handled modules. Include good contact surfaces for teleoperator grips on the module components.

- Keep the interfaces between the modules simple and self-aligning. Remote alignment using CCTV viewing can be very difficult.

- Design for the simplest motion. Pushing-pulling with a teleoperator is much easier than rotary motion.

- Standardize to the greatest practical extent, particularly fasteners and connectors. This minimizes the number of tools and spare parts required.

- Do not allow loose parts in the design which can be dropped (or float away). Use captured fasteners.

- Minimize the number of special tools or fixtures. Take advantage of the capabilities of the system.

An important point to keep in mind is that the designer must design for remote handling from the beginning. In many cases, retrofitting is virtually impossible and certainly expensive.

Design reviews are an important feature of any design process. They are particularly important when designing for remote handling. Equipment designs must satisfy handling requirements as well as functional requirements. The use of a design checklist, based on design guidelines such as those, can be a very useful tool.

The next critical area is that of development and demonstration. Never believe that designers/fabricators are perfect. Equipment should always be prototyped and complete disassembly and assembly demonstrated using the chosen teleoperator system. This may be a costly undertaking, but costs much less than being unable to repair equipment once in place.

Finally, planners must be painfully aware of the relative time efficiency achieved in performing tasks remotely. The well-established reference from extensive nuclear experience as well as many non-nuclear (not quite as extensive) applications is 8:1. Some tasks take less, as in the case for experiments discussed in this paper, but 8:1 is still the best data for planning purposes. Also keep in mind that the M-2 system is one of the most capable systems in the world. Lesser systems will certainly decrease the time efficiency. With the

tremendous emphasis on robot safety for the space station, one likely outcome is for the telerobotic devices to operate very slowly (and implied safely). If this does occur, then the time efficiency will be greatly reduced. This could be an overwhelming issue for those designing and planning for telerobots in space applications.

CONCLUSIONS

The ACCESS and refueling coupling remote handling experiments have demonstrated the feasibility of performing complex, space-related tasks by teleoperation. In both experiments, operators were able to achieve, with relatively little experience and practice, repeated performance of the tasks without incident in an almost routine manner although no equipment modifications were implemented for remote handling. This demonstrates the high level of adaptability of man-in-the-loop teleoperation to unstructured tasks. Operator fatigue in the second truss experiment was significant and suggests that telerobotic (automated) assembly would be beneficial where possible. The results of both experiments support conclusions that teleoperation represents a valuable enhancement to astronaut EVA. It must be recognized that equipment must be designed differently for remote handling than for hands-on operation. This will also improve EVA performance. General guidelines do exist that have been proved in other remote applications.

REFERENCES

1. T. W. Burgess, "The Remote Operations and Maintenance Demonstration Facility at the Oak Ridge National Laboratory," presented at the American Nuclear Society Topical Meeting on Waste Management and Decontamination and Decommissioning, Niagara Falls, NY.

2. J. N. Herndon et al., "The State-of-the-Art Model M-2 Maintenance System," pp. 147-154, Proceedings of the ANS Topical Meeting on Robotics and Remote Handling in Hostile Environments, Gatlinburg, TN, April 1984.

3. W. W. Hankins III et al., "Space Truss Assembly Using Teleoperated Manipulators," Proceedings of the Goddard Conference on Space Applications of Artificial Intelligence and Robotics, Greenbelt, MD, June 1987.
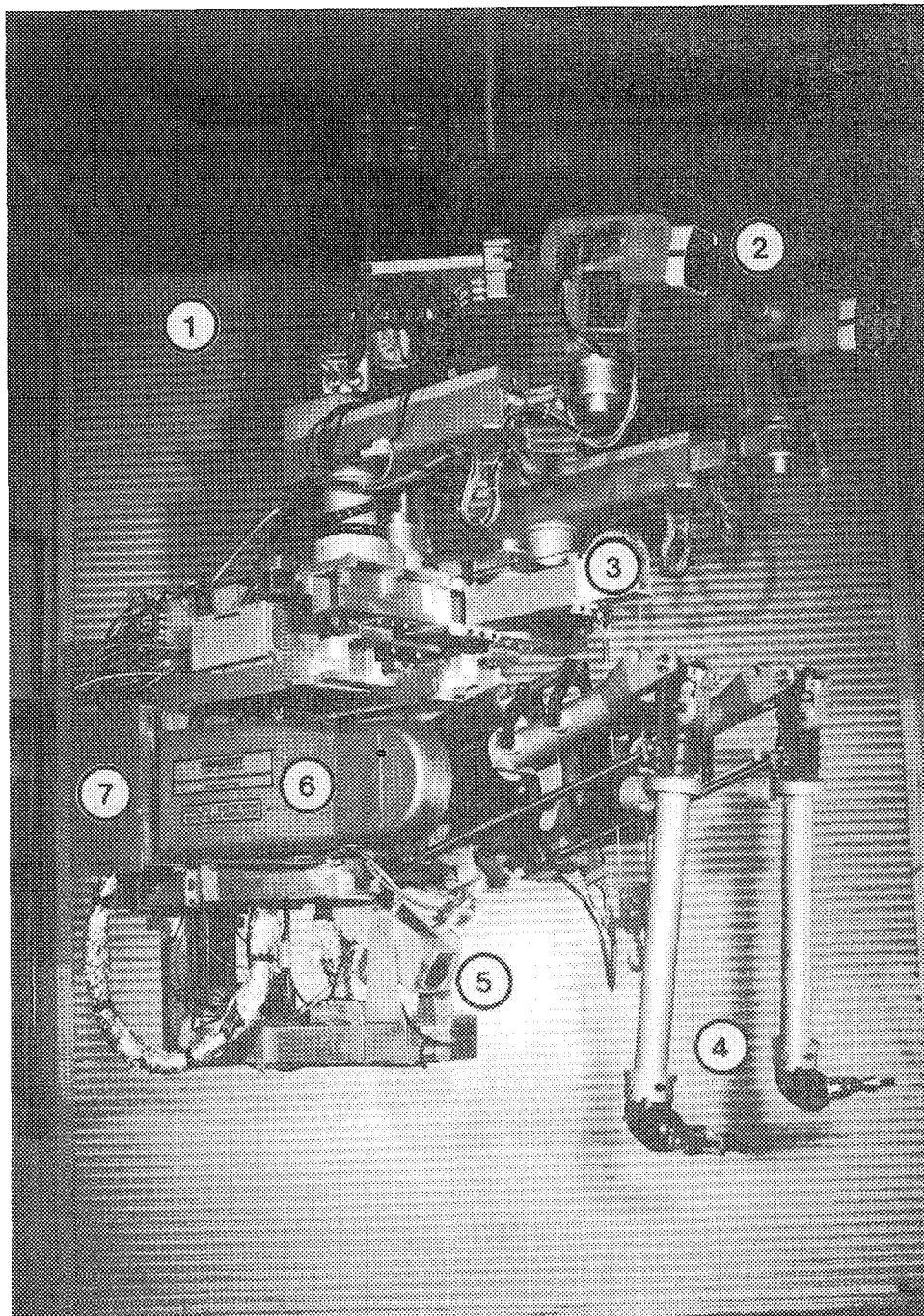
Fig. 1. The model M-2 teleoperator slave (1) transporter interface, (2) movable overhead cameras, (3) auxiliary hoist, (4) slave arms, (5) fixed lower camera, (6) servomotor housing, and (7) control electronics rack.

Fig. 2 The ROMD control room (1) model M-2 master control station,
(2) teleoperator transporter and facility camera control console.
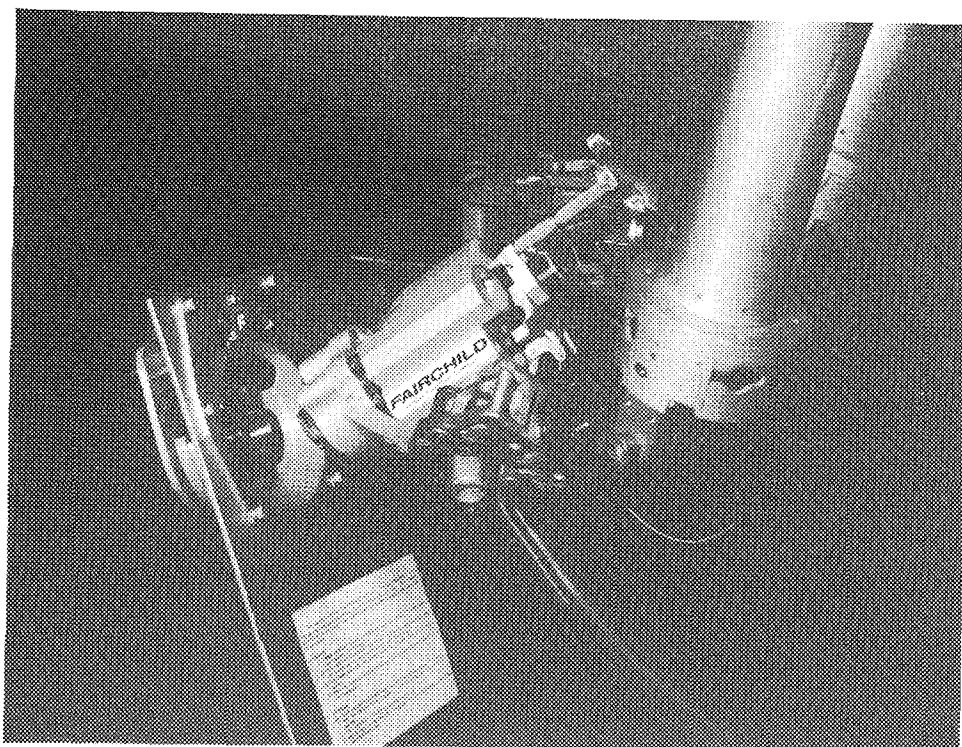
Fig. 3. Satellite refueling coupling remote handling operations.
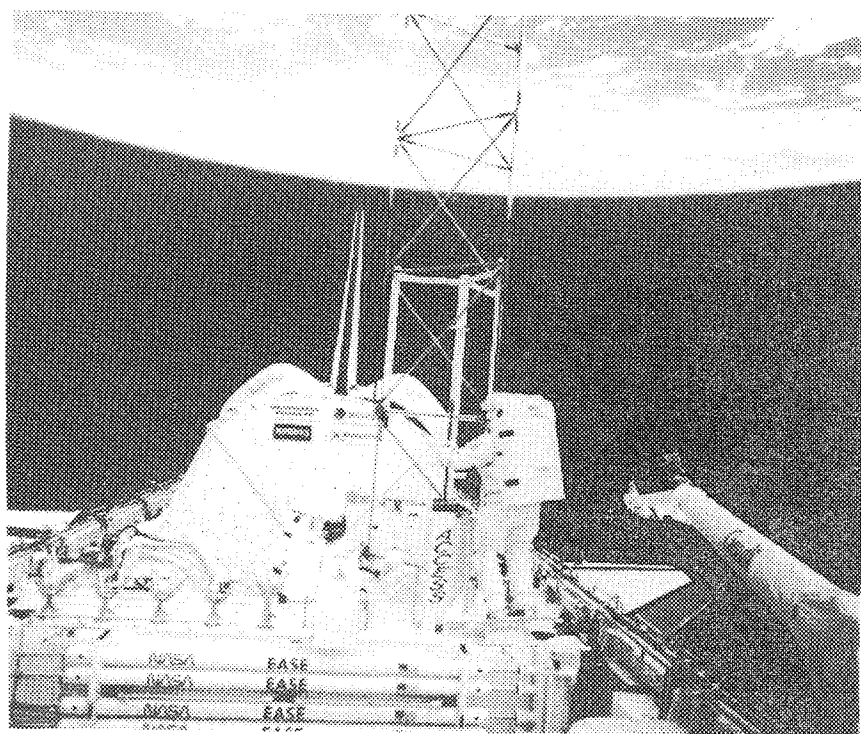
Fig. 4. ACCESS I EVA operations aboard shuttle mission STS—61b.
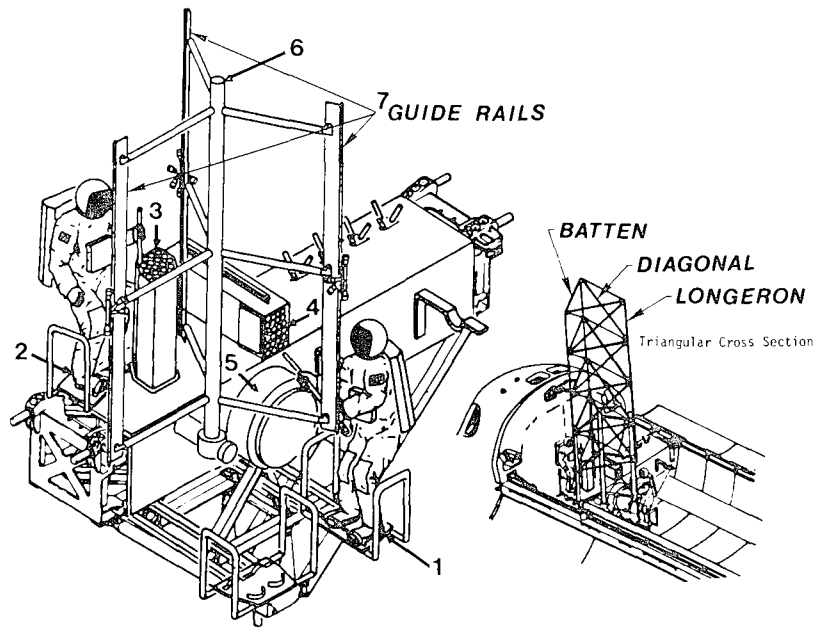
Fig. 5. Schematic showing EVA construction of ACCESS truss on assembly fixture.
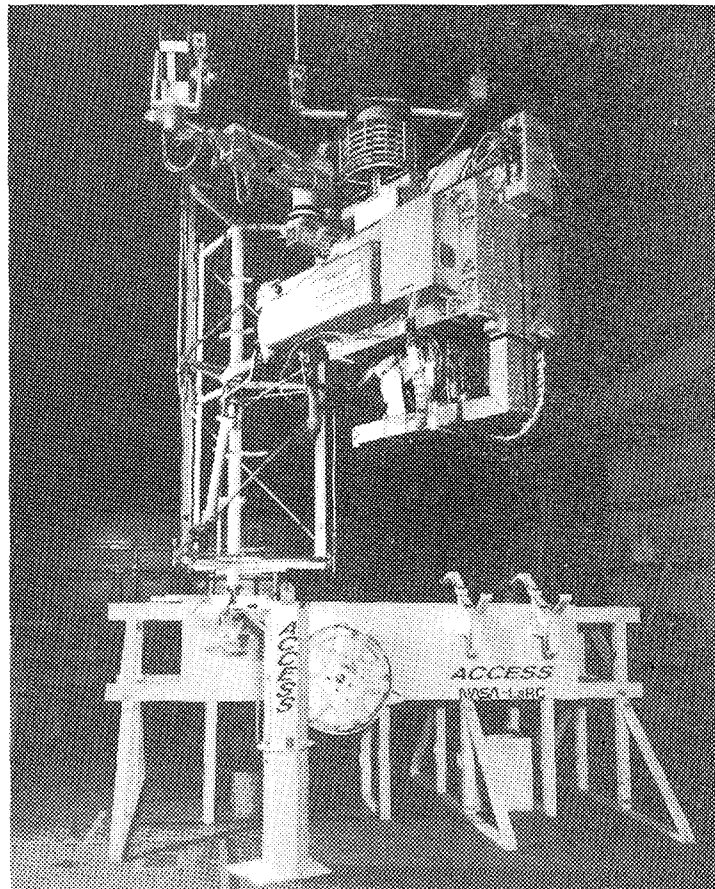
Fig. 6. ACCESS I assembly operations during Experiment I.

Fig. 7. Installing a node on a guide rail.
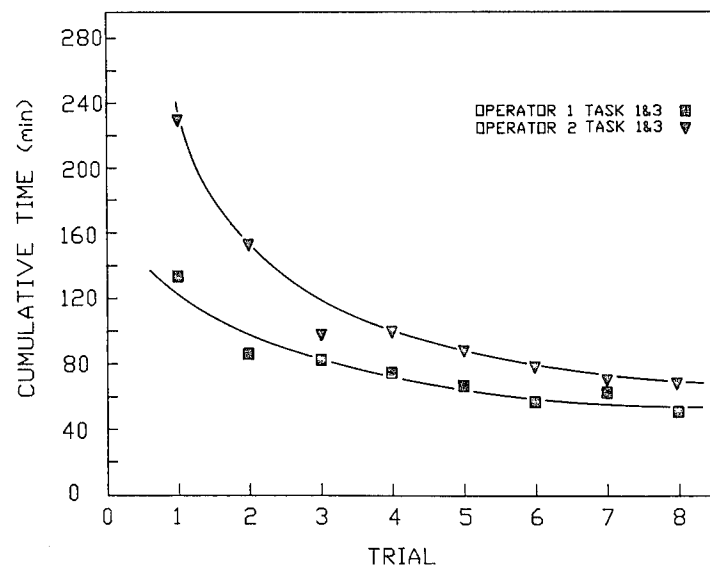
Fig. 8. Combined task completion time versus task trial for Experiment I.
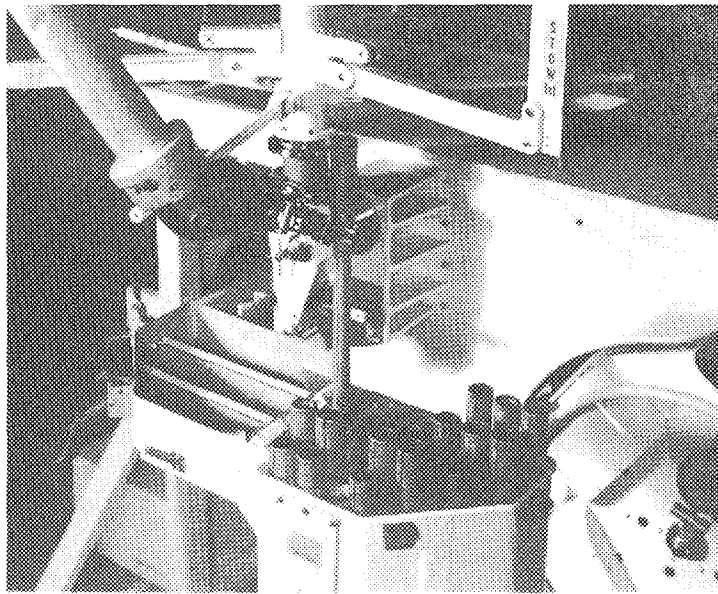
Fig. 9. Removing a strut from the storage canister.
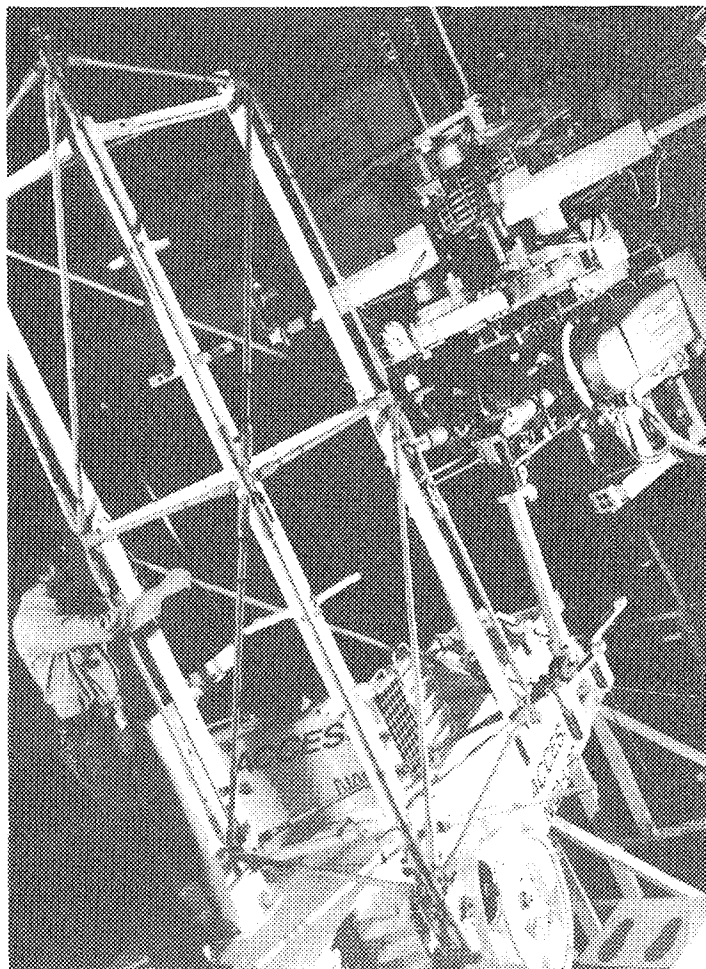
Fig. 10. Positioning of the model M-2 teleoperator for operations at Station 1.
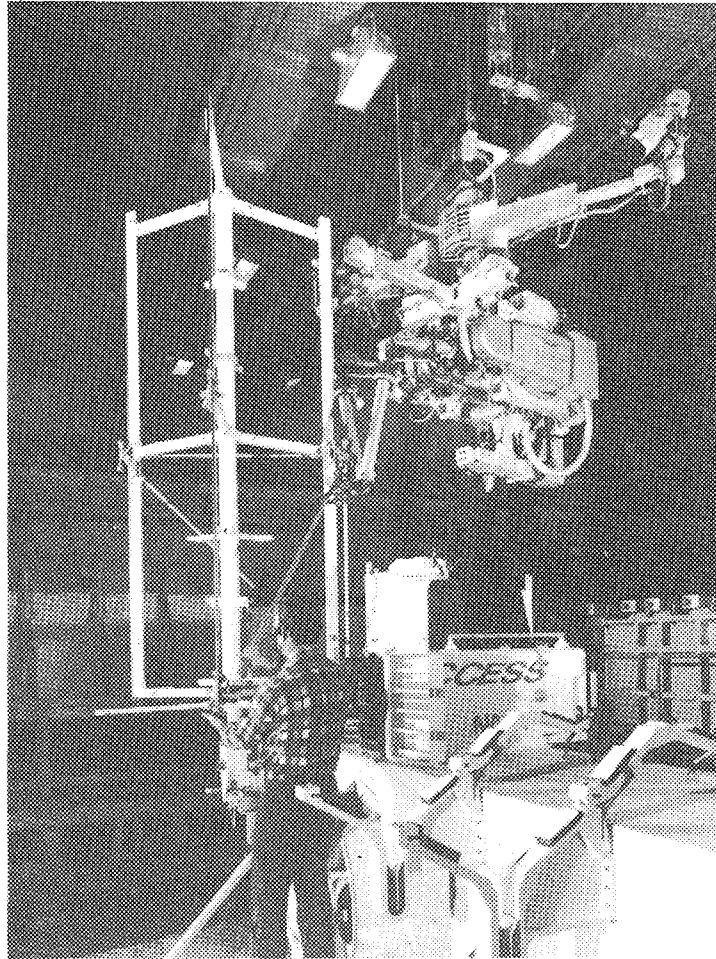
Fig. 11. Positioning of the model M-2 teleoperator for
operations at Station 2.
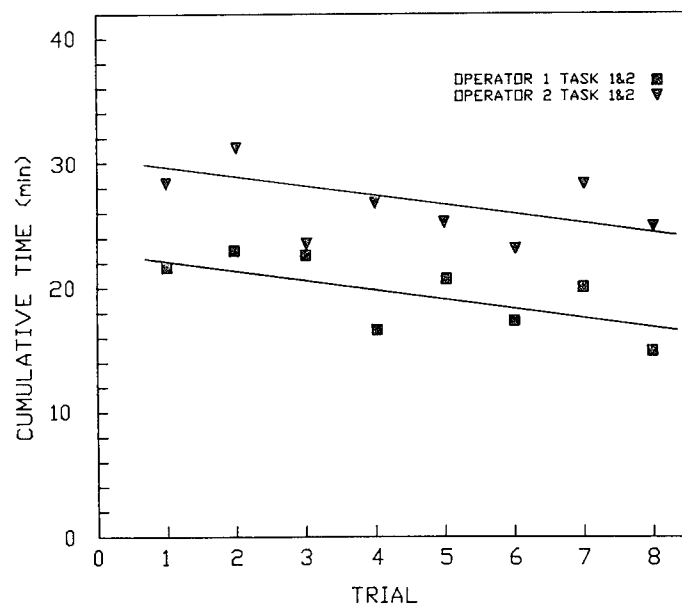
Fig. 12. Combined task completion time versus task trial
for Experiment II, Station I.
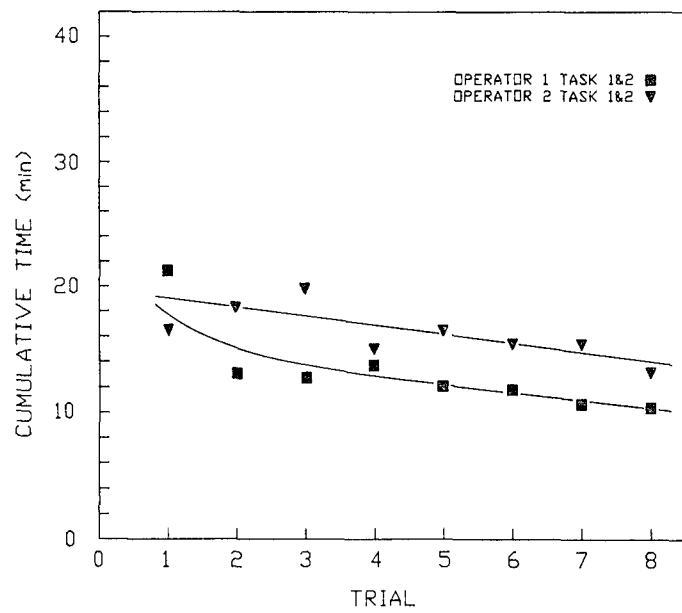
Fig. 13. Combined task completion time versus task trial
for Experiment II, Station 2.
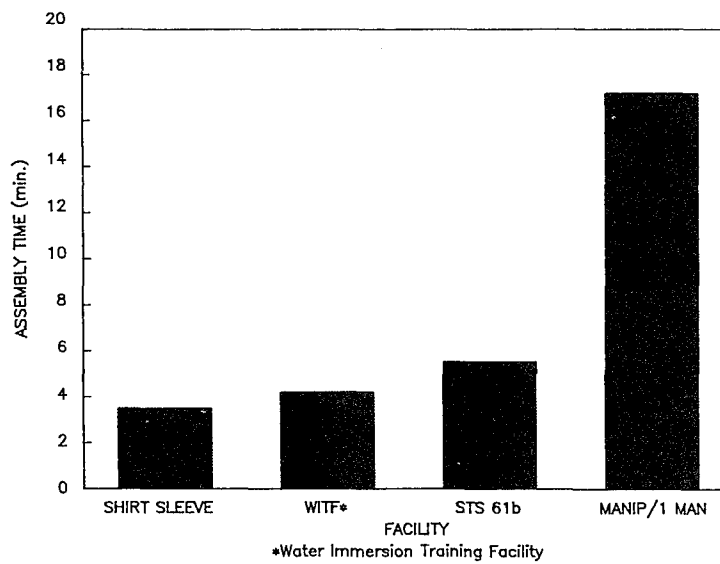
Fig. 14. Comparison of assembly time in different facilities.

ROBOTIC JOINT EXPERIMENTS UNDER ULTRAVACUUM

A. Borrien and L. Petitjean*

ABSTRACT

In the first part of the paper, various aspects of a robotic joint development program, including gearbox technology, electromechanical components, lubrication, and test results, are discussed.

A test prototype of the joint allowing simulation of robotic arm dynamic effects is presented in the second part of the paper. This prototype is tested under vacuum with different types of motors and sensors to characterize the functional parameters: angular position error, mechanical backlash, gearbox efficiency, and lifetime.

1. INTRODUCTION

The objectives of this paper are to present the gear technology, lubrication, and ultravacuum test results of a robotic joint with high Hertzian pressure on the gear teeth. Dynamic operation of the joint is studied to determine the influence of the control feedback law on significant parameters such as angular precision, speed variation, and damping rate of the joint. Finally, simulated lifetime results of the joint are discussed. After the ultravacuum lifetime test, mechanical and tribological reducer effects in the gearbox are examined to quantify wear level versus number of cycles.

2. JOINT DESIGN

2.1 General Specifications

Geometric, kinematic and dynamic specifications are based on system require-ments established for accomplishing the mission with the manipulator arm.

General specifications are the following:

.	Angular excursion	-90 deg to +90 deg
.	Maximum output motor torque	10 Nm
.	Holding output torque	60 Nm
.	Global stiffness	7000 Nm/Rad.
.	Maximum output backlash	2×10^{-3} Rad.
.	Lifetime under ultravacuum	250 hours
.	Vacuum level	10^{-8} torr
.	Maximum output speed	5×10^{-2} Rad./sec

*Centre National d'Etudes Spatiales (CNES), Toulouse, France

2.2 Technological Definition

The electromechanical joint consists of a DC brushless motor, two optical encoders (input and output), a gearbox, and an electromechanical brake.

a) Motor

Our nominal choice consists of a space-qualified electrical DC brushless motor. The most important advantages are electronic and feedback law simplicity and good stability over a wide dynamic operating range as well as good steady state system performance. An alternative choice is based on a space-qualified stepper motor driven with a special control law. A standard mechanical interface allows comparison of the two alternatives with the same joint.

b) Sensor Modules

Two sensor configurations are possible for measuring joint parameters such as output angular position and input motor speed. System studies have shown that the angular speed of the joint must be sensed on the motor shaft and the angular position on the output housing to satisfy stability and damping criteria of the control loop.

c) Brake

A brake is placed on the motor shaft to latch the joint. A solenoid is energized to release the brake whenever the joint is to be driven.

d) Gear Transmission Description (see Figure 1)

Trade-off studies have concluded that the best solution consists of a parallel-axis back-driveable gearbox with several stages. The main advantages are:

- relatively simple manufacturing
- good potential efficiency
- low backlash
- gear geometry consistent with dry lubrication technology.

Gearbox Definition (see Figure 2). The reducer is divided into two kinematically symmetrical closed parallel branches which consist of:

- external spur gears for the first and second stage
- internal gear wheel for the output stage.

The objective of this design is to allow a fine adjustment of backlash and equal load sharing between the two branches.

- Gear material : 35NCD16 – Air hardened 875 deg C
                           – Tempered 650 deg C
- Lubrication   : PTFE coating

Geometric Characteristics

Stage	Module (mm)	Width	Teeth number	Gear ratio
1	0,5	3	20 / 120	6
2	0.7	7	17 / 86	5.06
3	1	9	17 / 103	6.06
Total ratio				183,90

Stage		Bending stress	Allowable bending stress	Hertzian Stress	Allowable Hertzian Stress
1	P	7.3	48.8	52.3	80.4
	W	6.4	55.5	52.3	91.9
2		12.7	54.4	74.5	91.9
		10.2	76.8	74.5	104.5
3		22	60.4	83.3	104.5
		24.8	69.3	83.8	104.5

P : pinion   Stress : 0.1 N/mm^2
W : wheel

Theoretical calculations have shown that the most important parameter is Hertzian stress which occurs on the gear teeth and could induce fast coating wear and scuffing.

2.3 Description of the Joint Test Machine (see Figure 3)

a)   Joint Test Machine Objectives

The test machine, which consists of the electromechanical joint and an inertia simulation, has been designed to allow interchangeability of the electrical components while using the same joint.   Several configurations are available for testing:

.   Configuration 1: Brushless DC motor, angular potentiometer (output shaft) and optical encoder (input shaft)

.   Configuration 2: Brushless DC motor, optical encoder for input and output angular position sensing

.   Configuration 3: Stepper motor with the sensors of Configuration 2. This configuration is not presented in detail because some numerical problems must be resolved to achieve feedback law stability.

b)   Test Machine Technological Definition (see Figure 4)

The choice of electrical components has been made with the main criteria, vacuum operation without significant outgassing.   Also, bearing lubrication and materials have been selected to satisfy environmental conditions of low outgassing.

List of components:

.   Brushless DC motor: SAGEM 23 MCM90, space-qualified
.   Stepper motor SAGEM 23 PP, space-qualified
.   Brake: Binder magnetic 86: 61104, vacuum rated only
.   Optical encoder: Sopelem RI110: vacuum rated only

c)   Inertia Simulator (see Figure 5)

The objective is to simulate an inertia of 800 Kg m^2 on the output of the joint shaft.   Several solutions were examined.   Step-up gearing with a tooth belt was chosen to minimize mass and reduce volume in the vacuum chamber. Moreover, it allows a good simulation of the robotic arm inertia parameters.

.   Simulated inertia: 800 Kgm^2
.   Step-up gearing ratio: 125
.   Step-up gearing stiffness: 1950 Nm/Rad.

310

3. GEAR MATERIAL AND LUBRICATION PROCESSES

3.1 Material Trade-off

High contact stresses occur with the given requirements and lead to a material which provides good mechanical characteristics. These include yield strength, surface hardness, and contact pressure fatigue resistance. Good machinability is also required to obtain excellent geometric tolerances

Among different alloy and stainless steels, 35NCD16 steel was chosen, which has the following advantages:

- o   Air hardened, which produces minimum deformation
- o   Ease of plasma nitrided (if necessary)
- o   Use after tempering without other surface treatment
- o   Useful for heavy dynamic loads combined with fatigue, one of the best steels used in aircraft technology.

3.2 Lubrication Processes

In considering lubrication, the investigation was deliberately limited to dry lubricants. To ensure sufficient life and to avoid scuffing, a coating must be used which gives low friction coefficient and low wear rate.

Possibilities giving satisfaction in this case are:

- o   crystalline solids with lamellar structure (MoS_2)
- o   soft metals (Pb, Au, Ag)
- o   anti-wear ceramics (TiN, TiC)
- o   polymer materials (PTFE, polyamides, polyacetal)

To help choose the right solution, gears coated with different dry lubricants were tested on a "four square" (closed loop) gear test machine. These machines allow simulation of the speed and load environment of each reducer stage.

The selection criteria for the coatings are:

- o   no scuffing in ultravacuum
- o   low wear rate
- o   low friction coefficient
- o   no geometric modification during and after coating
- o   good adhesion between coating and substrate.

Five treatments were selected for preliminary experiments at atmospheric pressure. Those which gave better performance were later tested in a vacuum (10^{-7} Torr).

Descriptions of coatings, test machines and results in air were given in 1985 at the 2nd European Space Mechanisms and Tribology Symposium at Meersburg, Germany.

Performance classification is as follows:

| Heavy load | Medium load |
| Low speed | Medium speed |

	Heavy load / Low speed	Medium load / Medium speed
1	PTFE	PTFE
2	MoS_2	MoS_2
3	TiN	FeMoS
4	Ion nitriding	Ion nitriding
5	FeMoS	TiN

The underlined coatings give satisfactory results in air.

3.3 Vacuum Tests

In tests under vacuum, the field was narrowed to PTFE and MoS_2 for the final choice of coating (see Figure 6). The chronology of these tests was:

1) Running-in process with a small torque
2) Qualification test of 100 hours with the nominal torque
3) Qualitative examination of the teeth
4) Short test with step-by-step increasing torque from nominal to maximum value. Each step lasts five hours.
5) Endurance test of 100 hours with maximum torque to classify coatings and to evaluate their resistance under severe loading conditions.

In the case of medium speed (100 rev/min) and medium Hertzian pressure (450 N/mm^2), both coatings had satisfactory friction coefficient evolution, but PTFE provided less surface wear. In case of low speed (2 rev/min) and high Hertzian pressure (550 N/mm^2), only PTFE reached the end of the endurance test (84,000 revolutions) without damage.

It was not possible to estimate the real friction coefficient during this endurance test because of disturbances caused by debris located in the four-point angular contact ball bearings. Finally, PTFE performed best in vacuum and it had a rather good accommodation to misalignment. We finally chose it for the robotic joint application.

3.4 Robotic Joint Gears

The gears were tooled on a MIKRON milling machine. Then they were checked before and after PTFE deposition. Profile, lead, run-out, pitch deviation, and tooth thickness were controlled.

The ISO quality range after treatment was always better than or equal to 6, except for the internal ring whose quality was 7.

4. DYNAMIC ASPECTS OF THE JOINT

4.1 Feedback Loop Description

a) Configuration 1

The DC brushless motor operates as a servo actuator with an analog position feedback loop. The rotor angular position is sensed by an optical encoder, sampled and differentiated to obtain angular speed. A numerical speed loop is implemented to damp high frequency oscillations. The reducer output position is sensed by a potentiometer.

Functional Scheme
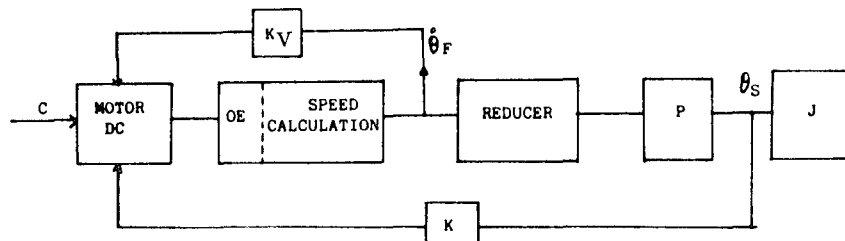
OE - Optical encoder   K - Position gain
P - Potentiometer K_V - Speed gain
J - Simulated inertia

b) Configuration 2

For this case, the potentiometer is replaced by an optical encoder which senses the output angular position.

c) Configuration 3

This configuration uses a stepper motor with a specific dynamic control law. A torque feedback control law has been simulated, but the first experiments indicated some stability problems due to the numerical speed calculation.

This configuration is not considered as a nominal solution because of the feedback complexity. Dynamic analysis and electronic improvement have been performed to prove the feasibility of the law. The results of these studies and experiments will be presented at the symposium.

4.2 Servo Loop Definition

The dynamic system can be treated as a second-order problem if rotor inertia, reducer output inertia, and the electrical constant of the motor are neglected.

The differential equation is:

$$J_s \ddot{\theta}_s + \frac{K_v \dot{\theta}_s + K\theta_s}{T_a} = T_m - T_R$$

θ_s: Output position T_a: Control torque
N: Reducer ratio T_m: Motor torque
K: Position gain T_R: Resisting torque
K_v: Speed gain J_s: Output inertia

with the usual 2nd order servo parameters:

$$\frac{J_s}{K} = \frac{1}{\omega_N^2}$$

ω_N : Undamped eigenfrequency

$$\frac{2\zeta}{\omega_N} = \frac{K_v}{K}$$

ζ : Damping rate

$$\frac{1}{K} = G$$

G : Static gain

With $\omega_N = 1.125$ Rad./sec and $\zeta = 1$

K and K_v are calculated to be

$$K = 1000 \text{ Nm/Rad.}$$
$$K_v = 1800 \text{ Nm/Rad./sec}$$

These theoretical gains have been introduced in the experimental servo electronics. Some stability problems in the high frequency range limit speed gain efficiency.

The phenomena can be explained by the following considerations: In the backlash range, the load inertia changes between two extreme values: low rotor inertia and high simulated inertia. The digital tachometer encoder cannot track these rapid changes in motor rate without significant phase lag. Rate sampling precision is poor because the samping frequency is low (5 msec).

To improve the servo loop stability, it is possible to add a low-pass filter in series with the digital tachometer output. It appears that one of the best solutions is to use an analog tachometer for the high frequency range and a digital tachometer for the low frequency range. This mix of the two types of rate feedback provides the desired characteristics, while attenuating undesirable phenomena.

5. PROTOTYPE JOINT EXPERIMENTS

5.1 Philosophy of Testing

The purpose of the tests was to achieve confidence in the performance of the electromechanical joint under heavy loading and long operation in an ultravacuum environment.

The main objective was to assess the performance of the dry-lubricant gear reducer and electrical components. Backlash and friction coefficient evolution are the most important parameters which characterize reducer transmission.

During preliminary analysis, dynamic performance of the joint was evaluated using different types of feedback loop. The angular excursion law consists of large amplitude movements, small oscillations and locking phases. This is considered a good simulation of the approach and grappling sequence. All dynamic parameters are easily modified, utilizing a "menu" on a computer. The following parameters are automatically recorded: output angular position, motor position, winding intensity, and motor speed (deduced from sampled angular position (200 Hz)).

5.2 Parameter Measurements Before Endurance Tests

- Backlash

After assembly, it is easy to check the residual backlash by comparing the information from the two optical encoders when rotational direction is changed. However, before final assembly, backlash has been checked by measuring the axial displacement of a comparator placed on the output gear of the reducer, the motor being locked. The measured backlash in this case was:

$$j = 5 \times 10^{-4} \text{ Rad.} \simeq 1.7 \text{ Arc min}$$

- Friction Torque

Joint friction torque was measured with an angular dynamometer before final assembly with an inertia simulator. Two values were obtained by rotating the joint successively by each extremity. The results were similar (T = 0.04 Ncm), proving good joint reversibility.

The multiplier mechanism had an effective friction torque of 0.6 Ncm, but there is a dispersion in the results, depending on the belt tension. The global resisting torque was about 0.65 Ncm.

- Efficiency

At maximum speed and nominal torque, the motor efficiency is determined as follows:

$$\eta_M = \frac{T \times \omega}{U \times I}$$

T - Torque ω - Angular velocity
I - Winding current   U - Voltage

$$\eta_M = \frac{\omega}{(R/K^2)T + \omega}$$

R - Winding resistance   R = 10.5 ohms
K - Torque constant   K = 0.06 Nm/A
                                 T = 0.08 Nm

so that

$$\eta_M \simeq 0.04$$

When the inertia decreases, motor efficiency rises to 0.3. Measurement was made of the global mechanical efficiency of the joint with a constant resisting torque of 0.09 Nm. A torque of 0.042 Nm on the motor shaft was obtained.

Then,

$$\eta_G = \frac{T_M \, \omega_M}{T_R \, \omega_R}$$

T_M = Motor torque ω_M = Motor speed
T_R = Resisting Torque ω_R = Output speed

The multiplier efficiency was also measured and found to be $\eta = 0.85$. An estimate of the reducer efficiency is then

$$\eta_\eta = \frac{\eta_G}{\eta} = \frac{0.69}{0.85} = 0.81$$

This corresponds to $\eta = 0.93$ for each meshing gear.

- Stiffness

To ensure good locking stiffness, a steel housing was placed on the joint. The joint torsional stiffness was calculated with individual shaft and gear contributions. A value of $K \simeq 1 \times 10^5$ Nm/rad was obtained. This value was checked by measuring the angular difference between the two encoders under the following conditions: the brake was locked and the output inertia mass was loaded by a static torque.

With an 11.85 Nm applied torque, an angular difference of 0.03 deg was measured. Global stiffness was deduced from the previous results to be K 23,000 Nm/rad.

The inertia simulator stiffness has been calculated to be K 2,000 Nm/rad.

- Inertia

Assuming a geometric design for the mechanical parts, we have:

- Joint output inertia : 0.84 m^2 kg
- Multiplier inertia : 800 m^2 kg
- Motor shaft inertia : 0.8 m^2 kg
- Ratio I load / I motor : 1,000

5.3 Preliminary Joint Experiments

- Maximum Static Torque Specification

A 56 Nm static torque was put on the joint using weights with the electromagnetic brake locked. One of the encoders was therefore fixed and the other rotated from 0 deg to 0.13 deg which confirmed the above stiffness value of about 25,000 Nm/rad. This test was repeated ten times without any angular position modification, thus demonstrating good behavior of the loaded gears and brake.

- Magnetic Brake Test

The brake was locked and the motor reversed from clockwise maximum torque to counterclockwise maximum torque. The motorshaft encoder was monitored to detect any rotation. No movement was observed.

In a second test, the brake was released for seven hours, which requires application of constant input voltage. Subsequently, after switching off the input voltage, the brake did not relock for several minutes. The reason for this may be the high temperature under vacuum, which increases the distance between the magnetic parts of the brake.

- Maximum Torque Motor Test

For this test, the output part of the joint was locked onto the housing and the motor driven from "0" to maximum current (0.17 Nm) with a linear rise during two minutes. This was repeated twenty times in succession. The motor was found reliable.

5.4 Endurance Tests

For all experiments, the minimum vacuum was 10^{-6} Torr, and was performed with a 600 ℓ/sec RIBER ion pump.

- Running in Process

With thick PTFE films (6 μm), the running-in process is very important. A low Hertzian pressure and small angular acceleration of 20 deg/sec (i.e., 1.52 Nm output torque was chosen. For run-in, the output gear was rotated 80 revolutions (40 clockwise and 40 counterclockwise).

- Cyclic Test Description

Two standard movements were recorded, one for large angular displacement with maximum dynamic performance and the other for large angular displacement combined with small oscillations to simulate a final capture.

The first standard movement, which is called A, consists of an angular excursion of 170 deg at the output of the joint. It begins with an accelerated phase (= 130 deg/sec , T = 10 Nm), followed by a constant angular rate of 500 deg/sec and finally, a decelerated phase with the same dynamic parameters. Then the joint comes back to the initial position with the same displacement law.

The second standard movement, B, has the same angular excursion and the same maximum angular rate, but the acceleration is limited to 65 deg/sec. Before coming back, four sinusoidal oscillations with a 1 deg amplitude are imposed on the joint.

- Endurance Test Procedure

The joint was tested with 1100 cycles of the A program (34 hours) and 1600 of the B program (87 hours), corresponding to a total of 121 hours lifetime.

318

The number of cyclic loads reached by each gear tooth was:

- Third stage internal ring :   5400
- Third stage pinion   :   32700
- Second stage wheel   :   32700
- Second stage pinion   : 165600
- First stage wheel   : 165600
- First stage pinion   : 1987200

The average torques which were applied to the gear teeth are shown in Figure 7.

- Parameter Control

Each standard cycle was divided into several phases depending on the driving law. For each phase, a reference clock time was defined at which the position and angular rate parameters were automatically recorded by a computer program.

The program calculates, for these times, the difference between the theoretical position and the effective position of the joint and the difference between angular position at the ends of the joint. After analyzing 120 cycles, the program draws the evolution curves of the parameters and calculates the mean value and standard deviation for each one.

The following curves depict joint parameter fluctuations:

- Static position error: (Θoutput – Θtheoretical at t = 0) (see Figure 8)
- Dynamic error, recorded for the accelerated phase (see Figure 9)
- Output angular rate (see Figure 10)
- (Θoutput – Θinput x R(Ratio)): backlash variation, machined-gear-tooth deviation, and elastic deformation due to the load (see Figure 11).

– Backlash Evolution

Several measurements of backlash were performed during the lifetime tests. The final value, after 121 hours, is j = 1.8 arc/min (Figure 12). Thus, no significant evolution could be detected. Backlash evolution is representative of output gear wear. However, it is not possible to draw any conclusions about the wear of the other gear stages.

– Friction Coefficient Evolution

An 8 gm weight is sufficient to move the joint (T $\simeq$ 0.5 Ncm). On the other hand, the minimum motor voltage to start the joint is 0.42V, i.e., T = 0.75 cmN. These values are similar and no evolution could be detected.

– Gear Tooth Examination

The gear housing has some circular holes that allow direct examination of gear teeth with an endoscopic cane. Unfortunately, it is possible to observe only the second stage of the reducer. The teeth looked polished, almost brilliant, near the top, and it appears that the two mat blue-gray extremeties of the pinion were never in contact after 120 hours of running. If the results of checking (wear and surface inspection) and the functional performances (output backlash, resistant torque, efficiency) are all found to be in accordance with the specifications, the endurance test duration will be increased to 150 hours of running in ultravacuum. A discussion of the final results will be presented at the symposium.

CONCLUSIONS

These robotic joint endurance experiments are a good simulation of the orbital
mission. The tests have confirmed behavior of the components after three
months under vacuum and 121 hours working time, except for the brake
which showed some problems due to increased temperature.

The feasibility of a robotic joint of 150 mm diameter and 100 mm length, with
10 Nm dynamic output torque and 60 Nm static torque, has been demonstrated for
more than 100 hours lifetime with dry lubrication. The backlash and friction
torque stability indicate a potential increased lifetime without significant
damage.

Some improvements in the feedback law must be implemented in the future to take
into account high frequency resonance problems, inertia simulator stiffness
effects and the effect of backlash.

Although the new torque requirements of the Hermes telemanipulator arm are much
higher than for the joint discussed in this paper, it seems that a joint with
force capability in the range 10 to 20 Nm could have several applications in
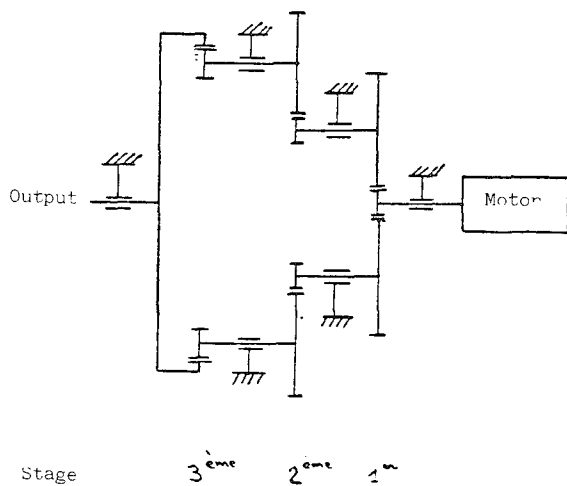orbital station manipulators.

Figure 1. Gear box description

Figure 2. Gear box arrangement
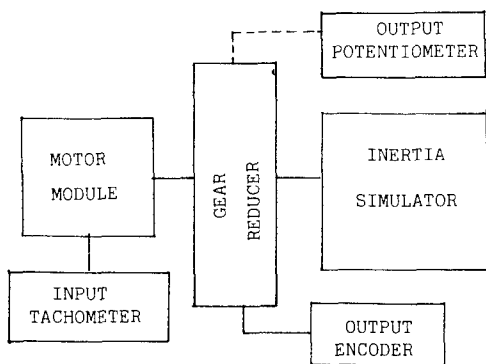
Figure 3. Joint prototype functionnal
definition
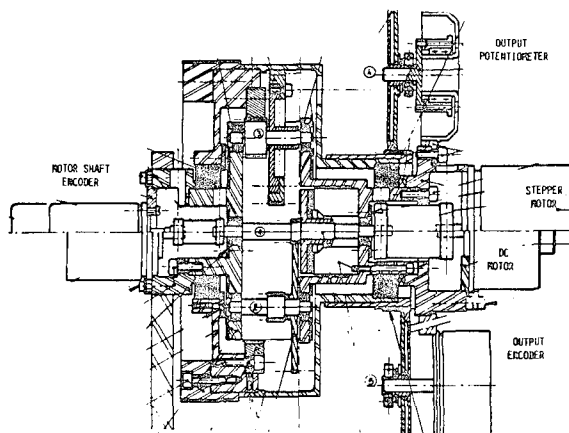
Figure 4. Prototype technological
definition joint

Figure 5. Inertia simulator
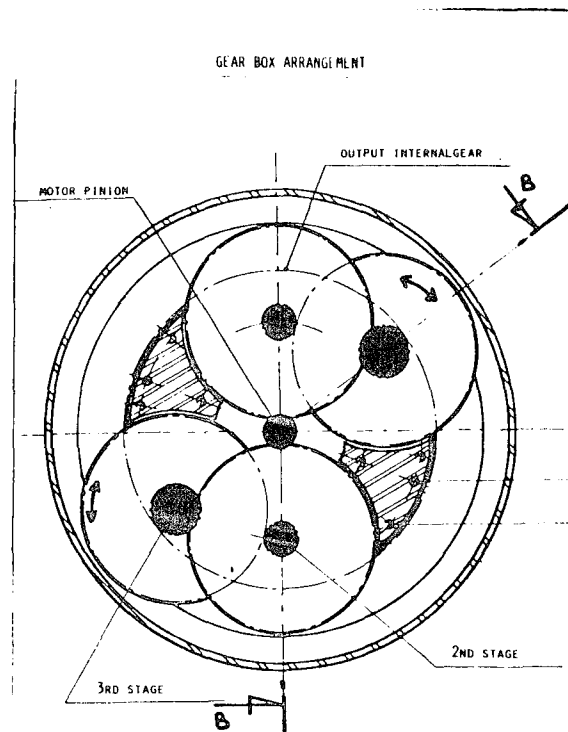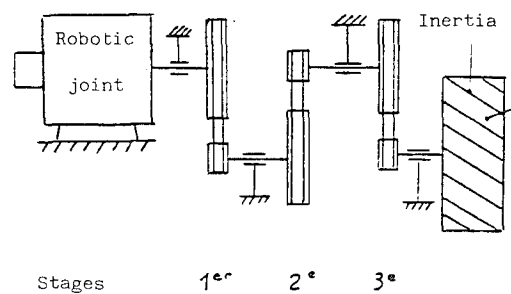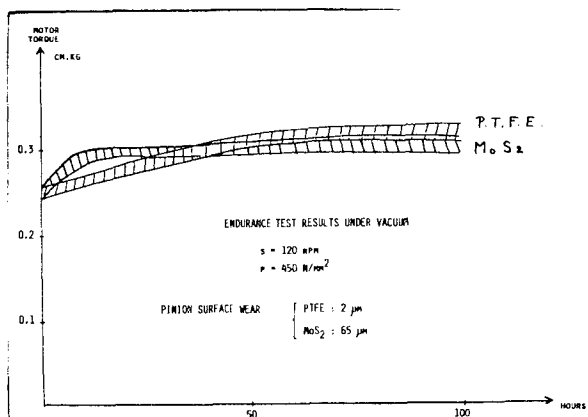
322

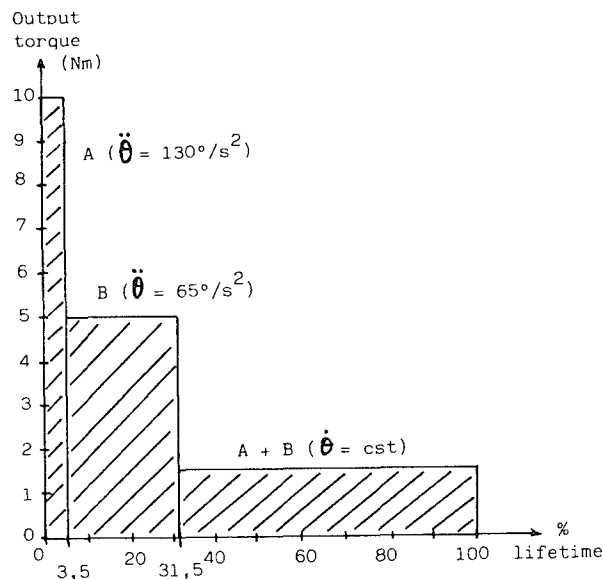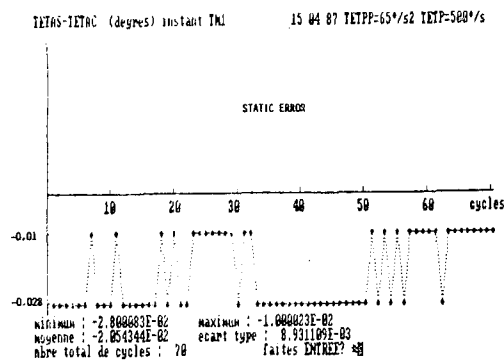Figure 6. Endurance tests MOS2/PTFE

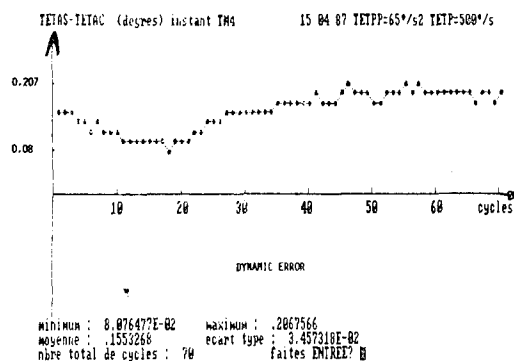Figure 7.

Figure 8. Static position error
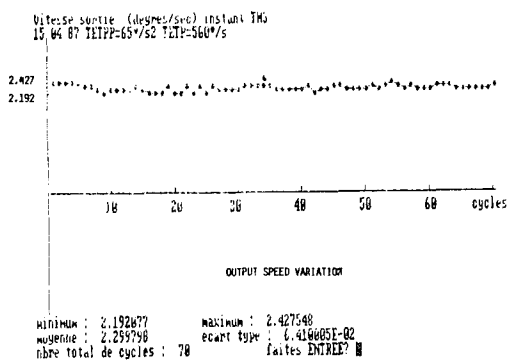

Figure 9. Dynamic error
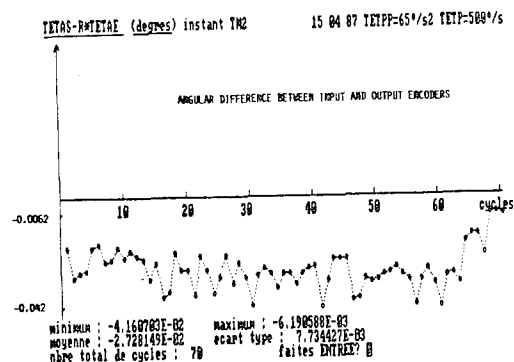

Figure 10. Output speed variation
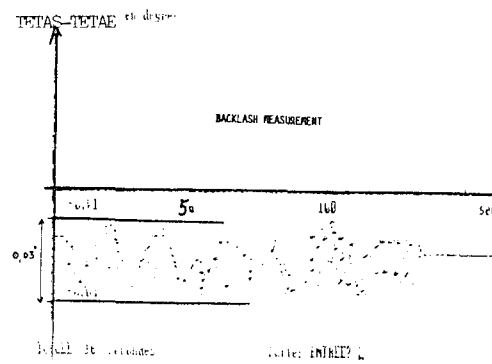

Figure 11. Backlash variation

323

Figure 12. Backlash measurement

324

SPACE STATION FULL-SCALE DOCKING/BERTHING MECHANISMS DEVELOPMENT

Gene C. Burns*
Harold A. Price*
David B. Buchanan*

ABSTRACT

One of the most critical operational functions for the Space Station is the orbital docking between the station and the STS[+] orbiter. This paper describes the program to design, fabricate, and test docking/berthing mechanisms for the Space Station. This 3-year program (May 1985 to April 1988) was conducted by McDonnell Douglas under a NASA Marshall Space Flight Center (MSFC) research and development contract. The design reflects Space Station overall requirements and consists of two mating docking mechanism halves. One half is designed for use on the shuttle orbiter and incorporates capture and energy attenuation systems using computer-controlled electromechanical actuators/attenuators. The mating half incorporates a flexible feature to allow two degrees of freedom at the module-to-module interface of the Space Station pressurized habitat volumes.

The design concepts developed for the prototype units may be used for the final Space Station flight hardware.

INTRODUCTION

Figure 1 shows a full-scale mockup of the docking/berthing mechanism. Figure 2 illustrates the orbiter's approach to dock with a Space Station module. The analysis and simulations of the STS orbiter docking to the Space Station have shown that an active capture and energy attenuation system is required in contrast to a passive system used on previous space docking systems. The location of the docking module in the orbiter forward cargo bay results in a 12.16 m (40 ft) offset between the docking line of action and the orbiter center of gravity. This offset produces an orbiter pitching movement at docking contact. The system designed to provide capture and energy attenuation consists of a capture ring with six degrees of freedom and remotely operated capture latches. The ring is supported and extended by eight computer-controlled, electromechanical actuators/attenuators. Through the proper design of the ball-screw actuators and the electronics that control them, these mechanical devices act as variable-rate, over-damped springs through the capture and attenuation phase of docking. Through the use of this active servo system that utilizes both force and position feedback loops, the docking forces and moments are minimized. After the docking energy is absorbed, the actuators align and pull the structural interfaces together.

The configuration of the Space Station uses a closed-loop pressurized module pattern. This pattern allows the crew to have dual egress from each module, but it presents mechanical problems in the assembly of the pattern because of module dimensional tolerances. For compensation, flexible couplings must be incorporated at

---
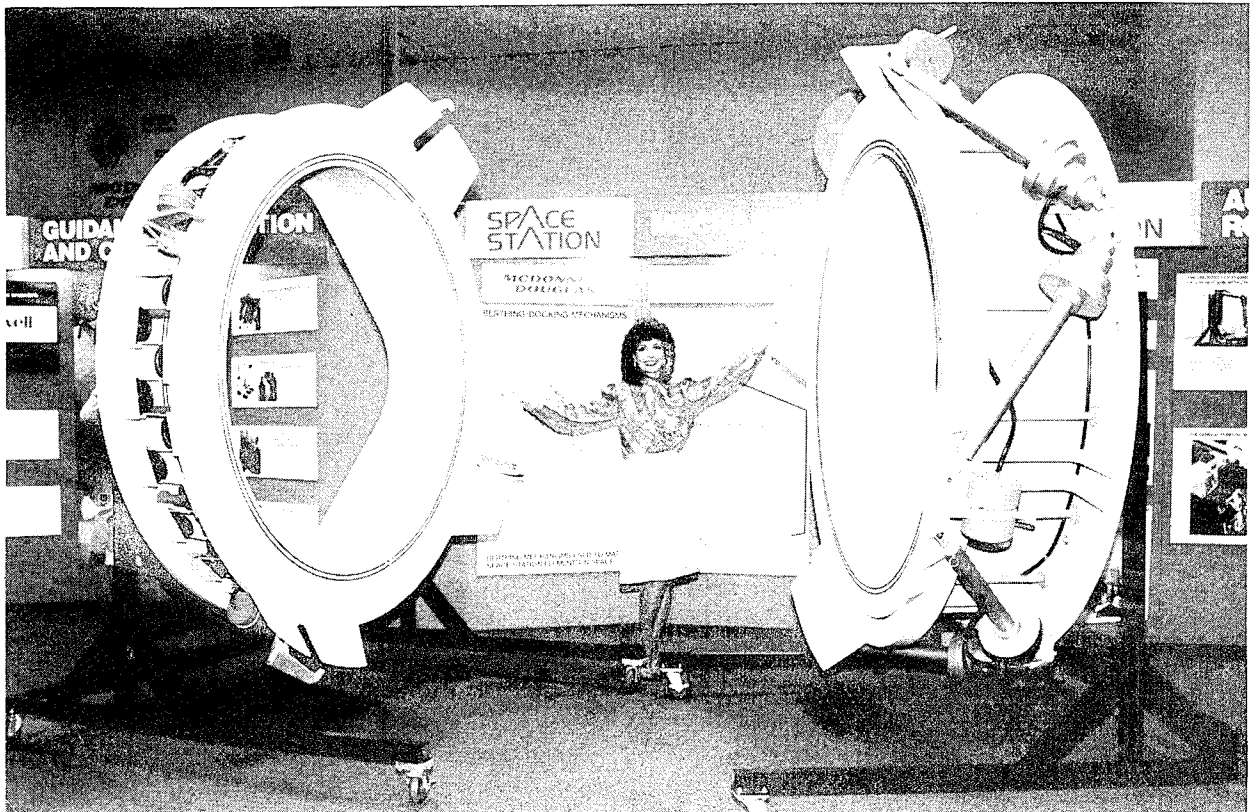
Figure 1. Space Station Berthing Mechanisms Mockup

Approach
- ☑ Module passive
- ▣ Orbiter active
  - ◦ Capture latches open
  - ◦ Structural latches open
  - ◦ Actuators/attenuators extended

Space Station
Pressurized Module

Docking
Mechanisms

12.16 m
(40 ft)

Orbiter Center of Gravity
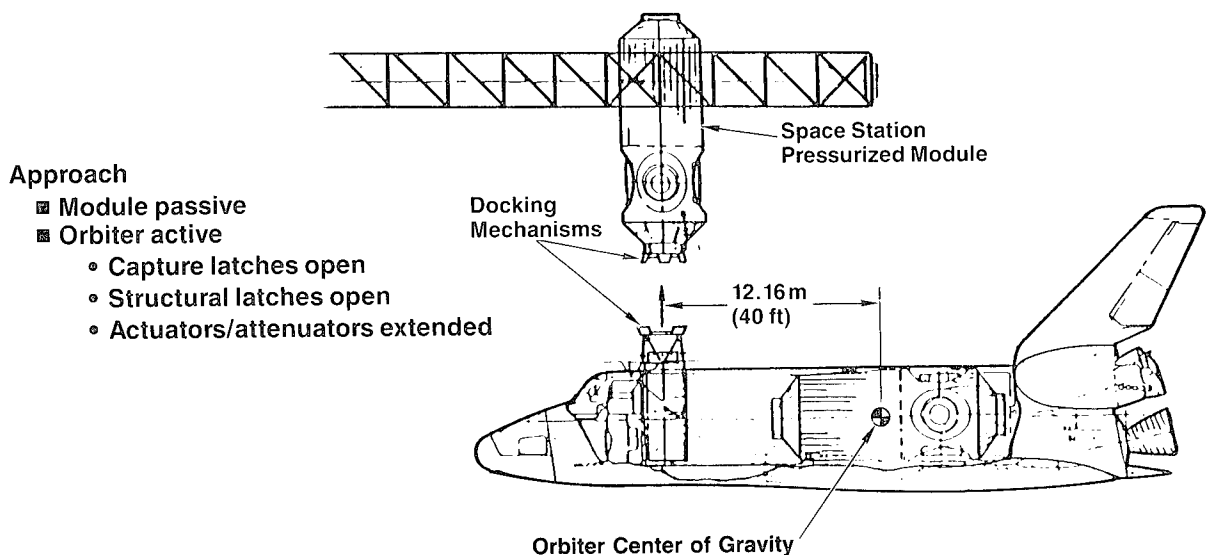
Figure 2. Orbiter Docking to Space Station

selected interfaces within the pattern. The berthing mechanism that was designed and
fabricated uses a 1.6 m (63 in.) diameter, 2 ply, 2219 aluminum bellows to provide
this flexibility. A cable and pulley restraint system is used to resist the axial
force on the bellows produced by the 1-atm internal pressure while at the same time
allowing the interface two degrees of motion flexibility. The fabrication and
assembly of the large-diameter aluminum bellows represents a significant development
issue.

The structural interface between the berthing mechanism halves uses manually operated structural latches and a triple redundant, androgynous pressure sealing system.

MECHANISM REQUIREMENTS

The two berthing/docking mechanism halves are designed specifically for two different sets of Space Station functional requirements plus a common set of general requirements.

The general requirements were established by the Space Station program during the concept definition phase and the Phase B preliminary design effort. The general requirements that apply to both of the mechanisms are as follows:

1.   Provide androgynous mating between any two berthing mechanism halves.
2.   Accommodate a clear 1.27 m (50 in.) square passageway.
3.   Provide 90-deg indexing for mating positions.
4.   Provide a redundantly sealed interface for an internal air pressure of 1 atm; air leakage to be less than 0.02 kg/day (0.05 lb/day).
5.   Furnish manual override backup capability for mechanical functions.
6.   Provide indefinite life through maintenance.
7.   Provide capture latches to engage and position the mating mechanism.
8.   Provide structural latches which are operable from both sides of the interface.
9.   Provide for internal module interconnect umbilicals for nonhazardous gases, liquids, electrical power, and data.
10.   Provide docking/berthing guides which will initiate indexing.
11.   Provide the capability to absorb the energy of berthing or docking of the orbiter to the Space Station.

The load-attenuating half of the berthing/docking mechanism is mounted in the orbiter cargo bay and provides the capture, energy disposition, alignment, and mating functions of the orbiter to Space Station interface. The conditions for both berthing and docking were analyzed to determine the worst case requirements for the mechanisms. Computer simulations of the STS orbiter's remote manipulator system (RMS) established berthing capture envelope and contact velocities. RMS joint runaway was considered in establishing maximum berthing contact velocities.

The Shuttle Engineering Simulator (SES) at NASA JSC was used to establish docking parameters. This man-in-the-loop simulation of docking the orbiter to the Space Station provided data on lateral and angular misalignments and rates at initial contact. The results of these two simulations were combined to establish the design parameters for the load-attenuating mechanism. Table 1 provides the berthing/docking contact conditions that the load-attenuating mechanism was designed to meet.

The flexible berthing mechanism half was developed to accommodate pattern assembly and tolerance compensation. It was determined that if two-degree-of-freedom, flexible interfaces were selectively placed within the module pattern, six degrees of freedom would result at the final or closing interface. Thus the requirement for the flexible berthing mechanism half is that it have ±2 deg of deflection capability about the X and Y axes and be restrained in the Z axis. The Z-axis restraint must be capable of supporting the load produced by the internal pressure of 1 atm multiplied by the area of the flexible interface.

Table 1. Berthing/Docking Contact Conditions

Condition [3]	[4][5] Berthing Module	Berthing Orbiter	[6] Docking Orbiter
Closing Velocity (m/sec) [1]	0.049	0.049	0.06
Lateral Velocity (m/sec)	±0.049	±0.027	±0.018
Angular Velocity (deg/sec)			
— Roll	±0.20	±0.02	±0.05
— Lateral	±0.52	±0.22	±0.15
Lateral Misalignment (m) [2]	±0.076	±0.101	±0.114
Angular Misalignment (deg) [2]			
— Roll	±1.5	±2.0	±3.0
— Lateral	±1.5	±2.0	±4.5
Relative CG Velocity (m/sec) [7]			
— Closing	0.039	0.018	0.063
— Lateral	0.012	0.012	0.021

Notes
1. Minimum closing velocity for docking shall be 0.015 m/sec
2. Maximum misalignments until capture (normal berthing)
3. Velocities and misalignments are defined relative to the docking ports
4. Berthing velocities are based on RMS joint runaways (PDRSS)
5. Berthing misalignments are based on nominal conditions
6. Docking values are based on SES data
7. Berthing CG velocities are based on elbow joint runaways
   (which give highest port closing velocities)
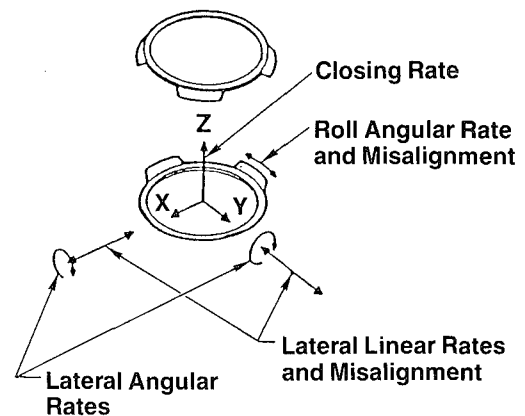
TRADES AND DESIGN CONCEPT SELECTIONS

OVERALL CONCEPTS

The overall berthing/docking mechanism concept was principally dictated by the requirements. The requirement for a clear passageway determined that the capture and latching be accomplished outside the passageway clearance. The size of the mechanism is dictated by the passageway size (hatch size) which was established by the Space Station Phase B study. The Space Station configuration and operational procedures dictate that four different and distinct functions must be accomplished at various berthing interfaces. A family of four berthing mechanism halves which satisfy these functions are: (1) a load-attenuating berthing mechanism for the orbiter side to capture, absorb energy, stabilize, and align the interface during an orbiter to Space Station berthing/docking maneuver; (2) a flexible berthing mechanism half to compensate for tolerances and allow assembly of a closed-loop module pattern; (3) a rigid berthing mechanism half to be used at all pressurized module interfaces where energy attenuation or flexibility is not required; and (4) an unpressurized berthing mechanism half to be used to berth the orbiter to the Space Station truss structure during buildup and that can potentially be used for unpressurized structural attachments and payloads. All of the four berthing mechanism halves will mate with each other and all berthing mechanism family members use common parts. Because of their complexity, the load-attenuating and the flexible mechanism halves were selected for advanced development.

Figure 3 illustrates the berthing mechanism evaluation areas and selections used in starting the final design. The following discussions summarize the choices and selections in each of the areas evaluated during this phase of the program.
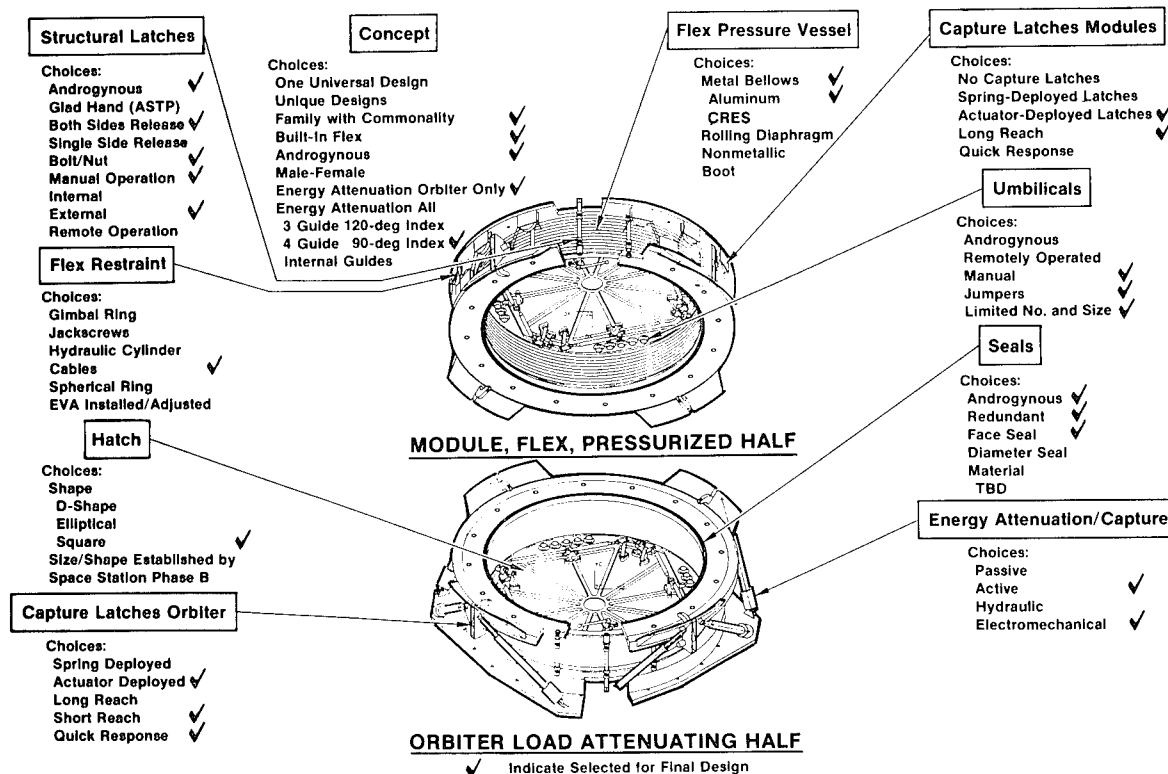
328

Structural Latches

Choices:
Androgynous ✓
Glad Hand (ASTP)
Both Sides Release ✓
Single Side Release
Bolt/Nut ✓
Manual Operation ✓
Internal
External ✓
Remote Operation

Concept

Choices:
One Universal Design
Unique Designs
Family with Commonality ✓
Built-In Flex ✓
Androgynous ✓
Male-Female
Energy Attenuation Orbiter Only ✓
Energy Attenuation All
3 Guide 120-deg Index
4 Guide 90-deg Index ✓
Internal Guides

Flex Pressure Vessel

Choices:
Metal Bellows ✓
Aluminum ✓
CRES
Rolling Diaphragm
Nonmetallic
Boot

Capture Latches Modules

Choices:
No Capture Latches
Spring-Deployed Latches
Actuator-Deployed Latches ✓
Long Reach ✓
Quick Response

Umbilicals

Choices:
Androgynous
Remotely Operated
Manual ✓
Jumpers ✓
Limited No. and Size ✓

Flex Restraint

Choices:
Gimbal Ring
Jackscrews
Hydraulic Cylinder
Cables ✓
Spherical Ring
EVA Installed/Adjusted

Seals

Choices:
Androgynous ✓
Redundant ✓
Face Seal ✓
Diameter Seal
Material
TBD

Hatch

Choices:
Shape
D-Shape
Elliptical
Square ✓
Size/Shape Established by
Space Station Phase B

Energy Attenuation/Capture

Choices:
Passive
Active ✓
Hydraulic
Electromechanical ✓

Capture Latches Orbiter

Choices:
Spring Deployed
Actuator Deployed ✓
Long Reach
Short Reach ✓
Quick Response ✓

MODULE, FLEX, PRESSURIZED HALF

ORBITER LOAD ATTENUATING HALF

✓ Indicate Selected for Final Design

Figure 3. Berthing Mechanisms Evaluation Areas and Selections

STRUCTURAL LATCHES

The concept chosen for the structural latch utilizes the bolt/nut attachment principle. The features are androgynous, both sides release, and manual operation. Although the basic latch design operates manually, a design for the incorporation of an electromechanical actuator was also included. The motor-driven latch may be operationally desirable for frequent docking operations such as orbiter to Space Station, logistics module to Space Station, and unpressurized interfaces.

FLEXIBLE PRESSURE VESSEL

A formed, two-ply, metal bellows was selected for the flexible pressure vessel. The material is 2219 aluminum which can be welded directly to the aluminum structure of the berthing mechanism. Twelve convolutions 38.1 mm (1.5 in.) deep provide 2-deg deflection about two axes.

FLEX RESTRAINT

A system of cables and pulleys carries the pressure-created tension load across the flexible bellows. The cable system transmits the tension load from one end of the bellows to the opposite end while allowing two-degree-of-freedom flexure of the bellows. The bellows structure provides adequate shear and torsion strength for the interface. Rigid struts may be added to the design to lock out the flexibility during Space Station buildup when the berthing port must be used for a cantilever module support.

CAPTURE LATCHES

The family of berthing mechanisms required the use of two capture latch designs. The requirements for the module-to-module interface dictate that the capture latch have a relatively long reach, but may be slow acting. The orbiter-to-Space Station interface requires that fact-acting, short-reach capture latches be provided for the berthing/docking operation. Both latch mechanisms use a conventional linkage powered by electric motors.

UMBILICALS

The internal umbilicals associated with the berthing mechanism interface incorporate manually installed jumper cables which will be attached to identical connectors installed in each berthing mechanism half. The connectors are located around the periphery of the hatch opening. The hook-ups will be accomplished in a shirtsleeve environment after the interfaces are mated and pressurized. Although space has been allocated in the design for umbilicals, no connectors have been installed in the prototype mechanisms.

HATCH

The size and shape of the hatch opening were established by the Space Station Phase B study. A 1.27 m (50 in.) square opening with 1.52 m (60 in.) diagonal to the corner radius has been selected. The size and shape of the hatch passageway establishes the overall size of the berthing mechanisms.

SEALS

Redundant, androgynous face seals were selected for the berthing mechanism design. Because of the androgynous nature of the interface, the face seal will mate and seal with an identical seal on the mating half. This seal-on-seal arrangement will be used to hold pressure at the interface until a replaceable seal is installed on orbit by a crew member.

ENERGY ATTENUATION/CAPTURE

The orbiter berthing mechanism half utilizes an extendable ring with guides and capture latches to engage the mating berthing mechanism half on the Space Station. The ring is supported on eight electromechanical actuators/attenuators which capture, absorb energy, stabilize, align, and retract to engage the structural latches of the interface. The active electromechanical approach allows the spring rates and damping to be tailored to provide a low spring rate during capture and then change to a high rate during stabilization. The eight actuators/attenuators are controlled by a processor which reads load position from the actuators and stabilizes the interface in accordance with a preprogrammed control law.

MECHANICAL DESIGN

The structure of the berthing mechanism halves is welded 6061 and 2219 aluminum construction and is generally not unique except for the large size, i.e. over 2 m (79 in.) in diameter.

The actuator/attenuator illustrated by Figure 4 has a relatively simple mechanical design. It utilizes a ball-bearing jack screw with a pitch diameter of 19.05 mm (0.75 in.) and a lead of 25.4 mm (1.0 in.). The jack screw is directly
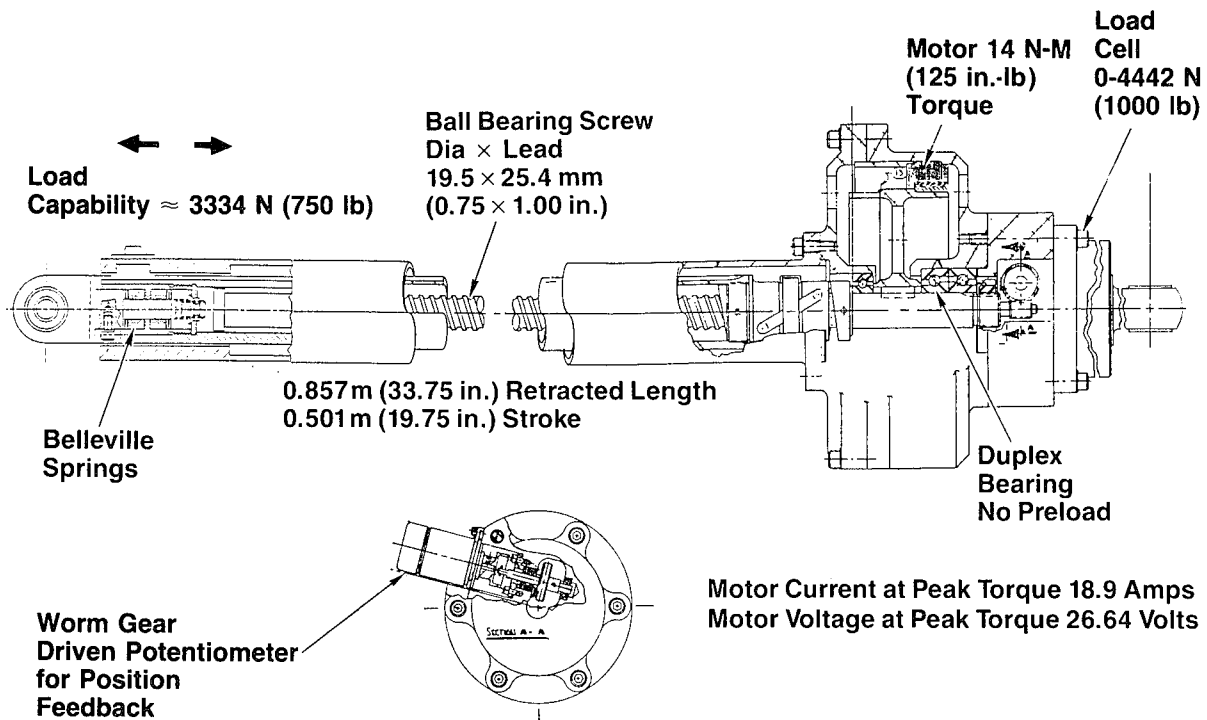
Figure 4. Berthing Mechanism Actuator/Attenuator Design

driven by a 40-pole brushless DC motor. The unit also contains a load cell and a potentiometer for control system feedback. A key design goal for the attenuator was to reduce back-drive friction and inertia to a minimum allowing the motor torque to shape the force stroke relation as a function of the control laws. The actuator rod incorporates a cartridge containing Belleville washers providing a spring rate of 874 Newtons/mm (5000 lb/in.). This compliance reduced the initial contact load spike allowing the servo loop to respond and control the load.

Figure 5 shows the orbiter docking module with the capture ring extended before the initial contact. The extension of the eight actuators/attenuators positions the active mechanism to latch securely with the mating mechanism, attenuate the energy, align the interfaces and retract to mate the seals and structural latches. The cross sections illustrated in Figure 6 show the capture ring in the retracted and extended positions. Four contact switches in the capture ring are connected in series to operate the four motor-driven over-center capture latches. The capture latches operate in approximately 50 m/s after the four contact switches are closed. The structural latches that tie the mated Space Station elements together are illustrated by Figure 7. These are 16 latches located around the periphery of the mechanism halves outside of the interface seals. The latch design features a nut and bolt principle with alternating units to provide androgynous mating. The bolt/nut combination uses a 0.500-20 UNF thread with a tailored nose on the bolt to allow misaligned entry and start without cross threading. The bolt and nut are fabricated of A286 CRES and use DOD-L-85645 (Dicronite) dry film lubrication. The attachment can be manually torqued from inside the pressure hull of the Space Station module after the interface has been placed into contact. The floating bolt/nut assemblies are intially retracted below the interfacing surfaces. By using friction-clamped, Delrin worm gears engaged to a thread on the external suface of the nut/bolt assembly, rotation of the assembly causes it to advance toward the mating half. When the bolt/nut advancement is restricted by engagement of the mating half, the clamped
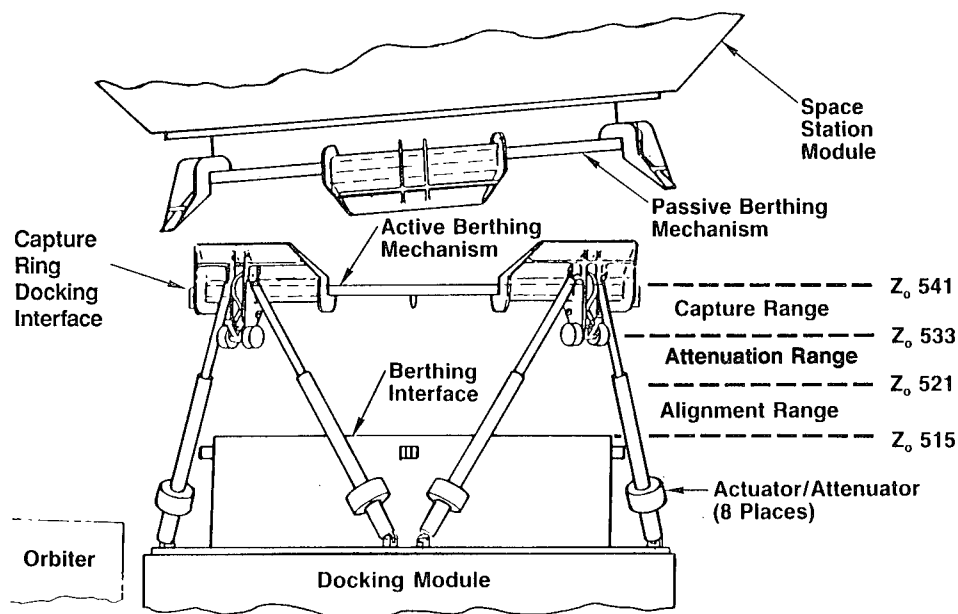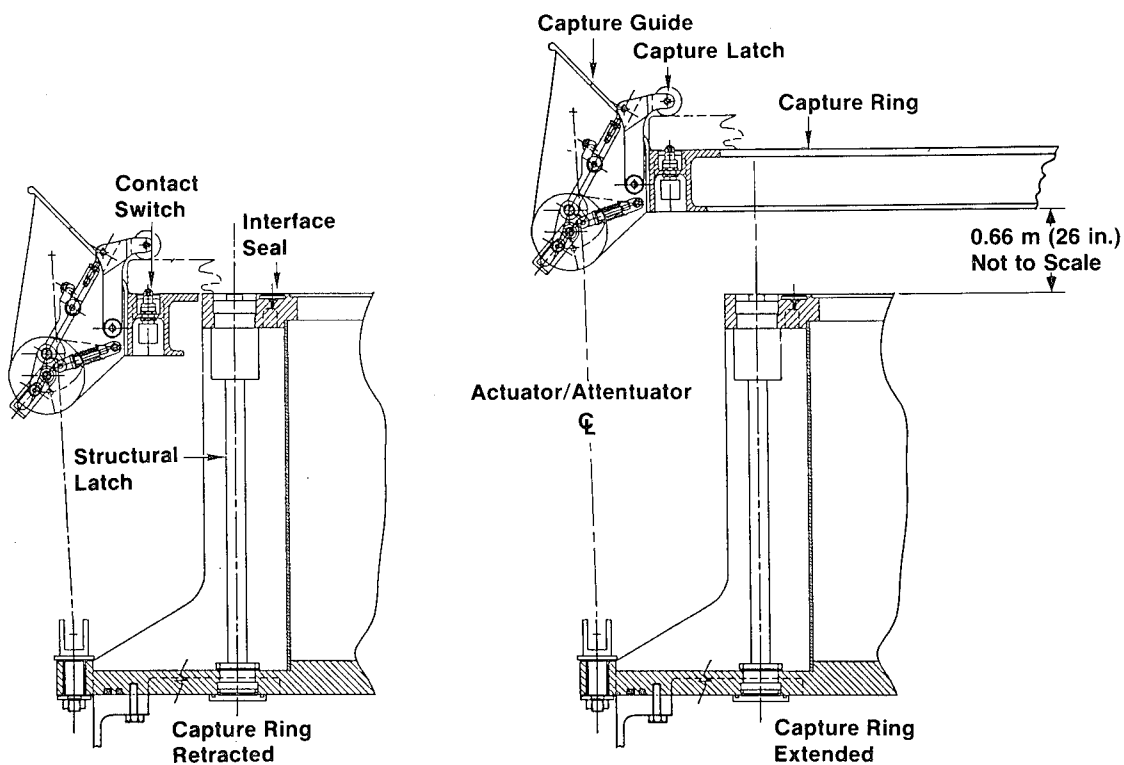
Figure 5. Initial Contact

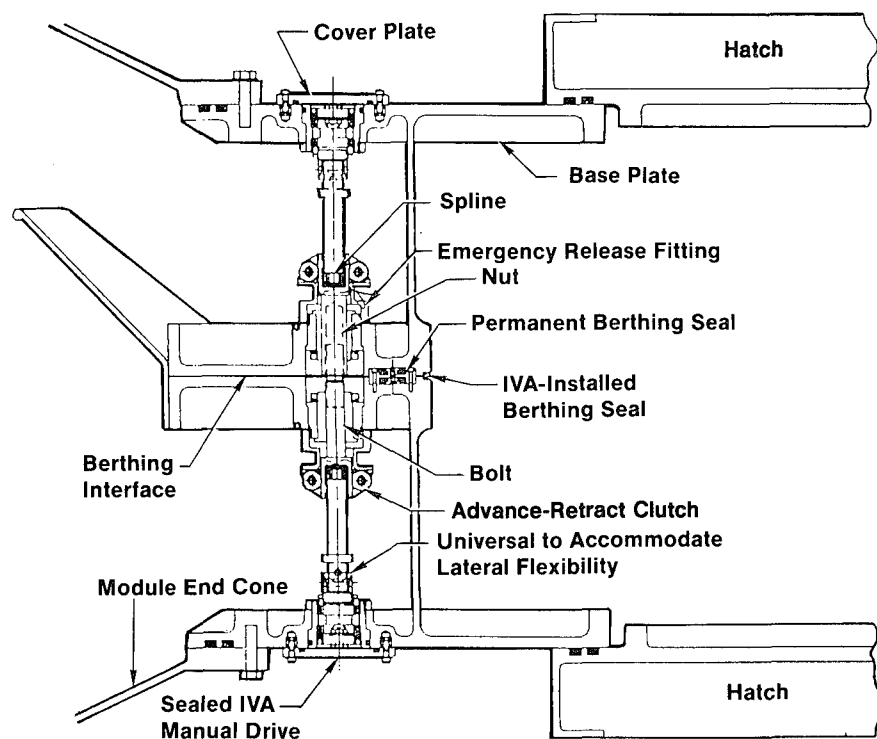Figure 6. Capture and Load-Attenuating Berthing Mechanism

332

Figure 7. Manually Driven Bolt/Nut Structural Latch

gears rotate and allow the bolt/nut assembly to rotate without advancement. The structural latch may be operated from either side of the interface. Each structural latch is designed for a tension load of 44,470 Newtons (10,000 lb).

The bellows and the cable restraint system for the flexible berthing mechanism half are illustrated by the cross section in Figure 8. The bellows are 1.6 m (63 in.) ID and are formed from 2 ply, 0.81 mm (0.032 in.) 2219 aluminum. The convolutions were roll formed with the material in the 0 temper condition (annealed). The bellows were not heat treated after forming for the prototype demonstrations because of the complex requirements for the process. Flight hardware will be heat treated to the T62 condition after forming and welding to the end rings.

The extension load caused by the internal module pressure is resisted by a closed-loop continuous cable/pulley system outside of the bellows. This system allows the two degree of freedom motion of the bellows while supporting the internal pressure load of approximately 221,233 Newtons (49,733 lb) at 1-atm internal pressure. The system is formed by a single cable and 47 pulleys; 24 attached to the base plate and 23 attached to the interface plate. The rigged cable compresses the bellows approximately 12 mm (0.5 in.) producing a total load in the system of 3706 Newtons (833 lb) for a bellows spring rate of 309 Newtons/mm (1767 lb/in.). For this load the tension in the cable is 77 Newtons (17.3 lb). The tension load in the cable at 1-atm internal pressure on the bellows is 4608 Newtons (1036 lb).

CONTROL SYSTEM DESIGN

The control system must accommodate three distinct phases of the docking operation: precapture, capture, and attenuation. During precapture, the capture ring is commanded from a start-up position to a new position at which initial contact with the approaching berthing mechanism occurs. The controller must maintain a stable
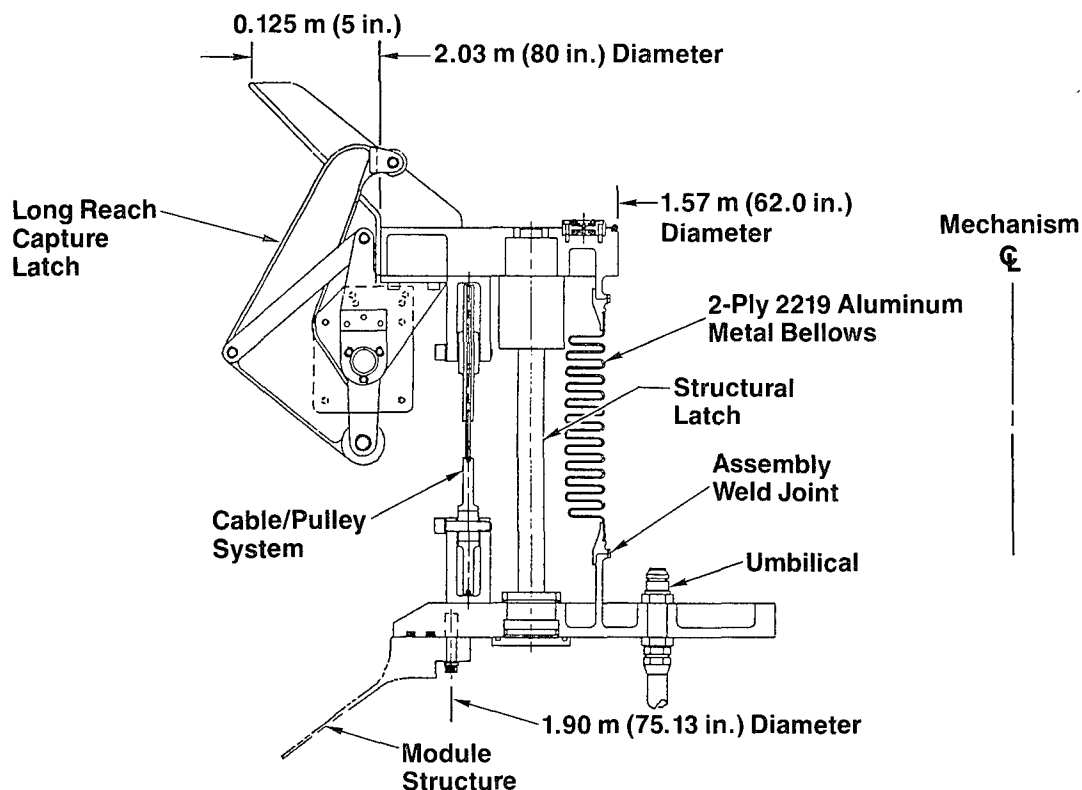
Figure 8. Flexible Berthing Mechanism Half With Cable/Pulley Structural Restraint

position without drifting. System loads consist only of the small mass associated with the capture ring.

Capture involves initial contact, camming of the capture ring for alignment with the mating interface, and clamping of the two berthing mechanisms together with the capture latches. The dynamics must consider the large orbiter CG offset from the berthing mechanism location.

During the attenuation phase, relative motion is zeroed out with the constraints that the capture ring position be within prescribed limits to maintain adequate clearances and that the individual actuator loads not exceed their force capability of about 2224 Newtons (500 lb). The effective controlled mass has increased from the capture ring to one that is equivalent to the station/orbiter. Control during follow-on centering and retraction for structural attachment is consistent with the attenuation phase because relative motion of the large station/orbiter masses is involved.

The control system design consists of an analog controller for each of the eight actuators and a digital controller that coordinates the motion of the actuators as a unit. An IBM PC-AT computer processes the measured actuator positions and commands a force to each actuator based upon programmed algorithms or control laws. Different algorithms are used for the various operational phases to compensate for the drastic changes in mass properties and for significant changes in functional requirements (i.e., soft spring during capture and stiff spring during attenuation). Figure 9 is a block diagram of the integrated control system.

Two computer tools were generated to analyze and develop the control system: a nonlinear time domain simulation written in FORTRAN to investigate system performance
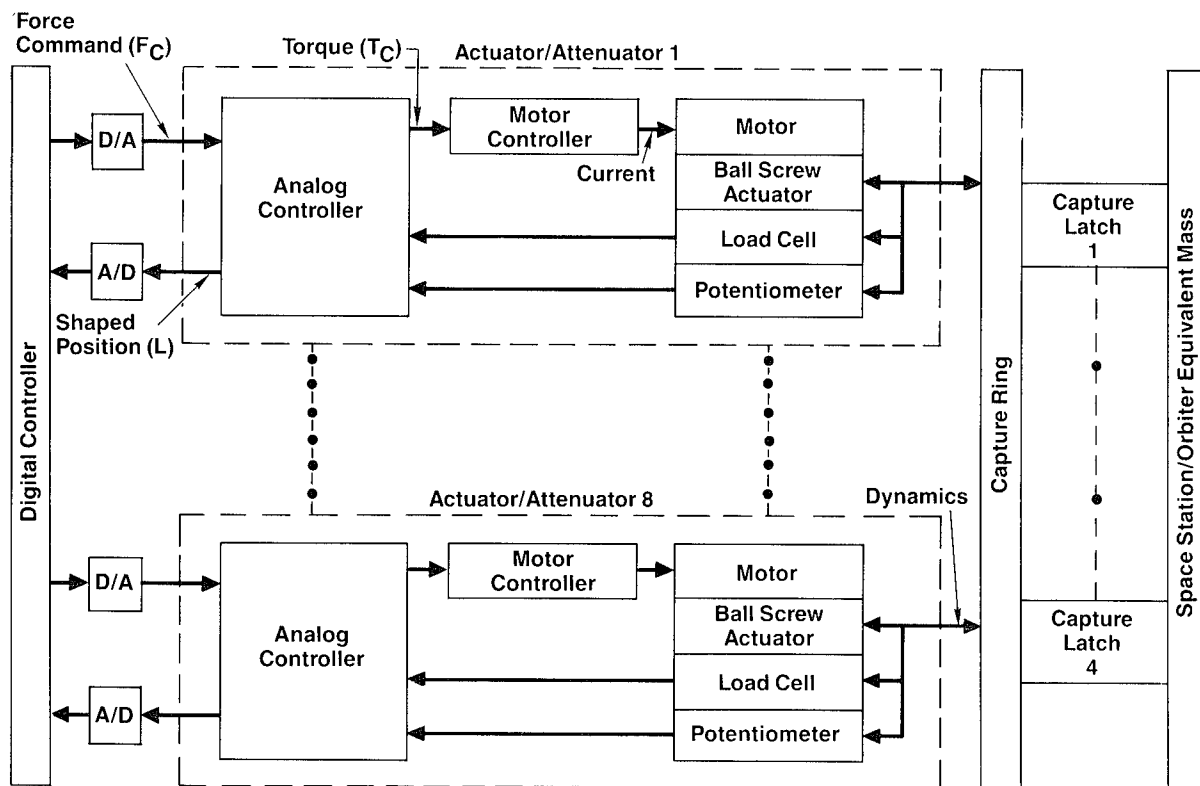
334

Figure 9. Control System Block Diagram

and a frequency response model written in CONTROL-C to check stability. The use of these analytical tools coupled with breadboard single-axis testing of an actuator/attenuator has resulted in the present controller design. Testing of the breadboard unit verified that our control technique was valid and led to actuator design changes that helped to simplify the control system. These changes included a reduction in motor inertia, an increase in ball screw lead, and the addition of a known compliance in the extension rod.

The analog controller for each actuator consists of a force loop that compensates for actuator friction and modeling errors, and a rate loop derived from actuator position that provides damping during the precapture and capture phases. Figure 10 provides a block diagram of this controller. It has been designed so that stability is independent of the mass driven by the actuator.

The digital controller uses actuation position data and algorithms to control force and make the eight actuators work as a unit. The algorithms are different as shown by Figure 11 for each phase of the docking operation. Note that with an input of position and output of force, the algorithm transfer function is analogous to the rate of a mechanical spring. For precapture, each actuator is controlled independently with a gain constant to prevent capture ring drifting. A force bias is used to compensate for gravity effects.

With capture, the same force bias is used to facilitate transition from precapture. In addition a small spring constant for each actuator coupled with a relatively high axial stiffness keeps the interfaces in contact while the capture ring cams into alignment. The axial stiffness component is accomplished by generating a force that is a function of the average of all the actuator lengths.
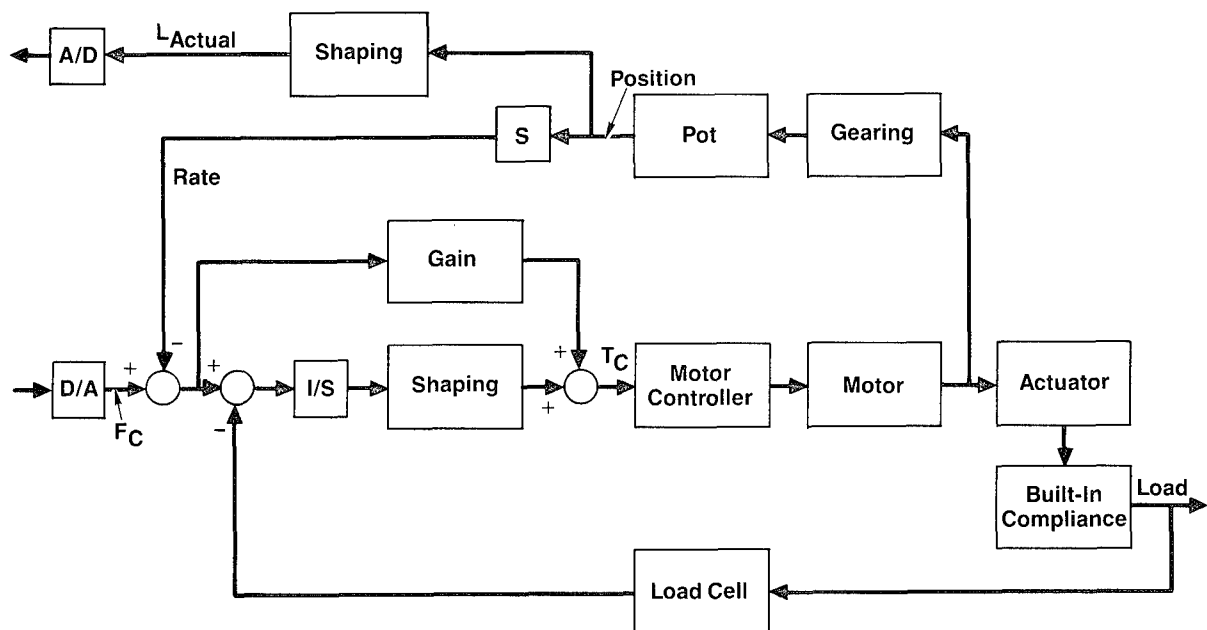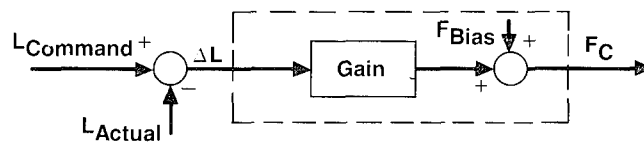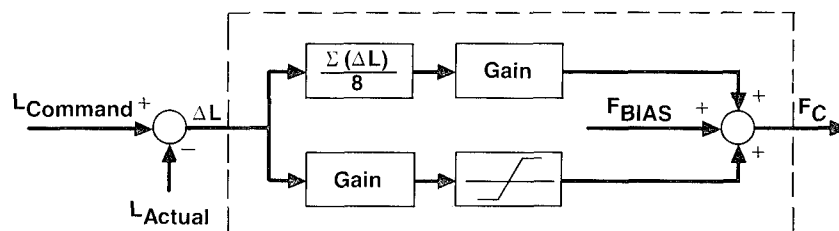
335

Figure 10. Actuator Analog Controller

PRECAPTURE

CAPTURE

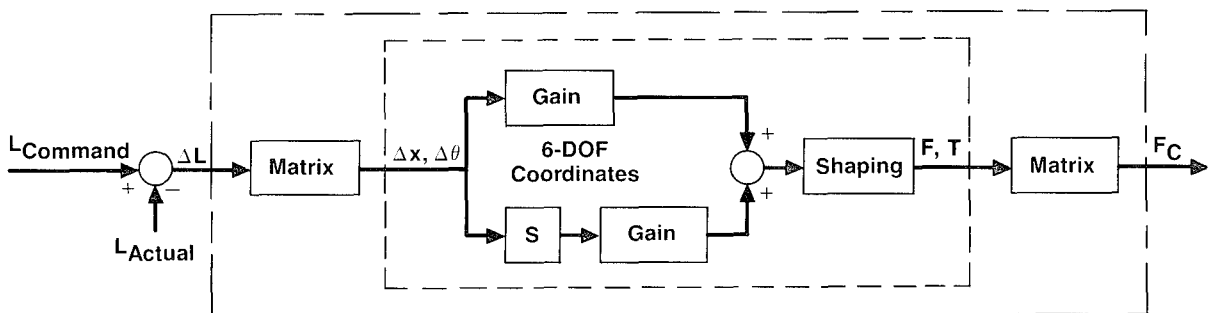ATTENUATION/ALIGNMENT/RETRACTION

Figure 11. Digital Control Laws

For attenuation, analysis has shown that six-degree-of-freedom control is necessary to limit actuator force and provide reasonable damping in all axes. Following transformation, position and rate gains generate forces and torques in the three translational and three rotational axes. Another transform provides commanded forces for each actuator. Analysis has shown that the transformation matrix can be normalized with respect to the precapture position thus avoiding the necessity of updating at each new position.

Examples of control system capture and attenuation performance obtained from the simulation are shown by Figures 12 through 15. Capture showing relative position and orientation for a very low approaching velocity of 15.2 mm/sec (0.5 ft/sec) is provided by Figures 12 and 13. This is a worst-case condition because it is difficult to make the capture ring cam into position at the low rates without rotating away from the interface.

The net axial attenuation force for a maximum contact rate of 61 mm/sec (0.2 ft/sec) imposed upon the berthing mechanism supporting structure is shown by Figure 14. The initial 890 Newtons (200 lb) impulsive force provides a 2.5 margin with respect to an arbitrarily imposed structural limit of 2224 Newtons (500 lb). Maximum actuator force during the same period is about 1780 Newtons (400 lb). Figure 15 provides an indication of the maximum generated torques.

FABRICATION AND TESTING

The two berthing/docking mechanism halves and the control system electronics were designed and fabricated as prototype one-of-a-kind units. The operating mechanisms such as actuators/attenuators, structural latches, capture latches, interface plates, bellows, bellows restraint system, capture ring and guides were designed to closely resemble the final flight designs. The structure used welded plate stock and is intended only to provide a pressure vessel with geometric accuracy for mounting the
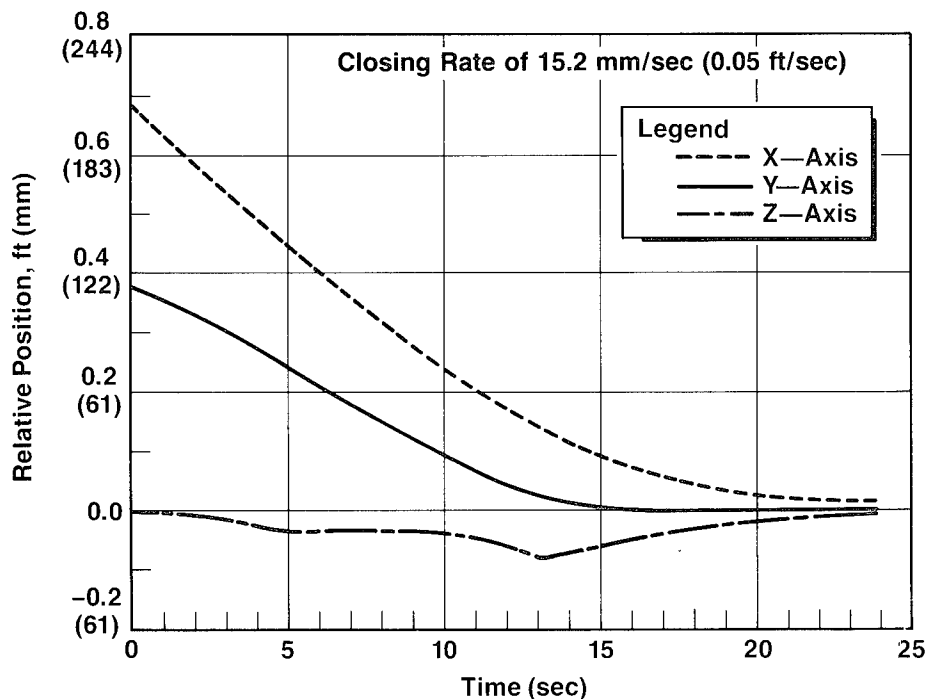

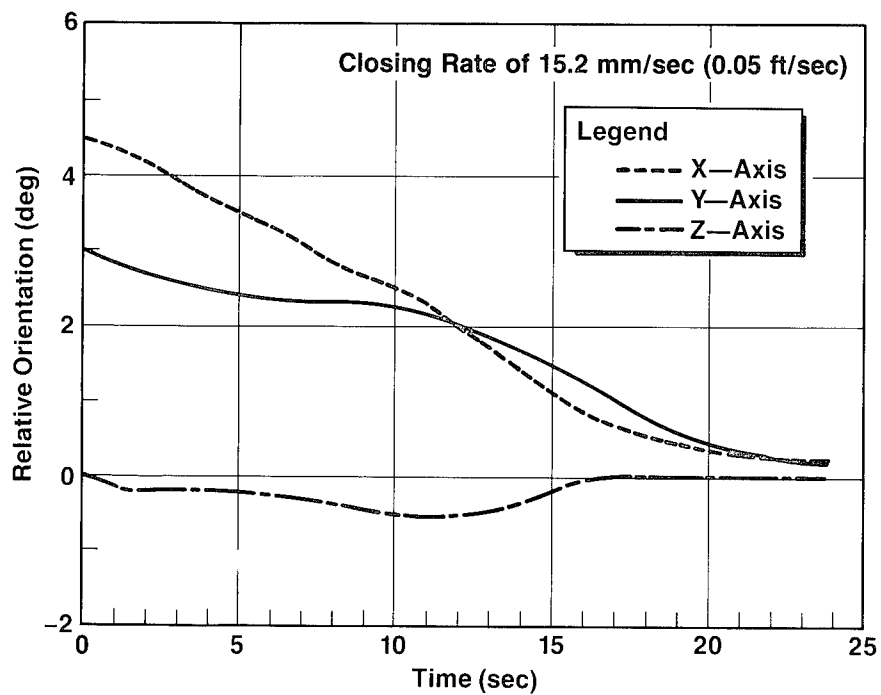Figure 12. Relative Position Between Mating Interfaces

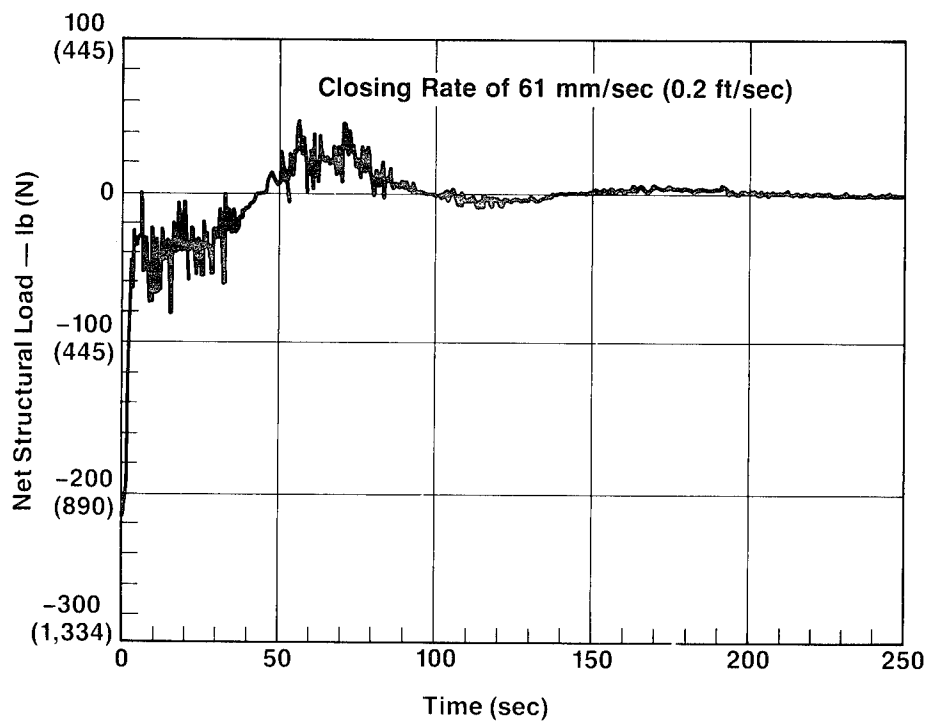**Figure 13. Relative Orientation Between Mating Interfaces**

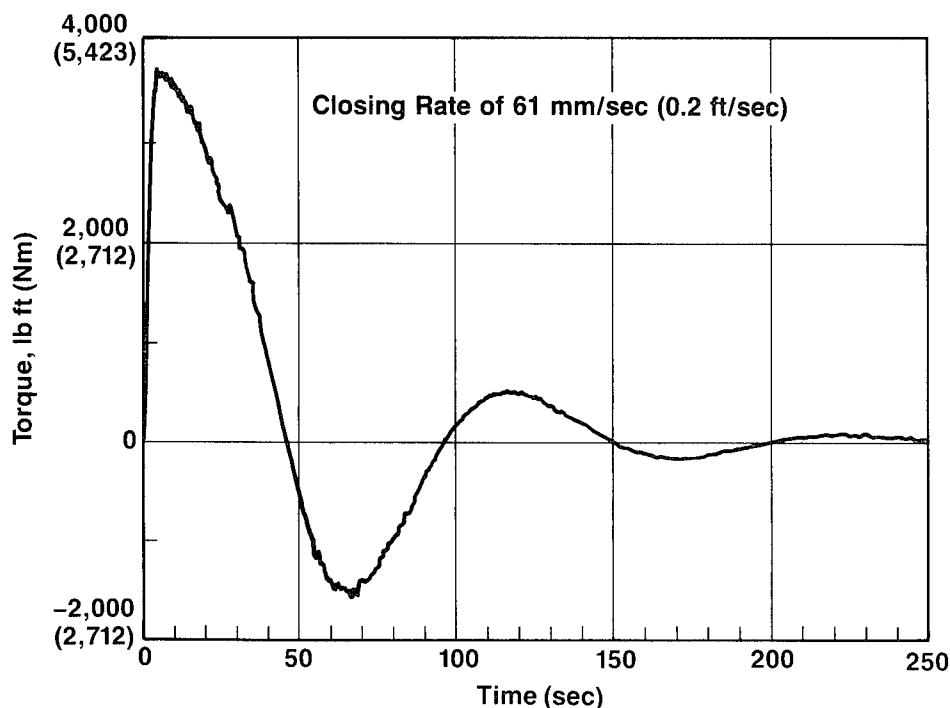**Figure 14. Axial Attenuation Force on Structure**

338

Figure 15. X-Axis Attenuation Torque

operating mechanisms. The hatch openings in the base plates were not cut out on the prototype unit which allow the two halves to be mated and pressurized for seal development.

The overall design of the mechanisms and the design and fabrication of the control system electronics were done by McDonnell Douglas Astronautics Company in Huntington Beach, California. The structure fabrication and the final assembly of the units were done by United Technologies Space Flight Systems in Huntsville, Alabama. Other suppliers participating in the program were: Beaver Precision Products, Troy, Michigan, actuators/attenuators; Sierracin Magnedyne, Carlsbad, California, actuator/attenuator motors; and Pathway Bellows Company Oak Ridge, Tennessee, bellows.

This paper was prepared in November 1987. Testing on this project is scheduled to be accomplished from January through April 1988. Testing results should be available for the oral presentation of the paper in May 1988. Pressure testing and overall systems checkout will be done at United Technologies. Dynamic testing will be done at NASA's Marshall Space Flight Center (MSFC) using a six-degreee-of-freedom (6 DOF) simulator. The MSFC six-degree-of-freedom moving base simulator has the capability to simulate the dynamics in space of the Space Station and the STS orbiter during the docking maneuver.

Figure 16 illustrates the MSFC six-degree-of-freedom facility on which the dynamic docking testing will be done. A total of 64 cases will be run encompassing the total range of contact velocities and misalignments expected.

Simulation of Vehicle Dynamics

Digital Computer

Zero Gravity Contact Forces and Torques

Berthing Mechanism

Relative Vehicle Motions

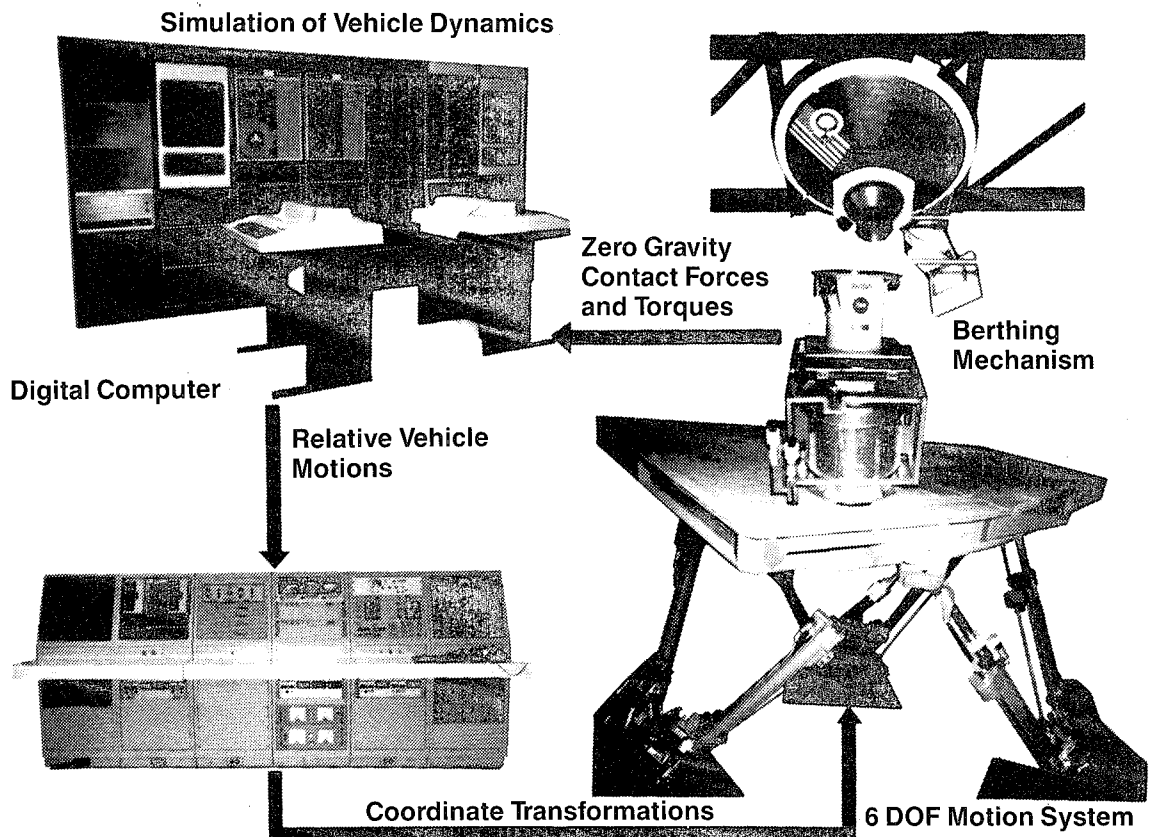**Coordinate Transformations**

6 DOF Motion System

Figure 16. The MSFC 6-DOF Facility

CONCLUSIONS

This program has provided proof-of-principle for a computer-controlled electromechanical system for docking the STS orbiter to the Space Station. In addition it has taught us valuable lessons in the mechanical design and fabrication of relatively large space mechanisms. During this program analysis demonstrated that an active docking system is required (1) to provide capture at low approach rates and (2) to reduce forces and moments to an acceptable level at maximum approach rates. An active docking system could be designed using either an electromechanical approach or a hydromechanical approach. The hydromechanical approach is considered undesirable for use in the orbiter cargo bay because of potential fluid leakage contamination. The active computer-controlled electromechanical energy attenuation system will meet the requirements for capture, energy attenuation, and structural attachment in space of the STS orbiter and the Space Station.

Further refinements are called for in the design of the actuator/attenuator and the control system to reduce the total electrical power requirements. The prototype system has a potential peak power requirement which could exceed 4 kW; this would be excessive for a flight configuration powered from the STS orbiter fuel-cell electrical power system.

Further refinement is needed in the design and fabrication techniques for the aluminum bellows used in the flexible mechanism. It required several attempts to fabricate the bellows using 2219 aluminum alloy. The bellows were not heat treated after forming because of the high temperature required and the potential distortion of the finished product. Other aluminum alloys should be considered as well as improved forming techniques and heat treat requirements for the flight system design.

AMMONIA TRANSFER ACROSS ROTATING JOINTS IN SPACE

Mark H. Warner*

ABSTRACT

Thermal control of future large space facilities, such as the Space Station, will require the transfer of anhydrous ammonia across rotating joints with near zero leakage. Anhydrous ammonia is the primary heat transfer fluid aboard the station, providing critical thermal management of habitat and payload systems. The solar radiator joints, as well as the various payload pointing systems, are obvious examples of the need for a reliable fluid transfer device. Low weight, tight temperature control, low parasitic drag torque, long life, and high reliability, in addition to near zero leakage, are important characteristics necessary for the successful operation of such a device. In late 1986, Lockheed initiated an IR&D project to develop a Rotary Transfer Coupling (RTC) directed toward Space Station requirements. Fabrication and assembly of this device is now complete and testing is scheduled for January 1988. This paper addresses the design and development of the face seal-type rotary fluid coupling that utilizes a unique 'cover gas' concept (an inert gas such as nitrogen) to provide full containment of the ammonia.

INTRODUCTION

The combined requirements of extremely low leakage, low frictional torque, and long life eliminate many of the rotary transfer methods considered in the past. Flexible hoses, though simple, experience relatively high ammonia diffusion rates in vacuum environments. In addition, pressurized hoses exhibit dramatic increases in drive torque at angular travel greater that 120-150 degrees. Also, hose-type devices either do not allow applications that require continuous rotation, or require the use of complicated 're-wind' mechanisms.

An O-ring type rotary coupling, as was used for Lockheed's Talon Gold Gimbal

---

* Lockheed Missiles and Space Co., Sunnyvale, California

Fluid Coupler, was rejected due to its relatively low life and excessive friction. This unit satisfied most of the performance objectives during testing, but operating torques were considerably higher than desired. Friction non-linearities place a high burden on gimbal controllability and can compromise both pointing accuracy and stability (jitter).

Other seal-type couplings were rejected for similar reasons: Lip seals, because of their high leakage rates; Ferro-fluidics, because of the increased complexity of the design and the multi-staging required to accept high pressure-differentials. Of the remaining available methods of sealing, a carbon graphite mechanical-type face seal best met the requirements of leakage, friction, and life, and was therefore selected as the baseline design (Figures 1-3).

This design approach was based on previous work with rotary coupler and heat pipe design, technology resulting from research at the Langley Research Center (LaRC), and the excellent industrial service record of ammonia pumping refrigeration equipment. The design includes novel solutions in the arrangement of multiple axial face seals, the use of 'scavenger' channels to facilitate internal leakage paths, and the use of a pressurized, nitrogen gas "cover" to eliminate external ammonia leakage.

DESIGN DESCRIPTION

As shown in Figure 4, the IR&D design uses annulus-type channels to provide the transfer capability of the coupling. The coupling was designed to accommodate the Space Station Radiator requirements shown in Figure 2. The device has the capacity to transfer eight separate lines/channels of anhydrous ammonia or, with minor modifications, other refrigerants such as monomethyhalamine or the common halocarbons. The RTC is approximately 14 inches in length, 5 inches in diameter, and has channels of two separate size: 0.688 inches in diameter for the vapor supply, and 0.438 inches in diameter for the liquid return.

The modular rotor and stator segments are machined from CRES 316 for corrosion resistance to the anhydrous ammonia. During the layout stage of the design, particular care was taken to minimize the overall size of the coupling, especially the diameter. This not only reduces the overall weight and the seal rubbing velocities, but causes a direct reduction of parasitic drag torque. In addition, the RTC assembly was sized for typical shuttle launch loads with adequate bearing load margins as shown in Figure 5. The IR&D coupling uses standard 52100 steel (440-C steel for flight) deep groove-type radial ball bearings, which are spring preloaded with a steel wave spring washer to accommodate thermal expansion. PTFE (Teflon) gaskets provide the static sealing between individual parts and were machined to account for any

342

cold-flow during installation.

In the RTC design, each of the 8 stationary carbon-graphite face seals (grade RP-8290) is positioned by a shrink-fit, stainless steel retaining ring which is keyed to prevent rotation. This arrangement forces the rotary sealing interface between the rotating shaft runner and the carbon graphite. The static secondary spring seal (also of PTFE) provides a seating force against the carbon graphite seals for start-up operations, in addition to acting as a radial and axial back-up seal. Because of the seal's compliant nature, tolerancing of parts is less critical. The carbon graphite seal is micro-lapped to a flatness of 1-2 lightbands (1.6 micro-inches RMS) to ensure full seal contact. This flatness is verified for each seal using a monochromatic light and an optical flat. The runner is a CRES 316 substrate with a 0.005 inch thick coating of tungsten carbide applied by a detonation gun. The tungsten carbide is sealed with a UCAR 100 epoxy for protection against bond layer corrosion and is also micro-lapped to 1-2 lightbands flatness.

As shown in Figure 6, the seal orientation allows the relative pressure differential between channels to provide a seal seating force in addition to that of the secondary seals. The actual seating force was a compromise between sealing pressure and the parasitic friction due to drag. All materials were selected for compatibility with anhydrous ammonia and for their very low out-gassing characteristics.

COVER GAS CONCEPT

A key design feature of the RTC is a scavenger/cover gas system. As shown in Figure 7, on both sides of the ammonia channels are scavenger channels. These channels provide internal containment of any leakage from the adjacent liquid or vapor ammonia channels. Outboard from these scavenger channels are nitrogen charged barrier annuli at a slightly higher pressure of 4 psid. This nitrogen is either supplied from a reservoir or carried in a separate line/channel to the coupling. With the nitrogen cover gas system, any ammonia leakage is contained within the scavenger line/channel and is not dissipated externally from the coupling.

PREDICTED PERFORMANCE

The five primary coupling performance characteristics are leakage rates, frictional torque, pressure drops, thermal cross-talk, and life. The performance of the RTC was predicted based primarily on two methods: analysis, and correlation to similar carbon face seal devices such as the LaRC rotary coupler. In addition, data

taken from industrial experience with sealing ammonia in refrigeration systems provided a reference during design.

The individual lines and annuli channel sizes are based on both flow rate and pressure drop requirements of the Space Station Radiators. As shown in Figure 8, the channels are sized to meet the RTC pressure drop requirements with margin. The predicted pressure drop was calculated using standard Mollier diagram-type analysis. The maximum pressure drop occurs at the maximum mass flow rate. This maximum mass flow rate occurs at the latent heat of the fluid saturation temperature. Note that the pressure drop across the RTC is a function of rotor-to-stator relative position. This is due to the change in direction and flow length as the rotor turns.

Figure 9 shows the total RTC drag torque (friction). For applications such as the various payload pointing systems on the Space Station, frictional torque must be kept to a minimum. As stated earlier, running friction, in addition to the non-linearities of start-up-friction, can compromise pointing accuracy and stability. This friction is due to a combination of both seal and bearing drag. The seal friction is due to the seating forces exerted by both the secondary seal and the vapor/liquid pressure differential between channels. Table 1 shows the coefficients of friction values for carbon graphite sliding on various materials. A value of 0.08 was selected for the performance analysis.

Depending on the application, very low thermal cross-talk between channels may be required. Radial and axial thermal conductance and convection between the liquid and vapor/liquid were calculated as a function of rotor position. Thermal conductance is at a maximum when the rotor port is 180 degress from, or opposite to, the stator port; the the heat transfer is then completely around the rotor annulus.

Life of the RTC is predicted to be a minimum of 120,000 revs over 10 years. This prediction is based both on analysis (PV factors) and from LaRC accelerated life test data. Volumetric wear of the carbon graphite can be calculated as follows:

$$\text{Wear} = \frac{(\text{Wear Coefficient})(\text{Seating Force})(\text{Sliding Distance})}{(\text{Material Hardness})}$$

Table 1 shows typical values for wear coefficients. Hardness of the carbon graphite (grade RP-8290) is approximately 450 Vickers. Seal wear is thus analytically predicted as 9×10^{-5} in^3/seal-year. This is equivalent to a thickness change of 5.6×10^{-5} in/seal-year. LaRC test data show lives in excess of 22 equivalent Space Station years (111,000 revs over 60 days continuous operation). LaRC disassembled and inspected the rotary coupling following this test and found extremely low wear of the carbon graphite face seals and corresponding runner.

Cross leakage on the order of 1×10^{-4} cc/yr is virtually impossible to predict

accurately due to the many second order factors influencing it, including surface flatness/finish, and thermo-mechanical distortions. This value, as well as external leakage, must be measured because it is so small.

DISCUSSION

Certain problems can arise when dealing with carbon graphite seals. Caution is necessary during the installation of the steel retaining rings which surround the carbon. Cracking of the brittle carbon graphite is possible due the shrink-fit nature of the retaining ring. A slight interference fit (0.0002-0.0003 in) allows adequate pressure without damaging the seal. When using larger interference fits, care must be taken to avoid over-stressing the carbon graphite.

When using PTFE (Teflon) type gaskets and O-rings for static seals, cold flow of the material must be accounted for. The ratio of final to initial bolt clamping force required for this 'creep' can be determined as follows:

$$\frac{\text{Final Clamp Force}}{\text{Initial Clamp Force}} = \frac{(53.3 - 190(\text{thickness}) - 0.2(\text{Temp. C}) - 33.7(\text{width}) + 3.6(\text{bolt length}))}{(100)}$$

It should be noted that 90 percent of the cold flow takes place in the first 24 hours.

The modular design of the RTC accommodates up to eight separate fluid/vapor channels by simply 'stacking' the required number of annuli together. One drawback, however, is the additive nature of the tolerance stackup. A minimum start-up seal seating force must be selected, and the corresponding minimum spring seal deflection determined from this. When summed, the individual part tolerances must not exceed the value that allows this minimum seating force.

The small diameter, seal anti-rotation pins pressed into the outside diameter of the retaining rings also presented a problem. The pins, which keep the carbon graphite seals stationary with respect to the coupling's stator, were sized for shear strength and not for stiffness. During initial assembly, the pins were deflecting excessively and were actually bending out of their mating holes on the retaining rings. A change to larger diameter pins was therefore required.

Designers of carbon face seals should be aware that a combined net force due to static seal spring forces and pressure differentials between channels is present and tends to move the rotor axially relative to the stator housing. The bearing preload spring (designed to accommodate thermal elongation of the coupling) was sized larger than this net force. If this force is larger than the restoring spring force, excessive

seal wear or loss of seating force may be experienced, depending upon seal orientation.

Certain applications, such as capillary-flow devices (heat pipes), are very sensitive to thermal cross-talk between the liquid and vapor lines of the transfer couplings used. An RTC designed for such applications must minimize the conduction and convection paths between channels. The use of Teflon-type gaskets and channel liners, as well as a switch to the less thermally conductive titanium in place of stainless steel for the RTC's rotor, may be warranted. Another solution would be vacuum venting 'blocking/barrier' channels in the coupling. Large decreases in thermal transfer are possible by opening various passages inside the coupling to the vacuum environment of space.

Designers must also recognize the special problems of ground based verification of two phase flow. Differences in the coupler's performance between a one-g and microgravity environment are expected in fluid pressure drops and thermal crosstalk. Differences in fluid pressure drops between one-g and microgravity environments occur only in the two-phase flow channels. Single-phase flow pressure drops are identical in both environments, but two-phase flow acts differently in micro-gravity. Design of the passages should be based on a 100% vapor or liquid flow (whichever is greater) which is larger than a X% quality, two-phase flow. This will ensure that the design has a more conservative pressure drop than that expected for the two-phase flow in a microgravity environment.

The problem with differences in two-phase flow between one-g and microgravity environments should not largely affect the value of the thermal crosstalk. The thermal crosstalk between the liquid and vapor lines is comprised of convective and conductive heat transfer. The thermal resistance due to conduction is the main resistance between the liquid and vapor. Any change in the heat transfer characteristics of the two-phase vapor flow between one-g and microgravity environments has a minor influence on the thermal cross-talk.

TESTING

Although RTC test data are unavailable at the time of this writing, certain special test considerations are needed to evaluate the performance of an anhydrous ammonia coupling with very small ($< 1 \times 10^{-4}$ cc/yr) leakage rates. The test equipment includes a sealed chamber that surrounds the coupling. Individual rotor exit lines will be routed back into the coupling. The corresponding exit port on the stator-side of the coupling is then capped. Leakage can be tested by pressurizing the inlet port. The chamber can be vented through a water bath and the corresponding pH change measured.

Calibration of the test apparatus can be done by introducing a known quantity of ammonia into the water bath and then recording the pH change. Also, because of similar molecule sizes, helium may be substituted for the anhydrous ammonia to facilitate leakage testing. By using readily available helium 'sniffers', the problems associated with ammonia can be avoided. A drive motor will be configured for both uni-directional and oscillating motion. In this manner, life and leakage rates can be evaluated in both modes.

Due to the extremely small wear of the carbon-graphite face seals predicted, it is difficult to make wear-rate measurements. A possible solution would be accurately weighing the seals before and after the extended life testing. Frictional torque, on the other hand, is relatively simple to determine by using a torque transducer.

CONCLUSIONS

Designers of carbon-face-seal rotary thermal couplings should be aware of the various points/problem areas addressed in this paper. Particular emphasis should be placed on minimizing the overall size of the coupling; a small diameter RTC not only reduces weight and seal rubbing velocities, but also minimizes any parasitic drag torque present. This friction, when experienced on sensitive pointing gimbals and rotary joints, can dramatically affect accuracy and stability. Depending upon the application of the coupling, thermal cross-talk between channels may also be excessive and should be evaluated early in the design stage. The same evaluation should also be done for flow pressure drops across the coupling.

The orientation and sizing of the static secondary seals, which provide the required initial seating force, must also be addressed. Proper compliance between the seal and runner is needed to ensure adequate, but not excessive, axial force. This trade-off between minimum required seating force and seal drag torque must be evaluated.

A carbon face seal, rotary thermal coupling, which uses a pressurized nitrogen gas 'cover' and separate scavenger annuli as leak paths, appears to be an effective design for transporting ammonia across rotating joints in space. In addition to negligible external leakage, this RTC satisfies the Space Station requirements of low drag torque and weight, long life, high reliability, and low thermal cross-talk.

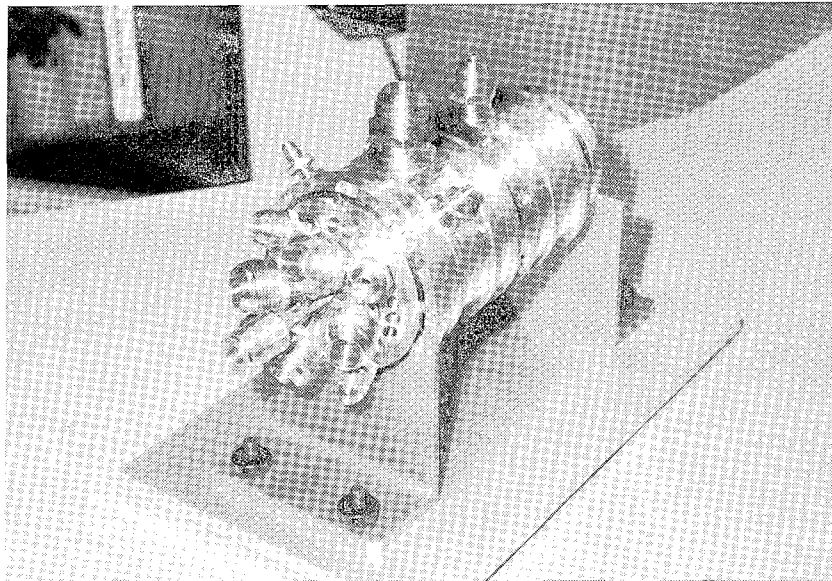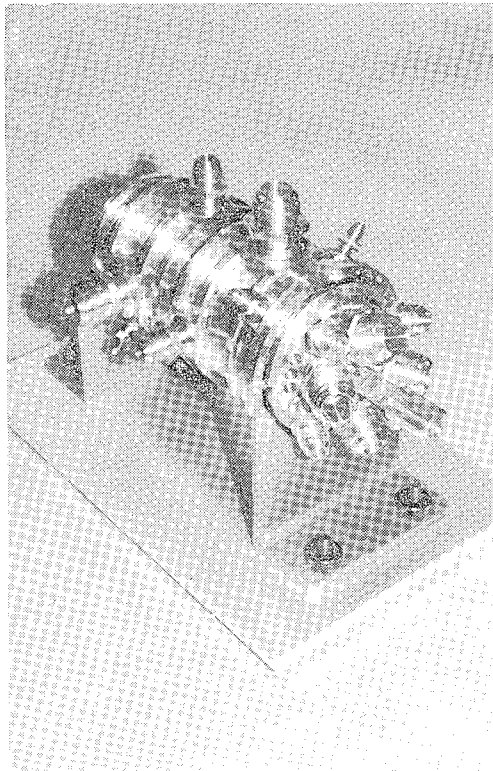**FIGURE 1. IR&D Rotary Thermal Coupler (RTC)**

<u>Space Station Radiator Joint Requirements</u>

-Vapor Supply, Liquid Return Lines
-Ammonia Compatible
-Max Flow Rate = 0.832 kg/s
-Max Line Press. Drop = 685 Pa
-Min Burst Pressure = 2.48×10^6 Pa
-Min Non-Maintenance Life = 5 years

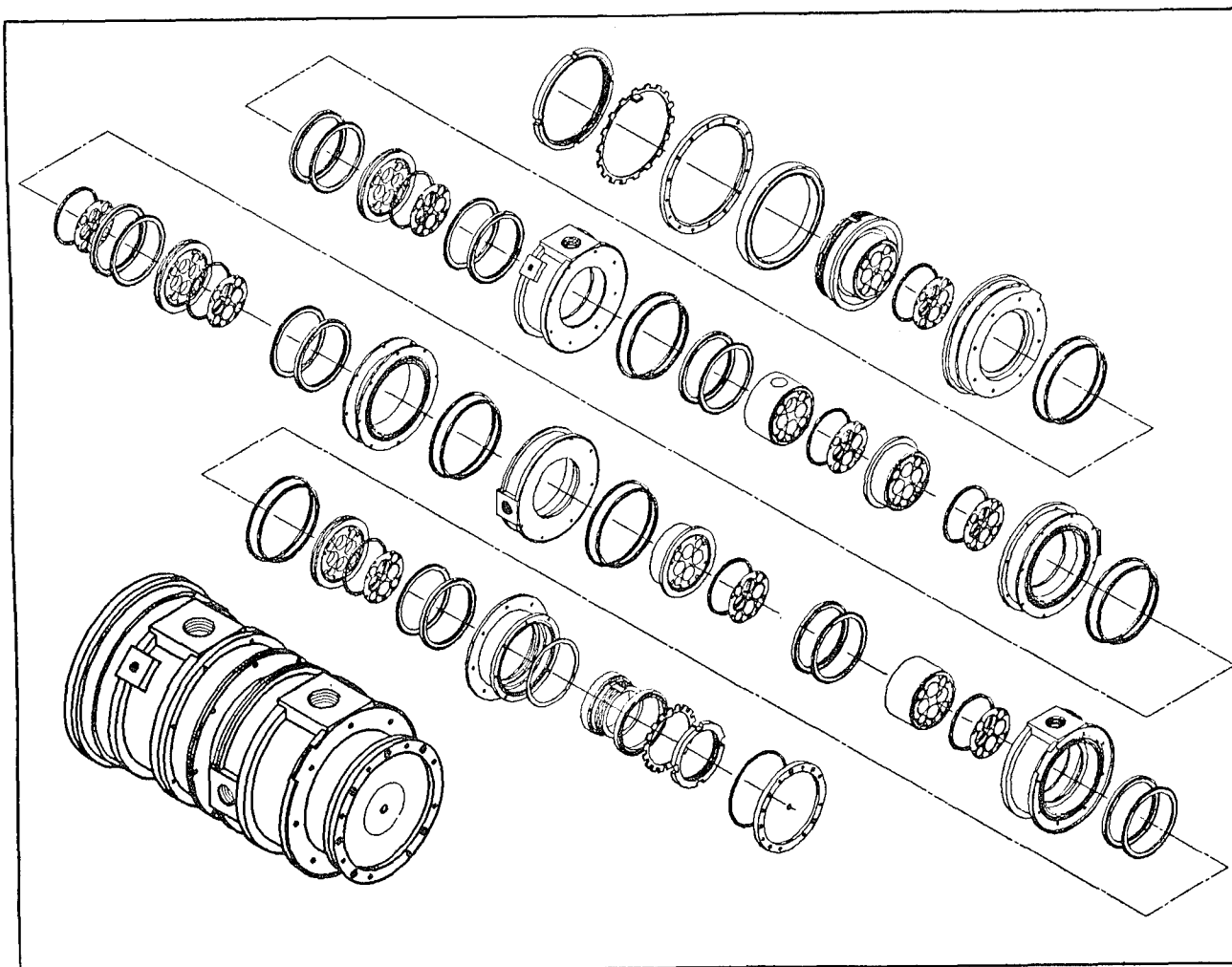**FIGURE 2. RTC Designed For Space Station Radiator Requirements**

FIGURE 3. 'Disassembled' Rotary Thermal Coupling (RTC)
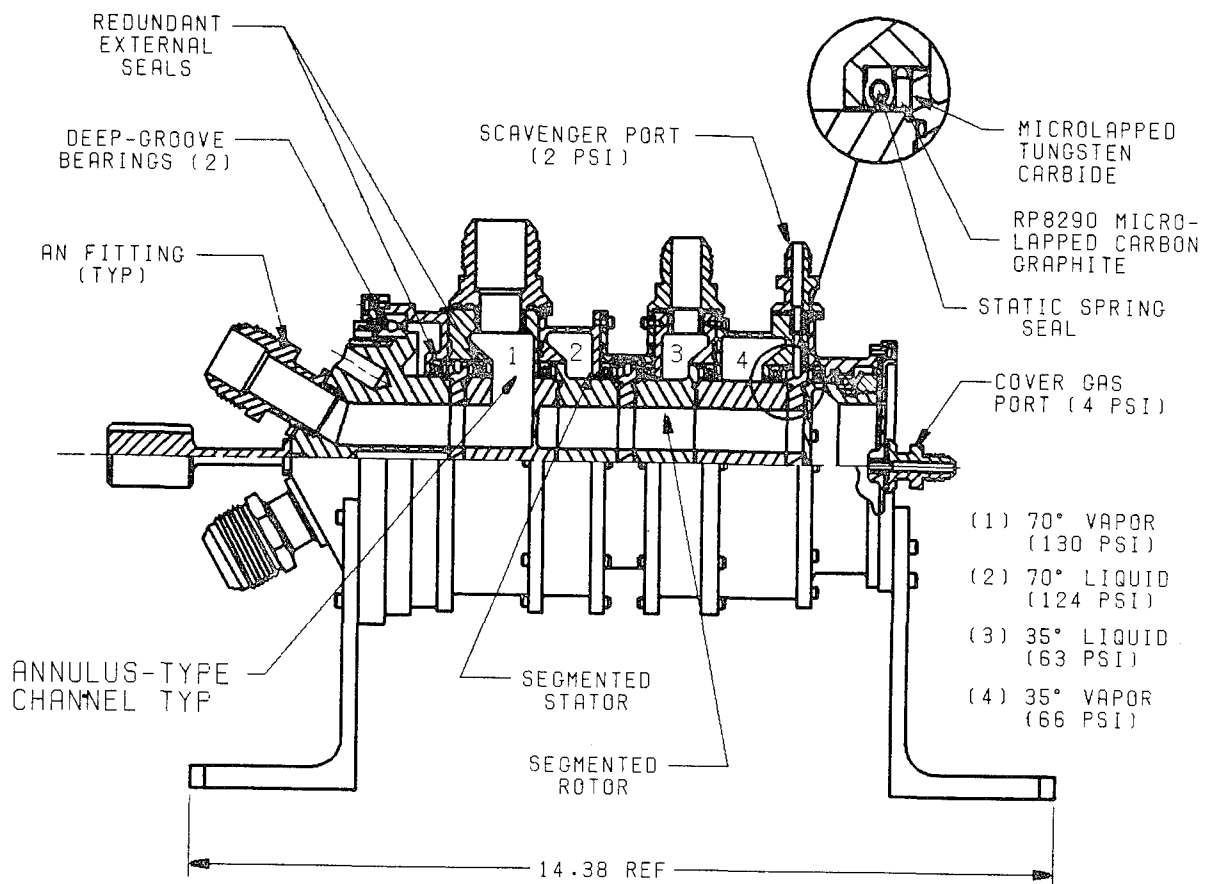
FIGURE 4. IR&D Rotary Thermal Coupler (RTC)

The following labels appear on the figure:

REDUNDANT EXTERNAL SEALS

DEEP-GROOVE BEARINGS (2)

AN FITTING (TYP)

SCAVENGER PORT (2 PSI)

MICROLAPPED TUNGSTEN CARBIDE

RP8290 MICRO-LAPPED CARBON GRAPHITE

STATIC SPRING SEAL

COVER GAS PORT (4 PSI)

ANNULUS-TYPE CHANNEL TYP

SEGMENTED STATOR

SEGMENTED ROTOR

(1) 70° VAPOR (130 PSI)

(2) 70° LIQUID (124 PSI)

(3) 35° LIQUID (63 PSI)

(4) 35° VAPOR (66 PSI)

14.38 REF
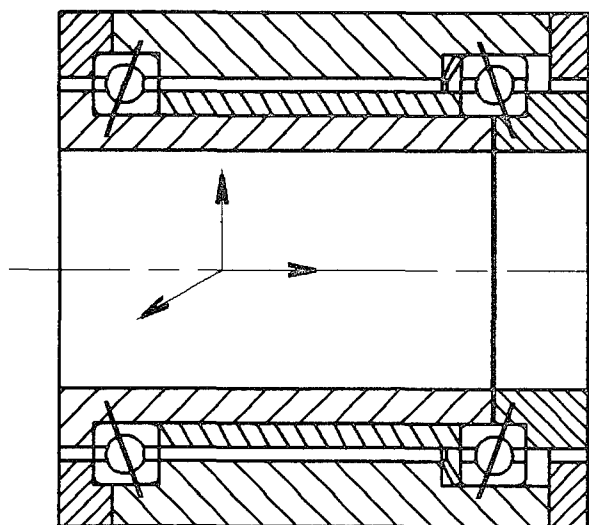
Shuttle Ascent = 6 G's

Assume Equal Load Sharing (Rotor = 9.1 lbm)
Radial Force = 54 Cos(45)/2 = 38 lbf
Axial Force = (54 +50)/2 = 52 lbf

Equiv. Radial Load = PR
PR = Radial Force +1.5(Axial Force) = 116 lbf

4"   Bearing Ascent Load Margin = 640%
2.5" Bearing Ascent Load Margin = 210%

**FIGURE 5. RTC Bearing Capacity Sized for Typical
Shuttle Launch Loads**

350
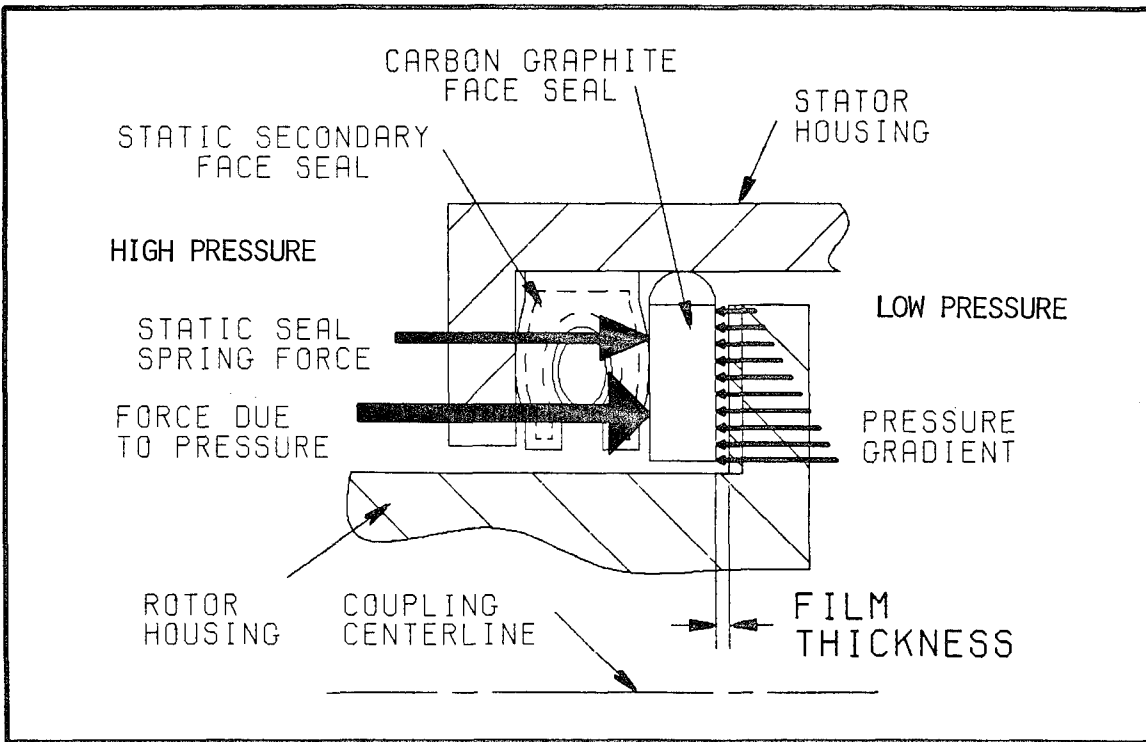
FIGURE 6. Carbon Graphite Seal Axial Loading
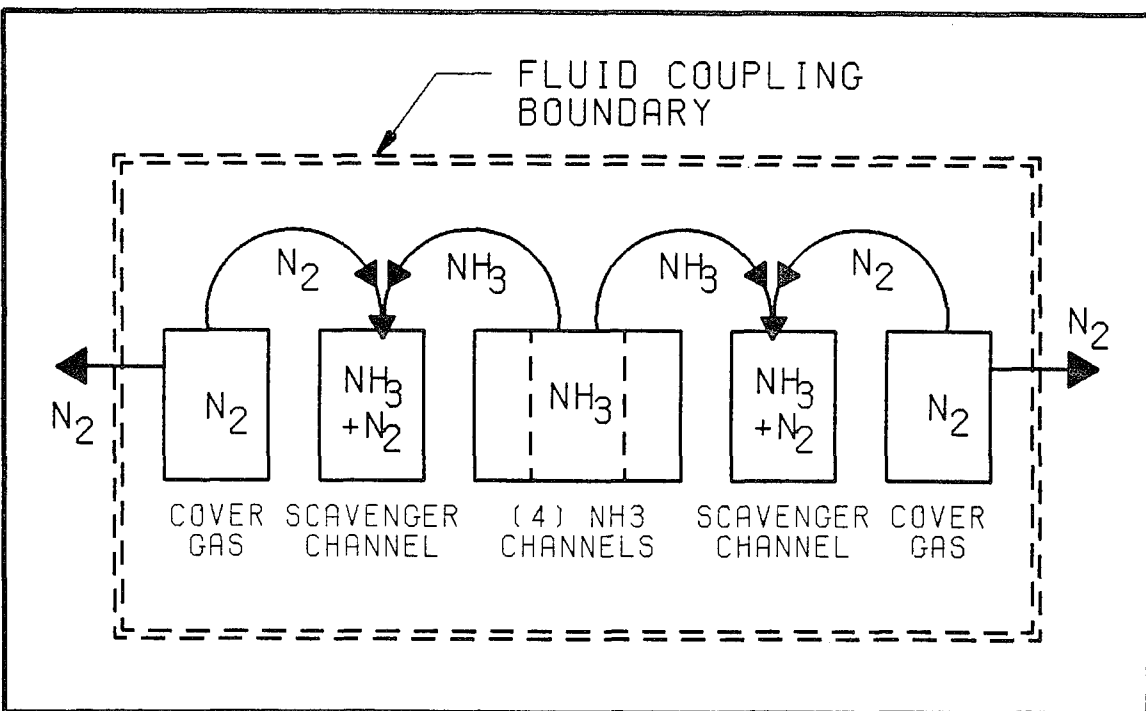
FIGURE 7. RTC Leak Path Schematic

351

VAPOR LINE PRESSURE DROP

LIQUID LINE PRESSURE DROP

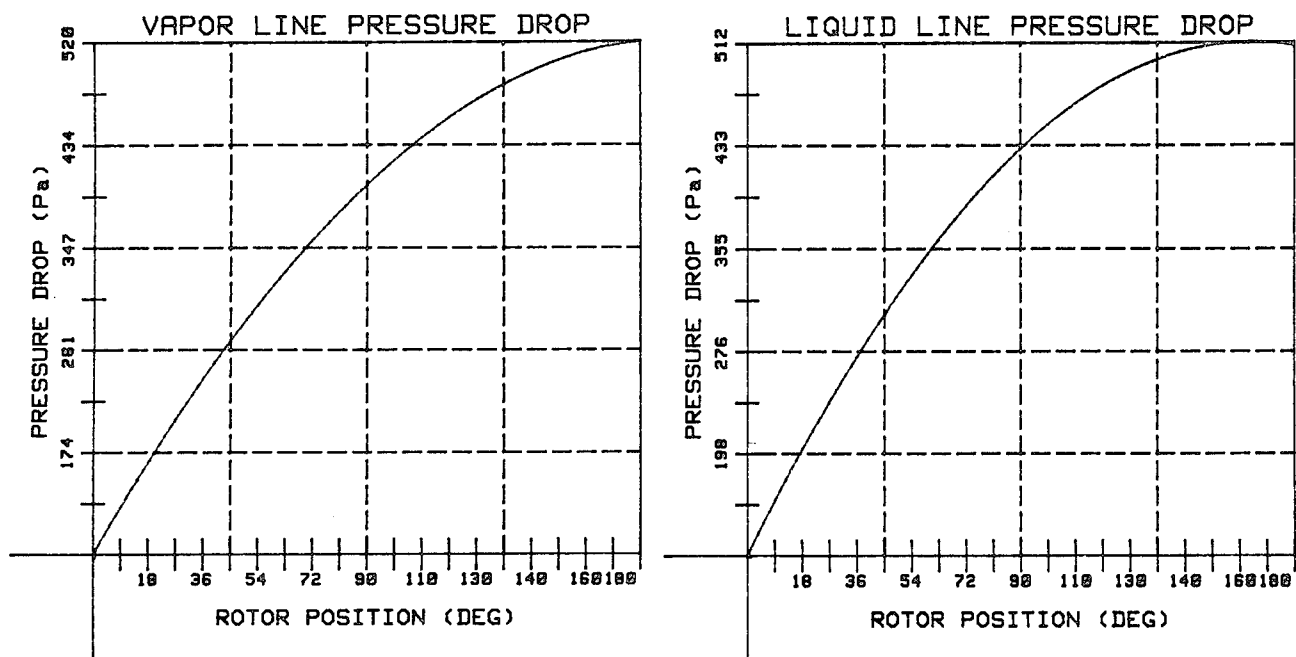**FIGURE 8. Pressure Drop as a Function of Rotor Position**
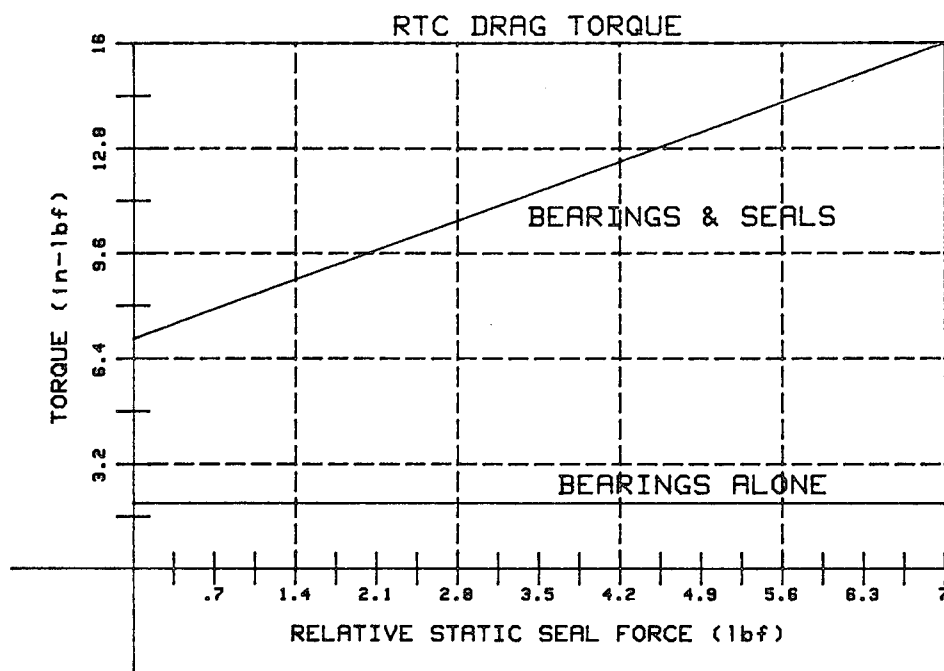
RTC DRAG TORQUE

BEARINGS & SEALS

BEARINGS ALONE

FIGURE 9. Rotary Thermal Coupling Drag Torque

Sliding Materials		Wear coefficient K	PV limit. bar · m/s	Friction coefficient f
Rotating	Stationary			
Carbon-graphite (resin-filled)	Nl-resist cast iron	10^{-6}	35	0.07
Carbon-graphite (resin-filled)	Ceramic (85% Al_2O_3)	10^{-7}		
Carbon-graphite (babbitt-filled)		10^{-7}		
Carbon-graphite (bronze-filled)	Tungsten carbide (6% cobalt)	10^{-8}	175	
Tungsten carbide (6% cobalt)		10^{-8}	42	0.08
Silicon carbide converted carbon	Silicon carbide converted carbon	10^{-9}	175	0.05

TABLE 1. Wear and Coeffients for Carbon Graphite
(*Mechanical Design & Systems*, Rothbart)

REFERENCES

-Etsion, E., and Strom, T.N., "Seals", *Mechanical Design and Systems Handbook*, Rothbart, H.A., McGraw-Hill, 1985.

BIBLIOGRAPHY

-Ludwig, L.P., and Greiner, H.F., "Designing Mechanical Face Seals for Improved Performance", *Mechanical Engineering*, November, 1978.

-Swick, R.H., "Designing the Leakproof Seal", *Machine Design*, January 22, 1976.

DEVELOPMENT OF A ROTARY FLUID TRANSFER
COUPLING AND SUPPORT MECHANISM FOR SPACE STATION

O. H. Bradley, Jr.*, J. A. Costulis*, and A. H. Porter**

ABSTRACT

A design has been developed for a rotary fluid coupling to transfer coolant fluids (primarily anhydrous ammonia) across rotating joints of the Space Station. Development testing using three conceptual designs yielded data which were used to establish the design of a multipass fluid coupling capable of handling three fluid circuits. In addition, a mechanism to support the fluid coupling and allow an astronaut to replace the coupling quickly and easily has been designed.

INTRODUCTION

A permanent manned Space Station, as currently envisioned, will be gravity gradient stabilized and incorporate rotating solar arrays and thermal radiator panels. The rotation of the solar arrays and radiators will provide much more efficient thermal and power systems, thereby reducing overall size, weight, and cost of the systems.

The rotation requirement calls for the development of structural, fluid, and electrical systems to provide for the transfer of loads, thermal control fluids (heat), and power across the rotation joints. As part of the advance development effort, an investigation was begun which would lead to the design of a rotary fluid coupling which allows 360° rotation and meet the severe design requirements of the Space Station.

The primary objectives of the development program were to demonstrate the design feasibility and to evaluate the particular design concepts proposed for a 360° continuous rotation joint. These objectives included the identification of manufacturing or assembly methods, identification of candidate materials and investigation of compatibility, selection of seals, determination of leakage rates, determination of drive power requirements, and lifetime assessment.

A set of design requirements was assembled based on the expected mission of the Space Station. Included in this set was a lifetime goal of 20 years of continuous rotation in orbit with little or no maintenance. The design rotation rate was one revolution per orbit period, or about 0.01 RPM.

*NASA Langley Research Center, Hampton, VA
**PRC - KENTRON, Inc. Hampton, VA

Anhydrous ammonia was the proposed coolant fluid, operating between saturated liquid and saturated vapor phases. As a goal, the leakage allowed from the rotary coupling was set at 454 g/yr (one pound per year), or .018 std.cc/sec. The flowrates of ammonia through the coupling were based on a total Space Station heat rejection capability of about 300 kilowatts (for two couplings). At the start of the investigation, the heat rejection was distributed among three separate fluid circuits as described in Table 1. Based on these flowrates, the coupling was to be sized to have a pressure drop of not more than 6.895 KPa (1 psi) for any circuit through the coupling.

Three conceptual designs for rotary couplings were investigated. An engineering model of each concept was designed and fabricated. Testing of each unit was then accomplished in an ammonia flow test facility which simulated the Space Station thermal bus. Based upon the results of the testing, an engineering prototype unit was designed and fabricated.

In addition to the rotary coupling designs, a support mechanism was designed which allows an astronaut to replace the fluid coupling quickly and easily. The objective was to design a device which allows essentially hands-off installation or removal of a coupling.

ROTARY COUPLING CONCEPTS

As mentioned, three concepts for rotary fluid couplings were evaluated. The evaluation was done in more of a serial fashion than in parallel so that results from previous testing and design experience could be factored into each design.

Each design included a shaft which rotated inside a stationary outer housing. The shaft contained flow passages which ran parallel to the rotating axis of the shaft, and then turned 90° out to annular passages between the outer diameter of the shaft and the inner diameter of the housing. Each of the annular passages was isolated by the use of various types of fluid seals. Each concept approached the problem of sealing in a slightly different manner.

Concept 1

The initial approach taken to designing the rotary fluid coupling is shown in figures 1 and 2. This design, called Concept 1, was fabricated of 316 stainless steel. A rotary shaft, which contained the seal glands, seals, and machined flow passages rotated inside of a mating smoothbore housing. The maximum internal diameter of the housing was 15.54 cm (6.12 in). The flow passage diameters were 1.27 cm (.50 in) for liquid and 2.54 cm (1.0 in) for gas. Four point contact bearings were used at each end of the shaft, exterior to the seals.

The interior surfaces of the housing were polished to a 2-4 microinch finish and then plated with electroless nickel to provide a

very smooth, hard surface for the seals. The exterior surfaces of the shaft were also plated with the nickel. Some previous compatibility testing with ammonia had indicated that either the electroless nickel or chrome plating would be acceptable with anhydrous ammonia. The electroless nickel does not hold up well at all, however, when exposed to ammonium hydroxide. This was a concern due to the great affinity which ammonia has for water. The chrome plating, while not exhibiting this problem, would have been difficult to polish on the surfaces requiring the "super" finishes.

The seals selected for evaluation in this unit were rotary shaft seals sized for .32 cm (1/8 in) glands and were similar in cross-section to that shown in figure 3. The material for the seals was a compound of teflon with 15 percent graphite to improve wear properties. A metal spring located in the seal provides the initial pressure on the surfaces of the shaft and housing necessary for sealing. Pressure on the interior surfaces from the fluid increases the contact force to improve sealing.

During assembly of Concept 1 it became evident that the seals could not be stretched over the shaft without incurring permanent inelastic deformation in the seals. This resulted in some initial looseness of the seals in the glands. When the shaft was inserted in the housing, however, the seals were forced back to a tight fit with the shaft by the tolerances between the shaft and housing.

Concept 2

To improve on the basic Concept 1 design, a second design was proposed as shown in figure 4. This Concept 2 hardware was designed for testing purposes to have no flow passages in the shaft. Instead, ports were provided in the housing to allow ammonia to be pumped through the unit while the shaft rotated. The seal glands for this unit were located in the housing. The housing and shaft were fabricated of 6061-T6 aluminum alloy. Previous testing with ammonia heat pipes had shown that this alloy could withstand long term exposure to the ammonia. The housing was sulfuric acid anodized, but the shaft was coated with a proprietary coating of the General Magnaplate Corporation designated as "Magnaplate HCR." This coating applies a tough teflon film to the surface which improves the hardness and frictional properties.

The seals in this unit were similar in cross-sectional appearance to the seals used in Concept 1. The seals used in Concept 2, however, were sized for .64 cm (1/4 in) glands. The seal material selected for investigation was virgin TFE teflon. Historically, teflon rubbing on teflon does not hold up well, but the design of this unit appeared to warrant further evaluation of this combination.

The assembly of Concept 2 was much simpler and easier than Concept 1. The seals slipped into the internal glands with only slight hand

manipulation. No permanent distortion of the seals was observed and the seals fit snugly into the housing. The installation of the shaft into the housing was done on a horizontal boring mill.

Concept 3

Concept 3, shown in figure 5, was designed to use mechanical face seals as the primary seals. To accomplish this, the housing was designed as a segmented unit. The shaft diameter was reduced to 7.62 cm (3.0 in) to accommodate commercially available seal designs. The sizes of the flow passages, however, remained the same as those used in Concept 1. The housing and shaft were fabricated of 6061-T6 aluminum alloy, as was Concept 2. The shaft was also coated using the Magnaplate HCR and the housing was sulfuric acid anodized.

The mechanical face seals used rotating rings of grade P-8290 carbon graphite from Pure Carbon Company. The mating rings were grade PS-9242 reaction bonded silicon carbide. Each ring was lapped to a flatness of 1-3 Helium light bands. The bellows and O-rings on the seal were fabricated of ethylene propylene.

Rotary shaft seals were used as backup seals in the design. These seals provided additional restriction for any leakage which would escape past the mechanical seals. Also, these seals would prevent the "rubber" parts of the mechanical seals from being exposed to a pressure in the range of the vapor pressure in the space environment. Ultrahigh molecular weight polyethylene was selected as the material for these secondary seals.

TESTING AND RESULTS

An ammonia flow test facility was designed and built to provide the range of flow and rotation rates required to simulate the Space Station coolant system. This system, shown in figure 6, was designed primarily to operate with liquid anhydrous ammonia. Flow rates from 0 to 0.167 l/s (0 to 2.65 gal/min) could be selected. A motor/gear drive provided rotation rates through the drive shaft of from 0.01 rpm to 1.00 rpm with an output torque of 667 N-m (5900 in-lb) available over the entire range. The temperature of the fluid within the system could be controlled from -37°C to +32°C (-35°F to 90 °F) using a separate temperature controlled liquid bath and heat exchanger.

Each unit was installed and tested in the ammonia flow facility until leakage of ammonia past the seals reached an unacceptable level or the target number of revolutions of the rotary coupling (116,800) were exceeded. The pressure within the test facility flow circuit was maintained between 786 KPa gage and 869 KPa gage (114 psig and 126 psig). This was controlled by maintaining the system temperature at 21 to 24 °C (70 to

75°F). The rotation rate was set at 1.0 rpm. This rate was somewhat arbitrary; however, the objective was to accelerate the test without modifying the performance of the seals.

Concept 1

The Concept 1 unit was tested through 31,560 revolutions before the test was stopped because of excessive leakage. The leakage past the primary seals was checked before rotation was started on unit, and it was found to be very high (95 scc/sec). The unit was rotated without ammonia for a period of one week to see if the seals would "seat." The leakage was checked with ammonia at that time and the leakage rate had dropped to .073 scc NH_3/sec. Although this rate exceeded the design goal, the decision was made to begin testing. The drive torque varied between 21.5 and 29.9 N-m (190 and 265 in-lb) during testing. The leakage past the primary seals ranged from .046 cc/sec to 1.65 cc/sec. Finally, after the unit had been driven through 31,560 revolutions (526 test hours) the leakage jumped to 50 scc NH_3/sec. The test was stopped at this point and the unit was pulled out of the test facility for inspection. While no specific cause for the leakage increase could be identified, several things were found which would contribute to the problem. First, considerable wear was noted on the seals. Residue from the seal wear was evident in the housing. Second, a bluish crystalline residue was also found in the housing. Analysis of the residue showed it to be primarily nickel. Apparently, the electroless nickel reacted with the trace ammonia vapor escaping past the seals and the water vapor from the air to form a salt compound. The presence of the residue in the housing could have contributed to the leakage failure; however, the leakage from this unit never achieved the desired goal.

Concept 2

The Concept 2 test unit accumulated 11,070 revolutions before it was removed from testing because of excessive leakage. The breakout torque for Concept 2 was 44.06 N-m (390 in-lb) at the start of testing. The running torque varied during testing from 20.79 to 23.73 N-m (184 to 210 in-lb). The leakage ranged from 2.6 to 20 scc NH_3/sec. This leakage also exceeded the design goal, but testing was continued to evaluate the long term performance of the unit. The leakage jumped sharply when the unit completed approximately 11,070 revolutions (184.5 hours). When the failure occurred, the leakage was high enough to cause significant ice formation on the unit, and attempts to measure the leakage would have put personnel at risk. When the unit was removed from the test facility and disassembled, a large amount of seal wear residue was found inside the housing. No other significant damage to the seals could be found other than the general uniform wear at the sliding interface. This would tend to confirm the undesirable performance of teflon rubbing on teflon. The surfaces of the housing and shaft were found to be virtually unaffected by the testing.

Concept 3

After 131,788 revolutions, the Concept 3 test was stopped. All performance goals for the unit had been exceeded, and examination of the unit was necessary to determine whether any design changes were required.

The unit was tested in the same manner as the other units except for the rotation rates. The initial rate was raised to 1.5 rpm. At 45,374 revolutions into the test, the test facility drive gear motor failed. A pump drive was quickly adapted, but this drive could only be controlled down to 3 rpm. Therefore, the remainder of the test was accomplished at this rate. The measured leakage from the test unit ranged between 1.9×10^{-6} and 2.0×10^{-5} scc NH_3/sec over the entire test. The torque value at breakout was 39.54 N-m (350 in-lb). The running torque was about 33.90 N-m (300 in-lb).

Disassembly of the unit revealed several latent problems. First, there was some corrosion of the shaft inboard of the outside set of secondary seals. Further in, where the ammonia concentration would have been higher, there was no corrosion. This led to the hypothesis that the corrosion was caused by ammonium hydroxide formed by the combination of ammonia vapor and water vapor from the air surrounding the test unit. A small test coupon of aluminum which had been coated with the Magnaplate HCR coating was exposed to ammonium hydroxide in an attempt to duplicate the type of corrosion found on the shaft. The coupon corroded in a similar fashion to the shaft. The second problem identified was due to the design of the silicon carbide mating rings in the mechanical face seals. The design did not include a retainer for the rings other than the spring force behind the rotating rings. When the system pressure was released, trapped gas between the primary and secondary seals caused the mating rings to act as pneumatic pistons to compress the springs. Movement of the mating rings allowed the rings to jam and prevented them from returning to their correct positions.

MULTIPASS COUPLING DESIGN

Based on the results from the testing program a multipass fluid coupling was designed which contains three separate flow circuits for different temperatures, pressures, and flowrates. The design, shown in figure 7, utilizes the technology of the Concept 3 test hardware with several improvements. Retaining snap rings were added to prevent the silicon carbide rings from moving out of position at system vent-down. Flanges were added to the secondary seals to prevent the possibility that the seals could slide at the wrong surface. New flange clamp rings were required to position and hold the seals using this approach. Metallic static seals were chosen to replace elastomeric o-rings between segments of the housing.

Currently, plans call for building one multipass coupling which will be evaluated in comparison testing with units built by other Space Station contractors.

SUPPORT MECHANISM DESIGN

As part of the total design of a rotary fluid coupling, in-orbit removal and replacement techniques were considered. In support of this effort, a conceptual design was created for a mechanism which would allow an astronaut to make a rotary coupling change quickly and easily.

The mechanism is illustrated in figure 8. The rotary coupling will be located in the center between two movable sealing plates. The fluid lines in and out of the rotary coupling will terminate at flanges on each end of the coupling. The movable sealing plates can be moved toward the coupling by a motor drive and lead screw. When the sealing plate reaches the correct position, mechanical stops will restrain the plate from advancing farther. A slide latch will be released at this point allowing the lead screw to continue to advance a drive collar which will serve as a hinge point for four latching jaws. The latching jaws will be driven inside of the flange on the rotary coupling and rotate out to grab a clamping lip on the coupling flange. The jaws will then apply a clamping force which will pull the coupling flange against the sealing plate. Some of the steps in this process are shown in figure 9.

Bellows will be used behind the sealing plate to allow the necessary movement of the plate relative to fixed hardware. The free position of the bellows will be about .32 cm (.125 in) away from the stopped position of the sealing plate. This will cause .32 cm (.125) stretch and 1.27 cm (.50 in) compression in the bellows over the entire movement.

Some development testing was performed to evaluate the capabilities of the static seals which would be required at the interface for each of the fluid lines. Shown in figure 10 is the design for a typical seal assembly. Figure 11 shows a cross-sectional view of the seal which was selected for this application. During testing, mating parts of the seal assembly were driven together using a load testing machine. The leakage external to the assembly was tested using helium gas at 862 KPa gage (125) psig internal to the assembly. A helium leak detector with a sensitivity of 1×10^{-10} scc He/sec could not detect leakage, even after bagging the unit for 24 hours.

The clamping load required between a coupling flange and a sealing plate is approximately 4448 N (1000 lbs) for each fluid line which must be sealed at the interface. Of this number, 3825 N (860 lbs) are due to the compression of the static seals.

CONCLUSIONS

The development program for a rotary fluid transfer coupling for Space Station identified a unit design (Concept 3) which exceeded the testing requirements that had been established. The design used mechanical face seals as the primary seals, with secondary rotary shaft seals

of ultrahigh molecular weight polyethylene. During testing, liquid anhydrous ammonia was flowed through the unit while the shaft was rotated for the equivalent of over 20 years of rotation life. The leakage external to the unit did not exceed 2.0 x 10^{-5} scc NH_3/sec throughout the test.

A prototype multipass fluid coupling design, which incorporates the Concept 3 test unit sealing principles, has been completed. This unit will accommodate up to three separate flow circuits operating at different temperatures, pressures, and flowrates. The design can be modified easily for more or fewer flow circuits as required.

A design has also been described for a mechanism which allows a rotary coupling to be removed or replaced in orbit. By actuating a motor drive, the mechanism will connect fluid lines to the rotary coupling, apply the necessary clamping forces, and mechanically link the coupling to the structure providing torque.

TABLE 1

Design Heat Rejection for Space Station

Circuit No.	Temperature, °C	Heat Rejection, KW	Ammonia Flowrates, Kg/hr
1	1.7	36	51.7
2	21	140.4	214.1
3	32	120	190.5

Leakage ports

Rotary shaft seal

Shaft

Housing
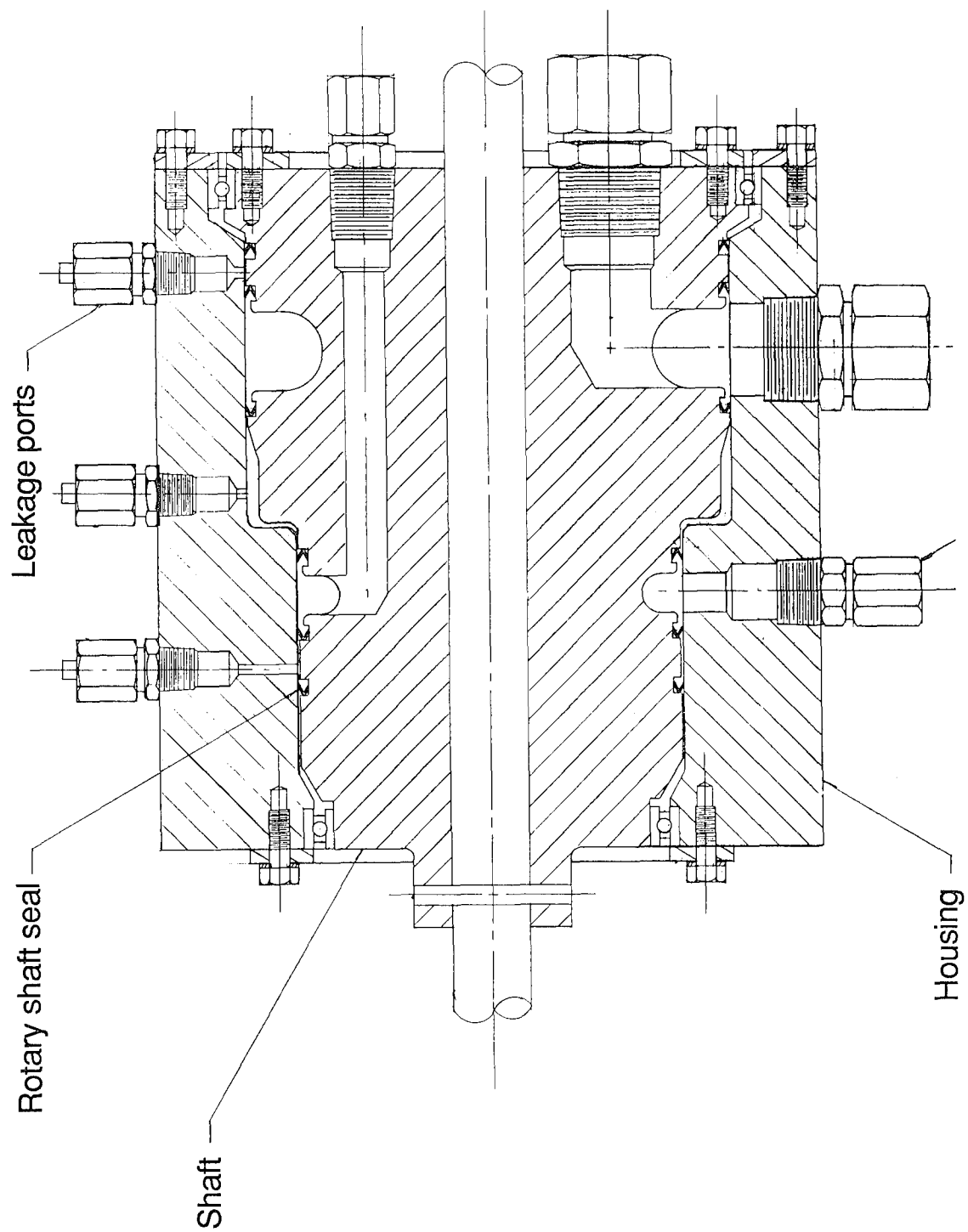
Figure 1. Concept 1 Rotary Coupling Design

363
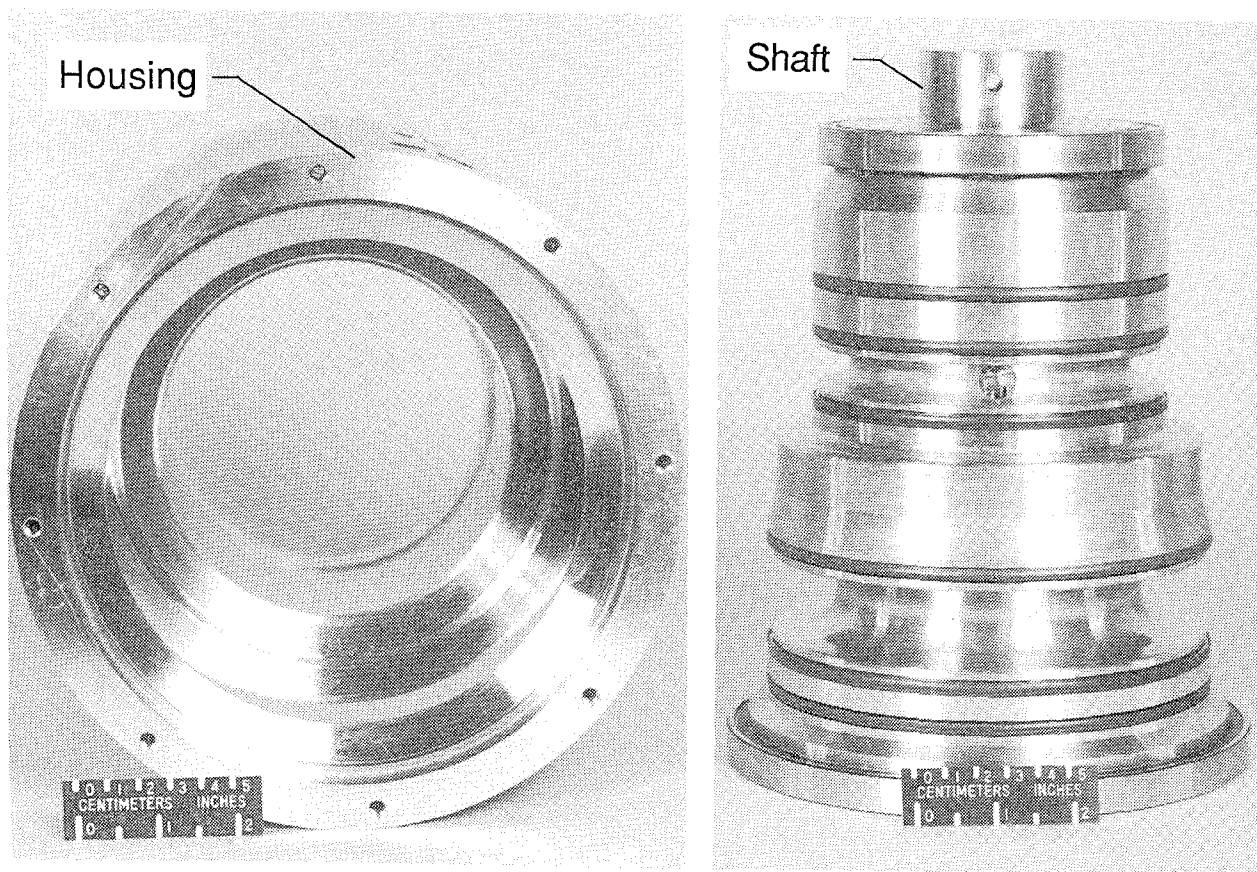
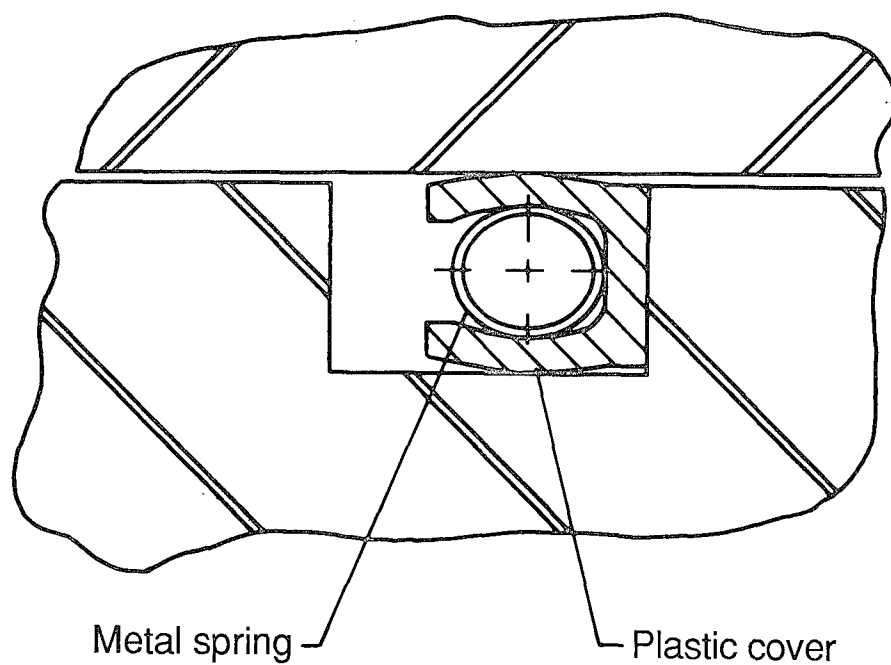Figure 2. Concept 1 Test Hardware

Metal spring ⌐   ⌐ Plastic cover
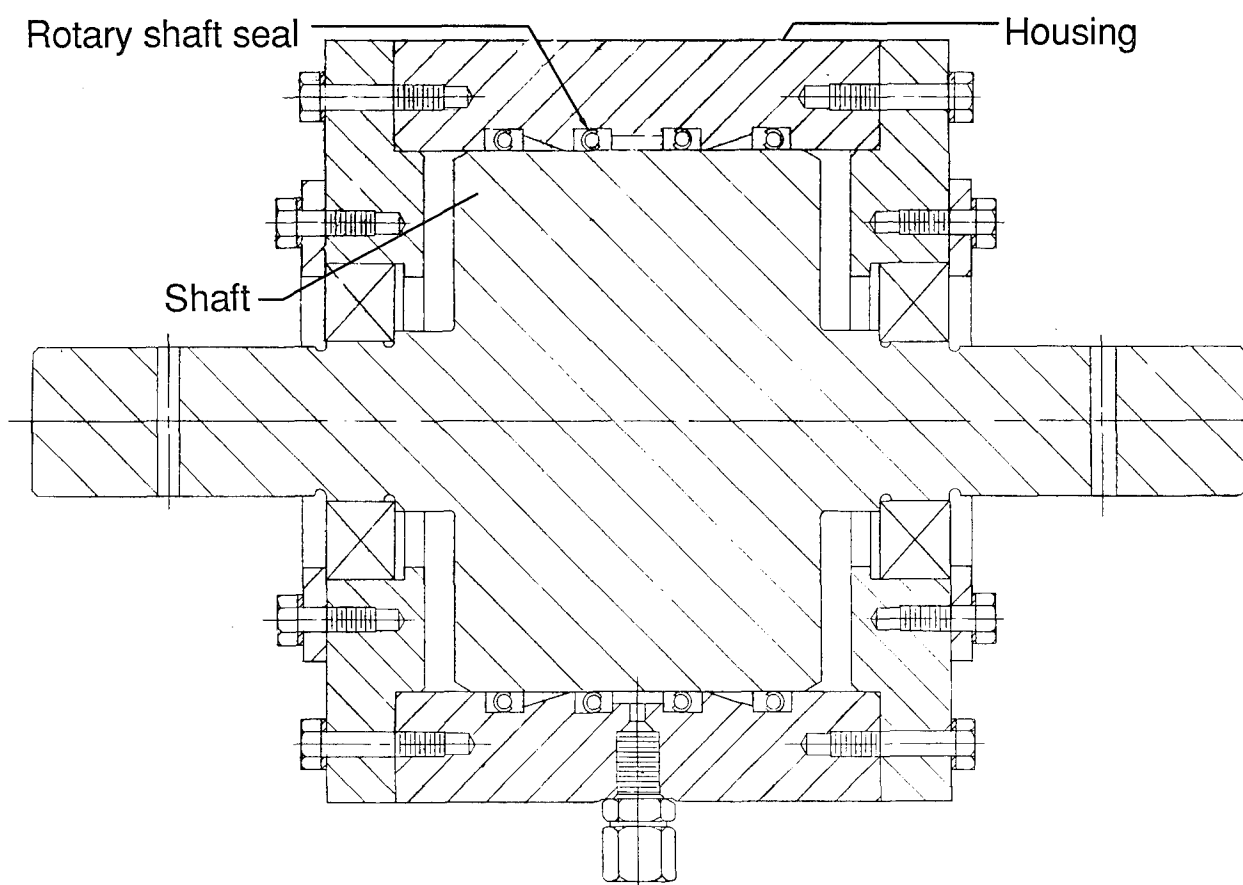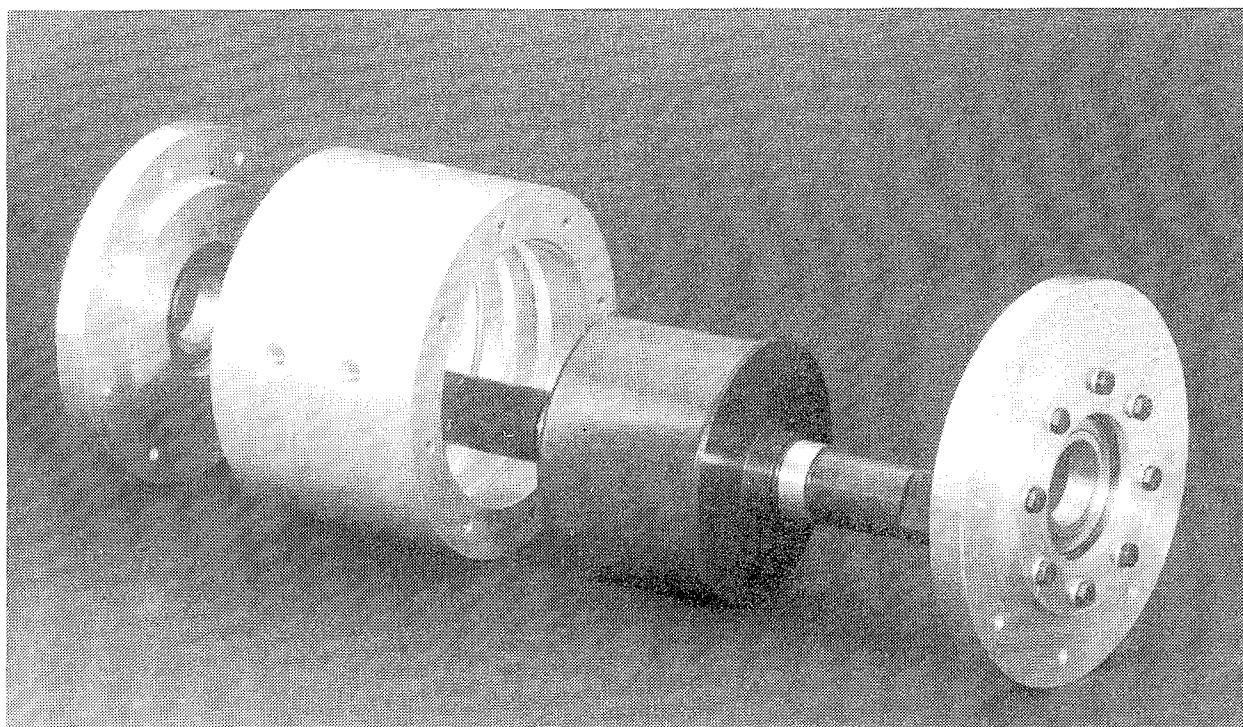
Figure 3. Typical Rotary Shaft Seal

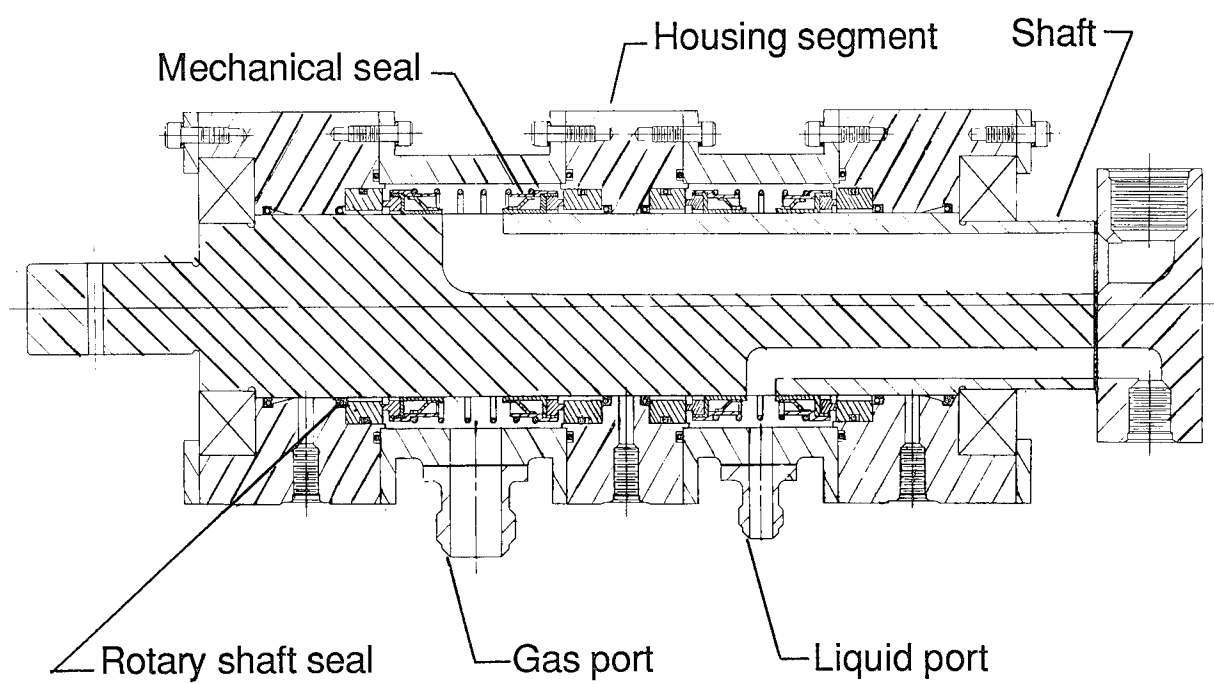Figure 4.   Concept 2 Rotary Coupling
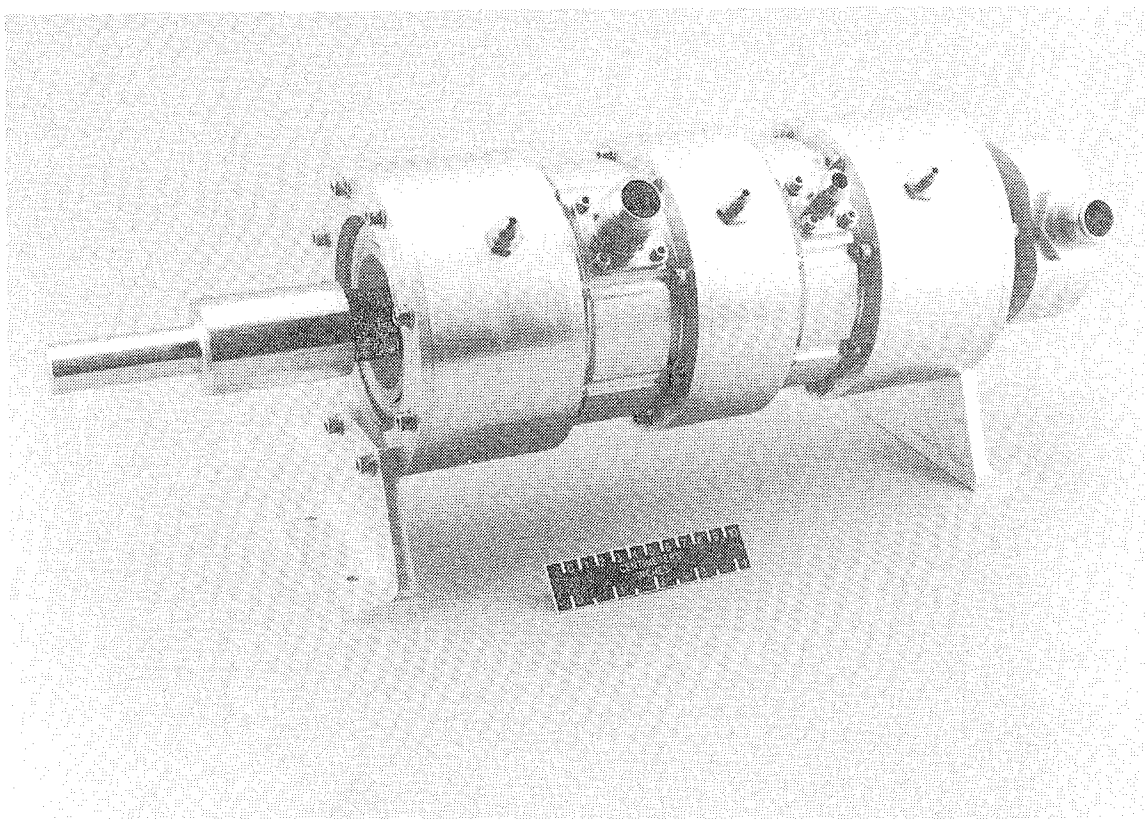
Figure 5. Concept 3 Rotary Coupling
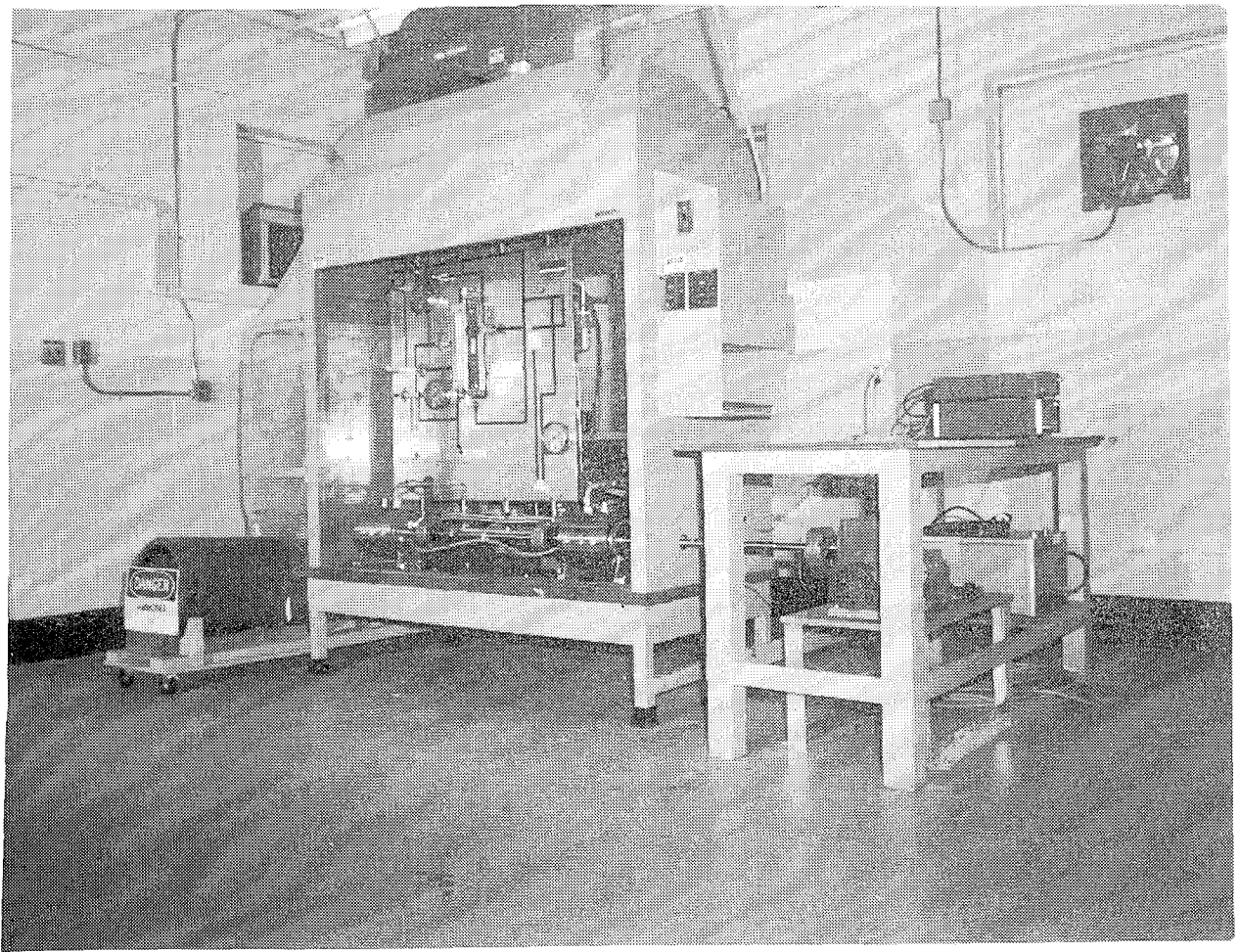
Figure 6. Ammonia Flow Test Facility
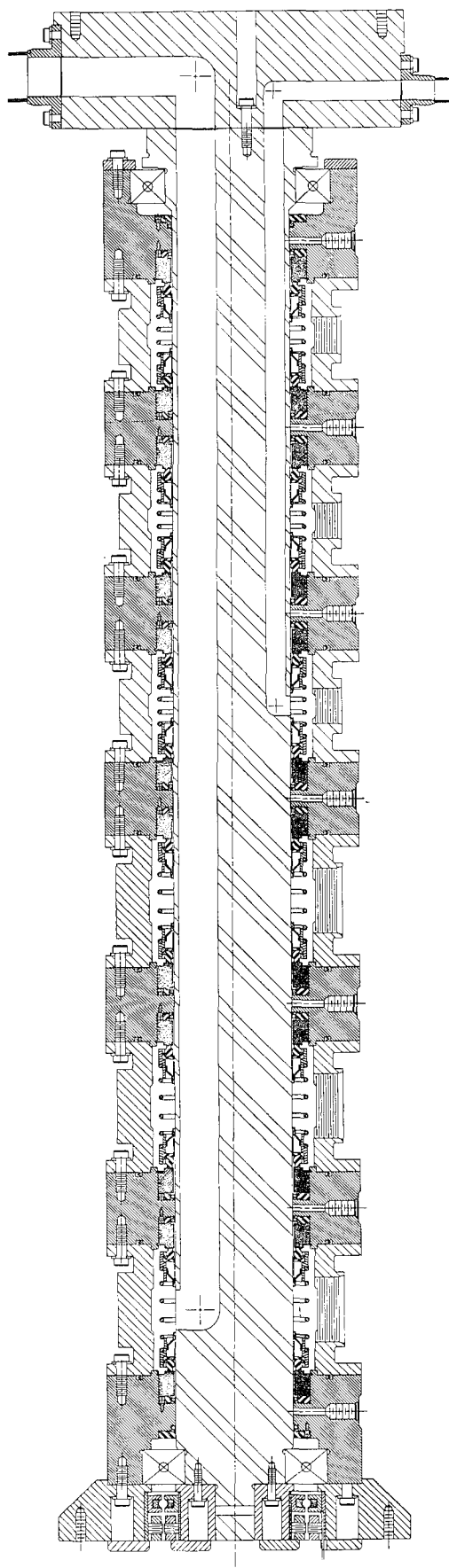
Figure 7. Expanded Concept 3 Design For Multiple Flow Passages

"Stationary" boom

Motor drive

Flange

Rotary fluid coupling

Sealing plate

"Rotating" boom

Motor drive
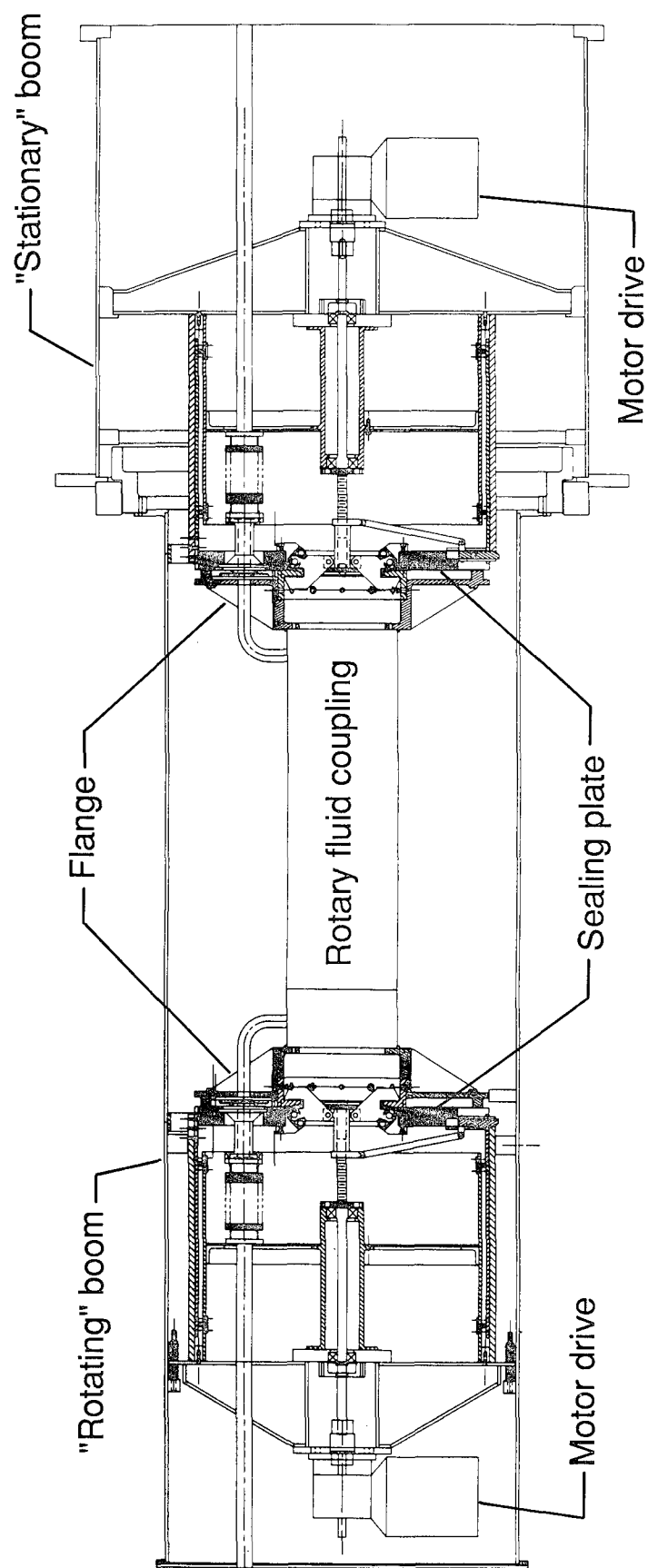
Figure 8. Support Mechanism For Rotary Coupling

369

Bellows

Rotary
coupling

Latching jaw

Slide latch

Latched

Rotary
coupling

Unlatched

Flange

Sealing plate

Rotary
coupling

Unlatched and

separated

Figure 9. Latching Mechanism Movement

370

Figure 10. Seal Assembly

Figure 11. Static Seal

ORBITER PROCESSING FACILITY SERVICE PLATFORM FAILURE AND REDESIGN

Jesse L. Harris*

THE MISHAP

On March 8, 1985, in high bay 2 of the Orbiter Processing Facility (OPF) at the Kennedy Space Center, technicians were preparing the space shuttle orbiter Discovery for rollout to the Vehicle Assembly Building (VAB). A service platform, commonly referred to as an "OPF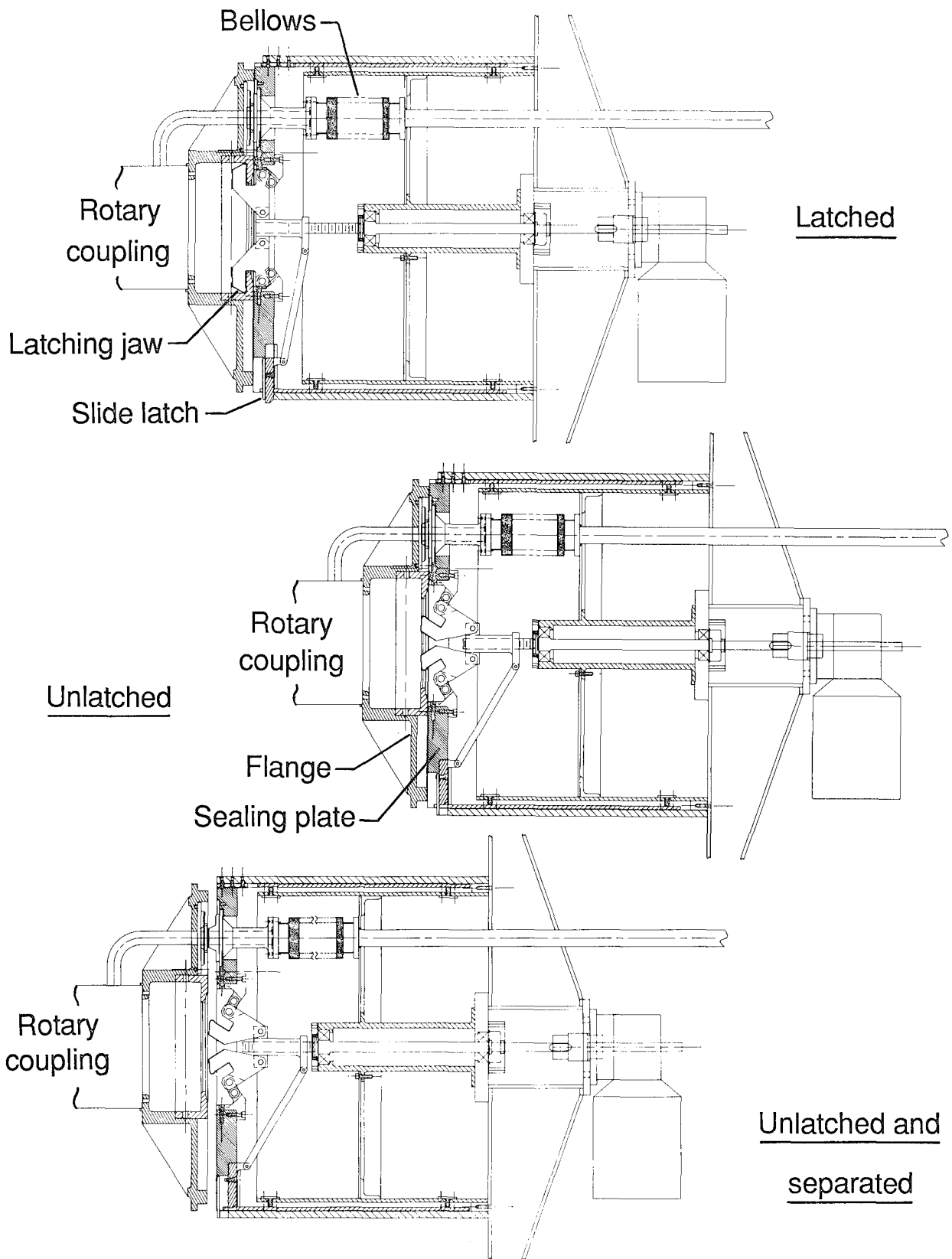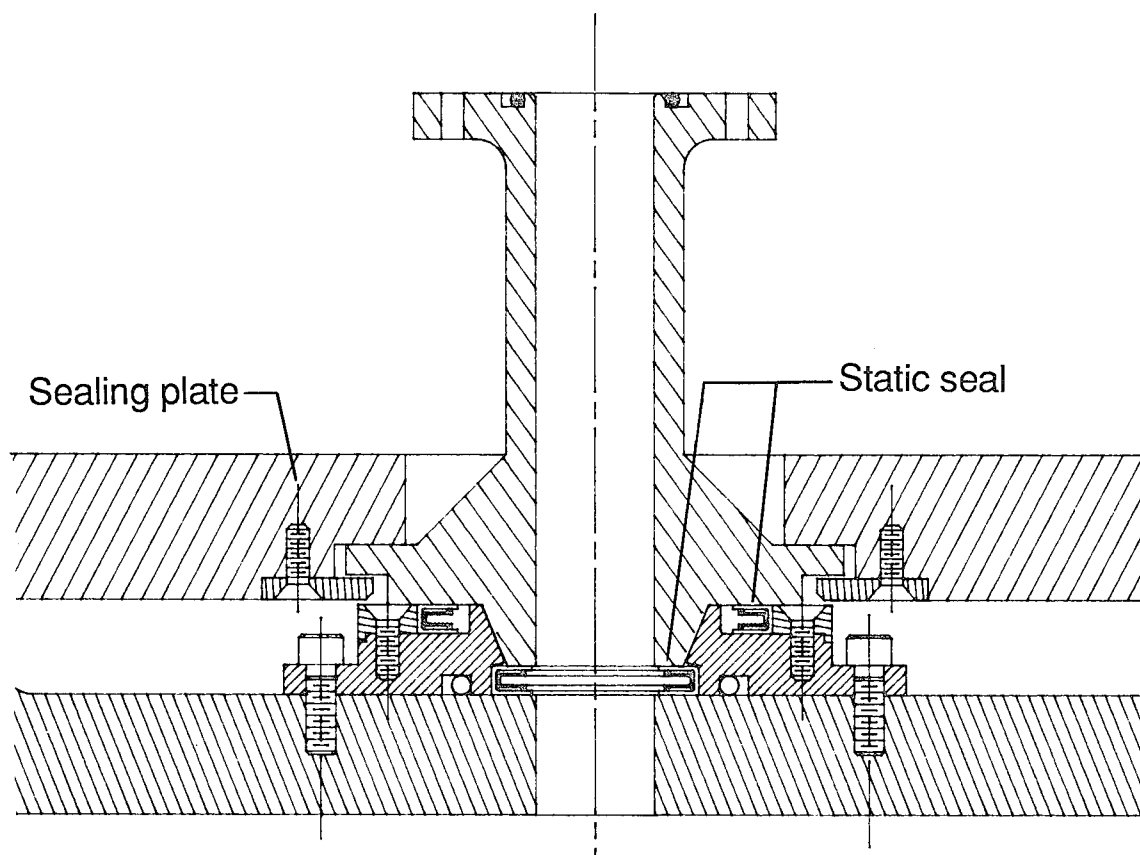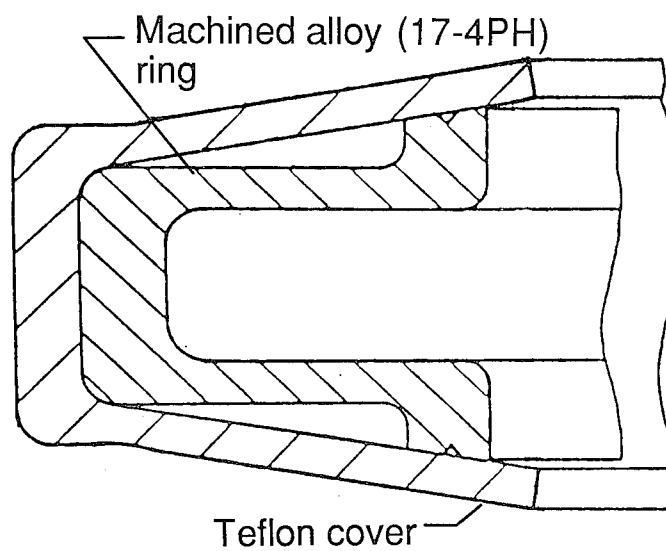 Bucket" was being retracted when it suddenly fell, striking a technician and impacting Discovery's payload bay door. A critical component in the OPF Bucket hoist system had failed, allowing the platform to fall. The incident was thoroughly investigated by both NASA and Lockheed Space Operations Co., revealing many design deficiencies within the system. This paper reviews the deficiencies and the design changes made to correct them. See Figures 1-14.

THE MECHANISM

The OPF Bucket system, Figures 1 & 2, consists of a pair of work platforms, telescoping tube assemblies, hoisting systems, and trolleys, both suspended from a common overhead bridge. Each orbiter payload bay may be accessed by two separate bridges, for a total of four Buckets per high bay.

THE WORK PLATFORM is made of aluminum, with a work area of 1 x 3 meters. A technician located in the Bucket has a hand operated rotation device with which he may rotate the Bucket one to two full revolutions. The first production set of OPF Buckets uses a chain drive system that allows the Bucket to rotate two revolutions but requires locking the Bucket into position after rotation. A later set of OPF Buckets uses a worm gear drive device which is self locking but rotates only one revolution. At the time of the mishap the Buckets had a rated capacity of 225 kg and were connected to the hoisting system thru the rotation device. An electrical control station, Figure 3, is available in the Bucket which controls the direction (up/down, east/west, and forward/aft) and speed (3 meters/min. and 1 meter/min.) of the Bucket motion drives.

THE TELESCOPING TUBE ASSEMBLY consists of four nested square steel tubes each 2.75 meters long allowing the Bucket to lower 6 meters into the orbiter payload bay. The telescoping tubes carry torsional loads preventing the Bucket from rotating in the horizontal plane and carry bending moments

----

*Lockheed Space Operations Co., Kennedy Space Center, Fla.

preventing eccentric loads from tipping the Bucket in the vertical plane. The tubes do not provide vertical support. The smallest of the tubes is 250 mm square and connected at its bottom to the Bucket thru the rotation device, the upper end of the tube has a travel stop which engages intermediate tubes above it. The two intermediate tubes, one 300 mm and the other 350 mm square, have bronze guides and travel stops which engage their adjacent tubes. The fixed upper tube is 400 mm square and is directly connected to the trolley chassis.

THE HOISTING SYSTEM, Figure 4 & 7, raises, lowers and provides vertical support for the Bucket and telescoping tubes. A two part reeved, dual wire rope hoist system using a commercial, off the shelf, wall mounted, 1350 kg capacity, AC electric hoist is used.

At the heart of the system is the hoist which has full depth, 20 degree involute, modified tooth form, straight spur gears, machined integrally with or splined to their shafts. The modified tooth form allows high addendum, small pitch diameter pinions, with higher strength teeth, to be used with low addendum gears more closely matching gear and pinion tooth strength and preventing undercutting of the pinion teeth. The hoist has an electrical solenoid operated drum type holding brake attached to its motor and an automatic Weston screw-and-disc type load brake mounted between the first and second gear reductions in the gearbox, Figure 5. The Weston load brake holds the load regardless of whether the power is on or off. When lowering the load the motor applies torque to the load brake causing the disc to unscrew and thus slip, allowing the load to lower. When raising, the motor causes the disc assembly to screw together, tightening the assembly. A ratchet pawl engages a ratchet on the disc preventing the load from backdriving when stationary.

The hoist is mounted to the outside of the fixed 400 mm upper tube and has two 10 mm stainless steel wire ropes anchored to its drum. The wire ropes pass through an upper snatchblock attached to the top of the fixed tube and, at the time of the mishap, routed down thru the telescoping tubes to a lower snatchblock attached to the Bucket rotation device. The rope is routed through the lower snatchblock terminating at the upper end of the fixed tube. With the two part reeving the hoisting system has a rated lifting capacity of 2700 kg.

THE TROLLEY provides support and east/west motion capability for the Bucket and telescoping tubes. It is a steel frame chassis with a commercial, underhung, four wheel trolley unit at each corner of the frame. Two of the wheeled trolley units have electric drive motors and geared drive wheels.

THE BRIDGE is a steel truss which supports two trolley/Bucket assemblies and provides the forward/aft motion capability of the system. The electric drive motor and gear box are centrally located on top of the truss, connected to drive shafts running to each end of the truss; chain drives connect the drive shafts to the drive wheels, Figure 6. The

bridge also has a control station that can control hoist, trolley and bridge drives for each bucket.

THE CAUSE OF THE MISHAP

The direct cause of the mishap was a failure of a hoist system master link, Figure 7, allowing the bucket to fall, Figure 8. The master link attached the lower snatchblock to the Bucket and was probably broken by locking up the Bucket's vertical hoisting system. The locking up resulted from the Bucket being raised until the telescoping tubes had reached their upper travel limit and were physically prevented from further motion. The hoist continued to drive applying an increasingly large force to the lower snatchblock and master link assembly causing the master link to break. An electrical limit switch designed to shut off power to the hoist prior to the tubes reaching their upper travel limit had been misadjusted and did not engage, Figure 9. The hoist system was designed to have redundant wire ropes, lower snatchblocks and master links loaded in parallel.

An earlier failure of one of the master links had occurred at which time the Bucket was removed from service and "Do Not Operate" tags were attached to the Bucket control stations. The mishap occurred upon failure of the second master link after the Bucket was tagged out. The primary cause of the mishap was attributed to operator error due to unauthorized use of the tagged out Bucket.

Investigation by NASA, Lockheed Space Operations Co., and a Lockheed Corp. protection consultant revealed many design related deficiencies with the OPF Bucket's hoisting and positioning mechanisms. These deficiencies were significant and if not corrected would have probably lead to another mishap. Below is a summary of these deficiencies.

1. The OPF Bucket system lacked a mechanical lock that would support the system and prevent its inadvertent use.

2. The system lacked an operational up travel stop switch thus allowing the Bucket operator to use the limit switch as an the operational stop. The system lacked any device that would indicate a failure of the limit switch.

3. The system was not provided with an overload protection device.

4. Main load carrying components were inaccessible and could not be readily inspected.

5. The electrical control system operated differently for the first production set of OPF Buckets than it did for the second production set.

6. The design of the control station switches would cause them to stick in the energized position after repeated use.

7. There were no visual aids to help the operator determine when he was

375

approaching the end of travel of the hoist system.

8. Inadequate clearance existed between the bottom of the OPF Bucket and the orbiter payload bay doors when the doors were being closed. This required the operator to retract the Buckets until the limit switch was reached.

9. The load capacity limit for the OPF Bucket was inadequate to support normal operations.

10. The master link failed at less than its rated capacity.

11. Other hoist system overload modes existed such as telescoping tubes which could bind then release and fall causing impact loads to the system. Bucket handrails could bottom out on other structures during retraction if the Bucket was not rotated to the proper orientation.

12. Downward overtravel could cause the hoist wire rope to rewind in the opposite direction on the hoist drum and cause the hoist load brake to be ineffective.

THE NEW DESIGN

Personnel and flight vehicle safety was the primary concern in the redesign effort. The design changes to correct the deficiencies in the system were not limited solely to beefing up the failed components but included a wide scope of changes including: improved maintenance capabilities, improved operation, increased load carrying capacities, electrical control reliability and safety enhancements. Improvement in reliability and the elimination of single failure points were also main goals of the redesign.

A review of OSHA and ANSI specifications revealed that there were no government or industrial standards for this particular type lifting mechanism. There were specifications for similar devices, however, such as exterior building maintenance platforms, typically used by painters and window washers for access to the outside of buildings. These specifications required that the platforms be maintained in a horizontal position with the failure of one of the hoisting ropes, that minimum safety factors of 10:1 be provided on the hoisting system and that the system have no single failure points. The new design would comply with the intent of these specifications.

INTERIM CHANGES were made immediately following the mishap to prevent a recurrence of the failure and allow returning the Buckets to service under restricted use. The changes included:

1. Redundant limit switches were installed at the upper end of the telescoping tubes. The switches were placed in series with the first switch located 45 mm below the physical upper travel limit and the second located

25 mm below the limit. The switches were also reoriented to eliminate the misalignment problem which contributed to the mishap. The change in alignment can be seen in Figures 9 & 13.

2. Visual aid stripes were painted on the telescoping tubes. The stripes are visible to the operator and when aligned indicate that the travel limit is being approached.

3. Inspection holes were cut in the lower end of the 250 mm telescoping tube allowing easy access and inspection of the master links and snatchblocks.

PERMANENT MODIFICATIONS were made to the system after completion of the mishap investigations that were intended to correct the design deficiencies identified by the various mishap investigation committees. An extensive failure modes and effects analysis was performed which identified system single failure points, latent failure points and hazards which were corrected where possible. Latent failure points, such as a failed-closed upper limit switch, are failure points in redundant systems in which the failure would be undetectable during normal use. These points were required to be inspected on a periodic basis if they could not be removed by design. The inspection requirement assured that if any failures occurred they would not go long undetected.

The importance of operator and user involvement in the redesign effort cannot be overemphasized. A key element in the redesign effort was the use of interviews by the design engineers with the Bucket operators. The operators knew the system well and had valuable information on how the system should be configured to suit their needs.

Inspection of the telescoping tube travel stops revealed damage caused by the tubes binding then working loose, freefalling and impacting the stops. Methods to individually drive each tube with jackscrews or wire ropes were rejected as being difficult to control and requiring too much space. It was decided that a method to control the fall of the tubes would be more practicable. The tubes if they should hang up would be allowed to fall but the descent velocity of the fall would be limited.

The selection of the descent control device involved trade off studies of different concepts including hydraulic cylinders and centrifugal brake type devices. The hydraulic cylinder concept appeared initially to be the most promising since the descent velocity could be controlled simply by selecting the correct size orifice for each size telescoping tube and the orifice size could be varied with ease. Problems with differing hydraulic fluid volumes between the downstroke and upstroke and concerns with the possibility of contaminating Space Shuttle payloads with leaking hydraulic fluid led to the rejection of the hydraulic cylinders as decent control devices.

The system finally selected was a commercial load control brake which

is actually a personnel escape device used by construction workers to jump off buildings in emergency situations. The device has an internal centrifugal brake that will limit angular velocity similar to the rotary dial in a dial type telephone forced in the counterclockwise direction. The load control brake is attached to the trolley chassis with an 8 mm wire rope routed down through a pulley on the telescoping tube, and back up to terminate at the trolley chassis, Figure 10.

A load sensing device, **Figures** 11 & 12, was installed that would sense high or low hoist loads and shut off power to the system. A load equalizing bar was also installed to maintain equal loading of the 10 mm wire ropes.

The hoisting system components, Figure 11 & 13, were repositioned to allow access for inspection of the wire ropes and wire rope pulleys. The lower snatchblock and master link assembly were eliminated.

To prevent inadvertent operation of one Bucket by an adjacent Bucket operator the control system circuitry was reconfigured. The Buckets in both OPF high bays were made to operate identically.

A study of the hoist revealed that the load control brake ratchet pawl stop, item 34 in Figure 5, a hex head screw, was located adjacent to the gearbox oil drain plug, item 33 in Figure 5. The two could be easily confused and inadvertent removal of the brake ratchet pawl stop would cause the brake to become nonfunctional. Labels were attached to the drain plug and the ratchet pawl stop bolt was sealed to the gearbox case.

Shunt trip circuit breakers were installed and mounted in a locked cabinet. Once tripped the circuit breakers cannot be reset without unlocking the cabinet. The circuit breakers are wired to the upper limit switches and to the load sensing switch. A tripped circuit breaker will indicate that there is problem with the system and that inspection or repairs are required.

Concepts are now under study to eliminate single failure points in the gear train of the commercial hoist. Concepts being considered are replacing the existing hoist with a commercial hoist that has no single failure points, installing a brake on the drum of the existing hoist or installing an inertia reel type load brake between the Bucket and the support structure. Control systems for telescoping tubes which could be used in lieu of the descent control devices are being investigated. Results of these studies are expected by the second or third quarter of 1988.

TESTING

Tests were conducted to verify that the load control brake used to control the descent of a falling telescoping tube would function correctly, and, that the hoist system components breaking strength was as assumed.

To test the load control brakes a full scale simulator, Figure 14, was

built to simulate the 350 mm telescoping tube and trolley chassis. Load cells were installed at the four corners of the trolley chassis, where the wheeled trolley units are located, to measure trolley loads and at the load brake wire rope termination to measure load brake loads. A linear transducer, "fish reel pot" was installed at the bottom of the telescoping tube to measure displacement and velocity. The telescoping tube was allowed to freefall with the load control brake connected and the loads at the trolley measured during impact of the tube travel stop. All load control brakes are qualification tested in this manner prior to installation on an OPF Bucket.

A failure test of the wire rope pulleys, Figure 13, and load limiting switch assembly, Figure 12, was conducted to verify that the manufacturers rated breaking strength was valid for the configuration in which they were being used. The test results confirmed that the weak link in the system was not the wire rope, which was analyzed as the weakest element, but **the** load limiting switch. The switch failed at 95% of its rated breaking strength. The test did confirm that adequate safety factors were provided for the system.

CONCLUSIONS

There are many lessons to be learned from the OPF Bucket failure, the most important of which is that equipment can be misused and probably will be if it does not meet the needs of its user. Design engineers must solicit the opinions and needs of the people who will use and operate the mechanisms that they design.

Latent failure points should be identified and dealt with, a failure in a redundant system that goes undetected in turn creates a single failure point. Often a latent failure point may be worse than a single failure point because it may instill a false sense of security in the system.

The failure of the master link at less than its specified breaking strength is an example of a manufacturer's desire to get the most from his product. In this case the rated breaking strength was based on unpublished test conditions. These conditions were not only omitted from his catalog and engineering design manuals, but were not even common knowledge of his engineers. When critical systems are involved it pays to test the components to determine their limitations.
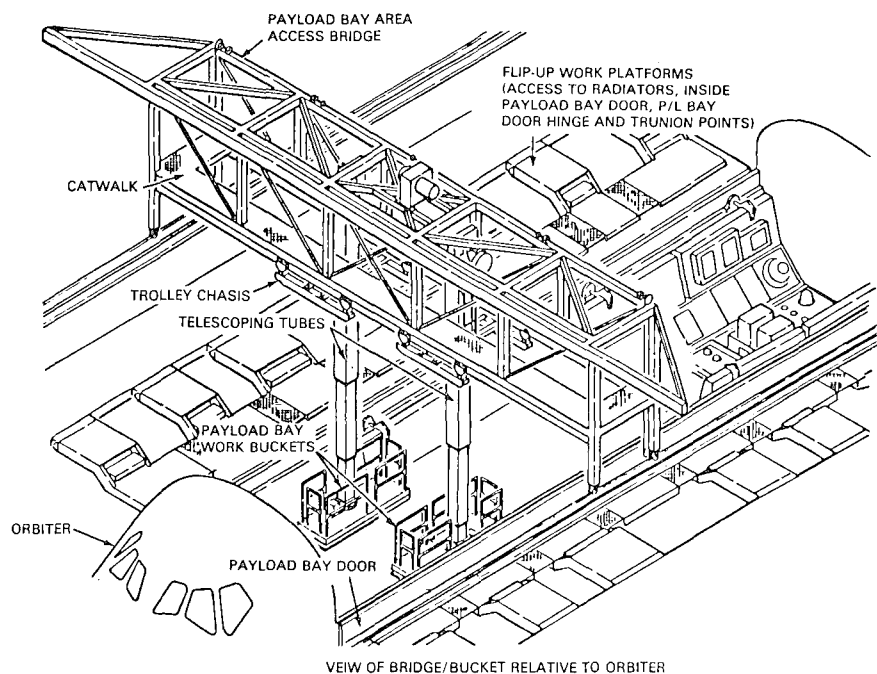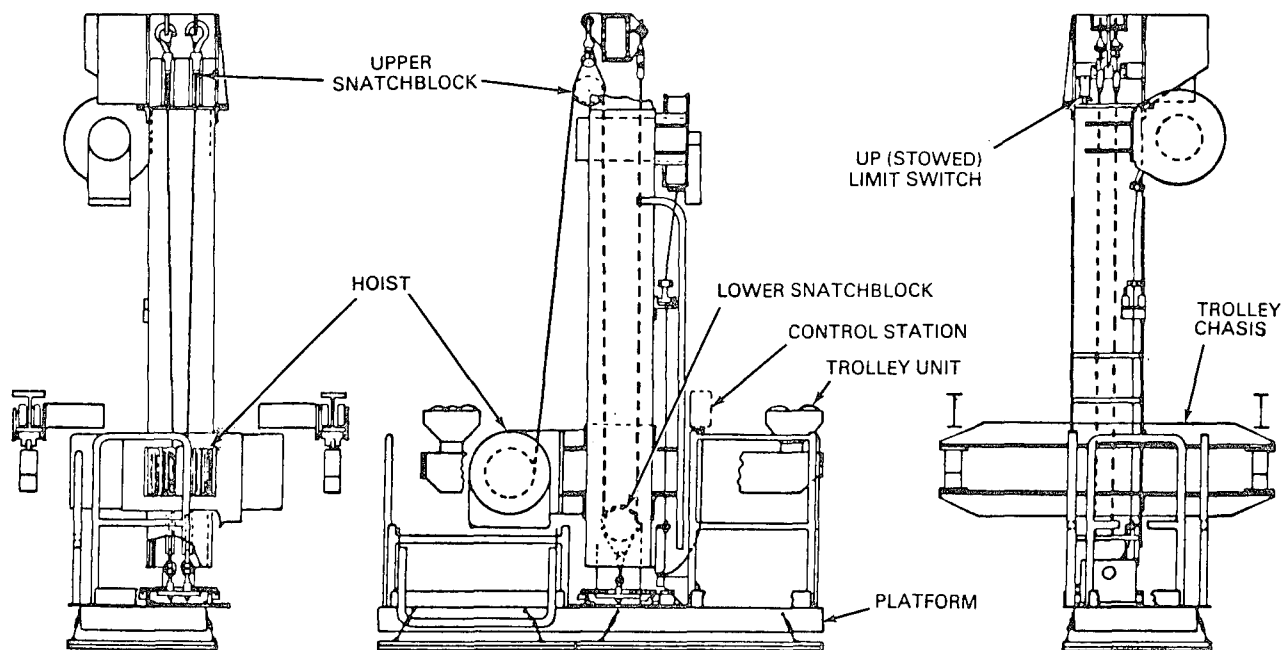
PAYLOAD BAY AREA
ACCESS BRIDGE

FLIP-UP WORK PLATFORMS
(ACCESS TO RADIATORS, INSIDE
PAYLOAD BAY DOOR, P/L BAY
DOOR HINGE AND TRUNION POINTS)

CATWALK

TROLLEY CHASIS

TELESCOPING TUBES

PAYLOAD BAY
WORK BUCKETS

ORBITER

PAYLOAD BAY DOOR

VEIW OF BRIDGE/BUCKET RELATIVE TO ORBITER

Figure 1

UPPER
SNATCHBLOCK

UP (STOWED)
LIMIT SWITCH

HOIST

LOWER SNATCHBLOCK

CONTROL STATION

TROLLEY UNIT

TROLLEY
CHASIS

PLATFORM

OPF BUCKET ASSEMBLY

Figure 2

380

CONTROL STATION
(BRIDGE AND BUCKET SYSTEM)

Figure 3

BUCKET DRIVE ASSEMBLY SCHEMATIC
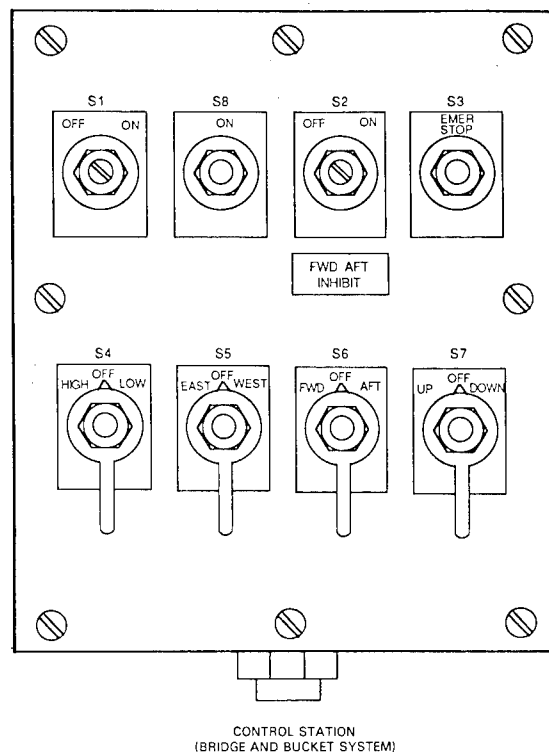
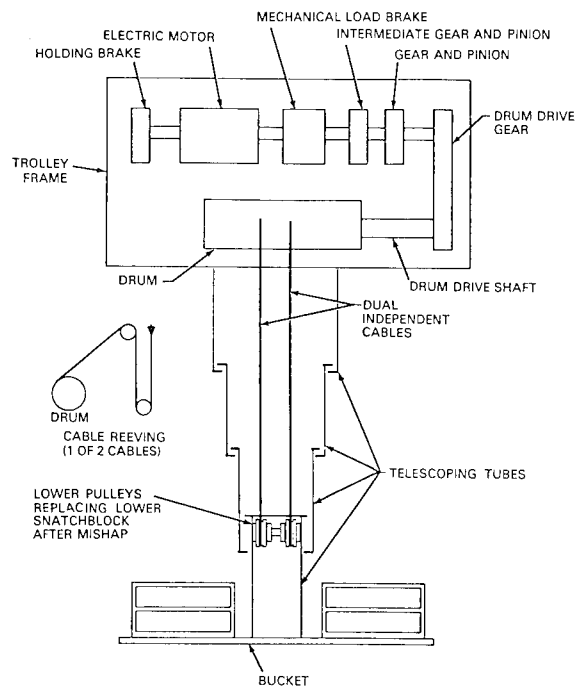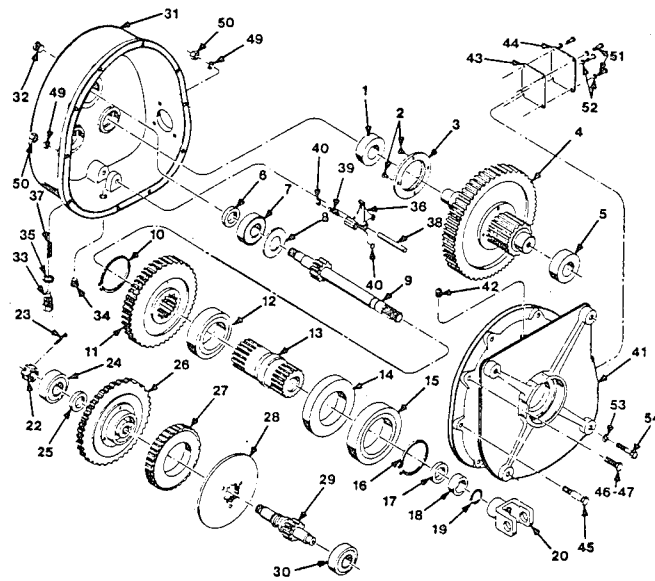Figure 4

HOIST GEARBOX EXPLODED VIEW

Figure 5

BRAKE   MOTOR   REDUCTION
                  GEAR

DRIVE
SPROCKET

DRIVE
CHAIN

DRIVE
CHAIN

DRIVE
SPROCKETS
AND SHAFT

DRIVE
CHAIN

DRIVE
WHEEL

DRIVE
WHEEL

BRIDGE DRIVE ASSEMBLY

DRIVE
SPROCKET

DRIVE SPROCKETS
AND SHAFT

TENSIONER

DRIVE
WHEEL

CHAIN DRIVE ARRANGEMENT

Figure 6

JAW CONNECTOR
SS PIN
SS ADAPTER PLATE
BOLT
EYE END TERMINAL

UPPER
SNATCHBLOCK

HOIST

400 mm
SQ. TUBE

350 mm ⎫
          ⎬ TELE-SCOPING
300 mm ⎬ SQ. TUBES
250 mm ⎭

10 MM DIA
SS WIRE ROPE

LOWER SNATCH BLOCK

MASTER LINK

CONNECTING LINK

SHOULDER EYE BOLT

CONFIGURATION AT TIME OF MISHAP

Figure 7

BUCKET POSITION BEFORE MISHAP

POSITION AFTER MISHAP

TROLLEY

TELESCOPING TUBES

PERSONNEL PLATFORM

ORBITER

BUCKET TRAJECTORY AT MISHAP
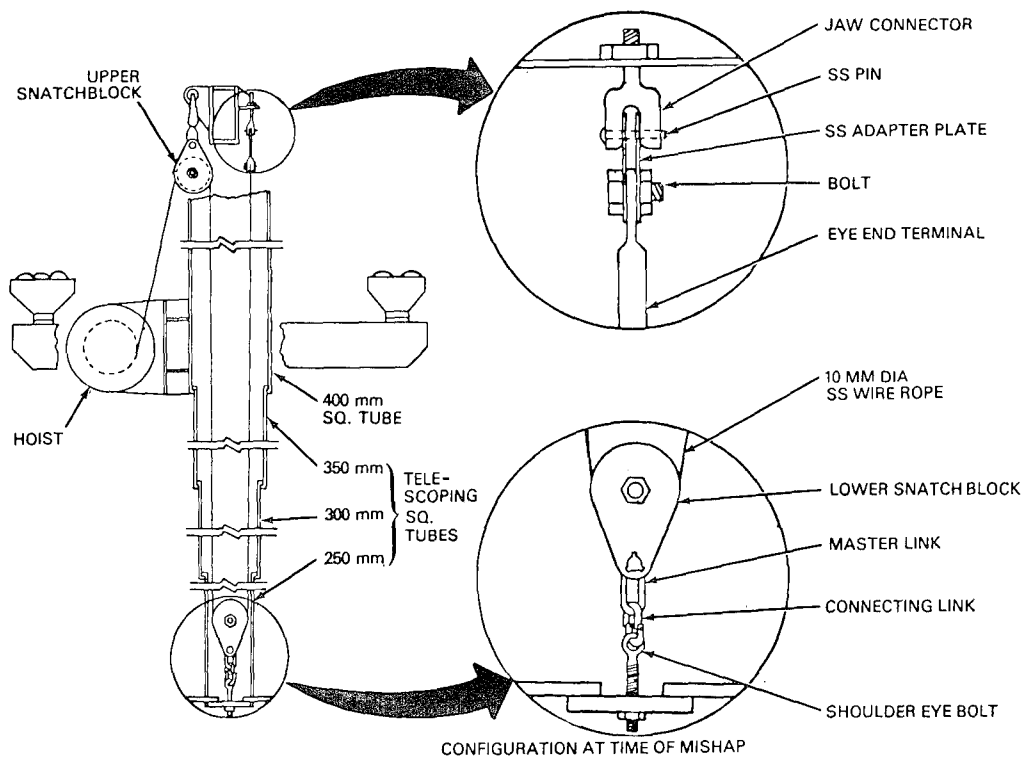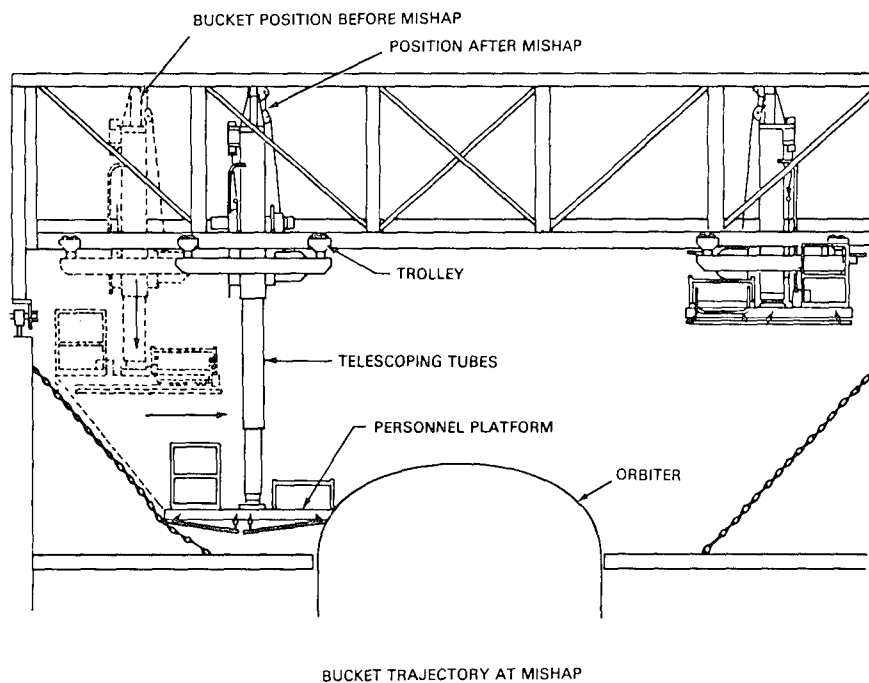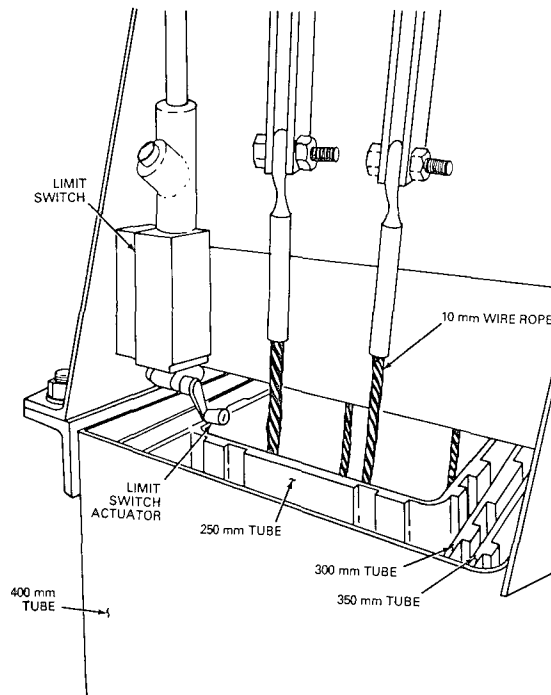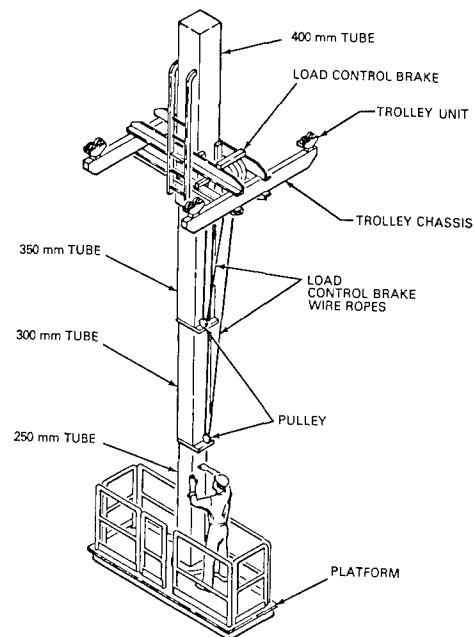
Figure 8

383

LIMIT SWITCH CONFIGURATION AT TIME OF MISHAP

Figure 9

OPF BUCKET WITH LOAD CONTROL BRAKE
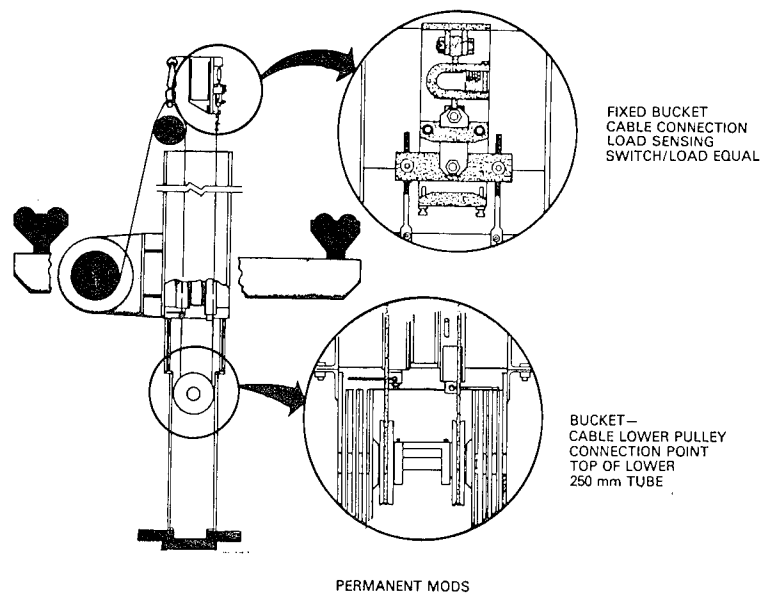
Figure 10

FIXED BUCKET
CABLE CONNECTION
LOAD SENSING
SWITCH/LOAD EQUAL

BUCKET—
CABLE LOWER PULLEY
CONNECTION POINT
TOP OF LOWER
250 mm TUBE

PERMANENT MODS

Figure 11

LOAD
SENSING SWITCH

EQUALIZER BAR

10 mm WIRE ROPE

LOAD SENSING SWITCH & LOAD EQUALIZER

Figure 12

UPPER LIMIT SWITCH

OPERATIONAL STOP SWITCH

10 mm WIRE ROPE

400 mm TUBE

250 mm TUBE

MECHANICAL LOCKOUT DEVICE

RELOCATED PULLEY

LOWER PULLERS, REDUNDANT LIMIT SWITCHES & MECHANICAL LOCK

Figure 13

CHAIN—FALL

SUPT STRUCTURE ADAPTER

QUICK—RELEASE

TROLLEY CHASSIS

BRIDGE STRUCTURE SIMULATOR

TEST ARTICLE

400 mm TUBE

LOAD CELL

LOAD CELL

ADAPTER (TROLLEY UNIT)

LOAD CONTROL BRAKE

LOAD CELL (DEAD END OF WIRE ROPE)

FISH REEL POT.

LOAD CONTROL BRAKE WIRE ROPE

350 mm TUBE

LOWER PULLEY

LOAD CONTROL BRAKE TEST RIG
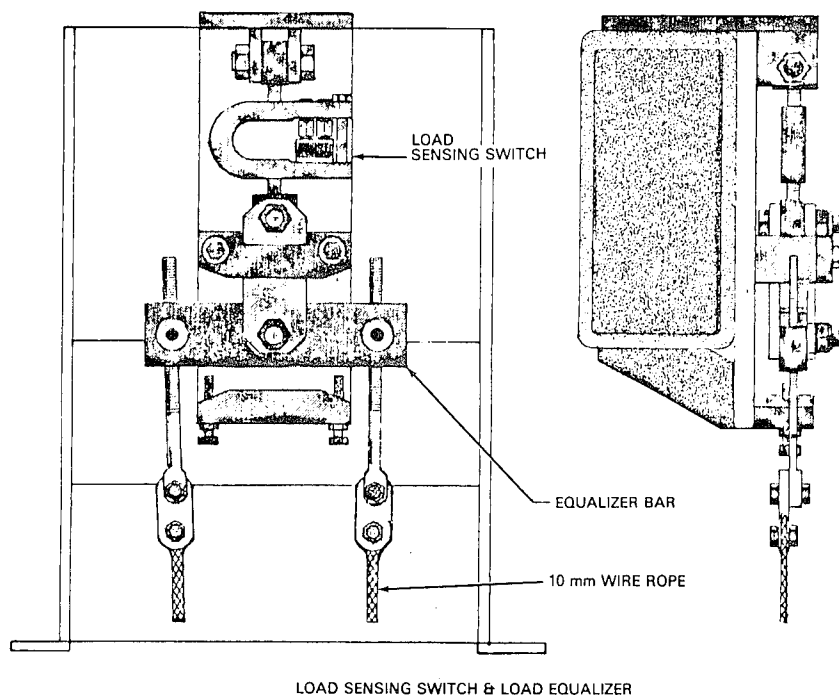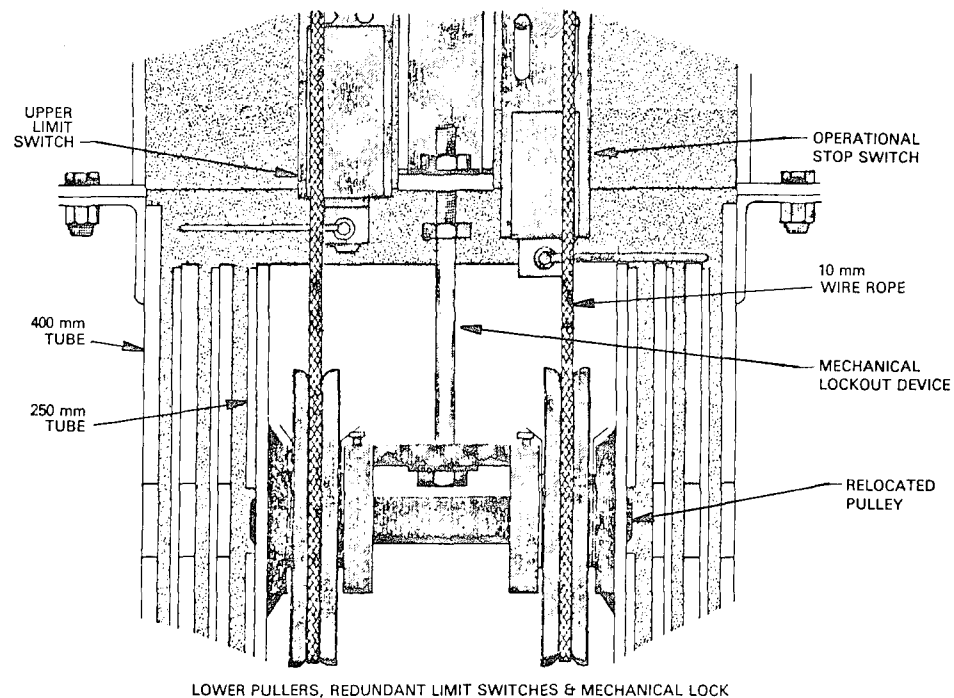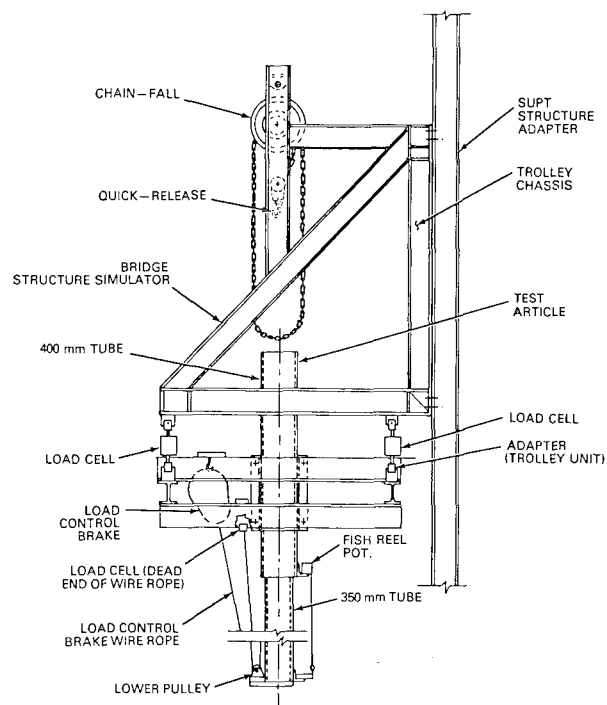
Figure 14

386

SPACE SHUTTLE SOLID ROCKET MOTOR
PROFILE MEASURING DEVICE (PMD)

John Redmon*

As a result of the space shuttle accident, a solid rocket motor redesign team was created at Marshall Space Flight Center, Alabama. One of the results of this team's efforts was the design, development, and testing of a device to accurately measure, record, and plot the diameters and deviations of the machined, mating surfaces of the solid rocket motor assembly interfaces commonly referred to as "field joints". This device, SRM Profile Measuring Device (PMD), P/N 97M50225, figure No. 1, has been developed, calibrated, tested, and is currently in operational use at Morton Thiokol Inc. (MTI), Brigham City, Utah, and is also scheduled for use at Kennedy Space Center. A description of the PMD is as follows:

The SRM PMD is an electromechanical tool used for measuring and recording the profile and diameters of the solid rocket motor segments, both Tang and Clevis ends. This system consists of a crossbeam assembly that mounts to the SRM segment using the existing assembly pin holes. The mounting configuration is such that the tool can be used to measure Clevis up/Tang down or Clevis up/Tang up.

The crossbeam assembly supports a radius measuring arm assembly that contains a digital electronic gauge, a resolver (for angular measurement), a gear train drive assembly (for rotating the above), and an adjustable counterweight. The crossbeam assembly is composed of four similar legs that interface at the center for ease of operations and mobility. The crossbeam assembly only needs to be mounted within plus or minus 1 inch of the SRM segment center and may remain in place during shaping operations. The crossbeam assembly weighs approximately 152 pounds. (See figure 1.) The associated electronics and plotter/printer system is packaged in an electronics cart, and is in turn, connected to the measuring system by a remote cable. (See figures 1-20.)

During measuring operations, the system functions as follows:

The digital linear gauge measures the relative distance on the SRM joint to a point at the approximate center of the SRM segment. (This point is also the center rotation of the

_____
*NASA/George C. Marshall Space Flight Center, Marshall Space Flight Center, Alabama

resolver/shaft and radius arm assembly.) The radius arm
assembly and resolver are driven radially by a servomotor
gear train assembly (1,000:1 ratio), while radial deviations
and angular positions are being stored. Measuring speed is
approximately 2 inches per second. An offset circle (based on
the true diameter of the SRM segment) is plotted. The data
obtained previously is then processed to give a least square fit
to the true offset circle. These differences are then plotted at
15 degree increments. A hard copy, for record, of the deviations
is then printed. This copy is printed 1:1 scale or up to 5:1
scale. This tool is calibrated and results checked by the use of
a helium neon laser system, as shown in figure 20.

        Development testing and calibration procedures were
developed at MSFC from June 1987 through September 1987. In
September of 1987 the PMD, along with the laser calibration
equipment, was shipped to MTI, in order to measure the first
flight segments for shuttle flight STS-26, prior to propellant
loading. As a result of these measuring operations, some
segments of the first flight SRB's were switched in order to
guarantee an interference fit at the mating field joints. Also,
during October 1987 and November 1987, the qualifications SRM's
were measured. Typical measurement results are shown in figures
18 and 19.

During November 1987, the MSFC PMD and calibration equipment was
formally turned over to MTI and two additional PMD's are being
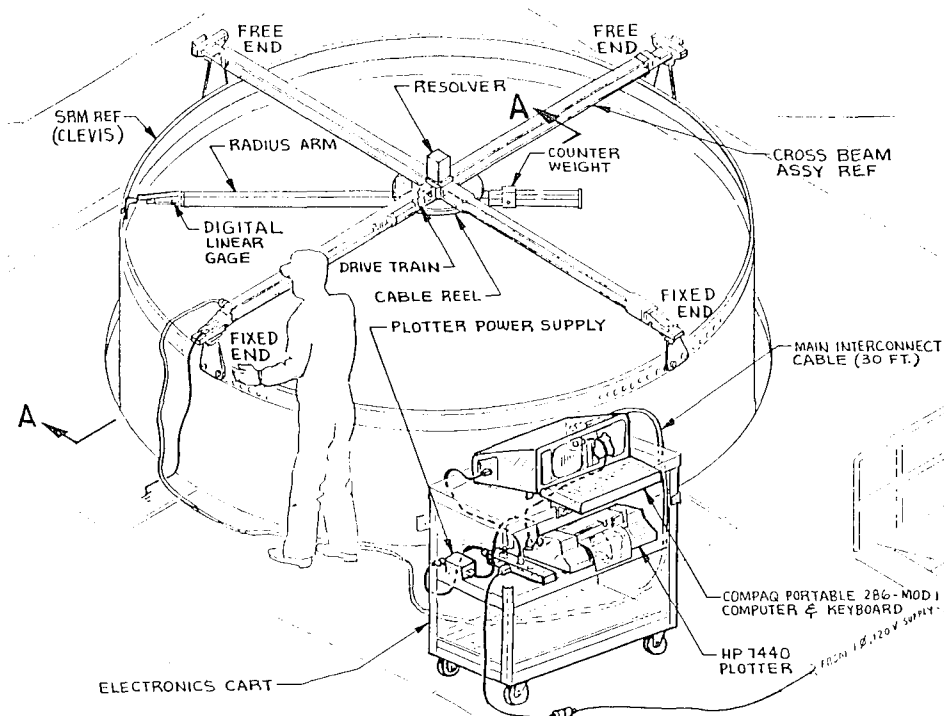procured for MTI usage.

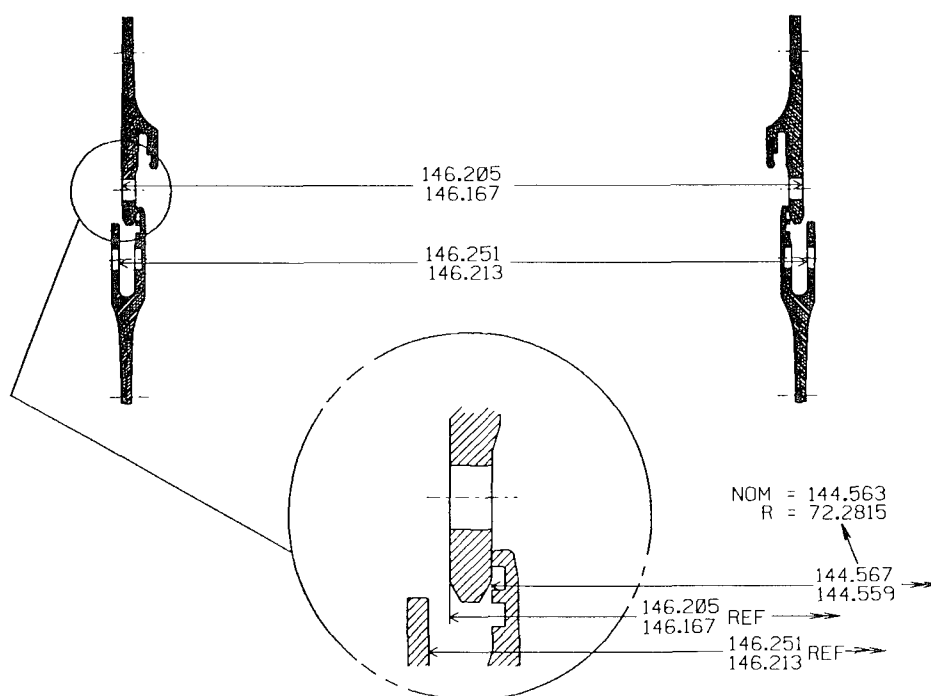Figure 1. SRM Measuring Tool Assembly, P/N 97M50225

Figure 2. Flight Field Joint

389
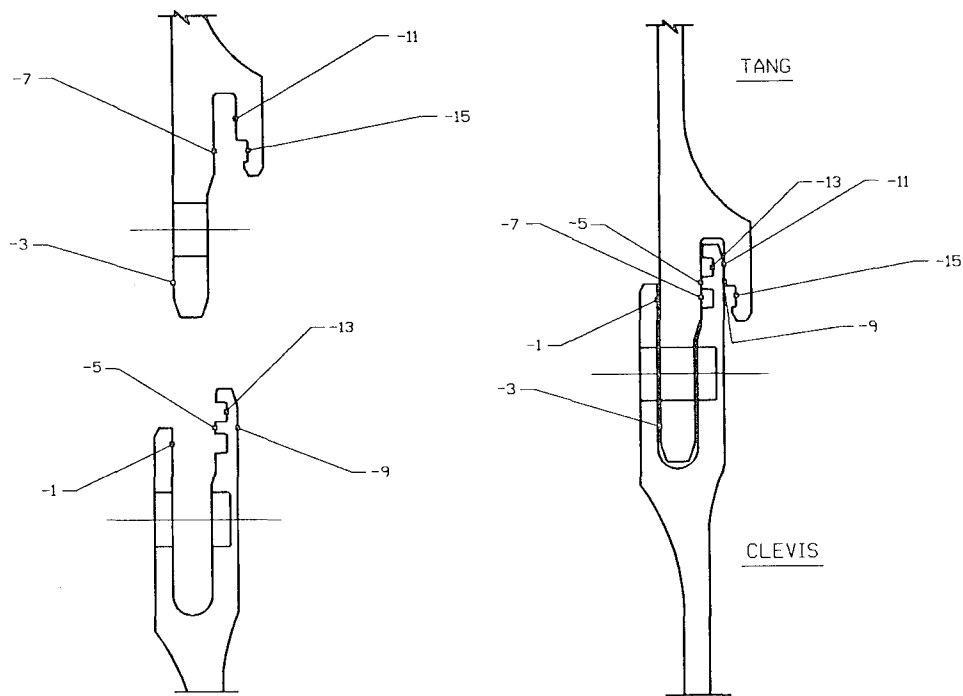
Figure 2A. Joint Surfaces to be Measured

Figure 3. SRM Profile Measuring Tool

CLEVIS (REF)

LOCKING ADJUSTABLE
SLIDE

BEAM (REF)

FIXED END
(REF)

ATTACH BOLT
(REF)

CLEVIS (REF)

Figure 4. SRM Profile Measuring Tool, Detail B

CLEVIS
(REF)

ATTACH BOLT
(REF)

BEAM
(REF)

FREE END
(REF)
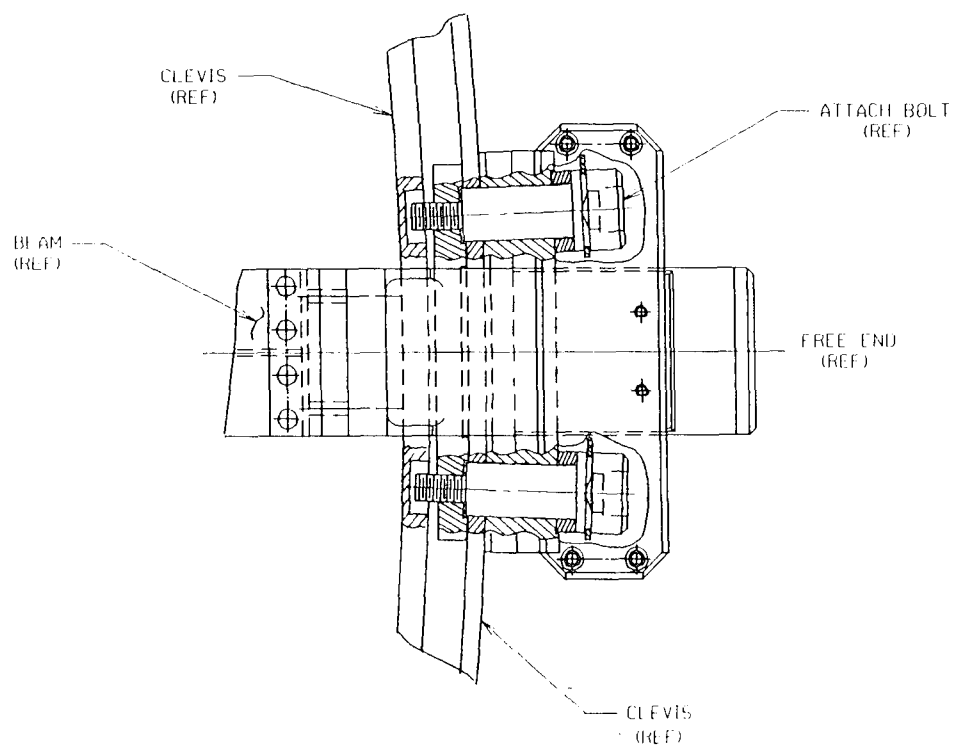
CLEVIS
(REF)

Figure 5. SRM Profile Measuring Tool, Detail C

391
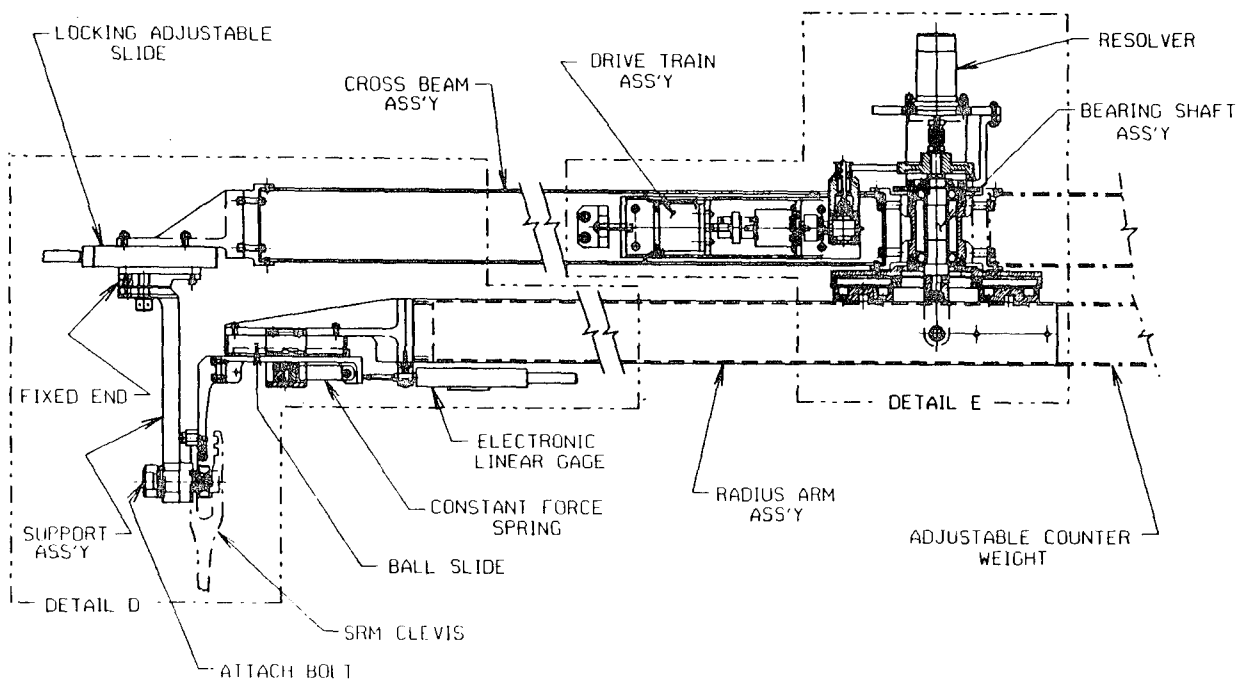
Figure 6. SRM Profile Measuring Tool, View A-A
(Clevis Measurement)
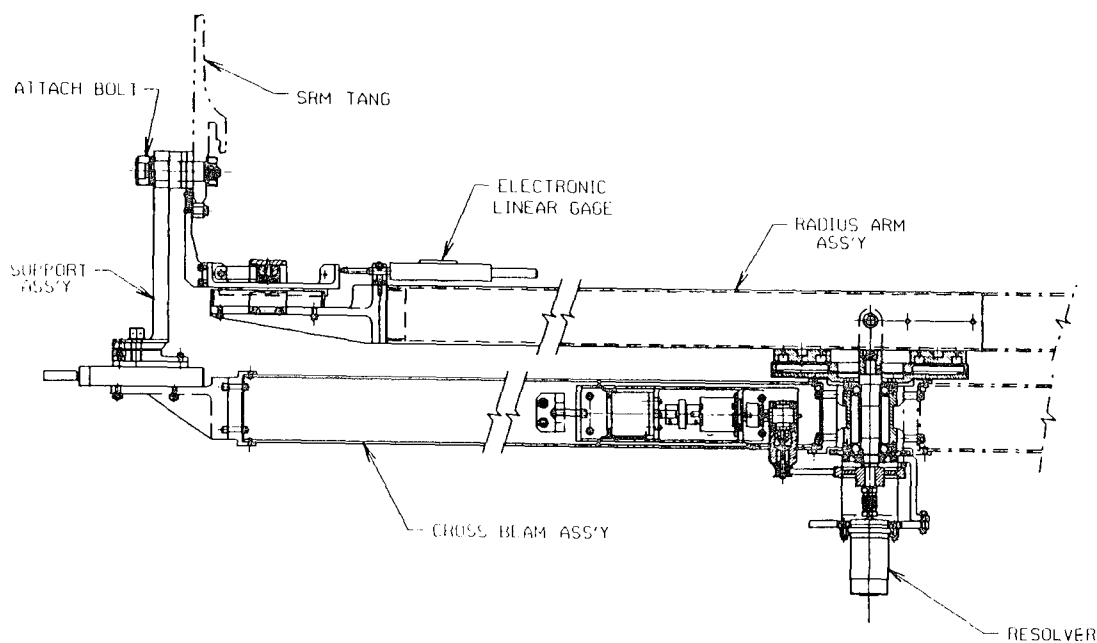
Figure 7. SRM Profile Measuring Tool, View A-A
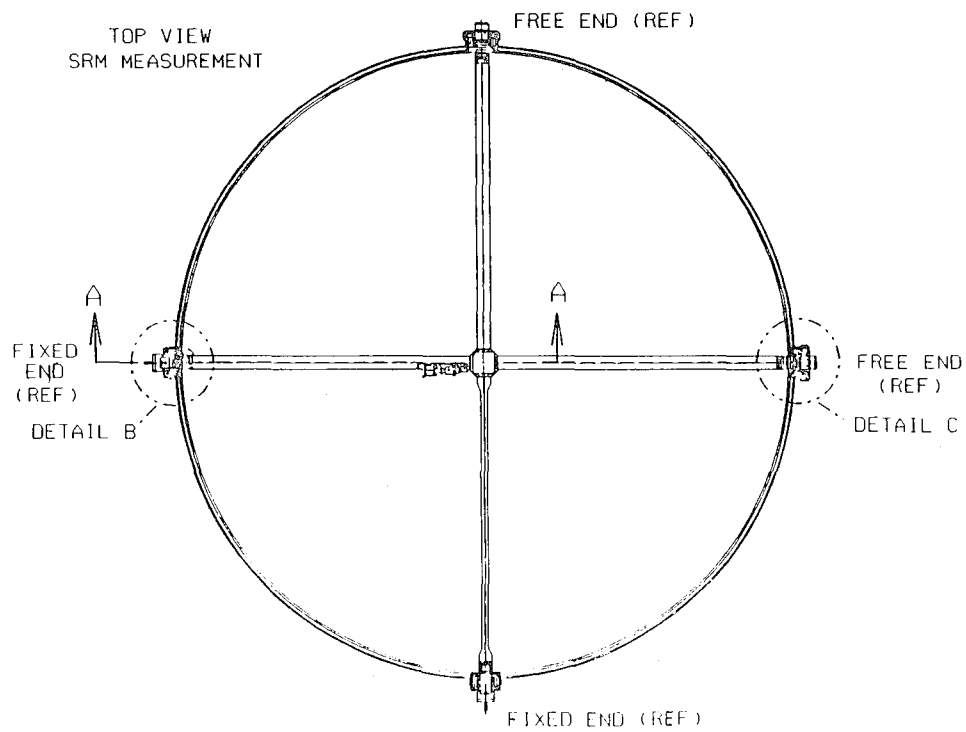(Tang Measurement)
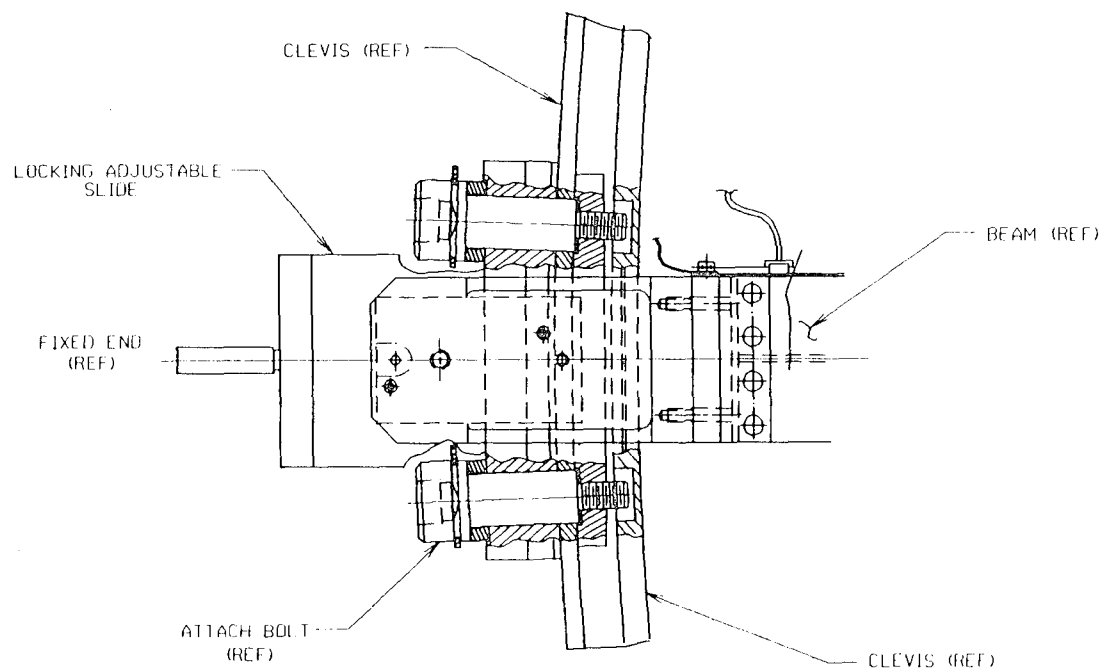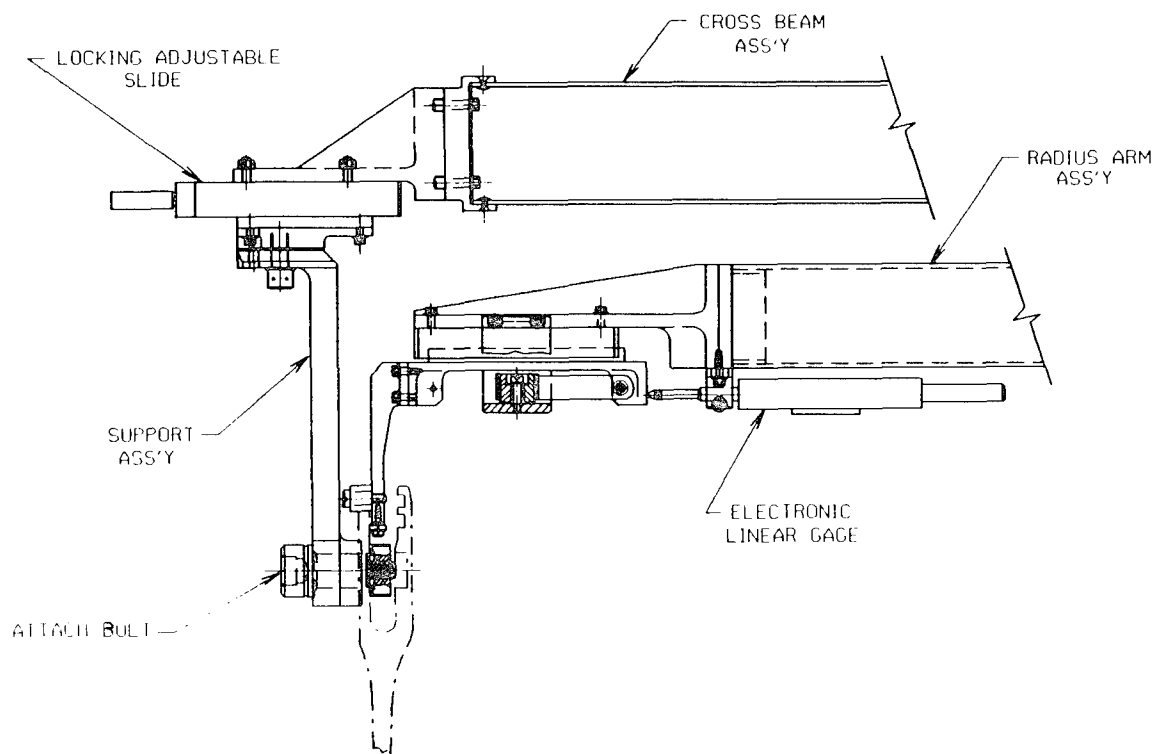
Figure 8.   SRM Profile Measuring Tool, Detail D
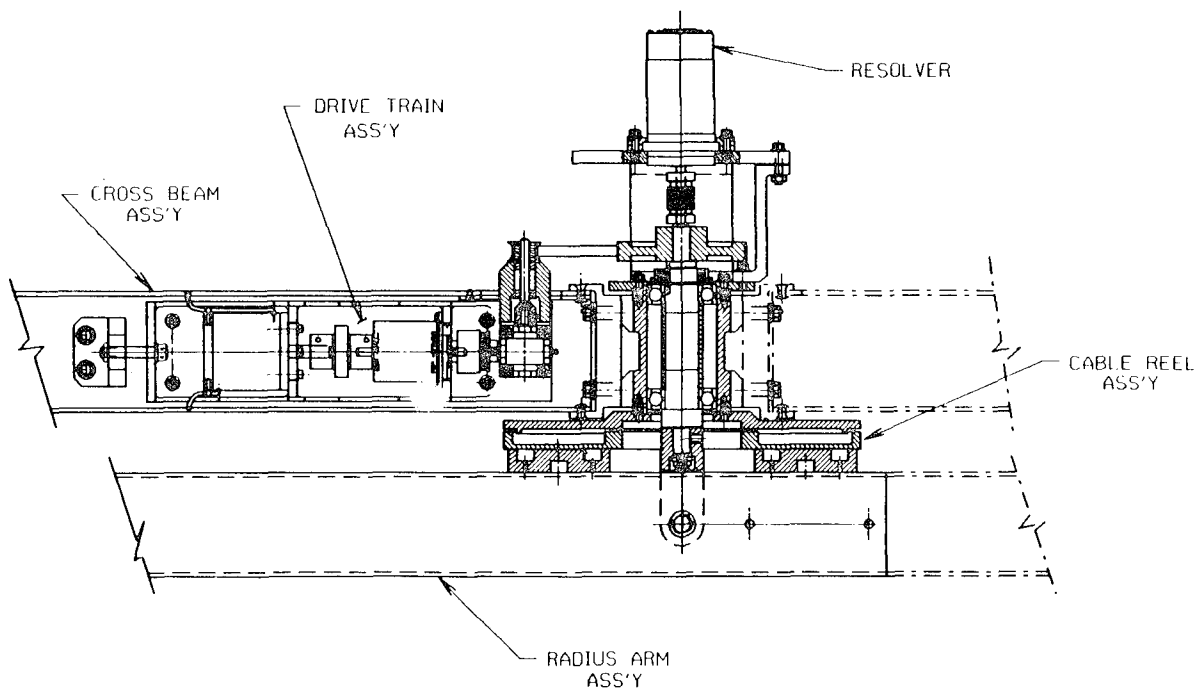
Figure 9.   SRM Profile Measuring Tool, Detail E

393
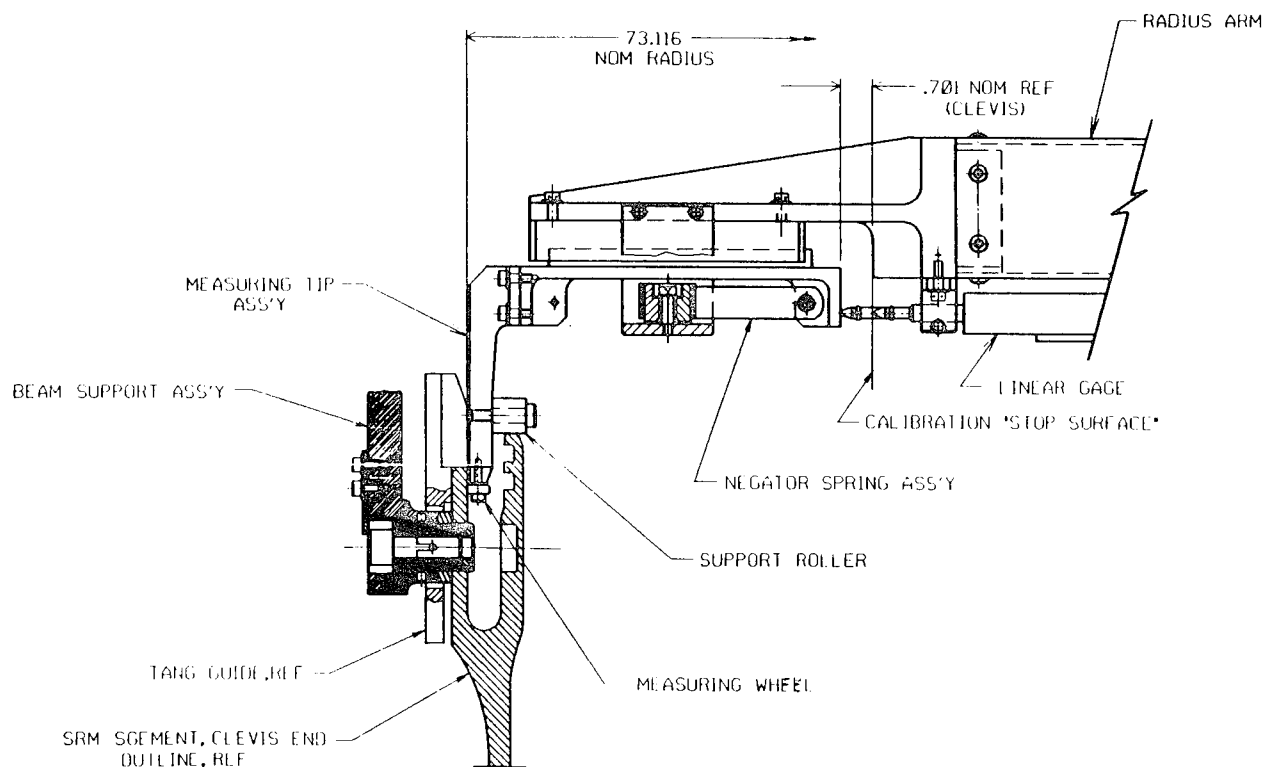
Figure 10. SRM Profile Measuring Tool, 97M50380-1,
Clevis Outer Leg I.D. With Tang Guide
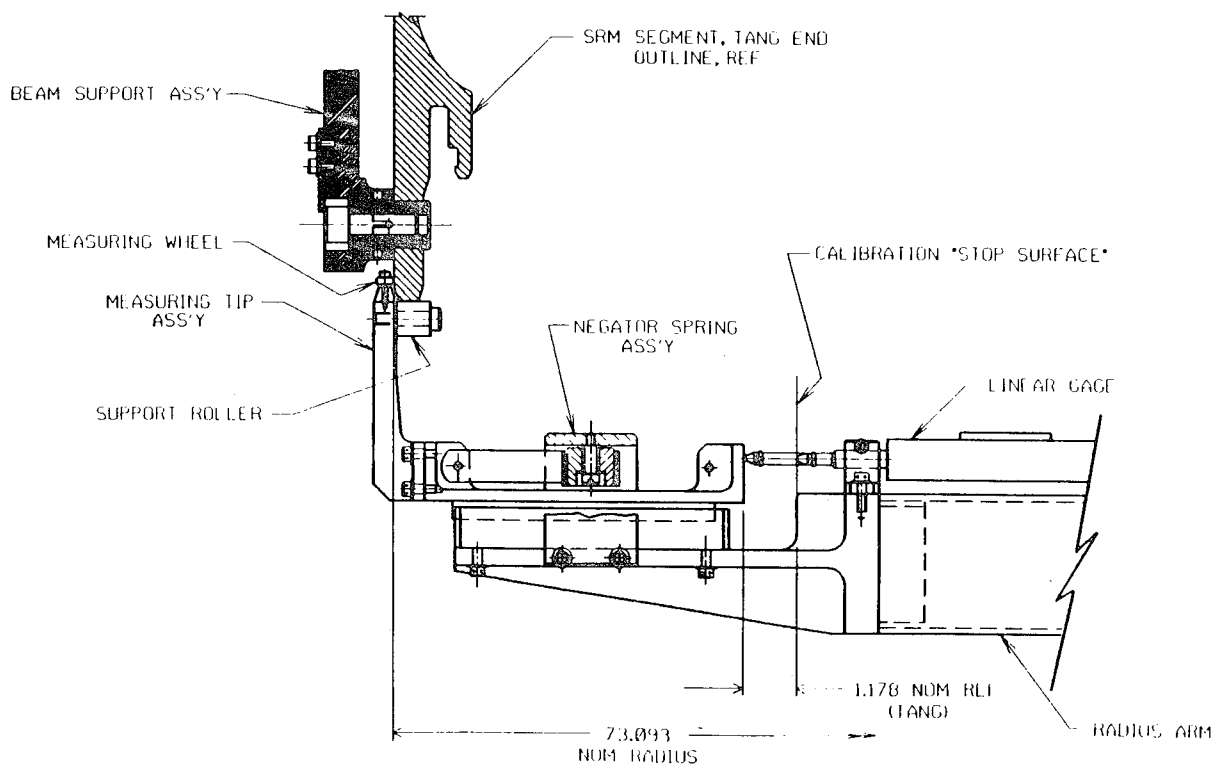
Figure 11. SRM Profile Measuring Tool, 97M50380-3,
Tang Outer Leg O.D.

394
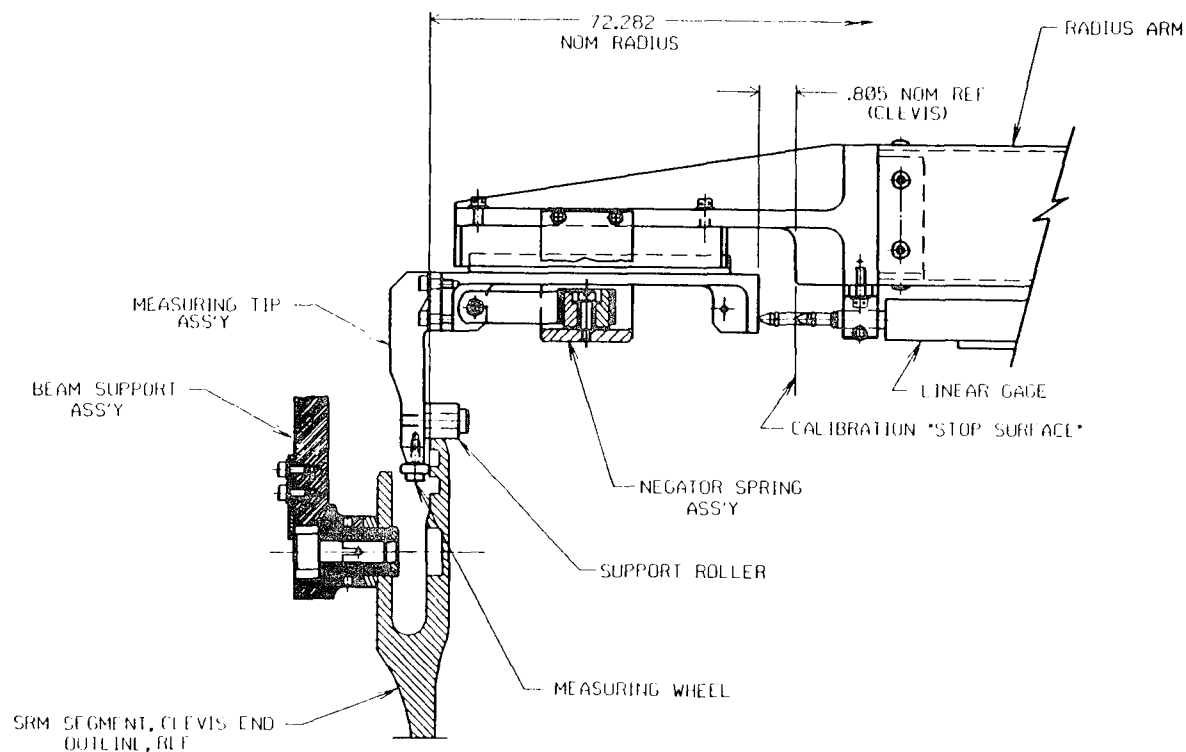
Figure 12.   SRM Profile Measuring Tool, 97M50380-5,
Clevis Inner Leg O.D.
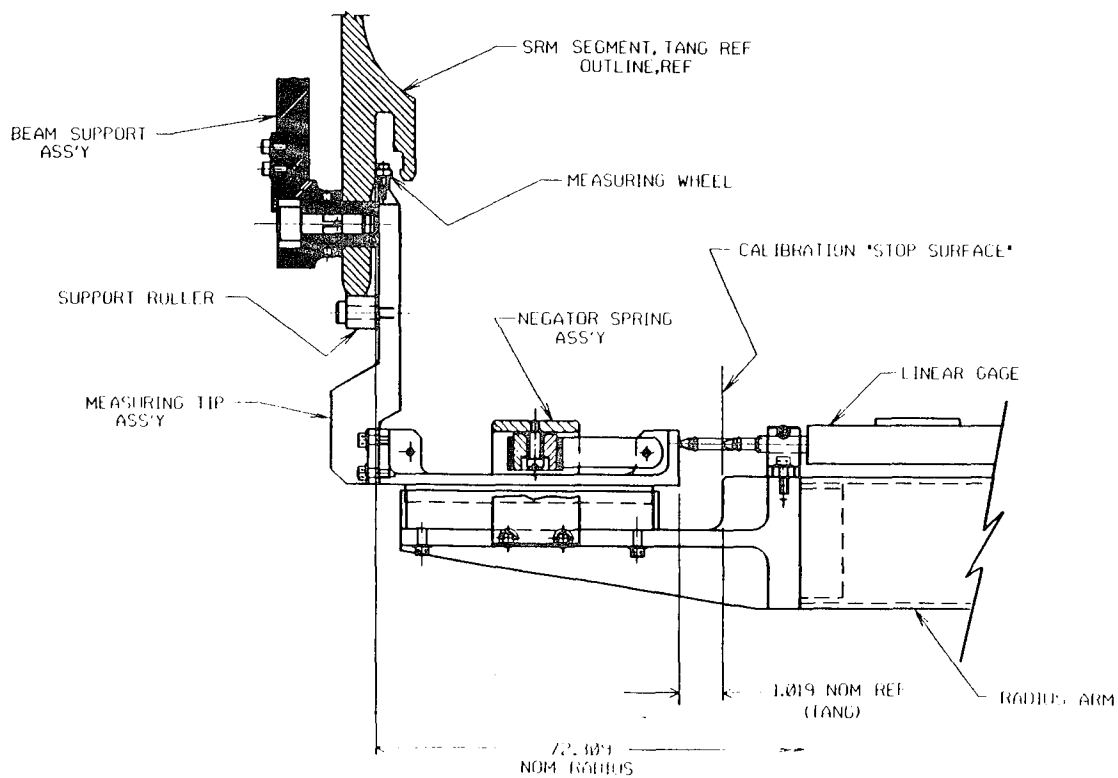
Figure 13.   SRM Profile Measuring Tool, 97M50380-7,
Tang Outer Leg I.D.

395
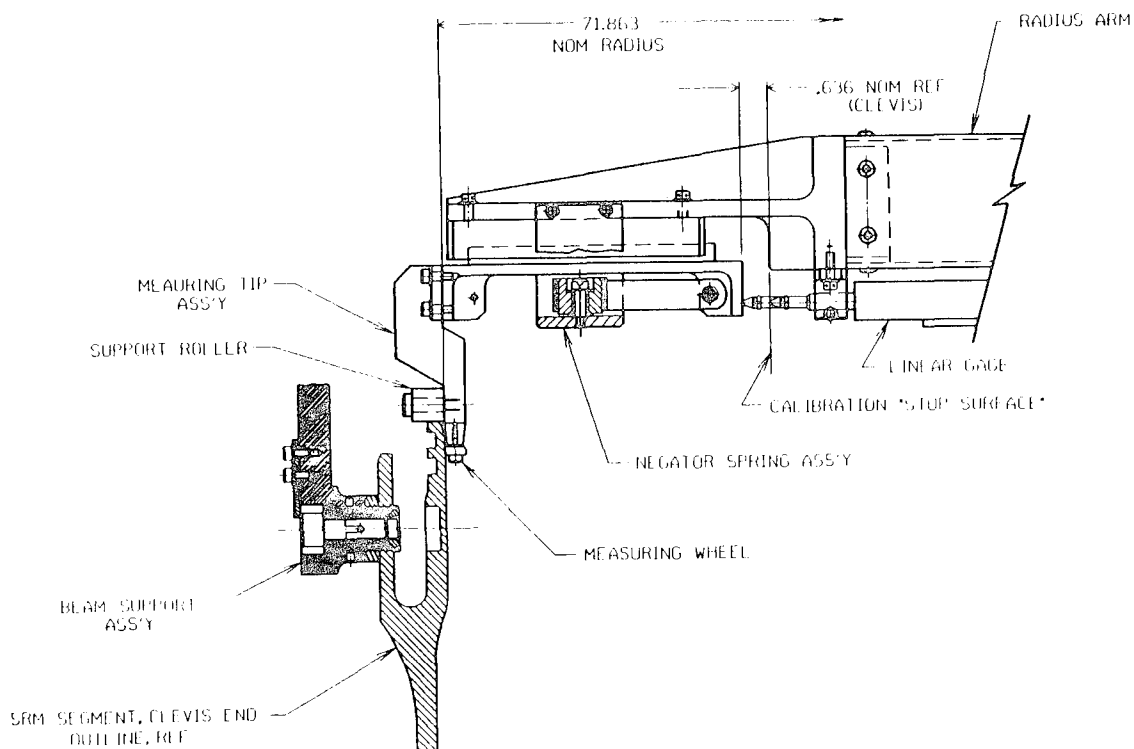
Figure 14. SRM Profile Measuring Tool, 97M50380-9,
Clevis Inner Leg I.D.
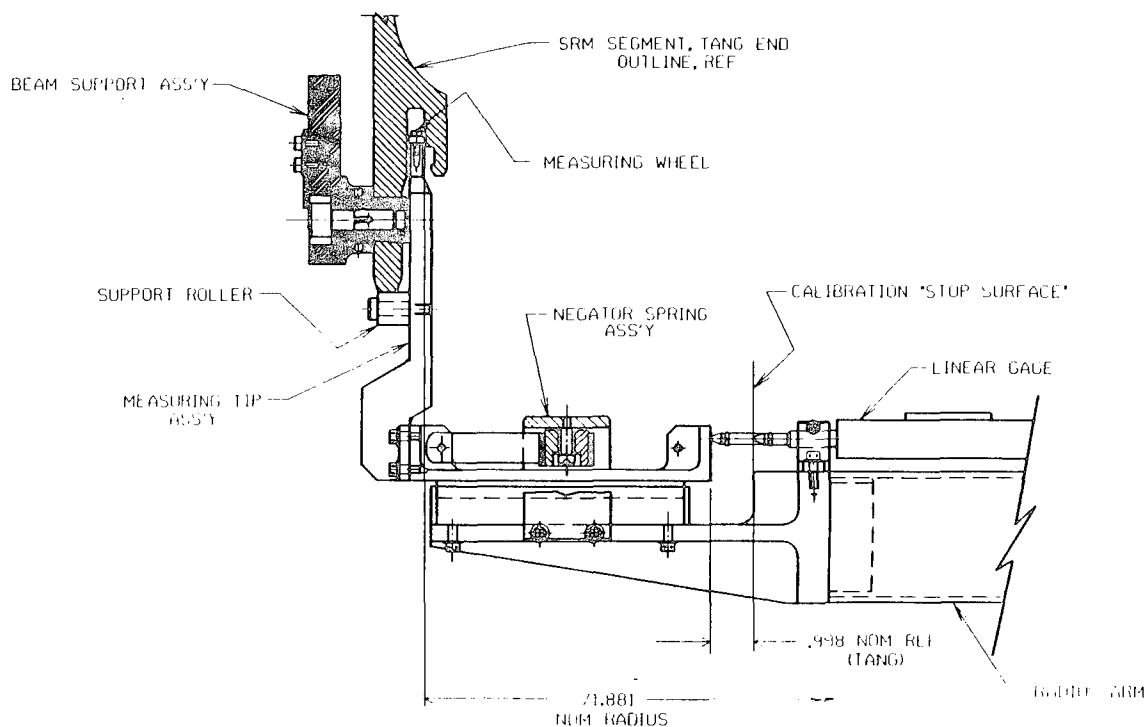
Figure 15. SRM Profile Measuring Tool, 97M50380-11,
Tang Inner Leg. I.D.

396
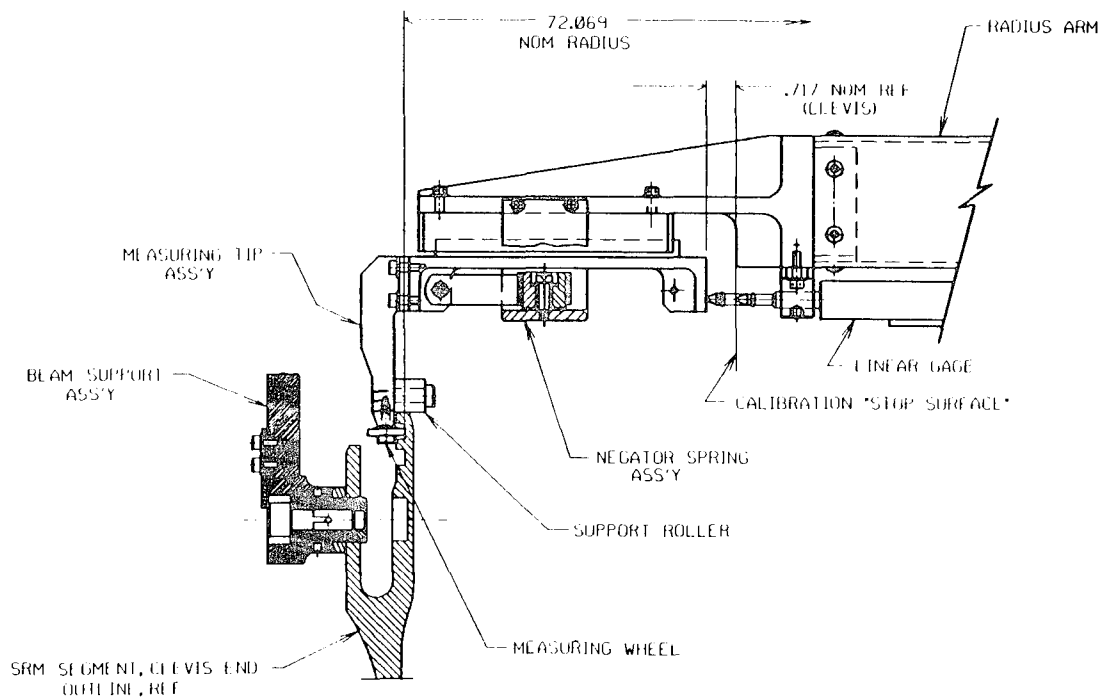
Figure 16.   SRM Profile Measuring Tool, 97M50380-13,
Clevis Inner Leg O-Ring
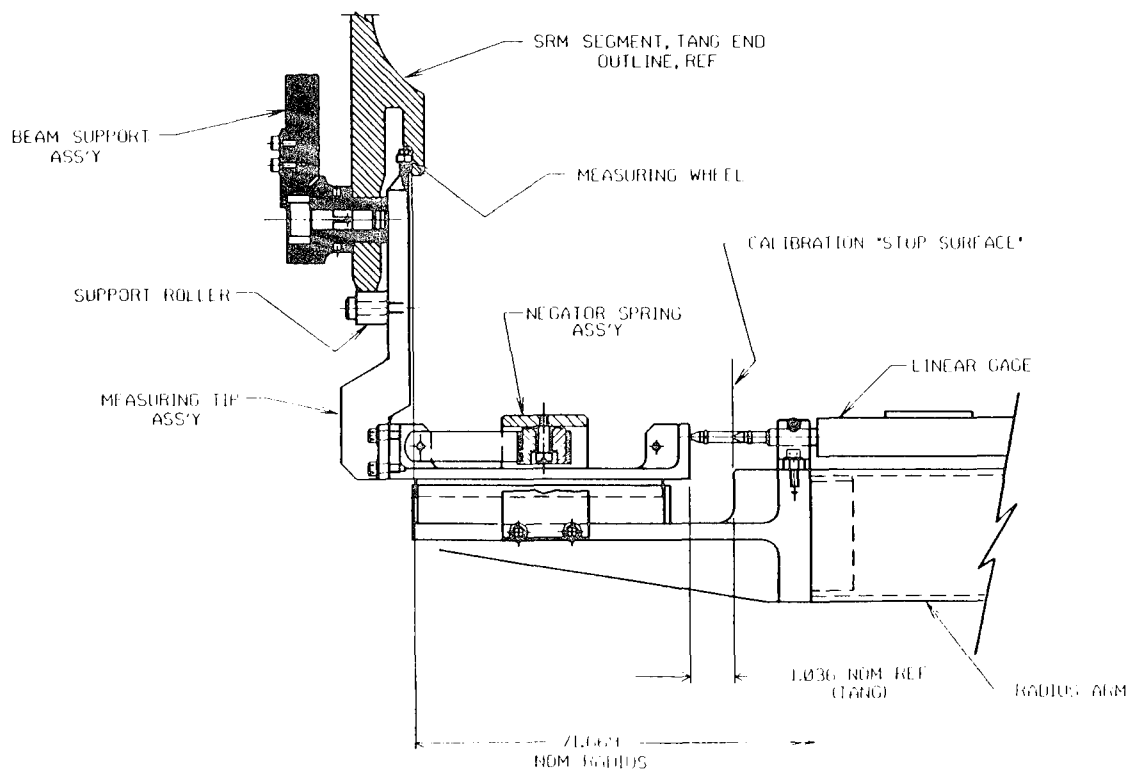
Figure 17.   SRM Profile Measuring Tool, 97M50380-15,
Tang Inner Leg O-Ring

397
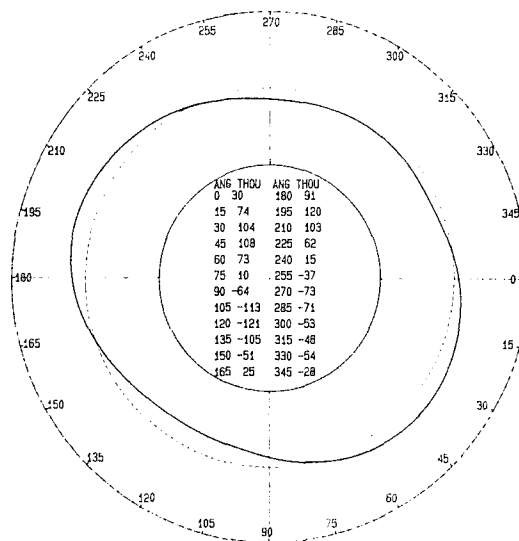
CASE: QM-7 AFT 1U50716-06 SN10R2 J7 RUN 1
FILENAME (DATE+TIME) 11026710.41 TIP 97M50380- 9 CLEVIS
SCALE: 1 INCH ON PLOT= 0.50 INCHES ACTUAL
RADIUS 71.8863 INCHES AT 80.5 DEG F   (71.8802 AT 68 DEG F)
DIAMETER 143.7605 INCHES AT 68 DEG F
DIAMETERS   0 DEG: 143.8937   90 DEG: 143.6357
OFFSETS   0: 0.001   90: 0.004
MAX + DEVIATION 0.120 AT 196 DEGREES
MAX - DEVIATION -0.122 AT 118 DEGREES
RMS OUT-OF-ROUND 0.076 INCHES

Figure 18.   Clevis Measurement (Surface 9)
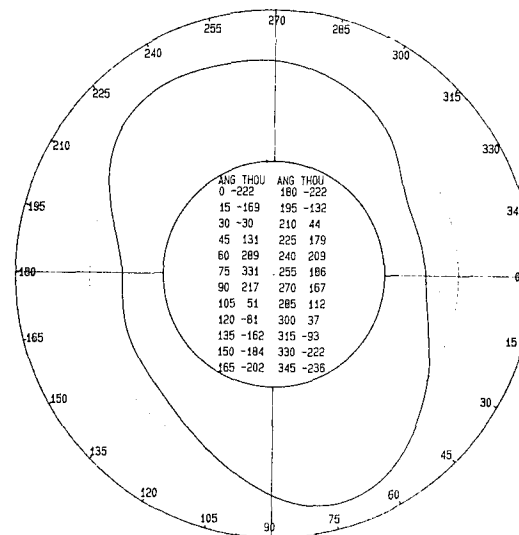
CASE: QM-7 FWD 1U52983-01 SN 6 FJ 3 RUN 1
FILENAME (DATE+TIME) 10288716.48 TIP 97M50380-11 TANG
SCALE: 1 INCH ON PLOT= 0.50 INCHES ACTUAL
RADIUS 71.8852 INCHES AT 80.8 DEG F   (71.8769 AT 68 DEG F)
DIAMETER 143.7578 INCHES AT 68 DEG F
DIAMETERS   0 DEG: 143.3250   90 DEG: 144.1524
OFFSETS   0: -.003   90: 0.005
MAX + DEVIATION 0.334 AT 73 DEGREES
MAX - DEVIATION -0.239 AT 339 DEGREES
RMS OUT-OF-ROUND 0.180 INCHES

Figure 19.   Tang Measurement (Surface 11)

398

ZERO STOP

MEASURING TIP

LASER CALIBRA. REFLECTOR
SLIDE ASS'Y

MITUTOYO GAGE, REF

CALIBRA. BEAM

ANGLE REFLECTOR
(MOVES)

LINEAR RETROREFLECTOR
(MOVES)

LINEAR INTERFEROMETER
(FIXED)

DETAIL D

TIP SHOWN AT ZERO STOP POSITION
SCALE 1 /2

MEASURING TIP

LASER CALIBRA. REFLECTOR
SLIDE ASS'Y

MITUTOYO GAGE, REF

CALIBRA. BEAM

ANGLE REFLECTOR
(MOVES)

LINEAR RETROREFLECTOR
(MOVES)

LINEAR INTERFEROMETER
(FIXED)

DETAIL D

TIP SHOWN AT CALIBRATED POSTION
SCALE 1 /2

ANGLE LASER, GFE

97M50225, REF

LASER CALIBRA. REFLECTOR
SLIDE ASS'Y

LINEAR LASER, GFE

4.25 REF

CALIBRA. BEAM

ANGLE REFLECTOR
(MOVES)

LINEAR RETROREFLECTOR
(MOVES)

LINEAR INTERFEROMETER
(FIXED)

FLOOR

VIEW A-A

SCALE: 1 /4

Figure 20. Laser Calibration

MITUTOYO=ZERO

MITUTOYO=ZERO

L
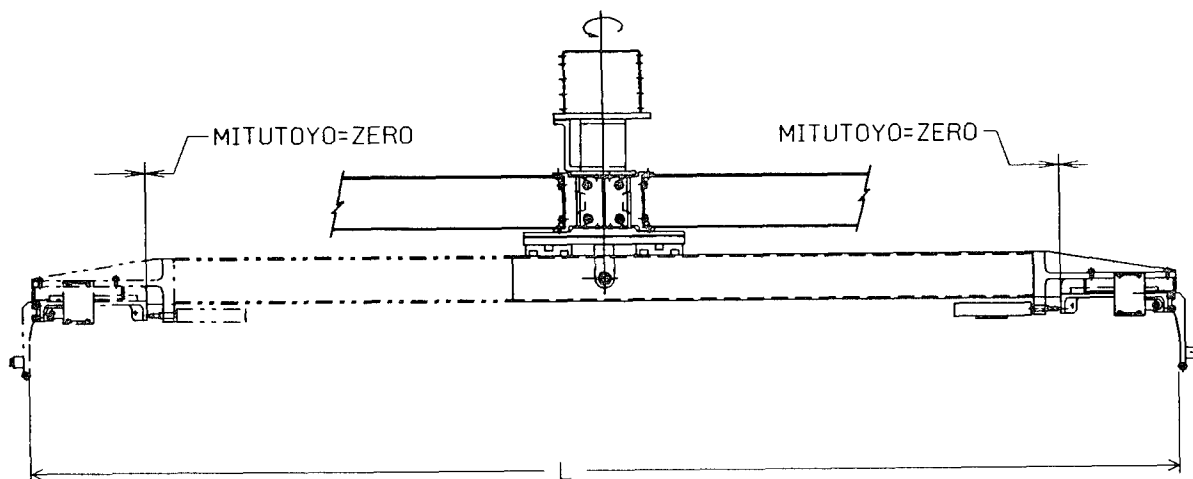
Figure 21. Radius Arm Calibration

MODIFICATION AND DEVELOPMENT OF

THE EXTERNAL TANK HYDROGEN VENT UMBILICAL SYSTEM

FOR THE SPACE SHUTTLE VEHICLE

Bemis C. Tatem, Jr.*

ABSTRACT

This paper describes the design and development of a new T-0 lock and secondary release mechanism (Figure 1) which is being introduced to the ET Hydrogen Vent Umbilical System (Figure 2) for the next launch of the Space Shuttle Vehicle (Figure 3). Critical analysis of the system in early 1986 indicated the need for an improvement in the secondary release system. The new T-0 lock increases the clearance with the vehicle during secondary disconnect and is described in this paper.

INTRODUCTION

As the Space Shuttle lifts off at Kennedy Space Center, it has a liftoff drift (Figure 4) which is generally in a north direction. The ET hydrogen vent umbilical system is attached to the external tank (ET) with a pyrobolt and disconnects and falls away at liftoff (T-0). It takes approximately 2.7 seconds for it to fall to its retracted position. During this time the vehicle drifts such that the left solid rocket booster (SRB) moves towards the falling ET hydrogen vent line. Analysis indicated for worst case of secondary disconnect (a simple lanyard disconnect with vehicle rise) actual contact with the SRB could occur. In order to provide adequate clearance a T-0 lock was designed and added to the secondary system to limit the amount of vehicle rise before lanyard release thus providing adequate clearance to the drifting vehicle.

DISCUSSION

With the existing system, the secondary release lanyard employed a tracking arm allowing for prelaunch motion and simply fell away from the vent line during retraction unmanaged. As such during a secondary release the carrier plate (vehicle) would have to lift as much as one meter in order to effect a secondary release. This permitted the SRB to drift closer to the normal

---

*Lockheed Space Operations Company, Kennedy Space Center, Florida

centerline of the ET (GH_2) vent line before disconnect due to the additional time to effect disconnect from the vehicle, and drift toward the vent line.

In order to solve this problem, two new features were incorporated into the system:

1. A T-0 lock was devised which would lock the weight end of the secondary release lanyard. This would limit the carrier plate rise to approximately 18 cm in order to accomplish a secondary disconnect.

2. A T-0 dropweight system was added to take up the slack of the secondary release lanyard.

Developmental testing of the new system was successfully completed on October 6, 1987 and the new system was installed on Pad B of Launch Complex 39 in December, 1987.

A primary disconnect has never failed to function; however, this new system provides a secondary release system with improved performance.

An SRB simulator was designed for clearance evaluation testing at the Launch Equipment Test Facility. This SRB simulator consisted of an adjustable position sector of SRB segments. It was adjusted to a worst-case drift position prior to the secondary disconnect. During disconnect and retract, the clearance was measured by means of multiple cameras, three fish reel deflecto-meters on different axes. For close clearance measurements (less than 30 cm), a laser measurement system was designed. As a back up to the laser system, monofilament nylon lines were employed approximately 15 cm from the SRB moldline. The laser beams and monofilament lines were not broken during the test. Test results indicated minimum clearance with the new secondary release system was 46 cm.

A more detailed description of the new secondary release system follows:

New Secondary (Backup) Release Mechanism. The secondary release mechanism is designed to increase the reliability of the ET vent system by providing a secondary disconnect function and a secondary latching function. A pair of 1.1 cm diameter lanyards connects the ground umbilical carrier plate (GUCP) to the spreader bar assembly attached to the underside of the flexhose support. Connected to the ends of the spreader bar is a short 1.4 cm diameter cable with a floating snatch block in the middle. A 1.6 cm diameter cable is routed from the snatch block assembly

through a system of sheaves to the T-0 lock assembly and a drop weight. The system is attached to the 58.2 m level of the fixed structural platform at Pad B up to the upper level where the T-0 lock is located. A 180 kg dropweight located under the T-0 lock keeps the cable taut before disconnect and takes up the slack in the cable after disconnect. After the dropweight has fallen, it is prevented from rising by a ratcheting mechanism, thus containing the ventline within the structure, should the primary latching system fail. The T-0 lock contains an 8.7 cm diameter by 1.6 m serrated rod which rests on the dropweight. This rod slides up and down inside the guide tube as the dropweight moves up and down with vehicle excursions. (See Figure 1). At T-0, when the ground umbilical carrier plate pyrotechnic separator is initiated, the T-0 lock pyrotechnic separator is also initiated, releasing the spring-loaded locking forks which lock the serrated rod in place. If the GUCP pyrotechnic separator fails, the vehicle continues to lift the carrier plate, and since the T-0 lock serrated rod prevents the dropweight from rising, the cable tension increases sufficiently to mechanically disconnect (break the pyrobolt) freeing the carrier plate from the ET. The length of the dropweight cable is adjusted by means of three cable clips located at the top end of the cable. The system is designed to allow approximately 1.9 cm of cable feedout prior to the secondary disconnect at approximately 18 cm of vehicle rise. The T-0 lock is contained in a protective enclosure, with hinged doors on either end and a removable cover.

BACKGROUND

The ET hydrogen vent umbilical system (Figure 5) provides the following major functions:

o Vents GH_2 from the hydrogen tank to the fixed service structure gaseous hydrogen venting system during and after LH_2 loading via a vacuumed double-walled, stainless steel vent pipe and vacuum-jacketed flex hoses.

o Provides a vent line pivot mechanism that permits the GH_2 vent line to track the Space Shuttle ET while it's connected to the ground umbilical carrier plate.

o Provides release, retract, and latchback mechanisms such that, at vehicle lift-off, the vent line assembly and the ground umbilical carrier plate are disconnected from the ET and dropped to a secured and latched-back position, clearing the vehicle lift-off path.

o Provides structural support and bulkheads for various pneumatic and electrical lines routed from the FSS* and the fixed structural platform to the ground umbilical carrier plate.

Withdrawal Mechanism. The withdrawal mechanism consists of a 680 kg withdrawal weight with wire-rope cable assemblies, guide sheaves, shock absorbers, and support structure. The withdrawal weight assembly is approximately 1.3 m high, 48 cm wide, and 15 cm deep and is a prefabricated steel shell filled with lead. The withdrawal weight is located at the back of the haunch and is mounted vertically between the 67 m level and the 63 m level (Pad B) of the fixed structural platform.

Two cable assemblies attached to the weight are routed over two guide sheaves in the rear of the haunch and are connected to the pivot arm. The suspended withdrawal weight exerts a constant 680 kg tension on the pivot arm, and subsequently on the vent line; and at T-0 when the ET umbilical carrier plate pyrotechnic separator is fired, the 680 kg tension pulls the vent line and carrier plate clear of the vehicle lift-off path as the vent line and carrier plate drop into the deceleration unit. Shock absorbers are mounted at the bottom of the withdrawal weight guide structure to absorb the energy of the dropping weight. An air-motor-driven winch is used to raise and reset the withdrawal weight.

Deceleration Unit. The deceleration unit is a mechanism used to absorb the rotational kinetic energy of the pivoting vent line and to latch it in a secured position. The unit is located under the haunch on the 58.2 m level of the fixed structural platform. The major element of the deceleration unit is a tension shock absorber with a 94 cm stroke capable of absorbing 3.457 mkg of energy.

The rod end of the vertically mounted shock absorber is attached to a guide sheave assembly through which a wire-rope cable is routed. The cable is routed to guide sheaves under the 61 m level, crossing the drop path of the vent line. The routing geometry of the cable allows the falling vent line to be decelerated and stopped approximately 2.3 m after its contact with the cable. A mechanical latching device secures the vent line in the retracted position. Should the deceleration shock absorber fail to move after the initial contact of the falling vent line into the cable assembly, a frangible link within the cable assembly will break, allowing the vent line motion to continue until latching is achieved. Tieback brackets for the vent line bridle cables are provided at the top of the

---

*Fixed service structure (FSS).

404

deceleration unit for use when the vent line is in a latched-back position. The cables are used as safety restraints during prelaunch operations.

Vent Line Assembly. The vent line assembly connects the ET ground umbilical carrier plate to the hydrogen vent system on FSS. It provides for continuous venting of the ET hydrogen tank during and after LH_2 loading and supports the pneumatic lines and umbilical interface. The vent line assembly consists of two vacuum-jacketed sections: an aft flex hose and a forward flex hose (with a double-wall vacuum hard line subassembly in between).

The aft flex hose has a 25 cm inside-diameter pipe size and is approximately 7.3 m long. This flex hose makes the connection between the hard line subassembly and the facility vent line interface. The forward flex hose has a 20 cm inside-diameter pipe size and is approximately 1.2 m long. It makes the connection between the hard line subassembly and the ground umbilical carrier plate.

The hard line subassembly is made up of a 20 cm diameter inner and a 51 cm diameter outer jacket and is approximately 7.6 m long. The aft end of the vent line is supported by the pivot arm located in the haunch. The pivot arm and withdrawal mechanism allow the line to be retracted approximately 60 cm away from the vehicle and rotated downward approximately 90^0 to the retracted position. The flex hose support mandrel is attached to the hard line near the pivot. This mandrel prevents the aft flex hose from exceeeding the minimum bend-radius limit during vertical rotation of the vent line.

The forward flex hose support bracket is located near the outboard end of the hard line. This support limits the movement of the forward flex hose during rotation of the hard line after umbilical disconnect. The support has a saddle attached to its lower edge to engage the arresting cable of the deceleration unit.

A gimbal fitting mounted at the outboard end of the hard line provides lugs for attachment of the bridle cables and line-handling cables. The bridle cables transfer the weight of the vent line assembly to the vehicle via the gound umbilical carrier plate. This prevents tension loads from being applied to the forward flex hose. The gimbal provides equalization of tension in the bridle cables, regardless of vehicle movement or misalignment.

Bridle Support. The bridle support provides a tension link between the ground umbilical carrier plate and the forward end of the vent line assembly hard line and alleviates tension loading of the forward flex hose. Wire cable assemblies attach to both sides of the ground umbilical carrier plate and to the gimballed fitting at the forward end of the vent line assembly hard line. The gimballed fitting allows for vehicle motion during wind and loading conditions.

Flex Hose Support. The flex hose support restrains the ground umbilical carrier plate end of the vent line assembly from recoiling at T-0 release. A saddle on the lower side of the flex hose support engages with the deceleration unit arresting cable, and a tab engages with the deceleration unit ratchet pawls that secure the vent line in a latched position.

Umbilical Carrier Plate Assembly and GUCP Pyrotechnic Separator. The umbilical carrier plate assembly and GUCP pyrotechnic separator form the interface connection between the Shuttle ET and the hydrogen vent umbilical system (see Figure 5). The carrier plate has two feet at the bottom that rest on pins on the ET. The GUCP pyrotechnic separator near the top center completes the attachment of the carrier plate to the ET. THE GUCP pyrotechnic separator is initiated at T-0 and is the primary disconnector. In the event the GUCP pyrotechnic separator fails to initiate, the secondary release lanyard (attached to two tabs near the top of the carrier plate) is the secondary disconnector. At disconnect, the vent line assembly pulls the carrier plate away from the ET, the feet at the bottom roll on the pins of the ET until unlock rotation is achieved, and the carrier plate completes its separation from the ET. The hydrogen vent umbilical side of the carrier plate has hard connections with the pneumatic lines and the electrical cables that are routed on the top of the vent line to the FSS facility interfaces. The ET side of the carrier plate has quick-disconnect fittings that interface with various systems of the ET.

CONCLUSION

An improved secondary release system has been successfully designed, developed, qualified and introduced for the ET (GH$_2$) Vent system for the Space Shuttle Vehicle Ground Support. In the unlikely event of a primary disconnect system failure, it provides secondary disconnects with assurance of adequate vehicle clearance.

ACKNOWLEDGMENT

ETV T-0 LOCK

REDUNDANT YOKES
(SPRING LOADED)

PIC CABLES

DROP WEIGHT

PYRO RELEASE BOLT

SECONDARY
ARM RETENTION
(RATCHET LOCK)

GUIDE TUBE

SERRATED TUBE

DROPWEIGHT

T-0 LOCK DETAIL

FIGURE 1: NEW T-0 LOCK

HAUNCH PIVOT
FIXTURE

VACUUM
JACKETED
VENT LINE
ASSY

FORWARD
FLEX HOSE

T-0 LOCK

MSFC
PYRO
BOLT

WITHDRAWAL
DROPWEIGHT

SECONDARY
RELEASE
DROPWEIGHT

TRUNNION

ET INTERFACE

SECONDARY
ARM RETENTION

VENT LINE
DROP PATH

DECELERATION
UNIT

SECONDARY
RELEASE
LANYARD

CARRIER
PLATE
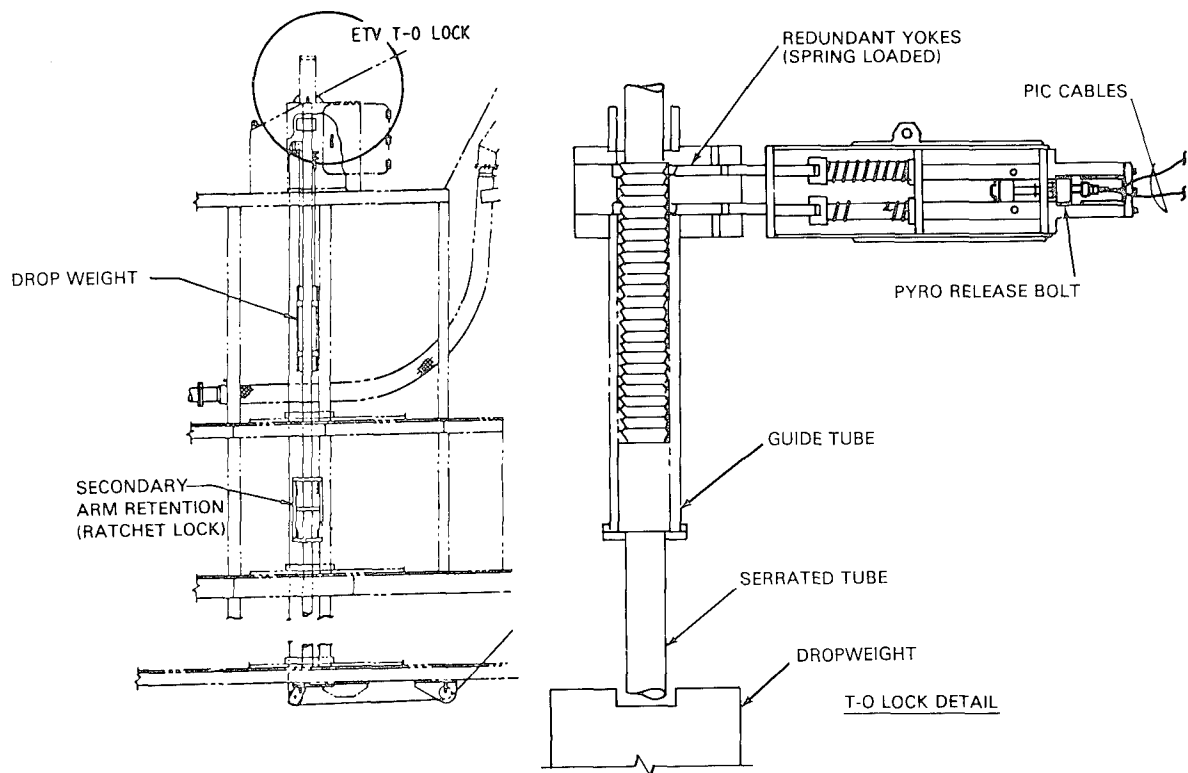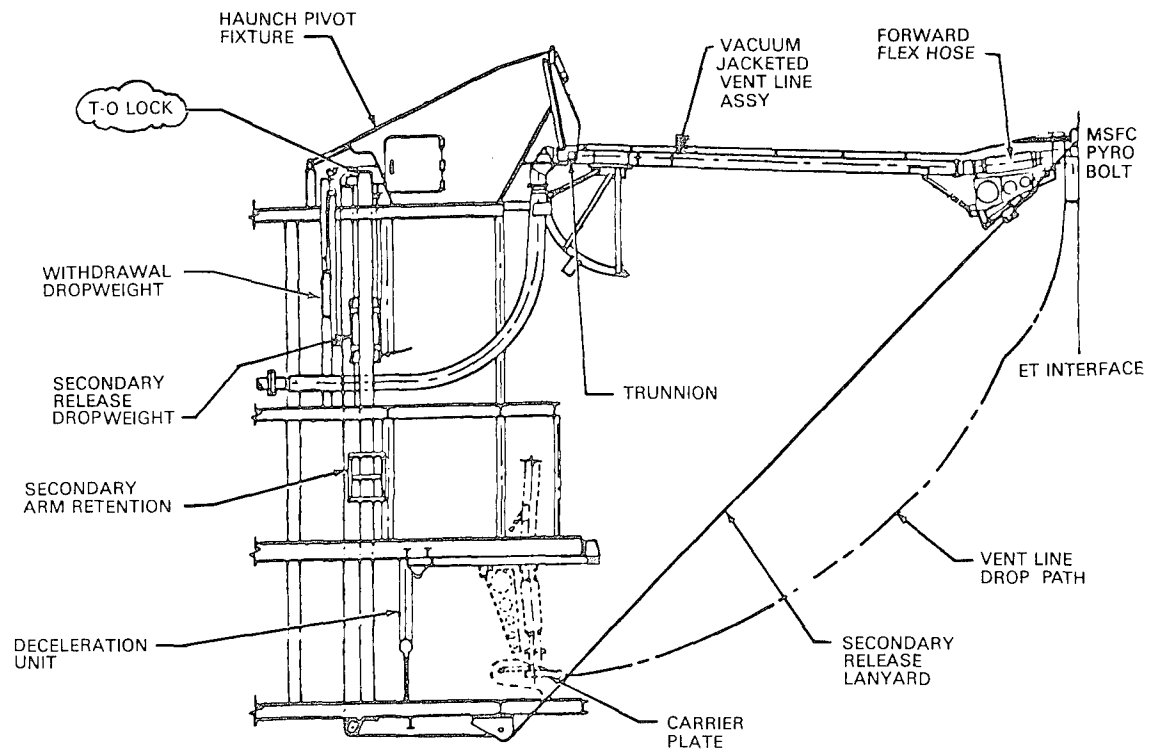
FIGURE 2: ET HYDROGEN VENT UMBILICAL SYSTEM

-X

-Y   -Z   NORTH

+Z   +Y

+X

ET GH2 VENT
SYSTEM
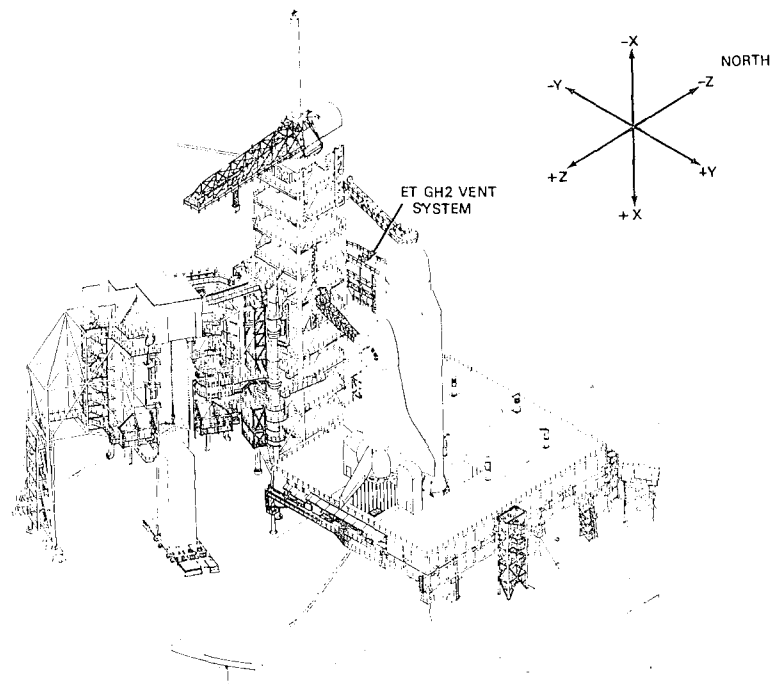
FIGURE 3: SPACE SHUTTLE VEHICLE LAUNCH PAD

TIME: T+1.62 SEC

N

38 cm
MINIMUM
CLEARANCE

12 cm

1.5 m

41 cm

NOMINAL
POSITION

• STATIC LANYARD DISCONNECT W/T-Ø LOCK
• 3σ WORST CASE DRIFT
• WORST CASE T-Ø
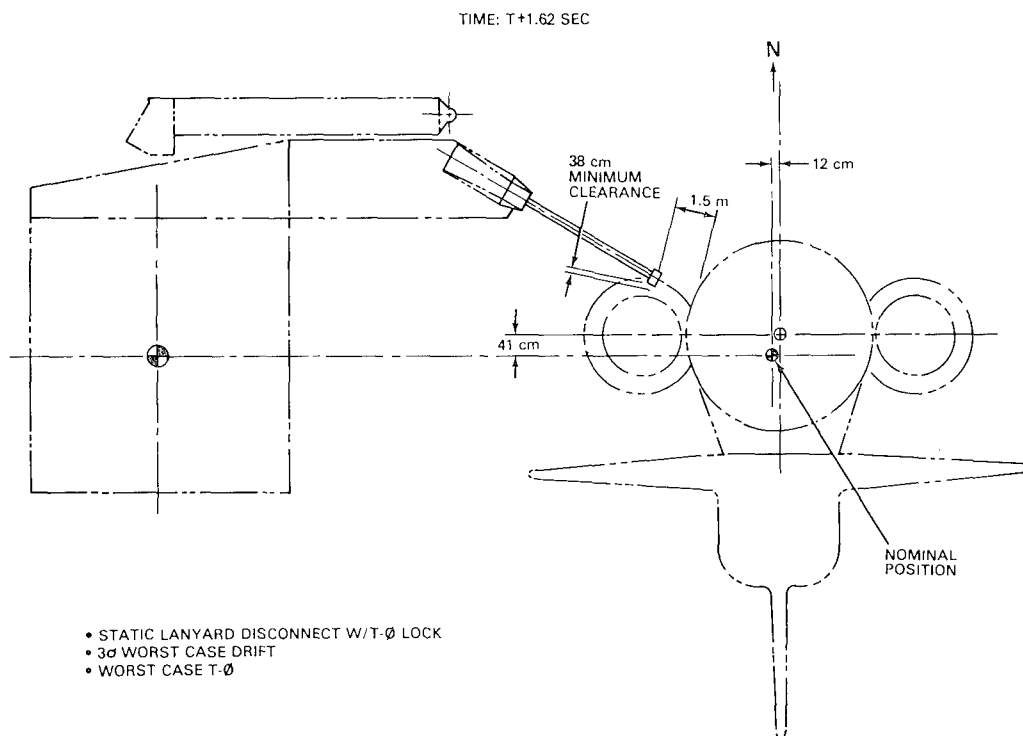
FIGURE 4: LIFTOFF - RETRACT CLEARANCE STUDY

409
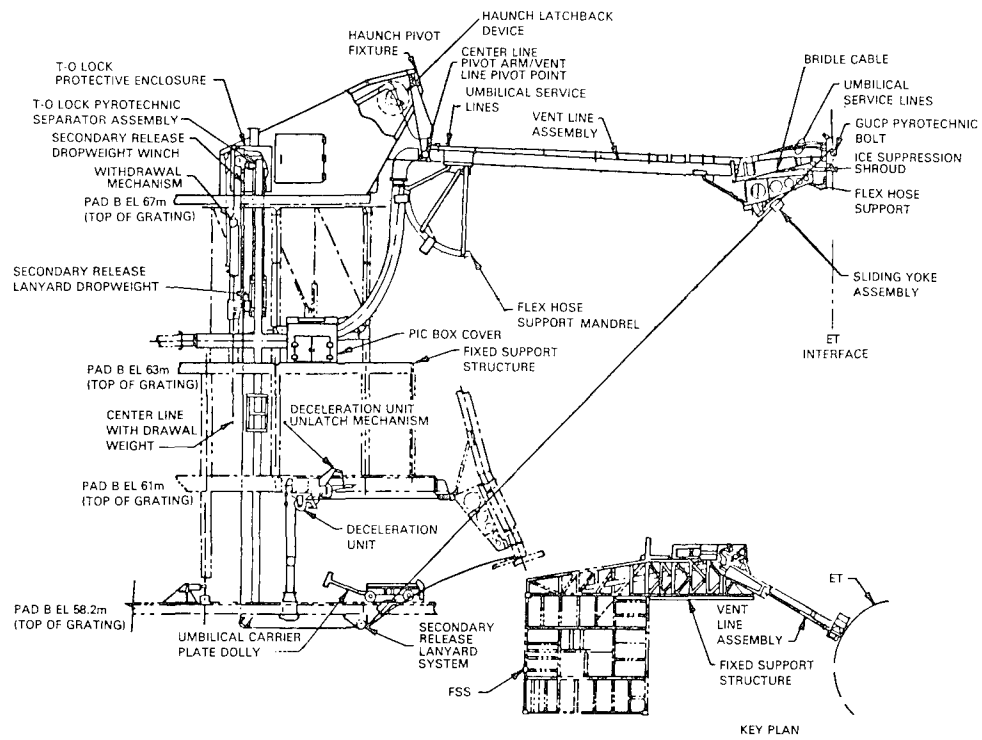
FIGURE 5: ET HYDROGEN VENT SYSTEM

410

APPENDIX

PANEL DISCUSSION SUMMARIES
21st AEROSPACE MECHANISMS SYMPOSIUM
APRIL 29 TO MAY 1, 1987
NASA - JOHNSON SPACE CENTER

Following the lively and successful panel discussion session held at the 20th Aerospace Mechanisms Symposium, the organizing committee selected two general themes for discussion at the 21st AMS, "Robotics for Space" and "Large Space Structures." A panel of three invited experts led the discussion during each of the two sessions by first presenting material on their view of the problem. Following each panelist's comments, the other panelists and audience attendees were given the opportunity to respond, ask questions and generally get involved.

Both discussion sessions were skillfully organized and moderated by Stuart Loewenthal, currently Senior Staff Engineer, Mechanisms, Servos and Robotics Department of LMSC, with 15 prior years of research and development in mechanical systems with NASA - LeRC.

The following summary records the highlights of the comments, questions and discussions brought out during the two panel sessions.

As reported by: Daniel P. Kuban, Section Head, Equipment Engineering
                                Martin Marietta Energy Systems
                                Oak Ridge National Laboratory

                  Douglas A. Rohn, Research Engineer, Structural Dynamics Branch
                                NASA Lewis Research Center

Stu Loewenthal opened the panel discussion by encouraging the audience to get
involved and to consider the panel as facilitators. He commented that there is a
lot of "hype" concerning "robotics." It is a common buzz word, called the "wave
of the future," but is it really anything new? We've actually been doing this for
many years. He cited the Surveyor and Viking exploratory probes as an example of
"robotic" devices to substantiate his claim. He then introduced the panel:
Professor Susan Hackwood, Director of the Center for Robotics in Micro-
electronics and Professor of Electrical and Computer Engineering at the
University of California - Santa Barbara, author of over 50 technical papers;
Mr. Geoffry Marks, Director of Engineering at Astro Aerospace Corporation,
responsible for mechanical systems on the RMS with a broad background in
actuators and deployable structures; and Dr. Byron Purves, Space Station
Automation and Robotics Manager at Boeing Aerospace Company, with a strong
background in robotic control systems, author of over 30 technical papers.

Mr. Geoffry Marks began the first area which concerned the safety of the EVA
astronaut while working with robots. He stated that on earth we rope off
robots from people, but in space we plan to let astronauts work in close
proximity to robots. He felt that EVA would be essential for Space Station
assembly and maintenance, but that since EVA was such a scarce commodity, a
crew member would have to work in conjunction with robots. The result is that
he is vulnerable! Marks then described four possibilities for how man and
robots could work together in space:

   1. Man controls the machine and machine does the work (classical
       teleoperations).

   2. Man works directly with machine on same task (very dangerous).

   3. Man does dexterous activities while machine serves him (hand
       parts).

   4. Man mounted on end of machine (presently RMS), i.e., man is
       essentially a dexterous end effector (EE).

He concluded by predicting that some day man would be safely in the Shuttle or
Station, and that's where he should be, but that it's too far away to affect the
Space Station (SS) unless the entire Station is designed from day one to be
completely assembled by robots.

Comments from the floor then centered more on design of the Space Station than
on astronaut safety. Should the SS be built for both man and robots? Why?
Some felt this would incur a large cost penalty. Others questioned what the

412

differences would really be, since an EVA astronaut's dexterity is reduced quite significantly due to his suit and gloves. Panelist Purves stated that the design of equipment was the most important factor for increasing the robots effectiveness. Many agreed with his thesis. Purves reinforced this point by stating that the present designs of spacecraft are barely maintainable by humans, let alone by robots.

Marks was then questioned as to why one would even consider putting man close to a robot when we NEVER do it on earth. The problem is the fragile suit -- if you make it safe as armor, then he can't move. Why do we want them together? Purves further stated that there's a "Frankenstein complex," that people have trouble accepting robots at all. This motivated the audience to consider the issue of why use a robot at all? Present state of the art is 10-20 years of spacecraft life, then why do we need to service? Just design the spacecraft for life, and accept the risk of failure. If it does fail, then take the risk. It's better to put more money into higher reliability than serviceability. Do a better job in the first place. We have a man up there -- let's use him! He has done well on satellite retrieval, on the end of RMS - why push him out? The audience answered its own question by saying that robots will eventually be more productive, efficient and cost effective -- the usual driver. Purves suggested that an easier way to implement robotics would be to start by redesigning specific components such as latches, bolts, etc., to accommodate robotic operation. It was then brought to the panel's attention that the Solar Max mission was repeated successfully on earth using the CRL teleoperator, proving that robots can accomplish EVA tasks, but that the issue of productivity still remains open.

The issue of growing complexity was then raised. As robots become more sophisticated (e.g., human-like) they also become less reliable. Software alone is expected to be immense. How can we believe robots will be safe? Hackwood replied that the complexity will develop gradually and that safety features must evolve with the technology. Marks stated that we're caught in an overlapping of technology -- the man is still here but the robots are coming into the picture. Far down the road the robot will do it all -- but until then -- we're caught in this transition and developing adequate safety rules will be just as challenging as the robot development.

Dr. Byron Purves then began the 2nd topic of "designing spacecraft for robotics." He started by showing an illustration from the National Commission on Space, which looked 50 years into the future of space programs. The report talked about robots playing a role, but all the illustrations showed only astronauts. He pointed out that this clearly reflects the dominate philosophy in NASA that "space" means "astronauts." He stated strongly that this must be turned around for robots to be effective. At present, he continued, equipment is not robot friendly. There is no benefit in using robots, since nobody wants to pay for the equipment to be designed for robots. The only way to get out of this viscous circle is for NASA to push equipment designers to change. Three ways out were then presented.

1. Keep equipment as is and provide a human-like robot. This is the worst choice since it's too far away. It is just a dream at this point.

2. Match equipment and robot -- this is acceptable only for special cases.

3. Design equipment to be robot friendly. This is the most important and productive. For this to be effective both robot designers and equipment designers must cooperate, interactively.

Purves then went on to list key areas requiring attention by both robot and spacecraft designers. Of utmost importance, he felt, was the need to keep accurate "as-built" equipment documentation.

Marks responded by repeating a key thesis from the first topic, that the spacecraft must be designed initially for robotic service. Loewenthal then turned to the audience and asked what impact this would have on the spacecraft. A very interactive and philosophical interaction developed on standard designs for spacecraft. Why don't we standardize? Why should we? Or even more to the point, can we? Loewenthal observed that we mechanism designers were at the bottom of the list in designing standard parts -- making every job a custom design/fab. The audience countered with the age-old "golden rule": He who has the gold makes the rules! Customers always change specs and, therefore, standard parts can't be achieved. Additionally, technology is always changing (hopefully improving) and, therefore, it's to our detriment to have standards. Hackwood offered that a solution would be to standardize interfaces, but this was also met with objections. It was then suggested that rather than standardizing the design, we would standardize the design process. It would be adequate to recognize that robots will be there and account for them early in the design. It was generally agreed upon that some level of standardization was good but it is uncertain where the line should be drawn. Opinions of the appropriate level of standardization ranged from standardizing simple nuts and bolts and grip points, all the way to (as Marks puts it) "If you make it cost effective to throw away a satellite, then what you've done is defined a satellite to be an ORU."

Prof. Susan Hackwood opened the final area of discussion which was industrial versus space robotics. She described ongoing robotics work in manufacturing of semiconductor products. She stressed that the area of greatest neglect in industrial robotics is mechanical design, and that mechanisms need much more attention. Robotics are being developed for semiconductor manufacture to operate in a vacuum and in very clean conditions. Hackwood showed a configuration of one large robot serving several small assembly robots. The work demonstrated that robots can operate reliably in a space environment, but that many areas still need to be addressed: materials, motors, lubrication, particle generation, and non-contacting mechanisms. Also the need for autonomous operation with even some self-repair was mentioned.

Loewenthal, after astutely observing the similarity to space manipulation, challenged the audience to take advantage of these developments. The audience felt that the manufacturing application was stricter even than space in two areas: cleanliness and precision. Hackwood then reminded us that NASA plans to "manufacture" in space and that we would inherit these requirements as well. This reinforced a recurring theme that NASA must push now for the entire SS to be designed for robotic operation and maintenance if robots are

to be effective. A NASA representative countered that this was a noble goal, but asked "which robot do we push"? Without a specific arm with reaches, envelope, capacity, etc., you can't design properly. That's why they've been pushing for maximum capability in the robot. Try to get it as close as possible to EVA. We know astronauts will be there. If a robot can approach EVA equivalence then the transition will be most successful.

The discussion concluded with some wise insights. One audience member felt that robots were just a subsystem, one of many subsystems that will comprise a successful Space Station. They cannot get special treatment, because from a practical standpoint, all subsystems end up compromising for the good of the whole. Robotics designers should not expect all other subsystems to bow before them as they optimize their design. Rather all subsystem designers must interact and together develop the best overall system.

"LARGE SPACE STRUCTURES"
21st AMS, APRIL 30, 1987

As reported by: Barry S. Leonard, Director of Spacecraft Engineering
                                Lockheed Missiles and Space Company

                  Douglas A. Rohn, Research Engineer, Structural Dynamics Branch
                                NASA Lewis Research Center

Stu Loewenthal began the second panel discussion by thanking the audience for
their strong participation in the previous day's robotics panel and noting
that this discussion topic should be just as stimulating. He posed the
question: Why should we be talking about large space structures? One
immediate answer is that the Space Station will be a whole new territory for
structures, bringing new problems which will drive mechanism designers.
Loewenthal pointed out that the Space Station will not be assembled on the
ground and thus will be a test laboratory itself. It will present a number of
system design problems, not the least of which is the fact that microgravity
experiments onboard cannot tolerate large vibratory excursions. Loewenthal
went on to highlight the subtopics each panel member would discuss. He then
introduced the panel: Mr. Don McCutchen, Technical Area Integration Manager
for Structures on Space Station at NASA Johnson Space Center, with extensive
background in structures and NASA programs including Apollo, Skylab and the Space
Shuttle; Mr. John Coyner, former Manager of Large Space Systems at Martin
Marietta Denver Aerospace Company, with numerous technical publications and 17
years experience in deployable structures; and Mr. Robert Crawford, Senior
Staff member at General Research Corporation, with 34 years of experience,
articles and patents in the design, analysis, and development of deployable
structures.

Mr. Don McCutchen began the first area of "deployable versus erectable" by
observing that the Space Station is an excellent example of a large space
structure, being 350 ft. by 450 ft. with a mass between 250,000 lbs. and
500,000 lbs. He made the point that it is not a vehicle, but a facility,
designed for long life, growth, modification and maintenance. As opposed to
other space missions, the Station will never be assembled on the ground nor
see launch loads, but be put in orbit as a box of "tinker-toys," then put
together. McCutchen observed parallels to large building construction,
specifically noting that as the pieces are assembled on a building site, men
are aided by machines - thereby providing a tie-in to the previous panel
discussion on robots in space.

In defining the difference between deployable and erectable structures, he
showed an example of the latter being assembled by an astronaut in a neutral
buoyancy tank. This procedure is heavily mechanized with component dispensers
and motorized work platforms, so that the man and the machines each do what
they do best. McCutchen went on to discuss the requirements for space
structures and how they relate to deployable and erectable designs, listing
light weight, high stiffness, predictable performance, low cost, thermal

stability, repairable, simple external interfaces, safety for the crew, and high strength. Deployables have been widely used, but McCutchen directed the audience to consider what trade studies are needed in order to accomplish the listed requirements in the future. For example, effective strut stiffness must include joint efficiency, and number and type of joints. McCutchen showed how pin joints are affected by freeplay; interference removes slop, but the joint is still left with hysteresis. Further, interference-type joints are difficult to use with deployable structures.

Comments from the audience related to the complexity of the task of erecting or deploying space structures. It was noted that installation of utilities onto a structure makes the whole a system. Mr. Coyner added that while looking at a large antenna with precision surfaces, it was found that a combination of the creative deployable and erectable concepts made the best use of resources available to assemble the antenna. Loewenthal raised the question of erectable versus deployable assembly time, considering EVA limitations. McCutchen responded with the observation that, for the Space Station, construction of the truss structure is planned to be only 8% of the total station construction EVA time. Attaching modules and stringing utilities are what really require time. A question was raised as to whether we should even consider erectable technology unmanned structures, which are usually deployable. Mr. Crawford responded that SDI is looking at numerous platforms, which would require a huge EVA workload, and suggested that perhaps robot assembly will be required.

Next, Mr. John Coyner discussed the area of flexible versus stiff structures including joint freeplay, damping, and control issues. He reviewed the mission requirements for several large antenna systems, with emphasis on the effort and high costs involved with very stiff structures and the resultant need for close cooperation between structural and controls disciplines. For one application, he highlighted structural configuration trades between four geometries (tetrahedral truss, hoop columnar, radial rib and box truss) considering cost, reliability, and basic attributes such as mass, stiffness, deployment ease, dynamic performance, etc.

Coyner also reviewed the results of two dynamic performance studies. The first was the effect of joint freeplay in a 20 m truss. Relative to zero freeplay, 1 mil freeplay decreased frequency, increased damping and showed non-linear response at lower inputs while still responding linearly at higher inputs. Further, 3 mil freeplay produced high damping and extreme non-linear response. The other study concerned the effects of damping. The results showed that while higher damping may cost in weight, it can have a payoff in reduced maneuver time or simpler controls.

Loewenthal addressed the panel with the question: how stiff is stiff enough? The panel agreed that there is a trade-off in reliability, cost, and weight. Coyner noted that for large space structures it is difficult to be too stiff. McCutchen observed that early in the design phase, we tend to use simple structural models and control engineers see them as fairly simple control

problems. However, as the design matures, the model gets structurally complicated. The panel recommended using complex models up front, and involving controls and structures people early, especially since damping is difficult to characterize.

A member of the audience suggested one possible advantage of low stiffness: to attenuate disturbance input sources. McCutchen agreed that local compliance is helpful. Another comment related to the COFFS-III work at NASA-LaRC pointed out the difficulty associated with working on scale models, particularly scaleability and joint linearity.

The third discussion area, design, development and operation of deployable large structures, was led by Mr. Robert Crawford. He discussed the proliferation of future spacecraft and their attendant deployable structures, such as large aperture antennas, dipole antennas, solar cell arrays, gravity-gradient stabilizer booms, extendable booms for experiments or nuclear power cells, tethered satellites, habitats, and manipulator/robot components. He perceptively argued that for these structural systems and the missions they support to be successful, the space community needs inspired, bright people to contribute innovative, deployable mechanisms ideas. Mr. Crawford went on to discuss the state of the art of several deployable structure concepts. He cited tubular booms, which are well developed and have flown on many missions including use as the Viking digger arm. Articulated lattice and coiling/folding booms have been used as magnetometer booms on Voyager, Galileo and others, as well as in concepts such as for the LOFT (low-frequency radio telescope) 1 mile diameter dish. He commented that methods to test these large, thin, light concepts in 1-G have not been adequately developed yet. Other deployable folding trusses and membrane mirrors were mentioned as only partially developed at this time.

Crawford concluded his talk by urging the audience, companies, and the Government to actively promote the development of deployable mechanisms. He noted that past advances have typically come from small, highly motivated groups. He suggested several means of motivation for further discussion, including: professional recognition, monetary incentives from corporate profits resulting from use of mechanisms, and user (e.g.: government) encouragement. The latter encouragement could consist of wider dissemination of specifications, more contracts for concept development, more generous patent rights sharing with inventors, less "not-invented-here" attitudes regarding user's competing concepts, and strict observation of proposal proprietary rights. These comments were heartily agreed to by the audience.

Loewenthal observed that the cumulative experience of the panel and the audience represents a "corporate resource" that needs to be transferred to younger members of our staffs. Many audience comments centered on the difficulty and urgency of this transfer. An AIAA committee study was mentioned, as well as several specific ways of getting experts and case studies into the engineering colleges. It was noted that while engineering

societies do a good job, their journals tend to emphasize mathematical treatments and thus, it is difficult for mechanism developers like ourselves to get our work published outside of the symposium. Dr. Coale mentioned that the AMS Organizing Committee has been considering the possibility of soliciting student papers for our symposium.

The panel session was concluded with brief but strong audience remarks in the area of government relations and proprietary rights. Industry is concerned about discussing new developments and possibly losing out on their R&D investment. A more critical observation was that the current trend in some government contracts requires companies to give up their proprietary rights. Considering the needs discussed earlier for advanced structural concepts, robotics, and general mechanism innovations, all agreed that the symposium attendees, as an industry/university/NASA technical community, should use whatever influence we have to maintain strong, innovative R&D in the aerospace mechanism industry.

CONCLUDING REMARKS

Once again, the symposium's goal to provide an open forum for designers, developers, and users of aerospace mechanisms was reinforced by thoughtful comments during the two panel sessions. The use of robots in space and the development of large space structures will certainly bring new and exciting challenges. In addition to the technical problems and solutions, the discussions highlighted the need for our continued diligence both in the education of future mechanism engineers as well as in the political arena.

Report Documentation Page

1. Report No. NASA CP-2506	2. Government Accession No.	3. Recipient's Catalog No.

4. Title and Subtitle	5. Report Date
22nd Aerospace Mechanisms Symposium	May 1988
	6. Performing Organization Code

7. Author(s)	8. Performing Organization Report No. L-16433
	10. Work Unit No.

9. Performing Organization Name and Address	11. Contract or Grant No.
NASA Langley Research Center Hampton, VA 23665-5225	
	13. Type of Report and Period Covered

12. Sponsoring Agency Name and Address	14. Sponsoring Agency Code
National Aeronautics and Space Administration Washington, D.C. 20546; California Institute of Technology, Pasadena, CA 91109; and Lockheed Missiles and Space Company, Inc., Sunnyvale, CA 94088	Conference Publication

15. Supplementary Notes

16. Abstract

The proceedings of the 22nd Aerospace Mechanisms Symposium, which was held at the NASA Langley Research Center, Hampton, Virginia, on May 4 to 6, 1988, are reported. Technological areas covered include space lubrication, bearings, aerodynamic devices, spacecraft latches, deployment, positioning, and pointing. Devices for Space Station docking and manipulator and teleoperator mechanisms are also described.

17. Key Words (Suggested by Author(s))	18. Distribution Statement
Docking devices Teleoperation Drive mechanisms Stress corrosion Actuators Thermal actuators Space lubricants Deployment devices Vibration isolation Magnetic Suspension	Unclassified - Unlimited Subject Category 39

19. Security Classif. (of this report)	20. Security Classif. (of this page)	21. No. of pages	22. Price
Unclassified	Unclassified	426	A19